Dario Compagnone
Francesco Baldini
Corrado Di Natale
Giovanni Betta
Pietro Siciliano
Editors

Sensors

Proceedings of the Second National
Conference on Sensors, Rome 19–21
February, 2014

Springer

Lecture Notes in Electrical Engineering

Volume 319

About this Series

"Lecture Notes in Electrical Engineering (LNEE)" is a book series which reports the latest research and developments in Electrical Engineering, namely:

- Communication, Networks, and Information Theory
- Computer Engineering
- Signal, Image, Speech and Information Processing
- Circuits and Systems
- Bioengineering

LNEE publishes authored monographs and contributed volumes which present cutting edge research information as well as new perspectives on classical fields, while maintaining Springer's high standards of academic excellence. Also considered for publication are lecture materials, proceedings, and other related materials of exceptionally high quality and interest. The subject matter should be original and timely, reporting the latest research and developments in all areas of electrical engineering.

The audience for the books in LNEE consists of advanced level students, researchers, and industry professionals working at the forefront of their fields. Much like Springer's other Lecture Notes series, LNEE will be distributed through Springer's print and electronic publishing channels.

More information about this series at http://www.springer.com/series/7818

Dario Compagnone • Francesco Baldini
Corrado Di Natale • Giovanni Betta
Pietro Siciliano
Editors

Sensors

Proceedings of the Second National
Conference on Sensors, Rome
19–21 February, 2014

Springer

Editors

Dario Compagnone
Faculty of Bioscience and Technologies for
Food Agriculture and Environment
University of Teramo
Mosciano S.A.
Teramo
Italy

Francesco Baldini
Institute of Applied Physics IFAC-CNR
Firenze
Italy

Corrado Di Natale
Dept. of Electronic Engineering
University of Rome Tor Vergata
Rome
Italy

Giovanni Betta
University of Cassino
Cassino
Italy

Pietro Siciliano
CNR, Head of Inst. of Microelectronics a
Lecce
Italy

Printed on acid-free paper

Preface

This book contains scientific contributions presented at the II National Conference on Sensors held in Rome in 19-21 February 2014. The conference has been organized by a partnership of the major Scientific Societies and Associations involved in the research area of sensors, the Italian Society of Chemistry (SCI), the Italian Association of Electric and Electronic Measures (GMEE), the Italian Association of Ambient Assisted Living (AITAAL), the Italian Society of Optics and Photonics (SIOF), the Italian Association of Sensors and Microsystems (AISEM) and was also under the patronage of the Italian Society of Pure and Applied Biophysics and the Italian Association of Photobiology.

The second edition of the Conference has confirmed a large participation with 59 oral presentations, 84 poster presentations and over 150 delegates. The driving idea of the First Conference, to gather scientists having different competences and with different cultural backgrounds, dealing with all the different aspects of sensors, has been demonstrated to be indeed successful again.

In this view, this book represent an invaluable and updated tool, to have an overall view on recent findings, strategies and possible new directions of the sensor research area in Italy. Different aspects of the research based on the development of new chemical, physical or biological sensors, assembling and characterization, signal treatment and data handling is reported. Electrochemical, optical and other detection strategies are applied to relevant issues in food, clinical environmental areas as well as industry oriented applications in the selection of papers reported.

The editors wish to acknowledge the Department of Chemistry of the University La Sapienza in Rome and the Head of Department Prof. Aldo Laganà for the warm hospitality, Drs. Antonella Taiani, Manuel Sergi, Chiara Cavaliere, Silvia Orlanducci and Prof. Franco Mazzei for the excellent work in the organization of the event.

Contents

Part IV   Physical Sensors

Contributors

Francesco Abate Department of Industrial Engineering, University of Salerno, Salerno, Italy

l. Abbamonte UTTP-MDB Department, ENEA, Italian Agency for New Technologies Energy and Sustainable Economic Development, C.R. Portici, Portici, NA, Italy

D. Accoto Laboratory of Biomedical Robotics and Biomicrosystems, CIR-Center for Integrated Research, University Campus Bio-Medico di Roma, Rome, Italy

Tommaso Addabbo Department of Information Engineering and Mathematics, University of Siena, Siena, Italy

Lorella Addari ENEA, UTAPRAD-DIM, Frascati, Italy

Annalisa Agresta UTTP/Basic Material and Devices Dept., ENEA Portici Research Centre, Portici, NA, Italy

UTTP/Basic Materials and Devices Department, ENEA RC Portici, Portici, NA, Italy

A. Alberti CNR-IMM Sezione di Catania, Catania, Italy

Roberto Alesii DEWS Center of Excellence, University of L'Aquila, L'Aquila, Italy

D. Alghisi Department of Information Engineering, University of Brescia, Brescia, Italy

Salvatore Almaviva ENEA, UTAPRAD-DIM, Frascati, Italy

D. Aloisio DIECII, University of Messina, Messina, Italy

Bruno Andò Dipartimento di Ingegneria Elettrica Elettronica e Informatica (DIEEI), University of Catania, Catania, Italy

Bruno Ando' Dipartimento di Ingegneria Elettrica Elettronica e Informatica (DIEEI), University of Catania, Catania, Italy

Riccardo Angeloni Department of Chemistry,"Sapienza", University of Rome, 00185 Rome, Italy

R. Anzalone CNR-IMM Sezione di Catania, Catania, Italy

Fabiana Arduini Dipartimento di Scienze e Tecnologie Chimiche, Università di Tor Vergata, Roma, Italy

F. Armani Department of Engineering and Architecture, APL laboratory, Trieste University, Trieste, Italy

Giuseppe Arrabito Department of Physics and Chemistry, University of Palermo, Palermo, Italy

M. Baù Dept. Information Engineering, University of Brescia, Brescia, Italy

Salvatore Baglio Dipartimento di Ingegneria Elettrica Elettronica e Informatica (DIEEI), University of Catania, Catania, Italy

F. Baldini IFAC-CNR, "Nello Carrara" Institute of Applied Physics, Sesto Fiorentino, FI, Italy

S. Baldo CNR-IMM Sezione di Catania, Catania, Italy

A. Ballo Dipartimento di Ingegneria Elettrica, Elettronica e Informatica Facolta' di Ingegneria, Universita' degli Studi di Catania, Catania, Italy

F. Barberis T&D Technologies Department, RSE-Ricerca sul Sistema Energetico, Milano, Italy

Giuseppe Barillaro Dipartimento di Ingegneria dell'Informazione, Università di Pisa, Pisa, Italy

Ruben Bartali Center for Materials and Microsystems, Fondazione Bruno Kessler, Trento, Italy

A. Barucci IFAC-CNR, "Nello Carrara" Institute of Applied Physics, Sesto Fiorentino, FI, Italy

A. Baschirotto Department of Physics, University of Milano-Bicocca, Milano, Italy

Mattia Bassi Materials Science Department, Solvay Specialty Polymers Research and Development Center, Bollate, MI, Italy

Tommaso Bellini Dipartimento di Biotecnologie Mediche e Medicina Traslazionale, Università degli Studi di Milano, Segrate, MI, Italy

Luca Belsito Istituto per la Microelettronica e i Microsistemi(IMM), CNR, Bologna, Italy

Natascia Bernacchia Dipartimento di Ingegneria e Scienze Matematiche, Università Politecnica delle Marche, Ancona, Italy

S. Berneschi IFAC-CNR, "Nello Carrara" Institute of Applied Physics, Sesto Fiorentino, FI, Italy

R. Bernini IREA-CNR, Institute for Electromagnetic Sensing of the Environment, Napoli, Italy

C. Berrettoni Information Engineering and Mathematics Department, University of Siena, Siena, Italy

IFAC-CNR, "Nello Carrara" Institute of Applied Physics, Sesto Fiorentino, Italy

Francesco Bertocci Department of Information Engineering and Mathematics, University of Siena, Siena, Italy

G. Betta Dipartimento di Ingegneria Elettrica e dell'Informazione, Università di Cassino e del Lazio MeridionaleVia G, Cassino, FR, Italy

F. Bettazzi Dipartimento di Chimica, Università degli Studi di Firenze, Sesto Fiorentino, Firenze, Italy

Paolo Bettotti Dipartimento di Fisica, Università di Trento, Povo, TN, Italy

Elena Biagi Dipartimento di Ingegneria dell'Informazione(DINFO), Università degli Studi di Firenze, Firenze, Italy

M. Bona Dipartimento di Ingegneria dell'Informazione, Università degli Studi di Brescia, Brescia, Italy

A. Boscolo Department of Engineering and Architecture, APL laboratory, Trieste University, Trieste, Italy

V. Bravatà Istituto di Bioimmagini e Fisiologia Molecolare (IBFM-CNR)—LATO, Cefalù PA Sicilia, Italy

M. Bressanutti Department of Engineering and Architecture, APL laboratory, Trieste University, Trieste, Italy

P. Bruschi Dipartimento di Ingegneria dell'Informazione, Università di Pisa, Pisa, Italy

Antonio Buonanno UTTP/Basic Material and Devices Dept., ENEA Portici Research Centre, Portici, NA, Italy

Marco Buscaglia Dipartimento di Biotecnologie Mediche e Medicina Traslazionale, Università degli Studi di Milano, Segrate, MI, Italy

F. Butti Dipartimento di Ingegneria dell'Informazione, Università di Pisa, Pisa, Italy

Franco Cacialli Department of Physics and Astronomy and London Centre for Nanotechnology, University College London, London, UK

Massimo Camarda CNR-IMM Sezione di Catania, Catania, Italy

F. P. Cammarata Istituto di Bioimmagini e Fisiologia Molecolare (IBFM-CNR)—LATO, Cefalù PA Sicilia, Italy

Luigi Campanella Department of Chemistry, "Sapienza" University of Rome, Rome, Italy

I. Capezzuto UTTP-MDB Department, ENEA, Italian Agency for New Technologies Energy and Sustainable Economic Development, C.R. Portici, Portici, NA, Italy

D. Capriglione Dipartimento di Ingegneria Elettrica e dell'Informazione, Università di Cassino e del Lazio MeridionaleVia G, Cassino, FR, Italy

D. Caputo Department of Information Engineering, Electronics and Telecommunications, "Sapienza" University of Rome, Rome, Italy

Estefanía Núñez Carmona Department of Life Sciences, University of Modena and Reggio Emilia, Reggio Emilia, Italy

CNR-IBF, Palermo, Italy

Andrea Caroppo CNR-IMM, Via Monteroni presso Campus Universitario, Lecce, Italy

Deborah Casinelli DIEI, Università di Cassino e del Lazio Meridionale, Cassino, Italy

Mauro Castrucci Department of Chemistry,"Sapienza", University of Rome, 00185 Rome, Italy

Erica Ceccarello Dipartimento di Biotecnologie Mediche e Medicina Traslazionale, Università degli Studi di Milano, Segrate, MI, Italy

Diego Centonze Dipartimento di Scienze Agrarie, degli Alimenti e dell'Ambiente, Università degli Studi di Foggia, Foggia, Italy

Roberto Cerbino Dipartimento di Biotecnologie Mediche e Medicina Traslazionale, Università degli Studi di Milano, Segrate, MI, Italy

Mattia Cettolin Department of Molecular Sciences and Nanosystems, University Ca' Foscari of Venice, Venice, Italy

Marcella Chiari Istituto di Chimica del Riconoscimento Molecolare—CNR, Milano, Italy

F. Chiavaioli Institute of Applied Physics "Nello Carrara", National Research Council, CNR-IFAC, Sesto Fiorentino, FI, Italy

Bice Chini Istituto di Neuroscienze—CNR, Milano, Italy

L. Ciaccheri CNR—Istituto di Fisica Applicata "Nello Carrara", Sesto Fiorentino, FI, Italy

Alessandro Ciattoni Consiglio Nazionale delle Ricerche, CNR-SPIN, L'Aquila, Italy

Nunzia Cicco Consiglio Nazionale delle Ricerche, Istituto di Metodologie per l'Analisi Ambientale, Tito Scalo (PZ), Italy

Stefano Cinti Dipartimento di Scienze e Tecnologie Chimiche, Università di Tor Vergata, Roma, Italy

Bianca Ciui Analytical Chemistry Department, Faculty of Pharmacy, Iuliu Haţieganu, University of Medicine and Pharmacy, Cluj-Napoca, Romania

Andrea Colarieti DEWS Center of Excellence, University of L'Aquila, L'Aquila, Italy

Adriano Colombelli CNR—Institute for Microelectronics and Microsystems, Unit of Lecce, Lecce, Italy

Department of Innovation Engineering, University of Salento, Lecce, Italy

G. Colonia Dipartimento di Ingegneria dell'Informazione, Elettronica e Telecomunicazioni, Sapienza Università di Roma, Roma, Italy

Dario Compagnone Faculty of Bioscience and Technologies for Food Agriculture and Environment, University of Teramo, Mosciano S.A., Italy

F. Conso Department of Electrical, Computer, and Biomedical Engineering, University of Pavia, Pavia, Italy

Annalisa Convertino CNR—Institute for Microelectronics and Microsystems, Unit of Roma, Roma, Italy

O. Cordovani Department of Information Engineering and Mathematics (Unita' GMEE Siena), University of Siena, Siena, Italy

M. Corvino Dipartimento di Ingegneria Elettrica e dell'Informazione, Università di Cassino e del Lazio MeridionaleVia G, Cassino, FR, Italy

Agnese Coscetta Dept of Industrial and Information Engineering, Seconda Università di Napoli, Aversa, Italy

F. Cosi IFAC-CNR, "Nello Carrara" Institute of Applied Physics, Sesto Fiorentino, FI, Italy

Cecilia Cristea Analytical Chemistry Department, Faculty of Pharmacy, Iuliu Haţieganu, University of Medicine and Pharmacy, Cluj-Napoca, Romania

Antonella Curulli ISMN CNR Istituto per lo Studio dei Materiali Nanostrutturati Consiglio Nazionale delle Ricerche, Roma, Italy

A. D'Amico Department of Electronic Engineering, University of Rome Tor Vergata, Rome, Italy

Ciro D'Apice Department of Electronic and Computer Engineering, University of Salerno, Salerno, Italy

Ravinder Dahiya Electronics and Nanoscale Engineering, University of Glasgow, Glasgow, UK

M. Dalle Feste Department of Engineering and Architecture, APL laboratory, Trieste University, Trieste, Italy

Francesco Damin Istituto di Chimica del Riconoscimento Molecolare—CNR, Milano, Italy

Principia Dardano Institute for Microelectronics and Microsystems, National Research Council, Napoli, Italy

C. De Berti Department of Electrical, Computer, and Biomedical Engineering, University of Pavia, Pavia, Italy

G. de Cesare Department of Information Engineering, Electronics and Telecommunications, "Sapienza" University of Rome, Rome, Italy

L. De Gara Food Science Human Nutrition Unit, CIR-Center for Integrated Research, University Campus Bio-Medico di Roma, Rome, Italy

N. De Leo Istituto Nazionale di Ricerca Metrologica, Torino, Italy

Massimiliano De Luca IDASC-CNR, Area della Ricerca di Roma Tor Vergata, Roma, Italy

Andrea De Marcellis Dipartimento di Scienze Fisiche e Chimiche, Università dell'Aquila, L'Aquila, Italy

Department of Industrial and Information Engineering and Economics—DIIIE, University of L'Aquila, L'Aquila, Italy

Antonella De Maria ENEA-Centro Ricerche di Portici, Portici, NA, Italy

Laura Maria De Plano Department of Environmental and Biological Sciences, University of Messina, Messina, Italy

Arturo De Risi Dipartimento Ingegneria dell'Innovazione, Universita' del Salento, Lecce, Italy

Luigi De Rosa UTTP/CHIA Department, ENEA Portici Research Centre, Portici, NA, Italy

A. De Vecchi Department of Engineering and Architecture, APL laboratory, Trieste University, Trieste, Italy

Saverio De Vito UTTP/Basic Material and Devices Dept., ENEA Portici Research Centre, Portici, NA, Italy

Michele Del Carlo Faculty of Bioscience and Technology for Food, Agriculture and Environment, University of Teramo, Teramo, Italy

F. Del Cesta Dipartimento di Ingegneria dell'Informazione, Università di Pisa, Pisa, Italy

Flavio Della Pelle Faculty of Bioscience and Technology for Food, Agriculture and Environment, University of Teramo, Teramo, Italy

Paola Delli Veneri ENEA-Centro Ricerche di Portici, Portici, NA, Italy

Daniela Di Camillo Department of Physical and Chemical Sciences, University of L'Aquila, Aquila, Via Vetoio, Coppito, Italy

Girolamo Di Francia UTTP/Basic Material and Devices Dept., ENEA Portici Research Centre, Portici, NA, Italy

Tiziana di luccio ENEA-Centro Ricerche di Portici, Portici, NA, Italy

Corrado Di Natale Department of Electronic Engineering, University of Tor Vergata, Rome, Italy

E. Di Nicolò Solvay Specialty Polymers, Research and Development Center, Bollate, MI, Italy

Alessia Di Pancrazio Dipartimento di Ingegneria dell'Informazione, University of Pisa, Pisa, Italy

Maria Dinescu Lasers Department, National Institute for Lasers, Plasma and Radiation Physics, Bucharest, Romania

A Donato DICEAM, University "Mediterranea" of Reggio Calabria, Reggio Calabria, Italy

N. Donato Dipartimento di Ingegneria Elettronica, Chimica e Ingegneria Industriale, Università degli Studi di Messina, Messina, Italy

C. Dossi DiSTA, University of Insubria, Varese, VA, Italy

AMEL Instruments, Milano, Italy

Alfinito Eleonora Università del Salento, Lecce, Italy

Ilaria Ercoli Dipartimento di Ingegneria e Scienze Matematiche, Università Politecnica delle Marche, Ancona, Italy

Vito Errico Department of Physics and Chemistry, University of Palermo, Palermo, Italy

Alberto Escarpa Department of Analytical Chemistry, Physical Chemistry and Chemical Engineering, Faculty of Chemistry, University of Alcalá, Alcalá de Henares, Madrid, Spain

Marco Faccio DEWS Center of Excellence, University of L'Aquila, L'Aquila, Italy

Luigi Falciola Dipartimento di Chimica, Università degli Studi di Milano, Milano, via Golgi 19, Italy

Christian Falconi Department of Physics and Chemistry, University of Palermo, Palermo, Italy

Christian Falconi Dept. of Electronic Engineering, University of Rome Tor Vergata, Rome, Italy

C. Fanelli Department of Environmental Biology, "Sapienza" University of Rome, Rome, Italy

D. Farnesi IFAC-CNR, "Nello Carrara" Institute of Applied Physics, Sesto Fiorentino, FI, Italy

Centro Studi e Ricerche "Enrico Fermi", Roma, Italy

Grazia Fattoruso UTTP/Basic Material and Devices Dept., ENEA Portici Research Centre, Portici, NA, Italy

Gabriele Favero Department of Chemistry and Pharmaceutical Technology, "Sapienza" University of Rome, Rome, Italy

Fabio Federici DEWS Center of Excellence, University of L'Aquila, L'Aquila, Italy

Filippo Fedi CNR-Institute for Composite and Biomedical Materials, Portici, NA, Italy

Marco Ferrari Dipartimento di Ingegneria dell'Informazione (DII), University of Brescia, Brescia, Italy

Vittorio Ferrari Dipartimento di Ingegneria dell'Informazione (DII), University of Brescia, Brescia, Italy

Giuseppe Ferri Department of Industrial and Information Engineering and Economics—DIIIE, University of L'Aquila, L'Aquila, Italy

Luigi Ferrigno DIEI, Università di Cassino e del Lazio Meridionale, Cassino, Italy

G. Fisicaro CNR-IMM Sezione di Catania, Catania, Italy

F. Formisano UTTP-MDB Department, ENEA, Italian Agency for New Technologies Energy and Sustainable Economic Development, C.R. Portici, Portici, NA, Italy

Ada Fort Department of Information Engineering and Mathematics, University of Siena, Siena, Italy

G. I. Forte Istituto di Bioimmagini e Fisiologia Molecolare (IBFM-CNR)—LATO, Cefalù PA Sicilia, Italy

M. Fretto Istituto Nazionale di Ricerca Metrologica, Torino, Italy

C. Gärtner Microfluidic ChipShop GmbH, Jena, Germany

Vincenzo Gattulli DEWS Center of Excellence, University of L'Aquila, L'Aquila, Italy

F. Genova Food Science Human Nutrition Unit, CIR-Center for Integrated Research, University Campus Bio-Medico di Roma, Rome, Italy

Daniele Giannetta Direzione di Esercizio, Ferrovie del Gargano, Foggia, Italy

A. Giannetti IFAC-CNR, "Nello Carrara" Institute of Applied Physics, Sesto Fiorentino, FI, Italy

Fabio Giavazzi Dipartimento di Biotecnologie Mediche e Medicina Traslazionale, Università degli Studi di Milano, Segrate, MI, Italy

M. C. Gilardi Istituto di Bioimmagini e Fisiologia Molecolare (IBFM-CNR)—LATO, Cefalù PA Sicilia, Italy

G. Giustolisi Dipartimento di Ingegneria Elettrica, Elettronica e Informatica Facolta' di Ingegneria, Universita' degli Studi di Catania, Catania, Italy

E. Golinelli T&D Technologies Department, RSE-Ricerca sul Sistema Energetico, Milano, Italy

María Cristina González Department of Analytical Chemistry, Physical Chemistry and Chemical Engineering, Faculty of Chemistry, University of Alcalá, Alcalá de Henares, Madrid, Spain

C. Granata Istituto di Cibernetica "E. Caianiello" del Coniglio Nazionale delle Ricerche, Pozzuoli, Napoli, Italy

Simona Granchi Dipartimento di Ingegneria dell'Informazione(DINFO), Università degli Studi di Firenze, Firenze, Italy

M. Grassi Department of Electrical, Computer, and Biomedical Engineering, University of Pavia, Pavia, Italy

S. Grasso Lab of Electronics for Sensor Systems, CIR-Center for Integrated Research, University Campus Bio-Medico di Roma, Rome, Italy

Fabio Graziosi DEWS Center of Excellence, University of L'Aquila, L'Aquila, Italy

Michele Gregorkiewitz Department of Physical sciences, Earth and Environment, University of Siena, Siena, Italy

I. A. Grimaldi IREA-CNR, Institute for Electromagnetic Sensing of the Environment, Napoli, Italy

Salvatore Guglielmino Department of Environmental and Biological Sciences, University of Messina, Messina, Italy

R. Guider Dipartimento di Fisica, Università di Trento, Povo, TN, Italy

Weihua Han Department of Physics and Chemistry, University of Palermo, Palermo, Italy

School of Physical Science and Technology, Lanzhou University, Lanzhou, P.R. China

Tibor Hianik Institute of Biochemistry and Animal Genetics, Slovak Academy of Sciences, Ivanka pri Dunaji, Slovakia

Sergio Iarossi IDASC-CNR, Area della Ricerca di Roma Tor Vergata, Roma, Italy

Luca Intaschi Dipartimento di Ingegneria dell'Informazione, University of Pisa, Pisa, Italy

Mario Iodice Institute for Microelectronics and Microsystems, National Research Council, Napoli, Italy

Mohammed Janneh Dipartimento di Ingegneria Industriale e dell'Informazione e di Economia, Università dell'Aquila, L'Aquila, Italy

J Jayaprakash Nanotechnology Laboratory, Sri Ramakrishna Mission Vidyalaya College of Arts and Science, Coimbatore, Tamil Nadu, India

N. Kumar Dipartimento di Fisica, Università di Trento, Povo, TN, Italy

W. Kutner Department of Physical Chemistry of Supramolecular Complexes, Institute of Physical Chemistry, Polish Academy Sciences, Warsaw, Poland

Vera La Ferrara ENEA-Centro Ricerche di Portici, Portici, NA, Italy

A. La Magna Istituto per la Microelettronica e Microsistemi, CNR, Catania, Catania, VIII Strada 5, Italy

F. La Via CNR-IMM Sezione di Catania, Catania, Italy

V. Lacquaniti Istituto Nazionale di Ricerca Metrologica, Torino, Italy

Antonia Lai ENEA, UTAPRAD-DIM, Frascati, Italy

Giovanni Landi Faculty of Mathematics and Computer Science, Fern Universität Hagen, Hagen, Germany

R. Lanfranco Dipartimento di Biotecnologie Mediche e Medicina Traslazionale, Università degli Studi di Milano, Segrate, MI, Italy

M. Latino DIECII, University of Messina, Messina, Italy

Stefano Lecci ENEA, UTAPRAD-DIM, Frascati, Italy

S. G. Leonardi Dipartimento di Ingegneria Elettronica, Chimica e Ingegneria Industriale, Università degli Studi di Messina, Messina, Italy

Alessandro Leone CNR-IMM, Via Monteroni presso Campus Universitario, Lecce, Italy

C. Liguori Dipartimento di Ingegneria Industriale, Università degli studi di Salerno, Fisciano, SA, Italy

Fabio Lo Castro IDASC-CNR, Area della Ricerca di Roma Tor Vergata, Roma, Italy

V. Locato Food Science Human Nutrition Unit, CIR-Center for Integrated Research, University Campus Bio-Medico di Roma, Rome, Italy

Cristian O. Lombardo Dipartimento di Ingegneria Elettrica Elettronica e Informatica (DIEEI), University of Catania, Catania, Italy

A. N. Longhitano Dipartimento di Ingegneria dell'Informazione, Università di Pisa, Pisa, Italy

Leandro Lorenzelli Center for Materials and Microsystems, Fondazione Bruno Kessler, Trento, Italy

Luca Lozzi Department of Physical and Chemical Sciences, University of L'Aquila, Aquila, Via Vetoio, Coppito, Italy

L. Lunelli FBK-Irst, Materials and Microsystems Centre, BioSInt Unit, Povo, TN, Italy

P. Malcovati Department of Electrical, Computer, and Biomedical Engineering, University of Pavia, Pavia, Italy

Cosimino Malitesta Laboratorio di Chimica Analitica, Dipartimento di Scienze e Tecnologie Biologiche e Ambientali (DiSTeBA), Università del Salento, Lecce, Italy

Maria Grazia Manera CNR—Institute for Microelectronics and Microsystems, Unit of Lecce, Lecce, Italy

Paolo Mantenuto Department of Industrial and Information Engineering and Economics—DIIIE, University of L'Aquila, L'Aquila, Italy

Rosanna Manzo Department of Electronic and Computer Engineering, University of Salerno, Salerno, Italy

Paolo Marchionni Dipartimento di Ingegneria e Scienze Matematiche, Università Politecnica delle Marche, Ancona, Italy

Andrea Mardegan Veneto Nanotech, Venice-Marghera, Italy

Vincenzo Marletta Dipartimento di Ingegneria Elettrica Elettronica e Informatica (DIEEI), University of Catania, Catania, Italy

W. Marmo Antica Azienda Agricola Brocchieri, Roma, Italy

Giovanna Marrazza Department of Chemistry "Ugo Schiff", University of Florence, Firenze, Via della Lastuccia 3, Sesto Fiorentino, Italy

Giancarlo Marrosu Facoltà di Ingegneria Civile e Industriale Dip. SBAI, Sapienza Università di Roma, Roma, Italy

Elisabetta Martini Department of Chemistry, "Sapienza" University of Rome, Rome, Italy

Marcello Mascini Faculty of Bioscience and Technology for Food, Agriculture and Environment, University of Teramo, Mosciano S.A., Italy

Ettore Massera ENEA UTTP-MDB Laboratory, R.C. Portici, Portici, NA, Italy

Andreea Matei Lasers Department, National Institute for Lasers, Plasma and Radiation Physics, Bucharest, Romania

Franco Mazzei Department of Chemistry and Pharmaceutical Technology, "Sapienza" University of Rome, Rome, Italy

Elisabetta Mazzotta Laboratorio di Chimica Analitica, Dipartimento di Scienze e Tecnologie Biologiche e Ambientali (DiSTeBA), Università del Salento, Lecce, Italy

A.A. Mencaglia CNR—Istituto di Fisica Applicata "Nello Carrara", Sesto Fiorentino, FI, Italy

Sandro Mengali CREO Consortium—Electro-Optics Research Centre, L'Aquila, Italy

Giovanni Merola Department of Chemistry, "Sapienza", University of Rome, 00185 Rome, Italy

Maria Lucia Miglietta ENEA UTTP-MDB Laboratory, R.C. Portici, Portici, NA, Italy

A.G. Mignani CNR—Istituto di Fisica Applicata "Nello Carrara", Sesto Fiorentino, FI, Italy

Marco Milanese Dipartimento Ingegneria dell'Innovazione, Universita' del Salento, Lecce, Italy

L. Minafra Istituto di Bioimmagini e Fisiologia Molecolare (IBFM-CNR)—LATO, Cefalù PA Sicilia, Italy

Aldo Minardo Dept of Industrial and Information Engineering, Seconda Università di Napoli, Aversa, Italy

Bogdana Mitu Lasers Department, National Institute for Lasers, Plasma and Radiation Physics, Bucharest, Romania

Giovanni Montagna CNR—Institute for Microelectronics and Microsystems, Unit of Lecce, Lecce, Italy

D. Monticelli DiSAT, University of Insubria, Como, CO, Italy

Ligia Maria Moretto Department of Molecular Sciences and Nanosystems, University Ca' Foscari of Venice, Venice, Italy

Antonio Morone Consiglio Nazionale delle Ricerche, Istituto di struttura della Materia, Tito Scalo (PZ), Italy

Alessia Mortari Center for Materials and Microsystems, Fondazione Bruno Kessler, Trento, Italy

Danila Moscone Dipartimento di Scienze e Tecnologie Chimiche, Università di Tor Vergata, Roma, Italy

Lucia Mosiello ENEA, Centro Ricerche Casaccia, S.Maria di Galeria, Rome, Italy

Marco Mugnaini Department of Information Engineering and Mathematics, University of Siena, Siena, Italy

S. Musazzi T&D Technologies Department, RSE-Ricerca sul Sistema Energetico, Milano, Italy

A. Nascetti Department of Astronautics, Electrical and Energy Engineering, "Sapienza" University of Rome, Rome, Italy

A. Negri IMT s.r.l., Rome, Italy

Heinz Christoph Neitzert Dipartimento di Ingegneria Industriale (DIIn), Università di Salerno, Fisciano, SA, Italy

G. Neri DIECII, University of Messina, Messina, Italy

Marco Nicolò Department of Environmental and Biological Sciences, University of Messina, Messina, Italy

G. Nunzi Conti IFAC-CNR, "Nello Carrara" Institute of Applied Physics, Sesto Fiorentino, FI, Italy

Vincenzo Paciello Department of Industrial Engineering, University of Salerno, Salerno, Italy

Elia Palange Dipartimento di Scienze Fisiche e Chimiche, Università dell'Aquila, L'Aquila, Italy

I. Palchetti Dipartimento di Chimica, Università degli Studi di Firenze, Sesto Fiorentino, Firenze, Italy

Giuseppe Palleschi Dipartimento di Scienze e Tecnologie Chimiche, Università di Tor Vergata, Roma, Italy

Antonio Palucci ENEA, UTAPRAD-DIM, Frascati, Italy

A. Paolillo Dipartimento di Ingegneria Industriale, Università degli studi di Salerno, Fisciano, SA, Italy

Francesco Pasanisi UTTP/CHIA Department, ENEA Portici Research Centre, Portici, NA, Italy

L. Pasquardini FBK-Irst, Materials and Microsystems Centre, BioSInt Unit, Povo, TN, Italy

C. Pederzolli FBK-Irst, Materials and Microsystems Centre, BioSInt Unit, Povo, TN, Italy

S. Pelli IFAC-CNR, "Nello Carrara" Institute of Applied Physics, Sesto Fiorentino, FI, Italy

Centro Studi e Ricerche "Enrico Fermi", Roma, Italy

G. Pennazza Lab of Electronics for Sensor Systems, CIR-Center for Integrated Research, University Campus Bio-Medico di Roma, Rome, Italy

C. Pepponi IMT s.r.l., Rome, Italy

M. Perelli IMT s.r.l., Rome, Italy

German Perez Laboratory of Computational and Theoretical Chemistry, Faculty of Chemistry, University of Havana, Havana, Cuba

Elisa A. Pergolizzi Dipartimento di Ingegneria Elettrica Elettronica e Informatica (DIEEI), University of Catania, Catania, Italy

U. Perini T&D Technologies Department, RSE-Ricerca sul Sistema Energetico, Milano, Italy

G. Perretti Department of Economic and Food Science, University of Perugia, Perugia, Italy

Gianluca Persichetti Institute for Electromagnetic Monitoring of the Environment (IREA), National Research Council (CNR), Milan, NA, Italy

R. Petruccelli CNR-Istituto per la Valorizzazione del Legno e delle Specie Arboree, Sesto Fiorentino, FI, Italy

Rita Petrucci Facoltà di Ingegneria Civile e Industriale Dip. SBAI, Sapienza Università di Roma, Roma, Italy

Antonio Pietrosanto Department of Industrial Engineering, University of Salerno, Salerno, Italy

Valentina Pifferi Dipartimento di Chimica, Università degli Studi di Milano, Milano, via Golgi 19, Italy

Laura Pigani Dipartimento di Scienze Chimiche e Geologiche, Università di Modena e Reggio Emilia, Modena, Italy

Ivan Pini Dept. of Electronic Engineering, University of Rome Tor Vergata, Rome, Italy

M. Piotto IEIIT-Pisa, CNR, Pisa, Italy

B. Piuzzi Department of Engineering and Architecture, APL laboratory, Trieste University, Trieste, Italy

Daniel Pizzoni Faculty of Bioscience and Technology for Food, Agriculture and Environment, University of Teramo, Mosciano S.A., Italy

S. Plattner Department of Chemistry, Sapienza University of Rome, Rome, Italy

Tiziana Polichetti ENEA UTTP-MDB Laboratory, R.C. Portici, Portici, NA, Italy

Jane Politi Institute for Microelectronics and Microsystems, National Research Council, Napoli, Italy

Department of Chemistry, University of Naples, Napoli, Italy

Giovanni Polito Dipartimento di Ingegneria dell'Informazione, Università di Pisa, Pisa, Italy

Maurizio Pollino UTMEA/Energy and Environmental Modeling Department, ENEA Casaccia Research Centre, Roma, Italy

Giuseppe Porcaro Tecnomatica SaS, Corso del Mezzogiorno III trav., Foggia, Italy

G. Porro Datamed Srl, Peschiera Borromeo, Italy

Alexandra Poturnayova Faculty of Mathematics, Physics and Informatics, Comenius University, Bratislava, Slovakia

Jeremy Pousset CNR-IMM, Lecce, Italy

T Prakash Nanotechnology Laboratory, Sri Ramakrishna Mission Vidyalaya College of Arts and Science, Coimbatore, Tamil Nadu, India

Andrea Pulvirenti Department of Life Sciences, University of Modena and Reggio Emilia, Reggio Emilia, Italy

CNR-INO SENSOR lab, Brescia, Italy

Adi R. Bulsara Space and Naval Warfare Systems Center Pacific, San Diego, CA, USA

Andrea Ravalli Department of Chemistry "Ugo Schiff", University of Florence, Firenze, Via della Lastuccia 3, Sesto Fiorentino, Italy

Ilaria Rea Institute for Microelectronics and Microsystems, National Research Council, Napoli, Italy

Lino Reggiani Università del Salento, Lecce, Italy

G. F. Regnicoli Department of Economic and Food Science, University of Perugia, Perugia, Italy

Roberto Rella CNR—Institute for Microelectronics and Microsystems, Unit of Lecce, Lecce, Italy

S. Rella Laboratorio di Chimica Analitica—Dipartimento di Scienze e Tecnologie Biologiche e Ambientali, Di.S.Te.B.A., Università del Salento, Lecce, Italy

Filiberto Ricciardella ENEA UTTP-MDB Laboratory, R.C. Portici, Portici, NA, Italy

Department of Physics, University of Naples 'Federico II', Naples, Italy

Alessandra Ricciardi Dipartimento Ingegneria dell'Innovazione, Universita' del Salento, Lecce, Italy

A. Ricelli CNR-Institute of Biomolecular Chemistry, Rome, Italy

G. C. Righini IFAC-CNR, "Nello Carrara" Institute of Applied Physics, Sesto Fiorentino, FI, Italy

Centro Studi e Ricerche "Enrico Fermi", Roma, Italy

Carlo Rizza Dipartimento di Scienza e Alta Tecnologia, Università dell'Insubria, Como, Italy

Valentina Robbiano Department of Physics and Astronomy and London Centre for Nanotechnology, University College London, London, UK

Santina Rocchi Department of Information Engineering and Mathematics, University of Siena, Siena, Italy

L. Romano Dipartimento di Fisica ed Astronomia, Università degli Studi di Catania, Catania, Italy

Alberto Roncaglia Istituto per la Microelettronica e i Microsistemi(IMM), CNR, Bologna, Italy

Alessandro Rufoloni ENEA, UTAPRAD-DIM, Frascati, Italy

G. Russo Istituto di Bioimmagini e Fisiologia Molecolare (IBFM-CNR)—LATO, Cefalù PA Sicilia, Italy

M. Salina Proxentia S.r.l., Milano, Italy

Matteo Salina Proxentia S.r.l., Segrate, MI, Italy

D. Salvalaggio Department of Engineering and Architecture, University of Trieste, Trieste, Italy

M. Salvato ENEA (Italian New Technologies, Energy and Sustainable economic development Agency), Portici Research Center, Portici, Italy

Robert Sandulescu Analytical Chemistry Department, Faculty of Pharmacy, Iuliu Hațieganu, University of Medicine and Pharmacy, Cluj-Napoca, Romania

M. Santonico Lab of Electronics for Sensor Systems, CIR-Center for Integrated Research, University Campus Bio-Medico di Roma, Rome, Italy

Gabriella Sanzò Department of Chemistry and Pharmaceutical Technology, "Sapienza" University of Rome, Rome, Italy

E. Sardini Dipartimento di Ingegneria dell'Informazione, Università degli Studi di Brescia, Brescia, Italy

Veronica Sberveglieri Department of Life Sciences, University of Modena and Reggio Emilia, Reggio Emilia, Italy

CNR-INO SENSOR lab, Brescia, Italy

S. Scalese Istituto per la Microelettronica e Microsistemi, CNR, Catania, Catania, VIII Strada 5, Italy

Lorenzo Scalise Dipartimento di Ingegneria e Scienze Matematiche, Università Politecnica delle Marche, Ancona, Italy

M. Scarpa Dipartimento di Fisica, Università di Trento, Povo, TN, Italy

R. Scipinotti Department of Information Engineering, Electronics and Telecommunications, "Sapienza" University of Rome, Rome, Italy

Paolo Scopece Veneto Nanotech, Venice-Marghera, Italy

V. Scuderi Istituto per la Microelettronica e Microsistemi, CNR, Catania, Catania, VIII Strada 5, Italy

Renato Seeber Dipartimento di Scienze Chimiche e Geologiche, Università di Modena e Reggio Emilia, Modena, Italy

M. Serpelloni Dipartimento di Ingegneria dell'Informazione, Università degli Studi di Brescia, Brescia, Italy

Luay Shahin Department of Information Engineering and Mathematics, University of Siena, Siena, Italy

Pietro Siciliano CNR-IMM, Via Monteroni presso Campus Universitario, Lecce, Italy

T. Siciliano Laboratorio Fisica e Chimica dell'Ambiente e dei Beni Culturali—Dipartimento di Beni Culturali, Università del Salento, Lecce, Italy

Morena Silvestrini Department of Molecular Sciences and Nanosystems, University Ca' Foscari of Venice, Venice, Italy

Maya Sneyedarkova Faculty of Mathematics, Physics and Informatics, Comenius University, Bratislava, Slovakia

Laura Sola Istituto di Chimica del Riconoscimento Molecolare—CNR, Milano, Italy

P. Sommella Dipartimento di Ingegneria Industriale, Università degli studi di Salerno, Fisciano, SA, Italy

S. Soria IFAC-CNR, "Nello Carrara" Institute of Applied Physics, Sesto Fiorentino, FI, Italy

M. Sosnowska Department of Physical Chemistry of Supramolecular Complexes, Institute of Physical Chemistry, Polish Academy Sciences, Warsaw, Poland

Katia Spinella Department of Chemistry, University of Roma, TorVergata, Rome, Italy

ENEA, Centro Ricerche Casaccia, S.Maria di Galeria, Rome, Italy

Roberto Spinicci Department of Information Engineering and Mathematics, University of Siena, Siena, Italy

Valeria Spizzichino ENEA, UTAPRAD-DIM, Frascati, Italy

Luca De Stefano Institute for Microelectronics and Microsystems, National Research Council, Napoli, Italy

F. Stropeni DiSTA, University of Insubria, Varese, VA, Italy

AMEL Instruments, Milano, Italy

A. Sudano Laboratory of Biomedical Robotics and Biomicrosystems, CIR-Center for Integrated Research, University Campus Bio-Medico di Roma, Rome, Italy

Salvatore Surdo Dipartimento di Ingegneria dell'Informazione, Università di Pisa, Pisa, Italy

Carlo Tebano UTTP/CHIA Department, ENEA Portici Research Centre, Portici, NA, Italy

A. Tepore Laboratorio Fisica e Chimica dell'Ambiente e dei Beni Culturali—Dipartimento di Beni Culturali, Università del Salento, Lecce, Italy

Fabio Terzi Dipartimento di Scienze Chimiche e Geologiche, Università di Modena e Reggio Emilia, Modena, Italy

Genni Testa Institute for Electromagnetic Monitoring of the Environment (IREA), National Research Council (CNR), Milan, NA, Italy

Sajina Tinku Center for Materials and Microsystems, Fondazione Bruno Kessler, Trento, Italy

Mauro Tomassetti Department of Chemistry, "Sapienza" University of Rome, Rome, Italy

S. Tombelli IFAC-CNR, "Nello Carrara" Institute of Applied Physics, Sesto Fiorentino, FI, Italy

Alessandro Trani ISMN CNR Istituto per lo Studio dei Materiali Nanostrutturati Consiglio Nazionale delle Ricerche, Roma, Italy

Giulia Tregnago Department of Physics and Astronomy and London Centre for Nanotechnology, University College London, London, UK

L. Tripodi Istituto per la Microelettronica e Microsistemi, CNR, Catania, Catania, VIII Strada 5, Italy

S Trocino DICEAM, University "Mediterranea" of Reggio Calabria, Reggio Calabria, Italy

C. Trono Institute of Applied Physics "Nello Carrara", National Research Council, CNR-IFAC, Sesto Fiorentino, FI, Italy

Antonio Turco Laboratorio di Chimica Analitica, Dipartimento di Scienze e Tecnologie Biologiche e Ambientali (DiSTeBA), Università del Salento, Lecce, Italy

Paolo Ugo Department of Molecular Sciences and Nanosystems, University Ca' Foscari of Venice, Venice, Italy

Enrico Vannacci Dipartimento di Ingegneria dell'Informazione(DINFO), Università degli Studi di Firenze, Firenze, Italy

Maria Verrastro Consiglio Nazionale delle Ricerche, Istituto di struttura della Materia, Tito Scalo (PZ), Italy

Scuola di Scienze Agrarie, Forestali, Alimentari ed Ambientali, Università degli Studi della Basilicata, Potenza, Italy, Potenza, Italy

A. Vettoliere Istituto di Cibernetica "E. Caianiello" del Coniglio Nazionale delle Ricerche, Pozzuoli, Napoli, Italy

Valerio Vignoli Department of Information Engineering and Mathematics, University of Siena, Siena, Italy

Diana Vilela Department of Analytical Chemistry, Physical Chemistry and Chemical Engineering, Faculty of Chemistry, University of Alcalá, Alcalá de Henares, Madrid, Spain

E. Viviani Department of Engineering and Architecture, APL laboratory, Trieste University, Trieste, Italy

D. Voccia Dipartimento di Chimica, Università degli Studi di Firenze, Sesto Fiorentino, Firenze, Italy

Chiara Zanardi Dipartimento di Scienze Chimiche e Geologiche, Università di Modena e Reggio Emilia, Modena, Italy

Luigi Zeni Dept of Industrial and Information Engineering, Seconda Università di Napoli, Aversa, Italy

M. Zweyer Clinical Department of Medical, Surgical and Health Sciences, Trieste University, Trieste, Italy

Part I
Biosensors

Chapter 1
Proteotronics: Electronic Devices Based on Proteins

Eleonora Alfinito, Lino Reggiani and Jeremy Pousset

The convergent interests of different scientific disciplines, from biochemistry to electronics, toward the investigation of protein electrical properties, has promoted the development of a novel bailiwick, the so called proteotronics. The main aim of proteotronics is to propose and achieve innovative electronic devices, based on the selective action of specific proteins. This paper gives a sketch of the fields of applications of proteotronics, by using as significant example the detection of a specific odorant molecule carried out by an olfactory receptor. The experiment is briefly reviewed and its theoretical interpretation given. Further experiments are envisioned and expected results discussed in the perspective of an experimental validation.

1.1 Introduction

Recently, science has changed its horizons, switching off overspecialization, and embracing a syncretic perspective. This movement sees the convergence of multiple interests, know-how and know-why, and therefore the need of a common language, with new keywords. In particular, in the field of electronics, more and more pressing requirements push toward the devising and setting up of very sensitive and fast detectors, useful for noninvasive diagnostics in medicine, food security etc. Biointegrated micro/nano-devices are the way followed by several groups for exploiting this trend. Accordingly, the new branch of science, conjugating electronics and proteomics, the large-scale study of proteins, was given the name of *proteotronics* [1].

E. Alfinito (✉) · L. Reggiani
Università del Salento, Lecce, Italy
e-mail: eleonora.alfinito@unisalento.it

J. Pousset
CNR-IMM, Lecce, Italy

1.2   Focus on Experiments

Recent investigations performed with chemical and physical approaches have definitely confirmed the possibility of detecting the protein activity by using electrical measurements [2, 3]. As a matter of fact, in spite of a completely different topological structure (highly not periodic), proteins seem to exhibit a conductivity like medium-gap semiconductors [1, 2], with electrical features deeply depending on protein conformation and environmental conditions. Proteins show very specific 3D structures in their native states, which, in the presence of specific stimuli, can significantly modify (active states). The detection of this conformational change is monitored by different techniques, both chemical-like, as electrochemical impedance spectroscopy (EIS) [3], and physical-like, as current-voltage or conductance measurements [4, 5]. In both the cases, the experimental set-up involves protein receptors anchored on specific substrates and used to detect the *in vitro* response to specific stimuli (small molecules capture or light absorption). In the following we recall the main data concerning the dose-response of rat OR-I7, used as a preliminary test for the development of a bio-electronic nose [3]. OR-I7 is an olfactory receptor, highly specific for the aldehyde group, showing a very good response to octanal. Samples were prepared by immobilizing OR-I7 proteins, in their membrane fraction, on a gold electrode, by using a self-assembled multilayer. The measurements were performed in an electrochemical cell whose working electrode is constituted by the functionalized gold electrode.

   The sensitivity to octanal has been explored over a range of about nine orders of magnitude of odorant concentration. The main results are a good selectivity with respect to other aldehydes, and a monotonic increase of sensitivity at increasing concentration. Figure 1.1 reports the experimental Nyquist plots at increasing octanal concentration (expressed in Molar). Data are analyzed by using a macroscopic circuit analogue called Randles cell, where the element most sensitive to the concentration variation is the polarization resistance: it decreases for about 18 % at an octanal concentration of 10^{-4} M.

1.3   Focus on Theory

A theoretical framework able to include all known results and predict new outcomes is the web on which proteotronics can develop. Accordingly, an numerical approach able to model the main electrical mechanisms revealed by experiments on proteins *in vitro* was set up [1, 2]. It focuses on the interactions between amino acids, that constitute the protein building-blocks, and as such are responsible of the specific sensing action of the given protein. As matter of fact, it is sufficient to change a single amino acid for producing a ill-functioning objects, like it happens for defective hemoglobins. These interactions may be described like a network covering the whole protein. In the case of interactions of electrical origin the simplest
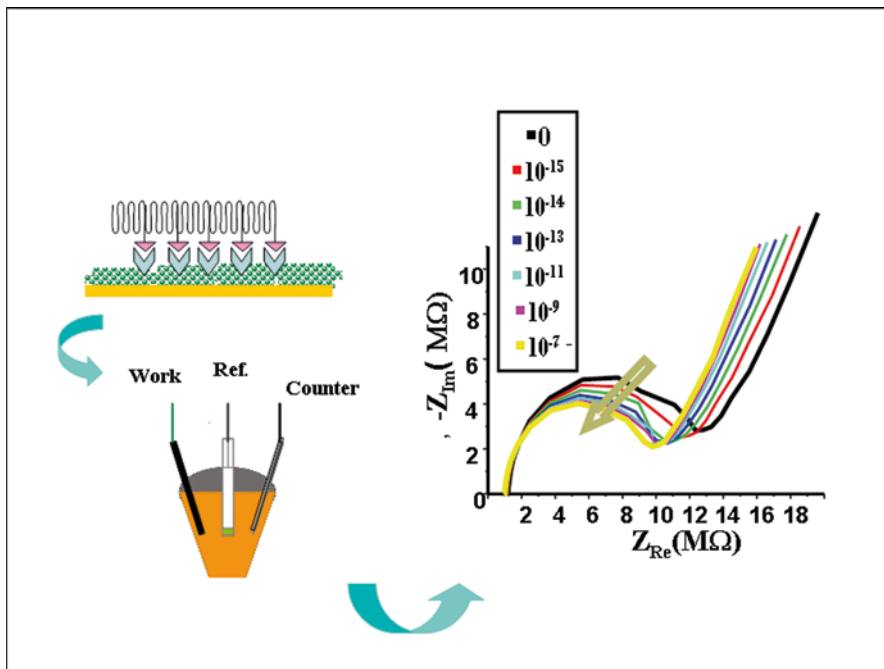
Fig. 1.1 Schematic representation of EIS measurements performed on samples of rat OR -I7 at increasing concentrations of the specific odorant, octanal. On the *left*: the sample and the electrochemical cell; on the *right*: the experimental results. The *straight arrow* indicates the increasing concentration of octanal

way to describe this web is the impedance network protein analogue (INPA) [1, 2] which, analogously to the well known Hodgkin-Huxley model, describes the interactions by using a set of linear equations, solved by a computational procedure. This procedure is based on the Kirchhoff's laws and therefore the equations are linear. Elements of non-linearity may be introduced by using stochastic terms within a Monte Carlo solving approach. More details of this approach can be found in Ref. [2]. Below the INPA is applied to the case of rat OR-I7. The model needs a few information concerning the protein under examination: the 3D structure, the kind of interaction between amino acids, the resistivity and polarizability of each amino acid. The model contains a free parameter, the interaction radius R_C, whose value can be correlated to the ligand dose [1, 2]. By using these input data it is possible (i) to reproduce experimental results with a satisfactory agreement; (ii) to predict the electrical properties of novel structures. In doing so, R_C is selected by the comparison of calculated data with experiments and its value is used to foresee new responses. In particular, the experimental results shown in previous section, select the value $R_C = 32$ Å, as reported in the inset of Fig. 1.2. This figure shows the calculated Nyquist plot of rat OR I7 in the native and active state. The calculated real impedance (ReZ) corresponds to the measured polarization resistance. The same figure

Fig. 1.2 I-V characteristics for rat OR I7 in the native (*continuous line*) and active (*dashed line*) states. In the inset: Nyquist plots for the same templates
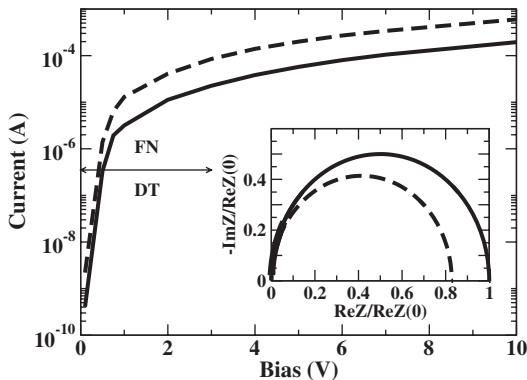
Fig. 1.3 Distribution of conductance fluctuations at different bias values for rat OR I7 in the native state
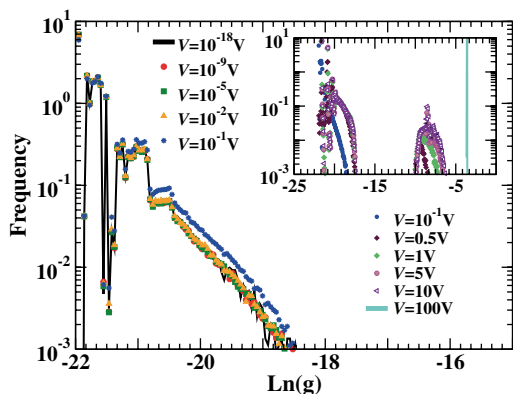
reports the I-V characteristics of rat OR I7 calculated with $R_C = 32$ Å, for the native and active state, to simulate the response in the presence/absence of octanal. The I-V characteristics are super-linear and this is attributed to a tunneling mechanism of charge transport [1, 2, 4]. In particular, by using a wide range of bias values, it is possible to observe two different tunneling regimes, the direct tunneling (DT) and the Fowler-Nordheim (FN). An efficient strategy for an accurate investigation of the DT-FN transition is given by the analysis of conductance fluctuations. This analysis is quite useful both for the general aim of a most deep understanding of the internal mechanisms driving the current transport [1] but also for an early monitoring of the protein response under a bias stress. Figure 1.3 reports the conductance fluctuation distribution (CFD) over a range of 20 orders of magnitude, clearly showing the DT regime, below 0.1 V, and the FN regime (in the inset) above 0.5 V. The change of regime is very sharp: in the low conductance region CDF has the same characteristic shape for more than 17 magnitude orders, a protein fingerprint. At higher conductance values the competition between DT and FN is indicated by the presence of a secondary peak. Finally, a new linear regime is established and a single sharp distribution appears.

1.4 Conclusions

Proteotronics is here introduced as a new branch of electronics devoted to investigate the electrical properties of proteins with the aim to develop new bio-electronic devices. As significant application, the case of rat olfactory receptor OR I7 acting as an odor sensor is considered. From the theoretical side, proteotronics has been used to predict the OR-I7 current-voltage characteristics in a wide range of applied voltages. The predicted I-V superlinear characteristics and the extreme conductance fluctuations still wait to be confirmed from an experimental side.

References

1. E. Alfinito, J. Pousset, L. Reggiani.: Protein-Based Electronics: Transport Properties and Application: Towards the Development of a Proteotronics., In Preparation for: Pan Stanford Publishing Pte. Ltd. Penthouse Level, Suntec Tower 3, 8 Temasek Boulevard, Singapore 038988
2. E. Alfinito, J. Pousset, L. Reggiani, in Olfactory Receptors: Methods and Protocols, ed by C. J. Crasto (Springer, Berlin Heidelberg New York, 2013), 67
3. Y. Hou et al. A novel detection strategy for odorant molecules based on controlled…. Biosensors and Bioelectronics **22** 1550–1555 (2007)
4. I. Casuso et al. Electron transport through supported biomembranes at the nanoscale…. Nanotechnology **18** 465503 (2007)
5. M. Marrakchi, et al. A new concept of olfactory biosensor based on interdigitated. European Biophysics Journal **36** 1015–1018 (2007):

Chapter 2
Study of the role of particle-particle dipole interaction in dielectrophoretic devices for biomarkers identification

Massimo Camarda, S. Baldo, G. Fisicaro, R. Anzalone, S. Scalese, A. Alberti, F. La Via, A. La Magna, A. Ballo, G. Giustolisi, L. Minafra, F. P. Cammarata, V. Bravatà, G. I. Forte, G. Russo and M. C. Gilardi

A three dimensional Coupled Monte Carlo-Poisson method has been used to evaluate the impact of particle-particle dipole interactions in the equilibrium distribution of a system of uncharged polarizable particles suspended in a static liquid medium under the action of an oscillating non-uniform electric field generated by polynomial electrodes. We compare the simulated distributions with experimental ones both for micro- (MDA-MB-231 breast tumor cells) and nano-(multiwall carbon nanotubes) particles. In both cases the equilibrium distributions near the electrodes are dominated by dipole interactions which locally enhance the DEP effect and promote long particles chains.

2.1 Introduction

The term "*dielectrophoresis*" [1] is used to describe the *"ponderomotive"* force exerted by a non-uniform electric field on polarizable neutral particles. Such force allows for the controlled manipulation of micro and nano-sized particles dispersed in colloidal solutions. Application fields include: cell partitioning and isolation [2], bio-structure assembling [3], nanostructure deposition [4], filtration systems for oils purification [5] etc. One of the problems that is hindering development and engineerization of DEP devices is the limited use of accurate numerical tools for their design which, in turn, is due to the computational complications arising by the

M. Camarda (✉) · S. Baldo · G. Fisicaro · R. Anzalone · S. Scalese · A. Alberti · F. La Via · A. La Magna
CNR-IMM Sezione di Catania, Z.I. VIII Strada 5, 95121 Catania, Italy
e-mail: camarda.massimo@gmail.com

A. Ballo · G. Giustolisi
Dipartimento di Ingegneria Elettrica, Elettronica e Informatica Facolta' di Ingegneria, Universita' degli Studi di Catania, Catania, Italy

L. Minafra · F. P. Cammarata · V. Bravatà · G. I. Forte · G. Russo · M. C. Gilardi
Istituto di Bioimmagini e Fisiologia Molecolare (IBFM-CNR)—LATO, Cefalù PA Sicilia, Italy

particle-particle dipole interaction. This many-particle effect can be simulated with high accuracy solving directly the equations of motion in the few-particles limit [6] or with some strong approximations using reaction-diffusion models [7] in large systems. Recently a coupled Monte Carlo-Poisson (MC-P) method [8] has been developed which allows simulating a large number of particles in large active zones (within the experimental range), explicitly including particle-particle interactions. The MC-P method has pointed out the relevance of this inclusion in the modeling predictions for the case of 2D systems (interdigitated electrodes). We have applied this methodology to the case of polynomial electrodes comparing the simulated results with experimental distributions of micro-(tumor cells) and nano-(multi-walled nanotubes, MWCNT) particles to evaluate the role of p-p interactions and definitively demonstrate the predictive potential of this methodology.

2.2   Computational Method

A detailed description of the method can be found in refs.[8, 9], here we summarize the equations used in the implemented KMC algorithm.

In the simulated kinetics the particles are considered as hard spheres with positions r_i and a configuration energy given by:

$$E\left(\{\mathbf{r}_1, ... \mathbf{r}_n\}\right) = \sum_i U_{eff}(\vec{r}_i) + \sum_{i,j} \bar{U}_{ij}(\vec{r}_i, \vec{r}_j)$$

$$\bar{U}_{eff}(\vec{r}) = -\frac{1}{2}\alpha_{eff} E_{rms}^2(\vec{r})$$

$$U_{ij} \cong \frac{1}{4\pi \mathrm{Re}(\varepsilon_m)} \alpha_{eff}^i \alpha_{eff}^j \frac{1 - 3\cos(\theta_{ij})\cos(\theta_{ij}^j)}{R_{ij}^3}\left(\vec{E}_{rms}(\vec{r}_i)\vec{E}_{rms}(\vec{r}_j)\right) \qquad (2.1)$$

where $\bar{U}_{eff}$ and $\bar{U}_{ij}$ represent the single-particle DEP energy and the dipole-dipole contribution, respectively. α_{eff} is the average polarizability of the particle defined as $\alpha_{eff} = 3V\,\mathrm{Re}(\varepsilon_m)\,\mathrm{Re}[f_{CM}(\omega)]$. V and ω are the particle volume and electric field frequency and $f_{CM}(\omega)$ is the Clausius-Mossotti factor which fully characterizes the dielectric response of the particle in the given medium [10, 11].

The simulated particles, after an initial random distribution, were allowed to move in a cubic computational box of dimensions $1600 \times 1600 \times 1500$ µm³ with four polynomial electrodes located at the bottom of the box (see Fig. 2.1, left) whose shapes can be described by the following parametric system:

$$D \le x \le L$$

$$y = \pm\sqrt{x^2 + D^2} \qquad (2.2)$$

where D represents half the distance of opposing electrodes whereas L is related to the electrode width. In this study we sat $D = 390$ µm and $L = 460$ µm.
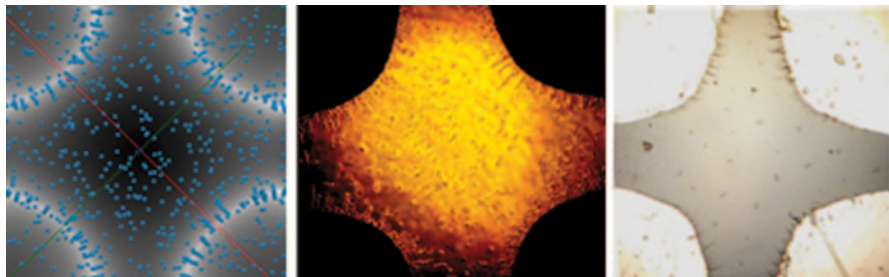
Fig 2.1 Comparison of the top view spatial distributions obtained with simulation and experiments: *left*) the Monte Carlo simulation with superimposed the intensity map of the electric field, *center*) Distribution of MDA-MB-231 after 180 s of DEP manipulation ($V_{pp}=8$V $f=1000$ kHz), *right*) Distribution of MWCNT after 10 min of DEP manipulation ($V_{pp}=80$V $f=300$ kHz)

2.3   Experimental Setup and Results

The polynomial electrode design described in the previous section, has been fabricated by deposition of 10 nm of Ti followed by 200 nm of Ni on a standard microscope glass. The electrodes were delineated by lithographic methods followed by wet etching. The device has been piloted by using a Protek 9205C signal generator which applied, consistently with simulated system, a sinusoidal voltage signal of $8V_{pp}$ peak-peak value at 1 MHz (DEP attractive force) for 180 s (to allow for cells equilibration). The human breast cancer cell line MDA-MB-231 used as test particles, cultured according to American Type Culture Collection (ATCC) instructions, and just before DEP tests, were suspended in a slightly conductive buffer composed of 9.5 % ultrapure sucrose, 0.3 % dextrose, and 0.1 % Pluronic F68 titrated to a conductivity of 30 mS/m (consistent with Monte Carlo simulations) with KCl. The cells, suspended in DEP buffer at concentration of 5×10^5 cells/ml were pipetted into an o-ring chamber (~ 100 µl) which was then sealed using a cover slip. In the case of MWCNT the system included further included a 1:20 step-up transformer which allows to increase the applied voltage up to $\sim 100V_{pp}$ at a fixed frequency of 300 kHz. In both cases (cells and MWCNT) the sinusoidal frequencies used results in a positive DEP (i.e. particles will be attracted by electrodes edges).

2.4   Results and Conclusions

Figure 2.1 shows a comparison between the simulation and the experimental cells distribution. As can be seen the two distributions are equivalent when the statistical approach of the equilibration is considered.

The final distribution is the result of the minimization of Eq. (2.1), which, being $f_{CM}(\omega) > 0$, will induce a movement towards the regions of high intensity field (minimization of the $\bar{U}_{eff}$ term) and an aligned/chaining of the cells along the

electric field lines (minimization of the $\bar{U}_{ij}$ term). From these results we can infer that particle-particle interactions compete with the dielectrophoretic force-field, which would otherwise massively trap (in p-DEP conditions) the particles in the regions where the gradient of the electric field is larger. The highest value of the cell concentration to avoid particle-particle interactions strongly depends on the electrodes and system geometry, on the particles dimensions and on the polarization factors. As a consequence a general prescription to neglect dipole-dipole interaction in the design of a device cannot be easily. For the specific considered system, an estimate for the density threshold governing the interaction free regime was suggested in ref. [9] as $\approx 3 \times 10^4$ cells/ml . Preliminary KMC simulations of MWCNT showed a significant quantitative discrepancy with the experimental results (Fig. 2.1, right). We could expect this results since the model (1) is reliable for spherical particles. Work is underway to evaluate the effects of polarization induced p-p interaction in the case the high aspect ratio object as the nanotubes compared to spherical particles (e.g. cells).

References

1. H. A. Pohl and R. Pethig, "Dielectric measurements using non-uniform electric field (dielectrophoretic) effects" *J. Phys. E: Sci. Instrum.* **10**, 190 (1977)
2. P. R. C. Gascoyne, J. Noshari, T. J. Anderson, F. F. Becker, "Isolation of rare cells from cell mixtures by dielectrophoresis" *Electrophoresis*, **30**, 1388 (2009)
3. J. Castillo, S. Tanzi, M. Dimaki, W. Svendsen, "Manipulation of self-assembly amyloid peptide nanotubes by dielectrophoresis" *Electrophoresis*, **29,** 5026 (2008)
4. M. Duchamp, K. Lee, B. Dwir, J. W. Seo, E. Kapon, L. Forro, and A. Magrez, "Controlled Positioning of Carbon Nanotubes by Dielectrophoresis: Insights into the Solvent and Substrate Role" *ACS Nano*, **4**, 279 (2010)
5. Y. Shen, E. Elele and B. Khusid, "A novel concept of dielectrophoretic engine oil filter" *Electrophoresis* **32**, 2559 (2011)
6. T. J. Arun, K. P. Singh, N. Aubry "Dielectrophoresis of nanoparticles" *Electrophoresis*, **25**, 3625 (2004)
7. O. E. Nicotra, A. La Magna, S. Coffa, "Particle-chain formation in a dc dielectrophoretic trap; a reaction-diffusion approach" *Appl. Phys. Lett.* **95**, 073702 (2009)
8. A. La Magna, M. Camarda, I. Deretzis, G. Fisicaro, and S. Coffa, "Coupled Monte Carlo-Poisson method for the simulation of particle-particle effects in dielectrophoretic devices" *Applied Physics Letters* **100**, 134104 (2012)
9. M. Camarda, L. Minafra, F. P Cammarata, V. Bravatà, G. I. Forte, G. Russo, M. C. Gilardi, A. Ballo, G. Giustolisi, G. Fisicaro, R. Anzalone, S. Scalese, A. alberti, F. La Via and A. La Magna, "Theoretical and experimental study of the role of cell-cell dipole interaction in dielectrophoretic devices: application to polynomial electrodes", *submitted to Biomedical Engineering Online*
10. O. F. Mossotti, Discussione analitica, Mem. Soc. Ital. 14, 49 (1850)
11. H. Morgan and N.G. Green, "Dielectrophoretic manipulation of rod-shaped viral particles" Journal of Electrostatics 42, 279 (1997)

Chapter 3
Portable, Multispot, Label-Free Immunoassay on a Phantom Perfluorinated Plastic

Fabio Giavazzi, Matteo Salina, Erica Ceccarello, Mattia Bassi, Francesco Damin, Laura Sola, Marcella Chiari, Bice Chini, Roberto Cerbino, Tommaso Bellini, Marco Buscaglia

Despite the continuous advancements in bio-molecular detection methods and fluidic integration approaches, the realization of portable and high performance devices for diagnostic applications still presents major difficulties, mostly due to the need of combining adequate sensitivity with low cost of production, operational simplicity and rapidity. In this context, we have previously proposed a compact device composed of a smartphone and a custom-designed cradle, containing only a disposable sensing cartridge, a tiny magnetic stirrer and a few passive optical components. The detection principle is named Reflective Phantom Interface and is based on measuring the intensity of light reflected by the surface of an amorphous fluoropolymer substrate having a refractive index very similar to that of water. The reflectivity of dozens of spots is monitored in real time by the smartphone's camera using the embedded flash LED as the illumination source. We tested the sensitivity and the repeatability of the combined device analyzing multiple spots of antibodies targeting an antigen commonly used as marker for diagnoses of HIV. Target concentrations as low as a few ng/ml can be rapidly and robustly determined by comparing the rate of increase of the signal after the addition of the sample with that measured after the subsequent addition of a standard solution with known concentration.

M. Buscaglia (✉) · F. Giavazzi · E. Ceccarello · R. Cerbino · T. Bellini
Dipartimento di Biotecnologie Mediche e Medicina Traslazionale,
Università degli Studi di Milano, via F.lli Cervi, 93, 20090 Segrate, MI, Italy
e-mail: marco.buscaglia@unimi.it

M. Salina
Proxentia S.r.l., via F.lli Cervi, 93, 20090 Segrate, MI, Italy

M. Bassi
Materials Science Department, Solvay Specialty Polymers Research and Development Center,
viale Lombardia, 20, 20021 Bollate, MI, Italy

F. Damin · L. Sola · M. Chiari
Istituto di Chimica del Riconoscimento Molecolare—CNR, via Mario Bianco, 9,
20131 Milano, Italy

B. Chini
Istituto di Neuroscienze—CNR, via Vanvitelli, 32, 20129 Milano, Italy

3.1 Introduction

In recent years, the increasing computational power and imaging capabilities embedded in current smartphones have stimulated their use as acquisition and elaboration units in various device schemes. In this context, we have proposed a custom-designed accessory that transforms a smartphone into a portable, label-free bio-sensing device [1] exploiting the Reflective Phantom Interface (RPI) detection method [2]. Antibodies are immobilized in spots on the surface of a plastic substrate with refractive index very close to that of water and the binding of specific antigens is monitored through the measurement of the intensity of the light reflected by each spot. Here we report the results of experiments aiming at detecting the HIV marker p24 in serum. The signal from multiple spots is analyzed in order to show the intra-chip variability.

3.2 The Device

Fluorinated polymer materials can be realized in order to have the same index of refraction as water, hence providing a very low reflectivity ($\sim 10^{-5}$) when in contact with an aqueous solution. In this conditions, the adhesion of carbon-based compounds, typically having a substantially higher refractive index, provides a large relative increase of reflectivity, which can be easily detected by consumer grade imaging detectors. Here we used the flash LED and the CMOS sensor of a smartphone (Desire HD, HTC, Taiwan) as illumination source and detector, respectively. The smartphone is combined to a simple, custom-designed cradle (Fig. 3.1) hosting the measuring sample cell and a small magnetic stirrer. The LED light is deviated in order to impinge on the diagonal surface of a right angle prism made of Hyflon® AD (Solvay Specialty Polymers, Bollate, Italy), which is contained in the sample
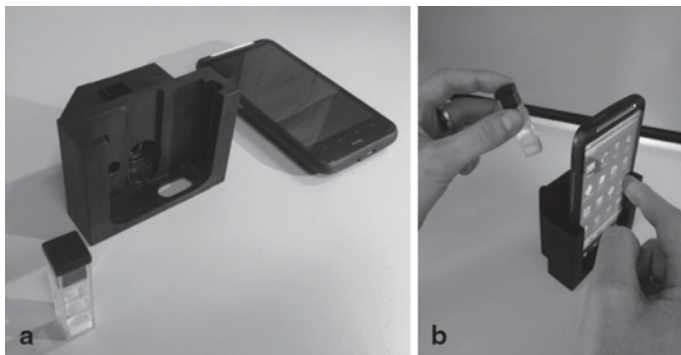
Fig. 3.1. Image of the smartphone-based set-up. **a** Custom cradle (*center*) designed to host the cuvette (*left*) and the smartphone (*right*). **b** Assembled device just before the insertion of the cuvette and the beginning of a measurement.

cuvette. The reflected light is then spatially filtered and imaged on the camera sensor. A custom application running on the smartphone controls the flash LED and acquires time sequences of the images of the light reflected by the sensing surface of the prism at 30 frame/s.

3.3 Results and Discussion

3.3.1 Multi-spot Detection in Serum

The sensing surface of the perfluorinated prism was coated with a multifunctional copolymer of dimethylacrylamide (DMA), N-acryloyloxysuccinimide (NAS), and 3(trimethoxysilyl) propyl methacrylate (MAPS)—copoly(DMA-NAS-MAPS) [3]. Antibodies targeting p24, HBsAg and β-lactoglobulin proteins were covalently immobilized in 200-μm spots by means of an automated noncontact dispensing system (sciFLEXARRAYER S5; Scienion AG). The prism was placed into the measuring cuvette, which was filled with a buffer solution consisting of 0.15 M NaCl, 0.02 % Tween 20, 1 % BSA, and 0.05 M Tris·HCl, pH 7.6 (Sigma Aldrich). After the acquisition of the initial baseline, a 1:10 dilution of bovine fetal serum (FBS, Sigma Aldrich) was placed into the cuvette and, afterwards, p24 was added to a final concentration of about 3 nM. Figure 3.2a shows that the non-specific adsorption of the serum components affected all the spots in a similar way. After 1 h, the p24 sample was added and a marked increase of reflectivity was observed only for the corresponding spots. Figure 3.2b shows that the two kinds of anti-p24 antibodies tested in this study, p24(c)Ab and p24(d)Ab, employed as coating and detection probes for a commercial ELISA kit (Dia.Pro Diagnostic Bioprobes, Italy), respectively, provided different responses. The p24(d)Ab showed a more pronounced increase of reflectivity indicating a larger amount of p24 binding to the spots.
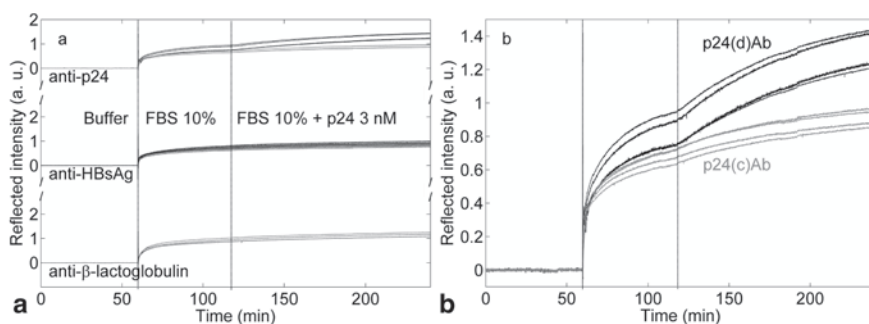
Fig. 3.2 Detection of p24 in serum. **a** The increase of reflectivity of the spots targeting p24(d)Ab (*upper black curves*), p24(c)Ab (*upper gray curves*), HBsAg (*middle curves*) and β–lactoglobulin (*lower curves*) was measured while fetal bovine serum and p24 were sequentially added in cuvette at the time indicated by the vertical lines. **b** Close-up of the p24 data of panel a.
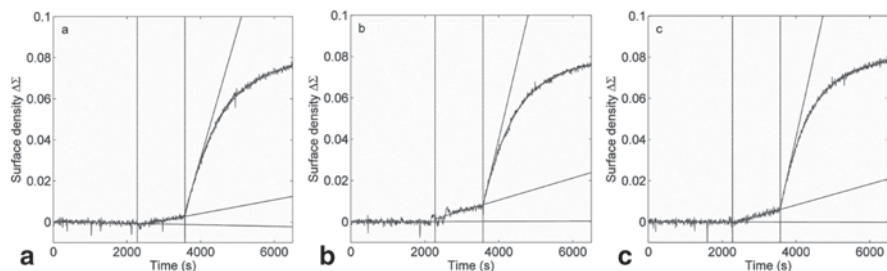
Fig. 3.3 Quantification of p24 concentration in serum. The p24 antigen was added to a concentration of 0.48 nM, followed by a second addition corresponding to a concentration in cuvette of 7.35 nM. The times of additions are represented by the vertical lines. The gray solid lines represent the slope of the signal curves in the proximity of the additions.

3.3.2   A Fast Assay Procedure

An unknown target concentration can be determined comparing the initial slope of the signal with that successively measured from the same spot after the addition of a standard sample with known target concentration. Figure 3.3 reports the signal measured from three different spots of p24(d)Ab in terms of surface density of antigen $\Delta\Sigma = (u(t)/u_0 - 1)^{1/2}$, where $u(t)$ is the spot brightness measured as a function of the time t and u_0 is the brightness of the bare prism surface. After the addition of FBS 1:10 and the acquisition of a steady baseline, p24 antigen was added to a concentration of about 0.5 nM, followed after half an hour by a second addition corresponding to a much higher concentration in cuvette. The ratio of the initial slopes of $\Delta\Sigma$ calculated for the three spots was 16.8, 14.4, and 15.9 for the data in Fig. 3.3a, b and c, respectively, thus in agreement within an error of 10 % with the value of 15.3 obtained as the ratio of the corresponding target concentrations.

3.4   Conclusions

Despite the slightly different non-specific responses of the spots to the addition of serum, the reported experiments show that the increase of reflectivity due to the binding of p24 is very similar for each species of antibody, hence demonstrating a limited intra-chip variability, corresponding to an error on the estimate of the target concentration of about 10 %.

References

1. F. Giavazzi, M. Salina, E. Ceccarello, A. Ilacqua, F. Damin, L. Sola, M. Chiari, B. Chini, R. Cerbino, T. Bellini, M. Buscaglia. A fast and simple label-free immunoassay based on a smartphone. Biosens. Bioelectron. **58**, 395–402 (2014)
2. F. Giavazzi, M. Salina, R. Cerbino, M. Bassi, D. Prosperi, E. Ceccarello, F. Damin, L. Sola, M. Rusnati, M. Chiari, B. Chini, T. Bellini, M. Buscaglia. Multispot, label-free biodetection at a phantom plastic–water interface. Proc Natl Acad Sci USA. **110** (23), 9350–9355 (2013)
3. M. Cretich, G. Pirri, F. Damin, I. Solinas, M. Chiari. A new polymeric coating for protein microarrays. Anal. Biochem. **332** (1), 67–74 (2004)

Chapter 4
Characterization of Bacilli Spores by Surface-Enhanced Raman Spectroscopy, a Fast and Reliable Technique for Early Warning of Biological Threats

Salvatore Almaviva, Antonia Lai, Valeria Spizzichino, Lorella Addari, Stefano Lecci, Alessandro Rufoloni and Antonio Palucci

It is demonstrated that Raman Spectroscopy is a fast and sensitive tool for the detection and classification of molecular species. The vibrational spectrum inherently serves as fingerprint of the chemical composition of each sample a thus makes identification and early warning of threats possible. Also microorganisms in areas susceptible to bacterial contamination can be sensed. However, to increase the sensitivity and selectivity of the technique various solutions have been studied such as Resonant Raman Spectroscopy or Surface-Enhanced Raman Spectroscopy (SERS). In this work we present our results on the application of the SERS technique for the characterization of *Bacillus atrophaeus* spores, a biological and genetic simulant of the deadly bacterium *Bacillus anthracis,* already used in terroristic attacks in 2001 against U.S. media and government offices causing the death of five people and the infection of other 22. This work is part of the RAMBO project (Rapid Air particle Monitoring against Biological threats) whose ultimate goal is the development of an advanced sensor with high performances, capable of detecting few spores or bacilli of dangerous species with good selectivity and reliability so as to be used as an early warning sensor. In this context, the SERS technique allows to recognize the characteristics vibrational bands of the spores with a scan duration of only few seconds, on amounts of few tenths of spores or less, demonstrating how it can be considered an effective and fast technique for early warning of biological threats as it has been considered in the RAMBO project.

4.1   Introduction

Recent accidental and terroristic events have, once again, demonstrated as bioagents can easily spread through the population: they can be transmitted by aerosol, via the water or the food supply, or by person-to-person contact. *Bacillus anthracis*

S. Almaviva (✉) · A. Lai · V. Spizzichino · L. Addari · S. Lecci · A. Rufoloni · A. Palucci
ENEA, UTAPRAD-DIM, VIA Enrico Fermi, 45 00044 Frascati, Italy
e-mail: salvatore.almaviva@enea.it

| Mag = 20.00 K X | 1 μm | EHT = 20.00 kV | Signal A = InLens | ENEA | Date :19 Nov 2013 |
| | | WD = 3.4 mm | Aperture Size = 20.00 μm | C. R. FRASCATI | Time :11:23:31 |
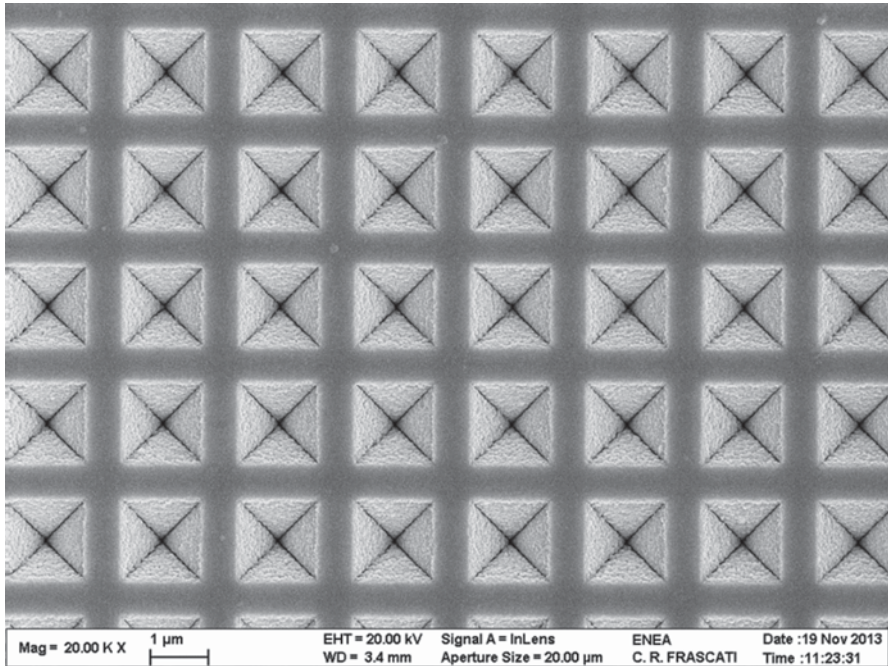
Fig. 4.1 SEM image of the SERS sensor

is the pathogen of a dangerous bacterial infection (Anthrax) that evolves when the spores are inhaled and, after germination, the bacteria release the virulence factors (i.e exo-toxins). A large number of deaths have been caused by this pathogen which started from the accident at a weapon facility in USSR in 1979, to the terroristic act of a Japanese religious sect in Tokyo in 1994, to the delivery of the same bioagent by mail to U.S. media and government offices in 2001.

To quickly identify these threats Raman spectroscopy has recently attracted a growing interest due to its high capability in the identification of molecular species. Sensitivity is an issue but much of this has been addressed by using enhancing techniques such as Surface Enhanced Raman Spectroscopy (SERS) [1]. Despite the mechanisms causing the SERS enhancement are not yet completely clear, it is well known that the intensity of the Raman signal gets increased by several orders of magnitude [1].

In these framework, the RAMBO project aims at classifying and identifying biological threats, i.e. anthrax, by two sensing techniques: SERS and Polymerase Chain Reaction [2], working in series in a microfluidic chip. RAMBO aims at developing an advanced sensor with high performances as good selectivity, rapid response time (<45 min), portability and high sensitivity (towards the one spore limit).
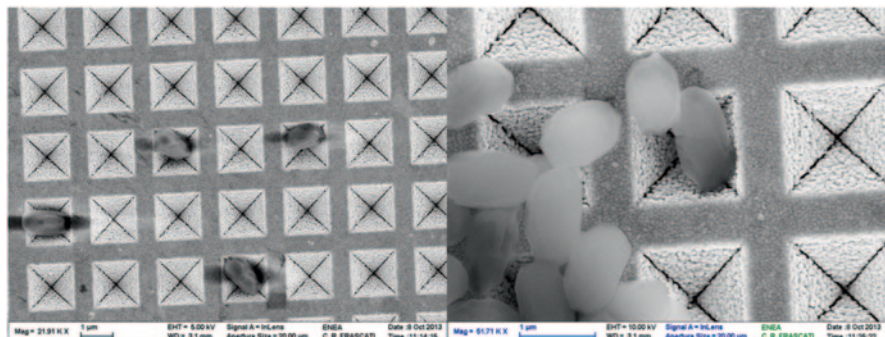
Fig. 4.2 SEM images of *Bacillus atrophaeus* spores on the klarite SERS sensor

4.2   Instrumentation and SERS Sensor.

An integrated table-top microscope-based Raman system [3] was used. The sampling laser, emitting at 785 nm (linewidth <0.3 nm), with 150 mW power is focused on the sample giving a laser spot of about 35–40 μm diameter. SERS sensors (Klarite®, Renishaw Diagnostics inc.) are composed of regular arrays of inverted pyramidal pits realized depositing a sputtered gold layer on a silicon substrate with an ordered nanostructure produced by electron beam lithography [4]. The regularity of the nanostructure guarantees a uniform enhancement of the weak Raman signal over the whole excited area. The full chip active area is 4×4 mm; each pit has an aperture of 1.5×1.5 μm and a total pitch size (aperture + distance to next microcavity) of 2 μm. The cavity depth is 1.06 μm. In Fig. 4.1 a Scanning Electron Microscope (SEM) image of a portion of the sensor:

4.3   Sample Preparation and Measurement.

Due to the level of danger of the *B. anthracis*, endospores of *Bacillus atrophaeus* var. *globigii* (ATCC 9372) were used as a simulant. This bacteria are generally utilized because they are phylogenetically similar between them [5]. Before being sampled, spores were diluted to a concentration of 10^4 CFU/ml. Then, a drop of 10 μl was deposited on the SERS sensor. Figure 4.2 shows a SEM image of some spores after deposition on the SERS sensor.

The spores appeared singly dispersed on the SERS sensor or clusterized in group of some tenths (Fig. 4.2) and it was possible to carry out the measures. A clear spectrum was obtained with an acquisition time of 10 s. A lot of spectral features have been observed and recognized from literature [6], as shown in Fig. 4.3, demonstrating the high sensitivity of the technique. These features are mainly due to dipicolinic acid, (2, 6-pyridinedicarboxylic acid; CaDPA) [7] that represents one of the major constituents of spores [7].

Molecular vibration	Raman shift (cm⁻¹)
Pyridine ring vibration (1)	≈ 660
C-COO⁻ stretching	≈ 820
Pyridine ring vibration (2)	≈ 1015
Symm – COO⁻ stretching	≈ 1394
Pyridine ring vibration (3)	≈ 1445
Asymm – COO⁻ stretching	≈ 1579
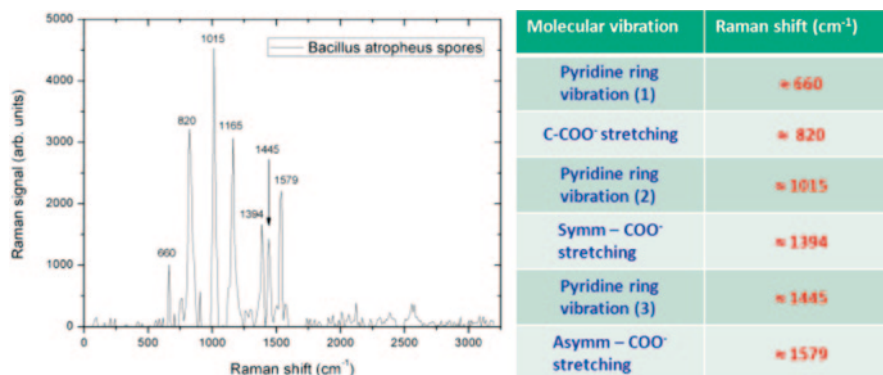
Fig. 4.3 SERS spectrum of *Bacillus atrophaeus* spores and band assignments

4.4   Conclusions

As part of the RAMBO project we performed SERS measurements on *Bacillus atrophaeus* spores, genetically similar to the deadly *Bacillus anthracis* to verify the high sensitivity of the technique even on few spores. The SERS spectra exhibited a satisfactory S/N ratio to identify the main spectral features that, compared with the results reported in literature, have been assigned to CaDPA. Spectra were obtained with only 10 s exposure, showing how SERS appears promising as a fast and reliable technique for early warning of biological threats.

References

1. E. Le Ru, P. Etchegoin, Principles of Surface-Enhanced Raman Spectroscopy and related plasmonic effects, (Elsevier, Amsterdam, 2009)
2. J. M. S. Bartlett, D. Stirling, A Short History of the Polymerase Chain Reaction. PCR Protoc. 226. 3–6 (2003). doi:10.1385/1-59259-384-4:3
3. S. Almaviva, S. Botti, L. Cantarini, R. Fantoni, S. Lecci, A. Palucci, A. Puiu, A. Rufoloni, Ultrasensitive RDX detection with commercial SERS substrates. J. Raman Spectrosc. 45, 41–46 (2014). doi: 10.1002/jrs.4413
4. T. A. Alexander, D. M. Le, Characterization of a commercialized SERS-active substrate and its application to the identification of intact *Bacillus* endospores. Appl. Opt. 46(18), 3878–3890 (2007)
5. C. Ash, J. A. E. Farrow, S. Wallbanks, M. D. Collins, Phylogenetic heterogeneity of the genus *Bacillus* revealed by comparative analysis of small subunit-ribosomal RNA sequences. Lett. Appl. Microbiolo. 13, 202–206 (1991)
6. J. K. De Gelder, P. Scheldeman, K. Leus, M. Heyndrickx, P. Vandenabeele, L. Moens, P. De Vos, Raman spectroscopic study of bacterial endospores. Anal. Bioanal. Chem. 389, 2143–2151 (2007). doi:10.1007/s00216-007-1616-1
7. P. Setlow, Spores of Bacillus subtilis: their resistance to and killing by radiation, heat and chemicals. J. Appl. Microbiol. 101, 514–525 (2006)

Chapter 5
Development of a Novel Snom Probe for in Liquid Biological Samples

F. Armani, A. Boscolo, M. Bressanutti, M. Dalle Feste, B. Piuzzi, A. De Vecchi, E. Viviani and M. Zweyer

This work is focused on the study and implementation of a novel method for the development of probes for Scanning Near-field Optical Microscopy (SNOM). The proposed approach is based on the mechanical impedance matching between the optical fiber tip and the resonating tuning fork. This methodology allowed an increase of the quality factor of the piezoelectric resonator used as atomic force transducer in the SNOM probe, thus increasing its overall sensitivity. This kind of probes are often used on biological soft samples in liquid. The presence of water medium has a strong dumping effect on probe sensitivity. Experimental validation of the proposed methodology showed an increase of robustness of SNOM probes also for in liquid samples

5.1 Introduction

Scanning Near Field Optical Microscopy (SNOM) is a branch of scanning probe techniques, which is based on the double interaction atomic force and light-tunneling effect. SNOM is gaining interest among other well consolidated techniques as SEM, AFM and TEM [1]. In particular SNOM is characterized by its unique capability to detect structures, through the near-field optical interaction up to 50 nm and by a low impact on the specimen, comparable or even better than standard

F. Armani (✉) · A. Boscolo · M. Bressanutti · M. Dalle Feste · B. Piuzzi · A. De Vecchi · E. Viviani
Department of Engineering and Architecture, APL laboratory, Trieste University, Trieste, Italy
e-mail: FRANCESCO.ARMANI@phd.units.it

A. Boscolo
e-mail: boscolo@units.it

E. Viviani
e-mail: EMANUELE.VIVIANI@studenti.units.it

M. Zweyer
Clinical Department of Medical, Surgical and Health Sciences, Trieste University, Trieste, Italy

Table 5.1 Performance comparison of SNOM probes built with different optimizations

Fiber layout	Quality Factor			
	Packaged quartz	Opened quartz	Quartz with fiber, in air	Quartz with fiber, in water
Standard	20,000	15,000	3000	500
APL Layout	20,000	15,000	4500	1800

AFM techniques [1, 2]. SNOM microscopy can be used with soft samples as it is characterized by low complexity in preparing samples, is less invasive and shows higher surface topographic resolution respect to conventional optical and confocal microscopes.

A SNOM probe is constituted of a primary and a secondary transducer. An optical fiber tip allows the near field interaction with the specimen while a second transducer exploits some electro-mechanical interaction to detect the weak atomic forces that occur between the tip and the surface [2].

As other emerging technologies, SNOM still presents issues related to imaging repeatability of in liquid samples. That is, the Q value of the probe, which is an important indicator of the sensitivity performance, abruptly decrease when the fiber is dived in the liquid cell [3, 4].

The performance enhancement of SNOM probes has been achieved through the study and complex activity of analysis, modeling and development of secondary transducers and related electronics, to meet the requirements of accuracy and repeatability necessary to bring in liquid SNOM microscopy to a high level of confidence.

5.2 Optimization

To optimize the SNOM probe, an electromechanical model of the resonator has been implemented on a commercial multiphysics finite element simulator (Comsol Multiphysics) which has been tuned using experimental data. This had permitted the identification of the zero-strain axis of the tuning fork, the zone with less strain during arm oscillation, and thereby determine the bonding area in which the resonator is less susceptible to fiber gluing with a consequential improvement of the Q factor (Table 5.1).

The SNOM probe has been characterized at different conditions of immersion in water and optical fiber layout using a HP4192A commercial electrical impedance analyzer. Secondly it has been mounted on a commercial SNOM microscope (TriA-SNOM by A.P.E. Research) and characterized as a force transducer to assess its sensitivity both in air and in water.
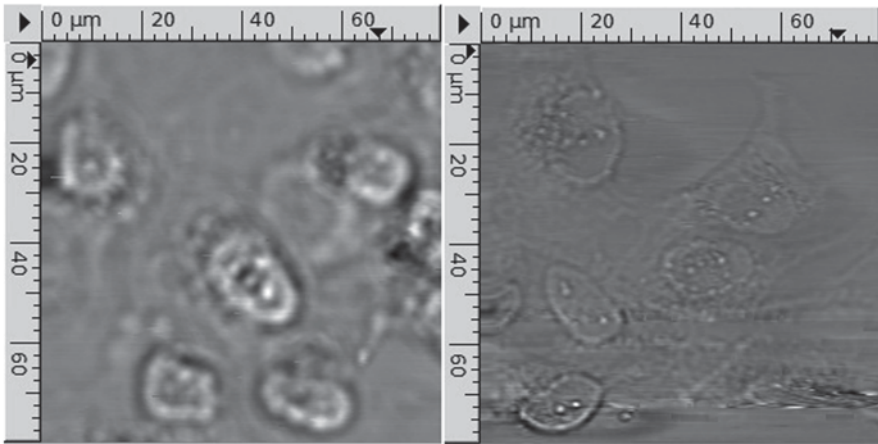
Fig. 5.1 Reflective near field (*left*) and transmission far field (*right*) of a gently bonded mesothelium in physiological solution

5.3 Characterization

The probe has then been tested with different samples as a brass plate, a strong fixed cell sample and a soft fixed one. Topographic, transmission and reflective optical images have been acquired (Fig. 5.1). SNOM probes metrological characterization was then performed using as reference a certified secondary standard. This was a Micromasch TGZ02, a silicon grating used for the characterization of SPM systems. Results (Figs. 5.2 and 5.3) has confirmed that the resolution of this probe is compatible with SPM probe standards; moreover it can perform with similar sensitivity both in air and in liquid.

5.4 Conclusions

The proposed work showed that an in depth physical modeling of SNOM probes is essential to optimize their performance. The use of a typical electronic approach, such as impedance matching, has been found to be very effective also when applied in a mechanical context. The use of the quality factor as an indicator of probe sensitivity is a good starting point for probes performance optimization.

The metrological characterization confirmed an improvement of probe sensitivity on a grating standard, both in air and in water. This increase in sensitivity is a promising achievement for the acquisition of high quality SNOM images for in liquid biological samples and gently fixed samples, which are usually destroyed by conventional scanning probes.

Fig. 5.2 Topographic image of a TGZ02 grating standard (*top*) and related depth profile (*bottom*)
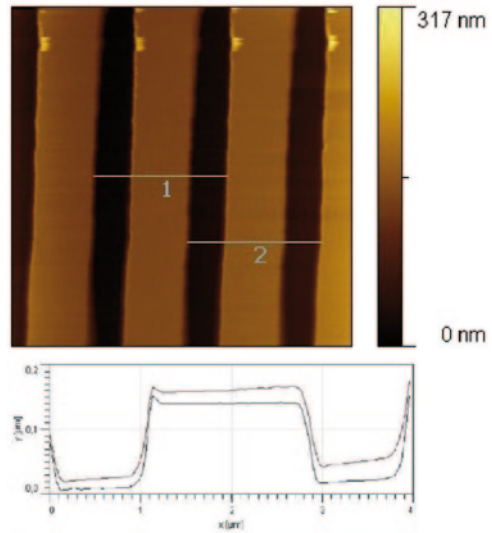
Fig. 5.3 TGZ02 grating standard in water images: topographical (*top*) and optical (*bottom*). This was realized in near field reflective mode with a 532 nm laser source
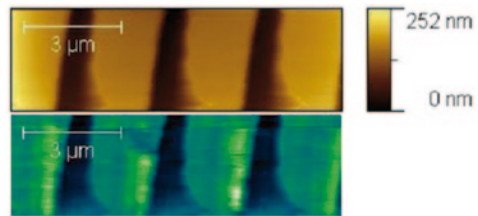
References

1. M. Zweyer, B. Troian, V. Spreafico, S. Prato, "SNOM on cell thin sections: Observation of Jurkat and MDAMB453 cells", Journal of Microscopy, 229, pp. 440–446, 2008.
2. R. Brunner, A. Bietsch, O. Hollricher, O. Marti, "Distance control in near-field optical microscopy with piezoelectrical shear-force detection suitable for imaging in liquids", Review of Scientific Instruments, 68 (4), pp. 1769–1772,1997.
3. W.H. Rensen, N.F. Van Hulst, A.G. Ruiter, P.E. West, "Atomic steps with tuning-fork-based noncontact atomic force microscopy", Applied Physics Letters,75, pp. 1640–1642, 1990.
4. F.J. Giessibl, "Atomic resolution on Si(111)-(7×7) by noncontact atomic force microscopy with a force sensor based on a quartz tuning fork", Applied Physics Letters, 76 (11), pp. 1470–1472, 2000.

Chapter 6
A Point-of-Care Device for Immunosuppressants Monitoring in Transplanted Patients

C. Berrettoni, C. Trono, S. Tombelli, A. Giannetti, S. Berneschi, F. Baldini, I. A. Grimaldi, G. Persichetti, G. Testa, R. Bernini, G. Porro and C. Gärtner

In the hospital Intensive Care Units (ICU) there is an even greater demand by the physicians for the continuous immunosuppressant drug monitoring in the transplanted patient therapy, in order to avoid different risks and diseases which may occur as result of some drug dosage related effect, such the rejection crisis or sepsis. Here we present a novel design of a point of care testing (POCT) device for the drug dose—adjustment in this kind of patients. The working principle of the device will be discussed. Preliminary tests on the immunoassay strategies for immunosuppressant drugs recognition such as on the optical chip realization and characterization are reported.

C. Berrettoni (✉)
Information Engineering and Mathematics Department, University of Siena, San Niccolò, Via Roma 56, 53100 Siena, Italy
e-mail: c.berrettoni@ifac.cnr.it

C. Berrettoni · C. Trono · S. Tombelli · A. Giannetti · S. Berneschi · F. Baldini
IFAC-CNR, "Nello Carrara" Institute of Applied Physics, Via Madonna del Piano 10, 50019 Sesto Fiorentino, Italy

I. A. Grimaldi · G. Persichetti · G. Testa · R. Bernini
IREA-CNR, Institute for Electromagnetic Sensing of the Environment, Via Diocleziano 328, 80124 Napoli, Italy

G. Porro
Datamed Srl, Via Achille Grandi 4/6, 20068 Peschiera Borromeo, Italy

C. Gärtner
Microfluidic ChipShop GmbH, Stockholmer Str. 20, 07747 Jena, Germany

6.1   Introduction

Therapeutic drug monitoring (TDM) in transplanted patients is one of the crucial aspects in order to define the correct drug dosage of immunosuppressants and make safe the patient health from some possible diseases. In fact, these drugs generally show a narrow therapeutic window. This means that a minimum increase of their concentration over a threshold value in the blood may cause a deficit response of the patient immune system, with the following risk to constrict an acute and danger-ous whole-body inflammation, like sepsis. On the contrary, an immunosuppressant under dosage may favor the body immune system response and the related rejection crisis. Hence, a fast and reliable response in the identification of the right dosage of these drugs is firmly desirable. For this purpose, different strategies are commonly adopted in the hospitals ICU. The standard TDM is based on the measurement of the so called trough concentration (i.e.: the drug plasma level measured just before the next dose) by use of analytical procedures such as laboratory immunoassays, high pressure liquid chromatography (HPLC) or liquid chromatography combined with mass spectroscopy (LCMS). The main drawback of these methods is represented by using one blood sample per dosing interval. Otherwise, recent clinical studies have demonstrated that multiple and sparse sampling, based on the assessment of the area under the concentration curve (AUC) of the drugs, offers a substantial improvement for the patient outcome [1]. In this field, better results will be expected from in-time continuous measurement of the AUC rather than a discrete estimation of it. For this reason, a novel POCT device, based on in–time and in–line immunosuppressant monitoring, can be a valuable tool for physicians for the dosage adjustment imme-diately after the transplantation [2].

6.2   The Design of the New TDM—POCT Chip

The device is an integrated multifunctional chip connected to the patient arm by an intravascular microdialysis catheter. This solution is minimally invasive for the patient and guarantees a better safety for his health. The chip is designed to be close to the patient and guarantees 48 hours online measurements, with a repetition rate of around 10–15 min between two consecutive sampling. It is constituted by dif-ferent parts: (i) a microfluidic circuit able to mix the dialysate, coming out from the catheter and containing the analytes of interest, with the chemical reagents for the immunoassays implementation; (ii) an optical device, which converts the con-centration changes of the analytes in luminescent signals; (iii) an electronic part, for driving and data elaboration. Preliminary results on the development both of a biochemical assay and of the optical chip are presented.

6.3   Results

6.3.1   Biochemical Assay

From a chemical point of view, among all the immunosuppressants of interest, we are focusing our attention on tacrolimus and a competitive heterogeneous assay was selected as possible strategy for its detection [3]. Tacrolimus and anti-tacrolimus monoclonal antibody from mouse (IgM, clone FK1) were purchased from Santa Cruz Biotechnology (Santa Cruz, CA). Donkey anti-mouse IgM labelled with Alexa Fluor® 647 (Jackson Immunoresearch, West Grove, PA) was used as secondary antibody. Tacrolimus-COOH derivative was kindly provided by Prof. G. Orellana (Universidad Complutense de Madrid, Spain). Prionex® Calbiochem was purchased from Merck Millipore (Darmstadt, Germany). The following optimized protocol for tacrolimus assay was adopted: (i) immobilization of a tacrolimus derivative (Tacrolimus-COOH) onto $-NH_2$ functionalized microfluidic titer plates in Topas (Microfluidic ChipShop GmbH, Jena, Deutschland); (ii) interaction with anti-tacrolimus antibody incubated with different concentrations of tacrolimus and (iii) interaction with anti-IgM antibody labeled with alexa-fluor 647 for fluorescence detection. The fluorescent layer was excited by means of a laser diode with emission at 635 nm (PicoQuant, LDH-P-C-635B), and the emitted fluorescence was collected by a plastic optical fiber (diameter 1 mm) (oriented at 45° with respect to the direction of the excitation beam) connected to a spectrometer (Andor Shamrock 303). The excitation and fluorescence light were filtered with a band-pass and a high-pass optical filter, respectively. By the optimization of the blocking agent Prionex and the anti-tacrolimus antibody concentrations, a limit of detection for tacrolimus of 0.15 ng/mL was achieved.

6.3.2   Optical Chip

The optical chip prototype has a heterogeneous structure, as reported in Fig. 6.1. It is comprised by two polymeric parts, with different refractive indexes (R.I.), bonded each other by an adhesive tape (ChipShop pressure sensitive tape; thickness: 140 μm; R.I.: 1.48 at 635 nm) in which a set of fluidics channels (length: 1 cm; width: 1 mm) was previously fabricated by a mechanical cutting procedure. The bottom part of the chip is a ZEONOR® foil (thickness: 188 μm; R.I.: 1.53 at 635 nm), while the upper part is represented by a PMMA slide (thickness: 1 mm; R.I.: 1.49 at 635 nm). The working principle of the device is based on total internal reflection fluorescence (TIRF) [4]. The light, coming from a He–Ne laser source (wavelength emission around 633 nm), is coupled by a prism into the ZEONOR® foil and propagates all along it by total internal reflection (TIR) ($n_{ZEONOR} > n_{TAPE}$). In such a way, the guided light is able to excite—by an evanescent field tail—the fluorescence coming from a particular fluorophore which labels the antibody anti-
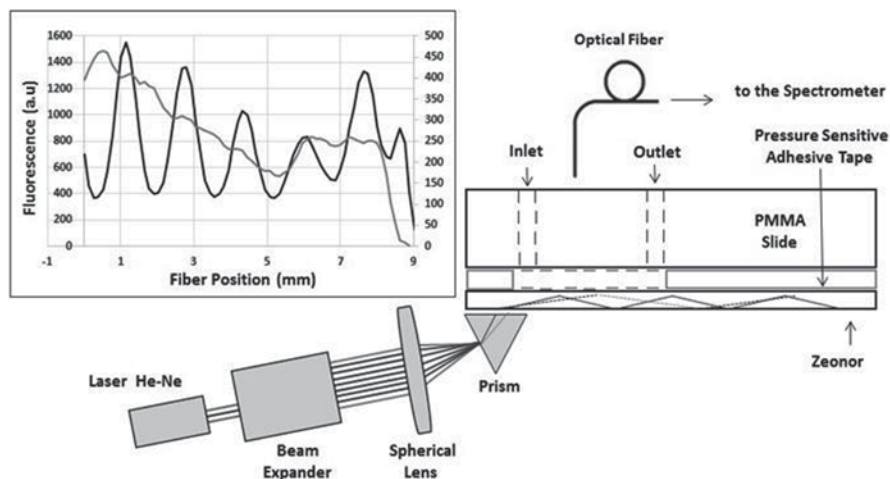
Fig. 6.1 Schetch of the optical set-up used to collect the fluorescence signal. In the inset, the collected fluorescence signal without (*black line*) and with (*gray line*) beam expander

analyte to be detected (i.e.: tacrolimus), when the specific biochemical binding to the same analyte derivative occurs on the bottom of the fluidic channels. Finally, due to fluorescence anisotropy [5], the fluorescent signal is driven to the PMMA cover part of the chip with the detection performed on the opposite side respect to the channels and all along their length. Preliminary fluorescence detection tests were performed on this chip. For this purpose a fluorescent layer, based on streptavidin labelled with ATTO647N, was excited into the fluidic channels. The emitted fluorescence was collected by an optical fiber (able to scan each channel for all its length) and connected to a spectrometer (in the final chip amorphous silicon photodetectors will be located along the whole length of the microchannel). The behavior of the fluorescence signal is reported in the inset of Fig. 6.1 with and without beam expander, respectively. The presence of a beam expander, before the focusing lens in the set-up, produces a more uniform distribution for the measured fluorescence signal (the gray line in the inset) due to the increase of the light beam diameter [6] and to the consequent excitation of more propagating modes.

6.4 Conclusions & Perspectives

The design of a novel TDM-POCT biochip for immunosuppressants detection in transplanted patients was presented. Preliminary tests on the biochemical assay and optical chip development were performed. The future steps will include: (i) the investigation of other bonding procedures; (ii) the integration of fluorescent magnetic nanoparticles and magnetic traps in the chip to enhance the luminescence sensitivity; (iii) the integration with the photodiodes.

References

1. G. R. Morris, G. R. Russ *et al.*, Ther. Drug. Monit. **24**, 479–486 (2002).
2. C. Berrettoni, C. Trono *et al.*, Proc. SPIE **8976**, 89760P (2014).
3. E. Fu, K. E. Nelson *et al.*, Anal. Chem. **81**, 3407–3413 (2009).
4. H. P. Lehr, A. Brandenburg, G. Sulz, Sens. Actuators B **92**, 303–314 (2003).
5. L. Polerecky´, J. Hamrle, and Brian D. MacCraith, Appl. Opt. **39**, 3968–3977 (2000).
6. A. Brandenburg, F. Curdt *et al.*, Sensors and Actuators B **139**, 245–251 (2009).

Chapter 7
Optical Detection of Surfactants by Means of Reflective Phantom Interface Method

R. Lanfranco, F. Giavazzi, M. Salina, E. Di Nicolò and M. Buscaglia

Surfactants are among the most relevant organic pollutants of water with threatening potential for the aquatic environment. The most common and widespread techniques to detect surfactants in water samples are typically expensive and time consuming. In this context, we propose a new kind of optical sensor, based on an amorphous fluorinated plastic iso-refractive to water and, therefore, barely visible in aqueous solutions. When a thin molecular layer with a different refractive index adsorbs at the interface, the intensity of reflected or scattered light markedly increases, hence enabling a simple and real-time detection. We investigated the interaction between the plastic iso-refractive to water and a non-ionic surfactant (Tween 20) by measuring the intensity of light reflected by a planar interface as a function of time after the addition of different concentrations of surfactant. This detection scheme has been also tested with natural water samples taken from the Lambro river across the city of Milan.

7.1 Introduction

Thanks to their amphiphilic nature, surfactants are massively used in many products, like soaps, detergents and wetting agents. More than 90 % of all surfactants are commonly removed in waste-water treatment plants, however trace amounts may

R. Lanfranco (✉) · F. Giavazzi · M. Buscaglia
Dipartimento di Biotecnologie Mediche e Medicina Traslazionale, Università degli Studi di Milano, via F.lli Cervi, 93, 20090 Segrate, MI, Italy
e-mail: roberta.lanfranco@unimi.it

M. Buscaglia
e-mail: marco.buscaglia@unimi.it

E. Di Nicolò
Solvay Specialty Polymers, Research and Development Center, Viale Lombardia, 20, 20021 Bollate, MI, Italy

M. Salina
Proxentia S.r.l., 20135 Milano, Italy

be released into the environment [1]. The common techniques to track down these polluting molecules in surface water are typically time consuming and expensive [2]. In this context, we propose a simple, low-cost and real time surfactant detection method, called Reflective Phantom Interface (RPI). The RPI method was previously used and applied to develop immunoassays for specific recognition and quantification of molecules in aqueous samples [3]. This technique is based on a fluorinated and amorphous plastic, Hyflon AD ®, having a refractive index $n_h = 1.327$, very close to that of water [3–5]. Accordingly, when in contact with water the optical reflectivity of a surface of Hyflon AD® is very small, less than 10^{-5}. In this configuration, when a thin molecular layer with a significantly different refractive index adsorbs on the surface, the reflectivity markedly increases respect to that of the bare surface. Through to the thin film reflection theory, this optical signal can be converted in an effective thickness of the adsorbed molecular layer.

7.2   Materials and Methods

Hyflon AD ® (trademark of Solvay Specialty Polymers, Bollate, Italy) is a copolymer of polytetrafluoroethylene, having the form of a transparent, hydrophobic solid with low refractive index. This material was shaped in the form of a right angle prism and placed inside a common 1-cm cuvette. The diagonal surface of the prism was illuminated by a He-Ne laser ($\lambda = 632.8$ nm) and the reflected light was measured by a photodiode. The measurements were performed adding increasing concentrations of surfactant into the cuvette, while the solution was continuously mixed by a magnetic stirrer.

Surfactants, driven by hydrophobic force, spontaneously adsorb on the plastic surface, causing an increase of reflectivity. This adsorption can be modeled by a simple Langmuir behavior. The fraction of occupied binding sites ϕ at equilibrium depends on the surfactant concentration c as $\phi = (1 + C_{eq}/c)^{-1}$, where C_{eq} is the concentration at which half of the binding sites are occupied. Using the RPI method, ϕ can be estimated from the reflectivity of the plastic surface. In fact, the reflectivity R can be converted into an effective thickness h through the following relation [3]:

$$h = h_0 \sqrt{\frac{R}{R_0} - 1} \tag{1}$$

where R_0 is the surface reflectivity in water and h_0 is a parameter that depends on the experimental conditions. Following this model, we analyzed the adsorption of a non-ionic surfactant, polysorbate 20 (Tween 20, from Sigma-Aldrich) dissolved in MilliQ water. The relevant parameters describing the surfactant are shown in Table 7.1. Given the refractive index of Tween 20 and the angle of incidence of 45° a value of h_0 of 1.14 nm is obtained.

Table 7.1 Characteristics of surfactant Tween 20. The molecular mass and the density ρ are taken from the data sheet. Critical micelle concentration (*CMC*) is obtained from conductivity measurements and the refractive index is measured with an Abbe refractometer

Molecular mass (g/mol)	Density (g/mL)	CMC (µM)	Refractive index
1227.54	1.10	512	1.4685

Natural samples of Lambro river water, taken before and after it crosses the city of Milan, were also analyzed with the RPI method. Before the measurements, the samples were mildly centrifuged and then filtered.

7.3 Results and Discussion

Figure 7.1a reports a measurement with surfactant Tween 20: after each surfactant addition (dashed vertical lines) the reflectivity R increases. From the fit of the adsorption curves as a function of time, we extracted the asymptotic plateau values at each concentration, which are reported in the graph of Fig. 7.1b. These values represent the equilibrium condition and so they are expected to follow a Langmuir behavior. From the fit with the Langmuir isotherm equation, we extracted the concentration of half surface covering $C_{eq} = 1.58 \ 10^{-6} \pm 0.54 \ 10^{-6}$ M.

From the plateau of the Langmuir curve reported in Fig. 1.b, through equation (1) we obtained the maximum thickness of the adsorbed layer, $h_{max} = 1.01 \pm 0.04$ nm. This value is in agreement with the expected thickness of a surfactant monolayer, grown on a solid-liquid interface [2, 6]. From h_{max} we obtained the maximum surface density of adsorbed molecules, $\sigma_0 = h_{max} * \rho = 1.1$ ng/mm^2.
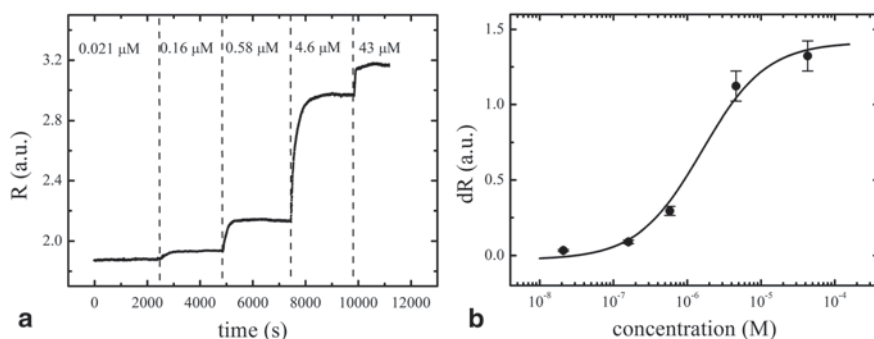
Fig. 7.1 Characterization of surfactant adsorption by Reflective Phantom Interface experiment. These data refer to non-ionic surfactant Tween 20. **a** In correspondence of the *dashed vertical lines*, increasing surfactant concentrations are added into the measuring cell (2.1×10^{-8} M, 1.6×10^{-7} M, 5.8×10^{-7} M, 4.6×10^{-6} M and 4.3×10^{-5} M, respectively). **b** The asymptotic value at equilibrium after each addition was fitted with a Langmuir Isotherm (*continuous curve*) in order to obtain the concentration of half surface covering $C_{eq.}$
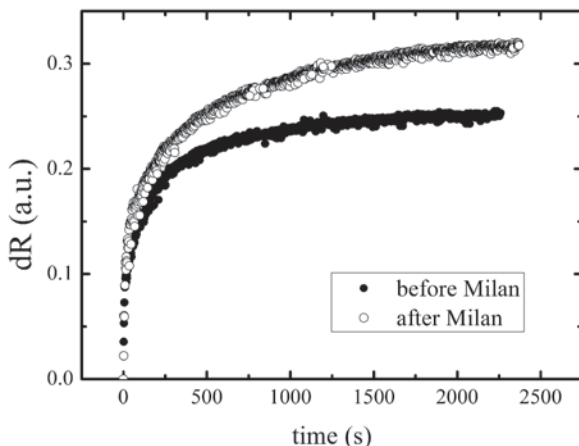
Fig. 7.2 Comparison between two samples of Lambro river water. In the sample taken *before Milan* (*full dots*) the adsorption on Hyflon AD ® prism is slower and the amplitude is smaller than the sample taken *after Milan* (*empty dots*)

Converting this value into number density, we find only 0.5 adsorbed molecules per nm^2, meaning that the surfactant layer is not dense and compact, but rather sparse and thin.

Adopting Tween 20's data as a reference, we analyzed two water samples taken from the Lambro river. Figure 7.2 shows how the reflectivity increases in these two cases. As expected, in the sample taken downstream of the city of Milan (empty dots) there were more self-adsorbing pollutants than in the one taken upstream (full dots). Moreover, comparing the plateau values and the characteristic growth times with the Tween 20 data, an estimation of the surfactant concentrations of the samples can be attempted, yielding about 0.4 µM for the sample before Milan and 0.7 µM for the sample after Milan.

7.4   Conclusions

In this work we used the RPI method to detect the spontaneous adsorption of surfactants at a barely visible water-plastic interface. In particular, we analyzed the affinity of a non-ionic surfactant to characterize the interaction with the plastic surface, extracting the half surface covering concentration C_{eq} and the surface density of binding sites σ_0. Moreover, we tested the RPI method with two natural river water samples, observing that after passing the city of Milan, the Lambro water became more polluted, as expected. This study demonstrates how the RPI method enables the real-time detection of surfactant with sensitivity down to about 10 nM.

References

1. World Health Organization, Linear alkylbenzenesulfates and related compounds; (Environmental Health Criteria 169, Geneve, 1996), 8.
2. S. Paria, K. C. Khilar, A review on experimental studies of surfactant adsorption at the hydrophilic solid–water interface Adv. Colloid. Interfac., 110 (3), pp 75–95, (2004)
3. F. Giavazzi, M. Salina, R. Cerbino, M. Bassi, D. Prosperi, E. Ceccarello, F. Damin, L. Sola, M. Rusnati, M. Chiari, B. Chini, T. Bellini, M. Buscaglia, Multispot, label-free biodetection at a phantom plastic–water interface PNAS USA 110 (23), pp 9350–9355, (2013)
4. A. Ghetta, D. Prosperi, F. Mantegazza, L. Panza, S. Riva, T. Bellini, Light scattered by model phantom bacteria reveals molecular interactions at their surface PNAS, 102, pp 15866–15870, (2005)
5. D. Prosperi, C. Morasso, F. Mantegazza, M. Buscaglia, L. Hough, T. Bellini, Phantom Nanoparticles as Probes of Biomolecular Interactions Small, 2, pp 1060–1067, (2006)
6. L. Shen, A. Guo, X. Zhu. Tween surfactants: adsorption, self-organization and protein resistance. Surf. Sci. 605, 494–499, (2011)

Chapter 8
Development of an Optical Sensing Strategy Based on Gold Nanoparticles Formation Driven by Polyphenols. Application to Food Samples

Flavio Della Pelle, Dario Compagnone, Michele Del Carlo, Diana Vilela, María Cristina González and Alberto Escarpa

In this work the basis for the development of two methods for evaluating the antioxidant capacity of food matrices were laid. One of the two methods involves the extraction of the phenolic fraction for the evaluation of the antioxidant capacity of polyphenols extract in aqueous solvent, while the other does not include a sample pre-treatment thus allowing an extraction free evaluation of the antioxidant capacity directly in the matrix. Both methods exploit the synthesis of gold nanoparticles (AuNPs), which present a diameter of a few tens of nm, via the reduction of chloroauric acid driven by the phenolic compounds. For the spectrophotometric reading, the absorption band of localized surface plasmon resonance (LSPR) that have produced AuNPs at 540 nm is used as analytical signal.

8.1 Introduction

Polyphenols play a key role in the maintenance of nutritional properties in the shelf life and in the definition of the characteristic of the organoleptic properties of olive oil [1] and other vegetables derived foods. Particularly the quality of foodstuff is strongly linked to its oxidative stability, being oxidative spoilage the main cause of its qualitative decay. As an example, among vegetable oils, extra virgin olive oil (EVOO) shows a higher resistance to oxidation due to its fatty acid composition, characterized by a high monounsaturated-to-polyunsaturated ratio and containing a large amount of compounds with antioxidant activity, being

F. D. Pelle (✉) · D. Compagnone · M. Del Carlo
Faculty of Bioscience and Technology for Food, Agriculture and Environment, University of Teramo, 64023 Teramo, Italy
e-mail: flaviod.p.86@hotmail.it

D. Vilela · M. C. González · A. Escarpa
Department of Analytical Chemistry, Physical Chemistry and Chemical Engineering, Faculty of Chemistry, University of Alcalá, 28871 Alcalá de Henares, Madrid, Spain

39

the majority polyphenols. Furthermore, among polyphenols, hydroxytyrosol and oleuropein derivatives have been tested in *in vitro* studies and have shown positive potential effects to prevent degenerative diseases [1, 2]. Currently, polyphenols derived by fruits and vegetables have been also recognized as potential nutraceutical compounds by food and pharmaceutical industries [3]. For this reasons, many different analytical approaches have been proposed to evaluate antioxidant activity and the total polyphenols content in food samples. Thanks to the unique properties of nanomaterials, they are widely used in various fields of analytical chemistry. In particular, gold nanoparticles (AuNPs) show high stability, unique optical properties and can be produced by various types of synthesis obtaining AuNPs with different diameter and being easily functionalizable with different molecules [4]. Scampicchio and his co-workers [5] were the first to introduce the idea of evaluating the antioxidant capacity of phenolics acids through the AuNP formation and growth. In this work, the ability of the polyphenols to reduce $HAuCl_4(III)$ to AuNPs(0) in aqueous and organic-aqueous solvent was demonstrated and the AuNPs optical absorption peak due to the localized surface plasmon resonance (LSPR) detected. More recently, Vilela and co-workers [6] have associated the AuNP formation driven by endogenous polyphenols in food samples to a sigmoidal function. In this work, two methods for the quantification of the antioxidant capacity are proposed. Both methods are based on the formation of gold nanoparticles mediated by endogenous polyphenols. For both methods, it was possible to obtain an antioxidant capacity index from AuNPs formation expressed as gallic equivalent antioxidant capacity (GEAC). The first method assesses the antioxidant capacity of polyphenols extracts in hydroalcoholic solvent. The second method assesses the antioxidant capacity of polyphenols, without requiring an extraction, in organic-aqueous solvent. The methods have been tested on different food samples including fruit and olive oil. In addition, we evaluated the influence of the non-polyphenolic compounds, with possible reducing power, present in the matrix.

8.2   Materials and Methods

8.2.1   Solid-Phase Extraction of the Phenolic Fraction

Commercially available octadecyl C18 cartridges (1 g, 6 mL) (International Sorbent Technology, UK) were used for the extraction of the phenolic fraction according to the following protocol: 1 g of olive oil was dissolved in 5 mL of hexane, and the obtained solution was loaded onto a column previously conditioned with 2×5 mL of methanol and 2×5 mL of hexane. The column was eluted with 2×5 mL of hexane to eliminate all the lipophilic fraction, and the retained polar compounds were recovered by eluting with 2×10 mL of methanol. Subsequently, the elute was placed in a conical flask and evaporated to dryness at room temperature (30 °C, 150 RPM) in a rotary evaporator. The extract was recovered with 0.5 ml of methanol and stored at −20 °C, in the dark.

8.2.2 Evaluation of the Antioxidant Capacity of Polyphenols Extract in Aqueous Solvent (Application to Olive Oil Extract)

AuNPs were obtained using the protocol described by Scampicchio et al. [5], modified according to Vilela et al. [6]. Phosphate buffer solution was used (pH 8.0; 1.0×10^{-2} mol L^{-1}) and then 10 μL of cetyltrimethylammonium chloride (8.0×10^{-1} mol L^{-1}), 25 μL of HAuCl4·3H$_2$O solution (2.0×10^{-2} mol L^{-1}), were added in the described order and finally different volumes of the standards or sample extract have been also added, reaching the final volume of 500 μL. Afterwards, the solution was stirred for 2 min and subsequently heated for 10 min at 45 °C in a water bath. Finally, the reaction was blocked using ice for 25 min. The absorbance was recorded between 400 and 800 nm. The evolution of the AuNP formation driven by polyphenols standards and extracts has been represented with a sigmoidal logistic curve (Eq. 8.1). In this curve the AuNP LSPR peak of absorbance (A_{540}) is a function of the standard/extracts polyphenol concentration (x).

$$A_{540} = \frac{A_{max}}{1 + e^{-kAuNPs\left(x - x_c^{50}\right)}} \qquad (8.1)$$

The two parameters exploited in this study are K_{AuNPs} and X_c^{50}. K_{AuNPs} is the slope of the sigmoidal curve and X_c^{50} is the concentration at which A_{540} reaches the half-value (the ratio $1/X_c^{50}$ was used, since it is directly proportional to the reducing power of the antioxidant compounds). The ratio K_{AuNPs}/X_c^{50} was also considered since the single parameter X_c^{50} and K_{AuNPs}, in some cases can only provide a partial information. For the EVOO extracts, an antioxidant index was calculated expressed as a function of gallic acid. The indexes were calculated by the ratio between the parameters (K_{sample}; $1/X_{c\ sample}^{50}$; $K_{sample}/X_{c\ sample}^{50}$) obtained from the sigmoidal curve of the extracts (were x = μL and y = A_{540}) and the respective parameters ($K_{Gal.Ac.}$; $1/X_{c\ Gal.Ac.}^{50}$; $K_{Gal.Ac.}/X_{c\ Gal.Ac.}^{50}$) obtained from the sigmoidal curve of gallic acid (were x = μg and y = A_{540}). In this way, three indexes expressed as gallic acid equivalent (GEAC) are obtained.

8.2.3 Evaluation of the Antioxidant Capacity Directly In the Matrix, Without Extraction (Application to Fruit Juices Samples)

AuNPs were formed, directly from the sample, in a organic-aqueous solution. Standard solutions or whole samples were dissolved in 240 μL of DMSO, the solution was stirred for 2 min. Subsequently 25 μL of HAuCl$_4$·3H$_2$O solution (2.0×10^{-2} mol L^{-1}), 10 of CTAC (8.0×10^{-1} mol L^{-1}) and phosphate buffer solution (pH 8.0; 1.0×10^{-2} mol L^{-1}) were added up to reach the final volume of 500 μL. After that, the solution
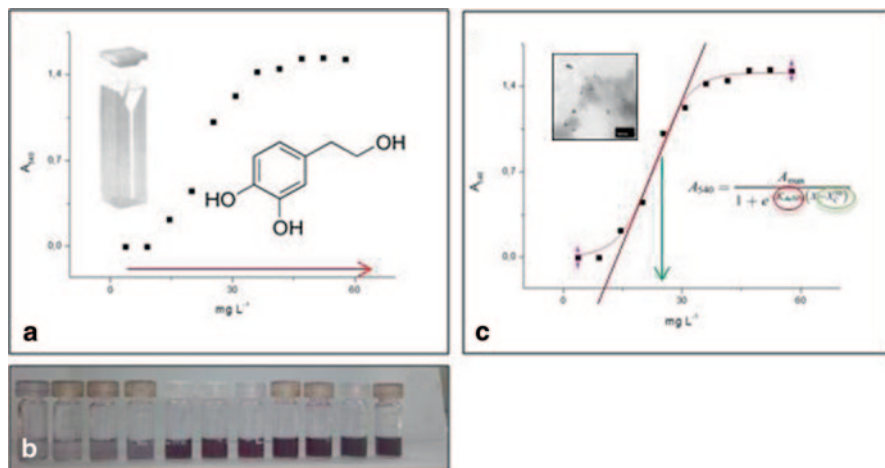
Fig. 8.1 a Points obtained by increasing the concentration of hydroxytyrosol and reading the absorbance at 540 nm. **b** The photograph shows the AuNPs formed with increasing concentrations of hydroxytirosol. **c** Sigmoidal curves obtained by increasing the concentrations of hydroxytyrosol and reading the absorbance at 540 nm. The inset TEM micrographs shows AuNPs formed with hydroxytyrosol. Inset it is also shown the sigmoidal formula from which are extracted parameters, used to calculate the antioxidant capacity

was stirred for 2 min and subsequently heated for 5 min at 45 °C in a water bath. Finally, the reaction was blocked using ice for 5 min. The absorbance was recorded between 400 and 800 nm. The antioxidant capacity quantification is performed with a calibration curve obtained with increasing concentrations of gallic acid.

8.3 Result and Discussion

In this work, two methods for the antioxidant capacity quantification are proposed. Both methods are based on the formation of gold nanoparticles mediated by polyphenols. The first method assesses the antioxidant capacity of polyphenols extract in *hydroalcoholic solvent.* The formation of AuNPs is described by a sigmoid curve (Fig. 8.1). The AuNPs absorbance signals (A_{540}) are dependent upon the concentration and type of the phenolic compounds (Figs. 8.1, 8.2, and 8.3).

Different parameters obtained from the sigmoidal curves employed for the antioxidant power evaluation of each polyphenol are proposed. The antioxidant capacity quantification of phenolic extracts is proposed as an antioxidant capacity index using the AuNPs formation (described by a sigmoid curve) as a function of a known standard, in this case, gallic acid equivalent antioxidant capacity (GEAC). A quantification of the antioxidant capacity (AuNPs GEAC index) of EVOO phenolic standards and extracts was performed. The best parameter for the evaluation of the antioxidant capacity is the K_{AuNPs}/X_c^{50}, this parameter is able to discriminate
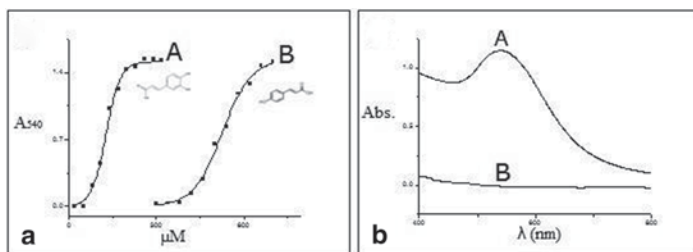
Fig. 8.2 a Sigmoidal curves obtained by increasing the concentration of polyphenols standards, reading the absorbance at 540 nm. Caffeic acid (*A*), p-coumaric acid (*B*). **b** AuNPs spectra formed with the same (140 μM) concentration of polyphenols standards. Caffeic acid (*A*), p-coumaric acid (*B*)
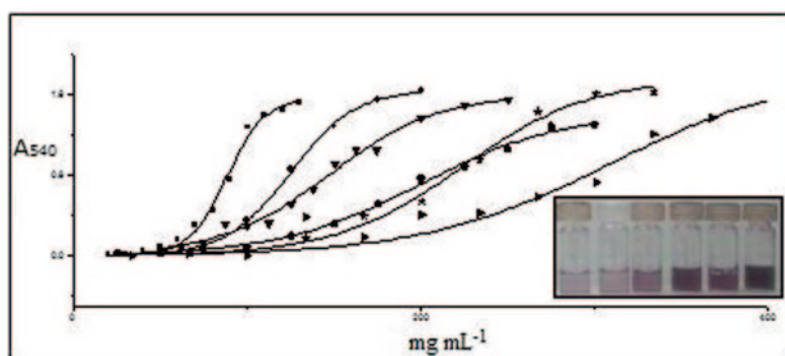
Fig. 8.3 Sigmoidal curves obtained by increasing the extract amount of six EVOO samples. The inset photograph shows the AuNPs formed with the six sample extracts, using the same concentration (140 mg mL^{-1})

sigmoids with similar slopes (K$_{AuNPs}$) and different X$_c^{50}$ and *vice versa*. GEAC (gallic equivalent antioxidant capacity expressed in mg mL^{-1}) indexes are calculated by the ratio between the average parameters obtained from the extracts with their respective average parameters obtained from gallic acid (standard compound).

The second method assesses the antioxidant capacity of polyphenols, without requiring an extraction, in *organic-aqueous solvent*. Again, also in this case, the AuNPs absorbance signals (A$_{540}$) are dependent upon the concentration and type of the phenolic compounds (Figs. 8.4, and 8.5). In this case the antioxidant capacity quantification is performed with a classical calibration curve obtained with increasing concentrations of gallic acid (Fig. 8.5).

Being an *in matrix* method, a study of the possible interfering compounds was carried out. This method is not affected by sugars content (Table 8.1) and neither by the presence of possible fruit juice interfering without significant loss of sensitivity (Fig. 8.4). A quantification of the antioxidant capacity (AuNPs GEAC index) of fruit juice phenolic standards and samples (Fig. 8.6) was performed. This method has proved to be usable for the antioxidant evaluation of fruit juice (apple, pear).
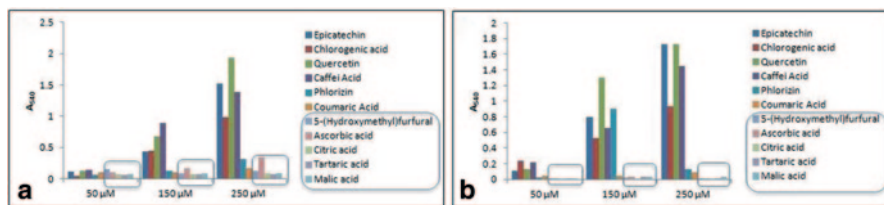
Fig. 8.4 AuNPs (absorbance at 540 nm) obtained by several typical fruit juices polyphenols standards and by possible interferences (highlighted ones). The AuNPs were formed with two methods: in hydroalcoholic solvent (**a**) and in organic-aqueous solvent (**b**)
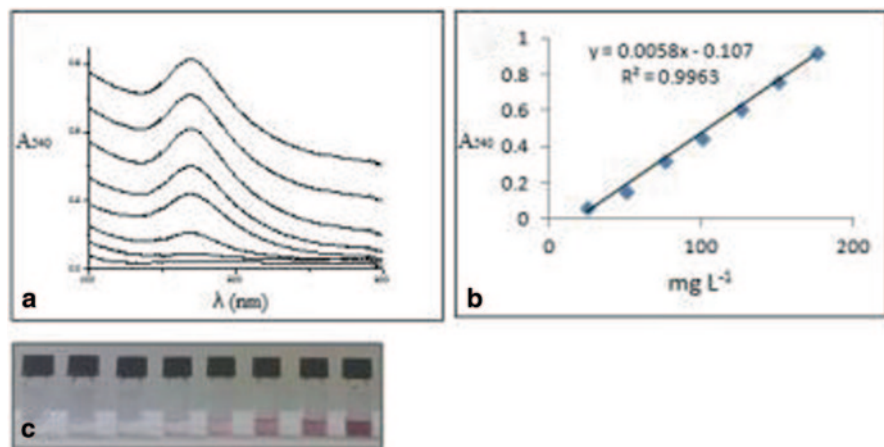
Fig. 8.5 **a** AuNPs spectra formed by increasing the concentration of gallic acid and reading the absorbance at 540 nm. **b** Calibration curve obtained by increasing concentrations of gallic acid and reading the absorbance at 540 nm. **c** The photograph shows the AuNPs formed with increasing concentrations of gallic acid

Table 8.1 Concentrations (g L^{-1}) of sugar solutions tested as reaction interferences. These sugars were tested in the concentrations reported, individually and as mixtures

	Mix 1	Mix 2	Mix 3
Sucrose	100	120	140
Fructose	30	50	70
Glucose	60	80	100

8.4 Conclusion

In this work, two different analytical approaches, based on the use of nanostructured materials applicable to samples of food interest, were obtained. The foundation for the development of the spectrophotometric methods for the selective determination of the antioxidant activity of phenolic compounds have been laid,
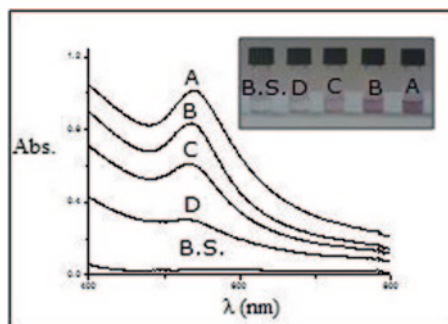
Fig. 8.6 AuNPs spectra formed with two volumes of two commercial fruit juices. Apple juice 60 µL (*A*), 30 µL (*B*) pear juice 60 µL (*C*), 30 µL (*D*); blank solution (*B.S.*). The inset photograph shows a blank solution (*B.S.*) and the AuNPs formed with the different fruit juices

exploiting their ability to reduce the gold (III) to gold (0) in the form of nanoparticles (diameter < 30 nm). For both methods it was possible to extrapolate the quantification of antioxidant capacity expressed as AuNPs gallic equivalent antioxidant capacity (AuNPs GEAC). It should be noticed that these methods do not require the use of radical compounds, with the related problems of stability, safety, disposal and analysis cost. Moreover both methods do not require long waiting times, they are selective for the polyphenols (despite the complex matrix) and are economic (final analysis volume: 500 µL). Furthermore the proposed method: "evaluation of the antioxidant capacity directly in the matrix in aqueous-organic medium", turns out to be simple and fast, it does not need the phase of extraction of phenolic compounds from the matrix (with the relative problems of reproducibility and partial recoveries), in fact it does not require any sample pre-treatment. It has also been revealed how the formation of AuNPs in aqueous-organic solvent reduces the interference of the possible non-phenolic reducing compounds, and enhances the ability of formation of AuNPs by phenolic compounds, thus increasing the selectivity and sensitivity of the method.

References

1. M. Servili, S. Esposto, R. Fabiani, S. Urbani, A. Taticchi, F. Mariucci, R. Selvaggini, G.F. Montedoro. Phenolic compounds in olive oil: antioxidant, health andorganoleptic activities according to their chemical structure. (2009) Inflammopharm. 17:76–84

2. R. Abe, J. Beckett, R. Abe, A. Nixon, A. Rochier, N. Yamashita, B. Sumpio. Olive oil polyphenol oleuropein inhibits smooth muscle cell. (2011) Olive Eur. J. Vasc. Endovasc. Surg. 41:814–820
3. H.K. Obied, P. Karuso, P.D. Prenzler, K. Robards. Novel secoiridoids with antioxidant activity from Australian olive mill waste. (2007) J. Agric. Food. Chem. 55:2848–53
4. H.E.Toma, V.M. Zamarion, S.H. Toma, K. Araki. The Coordination Chemistry at Gold Nanoparticles. (2010) J. Braz. Chem. Soc. 21:1158–1176
5. M. Scampicchio, J. Wang, A.J. Blasco, A. Sanchez, S. Mannino, A. Escarpa. Nanoparticle-based assays of antioxidant activity. (2006) Anal. Chem. 78:2060–2063
6. D. Vilela, M.C. González, A. Escarpa. Gold-nanosphere formation using food sample endogenous polyphenols for in-vitro assessment of antioxidant capacity. (2012) Anal. Bioanal. Chem. 404:341–349

Chapter 9
Deposition and Characterization of Laccase Thin Films Obtained by Matrix Assisted Pulsed Laser Evaporation

Nunzia Cicco, Antonio Morone, Maria Verrastro, Maria Dinescu, Andreea Matei, Bogdana Mitu and Diego Centonze

Matrix Assisted Pulsed Laser Evaporation (MAPLE) was used as an alternative technique within strategies for enzyme immobilization to produce Laccase thin films.

In order to characterize Laccase thin films, suitable deposition substrates were used. Laccase layers deposited onto silicon were investigated by Fourier Transform InfraRed Spectroscopy (FTIR) and Atomic Force Microscopy (AFM) to study molecular structure and surface morphology of Laccase thin films, respectively. Moreover, to estimate the amount of deposited enzyme, Quartz Cristal Microbalance (QCM) electrodes modified with Laccase films were used. Finally, glass and screen printed carbon electrodes were used as deposition substrates to test by colorimetric assay and amperometry the activity of the Laccase deposited. Experimental results have demonstrated that MAPLE enables the Laccase deposition that retains 10 % of the initial activity.

M. Verrastro (✉)
Consiglio Nazionale delle Ricerche, Istituto di struttura della Materia, Tito Scalo (PZ), Italy
e-mail: mariafilomena.verrastro@pz.imip.cnr.it

Scuola di Scienze Agrarie, Forestali, Alimentari ed Ambientali, Università degli Studi della Basilicata, Potenza, Italy

N. Cicco
Consiglio Nazionale delle Ricerche, Istituto di Metodologie per l'Analisi Ambientale, Tito Scalo (PZ), Italy

A. Morone
Consiglio Nazionale delle Ricerche, Istituto di struttura della Materia, Tito Scalo (PZ), Italy

M. Dinescu · A. Matei · B. Mitu
Lasers Department, National Institute for Lasers, Plasma and Radiation Physics, Bucharest, Romania

D. Centonze
Dipartimento di Scienze Agrarie, degli Alimenti e dell'Ambiente, Università degli Studi di Foggia, Foggia, Italy

9.1   Introduction

Matrix Assisted Pulsed Laser Evaporation (MAPLE) is a laser-based deposition technique used to deposit films of soft material [1]. In MAPLE, a pulsed laser beam is focused inside a vacuum chamber and impinges on the surface of a rotating target. The target consists of a frozen solution of the material of interest that is diluted in an appropriate solvent. Thus, when the laser beam impacts the target, the laser pulsed energy is mainly absorbed by the solvent and converted to thermal energy, allowing the solvent to vaporize while the material of interest is deposited as a thin film [1]. We have considered the MAPLE exploitable within strategies for enzyme immobilization [2] because of it is able to produce thin films of organic material [1]. We focused our attention on Laccase since it is an enzyme widely used as biological recognition component in biosensors for detecting polyphenols. These compounds have got an important role in environmental pollution and food industry fields [3].

In this study Laccase was deposited by Matrix Assisted Pulsed Laser Evaporation (MAPLE) and a characterization study was carried out.

9.2   Materials and Methods

Laccase powder purchased from Sigma (cod. 38429), with an estimated activity of 0.5 U/mg solid, was used in our experiments. Laccase thin films were obtained at room temperature by MAPLE using a Nd-YAG laser. The laser beam impinges on the rotating target at 45° with respect to the surface. A watery solution of the enzyme with a concentration equal to 1 % was flash frozen and used as target for MAPLE. The pressure in the deposition chamber was about 10^{-4} mbar. We report in Table 9.1 the working conditions used in MAPLE process.

Laccase layers deposited onto silicon were investigated by Fourier Transform InfraRed (FTIR) spectroscopy and Atomic Force Microscopy (AFM) to evaluate the characteristic chemical bonds and morphology, respectively. The laccase amount was measured by using quartz crystal microbalance (QCM) with a 33.2 mm^2 active area. Moreover, the activity of the Laccase thin film was tested by both colorimetric assay and amperometry by using glass and screen printed carbon electrode (DropSens 150) as deposition substrates, respectively.

Laccase deposited onto glass was first dissolved in 0.1 M phosphate buffer (PBS) pH 6.5, and the activity was tested as described by Ride [4]. Activity was also tested at SPE modified by Laccase thin films by recording the current signal after the addition of 100 μL PBS solution at pH 7.0, directly dropped onto the electrode (blank), and after the addition of catechol used as the enzymatic substrate.

Table 9.1 MAPLE deposition parameters

Parameter	Value
Pulse width	5–7 ns
Repetition rate	10 Hz
Fluence	0.6 J/cm^2
Target substrate distance	35 mm
Deposition time	900 s
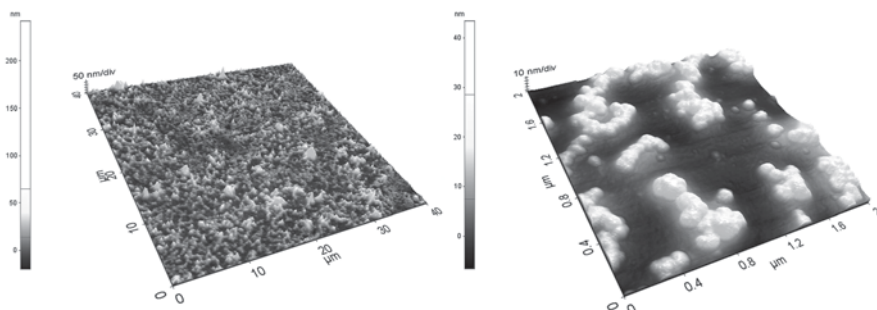
Fig. 9.1 AFM images of Laccase thin film obtained by MAPLE: A (40×40 μm^2) and B (2×2 μm^2)

9.3   Results and Discussion

9.3.1   AFM Analysis

Figure 9.1 shows the images from AFM analysis, where films obtained by MAPLE are displayed at different magnifications. The morphology of films is characterized by a basal layer with grains of hundreds of nanometres (1A) that cover the whole silicon substrate, giving a Laccase thin film. Scanning on a smaller area(1B), randomly round shape grains with sizes in the range 50–100 nm and inhomogeneously chained together can be observed.

9.3.2   FTIR Analysis

Figure 9.2 shows the comparison between the FTIR spectrum of Laccase obtained by drop-cast and those of Laccase deposited by MAPLE. The spectra are highly overlapped showing the same absorption peaks. FTIR analysis demonstrated that Laccase underwent no substantial modification in molecular structure during the deposition process. However, we have to underline that modifications of enzyme cannot be excluded even in the presence of identical FTIR spectra, indeed IR spectroscopy can give information only on primary and secondary structures of the enzyme [1, 5]. Therefore, the determination of the enzymatic activity is fundamental to claim structural integrity of the enzyme redox centres.
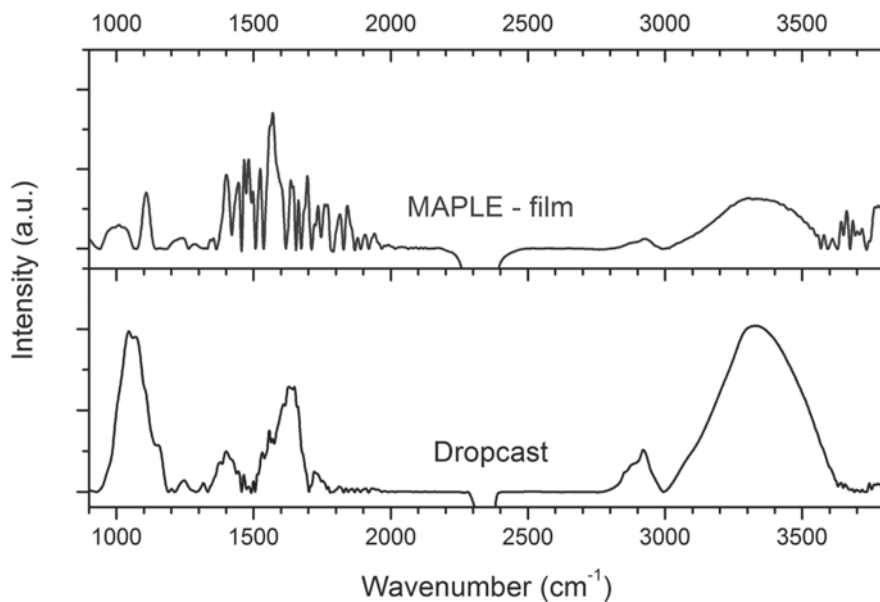
Fig. 9.2 FTIR spectra from Laccase dropcast and from Laccase thin film obtained by MAPLE

Fig. 9.3 Colour development from activity of Laccase thin film with respect to the blank (mixture without any Laccase)
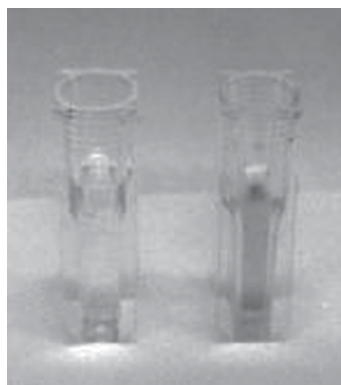
9.3.3   Amount and Activity Determination

The amount of Laccase deposited on QCM by MAPLE under the conditions above reported was equal to 1 µg. As far as the Laccase activity is concerned, the spectrophotometric assay, using syringaldazine as the enzyme substrate, showed that about 10 % of deposited enzyme was active (Fig. 9.3). This result was also corroborated by electrochemical analysis. The chronoamperometric response with respect to the blank (Fig. 9.4) showed a distinct signal due to the electrode reduction of the ortho-quinone produced from catechol by the enzymatic conversion.
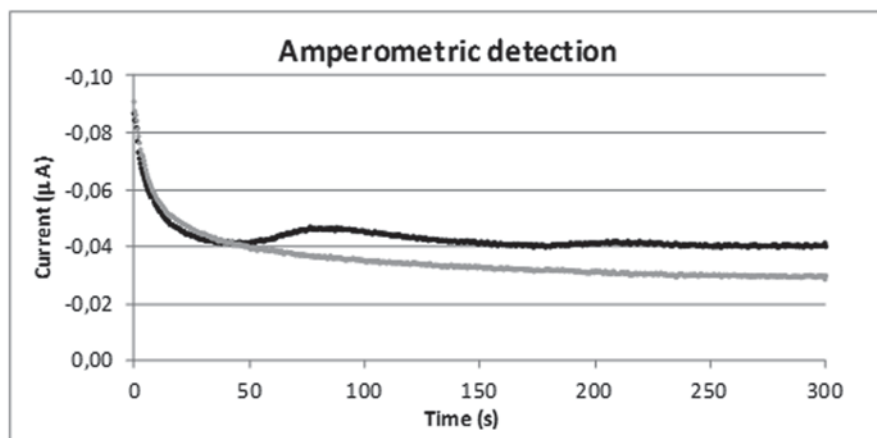
Fig. 9.4 Chronoamperometric responses of Laccase thin film obtained by MAPLE. Transients without (*grey* blank) and with (*black*) the addition of 1 mM catechol. Applied potential: −0.2 V

9.4   Conclusions

Experimental results demonstrated that MAPLE enables to deposit Laccase thin films, although partially active. Further investigations will be carried out to obtain improved performances of the enzyme deposited with MAPLE by optimizing the deposition conditions.

References

1. A. P. Caricato, A. Luches, Application of the matrix-assisted pulsed laser evaporation method for the deposition of organic, biological and nanoparticle thin films: a review, Appl. Phys. A, **105**, 565–582 (2011).
2. A. Sassolas, J. Blum, B. D. Leca-Bouvier, Immobilization strategies to develop enzymatic biosensors, Biotechnol. Adv. **30** 489-511 (2012).
3. F. Karim, A. N. M. Fakhruddin, Recent advances in the development of biosensor for phenol: a review, Rev. Environ. Sci. Biothecnol. **11**, 261–274 (2012).
4. J. P. Ride, The effect of induced lignification on the resistance of wheat cell walls to fungal degradation, Physiol. Plant Pathol. **16**, 187–196 (1980).
5. Y. Mei, L. Miller, W. Gao, R. A. Gross, Imaging the Distribution and Secondary Structure of Immobilized Enzymes Using Infrared Microspectroscopy, Biomacromolecules **4**, 70–74 (2003).

Chapter 10
Optical Characterization of Heavy Metal-Binding Proteins Bioconjugation on Porous Silicon Devices

Jane Politi, Principia Dardano, Mario Iodice, Ilaria Rea and Luca De Stefano

Biosensors are hot topic in recent years because of their versatility to different fields. Porous silicon devices are optical transducer sensitive to biological and chemical species which penetrate inside the pores after a proper functionalization with specific bioprobes. In this work, we reported a functionalization approach to obtain optical biosensors for heavy metal detection. Oligopeptides, namely Phytochelatins, were selected due to their ability to detect heavy metal ions. Spectroscopic reflectometry and Fourier transform infrared spectroscopy were used as characterization techniques. Data show successful and repeatable functionalization process. These results are very good starting step in development of heavy metal ions optical biosensors.

10.1 Introduction

Porous silicon (PSi) is a silicon-derived material widely studied in last 20 years due to its peculiar optical properties [1–4]. PSi is used as smart transducer material, since, on exposure at chemical substances, the average refractive index changes drastically [5]. PSi can be fabricated by electrochemical etching of doped crystalline silicon in hydrofluoric acid (HF) [6]. Tuning etching process parameters (etch time, HF concentration, doping level, and so on) allows a modulating of PSi porosity that permits to fabricate multilayer optical structures as 64 layers Thue-Morse (T-M) filters. This optical structure, due to characteristic alternation of porosity layers, is more sensitive than multilayers such as microcavity or rugate filters [7] and makes easier the study of biomolecules immobilization. Bioprobes useful for heavy

J. Politi (✉) · P. Dardano · M. Iodice · I. Rea · L. De Stefano
Institute for Microelectronics and Microsystems, National Research Council,
Unit of Naples, Via P. Castellino 111, 80131 Napoli, Italy
e-mail: jane.politi@na.imm.cnr.it

J. Politi
Department of Chemistry, University of Naples "Federico II", Via Cinthia, 80128 Napoli, Italy

metal ions detection are molecules that selectively bind them, such as Phytochelatins (PCs). PCs are small, heavy metal-binding proteins with the general structure of (γ-Glu-Cys)$_n$Gly ($n=2-11$) that complex with toxic metal ions protecting plants [8–10]. A proper bioconjugation of PC$_6$ on PSi T-M filters were studied and discussed.

10.2 Material and Methods

10.2.1 Fabrication of Thue-Morse Filters

Porous silicon structures were fabricated by electrochemical etching of crystalline silicon (0.001 Ωcm resistivity, <100> oriented, 500 μm thick) in hydrofluoric acid (HF, 50% in volume), water and ethanol solution (1:1:1) in dark and at room temperature (RT). Thue-Morse structure is generated following the substitution rules H->HL and L->LH, so that a 64 layers sequence can be expressly written as HHL-HLLHHLLHLHLHHLHLLHLHHLLH   HLHLLHHLLHLHHLLHHLHLLHLHL-HLLHHLLHLHHL. It was applied a current density equal to 100 mA/cm^2 for 1.6 s to obtain low refractive index, while high refractive index layer required 200 mA/cm^2 for 1.2 s, corresponding to $n_L = 1.53$ and $n_H = 1.79$, and thicknesses $d_L = 156$ nm and $d_H = 120$ nm, respectively. After the electrochemical process, pores dimension was increased by rinsing the "as-etched" porous silicon structures in KOH-ethanol solution (1.5 mM) for 15 min [11]. Devices were then thermally oxidized against uncontrolled environmental aging and corrosion in alkaline solutions [12]. The reflectivity spectra obtained are of very good quality in a wide range of wavelengths, as it is shown in Fig. 10.1.

10.2.2 Biomodification of Oxidized Porous Silicon Structures

Oxidized porous silicon surfaces were opportunely functionalized. As represented in Fig. 10.2, chips were treated in piranha solution (H_2SO_4:H_2O, 4:2) at RT for 30 min in order to activate Si-O-Si in Si-OH groups. After washes with distilled water (DI-H_2O) and drying under N_2, chips were treated with a solution of 5% 3-(aminopropyl)triethoxysilane (APTES) (Sigma Aldrich) in toluene anhydrous for 30 min at RT, washed with toluene anhydrous three times, curing on heater at 100 °C for 10 min and washed again twice with toluene anhydrous. The chips was then treated with cross-linker BS^3 (Bis [sulfosuccinimidyl] suberate) (Thermo scientific) 1.6 mM in PBS 1X at 4 °C for 4 h, then washed three times with PBS 1X and once with DI-H_2O. PC$_6$ (AnaSpec IGT group) was diluted in PBS 1X in order to obtain 1.5/3/6/10 mg/mL protein concentration and the incubation was made at 4 °C for 8 h. As experimental control for FTIR measurements was made a chip functionalized up to BS^3.

Fig. 10.1 Reflectivity spectrum of aperiodic PSi Thue-Morse structure

Fig. 10.2 Scheme of functionalization process of each chips

10.3   Results and Discussion

Chemical modification of inorganic surfaces such as porous silicon is needed for optical biosensors development due to highly hydrophobicity of as etched PSi devices that avoid infiltration of aqueous solution into sponge like matrix [13].

Table 10.1 Spectroscopic reflectometry data recorded after every functionalization step

	T1 (1.5 mg/ml)	T2 (3 mg/ml)	T3 (6 mg/ml)	T4 (10 mg/ml)
Oxidation	943.6 ± 0.1	942.3 ± 0.5	948.2 ± 0.2	950.4 ± 0.4
APTES	977.0 ± 0.3	974.4 ± 0.4	982.3 ± 0.2	985.3 ± 0.1
BS3	992.8 ± 0.4	991.4 ± 0.3	996.9 ± 0.5	1000.3 ± 0.5
PC6	988.5 ± 0.3	985.0 ± 0.1	995.3 ± 0.4	997.6 ± 0.5

Spotting condition of covalent approaches for proteins bioconjugation on inorganic surfaces has been previously studied [14]. The study revealed that APTES diluted in toluene dry for a period of incubation of 30 min generates a relatively smooth and homogenous layer. These results were useful in developing the bioconjugation strategy of PC_6 onto PSi surfaces. The homo-bifunctional cross-linker, BS^3, brings a sulfo-*N*-hydroxysulfosuccinimide (sulfo-NHS) group. Sulfo-NHS reacts with primary amines at pH 7–9 to form stable, covalent amide bonds [15], so it is able to bind primary amines on PSi surfaces, generated by silanization process, and primary amine of PC_6. The functionalization process of porous silicon optical structure can be easily attended by label-free techniques such as spectroscopic reflectometry. Data of peak shifts revealed by reflectometry spectra are shown in Table 10.1.

As it is showed, the APTES step generates a red shift of about 33 nm for each device, while cross-linker step generate a red shift of about 16 nm. These results induce us to conclude that the ability of APTES molecules to reticulate onto silanized surfaces generates a thicker layer than BS^3 [14] and it is optically traduced in a greater red shift. Good repeatability of functionalization process is also showed by reflectometry spectra data. The bioconjugation of PC_6 revealed a blue shift for each concentration of proteins. These results induce us to carefully conclude that sulfo-NHS leaving group of BS^3 have steric hindrance greater than PC_6 oligopeptide. Moreover, the blue shifts seem to be correlated with BS^3 functionalization grade, in fact: sample T3 shows the thinnest layer of BS^3 (14.6 nm of red shift) and have the less blue shift (1.6 nm) after PC_6 incubation; sample T4 shows a 15 nm of red shift after BS^3 and have 2.7 nm of blue shift after PC_6 incubation; sample T1 shows a 15.8 nm of red shift after BS^3 and have 4.3 nm of blue shift after PC_6 incubation, sample T2 shows the thickest layer of BS^3 (17 nm of red shift) and it shows he greatest blue shift (6.4 nm) after PC_6 incubation. These evidences seem to agree with our considerations about steric hindrance. To unequivocally highlight the presence of PC_6 into PSi matrix we did also FTIR investigation on a control (CTR) chip functionalized up to BS^3 step and sample T3. As Fig. 10.3 represents, the sample T3 shows characteristic peaks at: 2846 cm^{-1}, 2895 cm^{-1} that indicate the symmetrical stretching of the alkyl groups ($-CH_2$) linked to sulfur atoms present in lateral chain of cysteine of PC_6; while 2977 cm^{-1} indicate asymmetric stretching of alkyl groups ($-CH_2$) linked to sulfur atom present in lateral chain of cysteine of PC_6. CTR sample shows 2825 and 2870 cm^{-1} peaks that are characteristic of asymmetrical vibration of carbonyl groups linked to aliphatic chain, while peak at 2960 cm^{-1} is characteristic of $-CH_2$ asymmetric stretching linked to $-OCO-$ groups.

Fig. 10.3 FTIR spectra of control chip functionalized up to BS^3 and sample T3
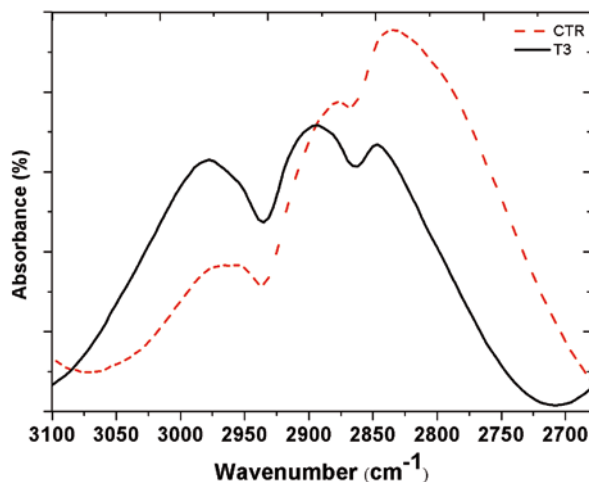
FTIR measurements demonstrate without any doubts the presence of proteins into PSi. These results encourage in developing new platform of optical biosensors for heavy metal detection.

10.4   Conclusions

Interesting topic of environmental monitoring are optical biosensors incorporated onto microdevices (lab-on-chip, LOC), since they allow wireless remote interrogation that avoid expansive costs of sampling of substrates that have to be analyzed (i.e. rent equipment, man-hours payment, etc.). LOCs need full development of a well-functionalized biosensor. In this study, we developed a good and repeatable kind of functionalization strategy to immobilize heavy metal-binding proteins such as oligopeptides, known as Phytochelatins, rich in cysteine able to sequester heavy metals (as lead, mercury and cadmium). The process was monitored by spectroscopic reflectometry and FTIR spectroscopy. The results showed the success of all steps of functionalization.

References

1. Cullis et al. J. Appl. Phys., Vol. 82, No. 3, 1997
2. Snow et al. J. Appl. Phys., Vol. 86, No. 4, 1999
3. Theifl et al., Surface Science Reports 29 (1997) 91–192
4. Lockwood et al., Solid State Communications, Volume 92, Issues 1–2, 1994, 101–112

5. De Stefano et al. IEEE Transactions On Nanotechnology, Vol. 3, No. 1, March 2004
6. Laurell et al. Sens. Actuators B, 31, 161 (1996).
7. Caliò, et al., J. Appl. Phys. 114, 134904 (2013).
8. Grill et al.,1985, Science 230, 674–676.
9. Tomaszewska et al. Science of Legume 3, 206–217.
10. Salt, et al. 1995, Plant Physiology 107, 1293–1301
11. Herino, et al. J. Electrochem. Soc. 134, 1994 (1987).
12. Chamard, et al. J. Appl. Phys. 84, 6659 (1998).
13. Ouyang, et al. Adv. Funct. Mater. 2005;15:1851–1859.
14. Terracciano et al. J. of Europ. Opt. Soc., 8, 13075 (2013)
15. Mattson et al. Mol. Biol. Rep., 17, 167-183 (1993)

Chapter 11
Label-Free Impedimetric Determination of miRNA Using Biotinylated Conducting Polymer Modified Carbon Electrodes

D. Voccia, M. Sosnowska, F. Bettazzi, I. Palchetti and W. Kutner

Preliminary results are reported on label-free miRNA determination with faradaic electrochemical impedance spectroscopy (EIS) measurements on glassy carbon electrodes (GCEs) and screen-printed carbon electrodes (SPCEs). These electrodes were coated with films of functionalized conducting polymers. For that, bis(2,2′-bithien-5-yl)-(4-hydroxyphenyl)methane biotin ester was used as the functional monomer. This monomer was potentiodynamically electropolymerized to result in deposition of thin polymer films on the electrodes. Next, streptavidin, and then the biotinylated DNA capture probe were immobilized via streptavidin–biotin interactions. Detectability of the resulting biosensor with respect to the complementary miRNA was well below 100 pM.

11.1 Introduction

An approximately 22 nucleotide long non-coding RNAs, known as microRNAs (miRNAs, miR), recently emerged as new clinical biomarkers [1–3]. A great effort has already been devoted to develop analytical procedures for miRNA determination with sufficient sensitivity, linear dynamic concentration range, and

D. Voccia (✉) · F. Bettazzi · I. Palchetti
Dipartimento di Chimica, Università degli Studi di Firenze, Via della Lastruccia 3 50019 Sesto Fiorentino, Firenze, Italy
e-mail: diego.voccia@unifi.it

I. Palchetti
e-mail: ilaria.palchetti@unifi.it

M. Sosnowska · W. Kutner
Department of Physical Chemistry of Supramolecular Complexes,
Institute of Physical Chemistry, Polish Academy Sciences,
Kasprzaka 44/52, 01-224 Warsaw, Poland
e-mail: wkutner@ichf.edu.pl

Scheme 11.1 Structural formula of the bis(2,2′-bithien-5-yl)-(4-hydroxyphenyl) methane biotin ester functional monomer [7]
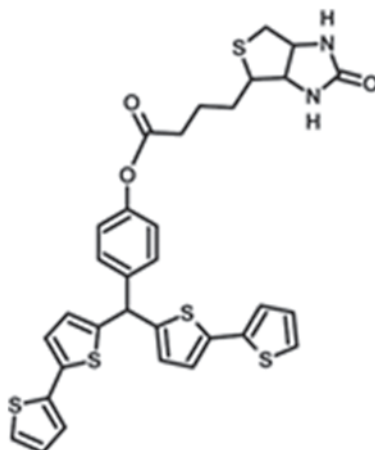
multiplexing capability without PCR. In this context, many different biosensor platforms have been reported [4–6]. In most of them, the target miRNA was labeled with a fluorophore [4], an enzyme [5–6], or nanoparticles for the determination. Although the miRNA determination was considerably improved that way, complexity of the miRNA labeling often introduced limitations in terms of the reagent cost and the assay time. Moreover, this labeling might introduce an additional bias. In contrast, label-free procedures represent attractive alternatives because they enable quantitative multiplexed miRNA expression profiling with minimal sample pretreatment and no need of using any assay reagents. The electrochemical impedance spectroscopy (EIS) detection is one of the promising signal transductions used in the label-free biosensors for nucleic acids. Beside the attractive features of electrochemical detection, EIS is largely nondestructive and highly sensitive to the presence of minute amounts of electron-transfer impeding materials on the biosensor surface.

Herein, an electrochemical label-free method of the miRNA determination is presented. This method is based on potentiodynamic electropolymerization of the bis(2,2′-bithien-5-yl)-(4-hydroxyphenyl)methane biotin ester, BMBE,

(Scheme 11.1) functional monomer [7]. This polymerization resulted in deposition of thin conducting polymer films onto surfaces of glassy carbon electrodes (GCEs) and disposable screen-printed carbon electrodes (SPCEs). In these films, the biotin moiety stayed intact remaining available for subsequent streptavidin immobilization. Then, the biotinylated DNA (DNA-biot) capture probe was tethered via the streptavidin-biotin binding. This layer-by-layer assembling of the (biotin-polymer)-streptavidin-(biotin-oligonucleotide) recognition film served to determine by EIS the label-free target oligonucleotide via complementary nucleobase pairing.

11.2   Experimental

11.2.1   Chemicals

Streptavidin from *Streptomyces avidinii* and ethanol (96%) were from Sigma-Aldrich. Disodium hydrogen phosphate, sodium dihydrogen phosphate, potassium hexacyanoferrate (III and II), sodium chloride, tetra-n-butylammonium bromide [(TBA)Br] and acetonitrile were from Merck. Bis(2,2′-bithien-5-yl)-(4-hydroxyphenyl)methane biotin ester was synthesized according to the literature procedure [7]. The 18.2 MΩ cm MilliQ water (DEPC treated for RNA analysis) was used for preparation of solutions. Synthetic oligonucleotides were from MWG Biotech AG.

Probe (DNA-biot): 5' GAA-ACC-CAG-CAG-ACA-ATG-TAG-CT—biotin 3'.
Target: 5' AGC-UAC-AUU-GUC-UGC-UGG-GUU-UC—3'.

11.2.2   Electrochemical Measurements

Electrochemical measurements were performed with a three-electrode cell using the Autolab PGSTAT10 electrochemical system equipped with the FRA2 module (EcoChemie). A Pt wire, Ag/AgCl, and glassy carbon disk served as the auxiliary, reference, and working electrode, respectively. The SPCE devices were composed of planar electrodes, i.e., a carbon auxiliary electrode, an Ag pseudo-reference electrode, and a carbon working electrode. The EIS measurements were performed with an alternating voltage of the 10 mV amplitude at open circuit potential (OCP) of +0.20 V used as the bias potential in the frequency range of 10 mHz to 50 kHz. The EIS spectra were plotted as the complex plane diagrams (Nyquist plots). All potentials are referred to the reference electrode or pseudo-reference electrode for measurements at the GCE or SPCE, respectively.

11.2.3   Electropolymerization

The biotinylated polymer film was deposited from the BMBE solution of 0.1 M (TBA)Br ethanol:acetonitrile, 1:1 (*v/v*) (for GCE), and 0.01 M (TBA)Br in ethanol:acetonitrile:water, 1:1:10 (*v/v/v*) (for SPCE). The potential scan limits were +0.50 and +1.30 V and the scan rate was 50 mV/s. For both electrodes, the electropolymerization conditions were optimized in order to reach the best analytical performance of the biosensors fabricated. For that, different numbers of potential cycles and monomer concentrations were tested (data not shown). The best conditions found are summarized in Table 11.1.

Table 11.1 Electropolymer-
ization optimized conditions

Electrode	Number of potential cycles	Monomer concentration
GCE	3 cycles	1 mM
SPCE	10 cycles	0.1 mM

11.2.4 Analytical Procedure

The working electrode surface, modified with the polymer film, was immersed in the 0.2 mg mL^{-1} streptavidin solution of 0.5 M phosphate buffer (PB) pH=7.2 for 20 min. Then, the electrode surface was exposed to the 4 μM DNA-biot probe in PB for 20 min. The immobilization step was followed by the biosensor surface treatment with the target solutions of different concentrations for 20 min. The EIS measurements were performed using 0.1 M [Fe(CN)$_6$]$^{3-/4-}$ (redox probe) in 0.1 M phosphate buffer saline (PBS) pH=7.2 at OCP. In order to determine the value of the electron-transfer resistance (R_{et}), used as the analytical parameter, the experimental data were fitted with electric parameters of the modified Randles-Ershler circuit.

11.3 Results and Discussion

The Nyquist plots for GCE and SPCE (Fig. 11.1a and b, respectively) were constructed for each step of the biosensor preparation, and then after immersing the biosensor in solutions of different concentrations of the target. Expectedly, R_{et} increased for each step of the procedure. This increase indicates that the film became more insulating and its electrical double-layer property approached those of an ideal capacitor. The DNA-biot was immobilized on the biotinylated polymer film, as demonstrated by the R_{et} increase compared to that for the polymer coated with the streptavidin layer. That is, the hybridization event was accompanied by the R_{et} increase. The R_{et} signal increased with the target concentration increase in the range of 100 pM to 10 nM (Fig. 11.1) with the signal for the 100 pM target clearly seen.

11.4 Conclusions

The combined use of the biotinylated functional monomer and EIS is promising for further investigations towards development of label-free biosensors for the miRNAs determination with high detectability, i.e., that reaching the level useful for the miRNAs determination in biological samples.
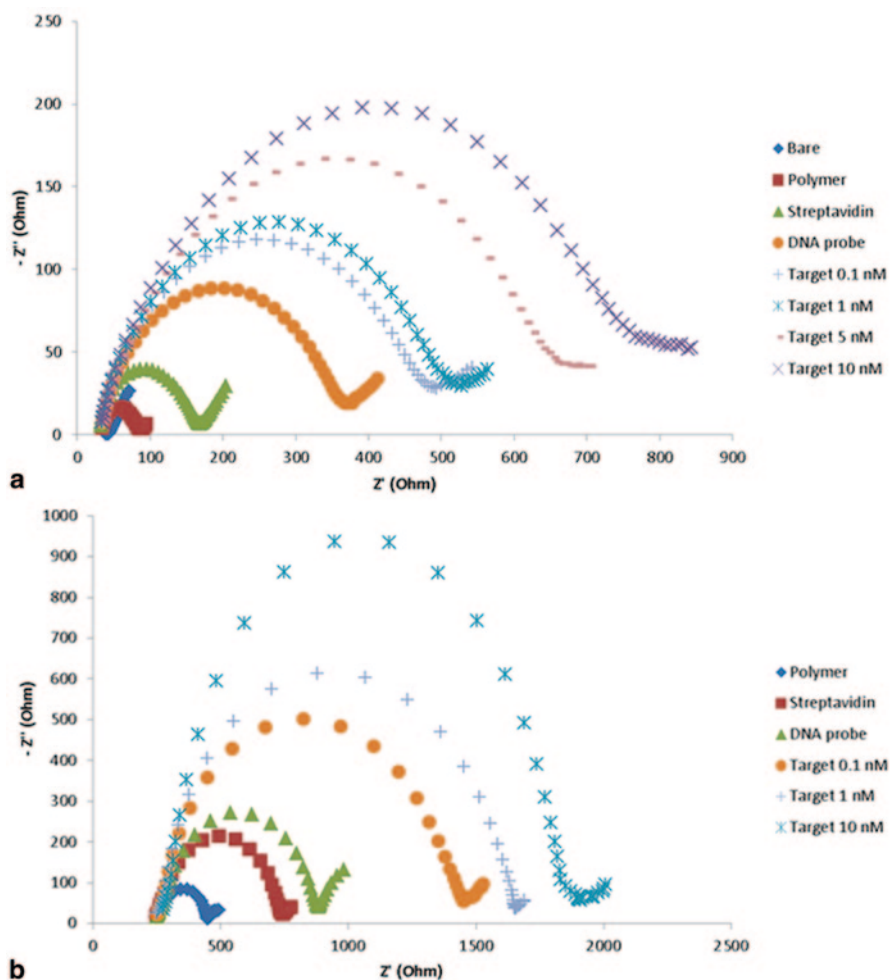
Fig. 11.1 The Nyquist plots for 0.1 M [Fe(CN)$_6$]$^{3-/4-}$ in 0.1 M PBS (pH = 7.2) at (**a**) GCE and (**b**) SPCE coated with the polymer film of biotinylated polymer, and then after consecutive immobilization of streptavidin from its 0.2 mg mL^{-1} PB solution, the DNA-biot probe from its 4 μM PB solution, and then the target oligonucleotide from its 0.1 to 10 nM solutions

References

1. B. Zhang, X. Pan, G. P. Cobb, T. A. Anderson, Dev. Biol. **302**, 1 (2008).
2. G. A. Calin, C. M. Croce, Nat. Rev. Cancer. **6**, 857 (2006).

3. M. V. Iorio, M. Ferracin, G. C. Liu, A. Veronese, R. Spizzo, S. Sabbioni, E. Magri, M. Pedriali, M. Fabbri, M. Campiglio, S. Menard, J. P. Palazzo, A. Rosenberg, P. Musiani, S. Volinia, I. Nenci, G. A. Calin, P. Querzoli, M. Negrini, C. M. Croce, Cancer Res. **65**, 7065 (2005).
4. A. A. Jamali, M. Pourhassan-Moghaddam, J. E. Dolatabadi, Y. Omidi, Trends Anal. Chem. **55**, 24 (2014).
5. M. Wang, H. Yin, N. Shen, Z. Xu, B. Sun, S. Ai, Biosens. Bioelectron. **53**, 232 (2014)
6. F. Bettazzi, E. Hamid-Asl, C.L. Esposito, C. Quintavalle, N. Formisano, S. Laschi, S. Catuogno, M. Iaboni M., G. Marrazza, M. Mascini, L. Cerchia, V. De Franciscis, G. Condorelli, I. Palchetti, Anal. Bioanal. Chem., **405**, 1025 (2013).
7. M. Sosnowska, P. Pieta, P. S. Sharma, R. Chitta, C. B. KC, V. Bandi, F. D'Souza, W. Kutner, Anal. Chem. **85**, 7454 (2013).

Chapter 12
Atrazine Determination Using Immunosensor Method Based on Surface Plasmon Resonance. Comparison with Two Other Immunological Methods Based on Screen-Printed and Classical Amperometric Devices

Mauro Tomassetti, Elisabetta Martini, Luigi Campanella, Gabriele Favero, Gabriella Sanzò and Franco Mazzei

12.1 Introduction

Analytical results for atrazine determination, obtained using a new immunosensor based on surface plasmon resonance (SPR), were compared with those obtained using both classical [1] and screen-printed [2] amperometric immunodevices. In the latter cases competitive formats were used while direct format was encouraged if the SPR method was applied. First applications involving bovine milk atrazine recovery were also carried out.

12.2 Methods

For the SPR measurements, performed using the flow operating mode (see Fig. 12.1), a BioSuplar 400T (Analytical μ-Systems–Dep. of Mivitec GmbH, Sinzing, Germany) was used. Classical and screen-printed immunosensors both used amperometric electrodes for hydrogen peroxide as transducers, with horseradish peroxidase as the enzymatic marker. In short, both a screen-printed immunosensor and a classical amperometric immunosensor were developed and in both these cases the measurement method was based on the formation of a labelled immunocomplex on a suitable (Immobilon) polymeric membrane of the immunosensor after competitive assay between the free antigen and a fixed concentration of enzyme

M. Tomassetti (✉) · E. Martini · L. Campanella
Department of Chemistry, "Sapienza" University of Rome, P.le Aldo Moro, 5, 00185 Rome, Italy
e-mail: mauro.tomassetti@uniroma1.it

G. Favero · G. Sanzò · F. Mazzei
Department of Chemistry and Pharmaceutical Technology, "Sapienza"
University of Rome, P.le Aldo Moro, 5, 00185 Rome, Italy
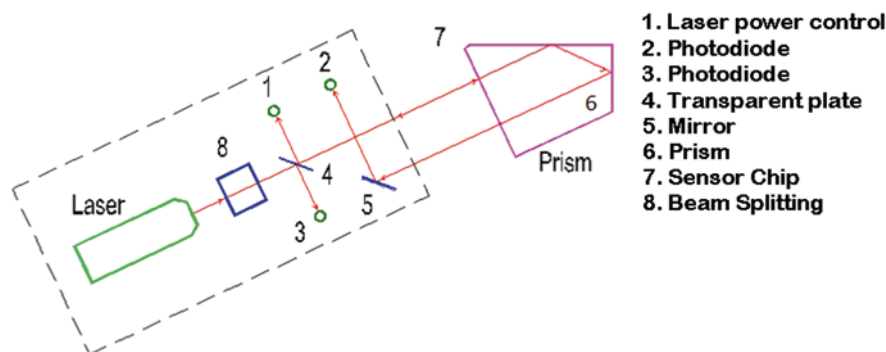
Fig. 12.1 Measurement scheme used for surface plasmon resonance operating in flow mode

labeled antigen for the anti-Atrazine immobilized in membrane (see Fig. 12.2). For the amperometric screen-printed measurements a wafer made of corundum ceramic was used as support and both working and counter electrodes were made of platinum. A Pt working electrode was modified with electrodeposited Prussian Blue, thus enabling H_2O_2 amperometric detection when polarized at 0 mV vs Ag/AgCl. The reference electrode was made of Silver. At the tip of the sensor there was a contacting field, connected to the active part by silver conducting paths, which were covered by a dielectric protection layer, while the bio-chemically active antibody immobilized on the Immobilon membrane was positioned on the working electrode
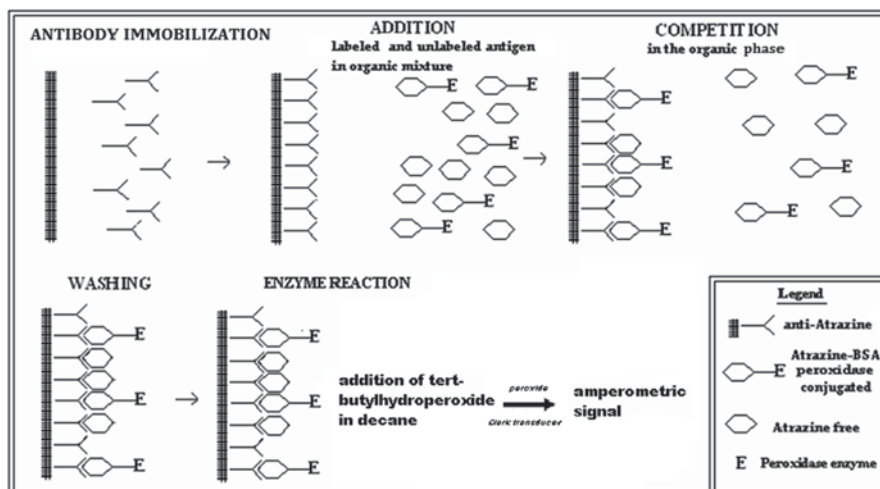
Fig. 12.2 Measurement: competition between atrazine and a fixed concentration of peroxidase atrazine conjugated, both free in organic phase solution, for the antibody immobilized in the membrane

Fig. 12.3 Behaviour of the screen-printed immunosensor response as a function of increasing atrazine concentration, using peroxidase enzyme as marker and an amperometric electrode for H_2O_2 as transducer
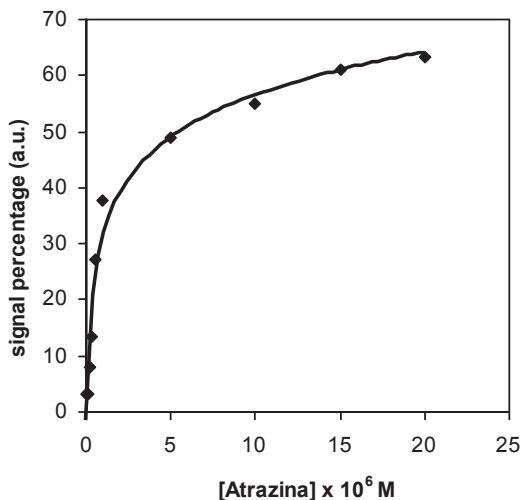
of the sensor. Finally the competitive assay for atrazine measurement, using the classical amperometric immunosensor was carried out using a commercial H_2O_2 amperometric sensor as transducer, overlapped by the Immobilon membrane for antibody immobilization.

12.3   Results

A comparison was made of the analytical features of the new SPR device with those of the other two immunosensors cited above and the advantages and disadvantages of the new SPR methods investigated: using the SPR device a calibration curve for Atrazine showed a linearity range from 1.0×10^{-7} to 1.5×10^{-6} μM and a LOD value of about 5×10^{-8} μM, while the linear range of the screen-printed and classical devices were of about three and five decades, respectively and the LOD values about 10^{-8} M and 5×10^{-11} M, respectively. However, the measurement time using the SPR device was found to be about half that required in the case of the two competitive formats.

The responses of the classical and screen-printed amperometric devices for increasing atrazine concentration are displayed respectively in Figs. 12.3 and 12.4.

In Fig. 12.5 the first results obtained for the detection of atrazine in bovine milk using SPR detection are reported for the sake of example.

In Fig. 12.5 the first and second lines where obtained simultaneously using the two-channel BioSuplar 400, with appropriately diluted raw milk flowing in the first channel (Curve 1) and milk spiked with atrazine in the second channel (Curve 2); the third curve represents the difference between the two signals. As can be seen, after stabilization for about 10 min, the added sample produces a signal increase in
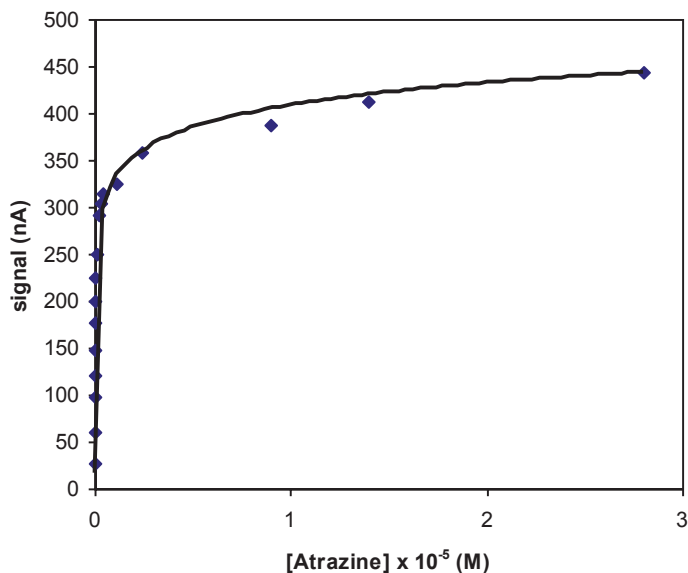
Fig. 12.4 Behaviour of the classical amperometric immunosensor response as a function of increasing atrazine concentration, using an H_2O_2 electrode as transducer and peroxidase enzyme as marker

Fig. 12.5 Typical measurement recorded for the detection of atrazine in bovine milk by SPR detection
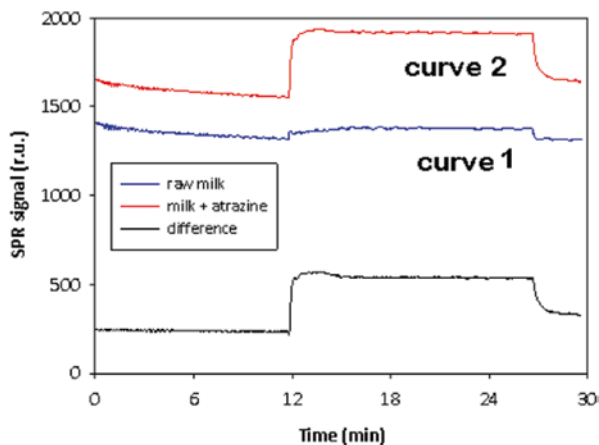
both cases but which is much more pronounced for the fortified sample. The successive washing with buffer leads to a signal decrease down to the baseline only in the case of raw milk, indicating the absence of atrazine in the raw sample, while in the case of fortified sample the signal attains a constant value higher than the baseline, as expected, taking into account that atrazine stably binds to the antibody

Table 12.1 Atrazine recoveries from spiked samples of bovine milk using the SPR immunosensor and the direct method

Pesticide	Added conc. (Final conc. Value) (x 10^7 M)	Found experimental conc. value (x 10^7 M)	% Recovery
Atrazine	1.89	2.01 ± 0.02	106.3%
Atrazine	2.64	2.40 ± 0.03	90.9%

Table 12.2 Atrazine recovery from spiked sample of bovine milk using the classical amperometric immunosensor and the competitive format illustrated in Fig 12.2

Pesticide	Added conc. (Final conc. Value) (x 10^8 M)	Found experimental conc. value (x 10^8 M)	% Recovery
Atrazine	1.00	0.98 ± 0.010	98.5%

immobilized on the sensor chip; this enables the detection and quantification of this pesticide in the real sample.

Finally, in Tables 12.1 and 12.2 results of some recovery tests are reported, performed on bovine milk samples, using both SPR and a classical amperometric immunosensor, obtaining satisfactory results.

12.4   Conclusion

Later tests confirm that new surface plasmon resonance is suitable, like the classical immunosensor method, for the analysis of triazinic pesticides in milk samples, with the advantage that the SPR measurements require about the half time of the classical immunosensor method.

References

1. L. Campanella, S. Eremin, D. Lelo, E. Martini., M. Tomassetti. Sens. Actuators B, 156 (2011) 50–62.
2. Mauro Tomassetti, Elisabetta Martini, Luigi Campanella, Gabriele Favero, Luciano Carlucci, Franco Mazzei J. Pharm. Biomed. Anal., 73 (2013) 90–98

Chapter 13
Acoustic Aptasensor for Aflatoxin B1 Determination

Katia Spinella, Lucia Mosiello, Alexandra Poturnayova, Maya Sneyedarkova and Tibor Hianik

13.1 Introduction

Over 20 years ago, aptamers were independently described by three groups as nucleic acid macromolecules of artificial single-stranded DNA or RNA sequences (ss-DNA, ss-RNA). These nucleic acid aptamers are capable of adopting stable secondary and tertiary structures, which enable specific interactions with other molecules. Aptamers are specially engineered to bind specifically to a target molecule, such as a protein, glycolipid, small molecule, or another DNA fragment. In addition, aptamers have high binding affinities in the nanomolar to picomolar range for large molecules, and in the micromolar range for small molecules. Aptamers, derived from an evolution process called SELEX (Systematic Evolution of Ligands by Exponential enrichment), are single strand nucleic acids capable of binding to their target molecules with high affinity and specificity [1]. In the past two decades, considerable growth of interest in DNA biosensors can be attributed to their important analytical properties. Most current DNA-based biosensors are based on DNA aptamers, and are referred to as aptasensors. DNA aptasensors exhibit excellent selectivity, high

K. Spinella (✉)
Department of Chemistry, University of Roma, TorVergata, Via della Ricerca Scientifica 1, 00133 Rome, Italy
e-mail: katia.spinella@enea.it, katiaspinella@libero.it

K. Spinella · L. Mosiello
ENEA, Centro Ricerche Casaccia, Via Anguillarese 301, 00123 S.Maria di Galeria, Rome, Italy

A. Poturnayova · M. Sneyedarkova
Faculty of Mathematics, Physics and Informatics, Comenius University, Mlynska dolina F1, 842 48 Bratislava, Slovakia

T. Hianik
Institute of Biochemistry and Animal Genetics, Slovak Academy of Sciences, Moyzesova 61, 900 28 Ivanka pri Dunaji, Slovakia

Table 13.1 Washing steps of quartz crystal surface

Cleaning steps	Time
Sodium dodecyl sulfate (1%)	30'
MQ water	15'
Acetone	5'
Ethanol	5'
Methanol	5'

sensitivity, and can be used for the rapid detection of different viruses, bacteria, and various chemical substances [2–4].

13.2 Experimental

The binding of AFLAB1 to the aptamers was analyzed by TSM method. TSM has certain analogy with QCM (Quartz Crystal Microbalance); however, in addition to mass, the TSM determines also the viscosity contribution arising from the friction between sensing layer and the surrounding buffer. This is important for detection of small molecules, such as AFLAB1 for which the QCM detection is difficult due to small molecular weight of the analyte. A TSM resonator consists of a thin disk of AT-cut quartz with gold electrodes deposited on both sides. Due to the piezoelectric properties and crystal orientation of the quartz, application of a voltage between the electrodes results in shear deformation of the crystal. An acoustic shear wave is generated and propagates through the sensing layer into the liquid. The viscous forces result in friction between the surrounding liquid and the layer immobilized at the surface of the crystal. This is reflected in an increase of Rm and a decrease of fs. The TSM experiments were performed at T=25 °C. For preparation of the aptasensor we used AT-cut quartz with a fundamental frequency of 8 MHz, covered on both sides by thin gold layers that served as electrodes (working area 0.2 cm²). The aptamers with the following nucleotide composition: 5′-thiol GTT GGG CAC GTG TTG TCT CTC TGT GTC TCG TGC CCT TCG CTA GGC CCA CA-3′ were immobilised on the gold layer of quartz crystal transducer. For this purpose the transducer was carefully cleaned (see Table 13.1 for details), sonicated, dried and mounted between two silicon O rings in the incubation cell.

Before of the immobilization of the thiolated aptamers onto the gold layer, dithiothreitol (DTT) was used as deprotecting agent for thiolated DNA as it has the tendency to form dimers in solution, especially in the presence of oxygen. Dimerization greatly lowers the efficiency of DNA immobilization on gold surface. DTT [1 mM] was incubated with PBS* (+0,2 mM CaCl2) and thiolated-DNA aptamer [5 µM] for 1 h to allow to react. Afterwards it is removed by filtration, using microspin column and the purified sample is eluted by centrifugation. The aptamers dissolved in binding buffer (PBS*) were added at the surface of gold electrode of quartz crystal, previously installed in closed cell preventing the solvent evaporation, for 17 h.
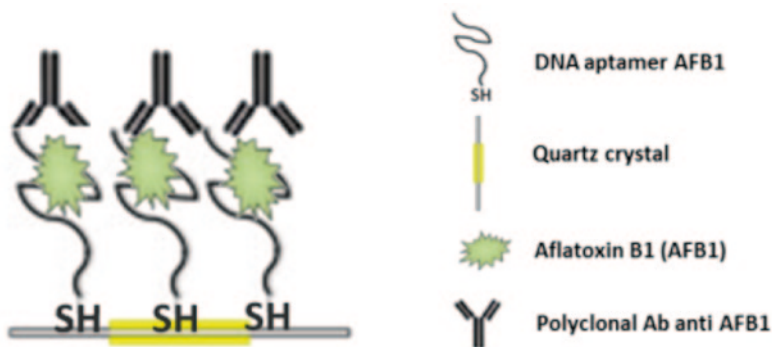
Fig. 13.1 Diagram of immobilization of Aptamers on the surface of quartz crystal

Once the immobilization was done, gold electrodes were rinsed in deionised water, dry in a gentle flow of nitrogen gas and incubated in 100 µl mercaptoethanol [100 µM] for 30 min for removing physically adsorbed aptamers and for blocking the naked electrode surface, thus avoiding non-specific binding. Then the aptamer-coated crystals were installed in flow-through cell. The sensor was rinsed with PBS* at a flow rate of 50 µl min^{-1} until a stable baseline was reached and after the analyte was introduced, each solution was applied until the resonance frequency stabilized. In Fig. 13.1 is shown the outline of the assay used

The interaction between aptamers and antibodies were tested for using these affinity biomolecules for detection of Aflatoxin B1. Addition of different concentration of polyclonal antibodies (1, 10, and 100 nM) on gold surface coated with aptamer didn't result in a decrease of fs and an increase of Rm and this means that there is not interaction between aptamers and antibodies (data not shown).

13.3   Results

The TSM method allows checking all steps of sensor preparation and to study the binding of AFLAB1 to the aptamers. As seen from Fig. 13.2, addition of AFLAB1 (0.05 ppb) caused a decrease of the frequency by 26 Hz and an increase of the motional resistance by 6 Ω.

However, after washing in buffer (PBS*) to remove unspecific interaction, we observed practically recovery of both fs and Rm. Thus, due to both rathers small concentration of AFLAB1 as well as its small molecular weight (312 Da) we did not observed changes of measured parameters. Therefore amplification of signal was performed by polyclonal antibodies. The molecular weight of antibodies is much larger (150 kDa), therefore we can expect more effect on acoustic parameters upon binding to the surface. We added antibody at different concentration (1 nM, 5 nMm,10 nM, 50 nM, 100 nM and 500 nM). Substantial decrease of the resonant
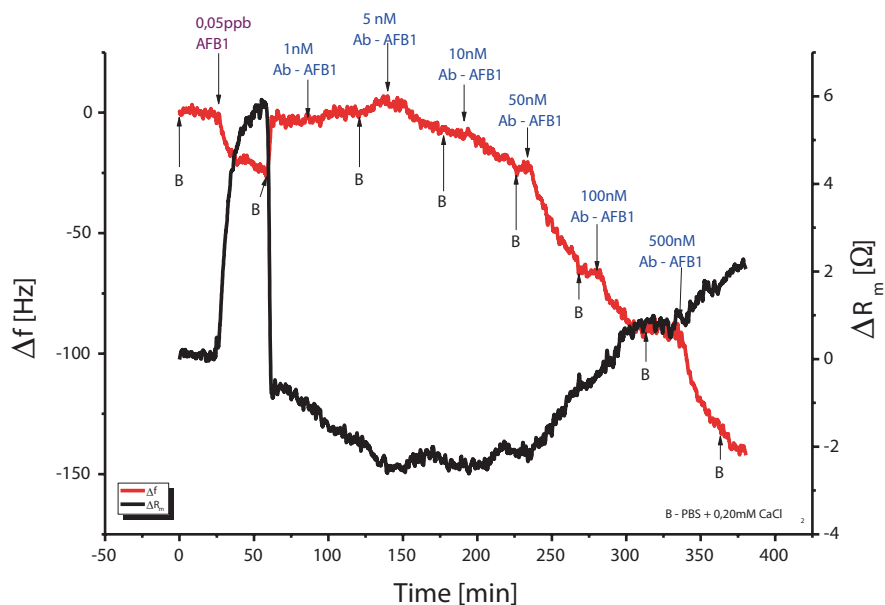
Fig. 13.2 Representative plot of the changes of Δfs (*red*), and ΔRm (*black*), following addition of 0.05 ppb AFLAB1 and different concentration of polyclonal Ab anti AFLAB1

frequency and in increase of motional resistance starting from 50 nM of antibody, while 1–5 nM antibody concentrations did not induce significant changes of the measured values.

13.4   Conclusions

These preliminary results, since they are related to a sandwich apta-immunoassay using polyclonal antibodies specific for Aflatoxin B1and aptamers immobilized on the surface of quartz crystal are of particular importance, since they show the applicability and feasibility of this sandwich assay. Unfortunately, we have found that the step of functionalization of the quartz crystals affect the success of the experiment, with this purpose in the future we would like characterize crystal surface with AFM to study interaction thiol group and gold surface. However, since the greater advantage of the TSM results in a label-free system that allows the identification of different analytes, in our system that characteristic not only is preserved, but, being applied to the identification of mycotoxins, can assume new application scenarios of the TSM, based on the use of antibodies and aptamers on a solid support in the field of food safety and, therefore, human health.

References

1. A.D. Ellington, J.W. Szostak: In vitro selection of RNA molecules that bind specific ligands. Nature. **346**, 818–22 (1990)
2. G. Castillo, I. Lamberti, L. Mosiello, T. Hianik: High-sensitive impedimetric aptasensor for detection ochratoxin A in food. Lecture Notes in Electrical Engineering. **109**, 31–35 (2012)
3. J. Tang, J. Xie, N. Shao, Y. Yan: The DNA aptamers that specifically recognize ricin toxin are selected by two in vitro selection methods. Electrophoresis. **27**, 1303–11 (2006)
4. J. He, Y. Liu, M. Fan, X. Liu, Isolation and identification of the DNA aptamer target to acetamiprid. J. Agric Food Chem. **9**, 1582–6 (2011)

Chapter 14
Respirometric Tests on Yeast Cells Located in a Small Satellite System

L. Campanella, G. Merola, S. Plattner, A. Negri, C. Pepponi and M. Perelli

The primary aim of the research is to investigate about the respiratory activity (thermodynamics and kinetics) of eukaryotic cells in micro gravity medium. This information can be precious both with reference to human activity in the same conditions and to possible applications to environmental sensing by respirometry. In a space platform, one of the human main activities is surely respiration as strictly related to life conditions. When breathing is not permitted, life expires. What happens to this function in a small satellite system? How do the specific conditions affect the capacity of oxygen uptake and the shape of a respiration curve? In this presentation we describe a research aiming to study the behavior of a well common respirometric system, *Saccharomyces Cerevisiae* yeast cells when located within a closed system positioned inside a small satellite system. More the consequently needed miniaturization of the Clark electrode to amperometrically determine oxygen brings to a further reason of uncertainness related to the high current density and consequent polarization. Some problems were faced such as the aggregation of the cells able to close the circuit where solution is flowing in the experimental system, the formation of gaseous bubbles going to constitute cause of increasing electric resistance, the rigorous stability of the applied tension, the miniaturization of reactor passed from a mean 20 mL model in normal lab to 1 mL and less model when located in a small satellite system.

L. Campanella (✉) · G. Merola · S. Plattner
Department of Chemistry, Sapienza University of Rome, Piazzale A. Moro 5, 00185 Rome, Italy
e-mail: luigi.campanella@uniroma1.it

A. Negri · C. Pepponi · M. Perelli
IMT s.r.l., Via Carlo Bartolomeo Piazza 8, 00161 Rome, Italy

A. Negri
e-mail: andrea.negri@imtsrl.it

14.1 Introduction

The aim of the research is to investigate about the respiratory activity (thermodynamics and kinetics) of eukaryotic cells in micro gravity medium. The development of an environmental sensor to be possible to applied to future human missions is important for future space application. Really the environmental factors in the space can be hazardous for the health of the human crew members: microgravity conditions, presence of electromagnetic and ionizing radiation, toxic or harmful substances at limit concentrations in the space environment. In this work, our group has designed and built an assay using a biosensor able to check environmental parameters with properties suitable for working in a space environment that can be embedded in a nanosatellite CubeSat class. The assay is based on the measurement of respiration of yeast cells (*Saccharomyces Cerevisiae*) in micro gravity conditions. The yeasts are among the organisms most sensitive to the variations of environmental conditions, including the presence of pollutants, in fact toxic substances slow down the oxidative metabolism of yeasts causing a decrease in the oxygen consumption. The yeast *Saccharomyces Cerevisiae* is evolutionarily closer to humans than other eukaryotes and is one of the most intensively studied organisms in molecular and cell biology because its culture is very simple, but, as an eukaryote, presents the complexity of the internal structure of plants and animals, which are also eukaryotes, in fact most of the scientific discoveries made using yeast as a model organism was true for mammals, including humans.

14.2 Measurement Methods

14.2.1 Classic Yeast Respirometric Test

The measurement of the metabolic activity of yeasts is carried out by the measurement of oxygen decrease after the addition of a nutrient substrate (glucose). In the presence of oxygen yeasts carry cellular respiration, consuming oxygen and producing carbon dioxide. The yeast cell respirometric test is a technique used successfully in laboratories to build biosensors for integral toxicity determination that can work with different type of real samples including (food, water, particulates, soil, etc.) [1–3].

14.2.2 Yeast Respirometric Test in Nanosatellite

The space environment and requirements of flight are much more restrictive than a normal laboratory activities, the difference is due primarily to variations of temperature and gravity, mechanical requirements such as resistance to vibration and
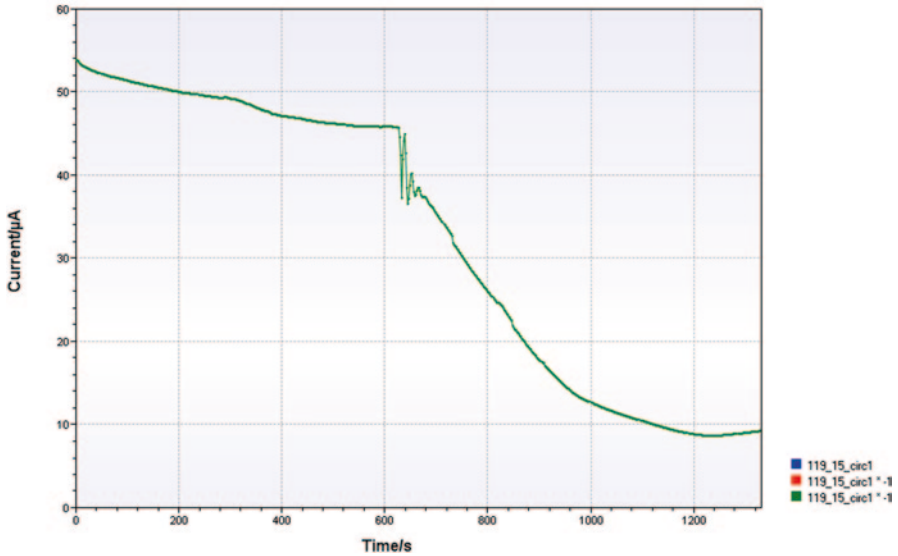
Fig. 14.1 Respirometric curve obtained in close-flow system

finally restriction on the weight and bulk of the device For the measurement of oxygen, due to space limitations, we chose an amperometric measurement system and, in particular, an SPE (screen printed electrode) transducer located in a custom IMT flow cell. The difference respect the classic respirometric test are:

- System is closed and isolated, and O_2.cannot be exchanged with outside
- Yeast cell and equipment working in microgravity conditions.
- Device must be miniaturized and fully stand-alone automatized.

For this system the behavior of respirometric curve is shown in Fig. 14.1.

The best value of the parameters experimentally found to obtain the highest reproducibility and sensitivity are shown in Table 14.1.

14.3   Experimental Device Assembly

The experimental device (Fig. 14.2) was assembled using: piezoelectric micro-pump, 3-way latching micro-valve, IMT Custom Flow-Cell, SPE electrode and IMT Custom Electronic control device

Table 14.1 Best value of the parameter for reproducing and sensitivity

Yeast concentration	100 g/l
Glucose concentration	100 g/l
Particle Size	Mechanical agitation and filtration through a 25 μm paper
Cleaning electrode surface	Anionic Surfactants (Sodium Laurylsolfate) 1 mg/l
Bubble gas	Removal through flushing system on the flow cell designed by IMT
Flow rate	3.5 ml/min (100 Hz)
aging of the yeast (agglomeration of more than 25 μm)	<6% in 72 h
	<8% in 720 h
Temperature Range	$20\,C < T < 50\,C$
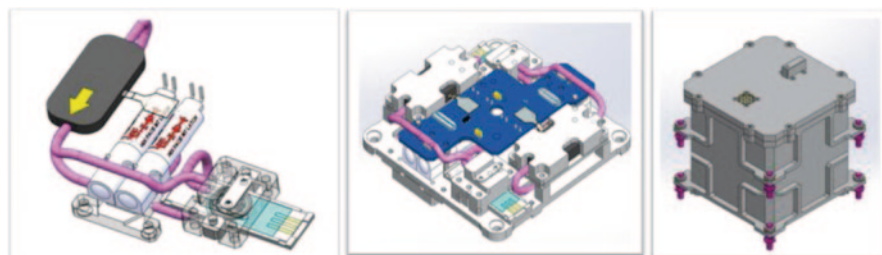
Fig. 14.2 Experimental device 3D-CAD

14.4   Results and Discussion

14.4.1   Reproducibility and Sensitivity

The experimental results obtained in the test session confirmed a good sensitivity and reproducibility of the method (RSD < 8 %) when observed parameter is dI/dt of the respirometric curve. Main analytical data are summarized in Table 14.2.

14.4.2   Robustness and Response Toward Toxic Agents

To check the values of robustness of the sensing system to toxic substances, the tests were also performed with the yeast into contact with toxic substance such as cationic surfactants, at various concentrations. In Fig. 14.3 the corresponding respirometric curve is shown.

Sensitivity toward Cationic surfactants (didecyl-dimethylammonium chloride) was obtained by measuring the ratio between this signal and that of a blank measured under the same conditions but in absence of toxic agent. Sensitivity to toxic

Table 14.2 Main analytical data

Reproducibility (observed parameter dI/ dt)	$\mu = 0.1132 \ \mu A/s$
	$\sigma = 0.0086 \ \mu A/s$ $\sigma/\mu = 0.0759$
	$\% \pm \sigma = 83\%$ $\% \pm 2\sigma = 100\%$ $\% \pm 3\sigma = 100\%$
Sensitivity of the method	$1.132*10^{-3} \ \mu A \ l/s \ g$
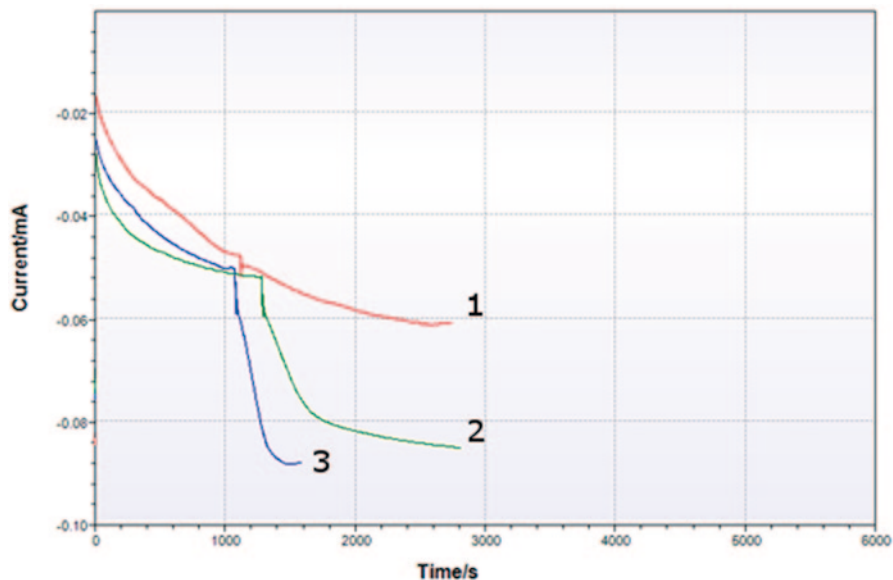
Fig. 14.3 Respirometric curve obtained with Cationic surfactants DDAC (Curve 1: 400 ppm; Curve 2: 160 ppM) and blank respirometric curve (Curve 3)

agents, attenuation rate of oxygen consumption in the presence of DDAC are 30.3 % with 160 ppm of DDAC and 7.6 % with 400 ppm of DDAC.

14.5   Conclusions

The respirometric test can be partially hypothized a monitoring approach in a satellite missions provided that some conditions (Table 14.1) are optimized

References

1. R. Dragone; C. Frazzoli; C. Grappelli; L. Campanella, Ecotoxicology and environmental safety 72, 2009, pp 273–279.
2. C. Frazzoli, R. Dragone, A. Mantovani, C. Massimi, L. Campanella, Analytical and bioanalytical chemistry 389, 2007, pp 2185–2194.
3. L. Campanella, R. Dragone, M.P. Sammartino, R. Trombini, Inquinamento 73, 2005, pp 64–68.

Chapter 15
Progress Toward the Development of a Lytic Bacteriophages-Based Impedance Microbiology for Agro-Food Application

Alessia Mortari, Leandro Lorenzelli, Laura Maria De Plano, Marco Nicolò and Salvatore Guglielmino

A novel approach to impedance microbiology (IM) has been under investigation. In our approach, solution resistance variations will be generated from bacteriophage (phage) lyses of host cell and the consequent release of endoplasmic material. To sensitively detect the lysis, bacteria cells have to be concentrated in a micro-electrochemical cell so that dilution of the released conductive molecules will be minimised. Therefore, the detection principle has been developed in conjunction with a sample preparation method for bacteria capture and concentration based on phage functionalised paramagnetic nanobeads and magnetic concentration. *Escherichia coli* has been used as target bacteria and the beads have been functionalised with selective lytic phages. The method has a potential detection limit slightly below 10 CFU/chamber. The whole assay detection time is bound to be below 30 min as it is strictly linked to the phages lytic cycle. The assay has potential for integration in automated systems.

15.1 Introduction

Hygiene regulation for foodstuffs [1] requires sensitive analysis of 10–25 gr samples [2]. Hazard Critical Control Points [3] have generated high testing rates in the agro-food industry. The general tendency is to provide analysis on-site but foodborne pathogen detection is a costly laboratory activity. A demand for cost-effective integrated system for viable foodborne pathogen testing is high [4].

A. Mortari (✉) · L. Lorenzelli
Center for Materials and Microsystems, Fondazione Bruno Kessler, Trento, Italy
e-mail: mortari@fbk.eu

M. Nicolò · S. Guglielmino · L. M. de Plano
Department of Environmental and Biological Sciences, University of Messina, Messina, Italy

Pathogen analysis requires sample preparation to increase bacteria concentration to a detectable level. Advanced methods also need matrix removal to circumvent inhibition of bio-chemical reaction and signal off-setting due to bio-fouling. Immunomagnetic separation is a recognised method, where bacteria are selectivelly captured and sample size is deceased. In addition, it is prone to system integration but antibodies are expensive and unstable at room temperature. Various types of recognition elements (REs) have been used in alternative to antibodies. Besides high specificity, an ideal RE must be produced at low-cost, be robust and stable at room temperature, have long shelf-life and be easy to immobilise on solid support with functional orientation. To the point, phage are viruses that have recently been suggested as promising RE [5]. Phages are highly specific to their target. After viral infection and amplification, the host cell wall is lysed and progeny phages are released with the endoplasmic material. A fit phage generates cell lysis in 30 min. Phages are easy to isolate, much cheaper to produce than antibodies, with a longer shelf life than the latter [5] and can be immobilised on surfaces with good orientation [6].

IM is an action method for the detection of viable cells. IM is based on solution resistance variation due to bacteria catabolism of non-conductive substrates, into conductive catabolites, such as sugars into organic acids. It employs bare electrodes, that are robust and reusable. However, IM relays on bacteria metabolic time frame and it is time consuming. It is also characterised by low sensitivity, which is mainly due to broth culture salinity and its off-setting effect but also in relation to the dilution that the conducting molecules experience in a high volume electrochemical cell [7].

Starting from the above discussions, an unconventional approach to IM has been under development in our laboratories. The method is based on: (i) magnetic capture of *E. coli* via phage functionalised paramagnetic nanobeads, (ii) micro-biochip further concentration via dielectrophoresis (DEP), (iii) signal variation generated by phages lysis of host cell, (iv) development of a low conductive growth medium and (v) impedance analysis in a microchamber. The preliminary results are here presented.

15.2   Results and Discussions

0.75 μm Ø paramagnetic beads (Chemicell screenMag-Amine) were functionalised via carbodiimide coupling chemistry with phages T4 (ATCC-11303-B4). The binding reaction targeted the carboxylic groups expressed in high concentration on the capsid, thus offering a simple, directional and functional immobilisation of the RE. The functionalisation was first confirmed in Raman Spectroscopy (Fig. 15.1) and was optimised starting from calculations based on spatial hindrance. Three phage:bead ratios were investigated: 84, 112 and 336 phages per bead. To evaluate the capture efficiency, the phages DNA was first deactivated via UV irradiation, thus
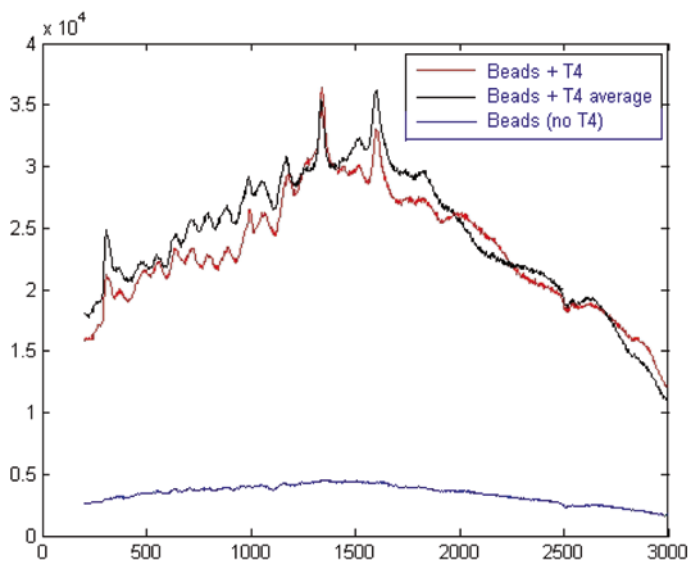
Fig. 15.1 Raman spectra (Raman Intensity, AU, vs. Raman Shift, cm^{-1}) of plain beads and phage functionalised beads

maintaining the phages recognition properties but circumventing the host infection. The captured bacteria (sample volumes from 0.25 to 1 mL; 10^6 CFU inoculation; reaction with functionalised beads from 10^6 to 10^8 in number) were counted on agar plates. The highest capture efficiency was obtained using beads with the 336 ratio.

A preliminary IM experiment was carried out. The experiment was performed using gold electrodes, previously fabricated, and included in a PDMS microchamber (Fig 15.2 right). The analysed *E. coli* samples were incubated off chip. The culture medium was a low conductive (LC) culture broth, similar to Luria Bertani (LB) and Half LB (HLB) broths where NaCl was substituted with mannitol (0.1 and 0.4 M respectively). Mannitol provided counterbalancing osmotic pressure to avoid cell burst. The broths conductivity decreased from the conventional LB broth, through the LC LB broth and to the LC HLB, which were 9.92, 2.09 and 0.039 mS/cm respectively. The bacteria growth in the LC broths was tested in comparison to the traditional LB broth and proved to be of the same order. Samples from *E. coli* cultures in both LC LB and LC HLB broths were analysed in impedance spectroscopy. The impedance spectra were collected at 50 frequencies logarithmically spaced between 1 KHz and 1 MHz, with a 100 mV excitation potential. The samples were at different concentrations, approximately between 10^4 and 10^7 CFU/mL which corresponded to in-chip concentrations between 1 and 10^3 cells. Quantification of cell count was performed with traditional microbiology plate count for validation. Two types of samples were analysed: viable cells and cell lysates. The lysates were produced by sonication as a proof of concept. The samples were sequentially injected (0.5 mL sample volume at 0.50 mL/min flow rate) and analysed in the chip after signal
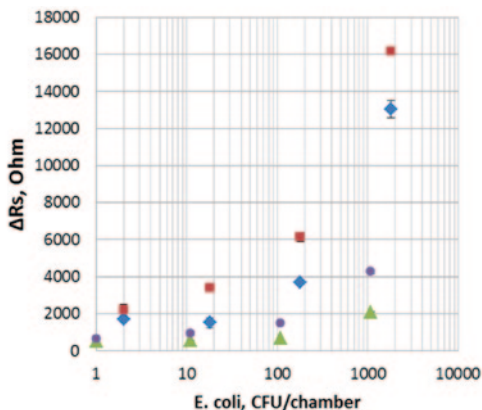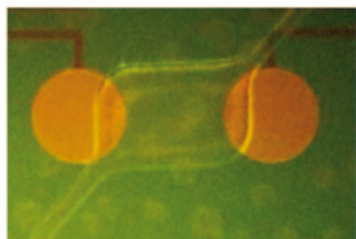
Fig. 15.2 Gold electrodes (500 μm in diameter) and 36 nL PDMS microchamber (*left*) and solution resistance variation (*right*): ■ sonicated cells in LC HLB; ♦ viable cells in LC HLB; ● sonicated cells in LC LB; ▲ sonicated cells in LC LB

stabilisation. The stabilisation was achieved 6 min after stopping the flow and an average results was obtained from the spectra collected at minute 8, 9 and 10. The variations between the broth culture and each sample were plotted (Fig 15.2 left). A proportional relation between solution resistance decrease and cell concentration increase was observed. The difference was larger with lysed cells than with viable cells. Viable cells produced a decrease in solution resistance in all probability due to their catabolic activity on nutrient substrate as per a conventional IM experiment. The signal variation with LC HLB broth was greater than with LC LB medium. This may be explained due to a greater off-set of the LC LB medium conductivity, which is of one order higher that the LC HLB one. Viable cells were detected from about 100 CFU/chamber, while lysed cells in LC HLB provided a detection limit slightly below 10 CFU/chamber.

Further on-chip bacteria concentration was achieved via DEP with gold castellated interdigitated electrodes (results not shown). The electrodes were 12 μm in width with 4 μm gap. Positive DEP was achieved with 2 V pick to pick potential at 1 KHz frequency in LB broth.

15.3   Conclusions

A novel and unconventional application of IM is under development. The method will relay on bacteria selective capture and concentration via lytic phages functionalised with paramagnetic nanobeads and on-chip concentration with DEP. The IM detection principle is based on the cytoplasm release consequent to the viral infection. Phages infection and amplification require viable cells, thus the method will be able to detect viable cells only. Low conductive broths have been developed to

dodge signal off-set. The method has a potential detection limit below 10 CFU/mL and it will have to be fast (30 min) to capture the host cell lyses in the microelectrochemical cell.

Further work will focus on IM analysis of phages lysates, methods integration and testing of milk samples.

References

1. EC. No 2073/2005 Microbiological criteria for foodstuffs. Off. J. EU (2005)
2. ISO. ISO 707:2008—Milk and milk products—Guidance on sampling (2008)
3. EC Health & Consumer Protection General Directorate. Implementation of procedures based on the HACCP principles, and facilitation of the implementation of the HACCP principles in certain food businesses (2005)
4. A. Mortari & L. Lorenzelli. Recent sensing technologies for pathogen detection in milk: A review. Biosens. & Bioelectr. **60**, 8–21 (2014)
5. L. Goodridge & M. Griffiths. Reporter bacteriophage assays as a means to detect foodborne pathogenic bacteria. Food Res. Int. **35**, 863–870 (2002)
6. L. Gervais, M. Gel, B. Allain, M. Tolba, L. Brovko, M. Zourob, R. Mandeville, M. Griffiths, S. Evoy. Immobilization of biotinylated bacteriophages on biosensor surfaces. Sens. & Act. B: Chem. **125**, 615–621 (2007)
7. R. Gómez, R. Bashir, A.K. Bhunia. Microscale electronic detection of bacterial metabolism. Sens. & Act. B: Chem. **86**, 198–208 (2002)

Chapter 16
Virtual Screening Peptide Selection for a Peptide Based Gas Sensors Array

Daniel Pizzoni, Marcello Mascini, Dario Compagnone, German Perez and Corrado Di Natale

A strategy for peptides selection, suitable for gas sensors arrays, is presented. Peptide selection was accomplished by using a virtual screening approach. In a first step, a complete tripeptide library (8000 elements) was generated. For each peptide, the geometry was optimized, and a set of their most representative conformers was considered. Docking simulations versus 160 different aroma molecules, representing different chemical classes with different shapes and dimensions, were carried out. Starting from the tri-peptide library results, the highest scoring 120 tripeptides selective for natural or synthetic strawberry aroma compounds (identified by GC-MS analysis) were selected for generating a 9300 tetrapeptide library in order to discriminate between the two different aromas (natural vs synthetic). The presence of unselective aminoacids, the ability of the peptides to give different scores with most natural/synthetic discriminating molecules, and the presence of aminoacids that can interfere during piezoelectric sensors functionalization were all taken into account in the selection process. Four tetrapeptides were then proposed as possible candidates for a gas sensor arrays to obtain a natural vs synthetic aroma molecules pattern recognition.

M. Mascini (✉) · D. Pizzoni · D. Compagnone
Faculty of Bioscience and Technology for Food, Agriculture and Environment, University of Teramo, 64023 Mosciano S.A., Italy
e-mail: mmascini@unite.it

G. Perez
Laboratory of Computational and Theoretical Chemistry, Faculty of Chemistry, University of Havana, 10400 Havana, Cuba

C. Di Natale
Department of Electronic Engineering, University of Tor Vergata, 00133 Rome, Italy

16.1   Introduction

In recent years the use of oligopeptide modified piezoelectric sensors has demonstrated to be a very useful tool for many different applications. Applications were proposed both in liquid and gas phase [1].

In a recent study [2] a good accordance between computational and experimental data was found in the analysis of the interaction of 14 different volatile compounds (with different chemical and physical properties) with a gold nanoparticles-peptide (GNP-peptide) based gas sensors array. Basing on these results, a method for the selection of peptides suitable for a specific sensing problem is reported. An application to a real case study (discrimination between a natural and a synthetic strawberry aroma) is hereby reported.

16.2   Materials and Methods

16.2.1   Gas Chromatography

Gas chromatography-mass spectrometric (GC-MS) analyses were performed on a Focus ISQ (Thermo-scientific, Milan, Italy) apparatus. A Thermo-scientific TRACE TR-5MS (0.25 mm i. d., 0.25 μm film thickness, 30 m lenght) capillary column was used.

500 μL head-space of liquid natural and synthetic strawberry aroma (both provided by Symrise srl, Milan, Italy) were injected in the GC-MS apparatus. The analysis were carried out in temperature gradient as follow: 3 min at 38 °C, temperature increase up to 150 °C at 7 °C min^{-1}, a final increase up to 250 °C at 30 °C min^{-1}. 25 major compounds were identified by MS spectra database (NIST MS search 2.0).

16.2.2   Virtual Screening

A group of 160 aroma molecules, representative of different chemical functions, was generated by converting standard IUPAC names into structures with LEXICHEM 2.1.0 package from OpenEye Scientific Software (OSS) [3]. The geometry of these structures was subsequently optimized *"in vacuo"* using Merck Molecular Force Field as implemented in SZYBKI 1.5.7 with MMFF94 atomic charges model. In order to account for ligands flexibility, OMEGA 2.4.6. was used to generate conformers with a difference of 0.5 Å^2 of Root Mean Square Deviation (RMSD). These compounds were assigned to different chemical classes (i.e., alcohols, esters, hydrocarbons, etc.) in agreement with their chemical function.

In an initial step, a library of 8000 tripeptides in zwitterionic form was generated. These structures were energy-minimized following the same protocol already used

for ligand molecules. For each peptide, several possible stable conformers were generated, accounting for molecular flexibility.

After the first docking step with the tripeptides library, hypotheses tests were conducted based on binding scores. The objective was to identify the most significant aminoacids and their positions in the sequences when interacting with each group of ligands. Based on this analysis, a subset of tripeptides was selected for lengthening their sequences using a combinatorial approach.

In a second step, this subset of tripeptides was used as scaffold for generating a second library of tetrapeptides. This library was the result of using a combinatorial approach, to insert all natural aminoacids (all but cysteine, excluded due to its ability to bond with GNP gold surface) in all possible positions in the selected tripeptides chains, and discarding redundant sequences. Energy minimization and conformers generation were carried out in an analogous way to previous library, described earlier. After docking the tetrapeptide library vs aroma ligands, a statistical analysis was carried out, aiming to maximize the difference of affinities for each group of ligands, and propose a final set of synthesis candidates. This incremental construction approach was used in a previous work [4]

In molecular docking, the peptides were treated as putative receptors, and their entire molecular surface was considered as possible binding sites for ligands. An exhaustive rigid body docking was conducted with OEDocking (from OSS) amongst multi-conformer both receptors and ligands. The best scores for each association complex formed were considered for the analysis of results.

16.3   Results

Based on the GC-MS data, 25 of the 160 aroma compounds were selected, corresponding to both natural and synthetic strawberry aromas, comprised in tree groups; alcohols, esters and hydrocarbons. The structural analysis of tripeptides showed that peptides rich in aromatic aminoacids had overall high affinity for all ligands. It also showed that negatively charged aminoacids D and E in 2nd position favored the association with alcohols alone. On the other hand, tripeptides with positively charged aminoacids H or R in 3rd position, exhibited better affinities for esters or hydrocarbon type aromas. Polar aminoacids, in general, tend to yield lower affinity. These results are resumed in Table 16.1.

Based on these results, and aiming to maximize differences between peptides to allow discrimination of ligands, 40 peptides targeting each group of ligand (totalizing 120 receptors) were selected for the next screening step.

In the second step, once redundant sequences were discarded, a total of 9300 tetrapeptides were generated (as described in Methods section) and screened versus the 25 designated aromas. A statistical analysis was carried out in order to identify the most relevant patterns in their sequences which allow future discrimination of these compounds based on their chemical characteristics. Finally, four peptides were selected according to their ability to discriminate between a single class and

Table 16.1 Hypotheses tests results showing the positions in which aminoacids are found in top scoring complexes ("good") and in lower scoring ("bad")

Position in sequence	Alcohols		Esters		Hydrocarbon	
	"Good"	"Bad"	"Good"	"Bad"	"Good"	"Bad"
1	F, R, W, Y	G, P, Q	F, W, Y	A, G, P, Q, S	F, R, W, Y	A, C, G, P, Q, S, V
2	D, E, W, Y	A, C, G, S, T	F, W, Y	A, C, G, N; V	F, H, W, Y	A, C, G, S, T
3	F, W, Y	A, C, G, N, S, T, V	F, H, R, W, Y	A, C, G, I, S, T, V	F, H, R, W, Y	A, C, G, S, T, V

Table 16.2 Score cross-reactivity of selected tetrapeptides vs. most representative both synthetic and natural aromas

Aromas (Ligand molecules)	Score cross reactivity (%)				Log(Nat/Syn)
	LGFD	KSDS	TGKF	LAWH	GCPeak area (AU)
7-methyl-3-methylene-octa-1,6- diene	50.8	0.7	75.7	91.4	−5.74
Ethanol	17.9	96.4	18.7	18.2	−1.39
(Z)-hex-3-en-1-ol	41.9	81.0	30.3	49.1	−0.59
(2S)-propane-1,2-diol	35.3	99.5	26.0	16.3	−0.48
[(Z)-hex-3-enyl] 2-methylpropanoate	77.1	0.2	36.3	83.1	0.57
Ethyl octanoate	68.8	0.1	41.2	91.6	6.68
Ethyl hexanoate	61.3	0.0	35.0	96.9	7.64

the rest, and chosen as possible candidates to be incorporated in a gas sensors array (adding a cysteine to the N-terminus for the self-assembling reaction). These results are summarized in Table 16.2.

These functionalized peptides were selected targeting: esters (C-LGFD), alcohols (C-KSDS), hydrocarbons (C-TGKF) and both esters and hydrocarbons (C-LAWH). The combination of these peptides in a sensor array device should be able to differentiate signals corresponding to each aroma group. Their sequences show conserved residues, marked as relevant in the tripeptides analysis.

16.4   Conclusions

In this work an approach for peptide selection, suitable for gas sensors arrays was presented. A complete tripeptide library was built and their binding scores against 160 volatile aroma molecules were calculated. The entire procedure was fairly fast and cheap (less than a month, including data preparation, steps overview, analysis of results, etc. all of these on a consumer laptop). The tripeptide library can be used for many other applications in the field of aroma studies, just selecting the target molecules of interest and generating the tetrapeptides as described.

References

1. D. Compagnone, G.C. Fusella, M. Del Carlo, P. Pittia, E. Martinelli, L. Tortora, R. Paolesse, C. Di Natale, Gold nanoparticles-peptide based gas sensor array for the detection of food aromas. Biosensors and Bioelectronics **42**, 618–625 (2013).
2. D. Pizzoni, M. Mascini, V. Lanzone, M. Del Carlo, C. Di Natale, D. Compagnone, Selection of peptide ligands for piezoelectric peptide based gas sensors arrays using a virtual screening approach. Biosensors and Bioelectronics **52**, 247–254 (2014).
3. OpenEye Scientific Software, Santa Fe, NM. http://www.eyesopen.com
4. G. Perez, M. Mascini, V. Lanzone, M. Sergi, M. Del Carlo, M. Esposito, D. Compagnone, Peptides Trapping Dioxins: A Docking-Based Inverse Screening Approach. Journal of Chemistry **2013**, 1–8 (2013).

Part II
Chemical Sensors

Chapter 17
Optofluidic Jet Waveguide Sensor for Raman Spectroscopy

Gianluca Persichetti, Genni Testa and Romeo Bernini

An optofluidic sensor based on a liquid jet waveguide has been successfully applied in Raman spectroscopy. The jet waveguide is obtained by ejecting the solution under analysis through a capillary nozzle. A self-aligned configuration allows to couple the liquid waveguide with an optical probe consisting of two optical fiber respectively used to excite and to detect the Raman signal. As the numerical aperture of a water jet exceeds the one of any other liquid waveguide, a liquid jet ensures high collection and excitation efficiency. Unlike common approaches, this method removes the signal background coming from the substrate avoiding any necessity to contain the solution by means of solid walls. Proof-of-concept measurements performed by means of ethanol-water solution at different concentrations, show limit of detection already competitive with respect different approaches.

17.1 Introduction

Raman spectroscopy (RS) is a powerful analytical technique widely recognized as one of the main tool for molecular identification. Raman scattering and fluorescence emission are two competing phenomena, for this reason, the fluorescence contribution affects the performances of a sensor based on Raman effect. Once the fluorescence background becomes large relative to the Raman signal, its contribution can no longer be subtracted effectively. Several time consuming approaches for reducing fluorescence have been proposed including time-resolved detection, photolytic destruction of fluorescent impurities, and quenching with added reagents. More practical solution are obtained by means of expensive techniques as for instance shifted-excitation Raman difference spectroscopy (SERDS) or Fourier transform infrared spectroscopy (FT-IR).

G. Persichetti (✉) · G. Testa · R. Bernini
Institute for Electromagnetic Monitoring of the Environment (IREA), National Research Council (CNR), Via Diocleziano 328, 80124 Naples, Italy
e-mail: persichetti.g@irea.cnr.it

Besides the background noise reduction attempts, as spontaneous Raman scattering is a weak optical effect, different methods in effective collection efficiency have been proposed as for instance the use of liquid core waveguides (LCWs) [1] or by means of hollow core photonic crystal fibers (HC-PCFs) [2].

Moreover, recent advances in microfluidics have greatly broadened the applicability of RS in lab on a chip devices [3]. Several factors affects the practical reliability of an optofluidic sensor for Raman spectroscopy. In microfluidic devices the main factors are the signal weakness and the background contamination from the substrate. In LCW approach, long capillary are required to enhance Raman signal and Teflon AF2400, the most performing material for capillary fabrication, exhibits autofluorescence. Despite HC-PCFs offer high collection efficiency, they are usually filled through capillary action. This slow technique prevent their practical use in real time monitoring. Moreover, the formation of air gaps in sample distribution affects light guidance within the microchannels. In this work, we report the successful application of a liquid jet waveguide for Raman spectroscopy. This approach, by exploiting the waveguiding nature of a water jet, is able to avoid or minimize the previously mentioned issues.

17.2   Jet Waveguide Sensor

The ejection of a liquid through a round nozzle depends on different forces acting on the liquid: the viscous drag, the surface tension, the gravitational and the inertial force. Depending on the liquid velocity, different regimes can arise. At low velocity, the quasi-static balance between inertial and surface tension will result in the formation of droplets (dripping regime). By increasing the velocity above a certain critical value, the kinetic energy will overcome the liquid surface energy, leading to a jetting regime where a continuous jet formation is observed. The jet has a continuous shape forming a regular cylinder up to a certain length (named breakup length), and then it breaks up into drops. The breakup length first increases linearly with jet velocity reaching a maximum (linear regime) and then it begins to decrease until a minimum of the breakup length. All the measurements performed by our jet waveguide sensor have been obtained in linear regime.

As for LCW, in a water jet, the Raman signal can be efficiently guided by means of total internal reflection (TIR) but in this case the numerical aperture and consequently the collection efficiency is greater ($NA_{water\ jet} = 0.88 > NA_{LCW} = 0.32$). HC-PCFs own a numerical aperture considerably larger than LCWs (≈ 0.68 for water core)[4]. But even in this case, the HC-PCF numerical aperture is well below the one achievable by means of a water jet waveguide. Jet waveguide sensors have been successfully applied in fluorescence spectroscopy [5] but never employed in the proposed configuration for Raman spectroscopy.

The working principle is shown in Fig. 17.1. A liquid stream of the solution to analyze is generated by means of a stainless steel capillary with internal diameter $ID = 0.508$ mm. In order to excite and detect the Raman signal, a simple probe
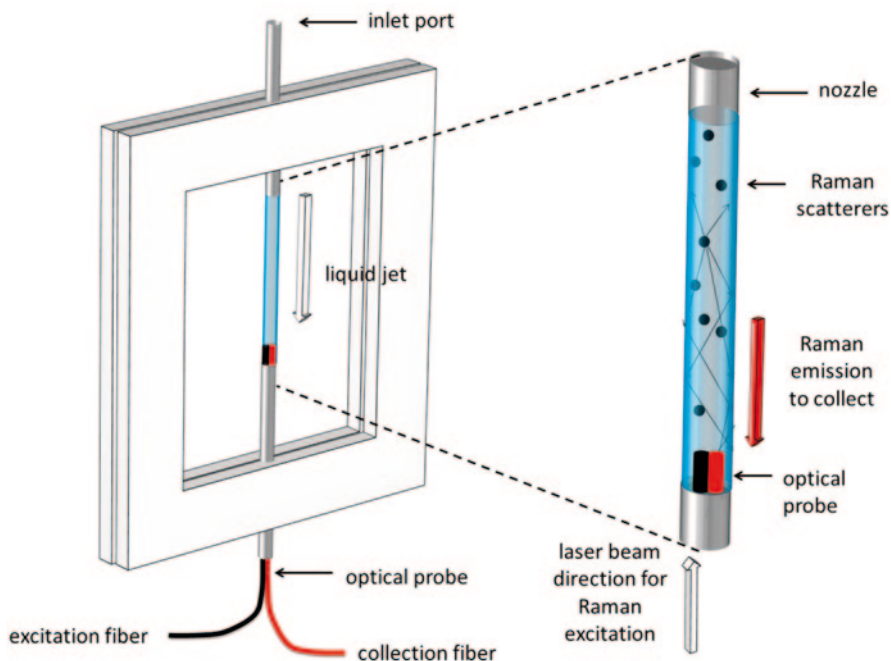
Fig. 17.1 Schematic of the optofluidic Raman sensor based on a water jet waveguide

composed of two optical fiber (diameter d=105 μm diameter, NA=0.22) has been used. One fiber is employed to excite the solution, whereas the other one is used to deliver the signal towards a spectrophotometer. The liquid jet is directly coupled with the optical probe in an alignment-free configuration enabling the excitation of the whole stream and an effective collection of the Raman signal. In contrast to commonly used methods in Raman detection, this configuration completely avoids any fluorescence background from the substrate or from solid walls used to contain the solution. The liquid jet length considered in our measurements was l=18 mm (distance nozzle-optical probe). This corresponds to an excited volume of around 3.53 μl.

In order to manufacture a suitable holding and alignment-free architecture a Polymethylmethacrylate (PMMA) frame was micromachined.

17.3   Experimental Measurements

A laser source at 532 nm (P_{out}=70 mW) was coupled with the exciting fiber of the optical probe by means of a collimator providing the 44% of the original emitted power. A syringe pump was used to drive the solution into the stainless steel capillary. The collecting fiber of the optical probe was directly coupled with a spectrom-
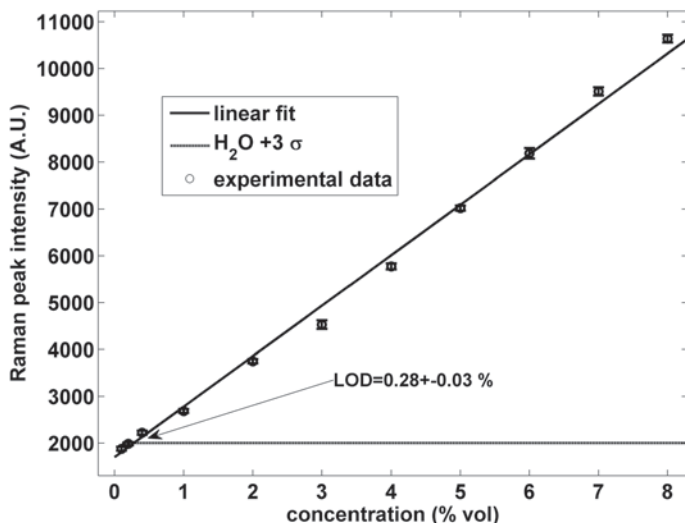
Fig. 17.2 Calibration curve for ethanol water solution ranging from 0.1 to 8%. The horizontal line is drawn considering the blank measurement plus three times the value of its standard deviation. The LOD is 0.28%

eter delivering the Raman signal towards this detector. The spectrometer used in the measurements was a Shamrock SR-3031(Andor Technology) employing a 600 lines per mm grating and a thermoelectrically cooled CCD camera (Newton, Andor Technology). An optical filter was employed to filter out the pump contribution at 532 nm in the detected spectra.

The performances of the system have been successfully tested considering ethanol-water solution at different concentrations. In particular for the measurements analysis, we have considered the Raman peak centered at 2932 cm^{-1} corresponding to the stretching symmetric vibration of the CH_3 group in water-ethanol system. Each experimental point of the calibration curve (Fig. 17.2) was obtained considering the average of 20 measurements performed with an integration time $t_{int} = 2$ s.

A limit of detection (LOD) of 0.28 ± 0.03% for ethanol-water solution has been obtained. Despite this present setup is not intended as a fully optimized system, the attained value of the LOD (0.28%) is competitive also if compared to more complex spectroscopic technique. For instance a LOD of 0.2% is reported using FT-Raman spectroscopy [6]. Also the comparison with sensors based on hollow core shows the effectiveness in ethanol detection of the proposed device. For instance ethanol concentration at the 1% level is reported for hollow core based sensor [7] (3 m long with internal volume of around 9 μl) using excitation wavelength at 532 nm.

17.4 Conclusions

An optofluidic sensor for Raman spectroscopy of liquid solutions has been developed. The NA provided from a liquid jet ensures very high collection efficiency, outperforming other liquid waveguides. Proof-of-concept measurements attest an LOD value which is suitable for sensing application. The intrinsic device simplicity establishes the basis for real world sensing applications and the absence of typical disadvantages affecting other approaches open new perspective in Raman spectroscopy.

References

1. D. Qi, A. J. Berger. Quantitative Analysis of Raman Signal Enhancement from Aqueous Samples in Liquid Core Optical Fibers. Appl. Spectrosc. **58** (10), 1165–1171 (2004).
2. S. Arismar Cerqueira Jr. Recent progress and novel applications of photonic crystal fibers. Rep. Prog. Phys. **73** (024401), 1–22 (2010)
3. P. C. Ashok, G. P. Singh, H. A. Rendall, T. F. Kraussa, K. Dholakia, Lab Chip **11**, 1262–1270 (2011)
4. F. Eftekhari, J. Irizar, L. Hulbert, A. S. Helmy. A comparative study of Raman enhancement in capillaries. J. Appl. Phys. **109**, 113104 (2011)
5. G. Persichetti, G. Testa, R. Bernini. High sensitivity UV fluorescence spectroscopy based on an optofluidic jet waveguide. Opt. Express **21**(20), 24219–24230 (2013).
6. L. S. Mendes, F. C. C. Oliveira, P. A. Z. Suarez and J. C. Rubim. Determination of ethanol in fuel ethanol and beverages by Fourier-transform (FT)-near-infra-red and FT Raman spectrometries. Anal. Chim. Acta **493**, 219–231 (2003)
7. C. Meneghini, S. Caron, A. C. Jacob Poulin, A. Proulx, F. Émond, P. Paradis, C. Paré, A. Fougères. Determination of Ethanol Concentration by Raman Spectroscopy in Liquid-Core Microstructured Optical Fiber IEEE Sens. J. **8**, 125–1255 (2008)

Chapter 18
Optical Sensors Based on Nanoporous Materials

Paolo Bettotti, N. Kumar, R. Guider and M. Scarpa

Nanoporous materials are ideal candidates to fabricate sensors with high sensitivities. Using nanoporous materials both the strength and the type of interactions between analytes and host matrix can be tuned at will, and their large surface area permit to achieve ultralow detection limit and to keep high loading capacity and, thus, large dynamic range. Despite these intriguing possibilities their use in sensing technology is still limited because several fundamental aspects are not fully understood. By comparing supported and free standing Porous Silicon membranes, we demonstrate that sensor's sensitivity is clearly overestimated if the sample is not properly washed. Moreover we underline the fact that, despite the reduced Q-factor of the resonant cavities, the strong interaction between the analyte and the optical modes in porous materials produces a large net sensitivity of the sensor. Finally, we show that the non-specific signal may have a linear response with the analyte concentration and it thus extremely difficult to separate it from the specific one. The work presented here is of importance in the design of nanoporous materials for sensing application. In fact it demonstrates that the final sensitivity of the device is not defined by its optical quality alone and that several other effects have to be considered to fabricate a reliable sensor.

18.1 Introduction

Nowadays, the large field of applications of sensors based on optical or electrical detection mechanisms has to deal with a poor chemical specificity of such systems and thus the contribution of Non Specific Signal (NSS) in the sensor response. Concerning porous materials based sensing systems, several materials were proposed so far as host matrices to fabricate nanoporous sensors [1–3]. Among all, Porous Silicon (PSi) is an ideal candidate for the fabrication of sensors because of the large

P. Bettotti (✉) · N. Kumar · R. Guider · M. Scarpa
Dipartimento di Fisica, Università di Trento, via Sommarive 14, 38123 Povo TN, Italy
e-mail: bettotti@science.unitn.it

tunability of its porous structure, its high optical quality, the multi-parametric sensor development opportunity and because of its well versatile surface chemistry [4, 5]. The use of porous material as sensor is accomplished using two different assay geometries. The first one is the Flow Over (FO) configuration where the sensor is bound to a solid substrate and the assay proceeds through the diffusion of the liquid phase into the pores of the device. Such technique allows quick and easy measurements, but suffers from a lack of specific binding in the holes, where non target molecules can easily remain trapped. The second one is the Flow Through technique (FT), where the molecules can pass through the functionalized open pores of the sensor (which are free standing membranes (FSM)), thus enabling an optimization of the binding reaction. In this article, we fabricate and investigate n-type PSi microcavities in FO and FT approaches for sensing applications and demonstrate that NSS is strongly reduced under FT conditions. Conversely, FO conditions lead to a systematic overestimation of the device sensitivity. These results support the superiority of the FT sensing scheme while raise some questions about the reliability of FO analyses performed on porous substrates.

18.2 Experimental Procedure

18.2.1 Samples Fabrication

N-type silicon wafer was used as precursor material and microcavities were fabricated through etching in aqueous solution containing 12.5% HF. The microcavity structures consist of two Bragg mirrors created by varying the applied etching current and enclosing a defect layer. More details about the PSi and the membranes fabrication can be found in [6]. MCs of different quality factor (Q=30, 50 and 70) were fabricated depending on the number of pair of alternating layers. As an example, transmittance spectra of MC with Q=50 are shown in Fig. 18.1b. The resonance for this sample is observed at around 1488 nm.

18.2.2 Sensing Experiments

Figure. 18.1a shows the shift of the MC resonance position when MCs with Q=50 is exposed to methanol-ethanol mixed solutions in FO condition. An increase of percentage in volume of ethanol with respect to methanol (from 0 to 100% v/v) shows a red shift due to the change in the refractive index of the sensor as liquid fills the pores. To quantify these results, we calculated the relative sensitivity of our devices by plotting the optical shift versus the refractive index of methanol-ethanol solution, assuming a linear variation of the refractive index of the solution according to their volume fraction. A sensitivity of ~ $1.7 * 10^{-4}$ is calculated from the observed slope of 510 nm/RIU for the fabricated MC samples.
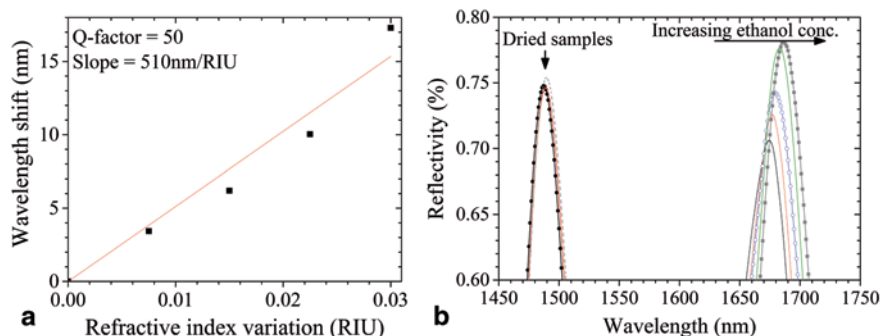
Fig. 18.1 a Shift of the resonance of the microcavity as a function of the refractive index variation obtained by filling the pores with different liquids. **b** Demonstration of the reproducibility of the sensor: after drying the signal goes back to its original position

Furthermore the reversibility of sensor was also tested leaving the samples to dry. As shown in Fig. 18.1b, the observed resonance initially was at 1488 nm before exposing to any organic liquid and shifts to higher wavelength after exposure. After letting the sample to dry, the resonance of MC goes back to nearly initial position at 1490 nm, which demonstrate the reversibility of the device. All these experiments confirm the great potential of PSi based MC for bio-sensing applications.

To check the limit of detection (LOD) of our sensors, we monitored the binding of bovine serum albumin (BSA) to the microcavity surface treated with glutaraldheyde (GA). In the first step pore's surface for both FT and FO configuration were modified by amino-silane (ATPES), which was treated with an excess of GA [6]. Then solutions containing increasing concentrations of BSA were injected in the sensor. Figure 18.2a shows the resonance shift corresponding to BSA concentration/ml for both configurations, and a sensitivity of 0.89 and 0.35 nm/mg was observed for FO and FT techniques respectively. With a resolution of 0.1 nm, the limit of detection (LOD) of "BSA" observed for these respective sensors is 0.11 and 0.29 mg/ml.

We noticed that the LOD is three times smaller in FO than in FT configuration, which was also noticed by Lisa A. De Louise for p-type MC structure used to sense water sucrose solution [7]. We suppose that such difference could be due to the presence of residues of bio-molecules or other impurity remaining in pore depth for FO configuration and that cannot be washed completely, resulting in an over estimation of sensor sensitivity.

In order to support our affirmation, we blocked all available sites for three set of samples (in both FO and FT configuration) by dipping them in glycine and BSA solution for whole night. After such treatment, the sensors were exposed again to high dose of BSA concentration. As expected, an average 2 nm positive shift is observed after exposing the FO sensors to BSA concentration, meanwhile a small negative shift of 0.6 nm is observed in the FT cases, which could be due to the removing of some glycine/BSA during washing procedure. Figure 18.2b shows observed relative shift for respective samples.
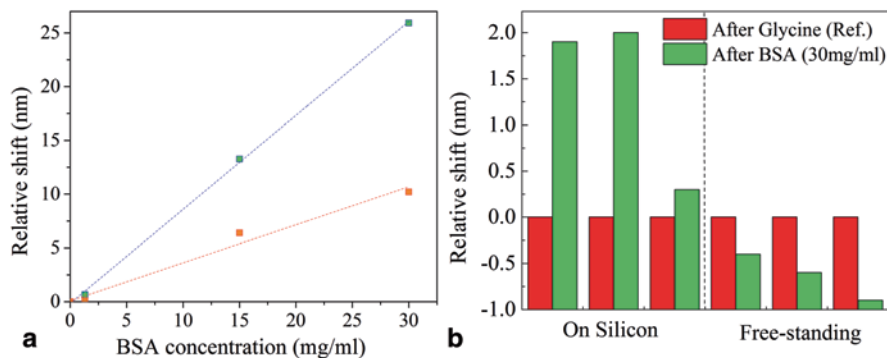
Fig. 18.2 a Shift of the resonance of the microcavity as a function of analyte concentration. The blue slope refers to the FO approach, while the red slope refers to an assay performed in FT configuration. The difference among the two is due to dielectric material that remains trapped within the pores and is not properly removed during the rinsing of the sample. **b** Contribution of non-specific binding in bio-sensing after blocking all available sites and again expose to high dose of BSA molecules

18.3   Conclusions

Nonspecific binding in FO and FT configuration is studied in this article. Free-standing and wafer supported n-type porous silicon multilayer structures with pore size (30–80 nm) are fabricated via conventional electro-chemical etching method. We have experimentally demonstrated the fabrication of bio sensors based on n-type PSi as well as the high influence of non-specific binding in FO techniques, resulting in an over estimation of LOD of such devices. In conclusion, we strongly believe that these results will be of great impact in the field of porous-based biosensors.

References

1. C. Cantalini, S. Agnoli, G. Granozzi, A.Z. Sadek, K. Kalantar-zadeh, W. Wlodarski. Comparison study of conductometric, optical and SAW gas sensors based on porous sol–gel silica films doped with NiO and Au nanocrystals. Sensors and Actuators B: Chemical **143**(2), 567–573 (2010)
2. T. N. Huan, T. Ganesh, K. S. Kim, S. Kim, S. H. Han, H. Chung. A three dimensional gold nanodendrite network porous structure and its application for an electrochemical sensing," Biosensors & Bioelectronics **27**(1), 183–186 (2011)
3. M. Scampicchio, A. Arecchi, A. Bianco, A. Bulbarello, C. Bertarelli, S. Mannino. Nylon nano-fibrous biosensors for glucose determination," Electroanalysis **22**(10), 1056–1060 (2010)

4. H. Zhang, Z. Jia, X. Lv, J. Zhou, L. Chen, R. Liu, J. Ma. Porous silicon optical microcavity biosensor on silicon-on-insulator wafer for sensitive DNA detection. Biosensors and Bioelectronics **44**(1), 89–94 (2013)

5. T. Jalkanen, E. Makila, Y. I. Suzuki, T. Urata, K. Fukami, T. Sakka, J. Salonen and Y. H. Ogata. Studies on Chemical Modification of Porous Silicon-Based Graded-Index Optical Microcavities for Improved Stability Under Alkaline Conditions. Advanced Functional Materials **22**(18), 3890–3898 (2012)

6. N. Kumar, S. Gennaro, P. V. W. Sasikumar, G.D. Soraru, P. Bettotti. Self detachment of free-standing porous silicon membranes in moderately doped n-type silicon. Appl. Phys. A (2013). doi: 10.1007/s00339–013-8104–6

7. J. A. Howarter, J. P. Youngblood. Optimization of Silica Silanization by 3-Aminopropyl-triethoxysilane. Langmuir **22**(26), 11142–11147 (2006)

Chapter 19
Modelling of Nanoantenna-Based Optical Sensors for High-Sensitivity High-Resolution Infrared Spectroscopy of Chemical Compounds

Mohammed Janneh, Andrea De Marcellis, Elia Palange, Carlo Rizza, Alessandro Ciattoni and Sandro Mengali

In this paper we investigate how to increase the functionalities of optical sensors based on metal nanoantennas (NA) arranged in 2D-arrays as sensitive spectroscopic tools for the identification of molecular species by using the Surface Enhanced InfraRed Absorption (SEIRA) technique. We will discuss the influence of the NA geometrical parameters (length, width and thickness) and 2D-array periodicity on the local electric field enhancement and 2D-array spectral response. Software based on the finite element method (FEM) is used to accurately simulate the NA 2D-array reflectivity response as a function of the wavelength of the probing light. In particular, by evaluating the optical response of rod and cross NA 2D-arrays we studied the influence of the NA geometrical parameters on the SEIRA response.

A. De Marcellis (✉) · E. Palange
Dipartimento di Scienze Fisiche e Chimiche, Università dell'Aquila, Via Vetoio 1, 67100 L'Aquila, Italy
e-mail: andrea.demarcellis@univaq.it

M. Janneh
Dipartimento di Ingegneria Industriale e dell'Informazione e di Economia, Università dell'Aquila, Via G. Gronchi 18, 67100 L'Aquila, Italy

C. Rizza
Dipartimento di Scienza e Alta Tecnologia, Università dell'Insubria, Via Valleggio 11, 22100 Como, Italy

A. Ciattoni
Consiglio Nazionale delle Ricerche, CNR-SPIN, Via Vetoio 1, 67100 L'Aquila, Italy

S. Mengali
CREO Consortium—Electro-Optics Research Centre, S.S.17 snc, Loc. Boschetto, 67100 L'Aquila, Italy

19.1   Introduction

The study of the optical properties of metal nanostructures (such as the NA) able to amplify the infrared vibrational and/or roto-vibrational absorption signals of adsorbed molecules is of great interest due to their potentiality to detect very small molar concentration of adsorbates. In this way, it is possible to increase the optical sensor sensitivity, especially, for applications in chemistry, biology and medicine. For the past years, remarkable progresses have been made on the understanding of the SEIRA effect by exploiting the potentiality of plasmon resonance in metal NA to enhance the infrared and the Raman signals [1–4]. Moreover, the use of surface plasmon excitations in NA has been demonstrated for the detection of specific chemical and biological molecules and their modifications under the presence of external analytes [5–7]. In this paper we will report on the study of how the NA shapes and their geometrical parameters as well as the periodicity of the 2D-array can influence the optical response and the SEIRA ability in determining the minimum molar concentration of adsorbed substance on the sensor.

19.2   Modelling and Optical Response of Metal NA-Based SEIRA Sensors

In general, the NA fabricated by lithographic processes on a semiconductor (e.g., Si, Ge and GaAs for near-, mid- and far-infrared applications) or dielectric substrates, are few tens of nanometer thick metal structures. The use of NA 2D-arrays as sensor for SEIRA effect is a quite general paradigm because, following the linearity of the Maxwell equations, a change of NA length (L), width (W) and thickness (S), as well as 2D-array periodicity (a and b), allows to centre the peak of the sensor reflection response at any specific wavelength. In this paper, we considered two geometrical structures of 2D-arrays of sub-wavelength gold NA having the shape of rods and crosses, as shown in Fig. 19.1 COMSOL Multiphysics software, based on FEM, was used for numerical simulations of the SEIRA responses of these optical sensors by fixing the following values for the geometrical parameters of the NA structures and of the 2D-arrays: $S=20$ nm, $W=200$ nm, $L=1.5$ μm and $a=b=2$ μm. These values allow to achieve a maximum of the peak reflectance at a wavelength equal to 9.5 μm when Si substrate is used. Moreover, an absorbing medium was described by a 20 nm thick film that uniformly covers the NA 2D-arrays with an absorption peak centred at 9.5 μm. As reported in Fig. 19.1, simulations show that the distribution of the reflected electric field is more localized and spatially confined near and around the edges of the NA. The resulting metasurface (i.e., the combination of both the NA 2D-array and the substrate) optically acts as a frequency filter for the reflected light. More in detail, Fig. 19.2 shows the far-field reflected spectral responses as a function of the wavelength of rod and cross NA 2D-arrays (see the red dotted curves). In the same Figure, are also reported the different absorption
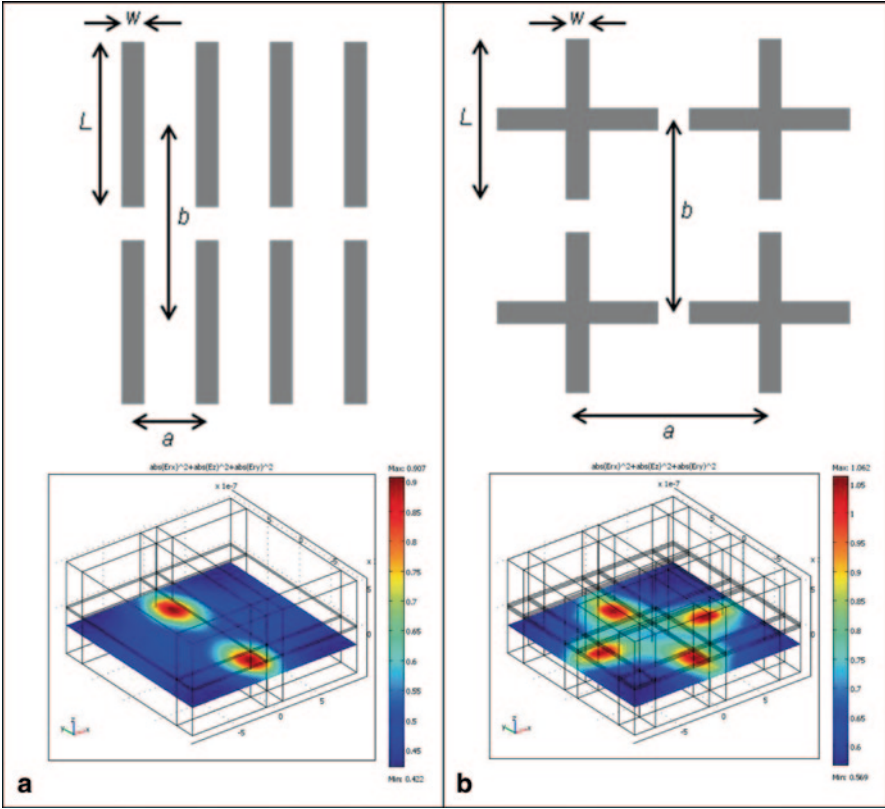
Fig. 19.1 2D-array configurations for rod and cross NA and 3D simulations showing the electric field amplitude enhancement when illuminated with a plane wave at normal incidence
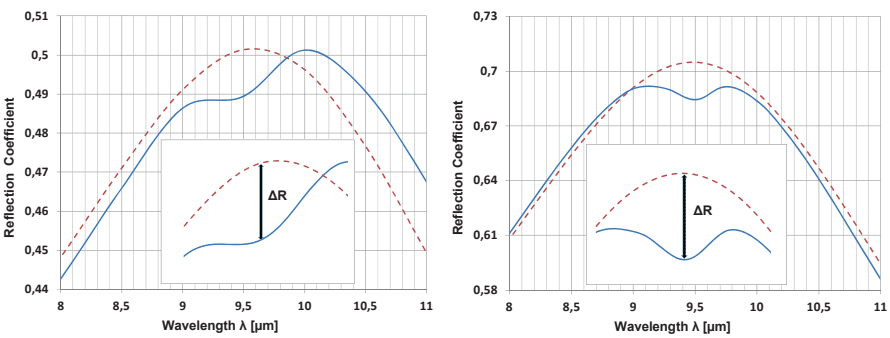
Fig. 19.2 Reflectance responses for the rod (*left*) and cross (*right*) NA 2D-arrays as a function of wavelength. Red dotted (*blue continuous*) curves are the 2D-array reflection response without (with) the presence of 20 nm thick absorbing substance. In the inset is magnified the variation of the 2D-array reflectivity due to the SEIRA effect

Table 19.1 Qualitative procedure to determine the optical sensor main reflectivity properties as a function of the NA and 2D-array geometrical parameters

NA and 2D-array parameter		Reflectivity peak value	Central wavelength
Length (L)	Increase	Increase	Increase
Width (W)		Increase	Increase
Thickness (S)		Increase	Decrease
2D-array periodicity (a)		Decrease	Increase
2D-array periodicity (b)		Decrease	Increase

peaks (ΔR) due to the presence of the absorbing medium on the NA 2D-array (see the blue continuous curves). For the comparison with the case in which the same film of absorbing medium is deposited on an unstructured flat gold substrate [8], it is possible to observe an enhancement of the absorption signal of more than two order of magnitude due to the SEIRA effect. Moreover, simulations demonstrate that the response of a 2D-array of cross NA is two times more sensitive respect to the same 2D-array composed of rod NA. As shown in Fig. 19.1, the enhancement of the absorption signal is related to the strong localisation of the electrical field of the reflected light that occurs near to the neighbouring NA edges. Physically, this is due to a combination of surface plasmon excitations at the NA surfaces and of light interference and diffraction. Moreover, as summarised in Table 19.1, optimization studies have been performed on the designed NA 2D-arrays in order to extract a qualitative method describing how their main geometrical properties allow to change the SEIRA sensor reflectivity peak value and the central wavelength.

19.3   Conclusions

In this paper we have shown how the geometrical parameters describing metal NA 2D-arrays can be varied in order to obtain specific SEIRA sensor reflectivity peak values and central wavelengths. Numerical simulations demonstrate that the enhancement of the SEIRA response of NA 2D-arrays respect to the simple absorption signal of an absorbing substance deposited on an unstructured flat surface is related to the strong increase of the light electric field that takes place around the NA neighbouring edges. In conclusion, the study of these structures enables to obtain promising results that can be used in optical sensor based applications for the detection of very low molar concentration of chemical and biological species.

References

1. F. Neubrech, A. Pucci, T. W. Cornelius, S. Karim, A. García-Etxarri, and J. Aizpurua. Resonances of individual metal nanowires in the infrared. Appl. Phys. Lett. **86**, 253104 (2006)
2. R. Adato, A. A. Yanik, J. J. Amsden, D. L. Kaplan, F. G. Omenetto, M. K. Hong, S. Erramilli, and H. Altug. Ultra-sensitive vibrational spectroscopy of protein monolayers with plasmonic nanoantenna arrays. PNAS **106**, 19227–19232 (2009)

3. L. V. Brown, K. Zhao, N. King, H. Sobhani, P. Nordlander, and N. J. Halas. Surface-enhanced infrared absorption using individual cross antennas tailored to chemical moieties. J. Am. Chem. Soc. **135**, 3688–3695 (2013)

4. C. D'Andrea, J. Bochterle, A. Toma, C. Huck, F. Neubrech, E. Messina, B. Fazio, O. M. Marago, E, D. Fabrizio, M. L. de La Chapelle, P. G. Gucciardi, and A. Pucci. Optical Nanoantennas for Multiband Surface-Enhanced Infrared and Raman Spectroscopy. ACSNANO **7**, 3522–3531 (2013)

5. J. Dostalek, J. Homola, and M. Miler. Rich information format surface plasmon resonance biosensor based on array of diffraction gratings. Sens. & Act. B **107**, 154–161 (2005)

6. D. Enders and A. Pucci. Surface enhanced infrared absorption of octadecanethiol on wet-chemically prepared Au nanoparticle films. Appl. Phys. Lett. **88**, 184104 (2006)

7. S. Mackowski, S. Wolrmke, A. J. Maier, T. H. P. Brotosudarmo, H. Harutyunyan, A. Hartschuh, A. O. Govorov, H. Scheer, and C. Bra1uchle. Metal-enhanced fluorescence of chlorophylls in single light-harvesting complexes. Nano. Lett. **8**, 558–564 (2006)

8. R. G. Greenler. Infrared study of absorbed molecules on metal surfaces by reflection techniques. J. Chem. Phys. **44**, 310 (1966)

Chapter 20
Surface Plasmon Resonance Optical Sensors for Engine Oil Monitoring

Alessandra Ricciardi, Adriano Colombelli, Giovanni Montagna, Maria Grazia Manera, Marco MIlanese, Arturo de Risi and Roberto Rella

Lubricant systems are fundamental in engines (automotive, aviation, rail etc.) and in any industrial system where surfaces of moving mechanical parts are in contact [1]. An improper lubrication due to oil degradation over a long period of time can lead to unwanted component failure and increased maintenance costs. Present study, unlike methods developed until now for detecting oil degradation (loss of mechanical, physical, chemical and optical properties) focuses on the development of a Surface Plasmon Resonance (SPR) transduction methodology able to measure lubricant degradation in real time observing the change in the refractive index. This approach answers to environmental regulation and user requirements on performance, lifetime expectancy and engine efficiency

20.1 Introduction

Lubricant systems are fundamental in automotive and in any industrial systems in order to guarantee the correct friction and to prevent dramatic failure of moving surface or mechanical parts in contact [2].

In particular, in automotive, although the substitution of lubricating oils follows a schedule specified by cars manifacturers, it's independent of the real state of oil, because doesn't take into account the operative conditions [3].

In fact, properties of lubricant depend on both external (e.g. temperature, humidity, etc.) and internal (e.g. aging, wear) factors: thus the quality of the lubricant changes over time [1].

M. G. Manera (✉) · A. Colombelli · G. Montagna · R. Rella
Istituto per la Microelettronica e i Microsistemi (IMM CNR) campus Ecotekne, via Monteroni, 73100 Lecce, Italy
e-mail: roberto.rella@cnr.it

A. Ricciardi · M. Milanese · A. De Risi
Dipartimento Ingegneria dell'Innovazione, Universita' del Salento, Via Monteroni, 73100 Lecce, Italy

From an environmental viewpoint it should be preferable to completely exploit oils before changing rather than the more conservative change on a schedule used at present [4].

In the last years, physical, mechanical, chemical and electrical properties of lubricant have received considerable attention from researchers, which have developed several methods for detecting oil degradation, but not able to give response in real time [5].

Differently, the present work focuses on the development of a new sensing device based on Surface Plasmon Resonance (SPR) technique able to measure, in real time, degradation of lubricant oils by observing the change of optical properties (refractive index).

In this paper both numerical simulations and experimental tests on newly developed SPR based sensors have been carried out to measure the variation in the refractive index of lubricant oil during exercise monitored.

20.1.1 Surface Plasmon Resonance

Surface plasmon resonance (SPR) is an optical phenomenon that results by the interaction between a transverse mode (TM) polarized electromagnetic incident wave and the conduction electrons present in a thin metal film. Kretshmann and Otto geometries are two fundamental SPR configurations, of which the first one is considered more suitable for sensing activities.

A TM light wave (Ei) propagating in the optical prism hits the metal film: a part of Ei is reflected back into the prism (Er) and an evanescent wave propagating in the metal film decays exponentially perpendicularly to the metal-prism interface to the outer boundary where couples with surface plasmons (PS). At optical wavelengths, gold and silver are the most commonly used metal films, whose thickness is less than 100 nm for visible–NIR light [6].

Once set up the incident light (wavelength and polarization) and the metal layer, the reflectance curve (R) in Kretschmann configuration shows a dip attributed to incident photons energy transfer to the SPs. The reflectance curve is very sensitive to the change of refractive index of dielectric medium (n_s) [7], making achievable to determine a relationship between R and wear of oil.

20.1.2 Experimental Details

A very schematic of the experimental setup used in this work is shown in Fig. 20.1.

The p-polarized radiation is generated by a monochromatic He-Ne laser ($\lambda = 632.8$ nm). A beam splitter provides two identical beams of which one reaches a first silicon photodiode (PD1), while the second beam that passes through the splitter, reaches the sensor surface (metal film coupled to SF10 glass prism) and undergoes to a further reflection. A second photodiode (PD2) measures the intensity of
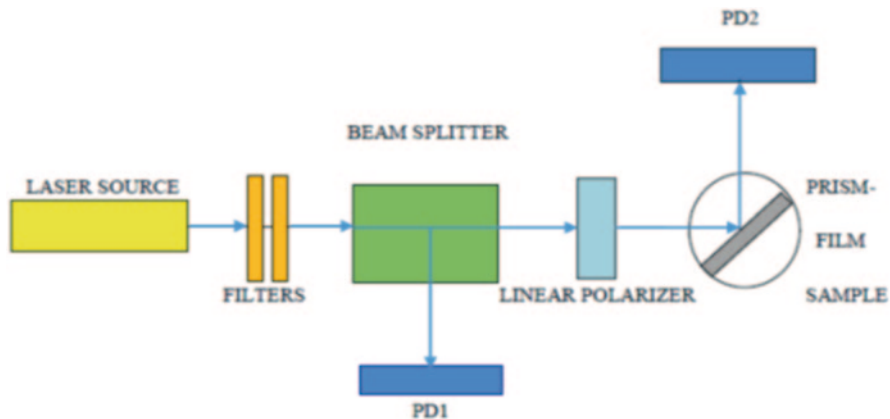
Fig. 20.1 Block diagram of SPR measurement bench

Table 20.1 Detection of variation of refractive index for each transducer

Transducers (numbers are referred to thickness-nm-of each metal layer)	Refractive index variation per 1000 km ($\Delta n/1000$ Km)
49Ag	$9*10^{-4}$
48Ag 2Ti	$1.6*10^{-3}$
48Au 2Ti	$1.9*10^{-3}$
23Ag27Au2Ti	$9*10^{-4}$

the beam reflected by the SPR sensor, thus allowing the calculation of the reflectivity as function of the incidence angle (SPR signal). The reflectance R is the ratio Er/Ei, that is the intensities of the light read by photodiodes PD2 andPD1 respectively after and before the reflection from the sensor surface. The prism-sample combination is performed to assure the contact oil-metallic film (optical transducer); the system is placed on a rotating structure that allows the user to control the angular position of the sample (resolution of 0.01).

Everything is managed by a dedicated software that allows the acquisition, processing and displaying of the data in real-time on a control panel.

In order to minimize optical noise, related to external light, the SPR bench has been shadowed through a teflon panel.

20.2   Realization of Suitable Transducers

In the present investigation four SPR sensor configurations were realized and analyzed, as shown in the following Table 20.1.

The system under investigation can be used to observe different fluids, whose degradation resulting in variation of their optical properties following the modification of the surface plasmon resonance curves.

In this work the relationship between degree of oil degradation and the variation of its optical properties has been found. Although the sensors don't provide an univocal response, all the experimental results are confident to realize suitable sensors for refractive index measurement in the investigated range. Thus the SPR transduction methodology can be used to do a real time oil control.

20.3 Conclusions

The present work focused on the development of a new sensing device based on surface plasmon resonance technique that, although cannot predict interactions between engine and lubricant, it has been demonstrated can measure in real time the increase of refractive index due to oil degradation. Obviously, the experiments carried out for this work, represent only a first step on the sensor design process, because it is necessary to study in deep further parameters, as influence of operating temperature of oil circuit, unwanted reactions between metallic film and lubricant, etc. Nevertheless, the device under investigation can represent an alternative to traditional methods of oil monitoring, so that the replacement of worn oil can be done only when it is necessary or when it is observed an unexpected rate of degradation. This predictive maintenance strategy can reduce not only unnecessary maintenance costs but also permits considerable environmental advantages.

References

1. L. Marton, F. van der Linden, Temperature dependent friction estimation: Application to lubricant health monitoring, Mechatronics 22 (2012) 1078–1084.
2. A. R. Caneca, M. F. Pimentel, R. K. H. Galvao, C. E. da Matta, F. R. de Carvalho, I. M. Raimundo Jr., C. Pasquini, J. J. R. Rohwedder, Assessment of infrared spectroscopy and multivariate techniques for monitoring the service condition of diesel-engine lubricants oils, Talanta 70 (2006), 344–352.
3. L. Marton, On analysis of limit cycles in positioning systems near Striebeck velocities, Mechatronics 48 (2008) 46–52.
4. J. D. Turner, L. Austin, Electral techniques for monitoring the condition of lubricant oil, Meas. Sci. Technol. 14 (2003) 1794–1800.
5. A. Agoston, C. Otsch, B. Jakoby, Viscosity sensors for engine oil condition monitoring—Application and interpretation of results, Sensors and actuators A 121 (2005) 327–332.
6. J. Homola, Electromagnetic theory of surface plasmons, Chemical Sensor and Biosensors 4 (2006) 3–44
7. G. Gupta, J. Kondoh, Tuning and sensitivity enhancement of surface plasmon resonance sensor, Sensors and Actuators B 122 (2007) 381–388.

Chapter 21
Advanced Materials for Electrode Modification in Sensoristic Applications for Trace Analysis

Valentina Pifferi and Luigi Falciola

This paper aims to provide a summary of our contribution in the field of the determination, by electroanalytical techniques, of some contaminants of emerging concern at trace level, particularly focusing the attention on the use of nanomaterials and innovative polymers for electrode modification.

21.1 Introduction

Trace analysis [1] (*i.e.* the analysis of analytes in concentration low enough to cause difficulty, generally under 1 ppm) albeit very challenging, in the last years has shown a tremendous growth, prompted by the urgent need of many International Organizations (US Environmental Protection Agency EPA, U.S. Food and Drug Administration FDA, European Food Safety Authority EFSA, World Health Organization WHO) looking for new analytical techniques for the detection of different molecules in different and increasingly more complex matrixes for the environmental monitoring, the food safety and the clinical diagnosis to the national security and the forensic investigation.

Among different reliable and robust analytical techniques suitable for the determination of trace analytes, electroanalytical techniques and particularly those based on pulsed voltammetry, seem to be a promising independent alternative in terms of very high precision, accuracy and sensitivity, simplicity of use, portability, easy automation and possibility of *on-line* and *on-site* monitoring without sample pretreatments and low costs. These methods are no more confined to the detection of inorganic species and have been already and successfully employed for the determination of organic compounds and environmental carcinogens [2–4], as the Barek UNESCO Laboratory of Environmental Electrochemistry and the Trace Element Satellite Centre has amply demonstrated in the last decades.

L. Falciola (✉) · V. Pifferi
Dipartimento di Chimica, Università degli Studi di Milano, 20133 Milano, via Golgi 19, Italy
e-mail: luigi.falciola@unimi.it

Moreover, very recently, the use of nanosized and/or nanostructured materials sometimes combined with the use of polymeric materials for the modification of electrodes has enhanced the chances of progress and growth of electroanalitycal methodologies for trace analysis, with the advantages of increasing the affinity for the analyte, increasing sensitivity, lowering the limits of detection and minimizing or completely avoiding interferences.

In this context, this paper aims to provide a summary of our contribution in this field, particularly focusing on the use of nanomaterials and innovative polymers.

21.2 Results and Discussion

21.2.1 *Electrodes Modified by Nanomaterials*

During the last years, nanomaterials appeared to be very promising for application in the field of sensors and biosensors. Among different types of nanomaterials, carbon nanotubes, metal and semiconductive nanoparticles, show very interesting properties and features for electrochemical performances and were chosen for the modification of electrodes to be used in selected trace electroanalytical applications.

All the new modified electrodes were firstly characterized and studied by Cyclic Voltammetry (CV) and Electrochemical Impedance Spectroscopy (EIS), in the presence or in the absence of a model probe molecule, in order to obtain information about electrochemical properties and the behaviour of the electrode in solution and with the redox probe. After the characterization study, some electrodes were used as sensors for the determination of relevant compounds or pollutants at trace level.

Carbon nanotubes (CNT) [5–6] are extensively employed in the electroanalytical field, due to their large surface area, electrocatalytic activity, fast electron transfer rate and easy functionalization. Since the procedure of purification with acids plays an important role for electrode performance, initially, a detailed study on different purification procedures was performed. 24 h sulfonitric mixture treatment appeared to be the best procedure for our CNTs yielding to materials characterized by an high metal nanoparticles removal, high amount of covalent acidity (responsible of CNTs activity), high surface area and mesoporosity. Moreover, the final removal of amorphous carbon by NaOH treatment highly improved the reversibility of the final device and favoured the diffusion mechanism of the process. The best type of purified and activated CNTs were employed for applications in electroanalysis, in particular in the determination of *o*-toluidine, benzidine and furan.

o-**toluidine** [6] was detected using Linear Sweep Voltammetry in the range 1.5–7 ppm with good linear correlation, obtaining a limit of detection of 0.16 ppm and excellent apparent recovery factors and repeatability, in comparison with carbon based-screen printed electrodes, which presented problems of fouling, probably due to polymerization products. This new method was used for the determination of *o*-toluidine during its photodegradation mediated by ZnO photocatalyst, showing

better performances than C-SPE and comparable with HPLC. Moreover, the methodology was also employed to monitor *o*-toluidine absorption by cyclodextrine nanosponges based on hydrogel polyamidoamines (PAA), allowing to discriminate among various types of resins and to obtain absorption kinetic parameters.

Benzidine [7] was determined by using Square Wave Voltammetry in the range 0.05–2.2 ppm, obtaining good correlation and good limits of detection at ppb level, with better apparent recovery factors and repeatability in comparison with the previously optimized technique based on C-SPE.

In the case of **furan** [8], preliminary promising results were obtained with deposition of Pt nanoparticles on carbon nanotubes by cycling voltammetry, but optimization of nanoparticles deposition procedure and application of other voltammetric techniques are still needed and are currently under investigation.

Metal and semiconductor nanoparticles present unique peculiar properties, dependent on their size and shape, very different from bulk materials, such as high active surface area, high surface-to-volume ratio, selectivity, easy functionalization and electrocatalysis, and for these reasons they are extensively employed in electroanalysis. In this work, gold, silver and titanium dioxide nanoparticles were studied and characterized.

Gold nanoparticles, synthesized by colloidal procedure with or without a protective polymer on carbon nanotubes as support, showed in comparison with CNTs, an increase in the peak current and capacitance, followed by the decrease of charge transfer resistance. The polymer, if the content of gold is low, is detrimental for the electrochemical behaviour, probably because it isolates the gold nanoparticles. The best results were obtained with 1 % Au or 5 % Au-Polymer. The optimized electrode was tested for the determination of glycerol using cyclic voltammetry obtaining really promising preliminary results.

Silver nanoparticles were synthesized via colloidal method using two different supports: Nafion membrane and carbon nanotubes. In the case of Nafion, Ag nanoparticles show higher current intensity than bare electrode, probably due to higher surface area, a change in the diffusion mechanism from planar to convergent and small double layer formation. This electrode was tested for the determination of halothane and dichloromethane, showing promising results [9]. In the case of CNTs, silver nanoparticles allowed the extension of the potential range towards negative values and peak currents were higher than the previous case with Nafion, showing the important contribute played by CNTs. Moreover, the use of a protective polymer (PVA) caused the decrease of the electrode activity, probably due to less available Ag nanoparticles.

Titanium dioxide nanorods were studied in combination with single-walled carbon nanotubes, in the dark or under UV illumination, considering the photoactivity of titania. The best electrochemical performances were obtained for SWCNTs, since titania, as semiconductor brings a more resistive behaviour. Differences between dark and irradiation appeared only in the presence of titania, as expected. UV irradiation caused a change in the model probe molecule diffusion through the nanomaterials, probably ascribable to excited electrons of the titanium dioxide.

21.2.2 Electrodes Modified by Polymeric Membranes

Among different electron conducting polymers [10–12], Brilliant Green (BG), belonging to the triphenylmethane family, was chosen as electroactive polymer for the production of modified electrodes, in combination with CNTs and PEDOT, another non-redox electron conducting polymer. CNTs in combination with PEDOT gave the best electrochemical performance in terms of capacitance and low resistance, but when the determination of hydrogen peroxide was considered, electrode with CNTs and polyBG gave the best results for the presence of the redox centre (LoD around 30 ppb) [13]. This electrode was also tested as biosensor for glucose and ethanol, immobilizing on it glucose oxidase (GOx) and alcohol oxidase (AlOx), respectively and showing very good results in comparison with the Literature, with limit of detections of 2 ppm for glucose and 1 ppm for ethanol. Moreover, the influence of oxygen was studied, obtaining better results in its presence for glucose detection and in its absence for ethanol determination, probably due to the aerobic or anaerobic character of the enzyme bacterium.

Among different proton conducting polymers sulphonated poly(aryl ether sulphone) (PES) was studied as a new material for the production of modified electrodes in comparison with Nafion. For its characterization, different parameters have been studied: the quantity and the form of the polymer, its storage, its method of drying and the casting solvent. In particular, 1 % linear PES in the acidic form, dried at 25 °C in oven, dissolved in N-methylpyrrolidone, showed the best performance, superior to Nafion. These polymers presented a very interesting behaviour, since without the redox probe, capacitance was comparable to glassy carbon, while when the redox probe was present, capacitance increased of two orders of magnitude and diffusion of the probe changed, probably due to variation of diffusion mechanism in the polymeric structure.

References

 1. D.T. Pierce, J.X. Zhao, in Trace Analysis with Nanomaterials (Wiley-VCH, Weinheim, Germany, 2010)
 2. J. Zima, I. Svancara, J. Barek, K. Vytras. Crit. Rev. Anal. Chem. **39**, 204–227 (2009)
 3. J. Barek, K. Peckova, V. Vyskocil. Current Anal. Chem. **4**, 242–249 (2008)
 4. J. Barek, J. Cvacka, A. Muck, V. Quaiserovà, J. Zima. Fres. J. Anal. Chem. **369**, 556–562 (2001)
 5. J. J. Gooding. Electrochimica Acta **50**, 3049–3060 (2005)
 6. V. Pifferi, G. Cappelletti, C. Di Bari, D. Meroni, F. Spadavecchia, L. Falciola. Anal. Chem. Submitted, (2014)
 7. L. Falciola, V. Pifferi, E. Mascheroni. Electroanalysis **24** (4), 767–775 (2012)
 8. L. Falciola, V. Pifferi, M. L. Possenti, V. Carrara. J. Electroanal. Chem. **664** (1), 100–104 (2012)
 9. V. Pifferi, V. Marona, M. Longhi, L. Falciola. Electrochimica Acta **109**, 447–453 (2013)
10. M.E. Ghica, C.M.A. Brett. Electroanalysis **18** (8), 748–756 (2006)
11. M.M. Barsan, E.M. Pinto, C.M.A. Brett. Electrochimica Acta **53**, 3973–3982 (2008)
12. M.E. Ghica, C.M.A. Brett. J. Electroanalytical Chemistry **629**, 35–42 (2009)
13. V. Pifferi, M. Barsan, M. Ghica, L. Falciola, C. Brett. Electrochimica Acta **98**, 199–207 (2013)

Chapter 22
Polyaniline Modified Thin-film Array for Sensor Applications

Andrea Ravalli, Giovanna Marrazza, Bianca Ciui, Cecilia Cristea, Robert Sandulescu, Daniela Di Camillo and Luca Lozzi

In this work, a pH sensor based on polyaniline-modified thin-film interdigitated array (IDA) microelectrodes was presented. Aniline was electropolymerized on the surface of IDA working electrodes by means of cyclic voltammetry. Scanning electron microscope and electrochemical measurements were used to characterize the polyaniline-modified sensor surface. Electrochemical impedance spectroscopy (EIS) was finally used to determinate the variation of pH in $[Fe(CN)_6]^{3-/4-}$ solutions.

22.1 Introduction

Thin-film interdigitated electrodes are one of the most used transducers in different technical and analytical applications with the particular importance in the field of (bio)sensing [1, 2]. They take advantages of the microelectrodes features enhancing the sensitivity and detection limits. Since conducting polymers show some numerous features such as lightweight, low cost, flexibility for sensing and biosensing, they have recently attracted a lot of attention in this field [3, 4]. Among all organic conjugated polymers, polyaniline (PANI) is a very attractive conducting polymer in the field of biosensing for its easy preparation, good level of electrical conductivity and environmental stability [5, 6]. In this work, we propose the use of innovative thin-film interdigitated arrays (IDAs) modified with polyaniline polymer. The IDAs are based on a four-electrodes system: two working, reference and auxiliary

G. Marrazza (✉) · A. Ravalli
Department of Chemistry "Ugo Schiff", University of Florence, Firenze, Via della Lastuccia 3, Sesto Fiorentino, Italy
e-mail: giovanna.marrazza@unifi.it

B. Ciui · C. Cristea · R. Sandulescu
Analytical Chemistry Department, Faculty of Pharmacy, Iuliu Haţieganu, University of Medicine and Pharmacy, Cluj-Napoca, Romania

D. Di Camillo · L. Lozzi
Department of Physical and Chemical Sciences, University of L'Aquila, Aquila, Via Vetoio, Coppito, Italy

electrodes. The gold working electrodes consists of two individually addressable arrays with an interdigitated approach. Aniline monomer was first electro-polymerized on the surface of gold arrays by means of cyclic voltammetry. The electrochemical characteristics of the modified sensors were obtained studying the electron transfer rates of potassium ferricyanide redox couple under different experimental conditions in cyclic voltammetry (CV) experiments and the electrochemical impedance spectroscopy (EIS). Preliminary experiments on polyaniline-modified IDA for pH determination were presented.

22.2   Materials and Methods

22.2.1   Chemicals

Aniline, perchloric acid, potassium ferricyanide(III) and potassium ferrocyanide(II) were purchased from Merk (Milan, Italy). Hydrochloric acid and potassium chloride were obtained from Sigma-Aldrich (Milan, Italy).

MilliQ (Millipore, USA) water was used throughout the work.

22.2.2   Electrochemical Apparatus

Thin-film interdigitated gold array microelectrodes (IDAs) and electrochemical-flow cell were obtained MicruX Fluidic (Oviedo, Spain).

Electrochemical measurements were conducted using a digital potentiostat/galvanostat AUTOLAB PGSTAT 30(2)/FRA2 controlled with the General Purpose Electrochemical System (GPES) and Frequency Response Analyzer (FRA2) 4.9 software (Eco Chemie, Utrecht, The Netherlands).

All the experiments were conducted at 25 °C using electrochemical flow cell.

Polyaniline-modified IDA electrodes images were obtained by Secondary Electron Microscope (SEM) equipped with In-Lens detector.

22.2.3   Electropolymerization of Aniline on Thin-film Interdigitated Gold Array Microelectrodes (IDA)

First, degassed 2.5 mM aniline solution prepared in 50 mM $HClO_4$ was injected in the electrochemical flow cell. Then, the potential was cycled between -0.4 V and 1 V for 10 cycles at 0.05 V s^{-1}. Finally, the modified sensors were washed with 0.1 M KCl solution.
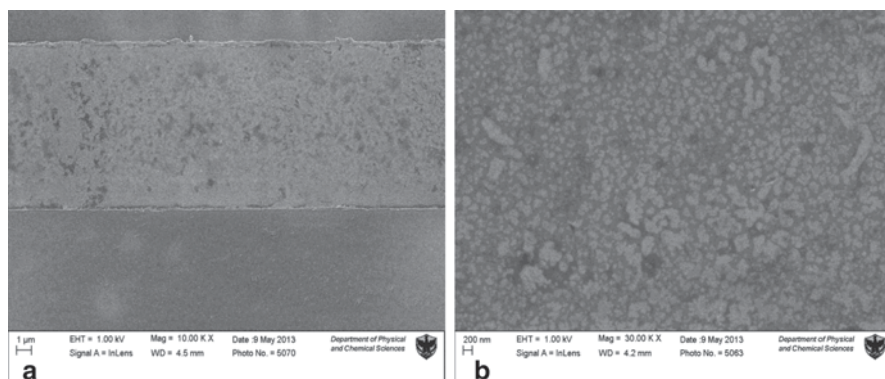
Fig. 22.1. SEM images of polyaniline-modified IDA electrode at different magnifications

22.2.4   Electrochemical Impedance Spectroscopy (EIS) measurements for pH determination

Equimolecular 1 mM $[Fe(CN)_6]^{3-/4-}$ solution prepared in 0.1 M KCl at pH 3, 5, 7 (using hydrochloric acid) was used as redox probe. Electrochemical impedance spectroscopy (EIS) measurements were performed on a single IDA working electrode using a voltage of 10 mV in amplitude (peak-to-peak), within the frequency range 100 kHz–10 mHz. Experimental spectra, presented in the form of complex plane diagrams (i.e. Nyquist plot), were fitted with proper equivalent circuits using the facilities of the FRA2 4.9.004 (EcoChemie) software. Charge transfer resistance (R_{ct}) values were taken as analytical signal.

22.3   Results and Discussion

22.3.1   Polyaniline-modified IDA Electrodes SEM Characterization

SEM analysis was conducted in order to verify the presences of the polyaniline on the surface of IDA electrodes. Results show the presence of polyaniline structures uniformly distributed onto the entire IDA electrode surface (Fig. 22.1)

22.3.2   Polyaniline-modified IDA Electrode for pH Measurements

Electropolymerization voltammograms of aniline onto IDA electrode surface were reported in Fig. 22.2. It was possible to observe an increase of both oxidation peaks

Fig. 22.2 Electropolymerization spectra of 2.5 mM aniline in 50 mM $HClO_4$. CV spectra were obtained as reported in Sect. 2.3
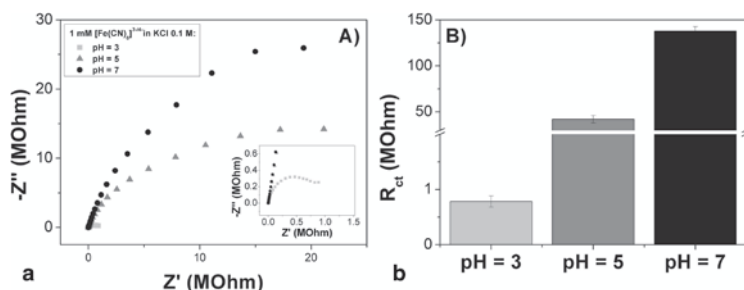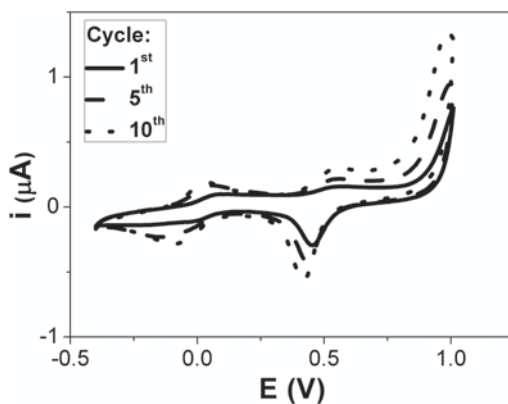
Fig. 22.3. **a** EIS spectra of polyaniline-modified IDA using 1 mM $[Fe(CN)_6]$ 0.1 M KCl redox mediator prepared at pH 3, pH 5, pH 7. **b** Average and standard deviation respect to the R_{ct} for polyaniline-modified IDA at pH 3.0, pH 5.0, pH 7.0

at $+0$ V and $+0.5$ V and the reduction peaks at -0.1 V and $+0.4$ V coherent with the formation of polyaniline film.

Polyaniline conductivity is strongly influenced by the degree of pronation, which is mainly controlled by the pH of the medium. Variation of protonation can be easily monitored using electrochemical impedance spectroscopy (EIS). EIS spectra acquired in presence of 1 mM $[Fe(CN)_6]^{3-/4-}$ redox mediator prepared in 0.1 M KCl at different pH are shown in Fig. 22.3.

An increase of resistance charge transfer (R_{ct}) values was observed with the increase of pH ($R_{ct}=0.8\pm0.1$ MOhm for pH 3.0, $R_{ct}=40\pm4$ MOhm for pH 5.0 and $R_{ct}=138\pm5$ MOhm for pH 7.0) in accordance with the decreasing of the conductivity of the polyaniline

22.4   Conclusions

In this work, the use of polyaniline-modified interdigitated arrays (IDAs) for detection of pH was presented. IDAs were successfully modified with conductive polymer offering a promising tool for sensor applications.

References

1. R. Ohno, H. Ohnuki, H. Wang, T. Yokoyama, H. Endo, D. Tsuya, M. Izumi. Electrochemical impedance spectroscopy biosensor with interdigitated electrode for detection of human immunoglobulin A. Biosensors and Bioelectronics **40** (1), 422–426 (2013)
2. K. V. Singh, D. K. Bhura, G. Nandamuri, A. M. Whited, D. Evans, J. King, R. Solanki. Nanoparticle-Enhanced Sensitivity of a Nanogap-Interdigitated Electrode Array Impedimetric Biosensor. Langmuir **27** (22), 13931–13939 (2011)
3. T. K. Das, S. Prusty. Review on conducting polymers and their applications. Polymer-Plastics Technology and Engineering **51** (14), 1487–1500 (2012)
4. Z. Taleat, A. Ravalli, M. Mazloum-Ardakani, G. Marrazza. CA 125 Immunosensor Based on Poly-Anthranilic Acid Modified Screen-Printed Electrodes. Electroanalysis **25** (1), 269–277 (2013)
5. F. Berti, S. Todros, D. Lakshmi, M. J. Whitcombe, I. Chianella, M. Ferroni, S. A. Piletsky, A. P. Turner, G. Marrazza. Quasi-monodimensional polyaniline nanostructures for enhanced molecularly imprinted polymer-based sensing. Biosensors and Bioelectronics **26** (2), 497 (2010)-503
6. R.-S. Saberi, S. Shahrokhian, G. Marrazza. Amplified Electrochemical DNA Sensor Based on Polyaniline Film and Gold Nanoparticles. Electroanalysis **25** (6), 1373–1380 (2013)

Chapter 23
Screen Printed Electrode-Flow Stripping Voltammetry for Inorganic Analysis

C. Dossi, F. Stropeni and D. Monticelli

The use of a commercial wall-jet cell for alumina-based screen printed sensors has regained new life to flow injection techniques in voltammetry. Of the many theoretical advantages of flow injection stripping, the possibility of using external calibration is of primary importance to the applied analytical chemist, since higher throughput is gained if compared to the commonly-used standard addition methodology. Adversely, external calibration in voltammetry heavily relies on the instrumental conditions, and needs careful optimization.

Flow injection voltammetry with wall-jet cells for SPE has been investigated using the new 4330 voltammetric instrument from Amel Instruments, Italy. The instrumental configuration has been optimized both in continuous flow (CF-SV) operations, where bubble formation during sample exchange must be minimized, and in flow-injection (FI-SV), where the analytical reproducibility is dependent on the peak shape. A new voltammetric software (VApeak[2]) has also been implemented for FIA and external calibration operations. Reproducibility was found to be very good under typical analytical conditions, with excellent calibration linearity, and limits of detection around 0.6 µg/L for Pb and 0.3 µg/L for Cd. Quantitation of Pb and Cd on real samples has been also carried out via external calibration, giving excellent results, particularly at low concentrations.

C. Dossi (✉) · F. Stropeni
DiSTA, University of Insubria, Via Dunant 2, 21100, Varese, VA, Italy
e-mail: carlo.dossi@uninsubria.it

C. Dossi · F. Stropeni
AMEL Instruments, Via S.G.Battista de la Salle 4, 20132, Milano, Italy

D. Monticelli
DiSAT, University of Insubria, Via Valleggio11, 22100, Como, CO, Italy

23.1   Introduction

Flow injection analysis for stripping voltammetric determination of trace analytes has appeared in the analytical literature in the 80's. It gained some interest in the scientific community, with good analytical figures of merit [1], but it was apparently undergoing a slow oblivion. In recent years, however, this instrumental approach has resurfaced [2]. One of the major reasons for this resurrection is to be due to the availability of new, automated instruments and to the commercial exploitations of wall-jet flow cells for screen printed electrodes. This approach has not simply improved automation, but it has open new possibilities, in terms of chemical modification of the electrode surface and lack of any problems in regenerating electrode surfaces. These new possibilities have been already exploited in organic analysis [3], whereas more work has to be done in inorganic trace analysis. This paper will focus on the optimization of a fluidic system for flow injection stripping voltammetry in inorganic analysis, trying to shade more light into the instrumental aspects and the analytical figures of merit in Pb and Cd analysis.

23.2   Experimental

An AMEL model 4330 multipolarograph (Amel Instruments, Italy) was used with VA_peak software for IBM-PC to control all the instruments and analytical data. A PERIMAX 12 peristaltic pump (Spetec, Germany) was interfaced to the AMEL 4330 instrument for full control. A wall-jet flow cell DRP-FLWCL (DropSens S.L., Spain) and screen-printed carbon electrodes DRP-C110, with both carbon or platinum counter electrodes, from DropSens were used as the electrochemical cell. Sample injections were done on a six-way valve (Omnifit, Cambridge, UK) equipped with a 0.5 mL loop. The flowrates were set to 1.0 mL/min. Degassing of eluent and samples with pure N_2 is controlled by the VA_peak software. Prior to analysis, a mercury film was plated on the screen printed electrode by flowing a plating solution ($HgCl_2$ 80 mg/L in 1.3 M HCl) at -1000 mV for 200 s. The plating solution was added at a 1% volume ratio to all the samples in order to renovate Hg film during analysis. In continuous-flow technique (CF-SV), the sample is continuously passed through the flowcell. Rinsing was undertaken between each sample with MilliQ water acidified at pH = 2 with HCl. In flow-injection technique (FI-SV), the six-way valve is used to inject the sample during the deposition step. A 0.8 mg/L solution of $HgCl_2$ in MilliQ water at pH = 2 is used as the eluent, and all samples are added with 1% plating solution.
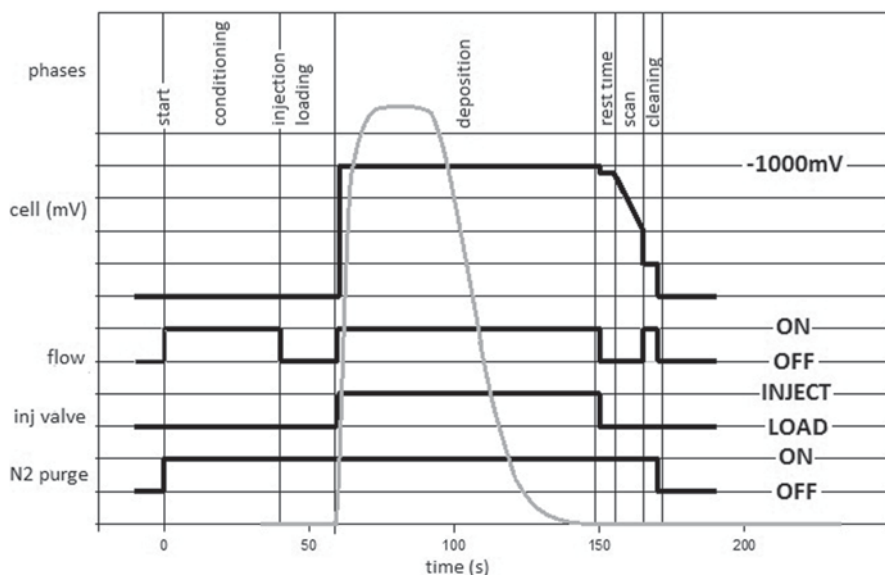
Fig. 23.1 Timings of all instrumental parameters in Fi-SV, superimposed to the peak shape

23.3 Results and Discussion

Two different techniques have been implemented on the same fluidic system, using a continuous flow of analyte (**CF-SV, continuous-flow stripping voltammetry**) or performing the stripping step under a single injection of analyte (**FI-SV, flow-injection stripping voltammetry**). In the latter technique, the optimization of the fluidic system is mandatory, for reducing all the dead volumes, and for ensuring a square-type injection peak with minimization of carryover times. The total volume of the plumbing system was found to be around 400 µL, with a 50 µL dead volume between the injection valve and the flowcell, leading to a prestep period of 5 s at 1 mL/min total flow. A 0.5 mL injection was then found to give a square shaped peak, returning to full baseline within less than 60 s. These figures are of primary importance, since the deposition step in flow-injection stripping voltammetry needs to start during the prestep period, and must last until the analyte peak has returned to full baseline (Fig. 23.1). A 90 s deposition time may be considered safe for a 0.5-mL injection; for bigger volumes, this time must be linearly increased.

The analysis of Cd and Pb in a synthetic water sample at pH=2 was done under differential pulse conditions, resulting in a reproducibility of the calibration curves between 0 and 40 µg/L below 5 %; on different screen printed electrodes, the reproducibility did not change significantly.

However, FI-SV always proved to be less noisy, at least five times lower, than CF-SV, in test analysis of Pb and Cd at 15 µg/L. On the basis of these considerations, the FI-SV technique, in spite of its greater complexity, proved significantly

Table 23.1 Quantitation of Cd and Pb in a synthetic water sample using the external calibration

Parameter	Pb (μg/L)	Err (%)	Cd (μg/L)	Err(%)
Expected concentration	5.0		5.0	
Found (sample #1)	4.78	4.6	4.84	3.2
Found (sample #2)	4.97	0.5	4.53	9.7
Found (sample #3)	4.84	3.3	4.78	4.4

superior to CF-SV, in terms of S/N ratio, immunity from bubble formation upon changing the sample, and electrode stability due to the use of a "clean" electrolyte during analysis and cleaning steps.

It is noteworthy that the analytical step, where the differential-pulse scan is used for analyte quantitation, is done under stopped flow conditions (Fig. 23.1), in order to minimize the noise of hydrodynamic mixing, and to optimize diffusional conditions. The very small volume of the wall-jet electrochemical cell will thus allow a linear calibration range up to 100 μg/L. Above this value, diffusional limitations may arise, leading to a bending of the calibration curve. The conservative value of 100 μg/L can be thus considered as a safe estimation of the Limit of Linearity (LOL) for both analytes at a 0.5 mL injection. The limit of detection (LOD) has been calculated following IUPAC guidelines, resulting in 0.62 μg/L for Pb and 0.32 μg/L for Cd, which are significantly lower than reported for conventional flowcell [4].

Real water samples of Lake Como have been successfully analyzed, showing a small decrease, generally less than 10 %, in the analytical figures of merit (LOD and calibration slopes) when compared to synthetic samples.

The good reproducibility in the calibration parameters may also avoid the use of the standard addition technique. A set of three water samples spiked with Cd and Pb at 5 μg/L have been analyzed with the external calibration method, and the results are reported in Table 23.1.

The results are consistent with the accepted precision of the method at 5 μg/L levels, with errors mostly below 5 %. Moreover, the external calibration may minimize the problems of the intercept errors in standard addition.

With real samples, our experiments showed that it is necessary to reproduce the sample matrix in the standard solutions for best results.

23.4   Conclusions

Screen printed electrodes have been demonstrated to revitalize flow-injection in inorganic voltammetry, as already observed for organic analysis [3]. Sensitivity and limits of detections are comparable to batch conditions, but S/N ratio and electrode stability are improved, and sample throughput is increased thanks to the applicability of external calibration.

References

1. A.Economou, Recent developments in on-line electrochemical stripping analysis—An overview of the last 12 years, Anal.Chim.Acta, **683**(1), 38 (2010).
2. K.C. Honeychurch, Screen-printed electrochemical sensors and biosensors for monitoring metal pollutants. Insciences Journal, **2** (1), 1–51 (2012).
3. J.D. Mozo, J. Carbajo, J.C. Sturm, L.J. Nunez-Vergara, P. Salgado, J.A. Squella, Determination of Nifuroxazide by flow injection linear adsorptive stripping voltammetry on a screen-printed carbon nanofiber modified electrode, Electroanal., **24** (3), 676–682 (2012).
4. J.F. van Staden, M.C. Matoetoe, Simultaneous determination of copper, lead, cadmium and zinc using differential pulse anodic stripping voltammetry in a flow system, Anal.Chim.Acta, **411**, 201–207 (2000).

Chapter 24
Electroanalytical Applications of Sensors Based on Pyrolized Photoresist Carbon Electrodes

Morena Silvestrini, Andrea Mardegan, Mattia Cettolin, Ligia Maria Moretto, Paolo Scopece and Paolo Ugo

M. Silvestrini and A. Mardegan contributed equally to this work.

Pyrolyzed photoresist carbon electrodes (PPCEs) fabricated by photolithographic micro-fabrication and pyrolysis of the epoxy-based photoresist named SU-8 are applied to electroanalysis. Bismuth-modified PPCEs (Bi-PPCEs) are used in the adsorptive cathodic stripping voltammetry (AdCSV) of Ni(II) and in the speciation of inorganic Cr, while PPEs are used in the cyclic voltammetric (CV) study of bilirubin (BR) in dimethyl sulfoxide.

24.1 Introduction

Carbon electrodes possess many advantages with respect to noble metals including low fabrication cost, good electrical conductivity, chemical and electrochemical stability and wide potential window accessible. In many cases, the electrochemical properties of these electrodes are even superior [1]. Recently, a new procedure to fabricate carbon electrodes by the controlled pyrolysis of organic polymer thin film used as microfabrication photoresist has been introduced [1]. The optimization of the preparation conditions allowed to obtain pyroloyzed photoresist carbon electrodes (PPCEs) in which the majority of the carbon is in the form of amorphous glassy carbon (GC) [2]. In this paper we show the applicability of PPCEs modified

L. M. Moretto (✉) · M. Silvestrini · M. Cettolin · P. Ugo
Department of Molecular Sciences and Nanosystems, University Ca' Foscari of Venice, Santa Marta 2137, 30123, Venice, Italy
e-mail: moretto@unive.it

A. Mardegan · P. Scopece
Veneto Nanotech, via delle Industrie 5, 30175, Venice-Marghera, Italy

with bismuth (Bi-PPCE) to the adsorptive cathodic stripping (AdCSV) determination of chromium(VI), a very toxic pollutant of great environmental concern. Moreover, we report the study of the electrochemical behavior of bilirubin (BR) demonstrating, for the first time, the possibility to use PPCEs in aprotic solvent, namely, dimethylsulfoxide (DMSO). Bilirubin is the yellow-orange bile pigment found in the body having the structure of a linear tetrapyrrole. It is an important serum biomarker traditionally used in clinical medicine for assessing hemolysis, hepatic function and cardiovascular risk; moreover, recent studies showed the importance of its antioxidant properties for assessing cardiovascular risk in pre-disease healthy population [3].

24.2   Experimental

BR (Frontier Scientific, ≥98%) and DMSO (Sigma Aldrich, ≥99.5%) were used without further purification. All other chemicals were reagent grade. Nitrogen was from SIAD (grade 5.0, purity 99.999%). SU-8 was obtained from MicroChem Inc. MA, USA. Purified water was obtained by using Milli-Ro plus Milli-Q (Millipore) water purification system.

All electrochemical measurements were carried out using a CHI440 electrochemical workstation at room temperature (22 °C). Electrochemical measurements were performed using a single compartment cell equipped with a PPCE or Bi-PPCE as the working electrode, a platinum wire as the counter electrode and an Ag/AgCl (KCl sat.) reference or a platinum pseudo-reference electrode, for aqueous or DMSO solution, respectively.

PPCEs were fabricated as previously reported [1, 2]. Before carrying out the electrochemical measurements, the electrodes were insulated with a Monokote® (Topflite, Champaign IL) or Kapton® (DuPont™; for measurements in DMSO) tape apart a hole which defines the geometric area of the electrode.

The Bi-PPCE used for the determination of Cr(VI) was prepared by adapting a method recently developed for Ni and Co analyses [4]; in particular, a bismuth film was deposited on the PPCE by electrochemical reduction at -1.2 V for 300 s in 2.5 µM $Bi(NO_3)_3$, 0.1 M acetate buffer (pH 4.5) solution. Afterwards, the Bi-PPCE was moved to an electrochemical cell containing 0.5 µM pyrocatechol violet (PCV), 0.1 M $NaNO_3$ in 0.01 M acetate buffer (pH 6). After an accumulation (adsorption) at -0.2 V for 60 s, a square-wave voltammogram (SWV) from -0.2 V to -1.2 V was recorded. The SW parameters were: pulse height 50 mV and frequency 25 Hz.

24.3   Results and Discussion

24.3.1   *Selective Cr(VI) Determination with Bi-PPCE*

Figure 24.1a presents the SW-AdCSVs recorded after accumulation at −0.2 V for 60 s, using a Bi-PPCE in electrolyte solution containing 5 µg L^{-1} Cr(III) and increasing concentrations of Cr(VI). The voltammograms display a well defined cathodic stripping peak at −0.65 V that increases linearly with the concentration of Cr(VI) in the range 5–25 µg L^{-1} (see Fig. 24.1b). These results indicate that the Bi-PPCE can be successfully used for the selective determination of Cr(VI), even in the presence of Cr(III). From these data, by using the 3 σ_b/m criterion, a limit of detection (LOD) of 0.1 µg L^{-1} was evaluated. The applicability of the method to real water samples was tested by determining Cr(VI) in tap water samples spiked with 12 µg L^{-1} Cr(VI), added as chromate. The sample was analyzed with the Bi-PPCEs and, for comparison, with the APAT CNR-IRSA standard method [5]. The concentration of Cr(VI) measured with the Bi-PPCE was 12.0±0.2 µg L^{-1} ($n=3$); it agrees with the expected value and with the concentration determined by standard method (12.0±0.1 µg L^{-1}).

24.3.2   *Voltammetric Characterization of BR in DMSO*

Figure 24.2 shows the CV pattern recorded with a PPCE in 1 mM BR, 0.1 M TBABF$_4$ in DMSO. This voltammogram is characterized by three oxidation peaks, namely A1 at+0.62 V, A2 at+0.80 V and a third peak near the anodic limit of the voltammogram (all vs Pt pseudo reference electrode). On the other hand, three main reduction peaks (C1, C2 and C3) are detected at rather negative potential values in the cathodic portion of the scan. Indeed, C1 is composed by two peaks C1' and C1'', rather close each other.
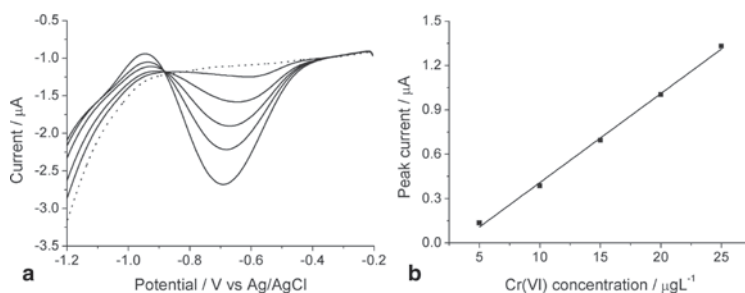
Fig. 24.1. a SW-AdCSVs at the ex-situ prepared Bi-PPCE in solution 5 µg L^{-1} of Cr(III) for increasing concentration of Cr(VI) (5, 10, 15, 20 and 25 µg L^{-1}); see section 24.2 for other experimental parameters. **b** Relevant calibration plot. Geometric electrode area: 0.07 cm^2
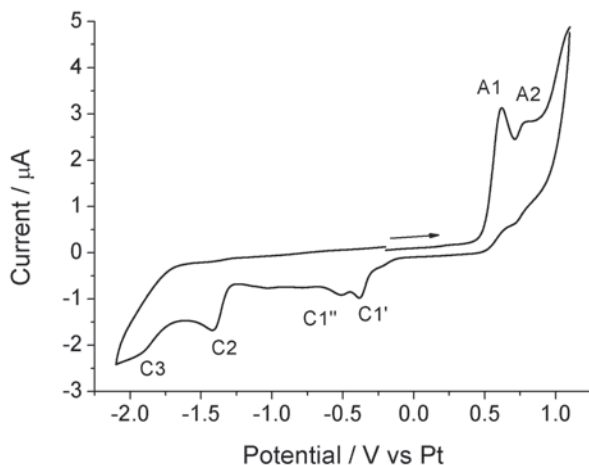
Fig. 24.2 Cyclic voltammogram recorded at a PPCE in 1 mM BR, 0.1 M TBABF$_4$, DMSO. Scan rate 20 mV s^{-1}. Geometric electrode area: 0.031 cm^2

The analysis of the voltammetric data together with the UV-Vis spectra recorded on the green solution produced by exhaustive electrolysis experiments at a potential close to peak A1 (data not shown), indicate that this peak is related to the oxidation of BR to biliverdin (BV). Similarly, macroelectrolysis experiments at a potential close to peak A2 produced a purple colored solution. The UV-Vis spectrum recorded on this solution is characterized by the appearance of three new absorption peaks at 336, 518 and 546 nm, indicating that at peak A2, BV is further oxidized to purpurin (Pu) [6]. Since the third anodic peak is detected at the positive limit of the accessible potential window, no detailed analysis was possible; however, on the basis of previous studies [6], it seems reasonable to ascribe this peak to the formation of choletelin (Ch). Further analyses of the CVs indicate that peaks C1' and C1'' are due to the reduction of the oxidation products of BR, while peaks C2 and C3 are related to the direct reduction of BR, to generate unknown dimerization or polymerization products; these results agree with what reported for BR reduction in DMSO at Hg and Au electrodes by Slifstein and Ariel [7].

24.4 Conclusions

PPC shows to be an electrode material comparable if not superior to GC. The results of this study, obtained in two very different analytical systems, confirm the wide applicability of PPCEs for sensing purposes. Finally, it is worth mentioning that, at variance with classical GCEs, PPCEs (obtained by the controlled pyrolysis of a photoresist) can be patterned by photolytography in a variety of electrode geometries and shapes, such as complex arrays suitable for generator-collector systems or sensors for multiplexed analyses.

References

1. S. Ranganathan, R.L. McCreery, S. M. Majji, M. Madou. Photoresist–derived carbon for microelectromechanical systems and electrochemical applications. J. Electrochem. Soc. **147** (1), 277–282 (2000)
2. A. Mardegan, R. Kamath, S. Sharma, P. Scopece, P. Ugo, M. Madou. Optimization of carbon electrodes derived from epoxy-based photoresist. J. Electrochem. Soc. **160** (8), B132–B137 (2013)
3. X. Wang, J.R. Chowdhury, N.R. Chowdhury. Bilirubin metabolism: applied physiology. Current Paediatrics **16**, 70–74 (2006)
4. A. Mardegan, S. Dal Borgo, P. Scopece, L.M. Moretto, S.B. Hočevar, P. Ugo. Simultaneous adsorptive cathodic stripping voltammetric determination of nickel(II) and cobalt(II) at an In Situ Bismuth-Modified Gold Electrode, Electroanalysis **25** (11), 2471–2479 (2013)
5. APAT IRSA CNR 3150B2, Italy
6. J.R. Pradko, S. Pons, S. Bandyopadhyay, J.F. McAleer, A.S. Hinman. A spectroelectrochemical investigation of the oxidation of bilirubin IX-α in dimethylformamide. Bioelectroch. Bioener. **13** (4–6), 267–285 (1984)
7. Ch. **S**lifstein, M. Ariel. The electrochemistry of bilirubin in dimethylsulfoxide. Electroanal. Chem. Interfacial Electrochem. **48** (3), 447–463 (1973)

Chapter 25
Three Different Sensor Methods for Methanol and Ethanol Determination

**Mauro Tomassetti, Riccardo Angeloni, Mauro Castrucci
and Giovanni Merola**

25.1 Introduction

Ethanol and methanol are two important alcohols used for different purposes. Consequently, also the analytical methods used to determine them are of considerable interest. Our team is therefore developing three different sensor-based methods for ethanol and methanol determination. Two of these consist of different enzyme electrodes and have been developed by immobilizing either alcohol oxidase or catalase in a k-Carrageenan gel layer overlapping an amperometric gaseous diffusion Clark type oxygen electrode (see Fig. 25.1). The third device, still under investigation, is a small commercial catalytic fuel cell used for analytical purposes, that is, direct methanol and ethanol detection.

25.2 Methods and Measurements Used for Enzymatic Biosensors

The variation of the oxygen concentration in the aqueous solution due to the enzymatic reactions was measured at a constant applied potential of - 650 mV. The responses of these biosensors toward standard solutions of methanol or ethanol were recorded, compared and discussed. In the case of the catalase electrode, the measurement was performed by adding hydrogen peroxide to a buffer solution which was diffused through the dialysis membrane towards the enzymatic layer when the reaction catalysed by the catalase enzyme took place:

$$H_2O_2 \xrightarrow{\text{Catalase}} \frac{1}{2}O_2 + H_2O \qquad (25.1)$$
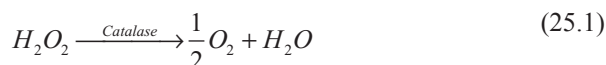
M. Tomassetti (✉) · R. Angeloni · M. Castrucci · G. Merola
Department of Chemistry, "Sapienza", University of Rome, piazzale A. Moro 5, 00185 Rome, Italy
e-mail: mauro.tomassetti@uniroma1.it

Fig. 25.1 Catalase and alcohol oxidase biosensor assembly

a:	electrode
b:	dielectric
c:	anode Ag/AgCl
d:	PTFE cap
f:	teflon membrane
g:	o-ring
h:	dialysis membrane
i:	k-carrageenan gel
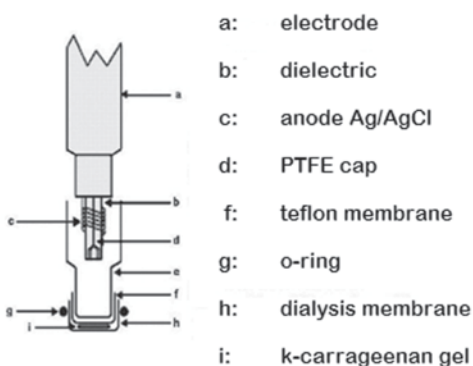
Since this reaction led to the production of oxygen, the concentration of the latter in the measurement solution increased. This increase triggered an increase in the cathodic current measured which increased from the original value to a new value corresponding to a new stationary state. At this stage further additions were made (equal to 20 μL) of a standard solution of 0.008 M of ethanol or methanol; after each addition a reaction of the following type occurred, which was catalyzed by catalase:

$$CH_3CH_2OH + H_2O_2 \xrightarrow{Catalase} CH_3CHO + 2H_2O \qquad (25.2)$$

The second reaction removed part of the H_2O_2 substrate from the first reaction, which was slowed down; this slowdown was accompanied by a decrease in the level of oxygen produced in the solution during the first reaction; this decrease was evidenced by the decrease in the measured cathodic current, which attained a new stationary state after each addition of alcohol solution. The current variation was read off after each alcohol addition [1]. With the biosensor operating with alcohol oxidase the operating procedure was much simpler as it consisted of directly making successive additions of the standard ethanol or methanol solution to a buffer solution in which the measurement was being performed. After each addition a reaction catalyzed by the alcohol oxidase enzyme of the following type took place:

$$CH_3CH_2OH + O_2 \xrightarrow{Alcohol\ Oxidase} CH_3CHO + 2H_2O_2 \qquad (25.3)$$
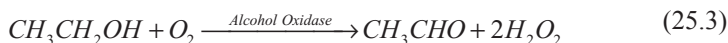
The reaction led to the oxygen present in the solution being consumed with a consequent decrease in the cathodic current measured until a new stationary state was reached. Also in this case, after each addition, the current variation was read off. All the experiments were carried out in a reaction cell thermostated at 23 °C containing 15 mL of 0.05 M phosphate buffer solution.

Table 25.1 Comparison of main analytical data of three sensors

Method	Linearity range		LOD		Life time
	Methanol	Ethanol	Methanol	Ethanol	
Catalase biosensor	$(9.5 \times 10^{-4} - 2.1 \times 10^{-2})$ M	$(2.0 \times 10^{-6} - 2.0 \times 10^{-5})$ M	3.5×10^{-4} M	0.4×10^{-6} M	30
Alcohol oxidase biosensor	$(8.2 \times 10^{-6} - 3.7 \times 10^{-4})$ M	$(9.2 \times 10^{-6} - 3.4 \times 10^{-4})$ M	2.2×10^{-6} M	3.6×10^{-6} M	7
Fuel cell OCV format	$(4.5 \times 10^{-4} - 4.5 \times 10^{-2})$ M	$(1.0 \times 10^{-4} - 1.0 \times 10^{-2})$ M	4.0×10^{-4} M	1.0×10^{-4} M	>60

Fig. 25.2 Picture of the fuel cell used and of the measurement apparatus
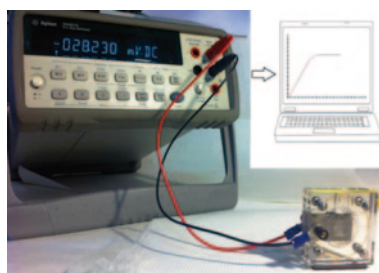
25.3   Analytical Results for Enzymatic Biosensors

The effect of pH on the response of two enzyme electrodes was investigated in detail and the best pH was found to be 7.5 for the catalase electrode and 8.0 for the alcohol oxidase electrode, respectively. Calibration curves for methanol and ethanol, obtained using both catalase biosensor and alcohol oxidase biosensor, were constructed. The catalase biosensor displayed a much greater sensitivity to ethanol than to methanol, unlike the alcohol oxidase biosensor. It also displayed a stability and a life-time at least triple that of the alcohol oxidase biosensor as well as an LOD vs. ethanol at least one decade lower (see Table 25.1). It also showed a better repeatability and reproducibility for ethanol and methanol solutions. The alcohol oxidase biosensor was instead found to be more sensitive to methanol than to ethanol but allowed the test to be carried out slightly faster than with the catalase device.

25.4   Fuel Cell Catalytic Sensor for Methanol and Ethanol Detection

Lastly our team is now investigating the feasibility of using a small catalytic 'fuel cell', originally constructed for the purpose of obtaining energy from methanol or ethanol, but now adapted for analytical purposes [2] [3] (see Fig. 25.2).
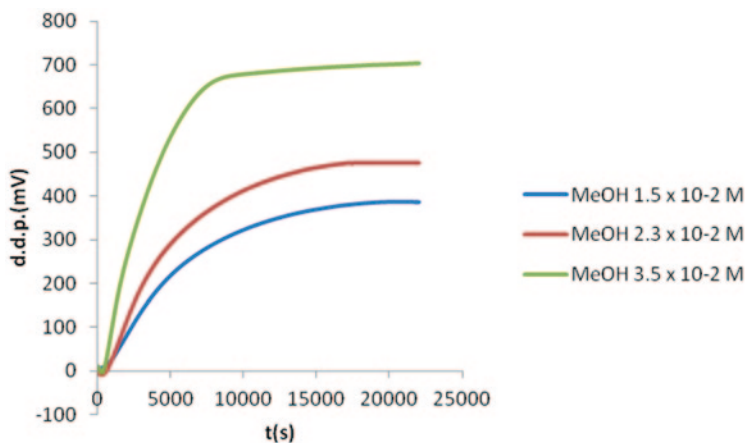
Fig. 25.3 Methanol
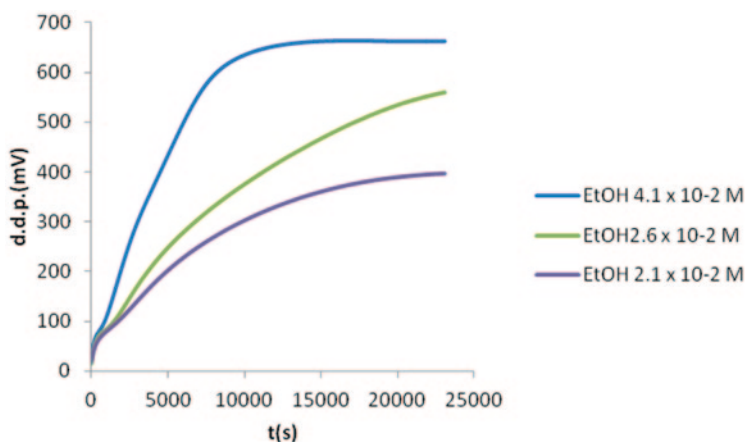
Fig. 25.4 Ethanol

Potential increase of the fuel cell at open circuit voltage (OCV) vs. time at different increasing methanol (Fig. 25.3) and ethanol (Fig. 25.4) concentrations

The aim is to see whether this kind of device can also be used for ethanol and methanol determination. To this end water-alcohol solutions containing increasing percentages of methanol or ethanol are added to the cell, then following the potential increase at the open circuit voltage that occurs at two electrodes of the cell and lastly reading off the maximum potential obtained after each alcohol addition (see Fig. 25.3 and 25.4). Although this part of the research is only at the preliminary stage it has already been possible to obtain calibration curves for both methanol and ethanol and main relative analytical data reported in the Table 25.1, found taking the

maximum measured voltage for each alcohol concentration. See in Table 25.1 the comparison of main analytical data with those of two enzymatic methods.

25.5 Conclusions

A comparison of the linearity ranges and LOD values obtained so far is shown in Table 25.1 using the three methods described. The catalase biosensor and fuel cell display a very similar linearity range and LOD toward methanol but different toward ethanol, while the values of both these parameters toward methanol are better for the alcohol oxidase biosensor. However, the lifetime of the latter biosensor is short compared with that of the catalase biosensor and very short compared with that of the fuel cell.

References

1. L. Campanella, G. Spuri Capesciotti, T. Gatta, M. Tomassetti, An innovative organic phase enzyme electrode (OPEE) for the determination of ethanol in leadless petrols, Sens. and Actuators, B 147 (2010) pp 78–86.
2. W. Sun, G. Sun, W. Yang, S. Yang, Q. Xin, A methanol concentration sensor using twin membrane electrode assemblies for direct methanol fuel cells, Int. J. Electrochem. Sci. 1 (2006) pp 160–170.
3. H. Zhaoa, J. Shen, J. Zhang, H. Wang, D. P. Wilkinson, C.E. Gua, Liquid methanol concentration sensors for direct methanol fuel cells, J. Power Sources 159 (2006) pp 626–636.

Chapter 26
Determination of Caffeine @ Gold Nanoparticles Modified Gold (Au) Electrode: A Preliminary Study

Alessandro Trani, Rita Petrucci, Giancarlo Marrosu and Antonella Curulli

Caffeine is a natural alkaloid exerting many physiological effects, such as stimulation of the central nervous system, diuresis and gastric acid secretion. It is widely distributed in plant products and beverages and its quantification is mainly of pharmaceutical and alimentary concern. In this paper, we describe an electrochemical study based on the modification of a gold electrode (Au) surface by deposition of functionalized gold nanoparticles by Cyclic Voltammetry (CV). The oxidation system is characterized by an anodic peak in the positive-going step and by the absence of any cathodic peak on the reverse scan, indicating that the oxidation is irreversible. At the modified electrode, the voltammetric peak height increases vs. that @ the bare one, depending on the nanoparticles functionalization. The best performances were observed @ Au electrode modified with colloidal gold nanoparticles (AuNPs) stabilized into a chitosan matrix. In order to optimize the influence of different electrolytes on the sensor response, different electrolytic solutions (nitric acid, sulfuric acid, phosphoric acid and hydrochloric acid) were used. The electrochemical behavior of caffeine was also studied in aprotic medium with the aim to clear up the different mechanisms the oxidative process occurs through in aqueous and in aprotic medium.

A. Curulli (✉) · A. Trani
ISMN CNR Istituto per lo Studio dei Materiali Nanostrutturati Consiglio Nazionale delle Ricerche, Via del Castro Laurenziano 7, 00161 Roma, Italy
e-mail: antonella.curulli@cnr.it

R. Petrucci · G. Marrosu
Facoltà di Ingegneria Civile e Industriale Dip. SBAI, Sapienza Università di Roma, Via del Castro Laurenziano 7, 00161 Roma, Italy

26.1   Introduction

Caffeine (3,7-dihydro-1,3,7-trimethyl-1H-purine-2,6-dione) is a natural alkaloid belonging to N-methyl derivatives of xanthine. Because of high popularity of coffee and other caffeine containing products (coca, tea, soft and energy drinks, cocoa, chocolate), it is the most commonly used psychoactive substance in daily human life. Caffeine (CAF) is also distributed in plants where it serves as a natural insecticide since it may paralyze and kill some insects feeding on the plant [1]. For humans, CAF has many important physiological effects, such as stimulation of the central nervous system, diuresis and gastric acid secretion [1]. However, the high amounts of CAF can cause trembling, nausea, nervousness and seizures [1] and mutation effects such as inhibition of DNA [1]. CAF is very attractive compounds for analytical chemists, thus its beverages (various type of coffee, tea, cola, cocoa, energy drinks) and drug formulations belong to the significant economic products in which the highest quality in international business is demanded [2]. Owing to its common use, the eventual abuse, the important effects in human system and in respect to the ascending number of samples, the novel and perspective analytical methods providing rapid, sensitive and reliable detection and determination of CAF are still necessary. Chromatographic and spectrophotometric methods are very popular in analytical laboratories in the context of determination of CAF; however, the disadvantages of these methods consist in time-consuming and complicated sample preparation as well as often lower sensitivity of analysis without preconcentration step. Besides, the demands for highly skilled personnel often restrict their use in routine analytical practice [1].

Electrochemical methods offer the practical advantages including operation simplicity, satisfactory sensitivity, wide linear concentration range, low expense of instrument, possibility of miniaturization, suitability for real-time detection and less sensitivity to matrix effects in comparison with separation and spectral methods [1]. For this reason, we have decided to investigate the electrochemical behavior of CAF @ bare (AuE) and AuNps gold modified electrode (AuNps/AuE) in aqueous solution and to compare the results obtained in aprotic medium. We would like to clear up the different mechanisms the oxidative process occurs through different media and, consequently, to set up a sensor for detecting caffeine in beverages.

26.2   Electrochemical Behavior of Caffeine @ Bare
and Gold Nanoparticles (Aunps) Gold Modified
Electrodes in Aqueous Solutions

Cyclic voltammetric measurements were performed to study the voltammetric behavior of caffeine at AuEs. The oxidation system is characterized by an anodic peak at the positive-moving step and by the absence of any cathodic peak on the reverse scan, indicating that the oxidation is irreversible. The oxidation mechanism

has already been elucidated [3, 4]. Several sensor architectures, involving surface modification with AuNps differently functionalized, were tested in order to choose the electrode configuration with the best electrochemical properties. In addition, the voltammetric behavior of caffeine was investigated at bare and modified AuE, in three different electrolyte solutions, in order to choose the best medium. The voltammetric behavior of caffeine at the bare AuE was examined by cyclic voltammetry (CV). The CV scan presents an anodic peak at a high potential around $+1.69$ V vs. Ag/AgCl, in phosphate buffer pH 7.4 and the absence of a cathodic peak on the reverse scan, indicating that the oxidation is irreversible,

26.2.1   The Influence of Different Surface Modifications on CAF Electrochemistry

Different gold surface modifications were done in order to assess possible enhancements of sensitivity of the caffeine electrochemical signal, namely gold nanoparticles, functionalized in different way, using cyclic voltammetry.

The synthesis of chitosan-stabilized and of cysteamine-stabilized AuNps was carried out by using a route, according to our recently published procedures from a $HAuCl_4$ aqueous solution and were characterized by UV-vis spectroscopy, as previously reported [5, 6].The resulting samples were labelled as AuCYST and AuOA−CHIT, where OA refers to the oxalic acid, used in the synthesis. After the polishing steps [5], Au electrodes were modified by drop casting 3 μL of AuNPs solution onto electrode surface and subsequent air drying at room temperature. All the AuNPs modified electrodes show an amplification of the electrochemical response with respect to bare gold reference electrode. The anodic peak potential (E_{pa}) values at AuNps modified electrodes for CAF do not differ significantly from those detected at bare electrode. The evident electroanalytical improvement concerns the higher anodic current intensity. The most pronounced signal amplification was obtained @ AuOA-CHIT/AuE in phosphate buffer 0.1 M pH 7.4. ($\Delta I_{pa} = 45\%$)

26.2.2   Evaluation of Different Media on CAF Electrochemistry

The electrochemical behavior of caffeine may be influenced by the nature of the electrolyte solution. In order to evaluate the effect of different media on the CAF electrochemical response, phosphate buffer, perchloric, sulphuric, hydrochloric and phosphoric acid solutions were tested and the electrochemical data in these media were obtained. All the AuNPs modified electrodes show an amplification of the electrochemical response with respect to bare gold reference electrode and a decrease in the overpotential oxidation in all acidic solutions ranging from $+1.69$ to $+1.48$ V vs. Ag/AgCl. The most pronounced signal amplification was obtained @AuOA-CHIT/AuE in H_3PO_4 0.085 M, ($\Delta I_{pa} = 131\%$), followed by hydrochloric acid 0.1M ($\Delta I_{pa} = 106\%$).

   The peak current value is influenced by the pH value of the solution, increasing from pH 3.0 to 7.0, and then decreasing at higher values of pH. Cyclic voltammograms, in solutions of pH higher than 8.0, have a broad oxidation wave, so accurate determination of caffeine was not possible. The results underline the advantage of this electrode that can be employed over a broad pH range, between 3 and 8. Consequently, further measurements could be performed in PBS pH 7.4, since at this pH the caffeine response was the highest. The influence of the scan rate in cyclic voltammetry on the oxidation peak current of caffeine was evaluated by recording CVs at different scan rates from 10 to 200 mV s^{-1} in 0.1 M PBS pH 7.4, containing 0.004 M caffeine. The anodic peak currents were linearly proportional to the square root of the scan rate (R = 0.999), so it can be deduced that the electrochemical oxidation of caffeine @ AuOA-CHIT/AuE is a diffusion-controlled process. Analytical parameters such as reproducibility, interference rejection, response time, storage and operational stability of the caffeine sensor have to be investigated.

26.3   Electrochemical Behavior of Caffeine @ Glassy Carbon (Gc) Electrode in Aprotic Solvent

The electrochemical behavior of caffeine in aqueous medium has been widely described in the literature, while very little is known on the oxidative process of caffeine in aprotic medium. Further, a ROS (Reactive Oxygen Species) scavenging activity of CAF has been recently suggested and a reactivity with ROS faster in nonpolar media than in aqueous solutions was predicted [7].

   So, the electrochemical behavior of CAF was studied in anhydrous acetonitrile to investigate the oxidative mechanism in a protons poor medium.

   A preliminary study evidenced for CAF a reversible oxidative mono-electronic process (by comparison with ferrocene in the same medium) occurring at 1.26 V vs Ag/AgCl likely to yield the corresponding radical cation. The dependence of the cathodic peak height in the reverse scan from the inversion potential value and scan rate suggests that a following chemical step may occur. Voltammetric data seem to agree with a following second order kinetics and a reaction with the substrate itself may not be excluded.

   When increasing amounts of water are added to the solution, the anodic peak increases till double of the starting one and the cathodic peak in the reverse scan disapperas: a nucleophilic attack may occur on the first oxidation product of CAF—the radical cation—leading to a product easily oxidable at the same potential of CAF. 8-hydroxycaffeine may be suggested as a product, in agreement with a product of chemical free radical oxidation of CAF in aqueous medium reported in literature [8]. Work is in progress to support this finding.

References

1. Ľubomír Švorc. Determination of Caffeine: A Comprehensive Review on Electrochemical Methods Int. J. Electrochem. Sci., **8** 5755–5773 (2013) and references cited therein.
2. P. S. Murthy, M. M. Naidu. Sustainable management of coffee industry by-products and value addition. A review. Resour. Conserv. Recy., **66** 45–58 (2012)
3. T. Alizadeh, M.R. Ganjali, M. Zare, P. Norouzi, Development of a voltammetric sensor based on a molecularly imprinted polymer (MIP) for caffeine measurement. Electrochim. Acta **55** 1568–1574 (2010).
4. N. Spataru, B.V. Sarada, D. Tryk, A. Fujishima. Anodic Voltammetry of Xanthine, Theophylline, Theobromine and Caffeine at Conductive Diamond Electrodes and Its Analytical Application Electroanalysis **14** 721–728. (2002)
5. G. Di Carlo, A. Curulli, R. G. Toro, C. Bianchini, T. De Caro, G. Padeletti, D. Zane, G. M. Ingo, Langmuir, **28**, 5471–5479 (2012)
6. G. Di Carlo, A. Trani, D. Zane, G. M. Ingo, M. Pasquali, A. Dell'Era, A. Curulli Electroanalysis accepted (2014)
7. J.R. León-Carmona, A. Galano, Is Caffeine a Good Scavenger of Oxygenated Free Radicals?, J. Phys. Chem. B, **115**, 4538–4546 (2011)
8. P. Telo, A.J.S.C. Vieira, Mechanism of free radical oxidation of caffeine in aqueous solution, J. Chem. Soc., Perkin Trans. 2, 1755–1757 (1997).

Chapter 27
Molecularly Imprinted Overoxidized Polypyrrole as Recognition Element in the Electrochemical Detection of Sulfadimethoxine

Antonio Turco, Cosimino Malitesta and Elisabetta Mazzotta

The present work describes the development of a simple and cost-effective electrochemical sensor for sulfadimethoxine (SDM) based on molecularly imprinted overoxidized polypyrrole (PPy). An all electrochemical approach is used for sensor fabrication and application. Several parameters influencing the imprinting effect are discussed and evaluated.

27.1 Introduction

In recent years, Molecularly Imprinted Polymers (MIPs) have been developed as a useful tool for the study of recognition phenomena and sensing. The molecular imprinting technique gives the possibility to easily and cheaply prepare materials containing cavities able to selectively recognize analytes ranging from biologically relevant markers, drugs and agrochemicals. In this work, we developed an electrochemical sensor for the detection of the antibiotic sulfadimethoxine (SDM) using an overoxidized molecularly imprinted PPy film as recognition element. In particular, galvanostatic polymerization of polypyrrole was carried out in the presence of SDM on a gold electrode. Subsequently, imprinted film was overoxidized, favouring the introduction of high electronic density oxygen containing groups that can cause electrostatical repulsion with negatively charged SDM thus leaving specific imprinted cavities within the film. The amperometric detection of SDM was performed in acidic solution (pH=2.6) to permit partial protonation of the target molecule thus promoting electrostatic interactions with overoxidized PPy. The imprinting process was analyzed by X-ray photoelectron spectroscopy (XPS) analyzing the presence of the template within MIP film before and after overoxidation. A good imprinting effect was verified comparing imprinted and not imprinted polymers (NIP) amperometric responses to the template molecule. Sensor responses were op-

A. Turco (✉) · C. Malitesta · E. Mazzotta
Laboratorio di Chimica Analitica, Dipartimento di Scienze e Tecnologie Biologiche e Ambientali (DiSTeBA), Università del Salento, via Monteroni Lecce, Lecce, Italy
e-mail: antonio.turco@unisalento.it

timized evaluating the effect of different parameters such as type of the electrolyte used in MIP electropolymerization and overoxidation conditions.

27.2 Experimental

27.2.1 *Reagents and Apparatus*

Pyrrole (Aldrich) was purified by distillation. All the reagents were purchased from Sigma and were analytical grade and used as received. Ultra-pure water (Millipore Milli-Q, 18.2 MΩcm^{-1}) was used in aqueous solutions and for buffer preparation. Britton-Robinson (BR) buffer pH 2.6 was prepared using H_3BO_3 0.04 M, H_3PO_4 0.04 M, CH_3COOH 0.04 M, NaOH 0.2 M. Stock solutions (17.5 mM) of SDM were prepared in the buffer and stored at 4 °C. Electrochemical experiments were carried out with a CHI 660D Potentiostat (CH Instruments, USA) controlled by computer. A one-compartment three electrodes cell was used, consisting of a gold working electrode (or a MIP-modified gold electrode, 2 mm diameter), a platinum wire as counter electrode and a saturated calomel electrode (SCE) or an Ag/Ag+ (0.1 M in acetonitrile) as reference electrode in aqueous and in acetonitrile (ACN) solution, respectively. XPS analysis was carried out using a Leybold LHS10 spectrometer equipped with an unmonochromatized AlKα source (operating at 10 kV and 17 mA) and a SPECS multi-channel detector. Surface charging was calculated considering C1s (BE=285.0 eV) as reference in order to estimate correct binding energy for each signal. Data analysis and peak deconvolution were performed by means of a suitable software CasaXPS.

27.2.2 *MIP Synthesis: Polypyrrole Electrosynthesis and Overoxidation*

MIP film was prepared by galvanostatic deposition (applied current: 0.2 mA, circulated charge density: 133 mC/cm^2) from a solution of pyrrole 0.1 M and SDM 5 mM in ACN containing LiClO$_4$ 0.1 M (films denoted as L) or TBAP 0.1 M (films denoted as T). Both films L and T were overoxidized by applying a fixed potential of 1.0 V overnight under the following experimental conditions: in NaOH 0.1 M (overoxidation 1), in NaOH 0.05 M (overoxidation 2), in phosphate buffer solution (PBS) pH 7.0 (overoxidation 3). Respective not imprinted polymers (NIPs) were prepared under the same condition but without SDM in polymerization solution.

27.2.3   Sulfadimethoxine Amperometric Detection

SDM was detected amperometrically at a fixed potential of 1.3 V in BR/ACN 50 % pH 2.6 [1]. Each calibration curve was repeated in triplicate. Sulfamethoxazole (SMX) was tested under the same conditions for evaluating sensor response selectivity.

27.3   Results and Discussion

27.3.1   Sulfadimethoxine Amperometric Detection

Among the tested overoxidation conditions, treatment in NaOH 0.1 M (overoxidation 1) revealed to be too strong on both films L and T determining an evident film detachment from gold substrate. Overoxidation was thus performed on both films L and T under 1.0 V overnight in two less strong environments, namely NaOH 0.05 M (overoxidation 2) and PBS pH 7 (overoxidation 3). The as prepared films were tested for amperometric detection of SDM evidencing a remarkably different behavior. It was observed that overoxidation in PBS did not produce significant imprinting effect in these experimental conditions, especially on film L and that MIP films prepared in TBAP solutions exhibit unstable current after the exposure to SDM, suggesting a less homogeneous film structure that permits SDM diffusion through MIP matrix and subsequent fouling of gold electrode surface [1]. Finally, also washings in NaOH 0.05 M solutions without applying any potential have been performed both on films L and T confirming the need to overoxidize PPy for template removal. From the above reported results, it is evident that MIP L prepared by overoxidation 2 is the system exhibiting the most satisfactory performance and further characterization has been focused on it.

27.3.2   MIP XPS Analysis and Amperometric Detection

XPS analysis has been carried out on films L to study the imprinting process. For this purpose, MIP films L before and after overoxidation 2 have been analyzed and compared. Figure 27.1 reports detailed spectra of C1s, N1s and S2p relevant to MIP L pristine (Fig. 27.1a) and after overoxidation 2 (Fig. 27.1b).

As expected [2], both C1s and N1s spectrum presents features indicative of overoxidized polypyrrole form. The atomic ratio between pyrrolic N1s and S2p suggests a template removal of about 33 %.

Figure 27.2a reports the calibration curve of SDM on as prepared MIP and the comparison with the relevant NIP film. A remarkable imprinting effect is clearly evidenced with an average imprinting factor (defined as the ratio between MIP
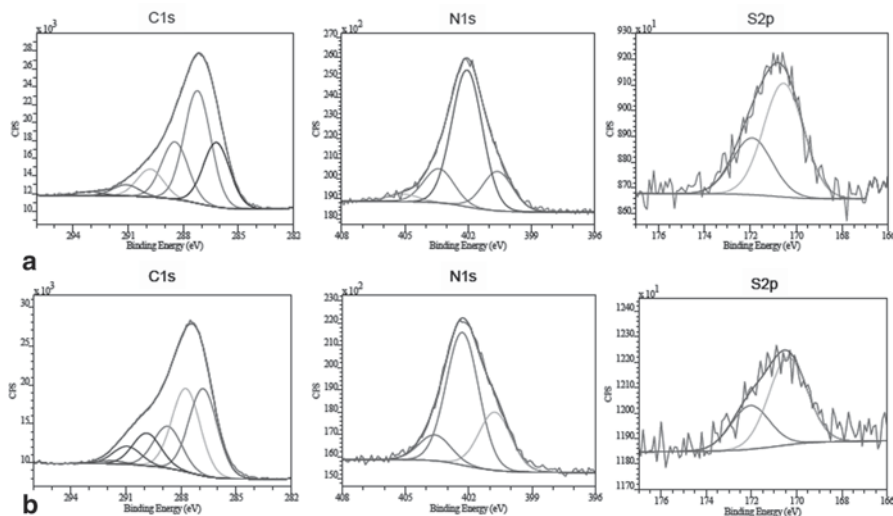
Fig. 27.1 XPS detailed spectra of C1s, N1s and S2p of MIP L pristine (**a**) and after overoxidation 2 (**b**). Curve fitting components and their resultants are also plotted. Spectra are not background subtracted and energy scale is not corrected for charging
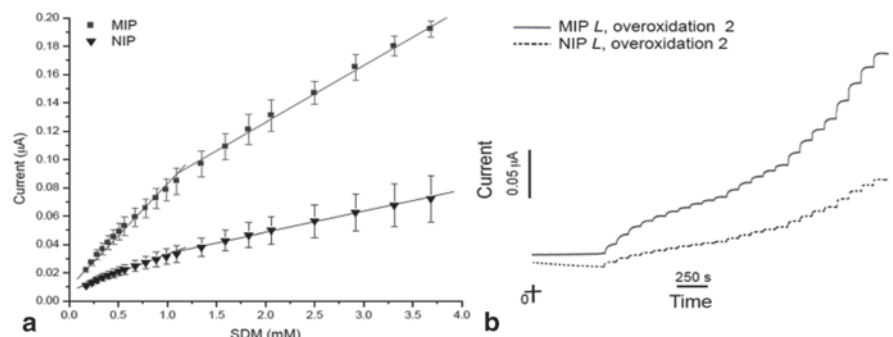
Fig. 27.2 Calibration curve (**a**) relevant to amperometric responses (**b**) of MIP (*circle*) and NIP (*triangle*) films L after overoxidation 2 to SDM 0.17–3.7 mM. Each measurement is performed in triplicate on three freshly prepared sensors

and NIP current response at each tested SDM concentration) of 2.5. Two linear range can be identified in MIP calibration curves being the first one extended from 0.17 mM to 1.1 mM (MIP: R=0.9971, NIP: R=0.9953) and the second one from 1.3 mM to 3.7 mM (MIP: R=0.9986, NIP: R=0.9981). A LOD value (S/N=3) of 70 μM was obtained on MIP film.

Moreover, MIP performances revealed to be satisfactory also in terms of reproducibility (RSD 4.2%, $n=9$) evidencing the reliability of the selected sensor development conditions and also MIP ability to act as an antifouling layer preventing SDM adsorption on gold electrode surface. With the aim to evaluate MIP selectiv-

ity, its amperometric response was analyzed also in the presence of SMX, a sulfonamide structurally similar to SDM. By comparing current responses, an interference ratio equal to 2.5 is achieved.

27.4 Conclusions

In this work a novel electrochemical sensor for SDM is presented based on overoxidized imprinted polypyrrole. A deep investigation of parameters influencing the imprinting effect and sensor performance has been performed being focused on the electrolyte used in MIP electropolymerization and on overoxidation conditions. Interestingly, a role of the cationic electrolyte has been proved to significantly influence stability/reproducibility of the amperometric responses. The efficacy of template removal has been evaluated by XPS. Under the best conditions, MIP-based sensor exhibited satisfactory sensing performances as well as good imprinting effect and antinterference properties.

References

1. Casella, I.G., Contursi, M., Gioia, D.: Development of a Liquid Chromatography/Amperometric Detection Method for the Determination of Multiresidue Sulfonamide Antibiotics in Meat-Based Baby Foods. Electroanalysis. **24**, 2125–2133 (2012).
2. Palmisano, F., Malitesta, C., Centonze, D., Zambonin, P.G.: Correlation between Permselectivity and Chemical Structure of Overoxidized Polypyrrole Membranes Used in Electroproduced Enzyme Biosensors. Anal. Chem. **67**, 2207–2211 (1995).

Chapter 28
Carbon Black/Gold Nanoparticles Composite for Efficient Amperometric Sensors

Chiara Zanardi, Laura Pigani, Renato Seeber, Fabio Terzi, Fabiana Arduini, Stefano Cinti, Danila Moscone and Giuseppe Palleschi

A screen-printed electrode (SPE) modified with a carbon black and Au nanoparticles bilayer was developed and proposed as an amperometric sensor for ascorbic acid quantification in pharmaceutical products and for dopamine estimation in the presence of large excess of ascorbic acid. Electrochemical investigations highlight the performances of the resulting modified electrode with respect to SPEs modified with a single component of the nano-composite.

28.1 Introduction

In the last decade, the scientific community has witnessed the diffusion of a large number of different nanosized materials devoted to a number of applications. Following an analogous trend, their use in electroanalysis has found so wide diffusion that, nowadays, electrode modifications based on these materials constitute the preferred approach to the development of efficient amperometric sensors [1]. The main advantage arising from the use of these materials lies in the activation of electrocatalytic processes, due to the particular reactivity of atoms located in correspondence to vertexes and edges of the nanostructure. This property results in voltammetric traces characterized by very sharp and repeatable peaks, anticipated with respect to those obtained when using bare electrode surfaces. Quite interestingly, the properties of nanosized materials can be further improved when two components strictly interact with each-other, i.e., by forming a proper nano-composite

---

C. Zanardi (✉) · L. Pigani · R. Seeber · F. Terzi
Dipartimento di Scienze Chimiche e Geologiche, Università di Modena e Reggio Emilia, Modena, Italy
e-mail: chiara.zanardi@unimore.it

F. Arduini · S. Cinti · D. Moscone · G. Palleschi
Dipartimento di Scienze e Tecnologie Chimiche, Università di Tor Vergata, Roma, Italy

material: a synergic action between them may improve the performance of the sensor system in terms of peak anticipation and even sensitivity [1].

   We report here the properties of a carbon black (CB)—Au nanoparticles (AuNPs) composite when used as an electrode coating to modify the working electrode of screen printed electrodes (SPEs), i.e., SPE:CB/AuNPs. The properties of this sensor system were tested in the presence of ascorbic acid (AA), demonstrating the activation of more marked electrocatalytic properties with respect to SPE modified either with CB or AuNPs as the single component, resulting in SPE:CB and SPE:AuNPs, respectively.

28.2   Experimental

Electrochemical tests were performed with an Autolab PGSTAT-30 electrochemical system (Eco Chemie, Utrecht, The Netherlands).

   SPEs were produced as previously reported [2]: they consist of a 3 mm diameter graphite working electrode, an Ag pseudo-reference and a graphite auxiliary electrode.

   Commercial CB N220 (19–25 nm diameter, 124 m^2/g surface area) was obtained from Cabot Corporation (Ravenna, Italy). AuNPs were synthesized by slightly modifying the procedure previously reported [3]: $HAuCl_4$ was used as the precursor instead of the relevant sodium salt. UV-vis spectra of the AuNPs solutions were recorded by a Perkin Elmer Lambda 650 spectrophotometer, showing a plasmonic band centred at 514 nm. The mean diameter of the NPs, calculated from TEM images (JEOL 2010, equipped with energy filter), was found equal to 5.8 ± 0.5 nm.

   SPE:CB and SPE:AuNPs were prepared by dropping three subsequent drops (2 μL each) either of 1 mg/mL CB dispersion in a 1:1 DMF:H_2O mixed solvent or of AuNPs solution, respectively, on a bare SPE. SPE:CB/AuNPs were prepared by dropping three drops (2 μL each) of AuNPs solution onto the SPE:CB. All SPEs containing AuNPs in the modifier underwent five subsequent cyclic voltammetric (CV) runs from to −0.2 to +1.5 V, 0.1 Vs^{-1} potential scan rate, in 0.1 M H_2SO_4, before use; a similar treatment was found useless on SPE:CB.

   Different modified SPEs have been compared on the basis of CV traces recorded both in 1 mM $[Fe(CN)_6]^{3-}$ and 1 mM AA, 0.1 M phosphate buffer solutions (PBS), at pH 7.0. Differential pulse voltammetry (DPV) was also used to obtain best signal-to-noise ratio; in this case the parameters used were 0.010 V potential pulse, 0.004 V potential step and 0.010 Vs^{-1} potential scan rate.

   The morphology of the working electrode surfaces was investigated by a Nova NanoSEM 450 scanning electron microscope (FEI Company, Oxford Instruments) working in high vacuum conditions, equipped with an Energy Dispersive Spectrometer (EDS Bruker QUANTAX-200). This instrumental setup confirmed the presence of well separated AuNPs, homogenously distributed on the CB coating.
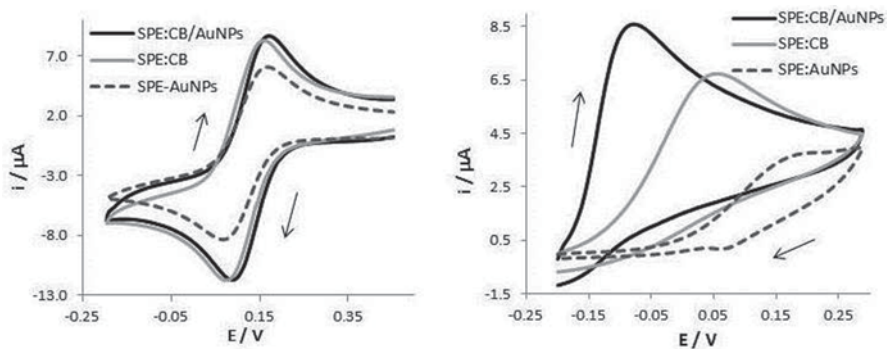
Fig. 28.1 CV recorded at different modified SPEs in **a** 1 mM [Fe(CN)$_6$]$^{3-}$ and **b** 1 mM AA, 0.1 M PBS. 0.05 Vs^{-1} potential scan rate

28.3   Results and Discussion

CV traces have been collected in 1 mM [Fe(CN)$_6$]$^{3-}$ solution in order to compare the behaviour of the three electrodes in an electrochemical process involving a typical reversible system (see Fig. 28.1a). The three different SPEs lead to voltammetric traces typical of diffusion controlled reversible charge transfer processes, with peak intensity proportional to electroactive area [4]. The results evidence that no meaningful differences are present between the total electroactive area of SPE:CB and of SPE:CB/AuNPs, whereas the area of SPE:AuNP results significantly smaller. This result indicates the active role played by CB in conditioning the morphology of the nanostructure; this conclusion is also supported by SEM images collected on different regions of the surfaces of different electrodes.

The electroanalytical performances of SPE:CB/AuNPs have been tested with respect to AA oxidation. As observed in Fig. 28.1b, a significant shift of the response toward less positive potential values is observed when using SPE:CB/AuNPs, with respect to both SPE:AuNPs and SPE:CB. This fact evidences a synergic action of the two components in the electrocatalysis of AA oxidation. From an analytical point of view, the peculiar efficiency of the composite material makes it possible to perform quantification at particularly low potential values, inducing resolution between the responses from different electroactive species; higher sensitivity is also evidenced.

The performance of SPE:CB/AuNPs in AA oxidation has been also tested in real samples. In particular, pharmaceutical formulations have been analysed with standard addition method, by comparing the voltammetric signals coming from electrode systems possessing similar electroactive area and similar inner resistance, namely SPE:CB/AuNPs and SPE:CB. As observed in Fig. Fig. 28.2, reporting the analysis of a multivitamin tablet, the oxidation peak due to AA oxidation at SPE:CB/AuNPs (Fig. 28.2a) is centred at low potential values and is significantly sharper with respect to that registered at SPE:CB (Fig. 28.2b). Moreover, as expected on the
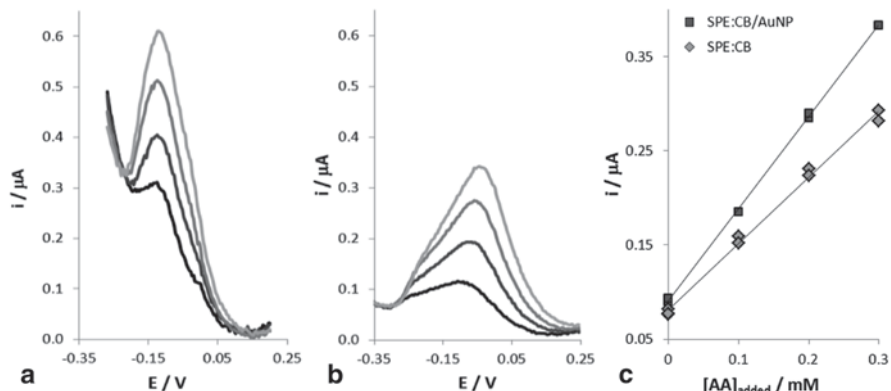
Fig. 28.2 DPV registered at **a** SPE:CB/AuNP and **b** SPE:CB in AA determination in a multivitamin tablet; standard addition method. The relevant i_p vs. [AA] plots are reported in (**c**); two replicates were performed with each electrode at each AA concentration

Fig. 28.3 DPV registered in 0.6 mM AA and 6 μM DP in 0.1 M PBS
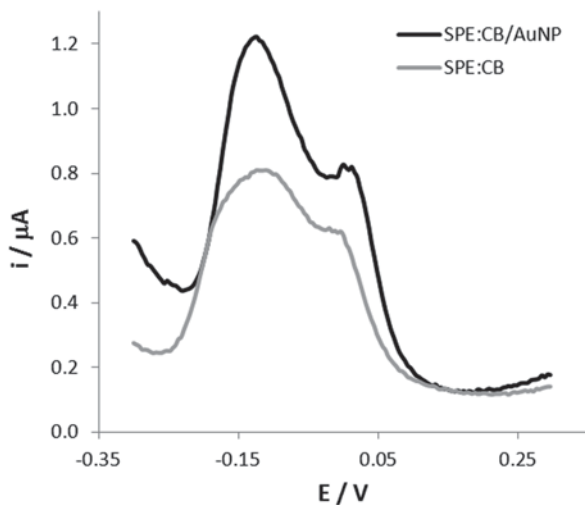
basis of voltammetric responses registered in buffer solution, the sensitivity of the nano-composite material is significantly higher (Fig. 28.2c).

In any case, the accuracy achieved by the two electrode systems seems quite good, although the results evidence that SPE:CB tends to overestimate the amount of AA contained. However, further determinations are necessary to confirm the actual significance of this result.

The advantages of the composite material with respect to SPE:CB have been also tested considering the possible determination of very low amounts of dopamine (DP) in the presence of AA, which accounts for a typical condition in many biological systems. As observed in Fig. 28.3, thanks to the marked anticipation of AA

oxidation occurring at SPE:CB/AuNPs, this determination becomes possible only at this sensor system. Moreover, the extraordinary sensitivity shown by this electrode allows the obtainment of significant signals even in the presence of particularly low DP concentrations.

28.4   Conclusions

SPE modified with a bilayer coating consisting of CB and AuNPs has been developed. The synergic action of the two nanosized materials, forming a composite film, results in an electrocatalytic efficiency well superior to that shown by SPE modified either with CB or with AuNPs. The applicability of this sensor system has been demonstrated for AA determination in pharmaceutical formulations, as well as for the possible quantification of DP in the presence of high amount of AA.

References

1. F. Terzi, C. Zanardi in Environmental analysis with electrochemical sensors and biosensors, ed. by L. Moretto and K. Kalcher (Springer, 2014) in press.
2. F. Arduini, F. Di Nardo, A. Amine, L. Micheli, G. Palleschi, D. Moscone, Electroanalysis 24 (2012) 743.
3. C. Zanardi, C. Baldoli, E. Licandro, F. Terzi, R. Seeber, J. Nanop. Res. 14 (2012) 1148
4. A. J. Bard, L. R. Faulkner, Electrochemical methods: fundamentals and applications, 2nd edn (John Wiley & Sons, New York, 2001)

Chapter 29
XPS Investigation of Electrosynthesized Conducting Polymer Nanostructures of Application in Sensors. Preliminary Results

S. Rella, C. Malitesta, E. Mazzotta, A. Turco, T. Siciliano and A. Tepore

One of the most important CPs is polypyrrole (PPy) because of its high stability, electronic conductivity, ion exchange capacity and biocompatibility. To improve the performance or extend the functions of the organic devices, CPs usually have to be nanostructured, in fact they are synthesized in the form of micro/nanotubes In this work electrosynthesized polypyrrole nanostructures prepared by a reported template-free method is investigated, in particular a preliminary analysis of high-resolution spectra, both for nanostructured sample and bulk sample has been performed.

29.1 Introduction

Conducting polymer nanostructures (CPNs), such as nanofibers, nanoparticles, etc are currently investigated as building blocks of nanoelectronic devices, sensors etc. Their electrochemical preparation appears as an effective and convenient method to finely tune their properties [1]. While confining electrochemical oxidation of monomers in porous hard templates (like zeolites, alumina and track-etched polymer membranes) has been widely explored, template-free approach seems desirable for avoiding multistep and post-treatment processes. Chemical characterization of CPNs is of paramount importance both for optimising preparation procedure and for clarifying chemical basis of novel properties of those materials. In this respect, XPS represents a suitable tool as, in this case, it can give both surface and bulk information. Separation of contributes can be performed by angle-resolved approach.

S. Rella (✉) · C. Malitesta · E. Mazzotta · A. Turco
Laboratorio di Chimica Analitica—Dipartimento di Scienze e Tecnologie Biologiche e Ambientali, Di.S.Te.B.A., Università del Salento, Via Monteroni, 73100 Lecce, Italy
e-mail: simona.rella@unisalento.it

T. Siciliano · A. Tepore
Laboratorio Fisica e Chimica dell'Ambiente e dei Beni Culturali—Dipartimento di Beni Culturali, Università del Salento, Via Monteroni, 73100 Lecce, Italy

However, XPS of nanostructured materials is not a routine method, yet, and caution must be exercised in interpreting collected data [2]. Preliminary XPS results on electrosynthesized polypyrrole (PPY) nanostructures prepared by a reported template-free method [3] are illustrated.

Comparison with conventional PPY suggests higher overoxidation that represents the main chemical difference.

29.2   Experimental

PPY nanofibers were potentiostatically grown at 0.85 V vs Ag/AgCl by a CHI-660D electrochemical station (CH Instrument Inc. USA) in an aqueous solution containing 0.1 M Py, 0.07 M LiClO$_4$ and 0.2 M PBS (phosphate buffer solution) pH 6.8. A platinum sheet was used as a working electrode and another platinum sheet as counter electrode.

PPY conventional was prepared as above, varying only the content of Py, 0.2 M.

XPS measurements have been performed by an Axis ULTRA DLD Spectrometer (Kratos Analytical, UK) with a monochromatic Al Kα source operating at 225 W (15 kV, 15 mA).

For each sample a wide-scan spectrum (WS) was acquired in the binding energy range 0–1200 eV with a pass energy of 160 eV, while high-resolution regions were acquired with a pass energy of 20 eV. In both cases, the area of analysis was about 700 * 300 μm. Data analysis was performed by CasaXPS software.

To evaluate the presence of micro/nanostructures on the surface of the films, a morphological analysis by means of scanning electron microscope (SEM) was conducted.

29.3   Results

Figure 29.1 shows a quite homogeneous PPY nanofiber network was obtained.

The orientation is highly random and the nanowires form a dense network with various overlaps. The chemical composition of the surface was evaluated.by XPS. Wide-scan spectra show the occurrence of O, N, C, Cl, P in the sample.

The Cl 2p and P 2p signals were assigned to anionic species originating from the electrolytes used during PPY electrosynthesis and overoxidation (ClO_4^- and PO_4^{2-}, respectively). Particular attention should be paid to the irradiation time of the sample. Infact, we noticed a change in the Cl 2p signal, as shown in Fig. 29.2, during prolonged exposure of the sample to X-rays.

At the beginning of the analysis, ClO_4^- represents the largely predominant species, while its extensive degradation is evident after a 1000 min. exposure.

High resolution C1 s, N1 s, O1 s, Cl2p and P2p spectra both for PPY nanofiber network and for PPY conventional were acquired. Ratios N/C, O/N and (Cl+P)/N

Fig. 29.1 SEM image of PPY
nanofiber network
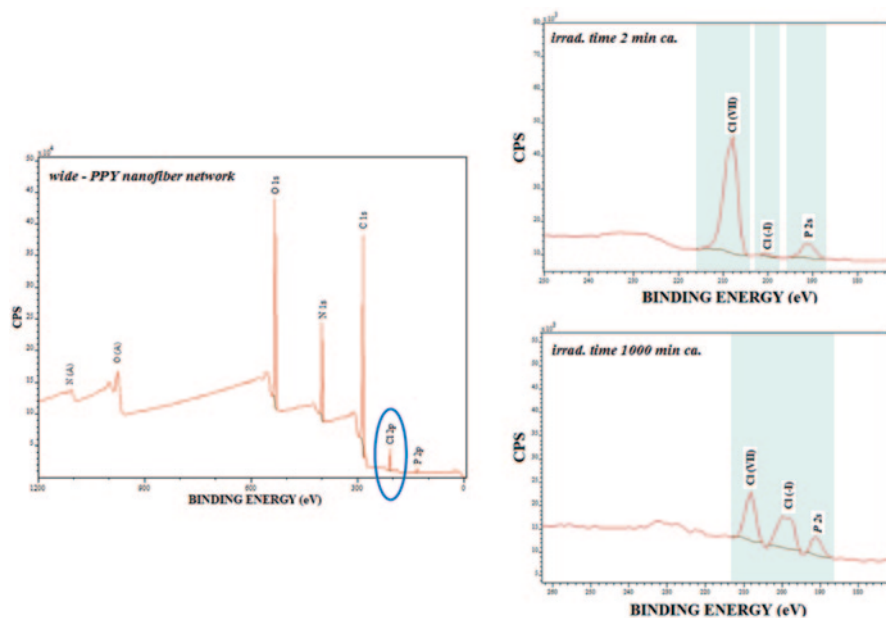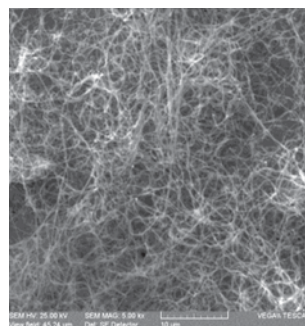
Fig. 29.2 Wide scan spectrum with a zoom for Cl 2p region

were calculated for both types of sample and the results were plotted to make the necessary comparisons (Fig. 29.3).

O1 s signal has been corrected taking into account the presence of ClO_4^- and PO_4^{2-}. As shown in Fig. 29.4, the nanostructured sample appears more overoxidized. A further comparison was made considering the N 1 s signal.

N1 s region shows an higher content of charged N in the conventional PPY. This is coherent with the trend observed in overoxidation.
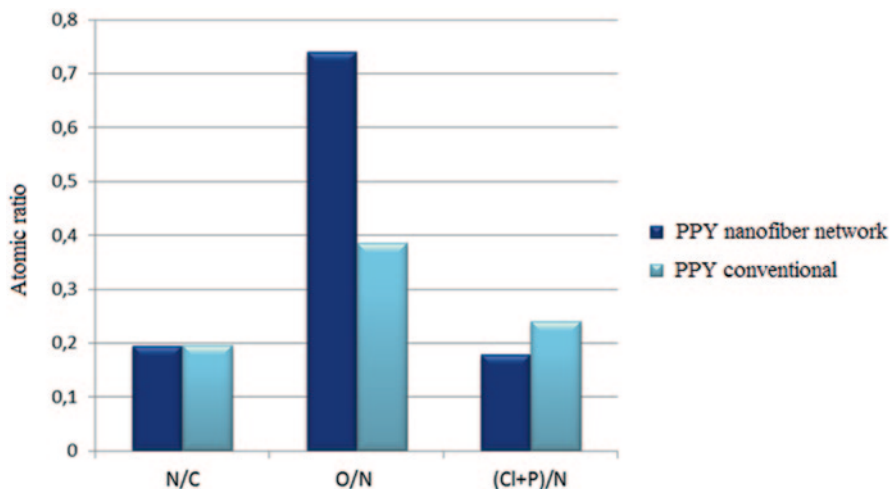
Fig. 29.3 Atomic ratios on PPYs
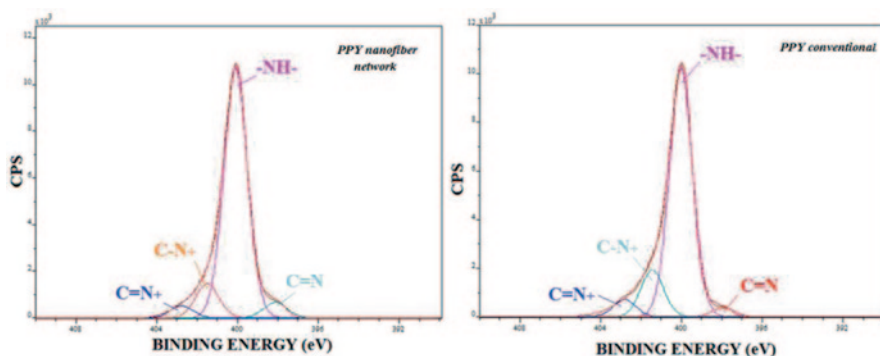
Fig. 29.4 N1 s signal

29.4 Conclusions

Preliminary comparison between nanostructured and conventional PPY samples has been performed with XPS in this work. Overoxidation extent seems the main difference between them. Homogeneity of the samples will be furtherly studied by imaging XPS. Conditions for avoiding and/or limiting perchlorate degradation under X-ray irradiation will be investigated.

References

1. C. Li, H. Bai, G. Shi, Chem. Soc. Rev. 38 (2009) 2397
2. C. Malitesta and E. Margapoti, Insights from XPS on nanosized inorganic materials, A. Dibene-detto and M. Aresta (Eds.), Inorganic Micro- and Nanomaterials, (2013) Walter de Gruyter GmbH, Berlin/Boston, pp. 47–55
3. J. Zang, C.M. Li, S.-J. Bao, X. Cui, Q. Bao, C.Q. Sun, Macromolecules 41 (2008) 7053

Chapter 30
Three-dimensional Plasmonic Materials for Chemical Sensor Application

Adriano Colombelli, Maria Grazia Manera, Giovanni Montagna, Roberto Rella and Annalisa Convertino

In this work, we perform a numerical and experimental comparison of 2D and 3D systems of plasmonic nanostructures in order to explore several key parameters for sensitivity enhancement of traditional LSPR biosensors. The optical properties and the sensing capabilities of planar and three-dimensional distributions of metal nanostructures have been theoretically and experimentally investigated. We developed a numerical model for calculating the absorption spectra and the sensitivity towards increasing refractive indexes of periodic array of plasmonic nanostructures. Our numerical results have been verified performing a sensitivity comparison of 2D and 3D nanostructured systems composed by the same kind of metal nanoparticles. As proof of concept, our experiment were conducted on a planar distribution of gold nano-spheres and an hybrid 3D plasmonic material composed by a disordered system of silica nanowires decorated with spherical gold nanoparticles.

30.1 Introduction

The remarkable interest in plasmonic nanostructures is based on the fascinating optical properties that they exhibit when stimulated by incident light under specific conditions [1]. Metallic nanostructures containing subwavelength nano-holes

---

A. Colombelli (✉) · M. G. Manera · G. Montagna · R. Rella
CNR—Institute for Microelectronics and Microsystems, Unit of Lecce, Lecce, Italy
e-mail: colombelli.adriano@gmail.com

A. Colombelli
Department of Innovation Engineering,University of Salento,Lecce, Italy

R. Rella
e-mail: roberto.rella@cnr.it

A. Convertino
CNR—Institute for Microelectronics and Microsystems, Unit of Roma, Roma, Italy

or nano-disks can greatly enhance the local electric fields near the particles surface and this phenomenon is known as Localized Surface Plasmon Resonance (LSPR). Although considerable progress has been made in improving bulk sensitivity of traditional LSPR biosensor, their performances are often limited by low LSPR signals due to the small active area of the metal NPs and their low density in the defined surface area. Many efforts have been devoted to increase the sensitivity of these systems by exploiting the high field confinement effect of 2D ordered array of closely packed metal NPs, or by increasing the NP ensemble density in three dimensional (3D) assemblies of NPs. In this paper, we perform a numerical and experimental analysis of 3D and 2D plasmonic materials, in order to compare their performances as chemical sensors. We develop a numerical model with the RF module of COMSOL Multiphysics for calculating the absorption spectra of highly ordered array of metallic nanostructures. Their sensitivities towards different refractive indexes have been calculated showing how the fabrication of 3D plasmonic architectures could represent a valid strategy for sensitivity enhancement of traditional LSPR biosensors. The outcomes of our numerical simulations have been confirmed performing a sensing comparison between planar and three-dimensional distributions of spherical gold nanoparticles. The 3D nanostructure consisted of a highly disordered system of silica nanowires (NWs) decorated with spherical Au NPs. This kind of system represent an efficient and cheap approach to obtain a very dense 3D metal NPs ensemble, easily accessible to biomolecules due to the micro-porous structure of the NW forest [2]. Similar NPs were deposited on a glass substrate in order to form a planar distribution. UV–Vis spectroscopy and SEM analysis were used to characterize the obtained structures. The sensing performances of the examined transductors have been investigated performing several refractometric tests. Their sensitivities have been compared confirming the outcomes of our numerical simulations.

30.2   Computational Methods

In this work, we numerically investigate the LSPR conditions of ordered arrays of metal NPs. distributed on a glass substrate. Square and cubic arrays of gold nano-spheres have been studied through 3D finite element simulations, in order to analyze their absorption spectra when the refractive index of the environment is changed. As built, the model can easily predicts the optical properties of metal nanoparticles characterized by different geometries. The simulation domain is composed by four layers with optimized thicknesses, and represents the unit cell of the analyzed periodic array (Fig. 30.1a). In order to avoid possible multiple reflections inside the simulation domain, Perfectly matched layers (PMLs) conditions have been set for the outer regions of the model. Port boundary conditions, automatically determine the reflection and transmission coefficients calculating the scattering parameters (S-parameters). Central domains represent the glass substrate and the environment and are characterized by wavelength dependent optical properties. A single gold nano-sphere with a diameter of 20 nm is placed near the substrate surface and

Floquet-periodic boundary conditions are used on four sides of the unit cell to simulate the infinite 2D array of NPs. The incident electromagnetic wave is excited from the port on the top of the model and can be linearly polarized in a desired direction. The optical response of the system was investigated in a particular wavelength range, corresponding to 300–800 nm. At these frequencies, gold can be modelled as having a complex refractive index, with real and imaginary components. In order to analyze the optical response of a 3D distribution of NPs, we modify the simulation geometry introducing multiple layers of NPs. As proof of concept a cubic array composed by eight layers of gold nano-spheres was analyzed.

30.3 Experimental Methods

Forests of silica NWs were produced by thermal annealing of Si NWs grown by plasma enhanced chemical vapor deposition (PECVD). The decoration of these structures with gold NPs was obtained by thermal evaporation of thin film of Au followed by a suitable thermal treatment for the activation of a metal de-wetting process. Further details on the fabrication process of these systems can be found in reference [2]. Using the same fabrication process we realize a planar distribution of Au NPs on a glass substrate. The morphology of these structures was investigated by SEM analysis while their optical properties have been studied in the spectral range between 400 and 800 nm by absorption measurements both in gaseous and liquid environment. By dipping these systems in different solvent and monitoring the variations of the LSPR absorption peak, we confirmed their ability to detect even small changes in the refractive index of the local environment. The response of each system was calibrated to bulk refractive index changes. Six refractive indexes standard solutions were prepared by ethanol diluted in deionized water.

30.4 Results and Discussions

The morphology of the systems was investigated by plan-view SEM analyses. As evidenced by the high magnification image in Fig. 30.1c, the wire surface is covered with Au nanoparticles, whose diameter varies from few nanometers to tens of nanometers. Similar structures have been observed for the planar distribution of Au NPs on glass substrate, as can be seen in Fig. 30.1d. The sensing performances of the simulated and real 2D and 3D plasmonic structures were investigated following the same strategy. In the first case we calculated the spectral shifts of the LSPR absorption peak, when the refractive index of the simulated environment was changed. In the second case, we monitored the integrated absorption intensity ($\Delta\lambda = 500$–600 nm) as function of time, as aqueous

solutions of ethanol with different concentrations and refractive indices flowed into the test chamber. Both the numerical and experimental results show a clear
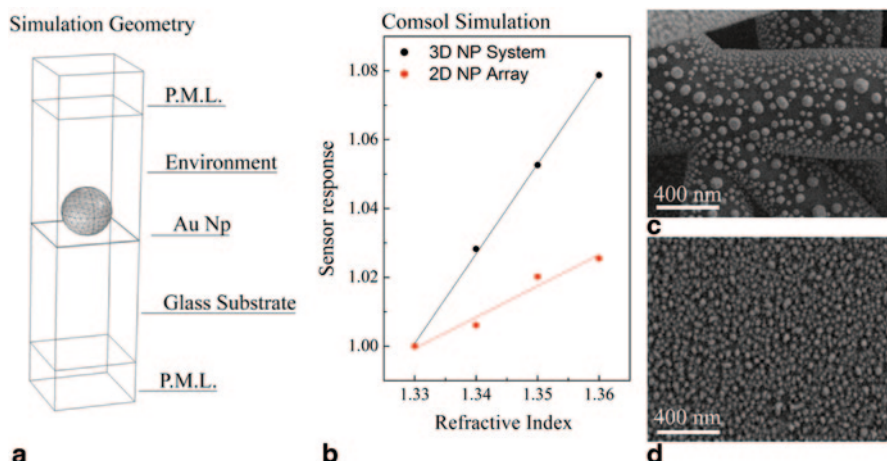
Fig. 30.1. **a** Simulation geometry used in Comsol Multiphysics, **b** Simulated calibration curves of the 2D and 3D theoretical systems immersed in different concentrations of ethanol, **c** and **d** SEM images of SIO$_2$ nanowire decorated with Au NPs and Au NPS generated on glass substrate

Table 30.1 Experimental sensitivity calculated for the examined 3D and 2D plasmonic systems; The sensitivity value is intended as Absorption Intensity Variations (%) per refractive index unit

Sensor system	Sensitivity
3D Silica NW with Au NPs	12.5
2D distribution of Au NPs	6.6

change in the absorption of the system, when the refractive index of the local environment is changed. In Fig. 30.1b the theoretical calibration curves are reported, where the sensor response is intended as the ratio of the signal intensity in presence of the analyte and the signal calculated in water. The slopes of these curves are proportional to the sensitivity of each system, and clearly demonstrate how the three-dimensional plasmonic transductors could represent an interesting strategy for the enhancement of traditional 2D LSPR sensors. The obtained experimental results confirmed the numerical ones. From the slopes of the experimental calibration curves, the bulk refractive index sensitivities were determined and reported in Table 30.1. A two-fold improvement in sensing performance can be seen when using this particular 3D plasmonic system as chemical sensor.

30.5   Conclusions

In order to demonstrate the higher sensing performances of 3D plasmonic structures, the sensitivity of 2D and 3D plasmonic materials have been theoretically and experimentally compared. We developed a numerical model for calculating the spectral shifts of the LSPR absorption peak when planar or three-dimensional peri-

odic array of NPs are exposed to different refractive indexes of the environment. As proof of concept, we confirmed the theoretical results comparing the sensitivities of a planar distribution and a 3D ensemble of metal NPs. A new class of plasmonic materials consisting of silica NWs decorated with metal NPs, have been used for this aim. The micro-porous structure of these NW forest allows the fabrication of 3D ensemble of metal NPs, easily accessible to liquids, vapors, or biomolecules.

References

1. Eliza Hutter, Janos H. Fendler, Exploitation of Localized Surface Plasmon Resonance, Adv. Mater., 16, No. 19, (2004)
2. A. Convertino, M. Cuscunà, F. Martelli, M. G. Manera and R. Rella, Silica Nanowires Decorated with Metal Nanoparticles for Refractive Index Sensors: Three-Dimensional Metal Arrays and Light Trapping at Plasmonic Resonances, J. Phys. Chem. C, **118**, 685–690, (2014)

Chapter 31
Multidimensional Approach to Solanaceae's Nutritional and Gustative Aspects

S. Grasso, F. Genova, M. Santonico, G. Pennazza, V. Locato, L. De Gara, D. Accoto, A. Sudano, A. D'Amico and W. Marmo

An innovative approach based on a potentiometric sensor has been employed for peppers characterization. Despite a great number of hot pepper varieties are cultivated worldwide and are consumed, a simple method to discriminate them does not exist yet. A multidimensional system centered on a liquid sensor was used to successfully characterize five different pepper species by means of an easy and rapid procedure. The information deriving from cyclic voltammetry analyses was acquired by the electronic system and further evaluated through a multivariate data analysis approach. The calculated models showed an efficiency of 100 % in the classification of the hot peppers and were able to predict with good accuracy the antioxidant content of the pepper exemplars.

S. Grasso (✉) · M. Santonico · G. Pennazza
Lab of Electronics for Sensor Systems, CIR-Center for Integrated Research, University Campus Bio-Medico di Roma, Rome, Italy
e-mail: S.Grasso@unicampus.it

F. Genova · V. Locato · L. De Gara
Food Science Human Nutrition Unit, CIR-Center for Integrated Research, University Campus Bio-Medico di Roma, Rome, Italy

D. Accoto · A. Sudano
Laboratory of Biomedical Robotics and Biomicrosystems, CIR-Center for Integrated Research, University Campus Bio-Medico di Roma, Rome, Italy

A. D'Amico
Department of Electronic Engineering, University of Rome Tor Vergata, Rome, Italy

W. Marmo
Antica Azienda Agricola Brocchieri, Roma, Italy

31.1   Introduction

Pepper is the fruit of plants from the genus Capsicum L., which belongs to the large
Solanaceae family. Peppers are commonly called "hot" or "sweet" depending on
their spiciness when consumed. The difference between the two kinds of peppers re-
sides in the amount of a specific alkaloid, the capsaicin, which the plant accumulates
in the fruits as a deterrent against premature consumption. Nevertheless, due to the
many other beneficial properties, peppers have become a common cooking ingredi-
ent worldwide. Taxonomy of Capsicum includes 39 existing species and nowadays
five of these are domesticated and cultivated since ancient times (5200–3400 B.C.)
[1]. From domesticated species a great number of varieties derives, different in col-
ors, shapes and spiciness. Despite a so wide choice of peppers, easy identification
criteria are currently not available and hot peppers are commonly identified only on
the basis of their spiciness. This classification method is reductive from a nutritional
standpoint, because peppers do not contain only capsaicin, but also several vitamins
and micro-nutrients [2]. Here we present a novel electronic system (BIONOTE)
based on a liquid sensor array that is able to discriminate from different pepper spe-
cies by means of a simple analytical procedure.

31.2   Materials and Methods

31.2.1   Sample Selection

Pepper fruits of the five domesticated species (*Capsicum annuum, Capsicum bac-
catum, Capsicum chinense, Capsicum frutescens, Capsicum pubescens*) were har-
vested on the basis of the correct maturation state and the absence of abnormalities.

31.2.2   Liquid Analysis

One gram of fresh tissue was isolated from each pepper exemplar paying attention
to leave out both seeds and placenta. Samples were fine homogenized in 30 mL of
double distilled water (pH 7.2) using an UltraTurrax instrument and the extracts
were clarified through a centrifugation at 8000 rcf and 4 °C. Finally, supernatants
were collected and stored in ice up to the analysis. Electronic interface and sensors
employed in the liquid analyses were the same as described in Santonico et al. 2013
[3]. Cyclic voltammetry in the range from −1 to 1 V was performed using a trian-
gular function at 10 mHz and a sampling interval of 1 s.

31.2.3 Trolox Equivalent Antioxidant Capacity (TEAC)

For lipophilic extraction, 1 g of fresh tissue was isolated from each pepper exemplar as described above. Samples were homogenized in a volume of 5 mL of acetone (Sigma-Aldrich, Milan, Italy) using mortar and pestle with the addition of a small amount of quartz sand. Homogenates were clarified through a centrifugation at 8000 rcf and 4 °C and the lipophilic fractions were collected. Remaining pellets were let to dry under flow hood to eliminate any acetone trace, thus were resuspended with 2 mL of 50 mM sodium phosphate buffer (pH 7.5). Mixtures were agitated vigorously for 1 min and the hydrophilic extracts were recovered from the upper phase after a centrifugation. The antioxidant potential of either the hydrophilic and lipophilic pepper extracts was evaluated through the TEAC assay [4]. Results were derived from a standard curve of Trolox (Sigma-Aldrich, Milan, Italy) ranging from 3 to 15 μM.

31.3 Results and Discussion

Pepper exemplars from the five domesticated species underwent extraction procedures before being characterized by means of either electrochemical and biochemical analyses. A screen-printed gold electrode (Aux.: Pt; Ref.: Ag) fabricated by DropSens S.L. (Llanera (Asturias), Spain) was employed as liquid sensor, while the electronic interface controlling it granted on the reference electrode a voltage input in the form of a triangular function and converted the out current from the working electrode in a an output voltage value. An array of 100 virtual sensor responses was obtained from a single physical sensor applying a 10 mHz triangular function as voltage input signal and recording one output value per second. By means of this setup, each pepper extract was evaluated through five consecutive independent measures and reproducibility of the system was confirmed by voltammetric curves overlapping (Fig. 31.1).

A data set array comprising all the acquired values was constructed and it was further analyzed using multivariate data analysis techniques. The score plot of the first two Principal Components (PCs) shows the ability of the system to sharply discriminate between the five pepper species (Fig. 31.2). Additionally, a Partial Least Square Discriminant Analysis (PLS-DA) model was calculated showing an efficiency of 100 % in the classification of the hot peppers in four independent repetitions each.

From a biochemical point of view, the antioxidant potential of either the hydrophilic and lipophilic pepper extracts was evaluated through the TEAC assay. Results showed quite differences between the two kinds of fraction in terms of antioxidant molecules concentration. In fact, while *C. frutescens* showed the highest value among the hydrophilic extracts, its lipophilic antioxidant molecules resulted only the 25 % of *C. chinense*'s ones (Fig. 31.3).
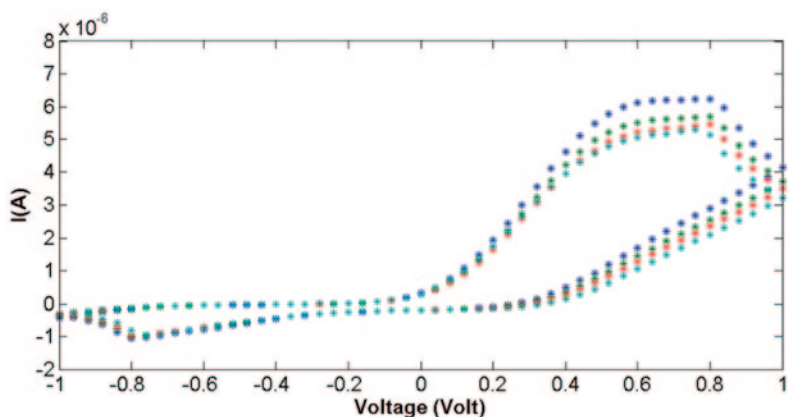
Fig. 31.1 Cyclic voltammogram of five *C. frutescens* consecutive independent measures
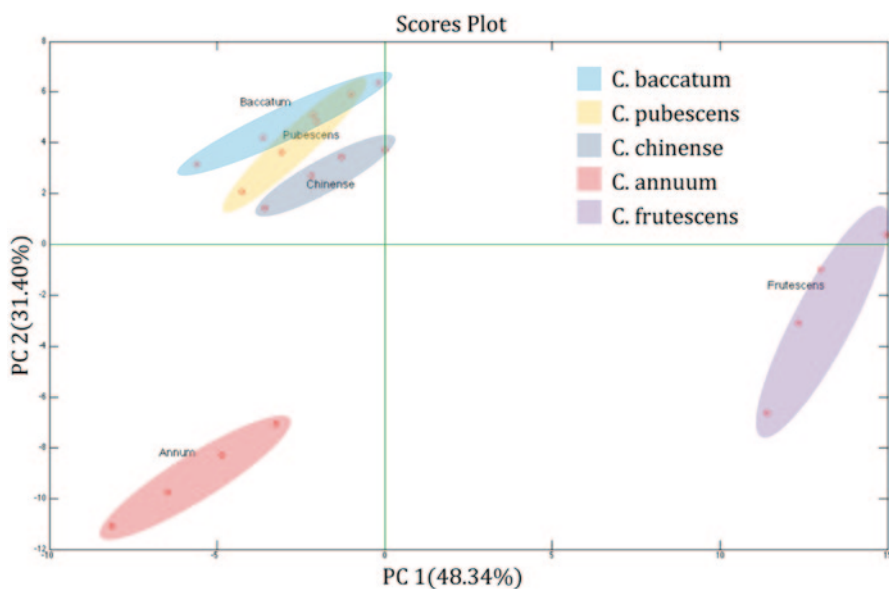
Fig. 31.2 Scores plot of the first two PCs of the PCA model built on the collected data

In general, the estimated total antioxidant capacity of the lipophilic pepper extracts was about one order of magnitude higher than hydrophilic counterparts.

Finally, a single data set comprising all the electrochemical and biochemical features was evaluated through a multivariate data analysis approach. PLS-DA model highlighted the excellent ability of BIONOTE to predict antioxidant content within hydrophilic extracts with a Root Mean Square Error in Cross Validation, using the Leave One Out criterion, of 0.29 μmol/g (Fig. 31.4).
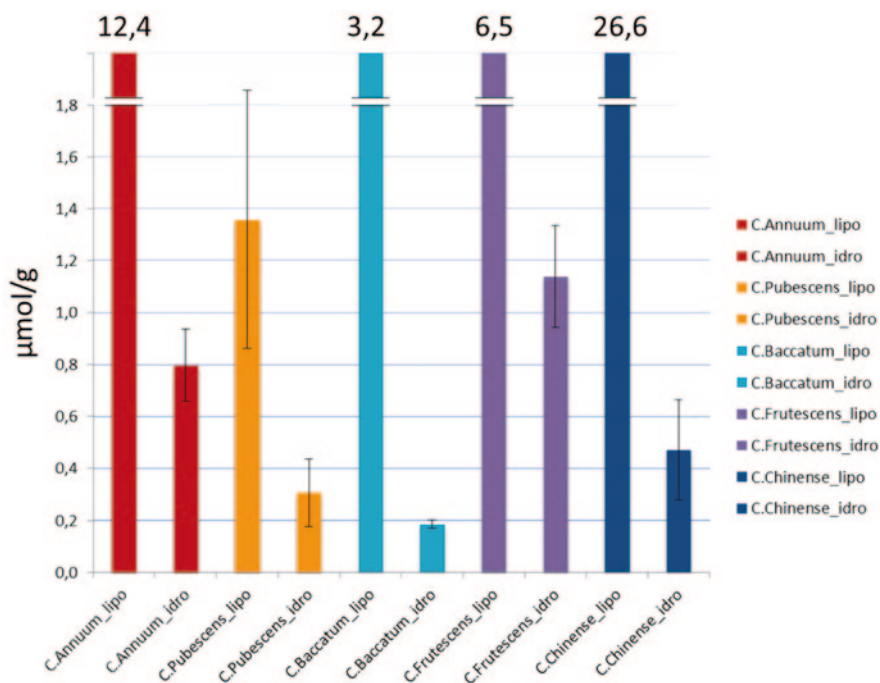
Fig. 31.3 Hydrophilic and lipophilic extracts evaluation by TEAC assay
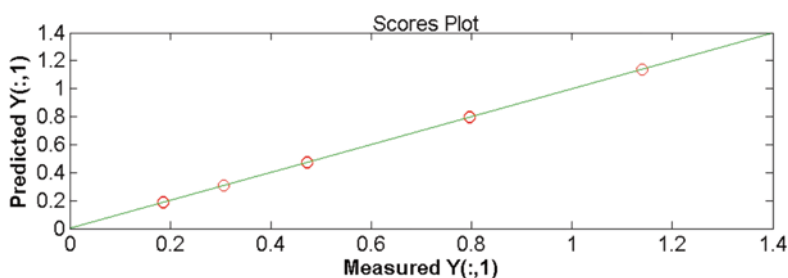
Fig. 31.4 PLS-DA model performed on antioxidant molecules concentrations versus predicted ones

On the contrary, the PLS-DA model did not seem to be able to calculate the lipophilic antioxidant molecules concentration with the same good accuracy. This discrepancy could be fundamentally attributed to the water based nature of the extract analyzed by the liquid sensor. In conclusion, BIONOTE system has demonstrated to recognize peppers of different species and to predict some biochemical features, thus opening the way to an easy-to-use device for farmers, manufacturers and consumers that actually lack of systems to analyze peppers and peppers derived products easily.

References

1. Perry, L., et al. Starch fossils and the domestication and dispersal of chili peppers (Capsicum spp. L.) in the Americas. Science, **315** (5814), 986–988 (2007)
2. M. Materska and I. Perucka. Antioxidant Activity of the Main Phenolic Compounds Isolated from Hot Pepper Fruit (Capsicum annuum L.). J. Agric. Food Chem. **53** (5), 1750–1756 (2005)
3. M. Santonico, G. Pennazza, S. Grasso, A. D'Amico, M. Bizzarri. Design and Test of a Biosensor-Based Multisensorial System: A Proof of Concept Study. Sensors **13**, 16625–16640 (2013)
4. Re R. et al. Antioxidant Activity applying an improved ABTS Radical Cation Decolorization Assay. Free Radical Biology & Medicine. **26**, 1231–1237 (1999)

Chapter 32
Whispering Gallery Modes Microresonators for Sensing and Biosensing Applications

A. Barucci, F. Baldini, S. Berneschi, F. Cosi, A. Giannetti, G. Nunzi Conti, S. Soria, S. Tombelli, C. Trono, D. Farnesi, S. Pelli, G. C. Righini, L. Lunelli, L. Pasquardini and C. Pederzolli

32.1 Introduction

Historically, the "whispering gallery" term was introduced for the first time by Lord Rayleigh in 1910 [1]. He discovered that the gallery curved surface of the St. Paul's Cathedral cupola in London refocused an acoustic wave in its propagation all along the same gallery. From a macroscopic and mechanical phenomenon to a microscopic and electromagnetic one. When an optical glass microsphere is opportunely excited by a suitable coupling system [2], the light inside the microcavity follows a zig—zag path, close to the microresonator surface and around the equatorial plane, by means of subsequent total internal reflections. Moreover, due to their small volumes, these particular resonant structures strongly increase the light—matter interaction, confirming the Galileo Galilei's eureka moment for which "[…] *smaller objects in nature are not just scaled replicas of similar big objects and in fact they have improved properties*" [3]. This unique property makes these optical devices attractive for investigation in many fundamental processes (e.g.: quantum electrodynamics or non—linear optics) and in more applied fields of photonics (e.g.: filters, microlasers and chemical/biological sensing). The key parameter which takes in account the microcavity capability of storing photons is the quality factor Q. The higher this quantity the longer the photon lifetime is and its interaction with

A. Barucci (✉) · F. Baldini · S. Berneschi · F. Cosi · A. Giannetti · G. Nunzi Conti · S. Soria · S. Tombelli · C. Trono · D. Farnesi · S. Pelli · G. C. Righini
IFAC-CNR, "Nello Carrara" Institute of Applied Physics, Via Madonna del Piano 10, 50019 Sesto Fiorentino FI, Italy
e-mail: a.barucci@ifac.cnr.it

D. Farnesi · S. Pelli · G. C. Righini
Centro Studi e Ricerche "Enrico Fermi", Piazza del Viminale 2, 00184 Roma, Italy

L. Lunelli · L. Pasquardini · C. Pederzolli
FBK-Irst, Materials and Microsystems Centre, BioSInt Unit, Via Sommarive 18, 38123 Povo TN, Italy

the surrounding medium. In particular, the sensing mechanism of these devices is strictly related to the morphological dependence of the whispering gallery modes (WGMs). Any change on the surface of the microresonator, due to the chemical/biochemical binding or in its surrounding medium, may cause a shift of the resonance position. This aspect is particularly useful for the development of high sensitive label-free sensors [4]. Here we present an overview on the main results obtained in our Labs about the implementation of these optical microcavities as suitable platform for sensing and biosensing applications.

32.2 Experimental

Optical silica microspheres was produced in our Labs partially melting a cleaved fiber tip by means of an arc discharge occurring between two metal electrodes. Due to the surface tension, a spherical shape was performed. Typical microspheres size used in our experiment was around 260 μm (in diameter). The light, coming from an external tunable cavity source, is coupled to the WGM resonator by means of a tapered fiber whose output is sent to a photodiode connected to an oscilloscope. By periodically scanning the laser the position of a WGM resonance, corresponding to a dip in the transmission, can be carefully monitored. We used a microfluidic flow system that incorporates the WGMR and the tapered optical fiber. A crucial step for the development of WGMs—based sensors is represented by the functionalization of the microresonator surface in order to specifically bind only the biochemical element to be recognized and, at the same time, maintain a good value for the Q factor.

32.2.1 *Optical Silica Microspheres as Aptasensor for Real Time Detection of Blood Proteins*

We have tested the binding capabilities of a thrombin DNA-aptamer both in buffer and in human serum. For this purpose, the silica microspheres surface was preventively silanized by dip coating using 3-mercaptopropyltrimethoxysilane (MPTMS). Hence, an incubation step of 10 μM aptamer solution (Thrombin Binding Aptamer TBA-15) in Coupling Buffer-CB was performed. Finally, these aptamer modified microspheres were further incubated for 30 min with purified human thrombin (5 μl of 0.3 mg/ml, THR) in diluted BioRecognition Buffer (BRB) and/or in non-filtered 1:10 human serum solution in BR buffer (v/v). The total volume of our microfluidic flow cell was 350 μl with the two entries connected to a peristaltic pump. Q factor measurements, performed at 773 nm, revealed high values both after silanization process (4.2×10^6) and thrombin covalent binding in BRB solution (8×10^5). Moreover, after the injection of 5 μl of 0.3 mg/ml of thrombin in human serum, the sensorgram revealed a wavelength shift of about 14.6 ± 0.1 pm in about 20 min [5].

32.2.2   Optical Silica Microspheres as IgG—anti-IgG Immunoassay

The silica microspheres were firstly functionalized by dip coating process in a diluted solution of 10 mM Eudragit® L100 in ethanol as reported in [6]. Then they were placed in a microfluidic open cell of 3 mL in volume. A peristaltic pump was used for filling the cell and injecting—in different steps—mouse and anti-mouse IgG both at a concentration of 100 mg·L^{-1}. Moreover, the anti-mouse IgG was labeled with fluorescein in order to check, at a fluorescence microscope, the quality of the detection layer so formed on the surface of the microsphere and visibly verify the effective binding between mouse and anti-mouse IgG. The main results of this investigation showed high Q factors values (1.5×10^5 at 1550 nm) in buffer solution after the IgG—anti-IgG binding. The uniform distribution of the labeled mouse anti—IgG, after the specific binding, was also confirmed by fluorescence microscope measurements. Moreover, a resonance wavelength shift of about 10.2 ± 0.3 pm after an injection of 10 μL of 50 mg·L^{-1} anti—IgG in the PBS solution was observed [7].

32.2.3   Optical Silica Microbubble Resonators as Refractometer

The main drawback in using silica microspheres for biosensing applications is represented by their worst integrability with the microfluidics part. In fact, in both of the aforementioned cases, the microsphere was slowly lowered down into the fluidic cell in order to make contact with the thinnest part of tapered fiber. Optical microbubble resonators (OMBR), with their intrinsic capability of microfluidics integration, well bypass this problem. We demonstrated the possibility to fabricate these resonant structures starting from a pressurized silica capillary, locally heated by a modified arc discharge system which is able to rotate all around the capillary axis. Typical diameter sizes were around 340 μm (outer diameter) with a wall thickness of 4 μm±0.5 μm. *Q* factor higher than 10^7 was measured at 1550 nm while a sensitivity of 0.5 nm/RIU with a LOD of about 10^{-6} RIU were obtained for our OMBR as refractometer [8].

32.2.4   A Novel Sensing Approach Based on a Fiber Ring Laser Loop with a WGM Microsphere

Usually, the typical sensing approach based on high *Q* WGMs microspheres consists in monitoring the resonance shift due to some chemical/biochemical binding on their functionalized surface or in the refractive index change of the surrounding medium. This requires high cost finely tunable laser source having a linewidth narrower than the resonance that has to be monitored. Instead of following the

resonance position of the WGMs microcavity, we proposed a new sensing method based on detecting the shift of a fiber ring laser containing a WGM microsphere in its loop. This approach is cheaper than the other one, because it requires the presence of an erbium doped fiber amplifier (EDFA). In our case the loop was closed on the microsphere by using two tapered fibers. A portion of the light circulating in the loop was extracted with a tap coupler and sent to a Fabry–Perot analyzer in order to accurately monitor the position of the fiber ring laser line. By a home—made thermostatic cell, we have thermally perturbed the system increasing, locally, the silica microsphere temperature of $0.5\,°C$. Consequently, we have observed the same behavior for the laser line as for the cavity resonance shifts. Because the measured laser linewidth of the loop was ≤ 1 MHz while that of the "passive" resonance was around 0.1 GHz, this method could also increase the sensor resolution [9].

32.3 Conclusions

An overview on the main activities performed in our Labs about silica WGMs microresonators was presented. We demonstrated the potentiality of these optical resonant structures as suitable platform for sensing and biosensing applications.

References

1. Lord Rayleigh, Philosophical Magazine **20**, 1001–1004 (1910).
2. G. Nunzi Conti, A. Barucci, S. Berneschi, M. Brenci, F. Cosi, D. Farnesi, S. Pelli, G.C. Righini, S. Soria, Proc. SPIE 8236, 82360V-1–82360V-8 (2012).
3. Galileo Galilei, "Dialogues Concerning Two New Sciences", Macmillan Company, 300 pages (1914).
4. M. Baaske, F. Vollmer, ChemPhysChem 13, 427–436 (2012).
5. L. Pasquardini, S. Berneschi, A. Barucci, F. Cosi, R. Dallapiccola, M. Insinna, L. Lunelli, G. Nunzi Conti, C. Pederzolli, S. Salvadori, S. Soria, J. Biophotonics 6, 178–187 (2013).
6. S. Soria, F. Baldini, S. Berneschi, F. Cosi, A. Giannetti, G. Nunzi Conti, S. Pelli, B. Tiribilli, G. C. Righini, Opt. Express 17, 14694–14699 (2009).
7. A. Giannetti, S. Berneschi, F. Baldini, F. Cosi, G. Nunzi Conti and S. Soria, Sensors 12, 14604–14611 (2012).
8. S. Berneschi, D. Farnesi, F. Cosi, G. Nunzi Conti, S. Pelli, G. C. Righini, and S. Soria, Opt. Lett. 36, 3521–3523 (2011).
9. G. Nunzi Conti, S. Berneschi, A. Barucci, F. Cosi, S. Soria, C. Trono, Opt. Lett. 37, 2697–2699 (2012).

Chapter 33
Development of Sensing Transducers on Compact Disc Substrates

M. Latino, D. Aloisio, N. Donato and G. Neri

Here is reported about the development of gold electrodes for sensors starting from high fidelity compact discs (CDs) as substrates. The CDs were chemically etched to remove the protective layers and to expose the metal one. Several transducer layouts were designed by means of electronic CAD, and then, realized with a LPKF rapid prototyping system (Protomat S103). The gold CDs transducers were employed in the realization of resistive sensors and electrochemical ones. Some examples of the use of the prototypes developed are also reported.

33.1 Introduction

Due to the wide-spread use of chemical sensors, the fabrication of printed electrodes has received great attention, thanks to its low cost and applicability to mass production. In previous works, we investigated printed electrodes on flexible plastic substrates in various application fields [1, 2].

In this work we focused our attention on the development of gold electrodes on plastic substrates. Gold is largely used in the formulation of printed electrodes, due to its high stability and high level of functionalization. In order to develop gold electrodes on plastic substrates, a low cost method is to employ gold compact discs (CDs). Generally, electrodes from CDs were obtained by means of several and tedious chemical etching procedures [3]. Here, we reported about the development of sensing transducers starting from gold CDs with a more simple mechanical prototyping procedure.

N. Donato (✉) · M. Latino · D. Aloisio · G. Neri
DIECII, University of Messina, Contrada di Dio, Messina, Italy
e-mail: ndonato@unime.it

Fig. 33.1 Schematic of the functional layers of a gold compact disc
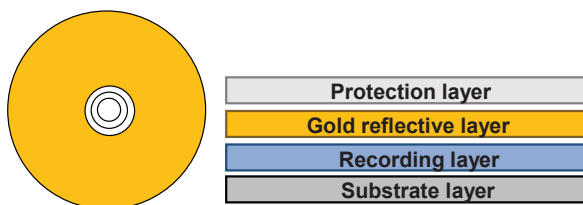
Fig. 33.2 Designed electrodes in Gerber format
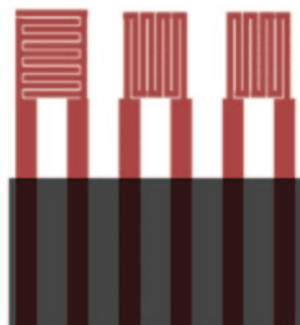
33.2 Experimental Details

Printed electrodes have been fabricated by employing CDs as substrates in a rapid prototyping system. In Fig. 33.1 is shown a schematic view of the functional layer composing a gold recordable compact disc: (a) polycarbonate base as substrate and mechanical support; (b) dye-photosensitive layer as recording one; (c) gold reflective layer; (d) one or two layers of polymeric film as protection ones.

To prepare the gold CD to be shaped by the rapid protoyping system, the protective films must be removed to expose the gold layer. This has been done using diluting nitric acid at 50 % in water as etching solution. Each disk was dipped, for a few minutes, in the etching solution heated at an operating temperature value of 80 °C, and then the disk was washed in distilled water and dried in air flow. The as prepared CD was then employed as substrate for the LPKF Protomat S103 rapid prototyping system. The main typologies of the developed electrodes are shown in Figs. 33.2 and 33.3.

The designed electrodes in Gerber format were then processed by the milling machine. The first transducer substrate fabricated is provided with an interdigitated couple of electrodes on the left side, a serpentine employed as heater in the middle and another one as temperature sensor on the right one. The second transducer was employed as electrode for electrochemical sensor.

Fig. 33.3 The developed electrode prototypes
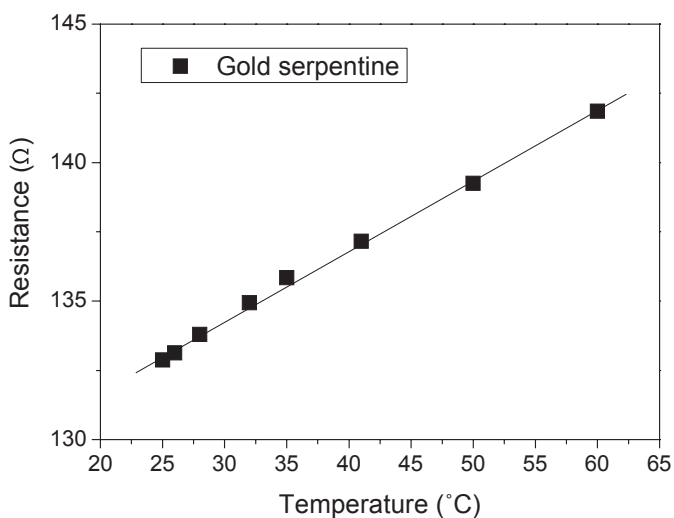
Fig. 33.4 Resistance vs temperature characterization of the gold serpentine

33.3 Results and Discussion

Some examples of the applications of the prototypes developed are reported below. In Fig. 33.4 is reported the calibration curve of the gold serpentine. It can be seen a linear response in a temperature range spanning from room temperature to 65 °C, allowing to the printed sensor to operate as a temperature sensor near ambient temperature.

The gold electrodes shown in Fig. 33.3 were employed as electrochemical platforms in the electrocatalytic oxidation of ascorbic acid (AA, Vitamin C). Ascorbic

Fig. 33.5 Electrochemical
response of the gold elec-
trodes to ascorbic acid
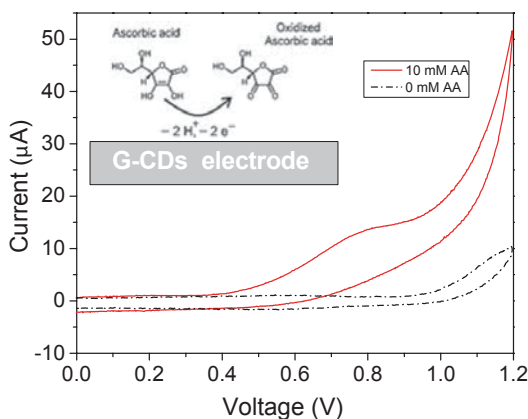
acid is water-soluble, is a powerful antioxidant and can be found in many biological
systems, foodstuffs (fresh vegetables and fruits) and pharmaceutical products.

The electrochemical behavior of the G-CDs electrodes in absence and in pres-
ence of AA in 0.1 M KCl has been investigated by cyclic voltammetry (Fig. 33.5).
The behavior of the G-CDs electrode in absence of AA is similar to that reported for
bulk gold electrodes, characterized by a rising of the anodic current at a potential
above 1.0 V and attributed to the electrocatalytic oxidation of water with evolution
of O_2. In the presence of AA, the oxidation of the analyte was evidenced by the
wave starting around 0.4 V. No cathodic peak has been registered on the reverse
scan, suggesting the irreversibility of the electrocatalytic process.

33.4 Conclusions

Because of the low cost and the fabrication simplicity, the proposed electrodes fab-
ricated from recordable G-CDs appear to be promising for practical applications
as resistive and electrochemical platforms. Indeed, by examining the preliminary
results above reported, it can be said that both the fabricated substrates can be suc-
cessfully employed in the development of reliable devices for resistive temperature
sensors and electrochemical sensors for vitamin C detection.

References

1. Arena, A, Donato, N., Saitta, G., Bonavita, A., Rizzo, G., Neri, G., Flexible ethanol sensors on
    glossy paper substrates operating at room temperature, Sens. Actuators, 145, 2010, 488–494,
2. Rizzo, G. Arena, A., Donato, N., Latino, M., Saitta, G., Bonavita, A., Neri, G., Flexible, all-
    organic ammonia sensor based on dodecylbenzene sulfonic acid-doped polyaniline films, Thin
    Solid Films 518, 2010, 7133–7137,
3. L. Angnes, E. M. Richter, M. A. Augelli, G. H. Kume, Gold electrodes from recordable CDs,
    Anal.Chem. 2000, 72, 5503–5506.

Chapter 34
Electrical Characterization of Nanostructured Sn-Doped ZnO Gas Sensors

S. Trocino, T. Prakash, J. Jayaprakash, A. Donato, G. Neri and N. Donato

Chemoresistive devices based on pure-Zinc Oxide (ZnO) and doped-ZnO nanostructures with tin as dopant were investigated. The nanostructured materials, prepared by a simple and fast microwave irradiation method, have been widely characterized by X-Ray Diffraction (XRD), Fourier Transform InfraRed spectroscopy (FT-IR), Scanning Electron Microscopy (SEM), Transmission Electron Microscopy (TEM), Energy Dispersive Spectroscopy (EDS). The electrical and gas sensing properties, by measuring the resistance value and the electrical impedance, of pure and Sn-doped ZnO nanoparticles were evaluated in the monitoring of reducing (CO) and oxidizing (NO_2) gases. Results demonstrated that, using tin-doped nanoparticles, a simple and low cost sensor device with improved properties in the detection of low concentrations of CO and NO_2 can be developed.

34.1 Introduction

ZnO (Zinc Oxide) is a group II–VI compound n-type semiconductor material with hexagonal wurtzite structure [1], a wide direct band gap (3.37 eV), a large exciton binding energy (60 meV) at room temperature, and a high degree of mechanical, chemical and thermal stability. Electrical properties of ZnO have been recognized from long time for applications in resistive chemical sensors [2]. However, sensors

N. Donato (✉) · G. Neri
DIECII, University of Messina, Contrada di Dio, Messina, Italy
e-mail: ndonato@unime.it

S. Trocino
DICEAM, University "Mediterranea" of Reggio Calabria, Via Graziella, Reggio Calabria, Italy

T. Prakash · J. Jayaprakash
Nanotechnology Laboratory, Sri Ramakrishna Mission Vidyalaya College of Arts and Science, Coimbatore, Tamil Nadu, India

A. Donato
DICEAM, University "Mediterranea" of Reggio Calabria, Via Graziella, Reggio Calabria, Italy

based on ZnO suffer from several problems, such as high operation temperature, poor sensitivity, long response and recovery time and so on [3]. Doping ZnO with different elements such as aluminum, iron, tin, titanium, copper, indium, etc., is generally adopted to overcome this problem [4].

34.2 Experimental Details

34.2.1 Materials and Samples Synthesis

Pure ZnO sample has been prepared by microwave irradiation method using a starting solution of zinc nitrate with 0.1 M concentration diluted in deionized water. Then, NH_3 was added, under constant stirring conditions, up to at the pH level of 8. The stirred mixture was irradiated by the microwave radiation of frequency 2.45 GHz, for 5 min continuously. The precipitates were collected and, washed with distilled water for several times until the extracts turns into a white product. The final product was annealed at 400 °C for 3 h. Sn-doped ZnO powders were prepared adding the suitable amount of a 0.1 M solution of $SnCl_4$ to obtain the 15 wt.% Sn-doped zinc oxide samples.

34.2.2 Samples Characterization and Sensing Tests

The microstructure of the samples was analyzed by X-ray diffraction (XRD) using a Bruker AXS D8 Advance instrument and the monochromatic CuKα_1 wavelength of 1.5406 Å. The Fourier transform infrared spectra (FT-IR) of the samples were recorded by using a 5DX FTIR spectrometer. The sample morphology was observed by Scanning Electron Microscopy (SEM-EDS), using a JEOL 5600LV microscope at an accelerating voltage of 10 kV. The Transmission electron microscopy (TEM) was recorded on a Philips CM200 using an operating voltages 20–200 kV.

Sensors were made by printing films (1–10 μm thick) of the nano-powders dispersed in water on alumina substrates (6×3 mm^2) with Pt interdigitated electrodes and a Pt heater located on the backside. A multimeter data acquisition unit Agilent 34970A was used for this purpose, while a dual-channel power supplier instrument Agilent E3632A was employed to bias the built-in heater of the sensor to perform measurements at super-ambient temperatures. The gas response for CO is defined as R_0/R where R_0 the baseline resistance in dry synthetic air (20% O_2 in nitrogen) and R is the electrical resistance of the sensor at different CO concentrations in dry synthetic air. Whereas for NO_2 R/R_0, where R is the electrical resistance of the sensor at different NO_2 concentrations in dry synthetic air and R_0 the baseline resistance in dry synthetic air. The impedance values were recorded by means of Agilent U1700 LCR Meter interfaced with a personal computer through a home made GUI interface developed with Matlab environment.
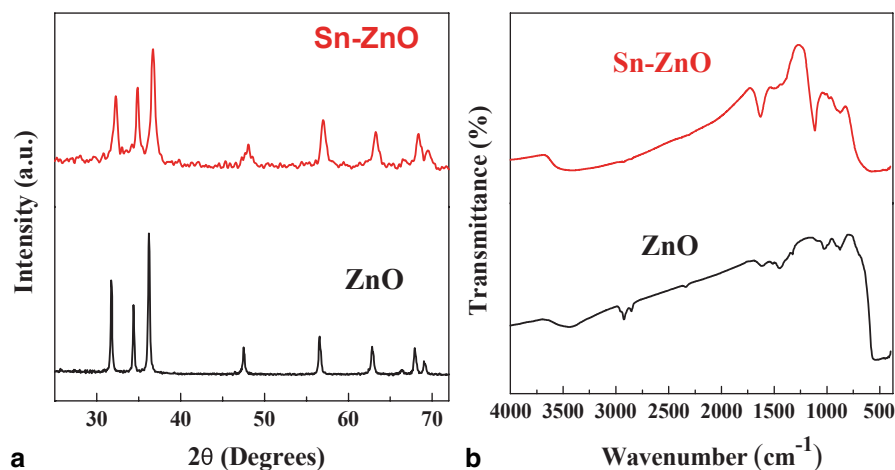
Fig. 34.1 a XRD analysis. **b** FT-IR characterization

34.3 Results and Discussion

34.3.1 Characterization Studies

In both the pure and Sn-doped sample, XRD analysis (Fig. 34.1a) reveals the existence of a pure ZnO single-phase in the hexagonal wurtzite structure (JCPDS 36-1451). It has been calculated through the Scherrer formula, applied to the full width at half-maximum of (101) peak, that on undoped ZnO sample the mean crystallite size is 58 nm, while on the Sn-doped sample is much smaller (27 nm).

FT-IR characterization (Fig. 34.1b) evidenced the broad peak in the range of $3452–3446 \ cm^{-1}$ due to the vibrational mode of O-H bond. Additionally broad adsorption peaks centered at around 1627, 1629 and $1631 \ cm^{-1}$ is caused by the O-H stretching of the absorbed water re-absorption during the storage of the sample in ambient air. Also the very weak peaks, located at 2349, 2337, 2318, 2920 and $2924 \ cm^{-1}$, and attributed to symmetric and asymmetric C-H bonds, respectively, appears due to an environmental contamination.

The needle-like structures for the pure ZnO sample are shown in Fig. 34.2a. The ZnO morphology change significantly by adding Sn to ZnO. Highly agglomerated ZnO nanoparticles characterize the morphology of the Sn-ZnO sample (Fig. 34.2b).

TEM micrograph, in Fig. 34.3a, shows the morphology of ZnO nanoparticles, having size about 40–60 nm. Figure 34.3b illustrates the round morphology of the Sn-ZnO nanoparticles having a diameter between 20 and 40 nm, in agreement with the mean crystallite size obtained from XRD line broadening.
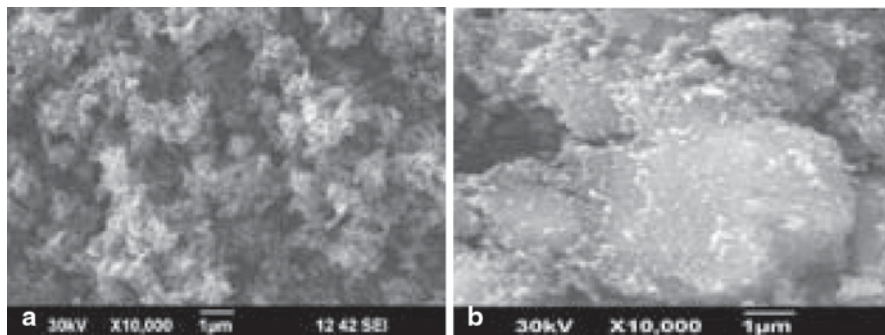
Fig. 34.2 SEM micrographs. **a** ZnO sample. **b** Sn-doped ZnO sample
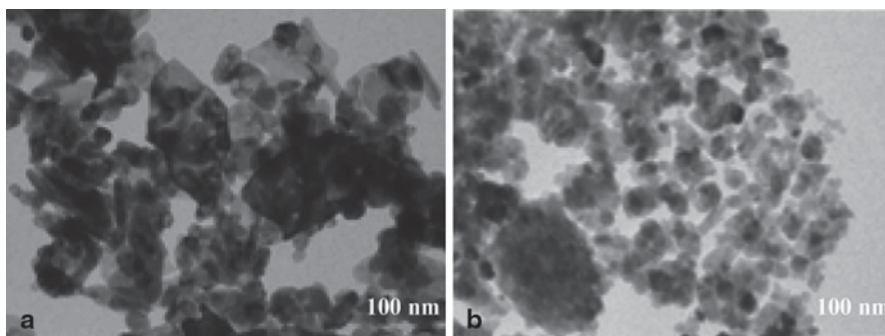
Fig. 34.3 TEM micrographs. **a** ZnO sample. **b** Sn-doped ZnO sample

34.3.2 Electrical and Sensing Tests

Electrical tests have shown that the resistance of tin-doped ZnO film is notably decreased when adding Sn (Fig. 34.4a), which is attributed to the increase of the electrons concentration caused by tin ions substituting the Zn^{2+} ions.

Figure 34.4b, c report CO tests at low concentration of CO (5–80 ppm) carried out at 300 and 400 °C. It can be noted that Sn doping increases the sensitivity to CO compared to ZnO and contemporary decreases the working temperature. On the basis of characterization results, the positive effect of Sn doping on gas response should be related to the presence of smaller particles respect to undoped ZnO.

Decreasing the working temperature, the doped sensor resulted sensitive to few ppm of NO_2 (Fig. 34.5a). Measurements were also carried out in a.c. at different frequencies, in order to optimize the operating conditions of the sensor. The a.c. measurements in range between 100 Hz and 100 kHz showed that the real part of impedance decrements by increasing the frequency (not reported). In Fig. 35.5b is
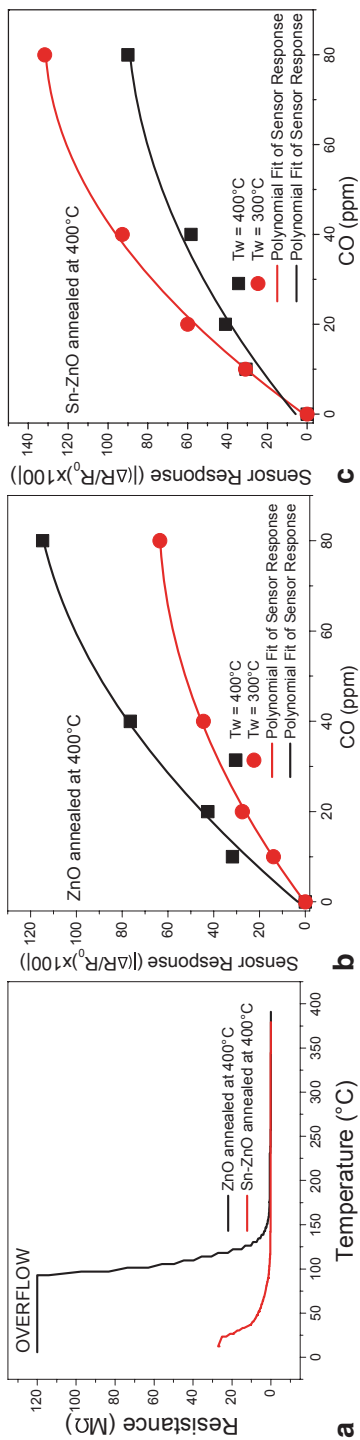
Fig. 34.4 a Electrical characterization, CO sensing test on: **b** ZnO sample. **c** Sn-ZnO sample
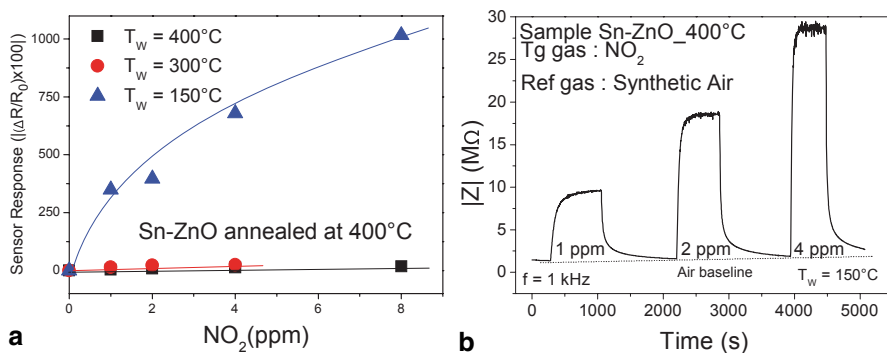
Fig. 34.5 **a** NO$_2$ sensing test on Sn-ZnO sample. **b** Dynamic response of Sn-ZnO sample to different concentrations of NO$_2$ at f = 1 kHz

reported the dynamic response (Z module) versus NO$_2$ concentrations in the range between 1 and 4 ppm at frequency value of 1 kHz.

34.4   Conclusions

The electrical and sensing characteristics of chemoresistive devices based on ZnO nanostructures on alumina substrates provided with Pt interdigitated electrodes were investigated. Addition of Sn allowed the development of a sensor device with improved sensitivity to low concentrations of CO and NO$_2$, good signal-to-noise ratio and short response/recovery time.

References

1. K. Nakahara, H. Takasu, P. Fons, A. Yamada, K. Iwata, K. Matsubara, R. Hunger, S. Niki. Interactions between gallium and nitrogen dopants in ZnO films grown by radical-source molecular-beam epitaxy. Appl. Phys. Lett. **79**, 4139 (2001)
2. B. R. Huang, J. C. Lin. Core–shell structure of zinc oxide/indium oxide nanorod based hydrogen sensors. Sens. Actuat. B-Chem. **174**, 389–393 (2012)
3. P. D. Yang, H. Q. Yan, S. Mao. Controlled growth of ZnO nanowires and their optical properties. Adv. Funct. Mater. **12**, 323–33 (2002)
4. A. Srivastava, Rashmi, K. Jain. Study on ZnO-doped tin oxide thick film gas sensors. Mater. Chem. Phys. **105**, 385–390 (2007)

Chapter 35
Vocs Sensors Based on Polyaniline/Graphene-Nanosheets Bilayer

Antonella De Maria, Vera La Ferrara, Ettore Massera, Maria Lucia Miglietta, Tiziana di luccio, Filippo Fedi, Girolamo Di Francia and Paola Delli Veneri

In this work chemical sensors based on polyaniline and on polyaniline/graphene-nanosheets bilayer were prepared by dip coating. Their morphology and volatile organic compounds (VOCs) sensing behavior were compared. In particular, the devices were investigated in presence of VOCs as limonene and ethanol. Furthermore the devices were characterized under relative humidity. Bilayer samples, exposed to limonene, show a higher relative response respect to only polyaniline, encouraging the graphene use in VOCs sensor devices.

35.1 Introduction

The pathogen attack and herbivore infestation cause considerable crop yield losses in greenhouse cultivation. A monitoring system to reveal plant health problems at an early stage would facilitate immediate actions and possibly diminish adverse effects. A promising method to provide plant health information is the analysis of volatile organic compounds (VOCs) produced by plants under stress in greenhouse atmosphere [1]. Sensors made by conductive polymers can play a crucial role in VOCs sensing because they offer several advantages respect to conventional materials: they work at room temperature, are easily synthesized by chemical or electrochemical processes, their molecular chain structure can be modified by co-polymerization or structural derivations. Furthermore, they exhibit good mechanical properties, which allow a simple fabrication of sensors [2]. When conductive polymers are modified by introducing nanostructured filler their sensing properties could be remarkably improved because of greater specific surface area [3]. Recently the polyaniline/graphene nanocomposites have been used as sensing devices because graphene possesses unique characteristics such as an excellent surface-to-volume ratio [4].

A. De Maria (✉) · V. La Ferrara · E. Massera · M. L. Miglietta · T. di luccio · F. Fedi · G. Di Francia · P. Delli Veneri
ENEA-Centro Ricerche di Portici, P.le E. Fermi 1, 80055 Portici, NA, Italy
e-mail: antonella.demaria@enea.it

In this work graphene nanosheets have been deposited by dip coating onto a pristine polyaniline (PANI) layer, obtaining PANI/graphene bilayer devices, named in this work as PANI-G. Sensing behavior under limonene and ethanol has been investigated comparing the response to pristine PANI devices, also realized by dip coating. In order to verify the sensing activity under different environmental conditions, PANI and PANI-G devices are tested at various percentages of relative humidity.

35.2 Experimental

PANI emeraldine salt dispersion in xylene (2–3 wt%) was purchased from Sigma-Aldrich. In a typical preparation 150 μL of suspension are diluted in 10 mL of tetrahydrofuran (THF) and sonicated for 30 min at room temperature. The PANI layer is deposited on alumina substrate with interdigitated gold electrodes by a dip coating deposition system (Holmarc HO-TH-01). The alumina substrates are vertically dipped and extracted at a speed of 500 μm/s, with 30 s dipping time. Each cycle in PANI solution is alternated with a cycle in deionized water, with a total number of 12.

The graphene nanosheets are prepared from graphite flakes (Sigma-Aldrich) through sonication assisted exfoliation in water/2-propanol mixture. In order to realize PANI-G devices, graphene nanosheets are deposited on pristine PANI layer, using the following dip coating process conditions: 250 μm/s dipping speed, 250 μm/s extraction speed, 10 s dipping time, for 2 cycles. After coating, all samples were quickly dried on hot plate at about 70 °C and stored in air. Pristine PANI and PANI-G device morphologies have been investigated by Focused Ion Beam (FIB) using a Dual Beam apparatus (FEI QUANTA 200 3D). Focused beam of gallium ions can be finely accelerated at low beam currents for imaging or at high beam currents for site specific milling. Thanks to these capabilities, the devices cross section has been milled by FIB.

The PANI and PANI-G conductance responses to different concentrations of ethanol, limonene and relative humidity are measured in a controlled environment with a Gas Sensor Charracterization System (Kenosistecequipment). Devices are installed in a stainless steel test chamber placed in a thermostatic box. A constant flow of nitrogen as gas carrier is inserted in the test chamber. Gas carrier can be properly humidified through a water bubbler placed in a thermostatic bath. In this environment, characterized by controlled temperature and humidity, the conductance value of the device in its equilibrium state is firstly measured (baseline) with high resolution Picoammeter (Keithley 6485) at a constant bias (precision power supply TTi QL355T). Successively an intentional disruption of the equilibrium state is produced by introducing a controlled amount of the analyte and mixing it with the gas carrier and/or changing the humidity grade. To validate and monitor the gas mixture, a thermo Antaris IGS FTIR analyzer is placed at the gas output to measure the chemical compound concentration in the test chamber down to the ppm range. Hardware and software implemented on a work station allow to control and record

Fig. 35.1 FIB cross section of pristine PANI device
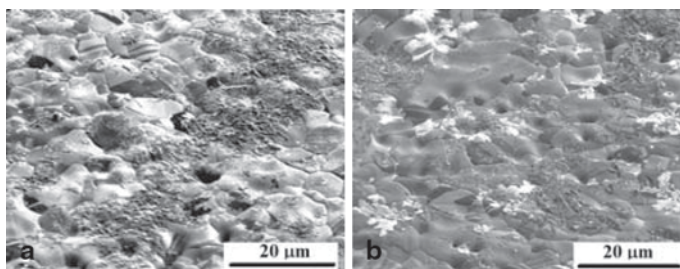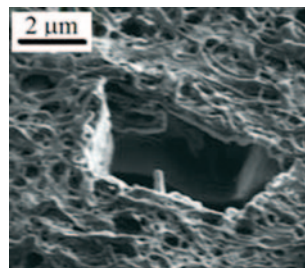
Fig. 35.2 FIB images of pristine PANI (**a**) and PANI-G (**b**) devices on interdigitated gold electrodes deposited on alumina substrate

environmental parameters, device bias and output signal, making possible to perform customizable automated tests on sensor devices.

35.3 Results and Discussion

Cross section of pristine PANI dip coated film obtained by FIB milling (Fig. 35.1) clearly shows a microporous and thinner layer compared to that one obtained by other deposition techniques, such as drop casting. FIB images of pristine PANI and PANI-G device surfaces are shown in Fig. 35.2. Graphene nanosheets are visible onto surface as indicated by the arrows in (Fig. 35.2b), thanks to image contrast due to the higher conductivity of graphene with respect to PANI. Graphene sheets are uniformly distributed over the PANI network.

The electrical responses of the pristine PANI and PANI-G sensors to limonene, ethanol and relative humidity are shown in Fig. 35.3, 35.4a and 35.4b, respectively.

PANI-G based sensors show a higher relative responses respect to pristine PANI in limonene, but the response time is slower (Fig. 35.3). In ethanol both PANI-G and PANI devices show relative conductance values that decrease with increasing of ethanol concentration, but pristine PANI has a greater sensitivity than PANI-G (Fig. 35.4a).
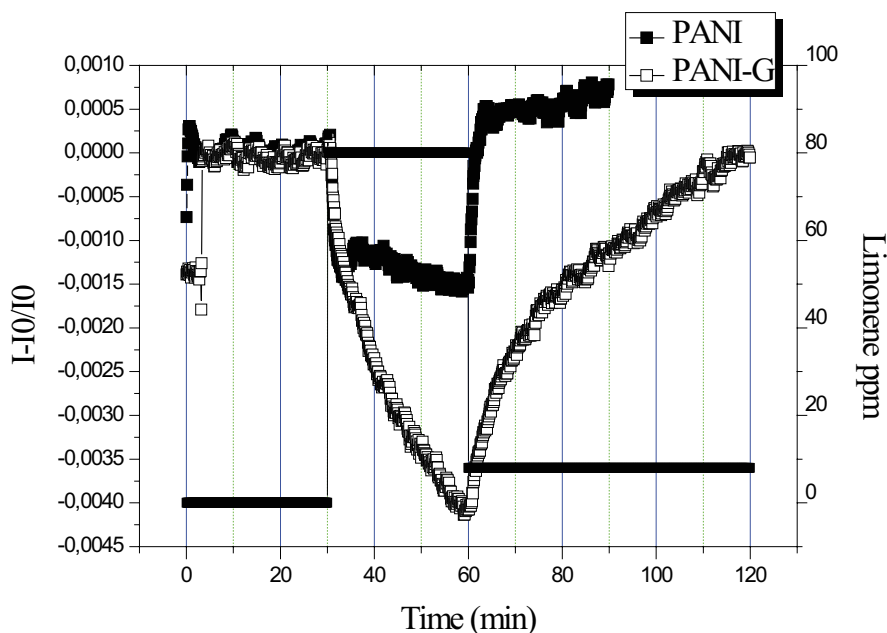
Fig. 35.3 PANI and PANI-G electrical responses to 30 min exposure in 80 ppm of limonene, at 30% relative humidity
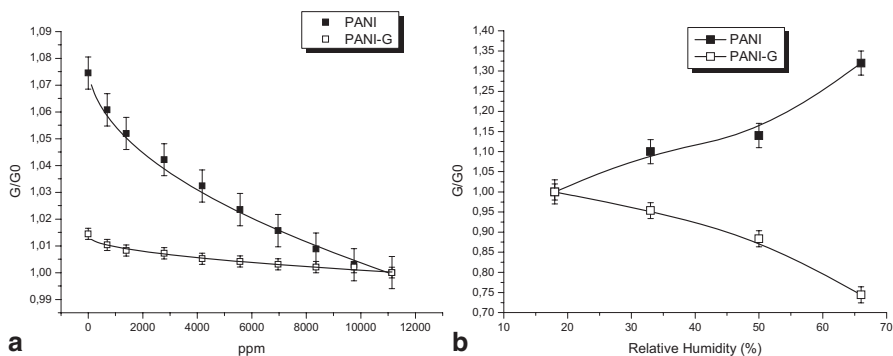
Fig. 35.4 a PANI and PANI-G conductance responses to different concentrations of ethanol, at 20% relative humidity. **b** PANI and PANI-G conductance response to various percentages of relative humidity

Conductance values of PANI sensors increase with increasing of relative humidity, while the opposite behavior is observed for PANI-G devices (Fig. 35.4b). These results show that graphene sheets deposited on pristine PANI change the response of device. In fact the nanosheets, though space separating, are however linked each other for the presence of polymer creating a net-like conductive path. Then graphene nanosheets have a functional role on the polymer behavior sensing

probably by the interlayer charge transport between the graphene basal plane and the π conjugated polymer chain [5].

35.4   Conclusions

Chemical sensors based on pristine PANI and PANI-G bilayers are successfully prepared by dip coating. Their role as VOCs sensors are investigated. The comparison between PANI and PANI-G based sensors reveals that the combination of graphene and PANI exhibit positive synergetic effects on detection of some VOCs produced by plants under stress as limonene, where PANI-G based sensors show a relative responses about four times higher.

These results suggest that graphene can be adopted as functional material for polymer sensing films and encourage to deepen the study of grapheme effects on electron transport in polymers.

References

1. R.M.C. Jansen, J.W. Hofstee, J. Wildt, F.W.A. Verstappen, H.J. Bouwmeester, M.A. Posthumus & E.J. van Henten, Health monitoring of plants by their emitted volatiles: trichome damage and cell membrane damage are detectable at greenhouse scale, Ann. App.l Biol. **154**, 441–452 (2009)
2. H. Bai and G. Shi, Gas Sensors Based on Conducting Polymers, Sensors **7**, 267–307 (2007)
3. K. H. An, S. Y. Jeong, H. R. Hwang, Y. H. Lee, Enhanced Sensitivity of a Gas Sensor Incorporating Single-Walled Carbon Nanotube-Polypyrrole Nanocomposites, Adv. Mater. **16**, 1005–1009 (2004)
4. M. Parmar, C. Balamurugan and D.-W. Lee, PANI and Graphene/PANI Nanocomposite Films – Comparative Toluene Gas Sensing Behavior, Sensors **13**, 16611–16624 (2013)
5. S. Biswas, L. T. Drzal, Multilayered Nanoarchitecture of Graphene Nanosheets and Polypyrrole Nanowires for High Performance Supercapacitor Electrodes, Chem. Mater. **22**, 5667–5671 (2010)

Chapter 36
Easy Recovery Method for Graphene-Based Chemi-Resistors

Filippo Fedi, Filiberto Ricciardella, Maria Lucia Miglietta, Tiziana Polichetti, Ettore Massera and Girolamo Di Francia

In this work we report on the development of a simple and fast method for re-generating exhaust graphene based chemi-resistors for NO_2 detection. A poisoning effect of the devices due to repeated exposure or to air exposure for >48 h results in an overall worsening of the sensing response. The presented method consists in the dipping of exhaust devices into ultrapure water at $100\,°C$ for 60 s. The device performances towards analyte are compared with those obtained after the restore by using the developed method.

36.1 Introduction

A bottleneck usually reported for the solid-state gas sensors operating at room temperature regards the slow and incomplete recovery to the initial conditions after the signal detection [1, 2]. Such behavior is mainly due to the interaction energy between sensitive materials and gases, as explained by the conventional transition state theory [3]. The goal of a recovery method is to remove polluting molecules from the sensitive layer in order to recreate a free interface, able to bind again target molecules. The usual approach is based on the increase of the analyte molecules mobility by providing a thermal energy sufficient for the desorption from the sensitive layer. Several solutions have been proposed in order to restore the devices at the initial conditions such as UV irradiation, thermal treatment and electric field applications [1, 4, 5].

F. Fedi (✉)
CNR-Institute for Composite and Biomedical Materials, Piazzale E. Fermi 1, 80055 Portici, NA, Italy
e-mail: f.fedi@hotmail.com

F. Ricciardella · M. L. Miglietta · T. Polichetti · E. Massera · G. Di Francia
ENEA UTTP-MDB Laboratory, R.C. Portici, Piazzale E. Fermi 1, 80055 Portici, NA, Italy

F. Ricciardella
Department of Physics, University of Naples 'Federico II', Via Cinthia, 80126 Naples, Italy

Herein, the method developed to restore the exhaust chemi-resistors used in the NO_2 detection relies on the capability to remove the adsorbates by a solvent, water being one of the most suitable [6]. The chemi-resistors performances towards 350 parts-per-billion (ppb) of NO_2 in wet N_2 environment (Relative Humidity = 50%, Temperature = 22 °C) were compared before and after the restore process. The effectiveness of the proposed method was also analyzed with respect to a thermal treatment at 130 °C in vacuum.

36.2   Materials and Method

The colloidal graphene suspension was prepared by Liquid Phase Exfoliation (LPE) dispersing the graphite flakes (Sigma-Aldrich, product N.332461) at 2.5 g/l in NMP (N-methyl-pyrrolidone, Sigma-Aldrich, product N.328634). A bath-sonication treatment at a low-power for 168 h was required to promote the graphite exfoliation [7, 8]. Films prepared from the colloidal suspension were characterized as reported in [7], confirming the presence of few-layers graphene.

Chemiresistor devices were fabricated by drop-casting few microliters of the colloidal dispersion onto alumina substrates with interdigitated Au electrodes [7].

36.2.1   Chemiresistors Testing

The chemi-resistors were mounted in a Gas Sensor Characterization System (GSCS, Kenosistec equipment) and tested under N_2 gas flow at atmospheric pressure, temperature and relative humidity RH set at 22 °C and 50%, respectively [9].

The standard exposure protocol consists of three steps: the baseline, the exposure window and the recovery phase, as described elsewhere [9].

The prepared devices were tested at three different times: as soon as prepared, after about 1 month, during which they were stored in air, and finally after two different restore processes: an usual approach which relies on the device annealing at 130 °C in vacuum for 120 min, a newly developed method which encompasses the dipping of exhaust devices into ultrapure water at 100 °C for 60 s followed by a drying step on the hot plate at 150 °C for 5 min.

36.3   Results and Discussion

The method proposed herein exploits the strong solubility of NO_2 in H_2O [6] to remove the adsorbed molecules, clearing sensitive sites for further adsorption processes and enhancing the sensing capability towards analyte.
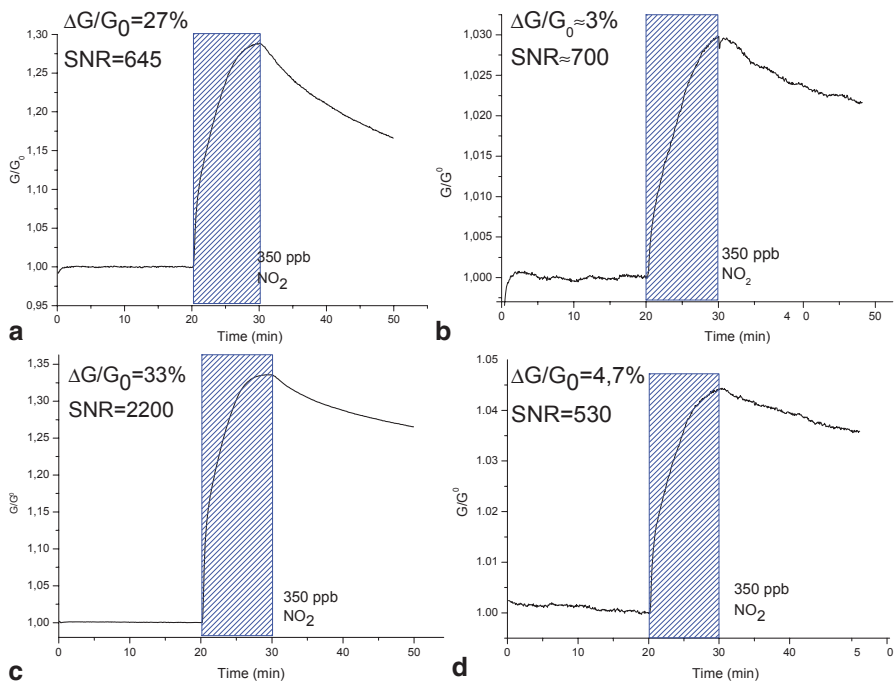
Fig. 36.1 Normalized electrical conductance behaviors for chemi-resistors towards 350 ppb of NO$_2$ in wet N$_2$ environment **a** as soon as prepared, **b** after 1 month, **c** after the restore by dipping method, and **d** after the restore by annealing method

Figure 36.1 reports the normalized conductance behavior of chemi-resistors exposed to NO$_2$, where G$_0$ represents the initial value soon before the introduction of the analyte (baseline) [7].

The effects of the restore approaches on the graphene-based devices can be clearly observed. After the first test, performed as soon as the solution was dropcasted onto the transducers (Fig. 36.1a), the chemi-resistor was left in air. When it was tested again after 1 month, it gave a conductance change dramatically lower than the previous one (3 % vs 27 %) towards the same analyte concentration, maybe due to the strong poisoning effect occurred in that period (Fig. 36.1b). The device was renewed by using the water based restore approach and then exposed again upon the same protocol. ΔG/G$_0$ in this case was not only dramatically increased with respect to that obtained by the exhaust device (33 % vs 3 %) but also even higher than the value provided by the freshly prepared device. The response of the device clearly evidences the effectiveness of the refresh method, confirming the water removing effects on the NO$_2$ molecules. In addition, the better performance compared to that shown by the freshly prepared device can be likely addresses to a cleaning of organic solvent residues deriving from the graphene film preparation.

In order to check the effectiveness of the restore method, a comparison with one of the usual recovery methods was carried out [1]. After leaving the device another month in air, a restoring in vacuum at 130 °C for 120 min was accomplished. The exposure test was performed and the behavior is reported in Fig. 36.1d. The conductance change is comparable with that given by the exhaust device (Fig. 36.1b), showing as the second recovery method affects the device less than the first one.

36.4 Conclusions

In summary, we have developed an easy method to recover the exhaust chemi-resistor after the exposure to NO_2 or after the storage in air. The new approach is basically based on the capability of the water to remove the adsorbed NO_2 molecules. The beneficial effects on the devices are confirmed by the fact that, after the restore, the chemi-resistor performances is comparable or even higher than those obtained when the device is freshly prepared.

References

1. F. Schedin, A. K. Geim, S. V. Morozov, E. H. Hill, P. Blake, M. I. Katsnelson, K. S. Novoselov. Detection of individual gas molecules adsorbed on graphene. Nature Mat. **6**, 652–655 (2007).
2. W. Yuan and G. Shi. Graphene-based gas sensors. J. Mater. Chem. A **1**, 10078–10091 (2013).
3. S. Peng, K. Cho, P. Qi, H. Dai. Ab initio study of CNT NO_2 gas sensor. Chem. Phys. Lett. **387**, 271–276 (2004).
4. R. Chen, N. R. Franklin, J. Kong, J. Cao, T. W. Tombler, Y. Zhang, H. Dai. Molecular photode-sorption from single-walled carbon nanotubes. Appl. Phys. Lett. **79**, 2258–2260 (2001).
5. M. P. Hyman and J. W. Medlin. Theoretical study of the adsorption and dissociation of oxygen on Pt (111) in the presence of homogeneous electric fields. J. Phys. Chem. B **109**, 6304–6310 (2005).
6. S.P. Tan and M. Piri. Modeling the Solubility of Nitrogen Dioxide in Water Using Perturbed-Chain Statistical Associating Fluid Theory. Industrial & Engineering Chemistry Research. **52**, 45, 16032–16043 (2013).
7. F. Fedi, F. Ricciardella, T. Polichetti, M. L. Miglietta, E. Massera, G. Di Francia. Exfoliation of graphite and dispersion of graphene in solutions of low boiling point solvents for use in gas sensors. Proc. of Sensors and Microsystems: AISEM 2013, Feb 5–7, Brescia (IT), 143–147 (2013).
8. U. Khan, A. O'Neill, M. Lotya, S. De, J.N. Coleman. High-Concentration Solvent Exfoliation of Graphene. Small **6**, 7, 864–871(2010).
9. E. Massera, M. L. Miglietta, T. Polichetti, F. Ricciardella, G. Di Francia. Reproducibility of the performances of graphene based gas sensitive chemiresistors. Proc. of Sensors and Microsystems: AISEM 2013, Feb 5–7, Brescia (IT), 121–125 (2013).

Chapter 37
Correlation Between Structural and Sensing Properties of Carbon Nanotube-Based Devices

S. Baldo, S. Scalese, V. Scuderi, L. Tripodi, A. La Magna, L. Romano, S. G. Leonardi and N. Donato

In this work we report the development of back-gated carbon nanotubes field-effect transistors (CNT-FET) and their electrical characterization for sensing applications. Different kinds of CNTs (MWCNTs produced by different techniques and SWCNT) have been used as channel layer in the FET structure and this allows the investigation of the role of defects on the sensing properties of the devices. In particular, defects due to the growth process or induced by chemical treatment on the CNT walls have been investigated.

37.1 Introduction

Carbon nanotubes (CNTs) have aroused great interest due to their exceptional properties like high current-carrying capacity, high thermal conductivity and reduced charge carrier scattering. The use of both individual nanotubes and CNT networks has been explored, depending on the specific applications [1].

In particular, due to very high surface-to-volume ratio, high electron mobility, great surface reactivity and high capability of gas adsorption, CNTs have been investigated as high-performance gas sensors [2].

Defects in CNTs play a crucial role on the electronic, optical and mechanical properties, and they can be wanted or unwanted, depending on the kind of application: for example, for sensor applications, defected nanotubes are considered more

S. Baldo (✉) · S. Scalese · V. Scuderi · L. Tripodi · A. La Magna
Istituto per la Microelettronica e Microsistemi, CNR, Catania, 95121 Catania, VIII Strada 5, Italy
e-mail: Salvatore.Baldo@imm.cnr.it

L. Romano
Dipartimento di Fisica ed Astronomia, Università degli Studi di Catania, Via S. Sofia, 95125 Catania, Italy

S. G. Leonardi · N. Donato
Dipartimento di Ingegneria Elettronica, Chimica e Ingegneria Industriale, Università degli Studi di Messina, Contrada di Dio, Salita Sperone 31, Messina, Italy

desirable than "perfect" CNTs [3, 4], due to a larger interaction of the adsorbing species with defective sites. The synthesis techniques and the chemical interactions, such as oxidation processes, introduce different point defects, in particular, adatoms, monovacancies, interstitial-vacancy defects, pentagon-heptagon pairs [5].

In this work, we report the development of back-gated CNT-FET devices and their electrical characterization for sensing applications. CNTs produced by different techniques have been used in order to investigate the role of defects (both native or generated by oxidation processes) on the sensing properties of the devices.

37.2   Experimental

Three kinds of nanotubes were used: (i) MWCNTs produced by arc discharge in liquid nitrogen and oxidized in H_2O_2 at 30 % for 2h in a ultrasonic bath; (ii) commercial MWCNTs (6–9 nm × 5 μm) purified by NaOH- and HCl-based treatment. (iii) commercial semiconducting SWCNTs (6, 5 chirality). The latter two kinds of CNTs were produced by Sigma-Aldrich CoMoCAT® catalytic CVD process.

The sensor preparation involves the use of a heavily doped silicon substrate (n++), used as back-gate, a silicon dioxide (SiO_2) layer (100 nm thickness) thermally grown on the substrate and, finally, Pt drain and source interdigitated electrodes defined by optical lithography. The CNTs were deposited on the interdigitated electrode region, using the electrophoretic deposition (EPD) method, as already described elsewhere [6, 7].

The devices were placed in T0-3 packages where they have been contacted by two 50 μm aluminum bond-wires.

A complete electrical characterization has been performed, both in air and in controlled gaseous environment (NO_2 and NH_3), using two source meters (SMU) in common source configuration. Both instruments, connected to a computer by GPIB interface, are totally controlled by a MATLAB graphical user interface (GUI) software.

37.3   Results and Discussion

In an EPD process, generally two electrodes are dipped in a solution containing the charged particles to be deposited. By applying a voltage to the electrodes a migration of the negative (positive) ions to the anode (cathode) takes place. Oxidative treatments of CNTs have two effects: removal of impurities and introduction of carboxylic groups on the surface of the tubes. The presence of carboxylic groups determines a negative surface charge on the CNTs dispersed in solution, allowing the deposition on the anode.

In Fig. 37.1 we report (a) a schematic of the device and (b) a SEM image showing a detail of the interdigitated electrodes where MWCNTs of type (i) (see Experimental section) have been deposited by EPD. The sample is formed by two sets of
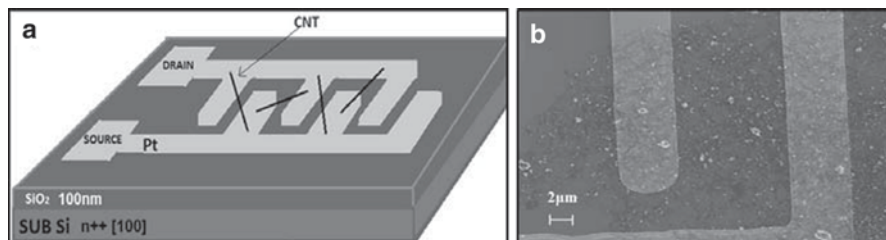
Fig. 37.1 Schematic **a** and SEM image of the strips **b** of the anode after EPD
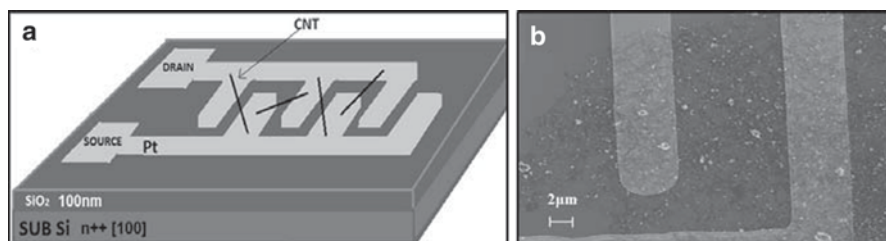
Fig. 37.2 CNT response to **a** NH$_3$ and **b** NO$_2$

ten Pt strips, connected to metallic pads. CNTs are deposited not only on the metallic strips but also between them.

All the samples, after deposition of the different kinds of CNTs, were characterized electrically, both in air and in controlled gaseous environment (NH$_3$ and NO$_2$). The I-V measurements, not reported here, show that devices with MWCNTs have a metallic behavior and no dependence on the gate voltage; on the contrary in the case of SWCNTs the device shows a non-linear I-V behavior and a dependence on the gate voltage. However, for all samples the conductance increases during the exposure to NO$_2$, and decreases after exposure to NH$_3$. This result can be explained by taking into account that NO$_2$ is an electro-attractor and thus induces an increase of the hole concentration in the CNT, while NH$_3$ has an electron pair that can be donated.

In Figs. 37.2a, b, we report the variations of the channel resistance, calculated with respect to a reference channel resistance value, observed for the different kinds of CNTs exposed to NH$_3$ and NO$_2$, respectively. In both cases SWCNTs show the highest sensitivity, probably due to a larger aspect ratio and, therefore, to a larger exposed area. In the case of MWCNTs the synthesis method and the corresponding structural differences play a role on the response towards the two gases under investigation.

The exposure to NH$_3$ induces a larger variation of the channel resistance in the MWCNTs treated with H$_2$O$_2$. Vice versa, during the exposure to NO$_2$, MWCNT

produced by CVD and treated in acid shows a larger sensitivity. These results depend on the different nature of the gaseous species interaction with CNT. In fact, the interaction between NH_3 molecules and CNT is favoured in the presence of–COOH groups on the CNT walls, and therefore MWCNTs of type (i) show a higher sensitivity. Vice versa, NO_2 molecules show a larger interaction with defects, like vacancies, and their adsorption is favoured on MWCNTs of type (ii), more defective than MWCNTs of type (i), as confirmed by Raman analysis, not reported here.

37.4   Conclusions

In this work we report the development and characterization of back-gated CNTs-based sensors. The sensors are developed starting from n++ Si substrate used as back-gate, where a SiO_2 layer was thermally grown. Finally, drain and source interdigitated Pt electrodes were defined by optical lithography. Different CNTs sensing networks were deposited on the electrodes by electrophoresis technique. Comparison between electrical and structural investigation indicates that–COOH groups are responsible for the interaction between the CNT and ammonia; vacancies, instead, are responsible of a better absorption of NO_2 on the CNT walls. Further studies have to be carried on in order to better understand the observed behaviors and to optimize the structural-sensing properties of such CNT-based devices.

References

1. O. Zhou, H. Shimoda, B. Gao, S. Oh, L. Flaming, G. Yue. Materials science of carbonnanotubes: Fabrication, integration, and properties of macroscopic structures of carbon nanotubes. Accounts Chem. Res. **35**, 1045–1053 (2002)
2. T. Zhang, S. Mubeen, N.V. Myung, M.A. Deshusses. Recent progress in carbon nanotube-based gas sensors. Nanotech. **19** 332001-4 (2008)
3. J.A. Robinson, E.S. Snow, Ş.C. Bǎldescu, T.L. Reinecke, F.K. Perkins. Role of Defects in Single-Walled Carbon Nanotube Chemical Sensors. Nano Lett. **6** 1747–1751 (2006).
4. N. Neophytou, S. Ahmed, G. Klimeck. Influence of vacancies on metallic nanotube transport properties. Appl Phys Lett **90** 182119-3 (2007)
5. V. Scuderi, C. Bongiorno, G. Faraci, S. Scalese. Effect of the liquid environment on the formation of carbon nanotubes and graphene layers by arcing processes. Carbon **50**, 2365–2369 (2012).
6. V. Scuderi, L. Tripodi, N. Piluso, C. Bongiorno, S. Di Franco, S. Scalese. Current-induced defect formation in multi-walled carbon nanotubes. J Nanopart. Reser. **16** (2) (2014)
7. V. Scuderi, A. La Magna, A. Pistone, N. Donato, G. Neri, S. Scalese. Use of the electric fields for the manipulation of MWCNTs. Carbon-Based Low Dimensional Materials – Proceedings of the 2nd CARBOMAT Workshop ISBN 978-88-124-5 86–89 (2012).

Chapter 38
NO$_x$ Sensors Based on YCoO$_3$ Perovskite

Tommaso Addabbo, Francesco Bertocci, Ada Fort, Marco Mugnaini, Luay Shahin, Valerio Vignoli, Santina Rocchi, Roberto Spinicci and Michele Gregorkiewitz

YCoO$_3$ perovskite powder was prepared by gel combustion method, which was extended to the preparation also of non-stoichiometric materials and samples containing Pt or Pd. This preparation route allows for increasing the surface area and hence the surface reactivity. The powders were characterized in terms of composition and microstructure using XRD and SEM-EDX; moreover, the powder surface properties were investigated by studying their adsorptive features towards oxygen and their redox behavior by means of TPD and TPR, respectively. Some sensors hosting sensing films obtained from the prepared powders were realized by a screen-printing technique. The response to NO$_x$ and to some interfering gases (CH$_4$, CO) were evaluated. Promising results were obtained at temperatures around 180 °C, where the sensitivities towards NO$_x$ result satisfactory high (2 %/ppm) and the responses result very fast, also in the recovery phase.

38.1 Introduction

Among toxic products of fossil fuel combustion nitrogen dioxide (NO$_2$) is the most hazardous with a TLV of 3 ppm. NO$_2$ also contributes to the formation of ground-level ozone, a major component of smog. NO is relatively less toxic with respect to NO$_2$. However, NO also causes acid rains, photochemical smog and production of ozone. For these reasons the detection and the emission control of nitrogen oxides are of the utmost importance to realize effective monitoring systems of environmental pollution.

V. Vignoli (✉) · T. Addabbo · F. Bertocci · A. Fort · M. Mugnaini · L. Shahin · S. Rocchi · R. Spinicci
Department of Information Engineering and Mathematics, University of Siena, Siena, Italy
e-mail: vignoli@dii.unisi.it

M. Gregorkiewitz
Department of Physical sciences, Earth and Environment, University of Siena, Siena, Italy

Currently, standard air pollution measurements are based on time-consuming and expensive analytical techniques. Gas sensors, and in particular semiconducting metal oxides chemiresistors, have been considered promising alternatives due to their low cost, high sensitivity, fast response. However, their performance including accuracy, selectivity, reliability, and low sensitivity to interfering gases must be further improved to meet the requirements of standard air pollution measurements.

The response of metal oxides sensors is due to an exchange of charge between the oxide surface and the gas phase which affects the electronic conduction, but many factors influence the overall sensor response, among which the geometry and the microstructure of the film, and the bulk and surface defect types. The film microstructure is important both because it determines the electric response to gas adsorption and because it determines the ratio surface-area/volume. Films obtained from nanostructured powders can ensure a very large value for this ratio; moreover the grains forming the film can more easily work close to the complete depletion causing the sensor resistance to be quickly modulated by the change of the gas concentration. Consequently, nanocrystalline and nanostructured materials are candidates for highly sensitive gas sensors in some specific applications [1]. In this paper the response to NO_x of seaweed nanostructured $YCoO_3$ materials obtained through gel combustion is studied.

38.2   Powder Preparation and Characterization

The material micro/nano-structure, that is fundamental in determining the gas sensing properties of a material, can be tuned selecting a suitable preparation route: in particular it is expected that a lower reaction temperature during material synthesis implies poor sintering and more opened or porous structure.

In this work seaweed nano-structured $YCoO_3$ powders were prepared by sol-gel combustion. A water solution of $Y(NO_3)_3 \cdot 6H_2O$ and $Co(NO_3)_2 \cdot 6H_2O$ is heated until it becomes a sol. The viscous sol is before transferred in a microwave oven, and brought to 380–400°C for 1 h, then is put in a furnace at 600°C increasing the temperature up to 900°C after 4 h. The gel bursts into flames after about 20 s. Figure 38.1 shows a SEM image of the obtained powders that are characterized by a surface area of 0.9 m^2/g and a mean crystallite size 300 nm.

As discussed in the introduction gas sensing properties of a chemoresitive material depend on its electronic properties, in particular by the introduction of bulk defects (acting as extrinsic levels) and surface defects. Based on previous results of the authors different types of semiconductors were obtained by preparing defective perovskite of the types $YCo_{1-x}O_3$ or $Y_{1-x}CoO_3$, selecting the salts concentrations in order to obtain an Y:Co atomic ratio of 1:(1−x) or (1−x):1, respectively, with x in the range 0.01–0.1. Moreover, $YCo_{1-x}Pd_xO_3$ powders were prepared by partly substituting Co with Pd, introduced, as usual, via Pd nitrate or acetate to the mixture of nitrates of Y and Co, with Co:Pd moles ratio in the range 0.03–0.1, before heating.

Fig. 38.1 SEM image of
prepared powders
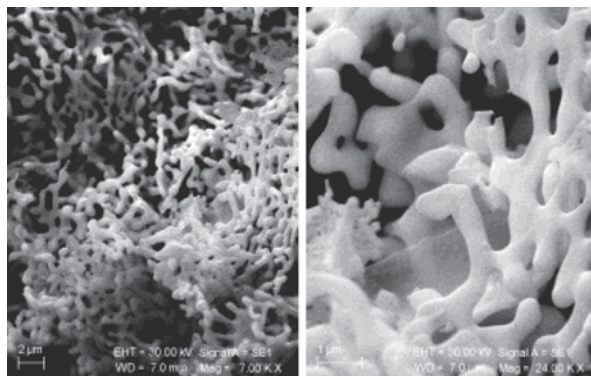
Finally surface impregnation with metallic Pd was obtained putting the prepared
powders in a solution with $Pd(NO_3)_2$ or $Pd(CH_3COO)_2$ in various percentages.

XRD analysis showed that all the prepared powders have a perovskitic structure.
Oxygen TPD and H_2 TPR were used to characterize the surface behavior. Both the
analyses showed that all the materials are absolutely stable up to 300°C, in fact even
in presence of a reducing gas (H_2) lattice oxygen (β-oxygen) is not involved in reac-
tions until 350°C. Moreover from TPD it can be seen that there is an evidence of a
small quantity of chemisorbed oxygen (α-oxygen) for all the samples with the only
exception of Pd doped powders.

These results point out that sensing must be based on a direct reaction of the tar-
get gas with the surface, and that adsorption sites for oxidizing gas are not saturated
by adsorbed oxygen.

38.3   Results and Discussion

Some sensors hosting sensing films obtained from the prepared powders were real-
ized by a screen-printing technique. The electric properties and responses to NO_x
and to some interfering gases (CH_4 and CO) were evaluated.

To test the sensors, a system specifically designed for the simultaneous char-
acterization of up to eight conductometric gas sensors was used. The system indi-
vidually controls the film temperatures or measures them with a resolution of about
0.1°C, and allows to accurately set the measurement conditions: gas concentrations
and flow, chamber temperature and humidity.

The characterization of the gas sensor response is obtained in terms of both
temperature and concentration dependence through a fully automatic measurement
campaign. The sensor response, r, is obtained with measurements under a constant
gas flow (200 mL/min) and is defined as $r = (R - R_0)/R_0$, where R_0 is the baseline
resistance value obtained at the considered temperature in a carrier gas, whereas R
is the value of the sensor resistance after a fixed duration exposure to the test gas

Table 38.1 Material response comparison. Data refer to the best temperature for each tested gas

	N_2+CO	N_2+NO	N_2+NO_2
$YCo_{0.91}Pd_{0.09}O_3$	270°C $T_{resp}=1.1$ min $T_{rec}=3.1$ min $r=12\%$ @500 ppm	180°C $T_{resp}=1$ min $T_{rec}=3.8$ min $r=-16\%$ @10 ppm	200°C $T_{resp}=0.6$ min $T_{rec}=2$ min $r=-14\%$ @10 ppm
$YCo_{0.9}O_3$	270°C $T_{resp}=1$ min $T_{rec}=4$ min $r=15\%$ @500 ppm	180°C $T_{resp}=0.8$ min $T_{rec}=1.5$ min $r=-18\%$ @10 ppm	180°C $T_{resp}=0.6$ min $T_{rec}=2$ min $r=-18\%$ @10 ppm
$YCoO_3$	280°C $T_{resp}=1$ min $T_{rec}=3$ min $r=7\%$ @500 ppm	210°C $T_{resp}=0.5$ min $T_{rec}=0.6$ min $r=-5\%$ @10 ppm	210°C $T_{resp}=0.5$ min $T_{rec}=0.9$ min $r=-5\%$ @10 ppm

mixture. All the $YCoO_3$ based sensors show p-type [2] semiconducting properties in every test environment within the temperature range of 100–380°C. For all the tested materials the response to NO_2 is given by the contribution of two different reactions: one implying the oxidation of the surface, which is faster and favored at low temperature, the other one implying the reduction of the surface, which is slower and favored at higher temperature. This last gives a weaker effect. A similar behavior is observed for NO. All sensors show satisfactory NO_2 sensitivity; the best results are found for Co defective powders: sensitivity 1.8%/ppm @10 ppm, very good stability, and fast response/recovery ($T_{resp}=0.6$ min; $T_{rec}=2$ min @ 180°C and @10 ppm). Moreover, low working temperatures (160–180°C) are required to grant these performance. The prepared sensors show no appreciable response to CH_4 with concentrations up to 10,000 ppm, whereas they have a very low response to CO for temperatures below 200°C. The performance of the different materials are shown in Table 38.1. The best performance in terms of NO_x sensitivity are granted by the Co defective materials which are characterized also by a large speed and a very low cross sensitivity to water vapor [3] (Fig. 38.2).

38.4   Conclusions

The good performance in terms of stability, sensitivity, speed and immunity to some interfering gases of $YCoO_3$ perovskite powders prepared by gel combustion is shown. The proposed material can be tuned to the target gas with the introduction of defects and or dopants.
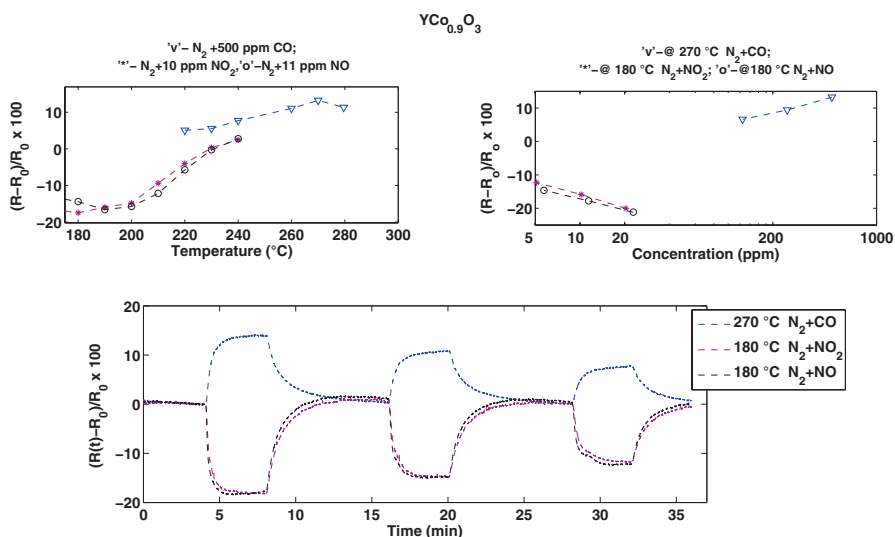
Fig. 38.2 Co defective materials: response in different test conditions. Experiments have been conducted with CO pulses of 1000, 500 and 250 ppm respectively. For NO2 with pulses of 24, 10 and 6 ppm while for NO with 24, 11 and 6 ppm.

References

1. A. Fort, M. Mugnaini, S. Rocchi, V. Vignoli, E. Comini, G. Faglia, A. Ponzoni. Metal-oxide nanowire sensors for CO detection: Characterization and modeling. Sens. and Actuat. B: Chem. **148** (1), 283–291 (2010)
2. A. Fort, T. Addabbo, V. Vignoli, F. Bertocci, M. Mugnaini, A. Atrei, M. Gregorkiewit. Gas-sensing properties and modeling of silver doped potassium hollandite. Sens. and Actuat. B: Chem., **194**, 427–439 (2014)
3. A. Fort, M. Mugnaini, I. Pasquini, S. Rocchi, V. Vignoli. Modeling of the influence of H2O on metal oxide sensor responses to CO. Sens. and Actuat. B: Chem. **159** (1), 82–91 (2011)

Chapter 39
Tinynose, an Auxiliary Smart Gas Sensor for RFID Tag in Vegetables Ripening Monitoring During Refrigerated Cargo Transport

Fabrizio Formisano, Ettore Massera, Saverio De Vito, Antonio Buonanno, Girolamo Di Francia and Paola Delli Veneri

Current state of the art's real time monitoring of fresh produce, provides only temperature and humidity information [1–3]. The idea is to develop new sensors and transport service assisted by ICT platform to monitor fresh produce quality. The technology will be based on radio frequency (RF) wireless network, and will provide real-time and in-site data-logging, enabling active management of food products in storage and transit. The RF sensor network design, allows an auxiliary sensor node to be "plugged in". In this contribution we present the commercial platform developed starting from o fork of open hardware on which we assemble an array of commercial sensors in an "open air" configuration. We developed for this Embedded Gas Sensor System Device (Tinynose) two set-up: the "Development set-up" that uses a star wireless network infrastructure to store all raw sensor output and associated measurement error in a server DB to define parameters in ripening mathematical model and the "TAG set-up" that performs ripening evaluation in ICT in-site platform.

39.1 Introduction and Method

The overall objective of the project is to improve the competitiveness of the national fruit and vegetable sector obtained by the exploitation of the goods transported, the maximization of customer satisfaction and environmental safeguard.

It intends to realize a prototype of innovative logistics platform, based on the use of ICT for fruit and vegetable national production of I and IV classification. Our research activity is to create innovative systems for evaluation and monitoring of product quality. In particular prototype sensor devices "TinyNose" able to evaluate

F. Formisano (✉) · E. Massera · S. De Vito · A. Buonanno · G. Di Francia · P. Delli Veneri
ENEA (Italian National Agency for New Technologies, Energy and Sustainable Economic Development), UTTP-MDB Laboratory, Portici Research Center, P.le E. Fermi 1, 80055, Portici, NA, Italy
e-mail: fabrizio.formisano@enea.it

a quality indicator (ripening parameter) of the vegetables product during transport, will be realized.

The RC ENEA is involved in several projects dealing with embedded technologies for gas sensing. We take into account all the steps starting from the investigation and test of the sensing materials, core of a chemical gas sensor, the calibration process dealing with the electrical characterization in controlled atmosphere up to the installation of the gas sensors on embedded technologies designed for the specific application and its break-in. Also in this scenario the methodology progresses from sensor film and transducer design, conditioning electronic and incorporation into the wireless network. The final stage of data analysis and algorithm provides a proof of concept for the world's first integrated wireless sensor system that directly detects changes in vegetables ripening.

39.1.1 Method

Main goal is to achieve prototype of sensor devices "TinyNose" able to evaluate a quality indicator (ripening parameter) of the vegetables product during transport and interact with monitoring RFID infrastructure.

For this purpose we provide a solution (TinyNose—TAG setup) that has the capacity to interact, through a USART bus, with a TAG-RFID inserted in acquisition RF network designed for refrigerated cargo transport. It implements a power management strategy to put the device in a low consumption state when it is not in use and it allows it to wake up only to acquire and process data (at periodic time according to transport characteristics) and to transmit, on request, the index correlated to the vegetable ripening. This index is a time-integral function depending on the vegetables transport parameters and sensors output (temperature, humidity and ethylene level). Possibility to modify many operating parameters and logging function, gives to the device remarkable ability to adapt to many operating scenarios, with the possibility of having available raw data for post travel depth analysis.

39.2 Experimental

In order to achieve the project goals it was necessary to develop TinyNose in a first version to study sensors behavior in a laboratory environment that simulates the final application scenario. In particular it will allow to define parameters value in ripening mathematical model.

We developed embedded Gas Sensor System Device (Tinynose) in "Development set-up" version. It is based on commercial hardware products by ®Libelium Comunicaciones Distribuidas (open hardware forked). We have used a star wireless network infrastructure, based on 802.14.4 protocol, to send and store all raw sensor output and associated measurement error in a open source server DB. Firmware that

Fig. 39.1 Metal oxide sensors installed on the GSCS test flange
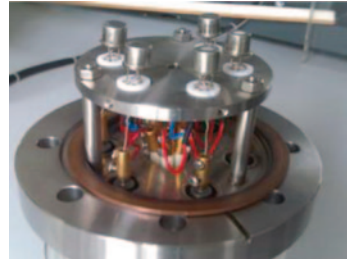
we have developed for this purpose, gives the possibility to easily modify the main parameters to control sensor operating mode and their power management strategy, signal conditioning output, data acquisition mode and network characteristics. It is possible also to perform firmware upgrades of individual Tinynose through the same wireless network (Firmware OnTheAir).

For the Solid State Gas Sensors choice, The scientific literature identifies ethylene as gas analyte reference in almost all of the processes of ripening of fruit and vegetables. Concentrations involved in these processes are extremely low, not exceeding 100 ppm with typical values of tens ppm. Choice of sensors suitable for the purpose was to ensure: high gas sensitivity, suitability for driving through portable electronics. We choose chemiresistive MOX sensors. For this aim, we have purchased and tested in ethylene the following classes of sensors of Figaro: TGS2600, TGS2620, TGS2602. Tests were performed with the system characterization sensors in a controlled environment (GSCS) (Fig. 39.1) at two temperatures and two rates of humidity level to get information on the interference of these two parameters on the responses to ethylene. The tests were repeated to evaluate the repeatability of the responses. Sensor sensitivity curves were measured in the range of 0–100 ppm ethylene.

39.3   Results

In Fig. 39.2 is shown the sensitivity curves to ethylene for the Figaro chemiresistors in controlled environment (constant relative humidity and temperature: RH=50%; T=20 °C). These sensors show a capability to detect ethylene up to few ppm.

TinyNose/development architecture has been tested in controlled environment. Devices (up to three) are placed in a closed box of steel (15 L) and exposed to controlled concentration of ethylene in constant temperature (8 °C) and humidity (30 % RH). Taking advantage of the implemented opportunity to easily modify the main operating parameters, has been identified their correct mix relating to sensor operating mode and their power management strategy, signal conditioning output, data acquisition mode and network characteristics.

Sensor outputs are transmitted to the gateway and stored in the mysql database table. Data is read through sql commands and plotted as shown in Fig 39.3
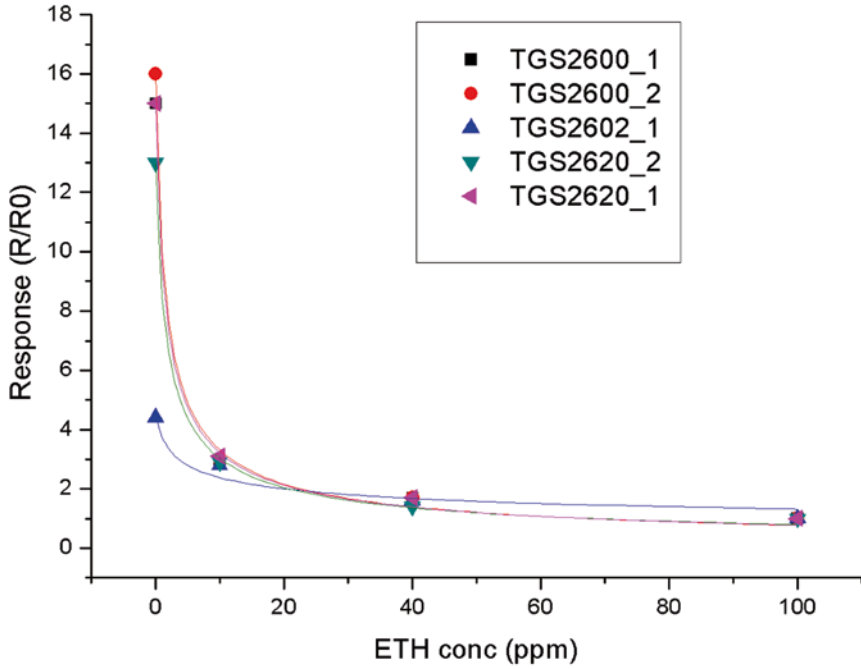
Fig. 39.2 Electrical Resistance sensibility curve to ethylene for Figaro sensors (at constant relative humidity and temperature: RH=50%; T=20 °C). R0 is sensor resistance at 100 ppm of ethylene
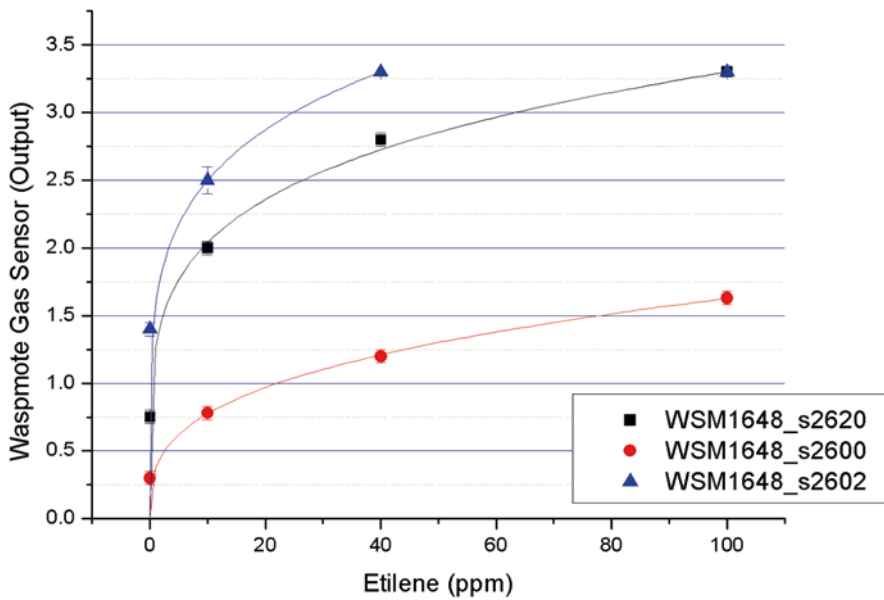
Fig. 39.3 Sensor output sensibility curve to ethylene for gas sensors installed on a single Tinynose (RH=50%; T=20 °C)

Also in this graph gas sensors installed on Tinynose confirm the capability to detect ethylene at few ppm.

39.4   Conclusions

The work presented show an approach to realize an embedded Gas Sensor System Device with ability to communicate to an RFID active sensor an index value correlated to the vegetables ripening. We realize a first prototype, tested in controlled environment. Works in progress are on:

- The study of correlation between sensors output and ripening evaluation simulating a refrigerated Cargo transport
- Completion of TinyNose-TagRFID
- Algorithm and mathematical model optimization
- Hardware and firmware optimization
- Final tests in operating scenario

References

1. Regulation EC/178 /2002, http://ec.europa.eu/food/food/foodlaw/principles/index_en.htm, 2013
2. RFID-F2F (RFID from Farm to Fork) project web page, http://www.rfid-f2f.eu/, 2013
3. I. Cuiñas, L. Catarinucci, and M. Trebar, RFID from farm to fork: traceability along the complete food chain, Proceedings of the Progress in Electromagnetics Research Symposium (PIERS '11) Marrakesh, pp. 1370–1374, March 2011

Chapter 40
Nanowire Technology to Asses the Bacterial Presence in Water and other Food Stuff

Veronica Sberveglieri, Estefanía Núñez Carmona and Andrea Pulvirenti

It has been broadly documented the presence of bacteria, yeast and mold in food processing like fermentations, ripening and also spoiling. The early detection of the contamination is critical to preserve the consumer's health and to avoid economic losses for the industry. The aim of this work was the establish a new fouling based on the cooperation between the use of a novel EN and classical techniques, like GC-MS coupled with classical microbiology, for the detection of bacterial presence in water and other foodstuff.

40.1 Introduction

The set of microorganisms present in a given food matrix may change greatly depending on the kind of the product, the stage of the processing food chain, and the storage time that this matrix is analyzed. The simplest food matrix that can be considered is water by itself or being part of other food matrix. It also important to bear in mind that water is the most important vector on microbiological contamination carried out by coliforms. On the other hand the group of Lactic Acid Bacteria (LAB) is one of the most important group of food processing microorganisms. LAB are involved in so many food matrix transformation both animal and vegetal origin, but at the same time are one of the most important spoilage microorganisms in food industry. This study proposes a solution based on physical (EN), chemical (GC-MS with SPME)

V. Sberveglieri (✉) · E. N. Carmona · A. Pulvirenti
Department of Life Sciences, University of Modena and Reggio Emilia, Via Amendola 2, 42014 Reggio Emilia, Italy
e-mail: veronica.sberveglieri@unimore.it

V. Sberveglieri · A. Pulvirenti
CNR-INO SENSOR lab, Via Branze 45, 25123 Brescia, Italy

E. N. Carmona
CNR-IBF, Via Ugo la Malfa 153, 90146 Palermo, Italy

and microbiological method for the rapid detection and identification of microorganisms in water and other foodstuff [1]. All the microbiological species produce a big amount of metabolites most of them volatiles, organic or/and inorganic compounds. The assay made by EN, based in the analysis of the head space, is able to reveal the present of this metabolites, given a different response for different kind of samples, and in some cases, individualizing species of the same group of microorganisms [2].

40.2 Materials and Methods

40.2.1 Samples Preparation

In this study an aliquot of water from WC and a well was dispersed in 2 Petri dishes with Violet Red Bile Agar (VRBA) (OXOID) and incubate at 30 °c during 24 h. Once the single colonies were visible one of each kind were picked and inoculated in liquid tubes of Brilliant Green Bile medium (OXOID) during 24 h at the optimal growth temperature for coliforms 35 °c. After 24 h the turbidity of the tubes was evident, and it was adjusted (diluted, using sterile Brilliant Green Bile medium) until the turbidity was the same as the number 3 of the McFarland series standards. To perform the samples of EN and GC-MS the used procedure was the same. Sterilized chromatographic vials containing 2 ml of Brilliant Green Bile media were inoculated with 100 µl of the number 3 of McFarland standards of the cultures prepared before. Once inoculated all the vials were cover with an aluminum crimp and a coated PTFE/silicon septum and crimped. The controls where performed adding 100 µl of sterile Brilliant Green Bile media.

On the other hand LAB were isolated from the chicken meat, were LAB are spoilers, in Man, Rogosa and Sharpe Agar medium (MRSA) (OXOID) and incubated during 48 h at 30 °c. Then the 48 h three random colonies were picked up and inoculated separately in a MRS liquid tube in order to obtain liquid cultures. The three typologies of tubes were incubated for 48 h at 30 °c. The samples for EN and GC-MS analysis were performed using the same procedure. Sterilized chromatographic vials (20 ml) containing 2 ml of MRSA media were inoculated separately with 100 µl of the number 3 of McFarland standards of the three kinds of liquid cultures prepared before. Once inoculated all the vials were cover with an aluminum crimp, a coated PTFE/silicon septum and crimped. The controls where performed just adding 100 µl of sterile MRSA medium to remain in the same range of volume as in the case of the inoculated one to maintain the uniformity in the preparation of the samples.

40.2.2 EN and GC-MS with SPME

The EN used in this work is EOS835 (SACMI IMOLA scarl, Imola, Italy) it's equipped with an array of six MOX gas sensors. Therefore this is a commercial device the sensor array has been modified in collaboration with INO Sensor lab,

Fig. 40.1 PCA score plot of
the coliforms analysis by EN
in the first 24 h
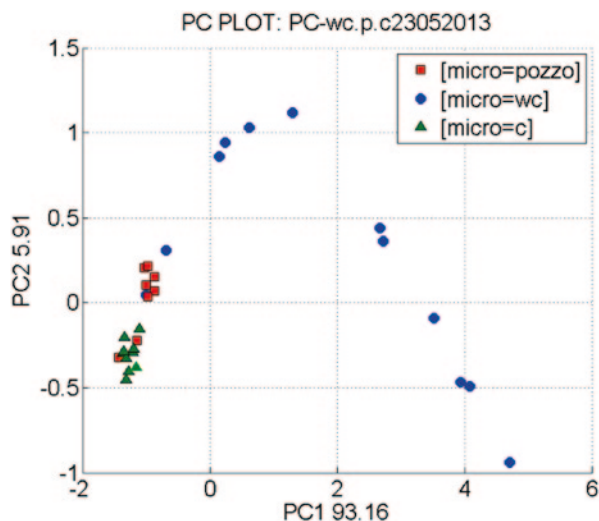
Brescia, Italy. Four of these sensors were prepared with the RGTO thin film tech-
nology [3], and the other two were constructed with nanowire technology [4]. Sin-
gle crystal nanostructures of tin oxides have been fabricated and characterized as
sensing materials to be implemented in an electronic nose. These nanowires exhibit
remarkable crystalline quality and a very high length-to-width ratio, resulting in
enhanced sensing performances as well as long-term stability for sustained opera-
tion [4]. Regarding to the analysis of EN, the vials were placed in a randomized
mode into the HT200 carousel. Each vial was incubated at 40 °C for 10 min into
the HT200 oven, by shaking it during all the incubation. The data analysis was run
by means of Principal Component Analysis (PCA), operated with the Nose Pattern
Editor software (SACMI Imola Scarl, Imola, Italy) [5].

It was selected GC-MS with SPME technique in order to characterize the volatile
profile of the microorganisms and proceed with the analysis in a similar way as EN.
The vials were incubated in an oven thermostatically regulated at 40 °c for 15 min
due to create the headspace equilibrium. In order to extract the volatile compound
of the samples was used a DVB/Carboxen/PDMS stable flex (50/30 μm) (Supelco
Co.Bellefonte, PA, USA) SPME fiber and a DB-WAX capillary column [6].

40.3   Results and Discussion

In the case of PCA score plot from the EN analysis of water from the well and wc
(Fig. 40.1) can be observed a two separate cluster very interesting results came
out from the isolated of the w.c., because it shows a kind of curve from bacterial
growth. The analysis of the sample's headspace shows that, acetone, 2-fluoroproen,
3-methyl butanal and 4-methyl thiazole characterize the organic volatile profile of
this microorganisms.
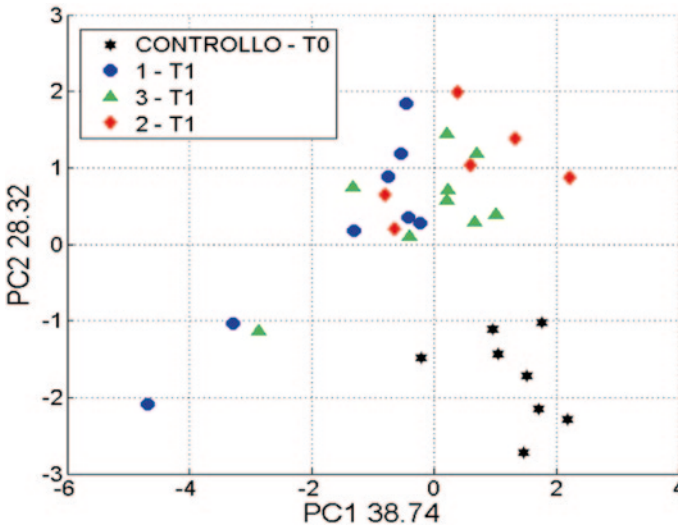
Fig. 40.2 PCA score plot of the LAB analysis by EN in the first 24 h

In the Fig. 40.2 are showed the result from the PCA analysis of LAB. It can be separate two principal clusters. One refer to the control (black stars), second one is formed for typologies, samples belonging to different colonies. The formation of cluster like this one can be due to the similarity of the colonies because of the same precedence of the samples, all them indigenous contaminants of the chicken meat. The obtained result of the GC-MS analysis shows that imidazolidone and carbonil sulfide were the compounds that characterize the head-space of this samples.

40.4   Conclusions

In conclusion is fear to say that the achieved results shows the EN very effective and fast tool for monitoring, of microbiological spoilage and food quality control and strongly recommend the use this kind of sensing technology like a quality control tool in industry laboratories [6].

References

1. M. Falasconi, I. Concina, E. Gobbi, V. Sberveglieri, A. Pulvirenti, and G. Sberveglieri, Electronic Nose for Microbiological Quality Control of Food Products. Int. J. Electrochem. A **2012**, 1–12 (2012).
2. I. Concina, M. Falasconi, V. Sberveglieri, Electronic noses as flexible tools to assess food quality and safety: Should we trust them? IEEE Sens. J. A **12** (11), 3232–3237 (2012).
3. G. Sberveglieri, G. Faglia, S. Groppelli, P. Nelli, A. Camanzi, A new technique for growing large surface-area SnO2 thin-film (RGTO technique). Semicond. Sci. Technol. A **5** (12) 1231–1233 (1990).
4. G. Sberveglieri, I. Concina, E. Comini, M. Falasconi, M. Ferroni, and V. Sberveglieri. Synthesis and integration of tin oxide nanowires into an electronic nose. Vacuum. A **86 (**5), 532–535 (2012).
5. E. Núñez Carmona, V. Sberveglieri and A. Pulvirenti. Detection of Microorganisms in Water and different Food Matrix by Electronic Nose. Proc. of the 7th International Conference on Sensing Technology ICST2013, Dec. 3–5, 2013, Wellington (NZ), 703–707 (2013).
6. V. Sberveglieri, E. Núñez Carmona, E. Comini, A. Ponzoni, D. Zappa, O. Pirrotta, A. Pulvirenti. A novel electronic nose as adaptable device to judge microbiological quality and safety in foodstuff. BioMed Res Int. A **2014**, 1–6 (2014).

Chapter 41
Characterization of Artificial Sweeteners Using Raman Spectroscopy

L. Ciaccheri, A.G. Mignani, A.A. Mencaglia and R. Petruccelli

Raman spectroscopy excited at 1064 nm was used to analyze a selection of artificial sweeteners that are commonly used in low-calorie diets. Aqueous solutions with different sweetener concentrations in the 5–30 % w/w range were analyzed, and a multivariate data processing of spectroscopic data was used to building a classification map. The map showed an excellent clustering according to sweetener type. These results indicate excellent potentials of Raman spectroscopy for measuring food quality indicators.

41.1 Artificial Sweeteners—The Modern Sugar Substitutes

Nowadays, artificial sweeteners contribute to consumer choice, since a growing number of people choose finished products that are prepared with these sugar substitutes or use them in food and drinks. Their sweetening capacity is hundreds of times higher than that of sugar, and the very little energy content, a few kcal per gram, can be regarded as negligible. Consequently, many consumers increasingly prefer artificial sweeteners to natural sugars for weight maintenance or reduction, dietary needs, or for a better oral health [1].

Optical spectroscopy is currently emerging as a modern and "green" analytical technique for intact food analyses, thanks to the non-destructive nature of light measurements which enable rapid checks without making use of reagents or chemical treatments, thus avoiding the problem of waste disposal [2]. While absorption and fluorescence spectra show broad peaks resulting from the convolution of the many

A. G. Mignani (✉) · L. Ciaccheri · A. A. Mencaglia
CNR—Istituto di Fisica Applicata "Nello Carrara", Sesto Fiorentino, FI, Italy
e-mail: a.g.mignani@ifac.cnr.it

R. Petruccelli
CNR-Istituto per la Valorizzazione del Legno e delle Specie Arboree, Sesto Fiorentino, FI, Italy

Table 41.1 The collection of table-top sweeteners analyzed

Brand (code)	"Soft" sweetener	"Hard sweetener"	Other factors
Tropicana slim (TS)	Sorbitol	Aspartame	Corn powder
Splenda (SP)	Dextrose	Sucralose	Maltodextrine
Stevia Misura (SM)	Erythritol	Rebaudioside-A	Cellulose powder
Sweet'n low (SL)	Dextrose	Sodium saccharine	Tartar cream, Ca_2O_4Si
Caless (CL)	Erythritol, Maltitol	Sucralose	Ca_2O_4Si

overlapping bands, which are poorly resolved for the purposes of multicomponent analysis, Raman spectra show sharp bands that identify the molecular composition, and can immediately lead to the detection of multiple components and their quantification [3].

The objective of this paper is to assess how Raman spectroscopy can be used for the recognition of different types of artificial sweeteners. Previous papers presented the use of Raman spectroscopy for determining the composition of artificial sweeteners [4], and for quantifying aspartame [5, 6]. In this paper, five popular table-top artificial sweeteners were selected, and Raman measurements were carried out on aqueous solutions with different sweetener concentrations. Principal Component Analysis was used for the dimensionality reduction and multivariate processing of spectroscopic data. This simple and straightforward data processing made it possible to build a classification map that showed an excellent clustering according to sweetener type.

41.2 The Table-Top Sweeteners Analyzed

Table 41.1 summarizes the table-top sweeteners considered in this study, the main ingredients, and the codes given for their rapid identification. Tropicana Slim was bought in Indonesia, Splenda and Sweet'n Low in USA, and Caless in China. They are made of popular "hard" sweeteners, such as aspartame, sucralose, and sodium saccharin, mixed with other "soft" sweeteners, such as erythritol, sorbitol and dextrose. Other additives which are used as stabilizers are typically based on corn, cellulose, and calcium silicate. Another sweetener made of the leaves of the Stevia plant was included, which was bought in Italy: it is popular in Central and South America, and was approved in Europe in November 2011, thus becoming a modern and increasingly used 0-calorie sweetener.

Aqueous solutions with sweetener concentration of 5%, 10%, 20%, and 30% w/w were prepared.
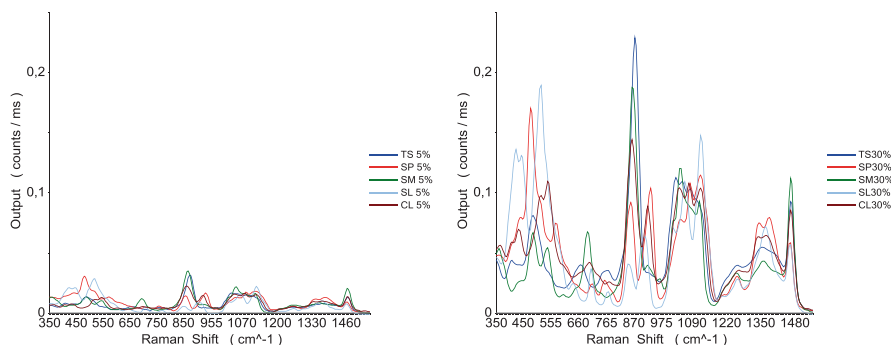
Fig. 41.1 Raman spectra of all sweetener solutions at minimum (*left*) and maximum (*right*) concentrations

41.3 Experimental Setup and Results

The instrument for Raman spectroscopy used in this experiment provides laser excitation at $\lambda = 1064$ nm, which is not the most popular wavelength for Raman experiments, since the Raman signal is inversely proportional to the fourth power of laser wavelength. However, this long excitation wavelength makes it possible to avoid fluorescence effects that are common in sweeteners and could overcome the weak Raman signal.

The detection unit is based on a dispersive scheme that provides a more compact unit with respect to Fourier-Transform configurations frequently used in Raman spectroscopy. Three spectrometers make it possible to operate over a wide wavenumber range (300–3200 cm^{-1}), and a thermoelectric cooled InGaAs array that is set at $-55\,^\circ$C serves as detector. A resolution of 4 cm^{-1} is obtained. An optical fiber is used for bringing the laser light to a microoptic unit. This unit is a compact device that makes it possible to optimize sample illumination and backscattered light collection, and also provides light guiding to the slit of the spectrometers. Liquid samples are analyzed within a 4 ml vial. The vial is inserted in a suitable holder which is butt-coupled to the microoptic unit. The instrument is suitable also for solid sample analyses using a fiber optic probe connected to the microoptic unit.

The entire instrument is portable. It is interfaced to a laptop PC which includes software for the management of hardware options and for spectra acquisition, display, and first processing [7].

Figure 41.1 shows the results of Raman spectroscopy of all sweeteners with solution concentration of 5% w/w (left) and 30% w/w (right). The spectra are displayed in the most significant band, which is 350–1500 cm^{-1}. All spectra underwent a baseline correction, which was estimated in the 2400–2600 cm^{-1} range, where samples do not scatter. The Raman spectrum of water was then subtracted from all spectra.

The Principal Component Analysis (PCA), which is a popular method for data dimensionality reduction and object classification purposes [8], was used for
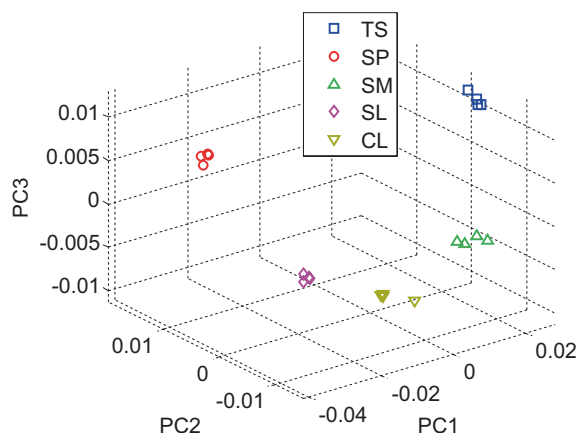
Fig. 41.2 3D plot of PCA scores clustering the sweeteners according to type

distinguishing the different types of sweeteners. PCA was applied on Raman spectra previously normalized to unit area within the 300–1600 cm^{-1} band, in order to remove the influence of concentration. Figure 41.2 shows the 3D plot of PCA scores. This classification map shows that the different sweeteners are sharply clustered according to type:

- PC1 splits the sweeteners containing erythritol or sorbitol (TS, SM, CL) from those containing dextrose (SP, SL);
- PC2 splits SP from SL: both contain dextrose, but the former makes use of sucralose while the latter saccharine; they also use different stabilizing agents;
- PC3 splits TS (sorbitol + aspartame) from SM (erythritol + stevia) and CL (erythritol + maltitol + sucralose).

41.4 Perspectives

Raman spectroscopy has demonstrated good potentials for distinguishing different types of table-top artificial sweeteners. This study is only the first step of a wider experiment, which will consider other artificial sweeteners worldwide, as well as mixtures of natural and artificial sweeteners.

References

1. International Sweeteners Association, http://www.sweeteners.org
2. S. Armenta, S. Garrigues, M. de la Guardia. Green Analytical Chemistry. Trends Anal. Chem., **27**, 497–511 (2008).
3. J. Moros, S. Garrigues, M. de la Guardia. Vibrational spectroscopy provides a green tool for multi-component analysis. Trends Anal. Chem., **29**, 578–591 (2010).
4. S. Armenta, S. Garrigues, M. de la Guardia. Sweeteners determination in table top formulations using FT-Raman spectrometry and chemometric analysis. Anal. Chim. Acta, **521**, 149–155 (2004).
5. S. Mazurek, R. Szostak. Quantification of aspartame in commercial sweeteners by FT-Raman spectroscopy. Food Chem., **125**, 1051–1057 (2011).
6. N. Peica. Identification and characterization of the E951 artificial food sweetener by vibrational spectroscopy and theoretical modelling. J. Raman Spec., **40**, 2144–2154 (2009).
7. Bayspec Inc. San Jose CA, USA (www.bayspec.com), model BRAM –1064–HR.
8. J.E. Jackson. A User's Guide to Principal Components (J. Wiley & Sons Inc., Hoboken NJ USA, 2003).

Chapter 42
Advanced Pattern Recognition Techniques for Fast and Reliable E-nose Response Analysis in NDTs Scenarios

S. De Vito, M. Salvato, E. Massera, M. Miglietta, G. Fattoruso and G. Di Francia

Non Destructive Tests (NDT) technologies have strong requirements in terms of fast response and reliability, these constraints are particularly stressed in aerospace industry, for safety and efficiency reasons. Composite panels bonding, essential to green aircraft concept, is still lacking a validated NDT technique that can guarantee the bond quality. E-noses appear to be a promising choice but they have to be adapted to the surface analysis task, furthermore they may require a significant amount of time to acquire a complete response pattern slowing the testing of large panels. In this paper, we present the results obtained by combining real time classifiers response on an adapted e-nose platform to obtain a rapid response while keeping the possibility to maximize accuracy awaiting for the end of the measurement cycle. A reject option is casted on the base of combined perceived reliability to nullify high safety costs false negatives while keeping low the false positive rate.

42.1 Motivation

In aerospace industry, the use of CFRP, namely Carbon Fiber Reinforced Polymers structures, induces considerable savings of fuel consumption and CO_2 emissions. However, the reliability of adhesive bonds strongly depends on the cleanliness state of the adherent surfaces before bonding take place. Contamination has actually been found to severely hamper mechanical properties of composite adhesive bonding. Indeed, the surface contamination significantly affect the mechanical strength of the CFRP panels adhesive bonds limiting adhesion performance either by physical screening or by chemical action on the surfaces. As an example, contamination by Skydrol500-B, a common fire resistant hydraulic fluid, can cause a reduction in the mode-1 fracture toughness of CFRP up to 25 % [2].

S. De Vito (✉) · M. Salvato · E. Massera · M. Miglietta · G. Fattoruso · G. Di Francia
ENEA (Italian New Technologies, Energy and Sustainable economic development Agency),
Portici Research Center, Portici, Italy
e-mail: saverio.devito@enea.it

NDTs are then needed for a fast and reliable assessment of the CFRP surface contamination in order to guarantee an high quality of the resulting adhesive bonding. Within this framework, a system built up by an electronic nose (e-nose) technologies together with suitable pattern recognition (PARC) techniques seems particularly promising to realize a NDT system allowing a "suitability for bonding" analysis.

Such a low cost tool with its relative responsiveness and potential portability, could be adapted to work in assembly or maintenance scenarios for surface contaminants detection. Notice that system quantification capability would also be particularly relevant to understand if the panel under analysis could qualify for adhesive bonding, should undergo a further cleaning process or just be discarded.

Surface analysis in an open environment is itself rarely addressed by artificial olfaction researchers. An adaptation process should be applied to these devices so to become able to obtain satisfactorily results in this unusual scenario. Anyway, e-nose should be able to rapidly check large CFRP surfaces for the presence of peculiar contaminants. Reliability, rapid response, portability, capability to deal with harsh contaminants (poisoning resilience) are extremely important factors if not mandatory requirements. Finally, as in most e-nose applications, the capability to be used by personnel that do not enjoy an ad-hoc artificial olfaction training is a must.

Here, we show an ad-hoc approach to fast testing by combining instantaneous samples contamination assessment.

42.2 Contamination Scenarios and Data Sampling Procedure

In this study, a $10 \times 5 cm^2$ panel of CFRP *M21* composite material have been contaminated by a water/contaminant solution based on skydrol 500-B™, a release agent (Frekote™) and moisture. Corresponding samples have been labeled respectively as SK, RE, MO. The UT label is employed for untreated panel, i.e. for panels that have not undergone the contamination process. Every agent solution have been produced with different levels of concentration. In particular, four are the contamination levels for release agent corresponding to (2.1–2.7%, 6.5–6.8%, 8.2–9.5%, 10.1–10.4%) ranges of XRF measured Si content on surface. The watery phase of stirred and settled Skydrol/water mixture have been used for Skydrol contamination samples. Three ph values (2;3;4) specify the SK contamination levels. Finally, MO contamination has been produced by exposure of the panels to different levels of RH for several days. In this case, the four mass uptake level, the selected contamination proxy, have been found to be [29%;0.79%;1.08%;1.26%].

Data sampling has made by an hybrid e-nose, GDA2 (see Fig. 42.1), composed by two metal-oxide sensors (MOX), a photoionization detector (PID), an electrochemical sensor (EC) and a IMS spectra bucketing, corresponding to additional four soft sensors.

Fig. 42.1 E-nose GDA2, sensors array depiction and a sampling process picture
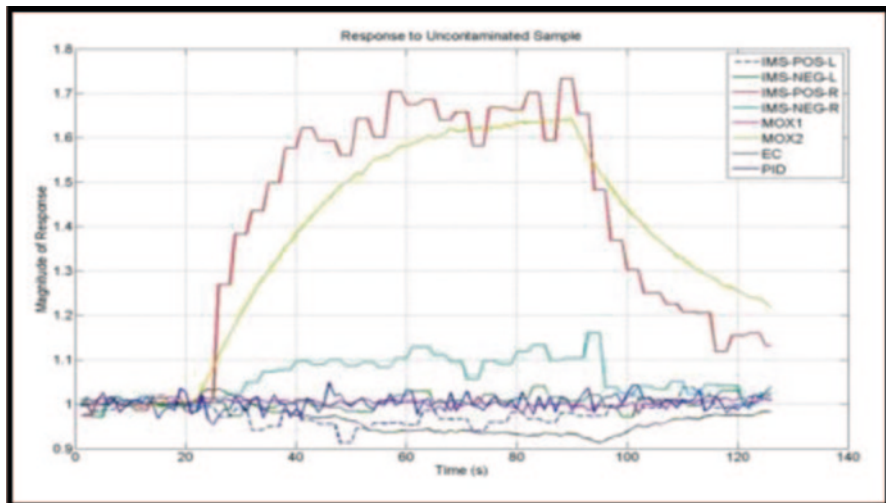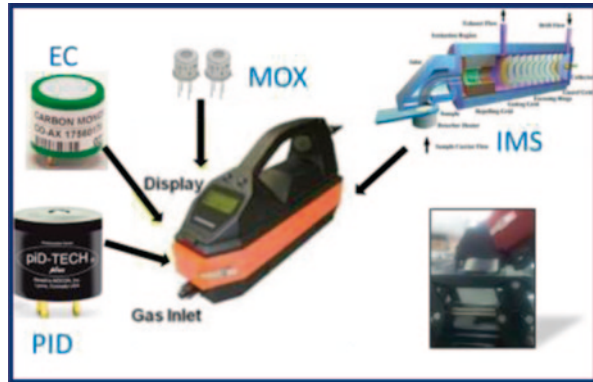
Fig. 42.2 E-nose response for an uncontaminated sample

The e-nose has been equipped with an infrared emitter (10 W halogen lamp) controlled via sw, to heat the surface thus helping the desorption of relevant volatiles. The e-nose response to chemical agents has been recorded by following a duty cycled scheme. The sampling of CFRP surfaces was performed at 1 Hz sampling frequency, exploiting the heat generated by an IR emitter that was powered for 30 s starting from the beginning of the measurements process. The basic measurement cycle (see Fig. 42.2) consists in three steps. The first one was focused on to baseline acquisition by exposing for 20 s the sensor array to filtered environmental air. The second one was characterized by 70 s of exposure to unfiltered air coming from the surface. During the first 30 s of this last phase the IR emitter was switched on. Sensors showed a transient response after which most of them reached a relatively

steady response phase. In the third step (sensors chamber flushing), the sensor responses were characterized by a slow recovery process.

42.3 Pattern Recognition and Results

The developed e-nose samples set is composed by forty different measurements of ten composite panels, for a total amount of 4400 instantaneous samples recorded during exposure phase. The aim of the pattern recognition subsystem was to simultaneously identify and discriminate contamination.

Discrimination among the four classes is obtained by an ANN classifier working on instantaneous sensors response in supervised mode. The class estimation for the entire cycle has been obtained by combining the NN winning output neuron of each sample classification estimate and, specifically, computing the maximum throughout all classes of the average Output Neuron level obtained by each class (winning class reliability):

$$WCR = max_j \left(\frac{1}{k} \sum_{i=1}^{k} ON_{i,j} \right) j = 1..T$$

with k being the number of sensor array readings i, and T the number of classes. The class j obtaining the maximum WCR is the winning class.

Of course, network training and test sets contain samples from different measurement cycles obtained from a random extraction from the entire dataset of all measurement cycles.

Accuracy performances have been obtained via cross validation to reduce performance estimation uncertainty. The process is based on a 90/10% partition of the dataset, on a measurement cycle base, and a 100x averaging scheme.

In this way, the obtained classification has been found to be in excess of 70%. The false positive rate is however too high settling at about 21%, but most of them are due to environmental humidity, misinterpreted as moisture contamination. The false negative rate, i.e. contaminated samples estimated as untreated, is instead approximately 5%. However it is to be considered unbearable considering the misclassification cost of the scenario. Errors are mainly found at lowest contamination levels. In this case, the system get confused by mistakenly estimate skydrol as moisture, moisture as skydrol or uncontaminated while at highest contamination level, instead, we get 95% classification accuracy. Winning class reliability WCR also provide an overall reliability measure of the cycle wide class estimation. Its distribution over the correctly classified CFRP panels has been found to differ significantly from that of CFRP wrongly classified panels (see fig. 42.3). The different form of the distributions and a quasi-Gaussian misclassification distribution suggest the possibility to improve accuracy results refusing to attempt a classification for values of low self-perceived reliability (WCR).
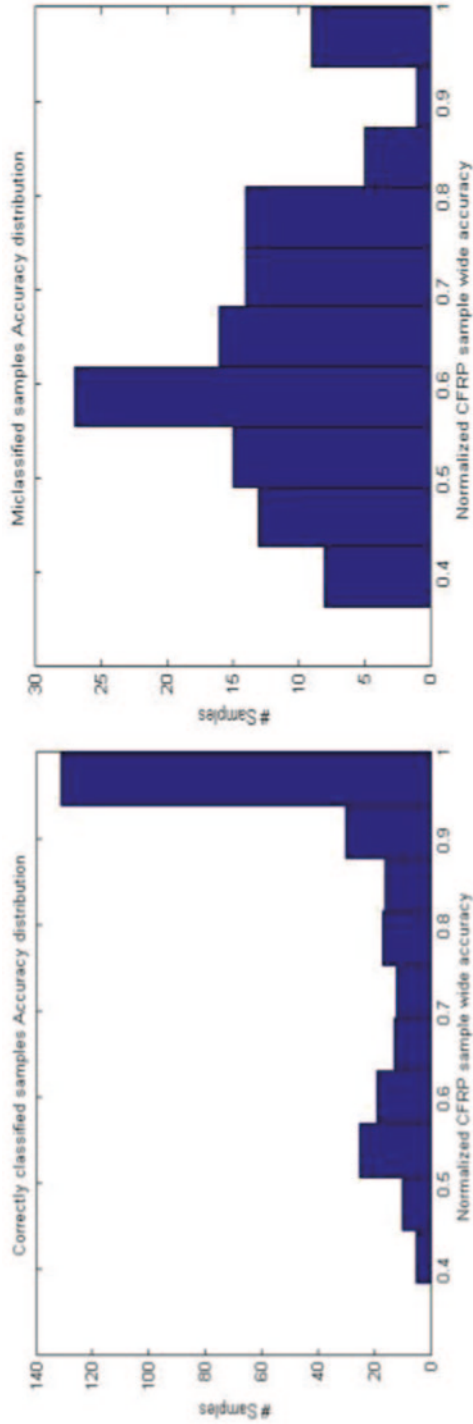
Fig. 42.3 Correctly and un-correctly classified samples accuracy distribution

On this base, a reject threshold have been set so to allow the e-nose to reject the samples whose classification do not meet an overall reliability criteria ([3]). After the rejection step, the obtained accuracy results definitely improve becoming interesting for such a demanding scenario. Specifically, by setting a 0.65 threshold value the false negative rate is zeroing and the cycle wide accuracy is approximately 84 %.

42.4 Conclusions

The reject option combined with the PARC architecture suggest that the e-nose can be capable to fulfill the requirement for a fast line contamination detection NDT tool in aerospace scenario. An unbiased estimation of the optimal reject threshold value, however, would have needed a further partition of the dataset that could be obtained only with a significant enlargement of the dataset.

References

1. TC Pearce, et al., Handbook of Machine Olfaction, Wiley Press, 2007.
2. D.N. Markatos, et al., Effects of manufacturing-induced and in-service related bonding quality reduction on the mode-I fracture toughness of composite bonded joints for aeronautical use, Composites Part B: Eng., Volume 45, Issue 1, February 2013, 556–564.
3. LP Cordella, et al., Reliability parameters to improve combination strategies in multi-expert systems, Pattern Analysis & Applications 2 (3), 205–214

Part III
Microsystems Technologies, Electronics and Integrated Sensing

Chapter 43
Synergic Integration of Conjugated Luminescent Polymers and Three-Dimensional Silicon Microstructures for the Effective Synthesis of Photoluminescent Light Source Arrays

Giovanni Polito, Salvatore Surdo, Valentina Robbiano, Giulia Tregnago, Franco Cacialli and Giuseppe Barillaro

In this work, a novel and straightforward technology for the fabrication of two-dimensional (2D) photoluminescent light source arrays by selective infiltration of conjugated luminescent polymers into three-dimensional (3D) silicon micro-structures is presented. Poly(9,9-di-*n*-octylfluorene-*alt*-benzothiadiazole) (F8BT) integration into 3D silicon microstructures is investigated by means of three different deposition techniques, namely, spin-coating, dip-coating and drop-casting/slow solvent evaporation. The microstructure is fabricated by electrochemical micromachining (ECM) technology and integrates 2D arrays of square holes with different sizes (about 40 and 4 μm), spatial periods (about 70 and 10 μm), and aspect ratios (ARs) (about one and ten). Notably, square holes with higher AR can be selectively filled with polymer using spin-coating and drop-casting techniques, whereas dip-coating technique allows selective polymer filling of square holes with lower AR. Independently of size, period and AR, each polymer-infiltrated hole behaves as a single light source, thus enabling the effective synthesis of 2D photoluminescent light source arrays

G. Barillaro (✉) · G. Polito · S. Surdo
Dipartimento di Ingegneria dell'Informazione, Università di Pisa, Via G. Caruso 16, 56122 Pisa, Italy
e-mail: g.barillaro@iet.unipi.it

V. Robbiano · G. Tregnago · F. Cacialli
Department of Physics and Astronomy and London Centre for Nanotechnology, University College London, Gower Street, WC1E 6BT London, UK

43.1   Introduction

Conjugated polymers (CPs) have been widely investigated over the past two decades because of their unique optical and semiconducting properties, with extensive application in the fields of organic electronics and photonic devices, of which CP-based light-emitting diodes (OLEDs), organic photovoltaic cells (OPVs), and organic field-effect transistors (OFET), are just a few remarkable examples. In spite of such a great research effort, integration of CPs with three-dimensional (3D) silicon mictrostructures has been overlooked so far. In this work, a novel and straightforward technology for the fabrication of two-dimensional (2D) photoluminescent light source arrays by selective infiltration of conjugated luminescent polymers into 3D silicon microstructures is presented [1]. Poly(9,9-di-*n*-octylfluorene-*alt*-benzothiadiazole) (F8BT) is a green-emitting polyfluorene derivative displaying good electron transport properties and a low-lying lowest unoccupied molecular orbital (LUMO), as well as high photoluminescence (PL) efficiency [2]. F8BT infiltration into 3D silicon microstructures is investigated using three different deposition techniques, namely, spin-coating, dip-coating, and drop-casting/slow solvent evaporation.

43.2   Experimental

The 3D silicon microstructure used for F8BT infiltration experiments is fabricated by means of electrochemical micromachining (ECM) technology [3] and consists of a 2D array of 4-μm-side square holes integrating a 2D array of 40-μm-side square holes featuring spatial periods of about 10 μm and 70 μm, respectively. The hole-depth is 50 μm for both the square hole arrays, thus resulting in holes with high (about ten) and low (about one) aspect ratio (AR) combined on the same silicon die. Typical scanning electron microscope (SEM) bird's eye view of the 3D silicon microstructure is reported in Fig. 43.1a. In the inset, a single unit of the periodic mictrostructure, composed of a low-AR hole surrounded by high-AR holes, is reported.

Toluene is used as solvent for F8BT polymer solution preparation. Both spin-coating and drop-casting experiments are carried out using polymer solutions with 1 and 2 wt% F8BT. As to spin-coating experiments, polymer deposition is performed also testing rotational speeds ranging from 500 to 1500 revolutions per minute (rpm) during a first 60 s spinning step, followed by a second 10 s spinning step at 4000 rpm. Drop-casting experiments are performed dispensing a volume of 0.25 mL of polymer solution onto the silicon microstructure, which is left 48 h at room temperature in nitrogen atmosphere for complete drying. Dip coating experiments are carried out at a prescribed vertical withdrawal speed of 0.13 μm s^{-1} using polymer solutions with 1 wt% F8BT.
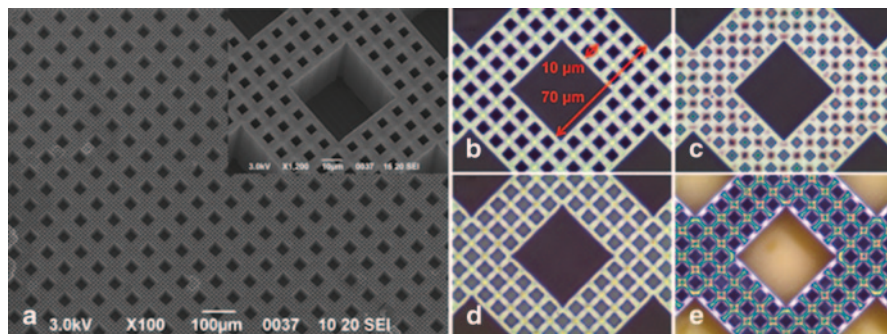
Fig. 43.1 a SEM micrograph of a 3D silicon microstructure featuring 2D arrays of square holes with different sizes, periods and ARs. The inset shows the single repeating unit. **b-e** Optical micrographs at 100× magnifications of microstructured samples before (**b**) and after spin-coating (**c**), drop-casting (**d**) and dip-coating (**e**) deposition experiments

43.3   Results and Discussion

In Fig. 43.1 (b, c, d, e), optical micrographs of the 3D silicon microstructure single unit at $100 \times$ magnifications before (b) and after polymer infiltration experiments (c, d, e) are reported. Figure 43.1 (c) shows polymer distribution in a sample spin-coated at 500 rpm with 1 wt% polymer solution. Figure 43.1 (d) shows polymer distribution in a sample drop-cast with 2 wt% polymer solution. For both spin-coating and drop-casting deposition experiments uniform polymer filling of high-AR holes is observed, whereas no polymer is present in low-AR holes. Conversely, Fig. 43.1 (e) shows that dip-coating deposition experiments allow uniform polymer infiltration of low-AR holes, while leaving high-AR holes free from polymer. In Fig. 43.2, typical fluorescence maps (a1, a2, a3) of the polymer-infiltrated microstructures in Fig. 43.1, along with 3D views of PL signal (b1, b2, b3), and luminescence intensity profiles (c1, c2, c3) acquired along a y-cross-section of fluorescence maps are shown. In fluorescence maps referring to spin-coating and drop-casting deposition experiments (Fig. 43.2(a1) and (a2)) PL signal only arises from high-AR holes, which are uniformly filled with polymer, while low-AR holes appear as a dark square hole array being free from polymer. Conversely, in fluorescence maps referring to dip-coating deposition experiments (Fig. 43.2 (a3)), PL signal mainly arises from polymer-infiltrated low-AR holes, which appear as a bright square hole array. Interestingly, 3D views (Fig. 43.2 (b1, b2, b3)) show a confinement effect exerted by the microstructure features on the polymer light-emission in the out-of-plane direction, thus enabling discrimination of the PL signal arising from each polymer-infiltrated hole, for both low- and high-AR holes, in spite of the very tiny dimensions and tight arrangement of the latter. Luminescence intensity profiles (Fig. 43.2 (c1, c2, c3)) allow selective polymer infiltration to be better appreciated.
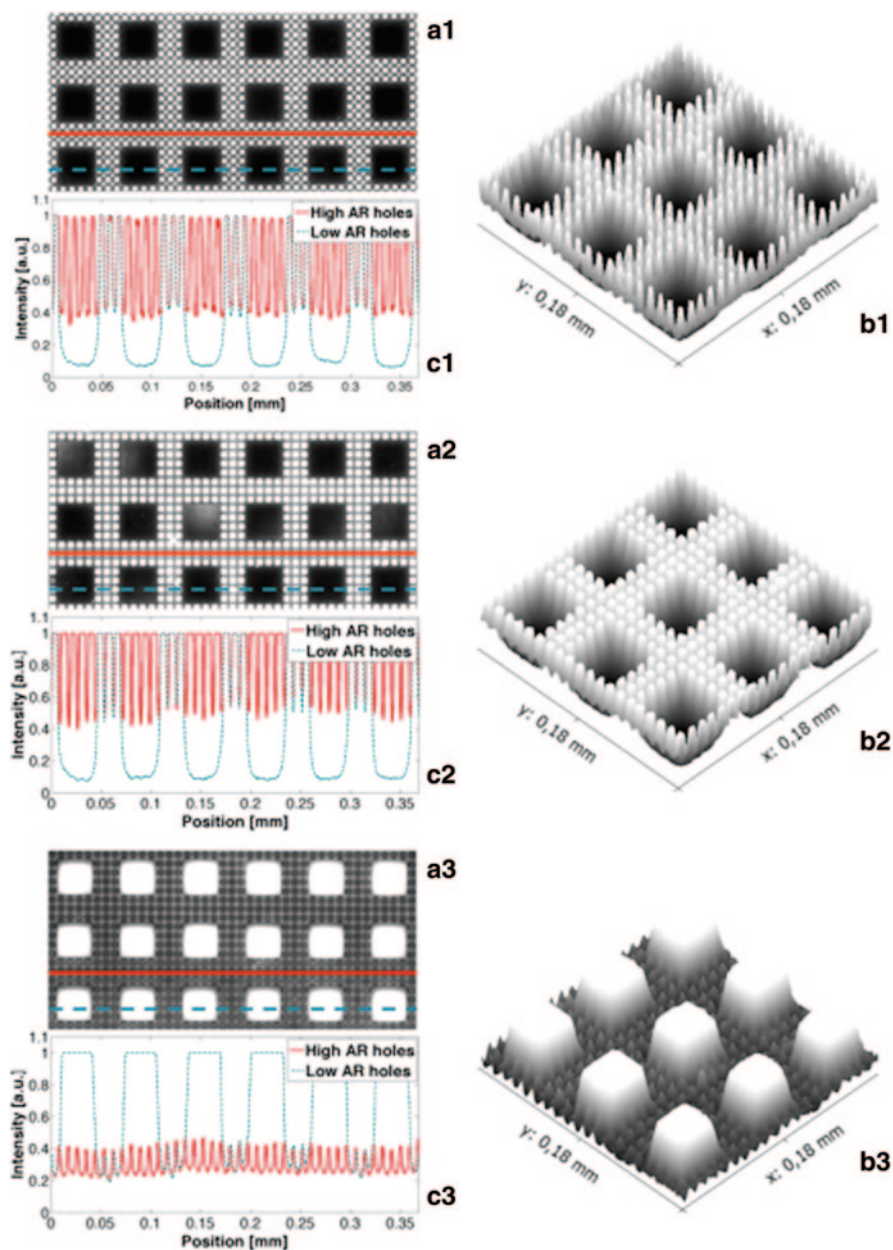
Fig. 43.2 **a** Typical fluorescence maps captured from spin-coated (*a1*), drop-cast (*a2*) and dip-coated (*a3*) microstructured samples of Fig. 43.1 (c, d, e). **b** Typical 3D views of PL signal arising from spin-coated (*b1*), drop-cast (*b2*) and dip-coated (*b3*) microstructured samples in (*a1*, *a2*, *a3*). **c** PL intensity profiles along a y-cross-section (solid and dashed lines in (*a1*, *a2*, *a3*)) of fluorescence maps of spin-coated (*c1*), drop-cast (*c2*) and dip-coated (*c3*) microstructured samples

43.4   Conclusions

Experimental evidences demonstrate that F8BT selective infiltration of high-AR and low-AR holes is attainable by spin-coating/drop-casting and dip-coating deposition methods, respectively. Independently of AR value, size and period, each polymer-infiltrated hole behaves as a single luminescent light source, thus enabling the effective synthesis of 2D arrays of photoluminescent light sources with tunable integration density. Such a synergic integration of CPs and 3D silicon microstructures envisages a plethora of applications, spanning from photonics (e.g., flat display) to diagnostics (e.g., tumor cell analysis).

References

1. G. Polito, S. Surdo, V. Robbiano, F. Cacialli, G. Barillaro. Two-dimensional array of photoluminescent light sources by selective integration of conjugated luminescent polymers into three-dimensional silicon microstructures. Adv. Optical Mater. **1** (12), 888–894 (2013)
2. L. Sardone, C. Sabatini, G. Latini, F. Barigelletti, G. Marletta, F. Cacialli, P. Samori. Scanning Force Microscopy and optical spectroscopy of phase-segregated thin films of poly –(9,9'-dioctylfluorene-*alt*-benzothiadiazole) and poly(ethylene oxide). J. Mater. Chem. **17** (14), 1378–91 (2007)
3. M. Bassu, S. Surdo, L.M. Strambini, G. Barillaro. Electrochemical micromachining as an enabling technology for advanced silicon micrtostructuring. Adv. Funct. Mater. **22** (6), 1222–28 (2012)

Chapter 44
Amorphous Silicon Photosensors for Food Quality Control Applications

D. Caputo, G. de Cesare, A. Nascetti, R. Scipinotti, C. Fanelli and A. Ricelli

In this paper we present an innovative, low cost and portable detection system for food quality control based on Thin Layer Chromatography method. The operating principle relies on the real-time monitoring of the chromatographic run through the measurement of the photocurrent induced in amorphous silicon (a-Si:H) photosensors by naturally fluorescent molecules present in the investigated sample. The integration in the system of the array of a-Si:H photosensor allows to achieve a sensitive and compact system without external optics for focusing the fluorescent light. The presented system was designed for detection and quantification of Ochratoxin A (OTA), a toxin due to food contamination by fungi. Tests for the detection of OTA were successfully performed achieving a minimum detectable quantity of 0.2 ng for both red wine extract and OTA standard solutions. Taking into account a 90 % of extraction efficiency and a volume of 2 µl which can be spotted on the HPTLC plate, we infer that a volume of only 5.5 ml of red wine is necessary to compare OTA level with the law limit.

D. Caputo (✉) · G. de Cesare · R. Scipinotti
Department of Information Engineering, Electronics and Telecommunications,
"Sapienza" University of Rome, Rome, Italy
e-mail: caputo@die.uniroma1.it

A. Nascetti
Department of Astronautics, Electrical and Energy Engineering,
"Sapienza" University of Rome, Rome, Italy

C. Fanelli
Department of Environmental Biology, "Sapienza" University of Rome, Rome, Italy

A. Ricelli
CNR-Institute of Biomolecular Chemistry, P.le Aldo Moro 5, Rome, Italy

44.1 Introduction

The deterioration of food commodities by biotic factors and, in particular, by fungi is a serious and widespread problem. Quality loss is due to the ability of different fungal species to produce mycotoxins like Ochratoxin A (OTA) [1]. Its high toxicity and the wide diffusion led the EU to define strict legal limits for the tolerable presence of OTA in different food commodities [2], such as cereals and grapes and in their products beer and wine.

Currently, the methods to detect OTA are based on immunochemical techniques (ELISA assay) that are fast, ease to operate but they give yes/no answers, as well as on High Performance Liquid Chromatography methods coupled with appropriate clean-up such as Immuno Affinity Columns [3], that give good results but they are very expensive, time consuming and require highly experienced operators. Recently, OTA detection methods based on the Surface Plasmon Resonance [4], on the Molecularly Imprinted Polymers [5] and on the Fluorescence Polarization Immunoassay [6] are being developed. However, even if some interesting results have been obtained, their use is related to laboratory and it is far from a real exploitation for in-field applications.

In this paper we present a novel OTA detection system, whose prototype was developed in the frame of the FP7 European project "OTASENS" [7]. The system exploits the Thin Layer Chromatography (TLC) method monitoring in real-time the natural fluorescence of the OTA molecules under ultraviolet (UV) radiation [8]. The emitted light is detected by an array of amorphous silicon (a-Si:H) photosensors [9] whose integration in the system avoids the need of external optics for focusing the fluorescent radiation [10] and leads to a sensitive, portable and ease-of-use system for in-field applications.

44.2 Description of the Prototype

The developed prototype, whose scheme is depicted in Fig. 44.1, includes: (a) an array of a-Si:H n-i-p stacked structure acting as active elements for the absorption of fluorescence; (b) a commercial High Performance TLC (HPTLC) plate where the extracts of food are spotted; (c) a vertical chromatographic chamber composed of a PTFE tank for the eluent and an upper side PET chamber, partially inserted in the tank, that hosts the a-Si:H array and the HPTLC plate; (d) a set of UV Light Emitting Diodes (LEDs) integrated on the upper side chamber and acting as UV excitation source.

The system also includes an electronic board to control the UV source, to acquire the signals generated by the photosensors and to handle the USB communication with a Graphic User Interface (GUI) on a computer for storage and analysis of the incoming data [11].

During the chromatographic run, the UV LEDs excite the naturally fluorescent OTA molecules, whose maximum absorption occurs at 330 nm and maximum emis-
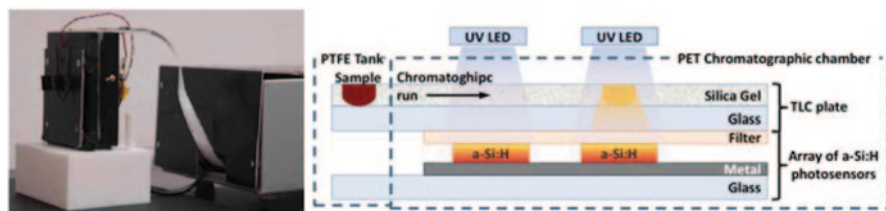
Fig. 44.1 Picture (*left*) and scheme (*right*) of the prototype of the system

sion occurs at 465 nm, and the re-emitted light is detected by the array of a-Si:H photosensors. The photosensors are glass/metal/n-i-p/metal structures whose photocurrents are proportional to the amount of the impinging light. Details of the fabrication process are reported in [12]. During the analysis, when the OTA chromatographic band is aligned with the photosensor, it is generated a photocurrent peak proportional to the amount of OTA contained in the investigated sample. Since the main objective of this prototype is a rapid screening to determine whether the OTA level is above or below the law limit, two parallel chromatographic runs, a reference sample and the food extract, are performed on the same TLC plate and monitored by two a-Si:H parallel linear arrays. Comparing the photocurrents resulting from the two parallel arrays it is possible to establish if the OTA quantity in the investigated sample is above or below the concentration allowed by European Regulations.

The investigated sample is extracted from the contaminated food by using a novel protocol based on a mixture of ethyl acetate and formic acid allowing a rapid, reliable and environmental friendly OTA retrieved. The reference sample is a solution containing OTA standard at the law limit.

44.3 Experimental Results

Figure 44.2 (left) reports the photocurrent values of two photodiodes during a chromatographic run. One monitors the effect of 4 ng of OTA standard spotted as reference, the other the effect of the eluent without spotting any food extract. Comparing the two curves, we see that the OTA signal is a Gaussian curve superimposed to a sigmoidal background signal due to the transmission of the UV radiation through the silica gel wetted by the eluent [13]. The OTA signal is the peak value extracted subtracting the baseline curve to the current signal. The baseline is individuated joining the beginning and the end of the OTA peak.

The system was then tested analysing 2 μl of OTA standard and extracted red wine fortified with OTA. The results, summarized in Fig. 44.2, show a very good linearity (R=0.987 for wine sample and R=0.999 for OTA standard) and a minimum detectable quantity of 0.2 ng for both sample and reference. Taking into account a 90% of extraction efficiency and a volume of 2 μl which can be spotted on the HPTLC plate, we infer that a volume of only 5.5 ml of red wine is necessary to determine whether OTA level is below the law limit.
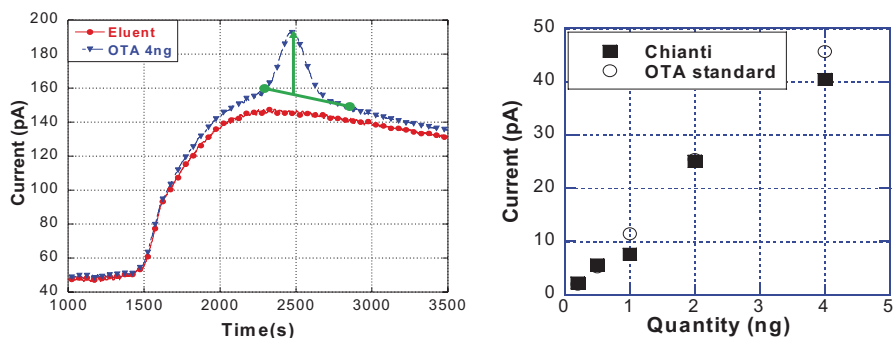
Fig. 44.2 *Left*: photosensor current with no OTA spotted (*circles*) and 4 ng of OTA (*triangle*). *Right*: quantitative characterization of fortified red wine (*squares*) compared with OTA standard (*circles*)

44.4 Conclusions

In this paper we presented the application of an amorphous silicon photosensors array to detect OTA in feed and food commodities. A prototype of the detection system was developed coupling the array of photosensors with a standard HPTLC plate both hosted in a PET-PTFE chromatographic chamber, achieving an innovative, low cost and portable device for rapid and reliable in-field analysis. The OTA detection is based on the real time monitoring of the chromatographic run of the extracted sample. Tests for the detection of OTA were successfully performed achieving a minimum detectable quantity of 0.2 ng for both red wine extract and OTA standard solutions.

References

1. P. De Rossi, M. Reverberi, A. Ricelli, A.A. Fabbri, D. Caputo, G. de Cesare, R. Scipinotti, C. Fanelli, "Early detection of ochratoxigenic fungi in wine grapes and of ochratoxin A in wine", Annals of Microbiology, **61**, 11–15 (2011).
2. Commission Regulation (EC) No 401/2006 of 23 February 2006.
3. H. Meng, Z. Wang, S. De Saeger, Y. Wang, K. Wen, S. Zhang, J. Shen, "Determination of Ochratoxin A in Cereals and Feeds by Ultra-performance Liquid Chromatography Coupled to Tandem Mass Spectrometry with Immunoaffinity Column Clean-up", Food Analytical Methods, **7** (4), 854–864 (2014).
4. Jing Yuan Dawei Deng Denis R. Lauren Marie-Isabel Aguilar Yinqiu Wu, "Surface plasmon resonance biosensor for the detection of ochratoxin A in cereals and beverages", Analytica Chimica Acta, **656** (1–2), 63–71 (2009),

5. Simon N. Zhou, Edward P. C. Lai, J. David Miller, "Analysis of wheat extracts for ochratoxin A by molecularly imprinted solid-phase extraction and pulsed elution", Analytical and Bioanalytical Chemistry, **378** (8), 1903–1906 (2004),

6. V. Lippolis, M. Pascale, S. Valenzano, A. C. R. Porricelli, M. Suman, A. Visconti, "Fluorescence Polarization Immunoassay for Rapid, Accurate and Sensitive Determination of Ochratoxin A in Wheat", Food Analytical Methods, **7** (2), 298–307 (2014)

7. http://www.ist-world.org/ProjectDetails.aspx?ProjectId= f86b851cf3f14f0d8f44afce1b443edc.

8. D. Caputo, G. de Cesare, C. Manetti, A. Nascetti, R. Scipinotti; "Smart thin layer chromatography plate" Lab on a Chip, **7**, 978 (2007).

9. D. Caputo, G. de Cesare, C. Fanelli, C. Manetti, A. Nascetti, A. Ricelli, and R. Scipinotti, "Linear Photosensor Array for On-Chip Food Quality Control Based on Thin Layer Chromatography". Sensor Lett. **8**, 465–469 (2010).

10. D. Caputo, G. de Cesare, A. Nascetti, R. Negri; "Spectral tuned amorphous silicon p-i-n for DNA detection", Journal of Non Crystalline Solids; **352**, 2004 (2006).

11. A. Nascetti, M. Truglio, P. Valerio, D. Caputo, G. de Cesare, " High Dynamic Range Current-to-Digital Readout Electronics for Lab-on-Chip applications" Proceedings of the 4th IEEE International Workshop on Advances in Sensors and Interfaces, IWASI 2011, art. no. 6004691, pp. 77–81, (2011).

12. D. Caputo, G. de Cesare, C. Fanelli, A. Nascetti, A. Ricelli, R. Scipinotti," Amorphous silicon photosensors for detection of Ochratoxin A in wine", IEEE Sensor Journal, **12** (8), 2674–2679 (2012).

13. D. Caputo, G. De Cesare, M. Nardini, A. Nascetti, R. Scipinotti, "Modeling of the photoresponse of a smart thin layer chromatography system", Proceedings of the 4th IEEE International Workshop on Advances in Sensors and Interfaces, IWASI 2011, art. no. 6004719, pp. 208–211 (2011).

Chapter 45
Characterisation of Gold Patterns on PDMS Substrates

Sajina Tinku, Ruben Bartali, Ravinder Dahiya and Leandro Lorenzelli

We present a technique for metal patterning on PDMS without cracks and adhesion issues. The adhesion strength of the metal patterns is characterized by micro scratch tests to check the effect of surface treatments of plasma on PDMS. The elongation of PDMS is also calculated with the applied force using the micro scratch test.

45.1 Introduction

Recently, there is a considerable research interest in the integration of microelectronics and sensors onto flexible substrates. Such possibilities of realizing the once rigid systems onto flexible substrates open up new horizons of applications. Especially in the area of biomedical wearable and implantable devices, the use of biocompatible polymers with incorporated specific functionality is garnering interest because of its flexibility and more sturdy nature compared to silicon based devices. Out of all the polymers, Polydimethylsiloxane (PDMS) is an inert and biocompatible polymer suited for biomedical applications as wearable and implantable devices [1]. However, the challenges of metal patterning on PDMS have prevented its wide use in various biomedical applications. Metal patterning on PDMS poses some main issues like crack formation on PDMS, poor adhesion of the metal on PDMS to name the few [2]. In this work we discuss an efficient metal patterning on PDMS for functional contact lens applications and adhesion characterization is performed by using a micro scratch tester.

S. Tinku (✉) · R. Bartali · L. Lorenzelli
Center for Materials and Microsystems, Fondazione Bruno Kessler, Trento, Italy
e-mail: tinku@fbk.eu

R. Dahiya
Electronics and Nanoscale Engineering, University of Glasgow, Glasgow, UK
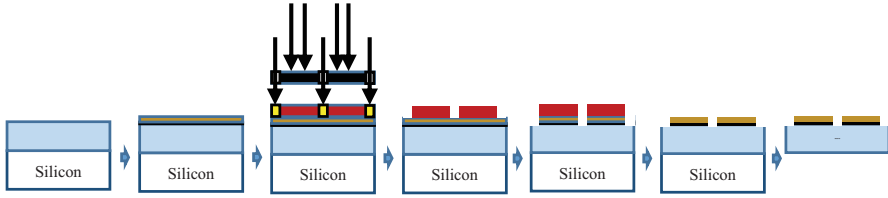
Fig. 45.1 Optimized micro fabrication steps for patterning gold on PDMS

Fig. 45.2 Set-up for micro scratch test
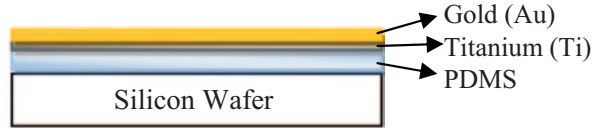
45.1.1 Micro Fabrication Steps for Metal Patterning

The step for patterning gold on PDMS is shown in Fig. 45.1. PDMS is spun coated on Silicon substrate and the patterning of gold is performed using metal deposition using e-beam evaporation technique, lithography and wet etching processes. The detailed information of this explained in a former work of the authors [3].

45.2 Micro Scratch Test of Patterned Gold on PDMS Substrates

Adhesion characterization of the patterned Au films on the PDMS substrates was carried out using a micro scratch tester. The test was carried out with a progressive load from 50 to 5000 mN with a set-up of sample as shown in Fig. 45.1.

The four samples as in Fig. 45.2 were prepared, with different plasma treatment on PDMS. The micro scratch test was performed in order to understand the effect of plasma treatment on the adhesion of the metal. The optical microscopic images were acquired before the scratch test as shown in Fig. 45.3.

The scratch test is performed with inputs of 'start force', 'end force', scan length and speed of the scratch. Start force was kept at 50 mN and the end force at 1500 mN, scan length and scan speed was 5 mm and 1 mm/min respectively. The scratch is performed and the micro scratch machine plots the graphs of penetration depth, acoustic emission, and frictional coefficient with respect to the applied force in real time. After the measurement, three pictures are acquired using the optical microscope (20x), which corresponds to three critical loads. First critical load or LC1 is the load at which the gold is removed and the underlying PDMS can be seen through the microscope. This point represents the maximum load to be applied to

| No plasma treatment | 15 sec plasma treatment | 20 sec plasma treatment | 30 sec plasma treatment |
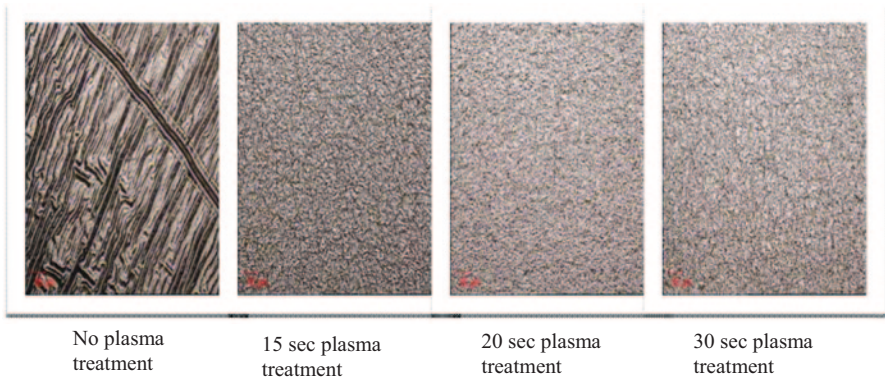
Fig. 45.3 Optical microscopic images of Au coated PDMS substrates with different plasma treatments before the micro scratch test
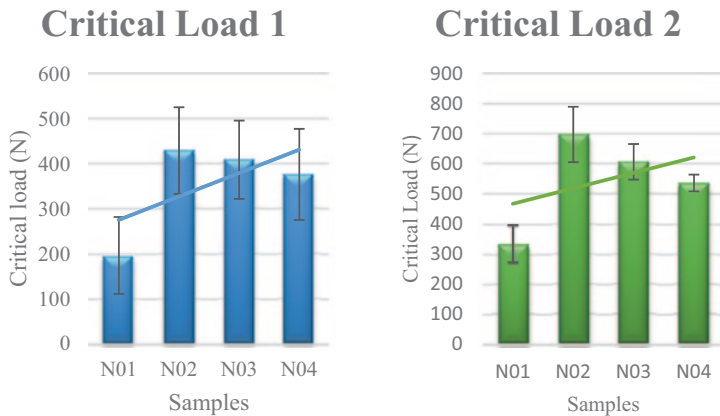
Fig. 45.4 First and second critical load measurement on Au coated PDMS, N01 (no plasma treatment), N02 (15 s plasma treatment), N03 (20 s plasma treatment), N04 (30 s of plasma treatment)

see the first real removal of gold from the substrate. Second critical load or LC2 is the point from where the delamination of gold is a continuous event. From LC2 onwards the gold gets scratched off until the LC3 or Critical load 3 where there is complete delamination of gold and only PDMS is present.

   The critical load measurements shown in Fig. 45.4 clearly points out the effect of plasma treatment on the surface of PDMS. The plasma treatment enhances the adhesion of the metal and this difference can be clearly seen from the graph where the critical load (LC1 and LC2) both increases, approximately doubles the load required to remove the deposited gold from PDMS.
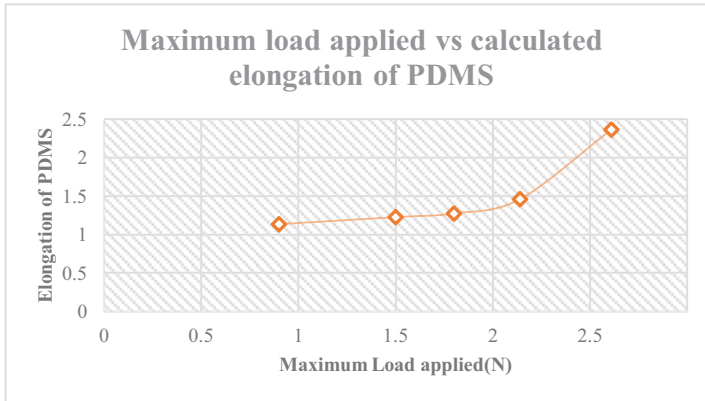
Fig. 45.5 Elongation of PDMS measured using micro scratch test with various applied loads

45.2.1 Elongation of PDMS with the Applied Force During the Micro Scratch Test

The results from the micro scratch test are obtained by analyzing the data obtained from two sensors: Sensor mounted on the tip of the scratch, which measures frictional force and acoustic emission in real time and Optical sensor, which shows the data after the scratch. When comparing the data from both of the sensors it reveals a clear difference in the position where the PDMS is critically damaged. The tip sensor, which collects the value in real time is happening during the elongation process of PDMS whereas the optical sensor collects the value after the process when the PDMS is in a relaxed state. We used this difference to estimate the elongation ratio of PDMS as a function of maximum applied load as illustrated in Fig. 45.5.

References

1. M. Fernandes, K. Lee, R. Ram, J. Corriera, P. Mendes. Flexible PDMS –based dry electrodes for electro-optic acquisition of ECG signals in wearable devices. Conference Proceedings IEEE Eng Med Biol Soc. 2010
2. H. Cong and T. Pan, "Micro fabrication of conductive PDMS on flexible substrates for biomedical applications," IEEE conference on Nano/ Micro Engineered and Molecular Systems, 2009, pp. 731–734
3. S. Tinku, C. Cristian, R. Dahiya, L. Lorenzelli. Smart contact lens with passive structures. Conference proceedings IEEE Sensors 2014 (In Press)

Chapter 46
Optimization of a Hybrid Silicon-Polymer Optical Ring Resonator

Genni Testa, Gianluca Persichetti and Romeo Bernini

In this paper we report the performance optimization of an integrated optofluidic ring resonator based on liquid core hybrid Antiresonant Reflecting Optical Waveguide (h-ARROW). Each optical element of the proposed ring has been simulated to find the optimized optical configuration which accomplishes single mode operation and reduced attenuation losses. We show that with an accurate design of the ring, quality factor up to 1.4×10^4 can be obtained.

46.1 Introduction

Optical ring resonators are of great interest in the field of sensing application because of the high sensitivity, low sample volume and compact-size. In particular optofluidic ring is very attractive as it integrates both sensing and fluidic functions, in the sense that the liquid sample flows within the waveguide core [1, 2]. However, complete integration of microfluidic part (comprising fluid inlet/outlet) is not an easy task using silicon technology and for this reason low cost polymer materials with simplified and cheaper fabrication process are more desirable [3, 4]. The great potentiality of these devices in the field of sensing application has led to developing innovative approaches which integrate microfluidic functions into the microring itself in order to improve the performances and to make these devices more adaptable to lab-on-a-chip applications. Here we propose an integrated hybrid liquid core optofluidic ring resonator (h-LCORR) based on liquid core hybrid ARROWs (h-ARROWs).

G. Testa (✉) · G. Persichetti · R. Bernini
Institute for Electromagnetic Monitoring of the Environment (IREA), National Research Council (CNR), Via Diocleziano, 328, 80124 Milan, NA, Italy
e-mail: testa.g@irea.cnr.it

G. Persichetti
e-mail: persichetti.g@irea.cnr.it
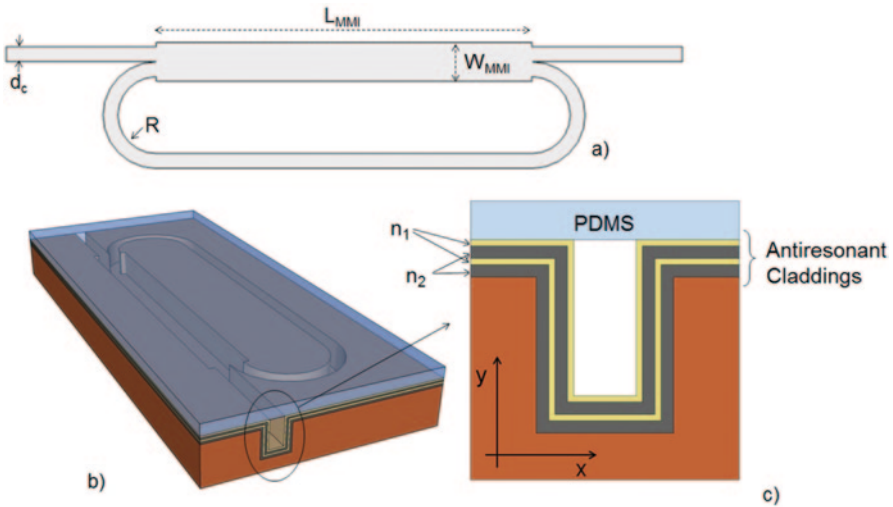
Fig. 46.1 a Schematic layout and **b** view drawing of the proposed hybrid ARROW optofluidic ring resonator. **c** Schematic cross section of an ARROW waveguide with four antiresonant cladding layers with refractive index n_1 and n_2

46.2 Simulation Results

A schematic of the ring resonator is showed in Fig. 46.1a. The resonator loop is obtained by using 90°-curved h-ARROW waveguides with curvature radius R and a hybrid multi-mode interference (h-MMI) liquid core ARROW as coupling element between the ring and the bus waveguide. The length and width of the MMI section are L_{MMI} and W_{MMI}, respectively, and d_c is the width of the waveguide core. A view drawing of the proposed h-ARROW optofluidic ring resonator is shown in Fig. 46.1b.

ARROWs are optical waveguides where the light is guided in a liquid core due to high- and low- refractive- index layers deposited on core sidewalls which act as a reflector. H-ARROWs consist of a silicon part with integrated a polydimethylsiloxane (PDMS)-layer which acts as optical elements and, at the same time, can incorporate microfluidic functions [5]. However, because h-ARROWs are leaky waveguides, an accurate optimization is required in order to ensure low propagation and coupling losses for a high sensitivity ring resonator with sharp resonances and high-quality factor. Numerical analysis of the h-ARROW modes has been performed with a two dimensional mode solver [FIMMWAVE, © Photon Design] by using the finite difference method. The waveguide has been designed at a wavelength of $\lambda = 770$ nm for a water-filled core (nc = 1.33). Three geometries which differ for the number of bi-layer claddings are studied. In particular, hybrid structures with one (1h-ARROW), two (2h-ARROW) and three (3h-ARROW) high and low-index layers are simulated by varying the core width (dc) and height (h). Figure 46.1c il-

Table 46.1 Fundamental mode attenuation losses

dc[μm]	1h-ARROW	2h-ARROW	3h-ARROW
2	28.551	7.291	3.979
3	11.022	4.599	3.476

Values of α_0 are expressed in unit of cm^{-1}
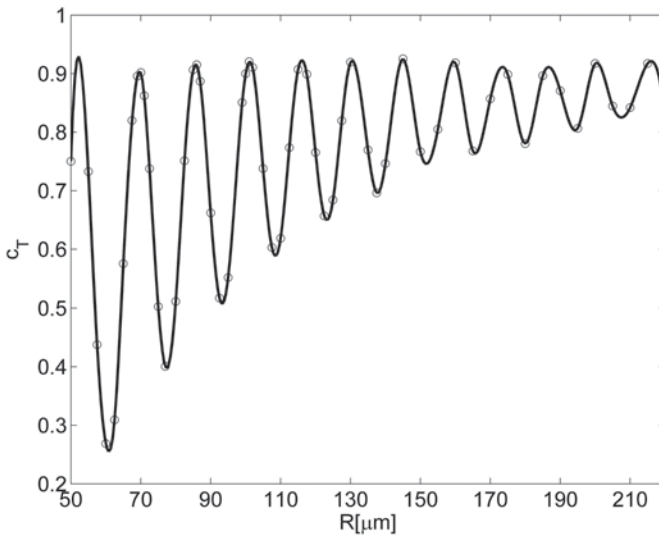
Fig. 46.2 Fundamental mode power transmission coefficient versus curvature radius R

lustrates the schematic cross section of a h-ARROW on which the proposed device is based. In Table 46.1 are summarized the fundamental mode losses α_0 versus dc in the particular case of $h = 12$ μm. From Table 46.1 it can be noticed that by using only two bi-layer (2h-ARROW) reduced attenuation losses can be obtained with respect to the 1h-ARROW configuration.

A further key parameter to be optimized is the shape of the bending waveguides of the ring loop structure. In fact a significant part of the power carried by the fundamental mode may be transferred to the higher order modes in the bend, especially at small curvature radius, thus deteriorating the ring performance. In order to estimate this effect, we have derived the amount of the power that is transmitted from the fundamental input mode to the fundamental output mode of a straight waveguide after propagating along the bend section by varying the curvature radius R. In Fig. 46.2 are shown the simulation results in the particular case of dc = 3 μm (2h-ARROW).

As it can be noticed, the transmission coefficient c_T varies in a damped oscillatory manner with the radius R. This phenomenon is the result of the multimodal interference (MMI) between the modes exited in the bend section. Values of c_T of about 0.9 can be obtained by suitably chosen the appropriate R. Another optical

Table 46.2 Ring optical parameters

MMI type	L_{MMI} [µm]	α_c^2	Qth	ER_{th}[dB]
A(50:50)	121	0.967	5.428×10^3	8.988
B(85:15)	322	0.901	1.378×10^4	10.043
C(72:28)	401	0.874	1.165×10^4	23.442

Fig. 46.3 Simulated transmitted spectrum for ring resonator based on 2h-ARROW
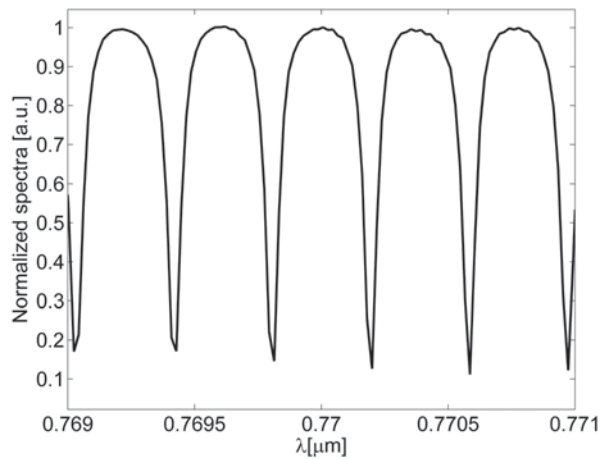
loss origin is given by the coupling mechanism between the bus waveguides and ring section. The coupling of light in the ring is obtained with a liquid core h-ARROW-based multimode interference (MMI) coupler. Three MMI configurations at the working wavelength of $\lambda = 770$ nm have been simulated with different splitting ratios between the two output ports. In particular, splitting ratios of 50:50 (type A MMI), 85:15 (type B MMI) and 72:28 (type C MMI) have been considered. Simulations have been performed using a 2d FDTD method (OMNISIM, © Photon Design). Table 46.2 lists the simulated coupling coefficient α_c^2 in the particular case of a 2h-ARROW waveguides with input/output core width of dc=2 µm. Based on the calculated coefficient, the expected quality factor Q_{th} and extinction ratio ER_{th} of the ring in the particular case of R=50 µm and dc=2 µm are also calculated using the analytical formula [6]. In order to confirm the expected behavior, spectral response of the entire device with MMI type B, R=50 µm and dc=2 µm has been simulated with 2d FDTD method. Quality factor Q_{sim} and extinction ratio ER_{sim} have been derived from the spectrum and compared with the expected results. Quality factor and extinction ratio calculated from the spectrum are $Q_{sim} = 1.338 \times 10^4$ and $ER_{sim} \approx 9$ dB, in good agreement with the expected values Fig. 46.3.

46.3   Conclusions

We have designed and optimized an integrated planar optofluidic ring resonator based on liquid core h-ARROWs. The optical performance of ring resonators which differ by MMI coupler has been compared. From simulations we demonstrate that quality factor up to 4×10^4 can be obtained by suitably designing each optical element constituting the ring structure.

References

1. G. Testa, Y. Huang, P. M. Sarro, L. Zeni, and R. Bernini. Integrated silicon optofluidic ring resonator. Appl. Phys. Lett. **97**, 131110 (2010).
2. I. M. White, H. Oveys, and X. Fan. Liquid-core optical ring-resonator sensors. Opt. Lett. **31**, 1319 (2006).
3. A. Nitkowski, L. Chen, and M. Lipson. Cavity-enhanced on-chip absorption spectroscopy using microring resonators. Opt. Exp. **16**, 11930 (2008).
4. S. M. Harazim, V.A. Bolaños Quiñones, S. Kiravittaya, S. Sanchez. And O. G. Schmidt, "Lab-in-a-tube: on-chip integration of glass optofluidic ring resonators for label-free sensing applications. Lab Chip **12**, 2649 (2012).
5. G. Testa, Y. Huang, L. Zeni, P.M. Sarro, and R. Bernini. Hybrid silicon-PDMS optofluidic ARROW waveguide. IEEE Photonic Tech. Lett. **24**, 1307 (2012).
6. A. Yariv. Universal relations for coupling of optical power between microresonators and dielectric waveguides. Electron. Lett. **36**, 321 (2000).

Chapter 47
Internally Curved Long Period Gratings for Improved Refractive Index Sensitivity

F. Chiavaioli, C. Trono and F. Baldini

A long period grating (LPG), characterized by a specially designed refractive index (RI) profile, is proposed. Each grating plane of the LPG is tilted at increasing angles, as moving away from the center of symmetry of the structure (grating plane with no tilt) towards its both edges. The RI sensitivity of an LPG to the external medium increases by means of this internally manufactured geometric structure, which mimics the external bending of an optical fiber. A three-fold improvement in the RI sensitivity has been experimentally showed for the sixth-order cladding mode. Therefore, this kind of LPGs displays the same spectral behavior of standard LPGs, with the advantage of increased RI sensitivity. The achieved results offer a novel and real scenario concerning the attainable improvements in the field of optical fiber LPG-based RI sensors.

47.1 Introduction

The Refractive index (RI) is a very remarkable physical measurand, the measurement of which is used in several fields, ranging from the control and characterization of materials, up to the sensing of physical parameters (e.g. liquid level) or chemical (impurities in mixtures such water content in gasoline) and biochemical (label-free bioassays) species. Optics allows to effectively evaluate RI changes using different approaches, such as surface plasmon resonance, interferometric configurations, optical resonators and, recently, optical fiber long period gratings (LPGs) [1]. Due to the peculiarity of optical fibers, the use of LPGs offers some advantages, such as high compatibility with telecommunication optoelectronic devices, multiplexing and remote measurement capability for distributed sensing.

F. Chiavaioli (✉) · C. Trono · F. Baldini
Institute of Applied Physics "Nello Carrara", National Research Council, CNR-IFAC, Via Madonna del Piano 10, 50019 Sesto Fiorentino, FI, Italy
e-mail: chiavaioli@dii.unisi.it
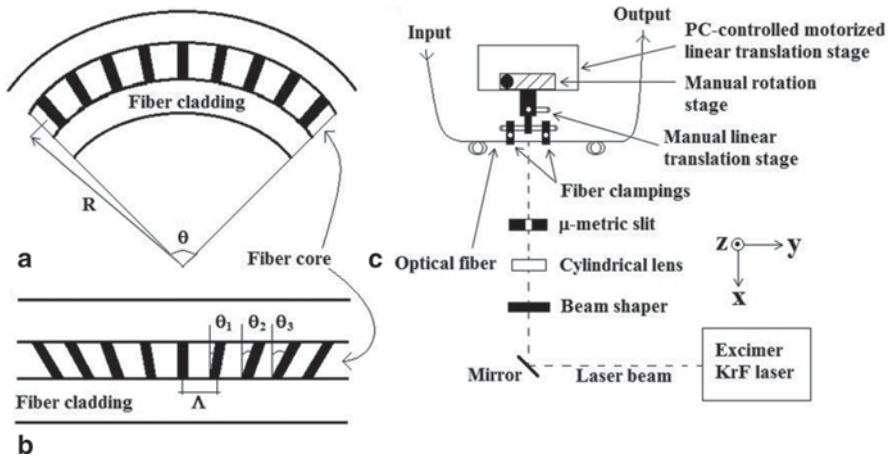
Fig. 47.1 Longitudinal views (not in scale) of **a** an optical fiber containing an LPG under the effect of an external bending and of **b** the same portion containing the internally curved LPG in a straight configuration. **c** Sketch of the manufacturing setup for writing internally curved LPGs

In order to improve the RI sensitivity of LPGs, different strategies have been proposed, among which the deposition of suitably designed coatings, cladding etching and fiber tapering are worthy to be mentioned. It was recently proved that better performance can be achieved by inducing an external bending along the LPG-containing region: the shorter the bending radius, the higher the RI sensitivity [2]. With this in mind, we designed an internally manufactured geometric structure of LPG, with a suitably designed RI profile, which mimics the same effect of an external bending, leaving unchanged the straight configuration of the fiber. The advantage of this approach lies in the easier design in the sensor configuration. Starting from our previous work [3], we experimentally showed an improvement in the RI sensitivity with a three-fold enhancement for the sixth-order cladding mode compared to a standard non-curved LPG.

47.2 Experimental Setup

47.2.1 Setup for Manufacturing Internally Curved LPGs

As opposed to an externally curved fiber structure (see Fig. 47.1a), the proposed structure preserved an external straight configuration of the fiber (see Fig. 47.1b). Each grating plane is tilted at monotonically increased angles with respect to the axis orthogonal to the fiber, as moving away from the center of symmetry of the structure (i.e. the grating plane with no tilt) towards its both edges. Looking at Fig. 47.1a, Λ is the grating period, R the bending radius and θ the bending angle.

Fig. 47.2 Comparison of the response curves between the internally curved (*black squares*) and standard (*grey circles*) LPG configurations. The solid lines account for the best rational data fitting
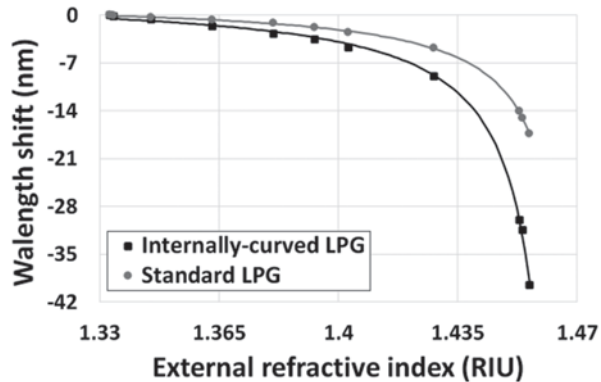
An ad-hoc customized setup to manufacture the novel LPG configuration was developed making use of proper stages, through which the structure of the grating planes of Fig. 47.1b can be manufactured [3]. By using the point-to-point method with an excimer KrF laser, the combined use of a PC-controlled motorized linear translation stage (1 μm resolution) and of a manual rotation stage (0.01° resolution) allowed to manufacture grating planes at desired angles. Another manual linear translation stage (1 μm resolution) was used for the exact positioning of the fiber with respect to the laser beam, since the position of the fiber changes due to the fiber rotation. The sketch of the manufacturing setup for writing internally curved LPGs is depicted in Fig. 47.1c. All the steps necessary for inscribing a tilted grating plane are described item by item in reference [3].

An internally curved LPG characterized by length of 20.35 mm, R = 66.2 mm, Λ = 370 μm and θ = 17.62° was manufactured and its performance was compared with that one of a standard non-curved LPG with the same grating period and considering the same cladding mode (sixth-order). LPGs were written using the same photosensitive optical fiber (FIBERCORE PS1250/1500).

47.2.2 Refractive Index Characterization of Internally Curved LPGs

By placing the sensor inside the thermo-stabilized flow cell [4] and by using different glycerol-in-water solutions with the RI ranging from 1.333 to 1.456 RIU, the response to external RI changes was studied for both the LPG configurations, the internally curved LPG and a standard LPG. Clearly, the solutions' RI was measured in advance by means of a commercial hand-held refractometer (ATAGO R-5000; 10^{-3} RIU resolution). The optical measuring setup consisted of a broadband superluminescent diode, of an optical spectrum analyzer (ANRITSU MS9030A-MS9701B) used for acquiring the transmission spectrum of LPG and of a peristaltic pump for pumping the solutions into the flow cell [4]. The temperature of the flow

Table 47.1 Comparison of the results achieved with the internally curved LPG and with a standard non-standard LPG

Type of LPG	Parameters related to the sixth-order cladding mode		
	Total wavelength shift	RI sensitivity near 1.333 RIU	RI sensitivity near 1.455 RIU
Internally curved	−39.5 nm	58.9 nm/RIU	4000 nm/RIU
Standard	−17.4 nm	29.8 nm/RIU	1154 nm/RIU

cell was kept constant at 23 °C and each solution was pumped inside the flow cell by following this protocol: flow rate of about 500 μL min^{-1} for approximately 4 min, then halting of the pump and acquisition of the spectrum for about 5 min (15 acquisitions for each measuring point).

47.3   Results and Discussion

The results of the RI characterization are showed in Fig. 47.2, together with the fitting of the experimental points with the rational curve. By using the fitted response curves, the internally curved LPG exhibited a two-fold enhancement of the RI sensitivity between 1.333–1.393 RIU and a more than three-fold enhancement between 1.454–1.456 RIU with respect to a standard non-curved LPG. All the other parameters (i.e. RI sensitivity, total wavelength shift) are gathered in Table 47.1.

Anyway, the reason of the improved RI sensitivity of curved LPGs was not entirely explained so far. This behavior should be figured out as the increase of the amount of optical radiation that interacts with the external medium, as well as the penetration depth of the related evanescent wave [1], due to the geometric structure of the grating planes.

47.4   Conclusions

An internally curved LPG, which mimics an external bending of the fiber, was manufactured for the first time thanks to the development of an ad-hoc setup. The proposed sensor showed better performance in terms of RI sensitivity than a standard non-curved LPG, with a three-fold improvement considering the sixth-order cladding mode. Moreover, the maintenance of an external straight configuration of the fiber is also worth mentioning. In addition, by reducing the bending radius, the RI sensitivity should increase, as well as by increasing the order of the cladding mode. Therefore, this kind of LPGs displayed the same spectral behavior of standard LPGs, with the advantage of increased RI sensitivity, offering the basis for a novel and real scenario in the field of optical fiber RI sensors based on LPGs.

References

1. F. Baldini, M. Brenci, F. Chiavaioli, A. Giannetti, C. Trono. Optical fibre gratings as tools for chemical and biochemical sensing. Anal. Bioanal. Chem. **402** (1), 109–116 (2012)
2. H. Tsuda, K. Urabe. Characterization of Long-period Grating Refractive Index Sensors and Their Applications. Sensors **9** (6), 4559–4571 (2009)
3. F. Chiavaioli, C. Trono, F. Baldini. Specially designed long period grating with internal geometric bending for enhanced refractive index sensitivity. Appl. Phys. Lett. **102** (23), 231109 (4 pp) (2013)
4. C. Trono, F. Baldini, M. Brenci, F. Chiavaioli, M. Mugnaini. Flow cell for strain- and temperature-compensated refractive index measurements by means of cascaded optical fibre long period and Bragg gratings. Meas. Sci. Technol. **22** (7), 075204 (9 pp) (2011)

Chapter 48
Zinc Oxide Nanowires on Printed Circuit Boards

Giuseppe Arrabito, Vito Errico, Weihua Han and Christian Falconi

Printed circuit boards (PCBs), which are widely used for the fabrication of electronic circuits, can only withstand rather low temperatures. For this reason, the fabrication of high-density, long ZnO nanostructures on PCBs still remains a complex task. In fact, in absence of a seed-layer, whose annealing would require high temperatures, solution-growth methods only allow to synthesize low-density arrays of nanowires. Here we evaluate methods for overcoming this issue and, as a prototype, demonstrate a simple displacement sensor.

48.1 Introduction

Zinc oxide is a wide band gap (3.37 eV) semiconductor with large exciton binding energy (~ 60 meV) with many outstanding optoelectronic, electrical, and piezoelectric properties [1]. In fact, quasi-1D (quasi-one-dimensional) ZnO nanostructures have been used as functional materials in many devices, including field-effect transistors, lasers, sensors, and solar cells. However, in many cases, the ZnO quasi-1D nanostructures should be sufficiently long and dense. Nevertheless, though ZnO nanowires of more than 100 microns were synthesized by using high-temperature physical vapour deposition (PVD) or chemical vapour deposition (CVD) [2], these methodologies are not suitable for substrates which cannot withstand high temperatures [3–5]. Wet-chemical synthesis methods are the best choice for such low-temperature resistant substrates, because of the simple, low temperature and scalable

C. Falconi (✉) · G. Arrabito · V. Errico · W. Han
Department of Physics and Chemistry, University of Palermo, V.le delle Scienze, Parco d'Orleans II 90128 Palermo, Italy
e-mail: falconi@eln.uniroma2.it

G. Arrabito
e-mail: giuseppedomenico.arrabito@unipa.it

W. Han
School of Physical Science and Technology, Lanzhou University, 730000 Lanzhou, P.R. China
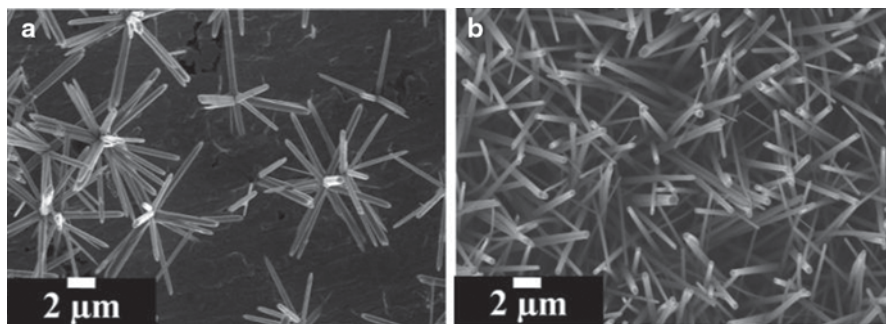
Fig. 48.1 Effect of adhesion layer. **a** ZnO NWs growth without adhesion layer leads to limited uniformity, low density and poor reproducibility, whereas the proposed treatment **b** permits to achieve good performances in terms of uniformity, density, and reproducibility

process; in practice, a water-soluble zinc precursor, often zinc nitrate mixed with a suitable amine, allows the in-liquid growth of the ZnO nanostructures; however, if high-density of the nanowires is also important, as it is generally the case, a seed-layer, whose annealing necessitates high-temperatures would be required. Here, we present an innovative approach for the solution-based, seedless growth of high-density and long ZnO nanowires on conventional ultra-low-cost PCB substrates by separately improving the density and the morphology.

48.1.1 Adhesion Layers to Improve the Nanowires Density

In order to enable high-density solution-growth of ZnO NWs we have deposited in-organic compounds of transition elements as reliable, low-cost and low-temperature adhesion film layers. In fact, the growth of nanowires without such adhesion layer results in the fabrication of samples with limited uniformity, low density and poor reproducibility, whereas the proposed, mild (<1 mM concentration) treatment permits to achieve good performances in terms of uniformity, density, and reproducibility (Fig. 48.1). Interestingly, the nanowires width is also reduced by the surface treatment, thus confirming the effect onto the nucleation density.

48.2 Solution Growth of ZnO Nanowires

Below we give the chemical reactions involved in the formation of ZnO nanowires during a growth in solution. Importantly, ammonium hydroxide plays a two-fold role in the growth process. First, it provides OH^-, which is the source of oxigen and it provides NH_4^+, which forms a complex with zinc ions as a buffering mechanism [6]. Concentration of ammonium hydroxide is kept in large excess (0.15 M) with
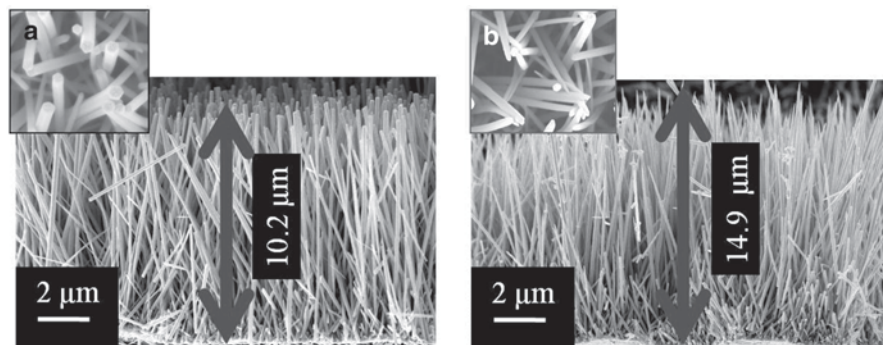
Fig. 48.2 ZnO NWs grown with the proposed method in absence (a) or in presence (b) of KCl. Polyethyleneimine permits to maintain a high amount of zinc into the solution phase by complexing zinc ions [8]

respect to zinc concentration (7.5 mM). Thermal decomposition of hexamethylenetetramine ($<100\,°C$) results in a pH increase of the solution, producing thermodynamically unstable zinc hydroxide, which spontaneously precipitates as ZnO [7].

$$NH_3 \cdot H_2O \leftrightarrow NH_4^+ + OH^- \tag{48.1}$$

$$C_6H_{12}N_4 + 6\,H_2O \rightarrow 4NH_3 + 6HCHO \tag{48.2}$$

$$NH_3 \cdot H_2O \leftrightarrow NH_3 \uparrow + H_2O \tag{48.3}$$

$$Zn^{2+} + 2OH^- \leftrightarrow Zn(OH)_2 \downarrow \tag{48.4}$$

$$Zn(OH)_2 + 4NH_3 \cdot H_2O \leftrightarrow Zn(NH_3)_4^{2+} + 4H_2O + 2OH^- \tag{48.5}$$
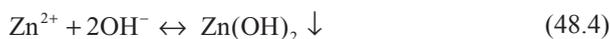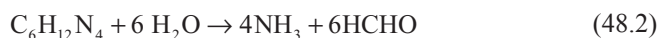
Polyethyleneimine (PEI) can chelate zinc ions in solution [8] at moderate concentrations (1–2 mM) by the amino groups that are present in the polymer chain. ZnO NWs growth in presence of PEI leads to high length NWs and high aspect ratio (up to 200). Moreover, here we demonstrate that chloride ions may result in further improvements of the ZnO nanowires length and aspect ratio. The NWs have quite sharp tip (<100 nm) and high length (>10 microns) (Fig. 48.2a). By adding KCl, due to electrostatic effects [9], it is possible to get high length alongside with pointed-tips (inset) and aspect ratio around 120 (Fig. 48.2b).
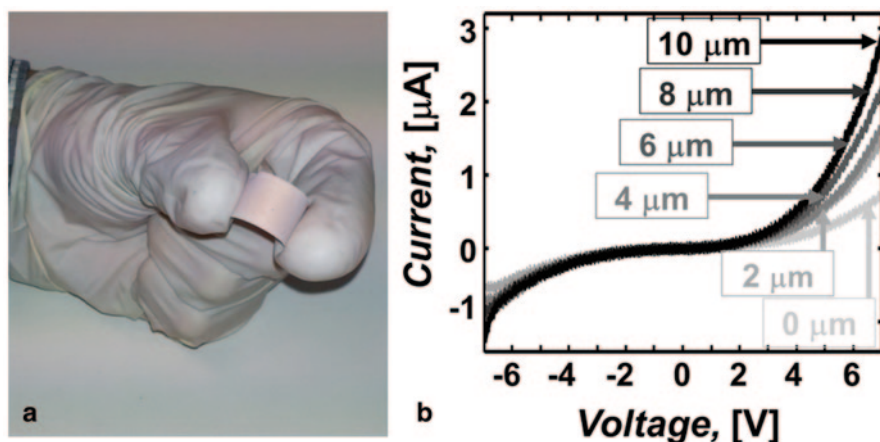
Fig. 48.3 Electrical characterization. **a** PCB displacement sensor with ZnO NWs. **b** The I–V sweep (from − 7 V to 7 V) shows sensitivity to the compression applied by a piezo-electric motor along the c-axis; the different displacements are given in the greyscale legend

48.3   Displacement Sensor

We took advantage of the method for fabricating low-cost, compression-sensitive devices based on flexible PCBs as shown in Fig. 48.3a. A piezo-motor, driven in closed-loop configuration, was used for applying controlled displacements parallel to the (average) *c*-axis of the nanowires. The ZnO NWs ensemble exhibit high sensitivity to the applied compression. Fig. 48.3b shows the measured I–V curves as a function of the different vertical displacements; the measured current clearly increases when increasing the NWs vertical stress.

48.4   Conclusions

Here we have shown the facile fabrication of high-density, long, high aspect ratio ZnO NWs onto copper PCB surfaces by a mild permanganate surface treatment and by optimizing a nutrient solution containing a zinc salt in presence of hexamethylenetetramine, ammonium hydroxide and polyethyleneimine.

We characterized the ZnO NWs by means of I–V curves, showing high sensitivity to compression.

References

1. S. Xu, Z.L. Wang, One-dimensional ZnO nanostructures: Solution growth and functional properties. Nano Research **4** (11), 1013–1098 (2011)
2. T.T. Ngo-Duc, J. Gacusan, N.P. Kobayashi, M. Sanghadasa, M. Meyyappan, M.M. Oye, Controlled growth of vertical ZnO nanowires on copper substrate. Applied Physics Letters **102** 083105 (2013)
3. T.J. Kuo, C.-N. Lin, C.L. Kuo and M.H. Huang, Growth of Ultralong ZnO Nanowires on Silicon Substrates by Vapor Transport and Their Use as Recyclable Photocatalysts, Chemistry of Materials **19** (21), 5143–5147 (2007)
4. G. Zhu, Y. Zhou, S. Wang, R. Yang, Y. Ding, X. Wang, Y. Bando and Z.L. Wang, Synthesis of vertically aligned ultra-long ZnO nanowires on heterogeneous substrates with catalyst at the root. Nanotechnology **23** (5), 55604 (2012)
5. L.Wen, K.M. Wong, Y. Fang, M. Wu, M. and Y. Lei, Fabrication and characterization of well-aligned, high density ZnO nanowire arrays and their realizations in Schottky device applications using a two-step approach. Journal of Materials Chemistry **21** (20), 7090–7097 (2011)
6. X. Wen, W. Wu, Y. Ding and Z.L. Wang, Seedless synthesis of patterned ZnO nanowire arrays on metal thin films (Au, Ag, Cu, Sn) and their application for flexible electromechanical sensing. Journal of Materials Chemistry **22** (19), 9469–9476 (2012)
7. L. Vayssieres, K. Keis, S. Lindquist and A. Hagfeldt, Purpose-Built Anisotropic Metal Oxide Material: 3D Highly Oriented Microrod Array of ZnO. J Phys Chem B **105** (17), 3350–3352 (2001)
8. K. Liu, W. Wu, B. CHen, X. Chen, N.Z. Continuous Growth and Improved PL Property of ZnO Nanoarrays with Assistance of Polyethylenimine. Nanoscale **5** (13), 5986–5993 (2013)
9. J. Joo, B.Y. Chow, M. Prakash, E.S. Boyden, Face-selective electrostatic control of hydrothermal zinc oxide nanowire synthesis. Nature Materials **10** (7), 1–6 (2011)

Chapter 49

Application of an Integrated Multi-Sensor Circuit for Tracing Quality and Safety Storage Parameters of Sliced Cheese

M. Grassi, P. Malcovati, G. F. Regnicoli and G. Perretti

In this work, storage environment and food preservation quality parameters of a specific kind of sample (Emmental sliced cheese) were monitored for 32 days under four different storage conditions thanks to the development of a dedicated multi-sensor smart tag. Dry matter, pH value, colour index, and water activity, have been analyzed to estimate the quality of preservation of the food samples over time. Furthermore, the long-term reliability and performance of the ad-hoc developed fully-integrated smart label system for food tracing has been validated. The low-power multi-sensor integrated circuit, employed to continuously monitor the conservation parameters for the sliced cheese samples, has been fabricated in 0.18 μm CMOS technology, and includes temperature, light intensity and optional humidity sensors with the respective interface circuits and a common A/D converter. Collected sensors data have been then studied together with physical and chemical analyses to find correlations between the conservation quality of food samples and the collected environmental data history.

49.1 Introduction

Smart food tracing is a powerful answer to guarantee a successful and safe delivery of degradable products. On this basis, low-cost miniaturized electronic tracing systems are becoming key elements in the food industry. These devices shall be able to identify the product, track its path along the complete food distribution chain, and monitor the environmental conditions under which the product is stored over time, in order to verify the effectiveness of preservation conditions. An integrated

M. Grassi (✉) · P. Malcovati
Department of Electrical, Computer, and Biomedical Engineering, University of Pavia, Pavia, Italy
e-mail: marco.grassi@unipv.it

G. F. Regnicoli · G. Perretti
Department of Economic and Food Science, University of Perugia, Perugia, Italy

microsystem which includes multiple sensors (temperature, light intensity and optional humidity) and very low power circuits (sensor interface circuits and A/D converter) is the first step to the implementation of a smart electronic label. Temperature, light intensity and humidity are fundamental storage parameters for the preservation of food products, and are good candidates to be quite easily measured with low-cost and low power integrated circuits. On the other hand, dry matter, pH value, colour index, and water activity are significant physical and chemical parameters to evaluate the quality of food conservation status.

49.2 The Multi-Sensor Tracing Smart Label

A multi-sensor smart label, performing temperature, light intensity, and humidity tracing has been designed, developed and characterized [1]. This prototype has been thought to grant a high versatility for the evaluation in the field of food production and delivery. In fact, temperature is the fundamental storage parameter that regulates the bioenzymatic reactions, while light intensity is a parameter of primary importance concerning the quality of preservation for food sensitive to photo oxidation and similar alterations activated by radiation, such in the case of oils and fats. Finally, humidity is an important parameter to be monitored for the storage of most kinds of food, like, for instance, intermediate bakery products. The multisensory tag has been thus designed to trace ambient temperature in the whole possible range for food distribution chain, to take note of light intensity from weak illumination of grocery shelves up to undesired, hopefully short-time direct sun-light exposure and optionally to measure relative humidity in food packaging in the $[10-90\%]$ range. The simplified block scheme of the smart tag is reported in Fig. 49.1, including a Li-Ion battery for a long term operation up to more than one year. The three environmental read-out sensors with their dedicated signal conditioning circuits are followed by a common A/D converter in order to save traced data in digital domain into a dedicated memory.

49.3 Smart Label Sensors and Read-Out Circuits Characterization

The microphotograph of the low power integrated microsystem, fabricated in 0.18 μm CMOS technology, and drawing only 50 μA (70 μA including optional humidity sensing) from a 1.8 V supply is shown in Fig. 49.2, mounted on the measurement setup main board. The chip occupies an area of 4 mm^2 including pads [1] and has been specifically characterized in controlled environment in terms of read-out absolute precision for the temperature and light intensity range of interest for food tracing environmental monitoring applications.
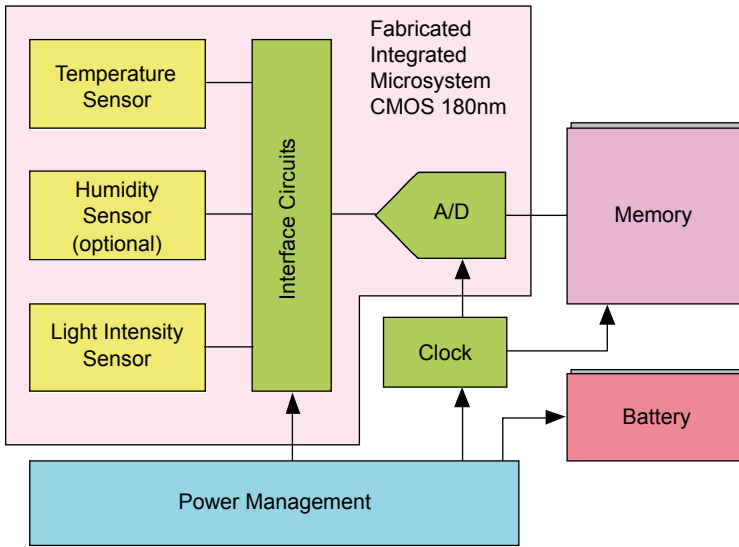
Fig. 49.1 Block diagram of the multi-sensor smart label for environmental data log
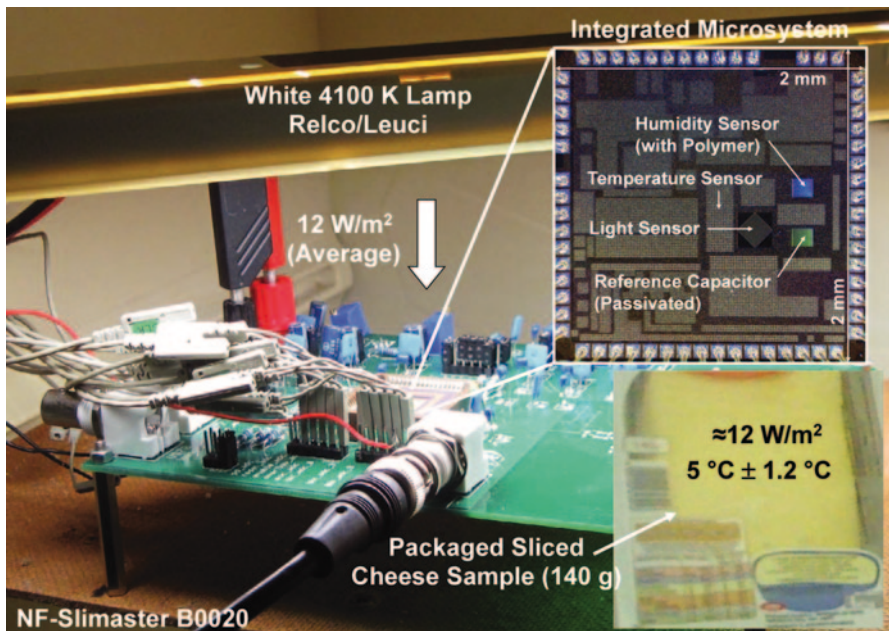
Fig. 49.2 Chip photograph and experimental setup for long term light exposure at low temperature
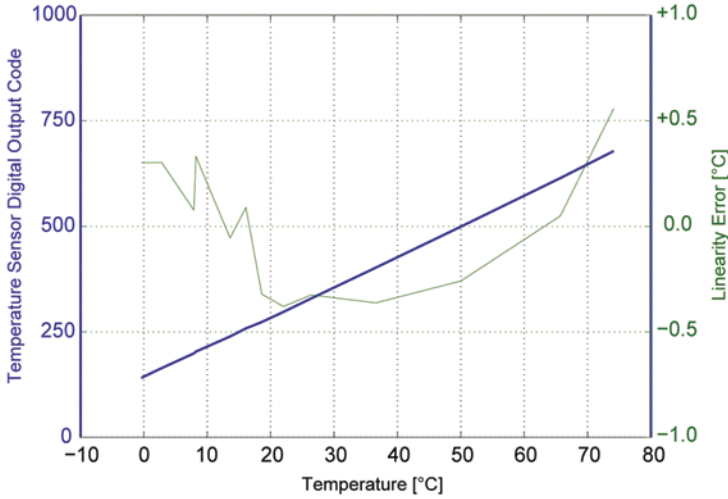
Fig. 49.3 Temperature sensor read—out response accuracy

Fig. 49.4 Light intensity sensor read—out response accuracy
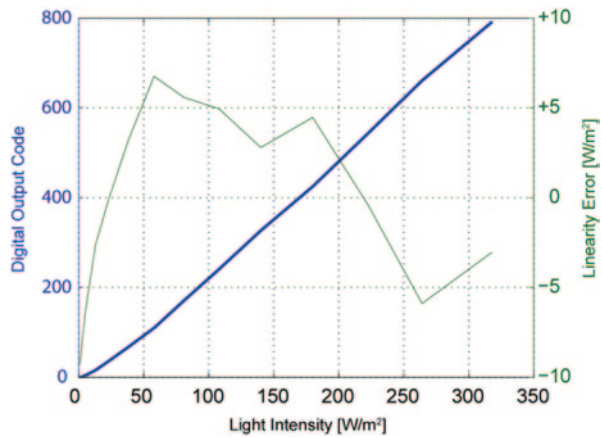
The developed microsystem showed a read-out precision of $\pm 0.5\,°C$ in the range $[-2\,°C, 75\,°C]$ and $\pm 6\ W/m^2$ in the range $[3\ W/m^2, 300\ W/m^2]$ for temperature and light intensity, respectively, as reported in Figs. 49.3 and 49.4. Finally, the successful continuous operation of the smart-label integrated circuit for the 32-days food storage case study is an encouraging reliability validation.

49.4   Long Term Environmental Storage Conditions Case Study

Packaged sliced Emmental cheese samples conservation status over 32 days has been monitored together with environmental conditions. More in detail, the food samples were kept under four different storage conditions [**LR:** exposure to *light* for 12 h/day at *room* temperature; **LF:** exposure to *light* for 12 h/day at *fridge* bank temperature; **DR:** *dark* at *room* temperature; **DF:** *dark* at *fridge* bank temperature]. When a 4100°K white light source (Relco/Leuci/13 W) is on duty (for LR, LF: 50% of time), samples are exposed to an average light intensity of 12 W/m², thus reproducing reasonable market fridge bank illumination condition.

The LR and DR, samples are just stored at the effective room temperature of 22.5 °C±2.5 °C, thus reproducing unsuitable thermal storage, while for LF and DF temperature is regulated by means of a NF-Slimaster B0020 chamber at 5.0 °C±1.5 °C thus reproducing correct temperature conservation conditions of an open fridge bank. An example of 24 hours sensors data logging is reported in Fig. 49.5. Smart tag log shows that samples have been stored at a temperature within the range T=[3.9–6.2 °C] over a complete day and that, during the daylight (lamp on, delivering about 12 W/m²), temperature chamber trend is positive, because of the significant internal lamp heating. A detail of residual temperature ripple in thermostatic chamber, characterized by a sinusoidal shape, a peak-to-peak amplitude of about 0.7 °C and a period of around 16 min, is reported in Fig. 49.6. Physical and chemical analyses show a significant increase of dry matter [2] content related to the storage time, as shown in Fig. 49.7. Moreover, the pH increases over time.
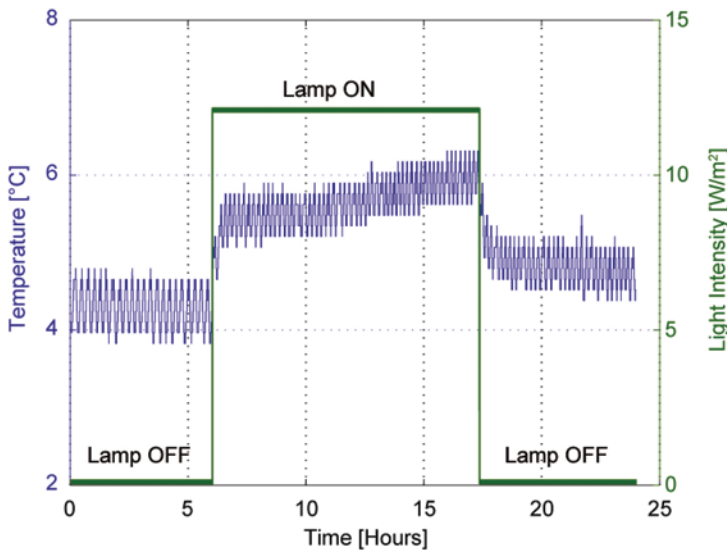
Fig. 49.5 Smart label environmental parameters log graph for 24 h
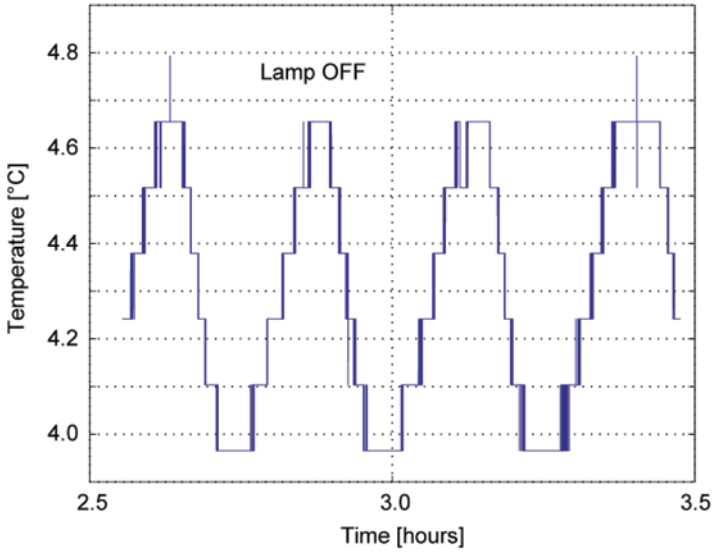
Fig. 49.6 Temperature ripple in the thermostatic chamber (1 h)
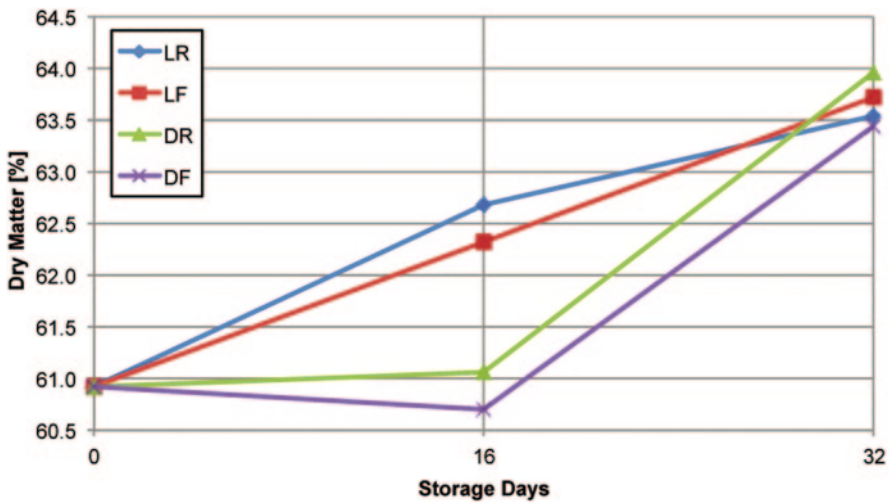
Fig. 49.7 Dry matter over time

The trend is greater for the samples stored at higher temperatures [2], with a maximum pH of 6.15 and 6.11 for samples stored at room temperature, exposed to light and dark respectively, as shown in Fig. 49.8. Significant ($P<0.05$) colour changes in the b* index occur, which indicate original yellow colour preservation for samples stored in the dark [3] and a decrease of the b* for those exposed to the
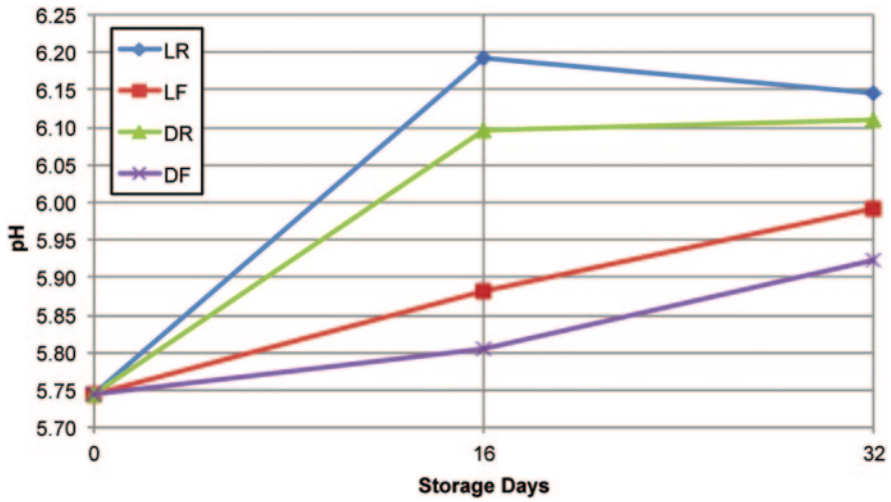
Fig. 49.8 pH over time
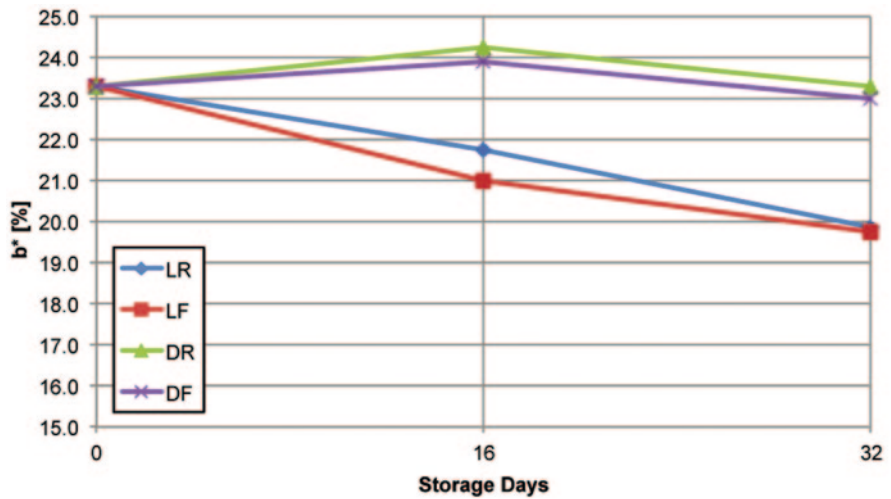
Fig. 49.9 Color index over time

light, that reaches the minimum values for b* of 19.7 for the cheese stored at 4 °C, as reported in Fig. 49.9. For the water activity, significant differences have not been detected, as reported in graph of Fig. 49.10. Physical and Chemical analyses can thus be related to the data collected by sensors and it is possible to define a correlation between the preservation conditions of the food samples and the environmental data history.
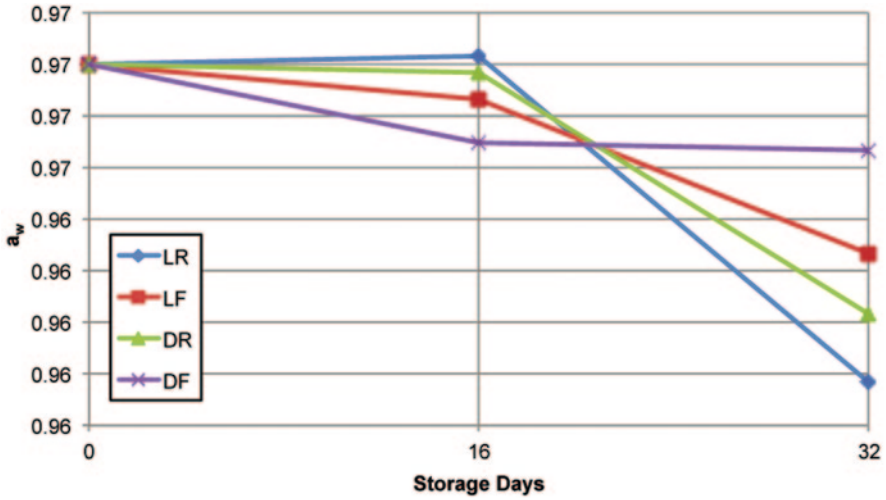
Fig. 49.10 Water activity over time

References

1. D. Cartasegna et al., "Integrated Microsystem with Humidity, Temperature and Light Sensors for Monitoring the Preservation Conditions of Food", proceedings of IEEE Sensors'11, Limerick, Nov. 2011, pp. 1859–1862, IEEE.
2. R. Rodriguez-Aguilera et al., "Effect on Modified Atmosphere Packaging on Quality Factors and Shelf Life of Mould Surface-Ripened Cheese: Part II Varying Storage Temperature", LWT – Food Science and Technology, vol. 44, issue 1, 2011, pp. 337–342, Elsevier.
3. A. Trobetas et al., "Light Induced Changes in Grated Graviera Hard Cheese Packaged Under Modified Atmospheres", International Dairy Journal, vol. 18, issue 2, 2008, pp. 1133–1139, Elsevier.

Chapter 50
Sophie: A General Purpose Sub-Picoamps Current Readout Electronics

A. Nascetti, G. Colonia, D. Caputo and G. De Cesare

SOPhIE is a eight-channel photocurrent readout electronic board that combines flexible selection of the current range (from femtoamps to hundreds of nanoamps), good noise performances and on-board sensor-bias voltage supply. Adjustable integration times allow digitizing up to 20 ksample/s with a resolution of 20 bit/sample. USB and UART data interfaces as well as eight additional general-purpose inputs and outputs pins are externally available. The noise level of the measured current, achieved when the board is connected to an array of hydrogenated amorphous silicon photodiodes, is less than 40 fA working at 5 sample/s and with a full-scale range of 1 nA. These features make SOPhIE suitable for low-level current sensing in lab-on-chip applications.

50.1 Introduction

Many sensing applications rely on the measurement of low-level currents, in the range of femtoamperes up to microamperes, produced by a transducer [1]. In the case of analytical devices, the transducer is often a thin film photodiode [2] that detects the radiation emitted by a chemiluminescent process [3, 4] or by the stimulated emission of a naturally fluorescent substance [5, 6] or a fluorescently labeled analyte [7]. Photodiodes are also used to detect the variation of an incident radiation source in absorption measurements [8]. In all the cases there is the need to reveal small current variations with a good signal to noise ratio. According to

A. Nascetti (✉)
Dipartimento di Ingegneria Astronautica Elettrica ed Energetica, Sapienza Università di Roma, Via Salaria 881, 00138 Roma, Italy
e-mail: augusto.nascetti@uniroma1.it

G. Colonia · D. Caputo · G. De Cesare
Dipartimento di Ingegneria dell'Informazione, Elettronica e Telecomunicazioni, Sapienza Università di Roma, Via Eudossiana 18, 00184 Roma, Italy
e-mail: caputo@die.uniroma1.it

these considerations, we developed SOPhIE (Simple Octal Photo-current Integration Electronics): a eight-channel photocurrent readout electronic board that combines flexible selection of the current range, good noise performances and on-board sensor-bias voltage supply.

50.2   System Description and Characterization

The circuit is built around the DDC118 *Current-Input Analog-to-Digital Converter from Texas Instruments* [9] used as low-noise sensor front-end. The chip has eight identical input channels each including a dual-switched integrator. It performs continuous signal integration (zero dead-time) over a wide range of currents (from femtoamps to hundreds of nanoamps) with adjustable integration times that allow digitizing up to 20 ksample/s with a resolution of 20 bit/sample. The timing and control signals are generated by a PIC18F4550 microcontroller from Microchip that also provides the communication interfaces, both USB and UART, to the host device. The microcontroller controls also a low noise Digital-to-Analog converter followed by an operational amplifier suited for driving large capacitive loads for the generation of the photodiode reverse bias voltage. Eight additional general purpose inputs and outputs (GPIO) pins are externally available for driving external hardware as pumps, radiation sources or reading digital alarms or analog sensors as humidity or temperature sensors. The microcontroller firmware has been developed to achieve the best behavior of the different devices, in terms of noise, speed and power consumption. On-board voltage regulator and electro-magnetic-interference (EMI) filter allow to supply the board either from the USB port or with an external unregulated AC/DC converter. A careful layout has been carried out in order to ensure optimal noise performances as well as a compact printed circuit board as shown in Fig 50.1.

Circuit characterization has been first performed using a Keithley 236 SMU as current source. Using 50 pf integration capacitance and 800 ms integration time (full-scale range equal to 250 pA) the output standard deviation measured with a constant input current of 10 pA was 15 fA, which is compatible with the noise level of the current source used for the tests. In Fig. 50.1 (right) the results achieved using the same parameters with an input current ranging from 105.0 pA up to 105.9 pA with 100 fA steps are shown.

50.3   Practical Application Example

In order to test the board in practical operating conditions, the readout circuit has been connected to an array of 30 thin film hydrogenated amorphous silicon photodiodes deposited on a glass substrate [10, 11]. The glass chip has been inserted in a card edge connector placed on an ad-hoc developed adapter board that has been
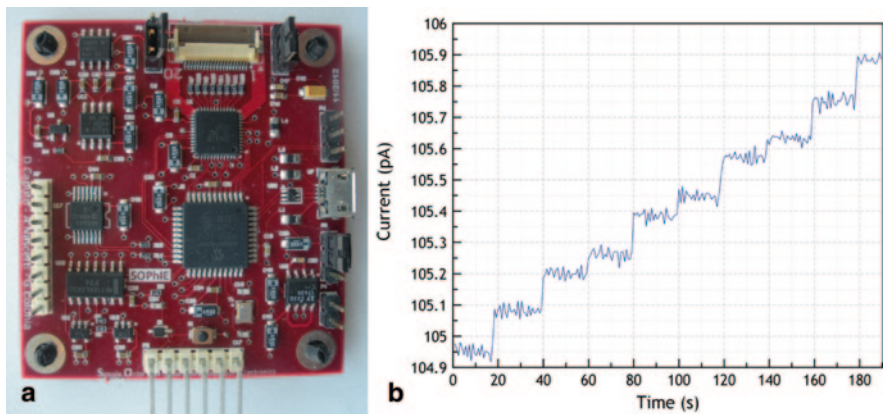
Fig. 50.1 *Left*: SOPhIE. Main specs include: continuous acquisition (no dead-time), range from femtoamps to microamps, integration time from 400 μs to 1 s, low noise bias supply (unlimited capacitive load), USB and UART interface, eight fully configurable GPIO pins, USB or external unregulated power supply, low power consumption, compact board size (70×70 mm^2). *Right*: electrical characterization results, the input current is sourced by a Keithley 236 Source Measure Unit. SOPhIE signal integration time is 800 ms and integration capacitance is 50 pF corresponding to a full-scale range equal to 250 pA

connected with a flex cable to the input connector of the SOPhIE board. A set of jumpers allows to connect eight photodiodes of the array to the eight input channels of SOPhIE. The photodiodes have been biased at low reverse voltage (25 mV) and the readout has been done using the 50 pF integration capacitance and 200 ms integration time with a resulting full-scale range of 1 nA. Due to the relatively large size of the thin-film photodiodes (2×2 mm^2), the estimated total capacitive load at the output of the on-board bias circuit, represented by the whole array, was larger than 10 nF [12]. The capacitive load at each input channel of SOPhIE was around 500 pF. In these conditions, the standard deviation of the measured dark current was less than 40 fA. By using a n-sample adjacent averaging post processing filter the noise can be reduced by a factor equal to the square root of n. As an example, using with 5-sample adjacent averaging, the measurement noise level decreases to about 15 fA. Figure 50.2 reports the results achieved using a 650 nm infrared light emitting diode to generate a photocurrent as low as about 75 fA. In the figure the raw data as well as the 5-sample adjacent averaging filtered values are reported, showing the ability of the circuit to detect low-level signals over a wide range.

50.4 Conclusions

We have presented a compact readout board, SOPhIE, that is suitable for current readout in lab-on-chip applications. Thanks to its flexibility in terms of readout speed and current range selection as well as to the additional features as low-noise
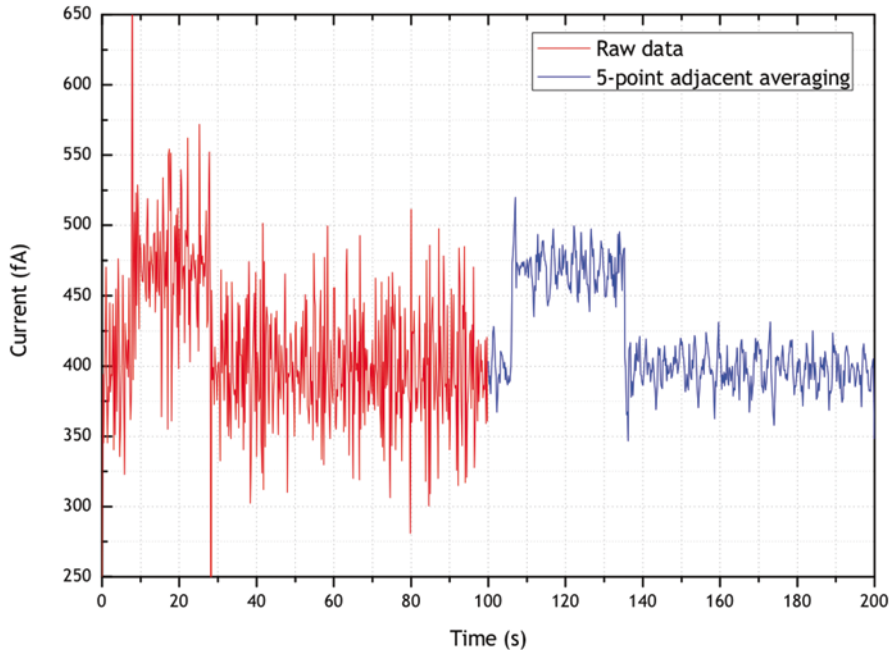
Fig. 50.2 Photodiode current acquired with SOPhIE with 50pF integration capacitance and 200 ms integration time (full-scale range equal to 1nA). The photocurrent signal is induced by a 650 nm LED. Up to 100 s the raw data, while after 100 s the 5-sample moving average are reported

bias voltage supply, USB and UART communication interfaces, additional GPIO channels and low power consumption, the board can be used for low-level current sensing applications not limited to photodiode readout.

References

1. H. Schafer, L. Scholer, K. Seibel, M. Bohm, "A monolithically integrated CMOS labchip using sensor devices", *Applied Surface Science*, **255**(3), 646–648 (2008)
2. T. Kamei, B.M. Paegel, J.R. Scherer, A..M. Skelley, R.A. Street, R.A. Mathies, "Integrated Hydrogenated Amorphous Si Photodiode Detector for Microfluidic Bioanalytical Devices", *Analytical Chemistry*, vol. 75 (20), pp. 5300–5305 (2003)
3. D. Caputo, G. de Cesare, R. Scipinotti, N. Stasio, F. Costantini, C. Manetti "On Chip Diagnosis Of Celiac Disease By An Amorphous Silicon Chemiluminescence Detector", AISEM 2013, Lecture Notes in Electrical Engineering, **268**, 183–187 (2014)
4. A.T. Pereira, A.C. Pimentel, V. Chu, D.M.F. Prazeres, J.P. Conde, "Chemiluminescent Detection of Horseradish Peroxidase Using an Integrated Amorphous Silicon Thin-Film Photosensor,", IEEE Sensors Journal,.**9**(10), 1282–1290 (2009)

5. D. Caputo, G. de Cesare, C. Fanelli, A. Nascetti, A. Ricelli, R. Scipinotti, "Amorphous silicon photosensors for detection of Ochratoxin A in wine", IEEE Sensor Journal, **12** (8), 2674–2679 (2012)

6. D. Caputo, G. de Cesare, C. Manetti, A. Nascetti, R. Scipinotti; "Smart thin layer chromatography plate" Lab on a Chip, **7**, 978 (2007)

7. D. Caputo, G. de Cesare, A. Nascetti, R. Negri; "Spectral tuned amorphous silicon p-i-n for DNA detection", Journal of Non Crystalline Solids; **352**, 2004 (2006)

8. G. de Cesare, D. Caputo, A. Nascetti, C. Guiducci, B. Riccò, "Hydrogenated amorphous silicon ultraviolet sensor for deoxyribonucleic acid analysis", Appl. Phys. Lett., **88**, 083904, (2006)

9.   http://www.ti.com/lit/ds/symlink/ddc118.pdf

10. D. Caputo, G. De Cesare, L.S. Dolci, M. Mirasoli, A. Nascetti, A. Roda, R. Scipinotti, "Microfluidic chip with integrated a-Si:H photodiodes for chemiluminescence-based bioassays", IEEE Sensors Journal, **13** (7), 2595–2602 (2013)

11. F. Costantini, A. Nascetti, R. Scipinotti, F. Domenici, S. Sennato, L. Gazza, F. Bordi, N. Pogna, C. Manetti, D. Caputo, G. de Cesare, "On-chip detection of multiple serum antibodies against epitopes of celiac disease by an array of amorphous silicon sensors", RSC Advances, **4** (4), 2073–2080 (2014)

12. R.A. Street, in "Hydrogenated amorphous silicon" Cambridge University Press, (1991)

Chapter 51
Non-Inverting CCII-based Astable Multivibrator and Its Application as Uncalibrated Wide-Range Capacitive Sensor Interface

Andrea De Marcellis, Giuseppe Ferri and Paolo Mantenuto

A novel wide-range capacitive sensor interface employing a non-inverting Second Generation Current Conveyor (*CCII*)-based astable multivibrator is here presented. With respect to typical Capacitance-to-time (*C-T*) conversion techniques, the circuit has been designed employing a reduced number of both active (only one *CCII*) and passive (three resistances and the capacitive sensor) devices, in order to keep power consumption reduced and allowing the development of a long-life portable tool. Test results, conducted on PCB, through the commercial AD844, have shown that the circuit is able to estimate large capacitance variations within [100 pF–10 μF] (about 5 decades), maintaining a reduced relative error. This makes the interface *uncalibrated* since a number of capacitive sensors can be employed maintaining the same oscillator features and making it suitable in those applications where the sensor baseline cannot be accurately estimated or is not well known a priori.

51.1 Introduction

Circuit miniaturization developments have led to the design of high accurate and small size sensor devices as MEMS [1–3]. They can be, typically, described as a planar capacitor (i.e., $C = \varepsilon A/d$, being ε the relative dielectric constant, A the actual parallel surface involved by the electric field and d the distance between capacitor metal plates) whose mechanical features are temporarily changed due to the measurand variation. In the literature, capacitive sensor interfaces typically concern

A. De Marcellis (✉) · G. Ferri · P. Mantenuto
Department of Industrial and Information Engineering and Economics—DIIIE,
University of L'Aquila, L'Aquila, Italy
e-mail: andrea.demarcellis@univaq.it

G. Ferri
e-mail: giuseppe.ferri@univaq.it

P. Mantenuto
e-mail: paolo.mantenuto@univaq.it

Capacitance-to-time (*C-T*) conversion techniques [4–6], where the measurand detection is possible through the output waveform period tracking. Here, a novel current-mode non-inverting astable multivibrator, based on a Second Generation Current Conveyor (*CCII*) [7–12], and its application as wide-range capacitive sensor interface [3], has been presented. The interface consists of only one *CCII*, three resistances and one capacitance (i.e., the capacitive sensor). The circuit working principle is based on a *CCII*-based inverting Schmitt trigger design [13–15]. Preliminary experimental tests on discrete PCB, performed by employing the AD844 as *CCII* [16, 17] and simple passive components, have shown good linearity and accuracy in the estimation of about 5 capacitive decades, within the interval [100 pF–10 µF].

51.2 CCII-based Proposed Interface

The CCII, whose symbol is shown in Fig. 51.1a, represents the fundamental block in the current-mode circuit design. Its ideal constitutive relationships are expressed in Eq. 51.1 and show that Y terminal voltage is buffered to X terminal while X node current is mirrored to the Z node. In particular, we refer to *CCII*+/− when current at Z terminal has the same/opposite X current flow. In Fig. 51.1b the proposed inverting Schmitt trigger-based oscillator is shown.

$$\begin{bmatrix} I_Y \\ V_X \\ I_Z \end{bmatrix} = \begin{bmatrix} 0 & 0 & 0 \\ 1 & 0 & 0 \\ 0 & \pm 1 & 0 \end{bmatrix} \cdot \begin{bmatrix} V_Y \\ I_X \\ V_Z \end{bmatrix} \tag{51.1}$$

According to Fig. 51.1b, the capacitance C_{SENS} is charged through the current which flows from both X and Z nodes, while R_1, R_2 and R_3 resistances have to be properly
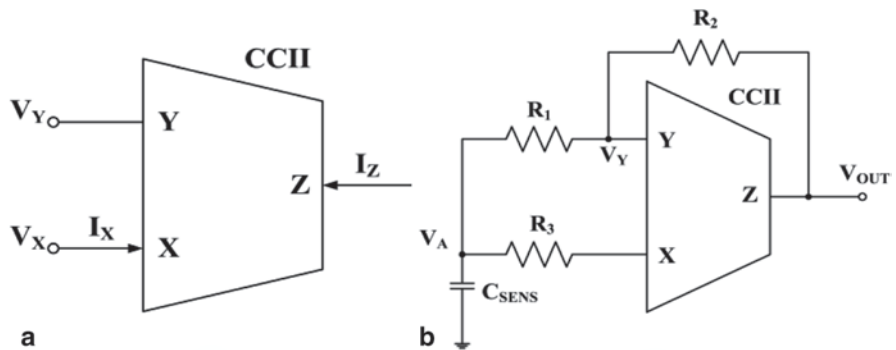
Fig. 51.1 a CCII symbol. **b** proposed current-mode non-inverting Schmitt oscillator configuration

set in order to impose I_Z and I_X maximum current values (i.e., the circuit power consumption and device life). In this manner, a current flows into the capacitor until the voltage V_A reaches the correspondent upper threshold voltage. This causes a current flux inversion, which discharges the capacitance until the lower threshold is reached, and so on. In particular, the resistance values set both the comparator threshold (see Eq. 51.2, where V_{OUT} is the output saturation voltage, $V_{SAT}^{\pm}$) and the output waveform period. In particular, by setting $R_1 \gg (R_2, R_3)$, the circuit oscillation period equation can be simplified, as shown in Eq. 51.3, performing a linear relationship with respect to C_{SENS}, R_1 and R_2.

$$V_{TH} = V_{OUT} \cdot \left(\frac{R_1 - R_3}{R_2 + R_3} \right) \tag{51.2}$$

$$T \approx (R_1 + R_2) \cdot C_{SENS} \tag{51.3}$$

51.3 Experimental Results

Figure 51.2 shows the oscillator main nodes time behavior. When V_A voltage arrives at the upper threshold, the output commutates until the lower threshold is reached and so on. Theoretical time responses and experimental measurements related to the period T of the output square waveform vs. capacitive sensor C_{SENS}, conducted through the use of the AD844 as *CCII*, are shown in Fig. 51.3. It can be seen that these quantities are in good agreement and a linear correspondence between the two trends is obtained for about 5 variation capacitive decades [100 pF, 10 µF], maintaining a reduced relative error in the range $(-8\%, +6\%)$.

Fig. 51.2 Experimental circuit main nodes behavior
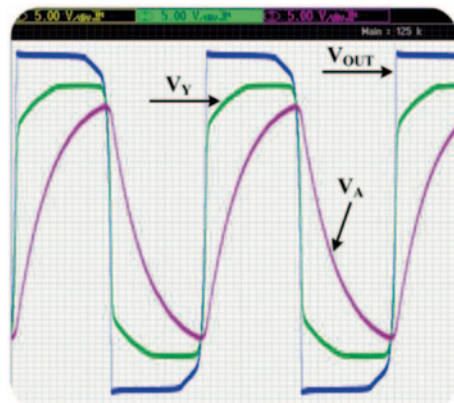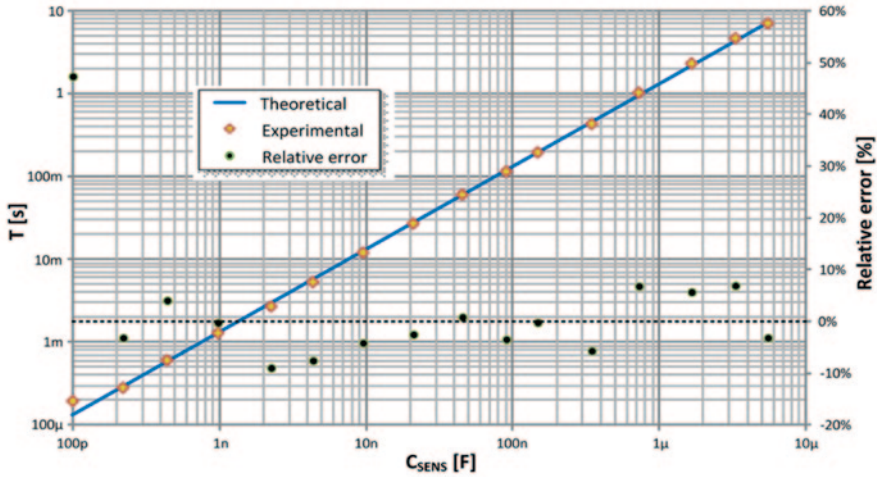
Fig. 51.3 Theoretical (continuous) and experimental (*yellow diamonds*) output waveform period (*left axis*) and relative error (*black dots, right axis*) vs. sensor capacitive value

51.4 Conclusions

In this paper, a novel simple architecture for a *CCII*-based non-inverting Schmitt trigger astable multivibrator has been proposed. Experimental tests conducted on a PCB, employing the commercial AD844, have shown the circuit capability to be employed as a capacitive interface performing the Capacitive-to-Time conversion. In particular, good linearity and accuracy in the estimation of about 5 capacitive decades have been provided.

References

1. S. Lachhman, C.A. Zorman, W.H. Ko, Multi-layered poly-dimethylsiloxane as a non-hermetic packaging material for medical MEMS, IEEE Engineering in Medicine and Biology Society. Conference 2012, 1655–1658 (2012)
2. A. Alogla, P. Scanlan, W.M. Shu, R.L. Reuben, A scalable syringe-actuated microgripper for biological manipulation, Sens Actuators A Phys **202**, 135–139 (2013)
3. T.A. Emadi, D.A. Buchanan, Multiple moving membrane CMUT with enlarged membrane displacement and low pull-down voltage, IEEE Electron Device Lett **34**, 1578–1580 (2013)
4. A. De Marcellis, G. Ferri, Analog Circuits and Systems for Voltage-Mode and Current-Mode Sensor Interfacing Applications, Springer, (2011).
5. A. De Marcellis, G. Ferri, P. Mantenuto, L. Giancaterini, C. Cantalini, WO$_3$ hydrogen resistive gas sensor and its wide-range current-mode electronic read-out circuit, IEEE Sensors Journal **13**, 2792–2798 (2013).
6. E.D. Kyriakis-Bitzaros, N.A. Stathopoulos, S. Pavlos, D. Goustouridis, S. Chatzandroulis, A reconfigurable multichannel capacitive sensor array interface, IEEE Transactions on Instrumentation and Measurement **60**, 3214–3221 (2011).

7. G. Ferri, N. Guerrini, Low-voltage low-power CMOS current-conveyors, Kluwer Academic Publisher (2003)
8. F. Kaçar, H. Kuntman, A new fully differential second generation current conveyor and its application. Paper presented at the 11th International Conference on Optimization of Electrical and Electronic Equipment, OPTIM 2008, 3–8 (2008).
9. A.M. Soliman, The inverting second generation current conveyors as universal building blocks. AEU—International Journal of Electronics and Communications **62**, 114–121 (2008)
10. A. De Marcellis, G. Ferri, N. C. Guerrini, G. Scotti, V. Stornelli, A. Trifiletti, A novel low-voltage low-power fully differential voltage and current gained CCII for floating impedance simulations, Microelectronics Journal **40**, 20–25 (2009).
11. C. Di Carlo, A. De Marcellis, V. Stornelli, G. Ferri, D. Tiberio, A novel LV LP CMOS internal topology of CCII + and its application in current-mode integrated circuits, Proc. IEEE PRIME 2009, 132–135 (2009).
12. F. Kaçar, B. Metin, H. Kuntman, O. Cicekoglu, A new high-performance CMOS fully differential second-generation current conveyor with application example of biquad filter realisation. International Journal of Electronics **97**, 499–510 (2010)
13. S. Del Re, A. De Marcellis, G. Ferri, V. Stornelli, Low voltage integrated astable multivibrator based on a single CCII, IEEE PRIME 2007, 177–180 (2007).
14. A. De Marcellis, G. Ferri, P. Mantenuto, F. Valente, C. Cantalini, L. Giancaterini, CCII-based interface for capacitive/resistive sensors, Proc. IEEE SENSORS 2011, 1133–1136 (2011).
15. A. De Marcellis, C. Di Carlo, G. Ferri, V. Stornelli, A CCII-based wide frequency range square waveform generator, International Journal of Circuit Theory and Applications **41**, 1–13 (2013)
16. J.A. Svoboda, L. McGory, S. Webb, Applications of a commercially available current conveyor, International Journal of Electronics **70**, pp. 159–164 (1991).
17. Internet resource: AD844 datasheet: http://www.analog.com.

Chapter 52
Above 160 dB Dynamic-Range Gas-Sensor-Grid Front-end Integrated Circuit with 500 °C, 1.5 °C/Pitch Temperature Gradient Synthesis, 20-Channel MUX, and I²C Interface

F. Conso, M. Grassi, C. De Berti, P. Malcovati and A. Baschirotto

A low-cost, reconfigurable integrated read-out circuit optimized for bi-dimensional arrays of metal-oxide (MOX) gas-sensors has been developed. The self-consistent ASIC for gas-sensor array interfacing, including temperature synthesis, has been fabricated in a 0.35 μm CMOS technology with 3.3 V supply and characterized. The device provides a measured read-out dynamic range of 162 dB and effective independent row temperature regulation of 1.5 °C within the range [25 °C ÷ 500 °C]. The ASIC can be completely configured and read-out through an embedded I²C interface. The gas-sensor read-out circuit consists of a resistance to digital converter and an intrinsic very low insertion loss 20-channel analog multiplexer, while the temperature regulation circuit consists of five closed-loop independent modules reading and driving their associated thermometers and heating actuators respectively, with the aim of reaching the assigned set-point temperature values in less than 50 ms with maximum 1 °C peak residual ripple.

52.1 Introduction

A fundamental aspect in the development of a novel gas-sensing system, especially for extensive analysis of air pollution in urban areas or in hostile environments, is portability. In these IC-based instruments the digitized outputs of several different unitary elements arranged in a sensor linear or bi-dimensional array are properly processed with dedicated digital pattern recognition algorithms. According to these requirements, a low-cost, reconfigurable integrated read-out circuit optimized for bi-dimensional arrays of MOX gas-sensors has been developed. The choice of

M. Grassi (✉) · F. Conso · C. De Berti · P. Malcovati
Department of Electrical, Computer, and Biomedical Engineering, University of Pavia, Pavia, Italy
e-mail: marco.grassi@unipv.it

A. Baschirotto
Department of Physics, University of Milano-Bicocca, Milano, Italy

Fig. 52.1 5×5 heteroge-
neous MOX gas-sensors grid
to be read-out
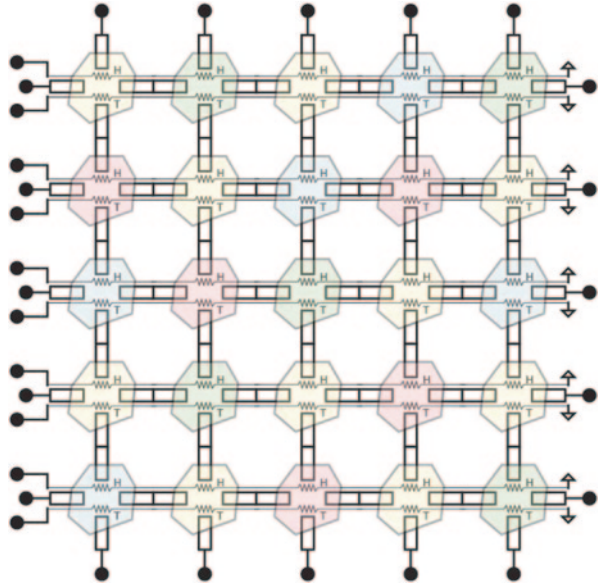
employing MOX elements is due to their versatility and compliance with integrated electronic systems, aiming to turn fixed bulky sensing spots, equipped with expensive laboratory instrumentation, into distributed portable devices. The idea of moving towards a bi-dimensional approach exploiting dynamic temperature patterns together with the choice of different kinds of metal for the membranes of the MOX elements [1] has instead with the objective of improving sensors selectivity. In order to meet these new portable instruments cutting edge requirements, a 0.35 μm CMOS complete 2D-gas-sensor array front-end ASIC has been developed. This candidate device for near tomorrow gas sensing smart instruments [2] has to provide better than 1 % precision in sensor resistance value measurement over a range of 6-decades, i.e. more than 160 dB Dynamic Range (DR).

52.2   Gas-Sensor-Grid Front-End Circuit

The developed integrated circuit converts into the digital domain the electrical information coming from a 5×5 bi-dimensional grid of MOX thick-film spots of different materials, hereinafter called membranes or elements, laid on standard dielectric substrate of silicon dioxide. The layout scheme of the 5×5 grid is shown in Fig. 52.1. The structure of the array is created connecting each membrane to adjacent sensing elements or to boundary leads through four interconnections towards cardinal directions. Heaters and temperature sensors of each row have been
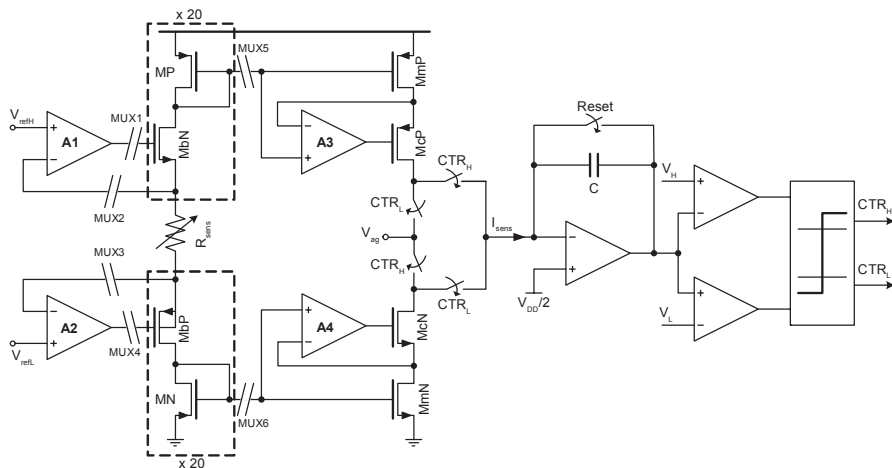
Fig. 52.2 Schematic of the sensor-grid read-out circuit

connected in series, so the membranes of each line will operate at identical temperature. Considering any possible couple of terminals on the perimeter and taking into account the polarity, 380 configurations may be setup. The use of a single shared read-out electronics for the matrix brings to a challenging input analog multiplexer design, but it strongly reduces the amount of area and power consumption for the overall device.

The gas-sensor read-out circuit of the developed ASIC consists of a resistance to digital converter and an intrinsic very low insertion loss 20-channel analog multiplexer, while the temperature regulation circuit consists of five closed loop independent modules reading and driving their associated thermometers and heating actuators, respectively. The schematic of the developed read-out circuit, based on resistance-to-digital conversion is illustrated in Fig. 52.2. The circuit includes the 20-channel very low leakage analog selector, a set of current mirrors, a Miller integrator, a couple of discriminators, and a control logic unit. In the developed ASIC, whose design specifications and implementation details are reported in [3], each equivalent chemo-resistive sensors combination to be measured is biased with a constant voltage drop to achieve higher linearity with respect to solutions with a variable bias over time. For the temperature regulation, five independent modules have been included, allowing the interconnection with up to a five-row sensor grid. Each module consists of a platinum thermometer read-out circuit, followed by a conditioning block to adjust the temperature signal dynamic swing for different sensor types, and by a 9-bit incremental A/D converter. The thermometer digital value is compared with a 9-bit digital set-point to regulate the duty cycle of the CMOS chain driving the heater power actuator device through a pulse-width modulation (PWM) control technique.

Fig. 52.3 Gas-sensing system ASIC microphotograph
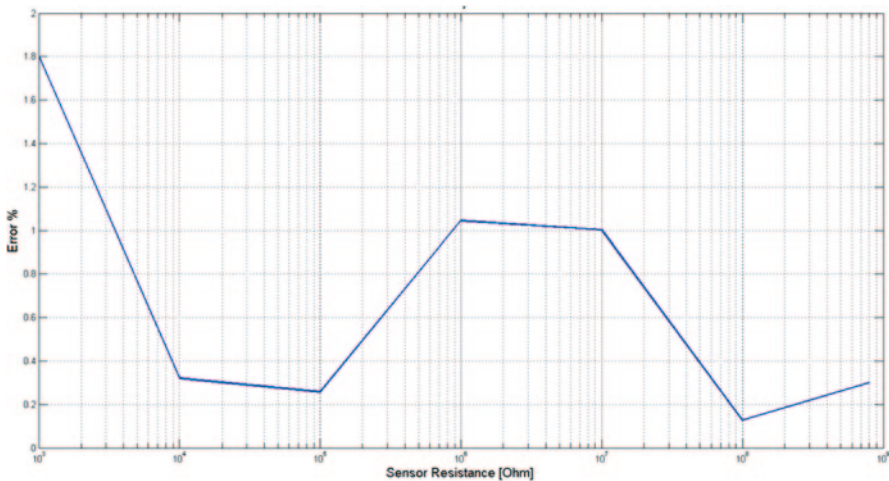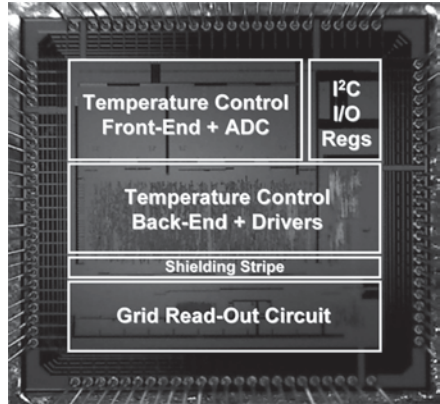
Fig. 52.4 Linearity error for sensor resistance read-out in [1 kΩ–1 GΩ] range

52.3 Measurements Results

The ASIC for gas-sensor array interfacing, including temperature synthesis, reported in this work, has been fabricated in a 0.35 μm CMOS technology with 3.3 V supply and characterized. The ASIC microphotograph is shown in Fig. 52.3. The device has a core area of only 5.75 mm^2 and consumes about 2 mW per sensing element. Linearity feature for the read-out circuit has been measured applying at the input of two addressed read-out terminals of the MUX high precision resistors of suitable log-stepped values in the range (1 kΩ–1 GΩ). Figure 52.4 shows that, over a range of 6-decades, the sensor resistance (R_{sens}) linearity measurement error is only $\pm 0.85\%$, i.e. about 162 dB DR. The performance of the read-out circuit does not depend on the grid-connection multiplexer configuration. This result widely satis-
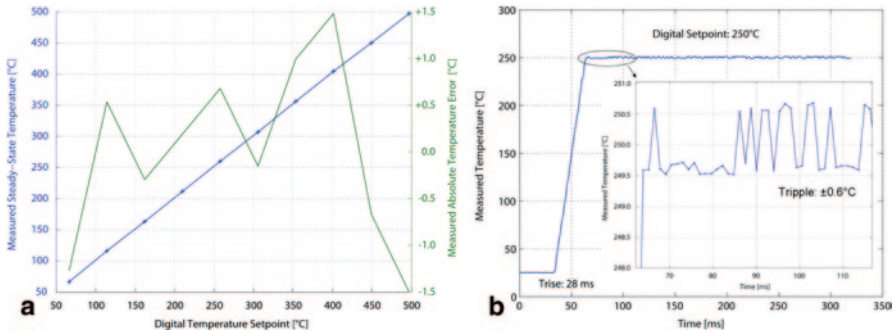
Fig. 52.5 Measured temperature synthesis accuracy over digital setpoint range (*left*)—Measured temperature response on digital setpoint step (25–250 °C) and residual ripple (*right*)

fies environmental monitoring gas sensing requirements in terms of sensor read-out precision and input resistance interval without the need of calibration techniques. Moreover, if we consider the worst-case MUX contribution, with a comprehensive linearity error of 0.94 %, the DR performance is still above 160 dB. Concerning thermal regulation, the left side of Fig. 52.5 reports the measured accuracy for steady-state temperature: the module shows a maximum temperature synthesis absolute error of 1.5 °C over the full digital set-point interval [25−500 °C]. Finally, the right side of Fig. 52.5 shows the measured temperature transient from 25 to 250 °C, actuated in less than 30 ms, and the residual steady-state ripple detail, which has a peak amplitude of less than 0.6 °C.

References

1. C. Di Natale, F. Davide, A. D'Amico. Pattern Recognition in Gas-Sensing: Well-StatedTechniques and Advances, Sensors and Actuators B: Chemical, vol. 23, issue 2–3, 1995, pp. 111–118, Elsevier.
2. P. Malcovati, M. Grassi, A. Baschirotto. Towards high-dynamic range CMOS integrated interface circuits for gas sensors, Sensors and Actuators B, Vol. 179, special issue in honour of prof. A. D'amico, March 2013, pp. 301–312, Elsevier.
3. F. Conso, M. Grassi, C. De Berti, P. Malcovati, A. Baschirotto. I²C System-on-Chip for bi-dimensional gas-sensor arrays providing extended dynamic-range A/D conversion and row temperature regulation, Proceedings of ICICDT'13, pp. 211–214, May 2013, IEEE.

Chapter 53
A Novel Compact Instrumentation Amplifier for Optimal Interfacing of Thermoelectric Sensors

M. Piotto, F. Butti, F. Del Cesta, A. N. Longhitano and P. Bruschi

An original architecture for the design of low-noise, low offset instrumentation amplifiers is described. The amplifier, based on a modified indirect current feedback structure, exploits chopper modulation to reject input offset voltage and low frequency noise. The key features of the proposed topology are: (i) embedding of the chopper modulation scheme into a 2nd order Gm-C low pass filter to obtain intrinsic chopper ripple rejection; (ii) equalization of the input and feedback common mode voltages for improved gain accuracy; (iii) biasing of the input devices in deep subthreshold region, to improve noise vs. power consumption efficiency. The effectiveness of the approach is illustrated by means of accurate electrical simulations.

53.1 Introduction

Thermoelectric sensors are widely used for the detection of a large variety of physical and chemical quantities, such as infrared radiation, flow rate and gas concentration. Interfacing of this kind of sensors involves the acquisition of voltages with sub-microvolt resolution, a task that is typically accomplished by means of instrumentation amplifiers [1]. The poor performances of MOSFETs, in terms of both gate referred offset voltage and flicker noise density, impose the use of dynamic techniques, such as chopper modulation, which has the drawback of producing an output signal affected by large disturbances at the clock frequency or higher harmonics (chopper ripple). The latter must be filtered by a low pass filter, which generally requires much more chip area than the amplifier core.

M. Piotto (✉)
IEIIT-Pisa, CNR, via Caruso 16, Pisa, Italy
e-mail: massimo.piotto@cnr.it

F. Butti · F. Del Cesta · A. N. Longhitano · P. Bruschi
Dipartimento di Ingegneria dell'Informazione, Università di Pisa, via Caruso 16, Pisa, Italy
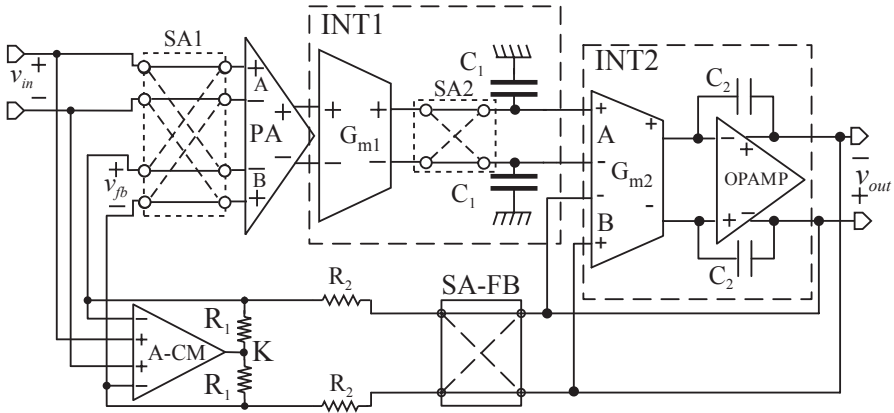
Fig. 53.1 Block diagram of the proposed instrumentation amplifier

In this work we demonstrate the feasibility of a chopper stabilized instrumentation amplifier, based on a recently proposed approach [2, 3] that embeds the filter into the amplifier, extending the benefits of chopper modulation to the filter itself, thus relaxing noise constraints on the latter and optimizing total area requirements.

53.2 Description of the Amplifier Architecture

A block diagram of the amplifier is shown in Fig. 53.1. Two integrators INT1 and INT2, based on a Gm C and Gm-Op-Amp topology, respectively, form a second order low pass filter with gain. The d.c. gain in ideal conditions is $R_2/R_1 = 200$, coinciding with the inverse of the feedback path gain.

Since it has been demonstrated that the only significant noise contribution comes from the first integrator, chopper modulation has been applied only to this block through modulators (switch matrices) SA1, SA2 and SA-FB. It can be easily shown that all disturbances deriving from the demodulator SA2 (chopper ripple, clock feedthrough) are filtered by the overall transfer function of the amplifier. A low pass Butterworth frequency response with a cut-off frequency of 200 Hz has been chosen. This bandwidth is perfectly adequate for a large variety of thermoelectric sensors and, at the same time, provides effective rejection of all artifacts at modulation frequency (20 kHz). Note that SA1 modulates the input signal V_{in} and alternates the preamplifier (PA) input ports between V_{in} and the feedback voltage V_{fb}. This alternation implements a DEM (Dynamic Element Matching) approach [2–4], reducing the impact of port mismatch on the overall gain. However, a remaining source of port mismatch originates from differences in the input and feedback common mode voltages. The main innovation of the amplifier proposed in this work is the use of a local common mode feedback loop (based on the A-CM
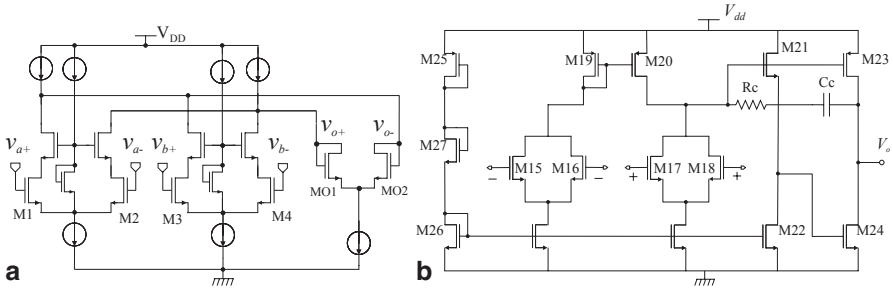
Fig. 53.2 Block diagram of the proposed instrumentation amplifier

amplifier) that forces the feedback common mode voltage to track the input common mode voltage (V_{CM}), eliminating the error due to common mode mismatch. The feedback voltage is modulated (SA-FB modulator) prior to the feedback attenuator (formed by resistors R_1 and R_2) in order to cancel the offset introduced by asymmetries of attenuator itself.

A telescopic cascode difference differential amplifier (DDA), shown in Fig. 53.2a, has been used for the preamplifier (gain=600). Input transistors operating in deep sub-threshold region have been used for this stage, in order to obtain an optimum trade-off between noise and power consumption, The common mode difference amplifier (A-CM) is a conventional class-AB operational amplifier with duplicated input devices, as shown in Fig. 53.2b.

53.3 Prototype Design and Performance Estimation

The amplifier has been designed using CMOS 0.32 μm devices from the Bipolar-DMOS-CMOS BCD6s process of STMicroelectronics and operates with a 3.3 single power supply voltage. Power consumption is 600 μW. The area occupation, estimated from the final layout, is 1.5×0.43 mm². Stationary State Transient (SST) simulations have been used to estimate the frequency response and output noise density shown in Fig. 53.3. In terms of noise, the absence of flicker contributions down to 1 Hz can be observed. The offset ripple on the output signal, estimated by means of Monte Carlo transient simulations, was smaller than 200 μV (less than 1 μV input referred). The low offset and high gain precision characteristics of the amplifier, estimated with SST Monte Carlo simulations, are demonstrated by the histograms in Fig. 53.4.

The effectiveness of the input common mode equalization approach is represented by the data in Table 53.1, where the gain error for various input common mode voltage is reported. The error is calculated as the deviation with respect to the gain at $V_{CM}=1.4$ V. These data clearly show that the effects of the input common mode voltage on the gain are less than 0.2 % for V_{CM} varying from 0.8 to 2.2 V.
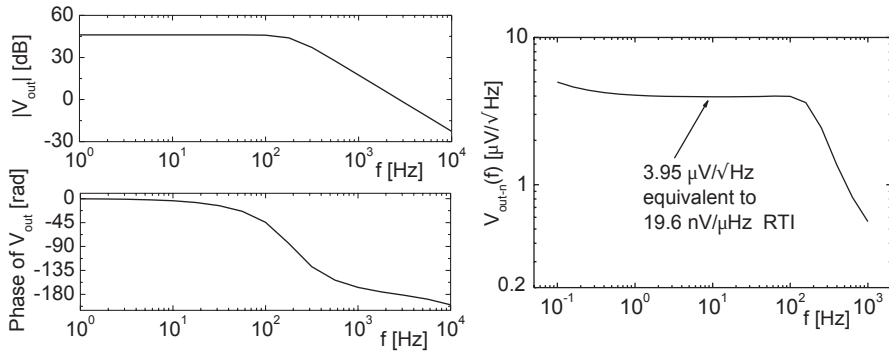
Fig. 53.3 Amplitude and phase response (*left*) and output noise density (*right*)
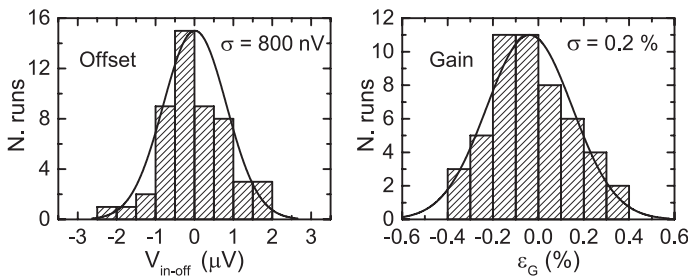
Fig. 53.4 Gain and offset spread from Monte-Carlo simulations

Table 53.1 Gain error as a function of the input common mode voltage

Input common mode voltage	Gain error
0.8	0.13%
1.2	0.08%
1.7	−0.06%
2.2	−0.17%

53.4   Conclusions

Simulation results indicate that an interesting combination of accuracy (low noise, low offset, low gain error) and low power consumption can be achieved with the proposed amplifier architecture. The absence of significant chopper ripple on the output voltage allows direct connection to a low sampling rate analog-to-digital converter with no need of additional time continuous filters.

References

1. M. Piotto, M. Dei, F. Butti, G. Pennelli, P. Bruschi. Smart Flow Sensor With On-Chip CMOS Interface Performing Offset and Pressure Effect Compensation. IEEE Sensors Journal, 12 (12) 3309–3317 (2012)
2. F. Butti, P. Bruschi, M. Dei, M. Piotto. A compact instrumentation amplifier for MEMS thermal sensor interfacing. Analog. Integr. Circ. Sig. Process. **72** (3), 585–594, (2012).
3. F. Butti, P. Bruschi, M. Piotto. A Chopper Modulated Low Noise Instrumentation Amplifier For MEMS Thermal Sensors Interfacing. Proc. of PRIME 2011, July 3–7, 2011, Trento (Italy) 133–136 (2011).
4. R. Wu, J. H. Huijsing, K.A.A. Makinwa. A Current-Feedback Instrumentation Amplifier With a Gain Error Reduction Loop and 0.06 % Untrimmed Gain Error. IEEE J. Solid State Circuits, **46** (12), 2794–2806 (2011)

Chapter 54
An App Based Air Quality Social Sensing System Built on Open Source Hw/Sw Tools

I. Capezzuto, l. Abbamonte, S. De Vito, G. Fattoruso, E. Massera, A. Buonanno, F. Formisano and G. Di Francia

The use of conventional tools of analysis for air quality has shown strong limitations in spatio-temporal coverage of urban scenarios. The required level of service needs for a distributed approach, based on a dense network of mobile sensor nodes. Developments in sensor technologies and communications, together with the constant social innovation make it now possible for citizens to cooperate together, producing and socializing data for the simultaneous benefit of the individual and the community. The following paper aims to develop this concept and apply it to the distributed monitoring of air quality. The goal is to enable individuals to monitor their exposure to air pollution, at the same time contributing to the construction of a map of the state of urban air quality through the sharing of data.

54.1 Introduction

A new concept of citizenship is spreading throughout all Europe. In their evolving smart cities, citizens want to become an active part of the intelligent management of their environment. At the center of this evolution is the ICT infrastructure, and in particular personal mobile devices. Introducing chemical sensing capability alongside these platforms can pave the way to a new model of citizen based smart atmospheric monitoring. Air pollution is actually one of the major concerns for public health: the UN estimates that it is responsible for the premature death of approximately 1.3 million people worldwide each year [1], and by 2050, according to the OECD [2], it may become the largest cause of mortality in the world, overcoming the scarcity of drinking water and poor health care.

Several authors have shown the limit of currently available air quality measuring networks, mainly because of their sparseness that does not allow to reach the correct

S. De Vito (✉) · I. Capezzuto · l. Abbamonte · G. Fattoruso · E. Massera · A. Buonanno · F. Formisano · G. Di Francia
UTTP-MDB Department, ENEA, Italian Agency for New Technologies Energy and Sustainable Economic Development, C.R. Portici, Portici, NA, Italy
e-mail: saverio.devito@enea.it

level of precision and accuracy even when using advanced modeling approaches [3, 4]. Cost is a main factor in determining network granularity but in some countries it's very difficult to install new conventional analyzers, due to their cumbersome dimensions and visual impact in the cultural heritage of relevant city centers. Fixed and/or mobile solid state multi-sensory device are increasingly believed to be a solution to improve the urban pollution monitoring conventional network [5].

In general, the availability of low cost, low power, portable personal analyzer and cooperative air quality monitoring models may help to significantly densify the urban pollution monitoring networks, eventually enabling good policies relying on high quality and high accuracy assesments and forecasting. In this work, we focus on providing a novel design of user centric approach to air quality monitoring, based on three sections: a mobile multi-sensory device; an Android APP for data gathering and visualization of personal exposure; a NoSQL high performance and high scalability database for data sharing and air quality heat maps generation.

54.2 Architecture

Because of its mobile nature, we defined the architecture according to the paradigm of Wireless Sensor Networks (WSN) (Fig. 54.1).

Within the framework, air quality sensors nodes connect via Bluetooth with users' personal mobility terminals (usually smartphones) that localize the data by means of GPS, A-GPS or IP based geolocalization facilities. Data is then sent by available network connectivity services to the backend server from which, through a model based approach, data is used to reconstruct city air pollution status for users availability anywhere.

54.3 Sensor Node

Aiming to involve the citizen at multiple stages of the monitoring process, the possibility for one to build his own node should be allowed. For this reason, we chose Arduino hardware. More precisely, because it provides an almost plug and play solution and it is aimed for developers, in this early stage we based our node on a commercial solution by Libelium Comunicaciones Ditribuidas S.L. named Waspmote PRO. The node architecture can be divided in two parts:

1. Gas Sensor Board, an expansion shield equipped with an array of chemical sensors, responsible for interacting with the environment and transforming gas concentrations in signals to be processed by a base board;
2. Waspmote PRO, the base board on which the Gas Sensor Board is mounted, responsible for trasmitting sensory data via Bluetooth.
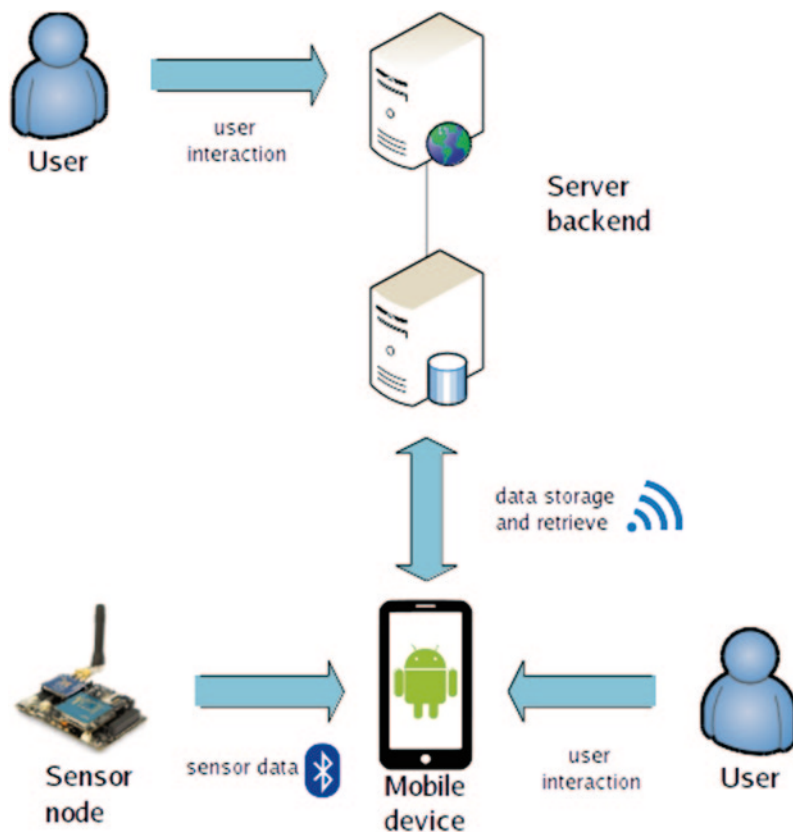
Fig. 54.1 Network diagram of the system

Table 54.1 Sensor node maximum power consumptions for the actual implementation

Waspmote PRO	Gas sensor board	Sensors	Bluetooth module	Total
9 mA	2 mA	63 mA	34 mA	108 mA

The node has been equipped with a Figaro TGS2442 sensor (CO), a MiCS 2710 sensor (NO_2) and a MiCS 5521 (VOC). RH and temperature sensors have also been added for the sake of environmental variables induced sensors drift counteraction. On a duty cycle of one sample per second, the heaters of chemical sensors are operated on pulsed mode so to strongly reduce the power needed for operation in a trade off with sensors sensitivity. Table 54.1 reports the maximum power consuption of a sensor node. Considering that supplied battery has a capacity of 6600 mAh, with this setup, autonomy is estimated in excess of 60 h, so to be comparable with medium intensity users smartphone recharge duty cycle. On field test has confirmed the capability to overcome the battery operation of the coupled smartphone.

Table 54.2 Default upper gas limits used in-app (ppm)

O_3	NO_2	CO	VOC
0.06	0.1	9.0	0.01

54.4 Android APP

The application primary goals are: to provide a gateway between sensor node and backend server geolocalizing gathered data; to provide the user with a real time and overall assessment of its personal exposition, and to allow the user to share its measurements both by relying on social networks platforms and by sending data the backend. The application was designed with focus on usability. With this in mind, we needed a simple, readily understandable synthetic index to allow the user to assess the pollution level. The choice was to use individual gases percentages of concentration limits derived from EU directives 2004/42 and 2008/50.

The overall index was instead computed as a simple Euclidean norm of the percentage vector. At this early stage, we chose to give equal weight to each variable in order to preserve a generality value, considering the many possible urban scenarios (Table 54.2).

54.5 Backend Server

Being the framework designed for the process of large amounts of information, methods and techniques of acquiring and handling data play a central role. We wanted the backend server and supporting infrastructure to be responsive, scalable, and most of all flexible, in order to allow the possibility to integrate different implementations of sensory nodes with different sensing capabilities. For this reason, we chose the Open Source NoSQL document database MongoDB, which can scale horizontally using the *sharding*, a process of storing data records across multiple independent machines, while making up one single logical database. The Android APP communicates with the server for two main operations: measurements submission and data retrieval.

Measurements submission is used to send sensory readings to server backend: this data is then used by the server to generate a heat map of air quality, which other users can visualize connecting to it via web. Data retrieval operation is used by the APP to retrieve user data logs from the database.

54.6 Conclusions

In this work we proposed a framework for highly distributed and user centric air quality monitoring, designed to involve the citizen in multiple stages of the monitoring process. Early tests conducted with the current implementation account for the users capability of *qualitative* assessment of their personal exposure. Social sharing possibility allows already for the wide sharing of the qualitative indexes obtained during mobility sessions. Next steps will include the on-field calibration of the sensory nodes with the aim of providing a *quantitative* measurement of pollutant concentrations.

References

1. World Health Organization. Tackling the global clean air challenge. http://www.who.int/mediacentre/news/releases/2011/air_pollution_20110926/en. Accessed 19 May 2014.
2. OECD. Environmental Outlook to 2050: The Consequences of Inaction. http://www.oecd.org/env/indicators-modelling-outlooks/oecdenvironmentaloutlookto2050theconsequencesofinaction.htm (2012). Accessed 19 May 2014.
3. M. Kamionka, P. Breuil, C. Pijolat, Calibration of a multivariate gas sensing device for atmospheric pollution measurement, Sens. Actuators B: Chem., 18 (2006), 323–327.
4. W. Tsujita, A. Yoshino, H. Ishida, T. Moriizumi. Gas sensor network for air-pollution monitoring, Sens. Actuators B: Chem., 110 (2005), 304–311.
5. Tim Watkins. The US EPA Roadmap for Next Generation Air Monitoring. EuNetAir second scientific meeting, Queens' College, Cambridge, Dec 18–20, 2013.

Chapter 55
Analysis and Implementation of Distributed Data Processing in a Wireless Sensor Network for Structural Health Monitoring

Fabio Federici, Roberto Alesii, Andrea Colarieti, Marco Faccio, Fabio Graziosi and Vincenzo Gattulli

In recent years, there has been a growing interest for possible application of wireless smart sensor networks. One area in which these platforms can offer considerable advantages over classical solutions is the monitoring of civil structures. This work analyze possible benefits and critical issues associated with the use of wireless sensor networks for vibrational monitoring of civil infrastructures. On the basis of the analysis of an experimental setup for the health monitoring of an heritage structure, the main advantages and limitations of a wireless sensor network for vibrational monitoring are outlined. A possible approach for the design of a sensor node supporting on-board vibrational data processing is discussed. Possible advantages of the proposed architecture are analyzed and a preliminary characterization of a custom prototype is presented.

55.1 Introduction

Structural health monitoring is an emerging tool for reliable assessment of civil infrastructures. Efficient monitoring programs may help in the characterization of the progressive decay of short term and long term structural performances, efficiently supporting maintenance and safety oriented strategies. Traditional structural monitoring solutions require the use of a large number of sensors deployed along the structure to be monitored and usually connected to one or more data acquisition units through wired communication channels. In recent years, technological advancements in the field of sensor miniaturization and progressive development of wireless sensor networks brought significant innovations in the field of monitoring systems [1]. Wireless sensor networks offer relevant advantages over traditional solutions, significantly reducing system's cost (it has been shown that a major fraction

F. Federici (✉) · R. Alesii · A. Colarieti · M. Faccio · F. Graziosi · V. Gattulli
DEWS Center of Excellence, University of L'Aquila, Via Giovanni Gronchi n. 18, 67100, L'Aquila, Italy
e-mail: fabio.federici@univaq.it
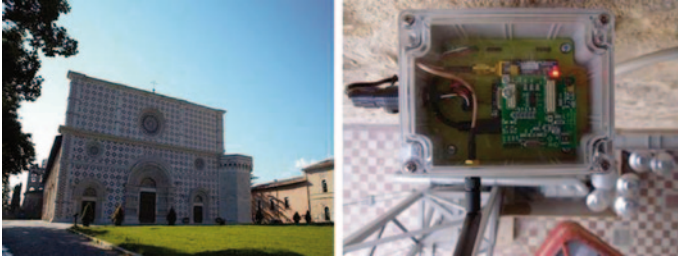
Fig. 55.1 The Basilica S. Maria di Collemaggio and a top view of an installed sensor node

of overall cost of a traditional structural monitoring system is primarily related to wiring costs[2]) and simplifying installation operations. However, their use in the context of structural health monitoring is still limited. One notable example is long period vibrational analysis of buildings.

Vibrational analysis, i.e. the analysis of structural behavior based on the measurement of buildings' dynamic response (usually expressed in terms of acceleration), is the basis for structural identification (modal analysis) and damage detection. Moreover, acceleration measurement can be extremely useful also in the characterization of the seismic response of a building. Vibrational monitoring oriented to modal analysis requires the acquisition and transmission of a notable amount of data, significantly reducing operating lifetime of battery-operated nodes (as radio communication is usually the most significant source of energy consumption for a wireless sensor node). Network synchronization errors may significantly affect structural analysis results. Duty cycling based sensor networks may have poor performance in the detection of random short length events (e.g. the detection of microtremors due low magnitude earthquakes).

An experimental setup, the structural monitoring of the Basilica S. Maria di Collemaggio (L'Aquila, Italy), allowed to deeply analyze highlighted problems. On the basis of this analysis, limitations of general purpose wireless sensor nodes will be discussed and a possible strategy for the design of a custom node able to overcome outlined problems will be detailed. Proposed approach will be evaluated on the basis of the analysis of a full-custom prototype.

55.2 A Real-World Case Study

The Basilica S. Maria di Collemaggio (Fig. 55.1) is one of the most important churches of the city of L'Aquila. The earthquake that interested the city and its surrounding area in April 2009 heavily damaged the structure of the church. After the seismic event, which caused a collapse of the structure in the transept area and serious damages on the external walls, a permanent monitoring system has been installed inside the structure [2]. The system is based on a wireless sensor network and includes 16 nodes (MEMSIC Imote2 with SHM-A sensor board) equipped with a tri-axial MEMS accelerometer sensor (ST Microelectronics LIS344ALH).
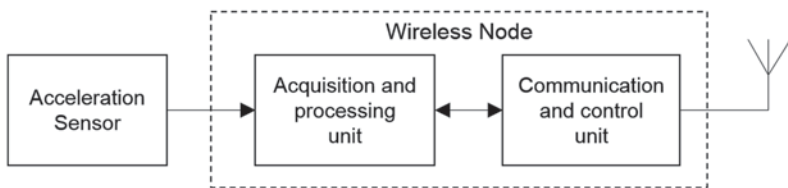
Fig. 55.2 Schematization of proposed node architecture

The use of MEMS accelerometers and general-purpose sensor nodes posed several problems in relation to structural analysis requirements. Among the various mentioned issues, the attention is here focused on two specific problems: sensors' selection and the satisfaction of operating lifetime requirements.

In recent years, there has been a wide diffusion of low cost MEMS accelerometers. Such sensors have the advantage of extremely low cost, reduced power consumption and high level of integration. For these reasons, these sensors have been often used in structural monitoring applications based on wireless sensor networks (for example, in bridge monitoring). However, for specific structures' typologies (e.g. masonry buildings), their resolution may result inadequate, especially for certain types of structural tests (e.g., environmental excitation response measurement). In the case of Collemaggio, it has been possible to overcome this problem by adopting identification procedures based on the analysis of the structural response to low-amplitude earthquakes. This has been possible thanks to a continuous monitoring of the structure, which, however, required the adoption of mains powered nodes (battery replacement would have been difficult, as nodes are placed at notable heights [3]).

55.3 Proposed Approach for Sensor Node Design

Ideally, a sensor node for vibrational monitoring should be able to operate for long periods (months or even years), running on battery power. It should include a high-resolution accelerometer sensor with low power consumption, and it must be able to continuously monitor the structure, detecting notable events. In order to satisfy these conflicting requirements, the following characteristics for custom node can be outlined:

- Support for distributed processing: a node able to locally process acquired data can reduce the amount of data to be transmitted. This can significantly optimize power consumption.
- Dedicated hardware for continuous operation: a node including a custom, very low power hardware block for specific data processing (e.g. event detection) can operate continuously over long periods (as this block can be the unique active block for the majority of time).

Figure 55.2 shows a feasible architecture able to support outlined requirements.

The acquisition and processing unit is a low power, specialized circuit able to continuously acquire data from the sensor and to process them (for example performing feature extraction or event detection) with reduced energy consumption. The control and communication unit is a block including a microcontroller unit along with a radio transceiver. This block supervises global node operations and manages its communication with the other nodes in the network. Moreover, it can perform data processing, effectively supporting distributed structural analysis.

The following section shows a preliminary analysis of a prototype version of the proposed architecture. Spectral analysis by means of embedded FFT algorithm has been selected as local data processing technique, as frequency domain analysis is a good example of distributed structural identification process [4].

55.4 Preliminary Evaluation of a Node Prototype

As part of the Basilica S. Maria di Collemaggio monitoring project, a custom sensor node specifically targeting long-term monitoring applications has been designed [5]. The sensor node is based on Atmel Zigbit (ATZB-900-B0) module and features an on-board 16 bit analog front end and an advanced power section. ST Microelectronics LIS3DSH has been selected as target accelerometer. This sensor natively integrates two finite state machines for autonomous processing of sensor data and can be used for the implementation of event detection strategies. The performance of the prototype system has been verified through an experimental setup (environmental and forced excitation tests on an experimental frame). The MEMS sensor showed satisfactory performance in forced excitation tests and event detection via embedded finite state machines (average current consumption of 35 µA in lowest power mode for the entire node). Embedded FFT calculation for spectral analysis has been implemented on the Zigbit module (average node current consumption of 12.5 mA). Anyhow, sensor resolution still resulted inadequate for environmental noise tests.

55.5 Conclusions

This paper described a possible approach for the design of an advanced wireless sensor node specifically oriented to vibrational monitoring of infrastructures. Experimental results obtained in the monitoring of the Basilica of S. Maria di Collemaggio allowed to identify some of the limitations of traditional sensor nodes with regard to vibrational monitoring applications requirements. A possible approach to the design of a dedicated sensor node has been detailed, and a node prototype based on a custom wireless sensing platform has been proposed. In the next future, an integrated solution specifically designed according to the outlined approach will be implemented, and its performances will be analyzed in real-world application scenarios.

References

1. F. Federici, F. Graziosi, M. Faccio, V. Gattulli, M. Lepidi, F. Potenza. An integrated approach to the design of Wireless Sensor Networks for Structural Health Monitoring. International Journal of Distributed Sensor Networks, (2012). doi:10.1155/2012/594842
2. M. Çelebi. Seismic instrumentation of buildings (with emphasis on federal buildings). Geological Survey, Tech. Rep. 0-7460-68170 (2002)
3. V. Gattulli, F. Graziosi, F. Federici, F. Potenza, A. Colarieti, M. Lepidi. Structural Health Monitoring of the Basilica S. Maria di Collemaggio. Proc. of the Fifth International Conference on Structural Engineering, Mechanics and Computation (SEMC 2013), Sep 2–4, 2013, Cape Town (ZA), 823–824 (2013)
4. A. T. Zimmerman, M. Shiraishi, R. A. Swartz, and J. P. Lynch. Automated modal parameter estimation by parallel processing within wireless monitoring systems, Journal of Infrastructure Systems **14**(1), 102–113 (2008)
5. F. Federici, R. Alesii, A. Colarieti, F. Graziosi, M. Faccio. Design and validation of a wireless sensor node for long term structural health monitoring. Proc. of IEEE Sensors 2013, Nov 4–6, 2013, Baltimore (MD), 1204–1207 (2013)

Chapter 56
Applying the SWE Framework in Smart Water Utilities Domain

Grazia Fattoruso, Carlo Tebano, Annalisa Agresta, Antonio Buonanno, Luigi De Rosa, Saverio De Vito and Girolamo Di Francia

Water leakage, water contamination, inability to detect water quality are some of the problems affecting the existing drinking water infrastructures. Unmanaged wastewater can be a source of pollution, a hazard for the health of human populations and the environment alike. The majority of wastewater infrastructures results in massive run-off and flooding of cities in case of extreme rainfall events. One of the ways to address these problems is by creating *smart* water utilities, equipping them of smart distributed sensing systems, integrated with advanced information systems. The integration of the diverse networked sensors involved in the water utilities management is not straightforward. The objective of this research work has been to develop a OGC SWE (Sensor Web Enablement) architecture across different applications in the smart water utilities domain, capable of integrating the various networks of in-situ sensors and processing sensor observations into decision support systems, realizing sensor related services and data delivery.

56.1 Introduction

The world is facing a global water quantity and quality crisis. The ageing infrastructure of the water systems coupled with the increasing demand is adding pressure to the water networks. Many problems arise in terms of water leakage, water contamination, inability to detect water quality and so forth.

Unmanaged wastewater can be a source of pollution, a hazard for the health of human populations and the environment alike. Wastewater can be contaminated

G. Fattoruso (✉) · A. Agresta · A. Buonanno · S. De Vito · G. Di Francia
UTTP/Basic Material and Devices Dept., ENEA Portici Research Centre, P.le E. Fermi 1,
80055 Portici, NA, Italy
e-mail: grazia.fattoruso@enea.it

C. Tebano · L. De Rosa
UTTP/CHIA Department, ENEA Portici Research Centre, P.le E. Fermi 1,
80055 Portici, NA, Italy

with a myriad of different components: pathogens, organic compounds, synthetic chemicals, nutrients, organic matter and heavy metals. They are either in solution or as particulate matter and are carried along in the water from different sources, affecting water quality. Also, existing wastewater infrastructures of most cities are no longer appropriate resulting in massive run-off and flooding of cities in case of extreme rainfall events.

One of the ways to address these problems is by creating smart drinking water and wastewater networks that involve the use of smart sensing systems distributed along the infrastructures and in the surrounding environment, integrated with advanced information systems (e.g. GIS; DSS; SCADA, etc.) and dynamics and analytics modeling components, providing the operators with a comprehensive and more effective set of decision-making capabilities for a sustainable water utilities management. A constant and real time stream of data by sensor networks coupled with predictive modeling capabilities, enables operators of the water utilities to quickly assess events as they occur, identify potential problems before they reach a critical level, respond to operational challenges, and minimize downstream effects. The observation systems have to be involved in the water utilities management are essentially based on diverse sensors. Nevertheless, their integration is not straightforward due to the variety of sensor protocols and interfaces. Within this framework, the objective of this research work has been to investigate and develop a OGC SWE (Sensor Web Enablement) architecture across different applications in the smart water utilities domain, capable of integrating the various networks of in-situ sensors and processing sensor observations into decision support systems, realizing sensor related services and data delivery. The developed SWE architecture has been applied within two real water utilities management scenarios. More specifically, one scenario was centered on water quality dynamics monitoring and predicting along the real Santa Sofia aqueduct (Southern Italy). The second scenario focused on building a monitoring and warning system for contaminations along the wastewater network of the Massa Lubrense city (Southern Italy).

56.2   The SWE Architecture

Within water utilities monitoring and management systems, the developed SWE architecture provides functions ranging from integrating and accessing the various networked sensors involved, to retrieving events and alerts triggered through sensors, as well as browsing, querying the real time observation data through a sensor web client and a QGIS SOS client application, developed ad-hoc. This architecture (Fig. 56.1) consists of the services SOS (Sensor Observation Service), SES (Sensor Event Service) and WNS (Web Notification Service) [1].

The SOS component allows clients (e.g. QGIS SOS client developed ad-hoc by ENEA) to access descriptions of associated sensors and their collected observations by a standardized web service interface. SES provides notification services, with stream processing capabilities. Alerting and notification capabilities provides
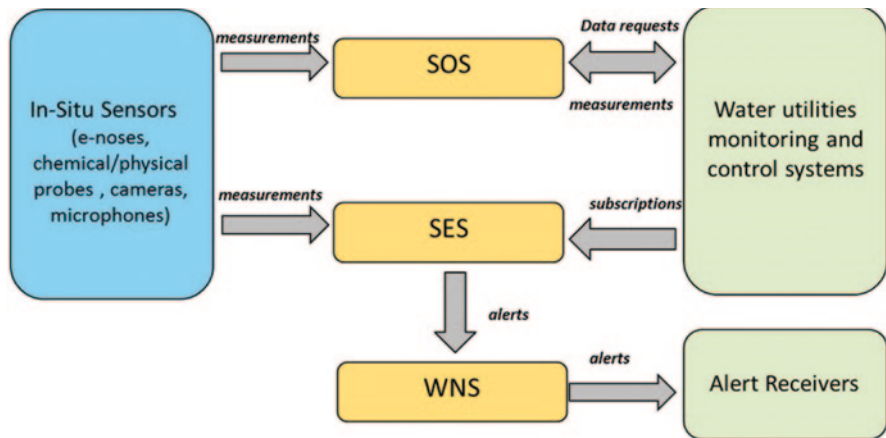
Fig. 56.1 The SWE architecture developed for water utilities monitoring and control systems

support for creating alarms and filter constructs by system users. Users may hence use created alarm constructs to subscribe to live sensor feeds and continuously receive notifications once events are detected during live streams processing. The notifications are processed by WNS that notifies the user by sending an email or sms with the notification received by SES.

The implementation of the proposed SWE architecture has been deployed by 52°North framework [2] version 4.0 and OGC SOS 2.0 standards. The deployed SOS endpoint uses a PostgreSQL database with a PostGIS spatial extension to store observation values and sensor metadata.

56.2.1   The QGIS SOS Client

A web SOS client has been developed as a web-based browser application extending the open source Sensor Web Client. It acts as an application layer to handle via web the rendering of queried observations in the form of graph, time series and geographic maps. A QGIS SOS client application (Fig. 56.2) has been developed by ENEA for adding the ability to the open source GIS desktop QGIS to access sensor data served by SOS and delivering them to the simulation models (i.e SWMM, Epanet/MSX), the latters integrated in the QGIS as plugins (e.g. GHydraulics). Thus, the developed QGIS SOS client offers easy to use interfaces within QGIS to run the *GetCapabilities* operation by SOS to request a service description containing the spatial and temporal extent of the offered observations as well as a list of the sensors and observed features. Similarity, the *GetObservation* operation, the core functionality of the SOS, is run by a specific interface allowing to access observations data within the QGIS viewer by table views. By another interface, new sensors can be easily registered and observations inserted, implementing the *Transactional profile* of the SOS specification.
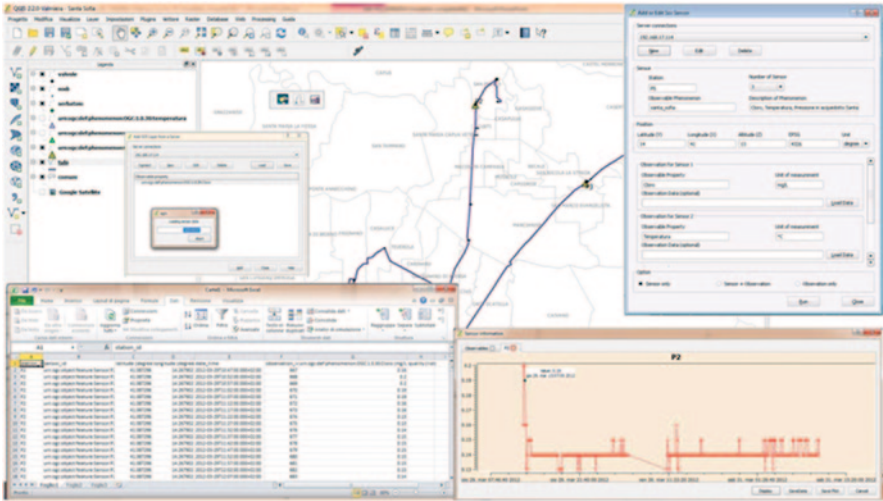
Fig. 56.2 The developed **QGIS SOS client application** for the real use case of Santa Sofia Aqueduct

Thus, this client hides technical details of SWE services and protocols, so that even non-experts can use all components of the developed SWE architecture, transparently.

56.3 The Use Cases

The developed SWE architecture has been applied to two real water quality monitoring and controlling scenarios along an aqueduct and a urban sewage system. One scenario concerns the water quality dynamics (i.e. DBPs formation as well as free chlorine decay) to be monitored and predicted along the real Santa Sofia aqueduct. Thus, a wireless network of sensors was installed along the system which monitors physical and chemical water parameters (i.e. pressure, residual chlorine, conductivity, temperature and pH) and delivers data to hydraulic and water quality simulation models [3]. Additionally, on-demand deployable sensor platforms for measuring DBPs were used. The different sensor types have been encapsulated by SOS servers to allow a standardized access to the gathered data by the developed web client or the QGIS SOS client. The alerting functionalities of the SWE system have been provided using a SES instance in conjunction with a WNS. Thus, a sms is sent when critical scenarios occur i.e. water contaminants levels do not meet regulatory requirements (e.g., a disinfection residual higher than 0.2 mg/l for free chlorine and DBPs concentrations higher than 30 µg/l). The second scenario concerns the development of a monitoring and warning system for contaminations along the wastewater network of the Massa Lubrense city. Different sensor types have been used

in this use case ranging from total immersion probes for monitoring qualitative and quantitative parameters such as PH, COD, NH_3, and water level and conductivity to multi-sensor platforms composed by an e-nose for NH_3, H_2S, in conjunction with temperature and humidity sensors for adjusting the gas readings, and a microphone. The networked sensor platforms have been, installed in strategic locations of the wastewater network. Displaying time series data is fulfilled by SOS instance. For the real-time notification, the sensor data are transferred to the SES instance which filters the incoming data with regard to alert criteria specified. Thus, if a matching alert condition is found by the SES, the according alert is dispatched, by sending the notification request to the WNS instance.

56.4   Conclusions

Through the shown use cases, the proposed SWE architecture has fundamentally proven its applicability to smart water utilities domain. It is ready to be used for building sensor based systems for monitoring and controlling water utilities. For the future, this architecture will be integrated with SPS services.

References

1. 52 North Sensor Web Community. [Online]. http://52north.org/communities/sensorweb
2. J. Simon, A. Bröring, and C. Stasch. Applying OGC Sensor Web Enablement to risk monitoring and disaster management. GSDI 11 World Conference, Rotterdam - NL (2009)
3. G. Fattoruso, D. De Chiara, S. De Vito, V. La Ferrara, G. Di Francia, A. Leopardi, E. Cocozza, M. Viscusi, M. Fontana. Simulation of Chlorine Decay in Drinking Water Distribution Systems: Case Study of Santa Sofia Network (Southern Italy). Sensors and Microsystems, Lecture Notes in Electrical Engineering Volume 268, pp 471–474 (2014)

Chapter 57
Integration of Wireless Sensor Network and Hydrologic/Hydraulic Ontologies for Flooding Forecasting

Grazia Fattoruso, Annalisa Agresta, Maurizio Pollino, Francesco Pasanisi, Saverio De Vito and Girolamo Di Francia

Sensors are quickly becoming ubiquitous and can be found in a vast range of environments. The increase of sensor systems is accompanied by an increasing volume of data, as well as an increasing heterogeneity of devices, data formats, and measurement procedures. Shared semantic definitions help not only with data integration from multiple sources, but can also assist in integrating data into temporal and spatial contexts. It is well recognized that ontologies have an important role to play in data integration. In this research work, an ontology by integration is developed for floods risk prevision based on continuous measurements of water parameters gathered in the watersheds and along the sewers and delivered to simulation models. The objective of this ontology is to promote the interoperability of components across hydrologic/hydraulic and wireless sensor network domains in order to forecast flooding risk scenarios.

57.1 Introduction

Today sensor networks are found in a vast range of applications (e.g., water, air, home etc.) and there are multitudes of ways in which sensors generate and represent observation data. In the study of flooding risk forecasting, data from different sensors types (e.g. temperature, rain, hydrometric gauges) are needed, to be managed

G. Fattoruso (✉) · A. Agresta · S. De Vito · G. Di Francia
UTTP/Basic Materials and Devices Department, ENEA RC Portici, P.le E. Fermi 1,
80055 Portici, NA, Italy
e-mail: grazia.fattoruso@enea.it

M. Pollino
UTMEA/Energy and Environmental Modeling Department, ENEA Casaccia Research Centre,
Via Anguillarese 301, 00123 Roma, Italy

F. Pasanisi
UTTP/CHIA Department, ENEA Portici Research Centre, P.le E. Fermi 1,
80055 Portici, NA, Italy

Fig. 57.1 A segment of FloodOntology in the Protégé framework: example of hierarchy classes, property and definition class

and processed by different software systems [1]. More accurate and complete information can be obtained by aggregating the available heterogeneous data. It is evident that the growing prevalence of sensing devices and systems makes essential their management and of the related volume of data gathered. Within this context, shared semantic definitions can help not only with data integration from multiple sources, but can also assist in temporal and spatial integration of data. Modern approaches to achieve the integration of different knowledge bases are mainly ontology-based [2]. The ontological capability of integrating, reusing and sharing knowledge is the main reason why building an ontology for flooding forecasting and management, too. In this research work, an ontology by integration, named FloodOntology, is developed for flooding risk prevision based on continuous measurements of water parameters gathered by networked sensors in the watersheds and along the sewers and delivered to hydrologic and hydraulic simulation models. The developed ontology capture the concepts and relationships across the three involved domains i.e. the hydrological, hydraulic and sensor network domains realizing the interoperability of their components in order to forecast flooding risk scenarios.

57.2 The Methodology

A growing number of methods have been proposed in recent years to address the issues of ontology development [3]. For designing our ontology, the widely accepted skeletal methodology described by Uschold and Gruninge [4] has been used. The first step for realizing this approach is to define the purpose of the ontology and its design requirements. The second step is to accomplish the ontology by three phases: (1) concept capture, (2) coding, and (3) integration with complementary ontologies. In the first phase, the classes, their definitions (glossary) and hierarchies are defined for capture concepts and they are attached through properties and semantic constraints (Fig. 57.1).

By the coding phase, an explicit representation of the conceptualization captured in the previous stage is performed by using formal languages. Ontology coding phase includes the specification of the meta-ontology and the identification of the representation language for the ontology. During either or both of the capture and coding processes there is the question of how and whether to use all or part of ontologies that already exist (integration of ontologies). In the used method, the integration of existing ontologies is considered as essential part of ontology development process. Integration is the process of building ontology in one subject, reusing one or more ontologies in different subjects [3]. However few of the available methods for building ontologies address integration in detail. In the integration process, different ontologies of the same phenomena or process are aggregated, combined, and assembled together, to form the resulting ontology. In this process, ontologies can, possibly after be reused, have suffered some changes such as extension, specialization or adaptation.

This research work develops FloodOntology by integrating the existing Semantic Sensor Network (SSN) ontology [5] with hydrologic/hydraulic ontologies, developed ad-hoc, obtaining an ontology for flooding risk forecasting. The main concepts modelled into the developed hydrological/hydraulic ontology are related to the watersheds and urban drainage systems i.e. the geometry and topology of the water network as well as the characteristics of the channels such as their slope, roughness, hydraulic sections and forth on, in order to provide an estimate on water levels, flows and velocities along a river as well as a sewer system. They are captured and modeled in the ontology as classes and subclasses, relationships and properties. In the following figures, some classes hierarchies are shown.

Networked sensors employed within flooding risk management scenarios take many forms and cover various geographical and temporal scales. They range from remote sensing satellites, to sensing devices situated along drainage networks (rivers and sewers) and within drainage basins, providing highly-detailed point-based information from single site. Only sensors and networked sensors for monitoring meteorological data (e.g. temperature, rainfall, humidity, pressure and wind speeds and directions) by weather station networks as well as hydrometric data (on the level of rivers and streams and the discharge rates) have been modelled into FloodOntology in terms of capabilities, measurement processes, observations and deployments, by re-using some segments of the SSN ontology.

The adopted approach for integrating the ontologies into FloodOntology argues for an integrated view instead of purely sensor-centric one. In fact, sensor concepts (i.e., how observations are performed) are related with hydrologic/hydraulic domain concepts (i.e., observed properties and their associated hydrologic/hydraulic entities). The correlation between the domains is realized by the definition of properties. For example, the category "watershed", related to hydrologic domain, is connected to sensor device "pluviometers", related to sensor network domain, through the "measurement" property (Fig. 57.2).

Flood Ontology is created by using Protégé, that is the most commonly used ontology editor and a knowledge architecture for the creation of customized knowledge-based application [6]. Protégé uses OWL (Ontology Web Language) for coding ontologies, a language appropriate when the information needs to be processed by an application, rather than just to be presented.
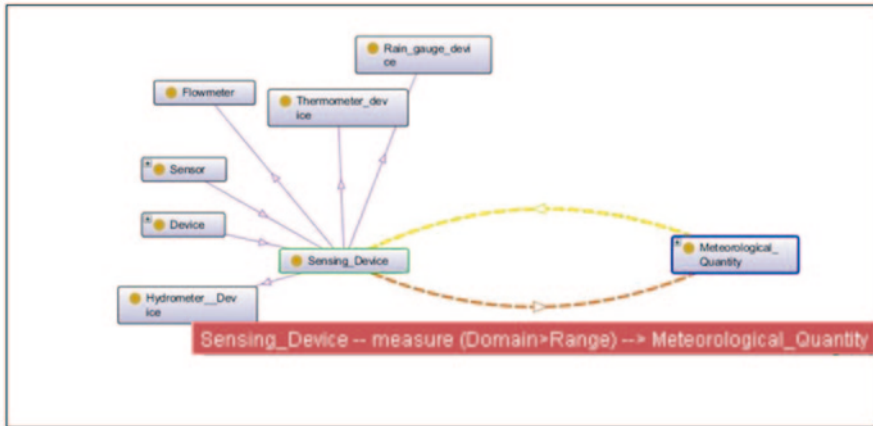
Fig. 57.2 Example of integration between SSN ontology and hydrologic domain

57.3   Results and Discussion

FloodOntolgy is realized through the integration of the existing SSN ontology with hydrologic/hydraulic domains ontologies, developed ad—hoc, for flooding forecasting and management applications. *FloodOntology* constitutes a headway in the capability of managing heterogeneous data and the capability of inferring new knowledge in the flooding forecasting. The creation of flood-forecasting and management applications centralized on this ontology allow to overcome recognized issues related to data heterogeneity within and across the involved domains.

References

1. Agresta A., Fattoruso G., Pollino M., Pasanisi F., Tebano C., De Vito S., Di Francia G. An Ontology framework for flooding forecasting (2014) The 14th International Conference on Computational Science and Its Applications (ICCSA 2014)
2. Taylor, K., & Leidinger, L. (2011). Ontology-driven complex event processing in heterogeneous sensor networks. In The Semanic Web: Research and Applications (pp. 285–299). Springer Berlin Heidelberg.
3. Y. Kalfoglou and M. Schorlemmer, Ontology Mapping: The State of the Art, in Proceedings of Dagstuhl Seminar -Semantic Interoperability and Integration, 2005.
4. N. Noy and D. McGuinness. Ontology Development 101: A Guide to Creating Your First Ontology, Technical Report, Stanford, 2001.
5. Compton, M., Barnaghi, P., Bermudez, L., García-Castro, R., Corcho, O., Cox, S., & Taylor, K. (2012). The SSN ontology of the W3 semantic sensor network incubator group. Web Semantics: Science, Services and Agents on the World Wide Web, 17, 25–32.
6. The Protégé Ontology Editor and Knowledge Acquisition System http://protege.stanford.edu

Part IV
Physical Sensors

Chapter 58
Influence of the Contact Metallization on the Characteristics of Resistive Temperature Sensors Based on EPOXY/MWCNT Composites

Heinz Christoph Neitzert and Giovanni Landi

The influence of different contact metallization materials and geometries on stability, sensitivity and linearity of epoxy/carbon nanotube based temperature sensors has been investigated. In our experiments, we found a perfect linear current-voltage characteristics and a stable conductance-temperature characteristics in the case of the sensor structures with the evaporated niobium contacts and a non-linear and noisy current-voltage characteristic with hysteresis in the case of the copper wire contacts. After a burn-in procedure, however, we could partially stabilize the electrical characteristics of the copper-wire contact based devices. However, in the latter case, even if a higher sensor sensitivity has been measured, the temperature sensing characteristics remained rather noisy and an acceptable long-term stability could not be achieved.

58.1 Introduction

Various temperature sensors based on single carbon nanotubes [1], carbon nanotube bundles without matrix [1] or in a polymeric [2] or even biological cell matrix [3] have been reported in literature, but fewer attention has been given to the electrical contacts. Epoxy resins, with the addition of 0.5 wt% multi-walled carbon nanotubes (MWCNTs) have been shown to be useful as active material for temperature [4] and humidity [5] sensors, applicable in a wide range of operating conditions. Using coplanar gold electrodes, ideal ohmical behavior [4] and excellent long-term stability has been demonstrated [5]. The DC electrical conductivity of this epoxy/MWCNT composite with 0.5 wt% CNTs has been reported to have a high value of

---

H. C. Neitzert (✉)
Dipartimento di Ingegneria Industriale (DIIn), Università di Salerno, Via Giovanni Paolo II 132, 84084 Fisciano, SA, Italy
e-mail: neitzert@unisa.it

G. Landi
Faculty of Mathematics and Computer Science, Fern Universität Hagen, 58084 Hagen, Germany
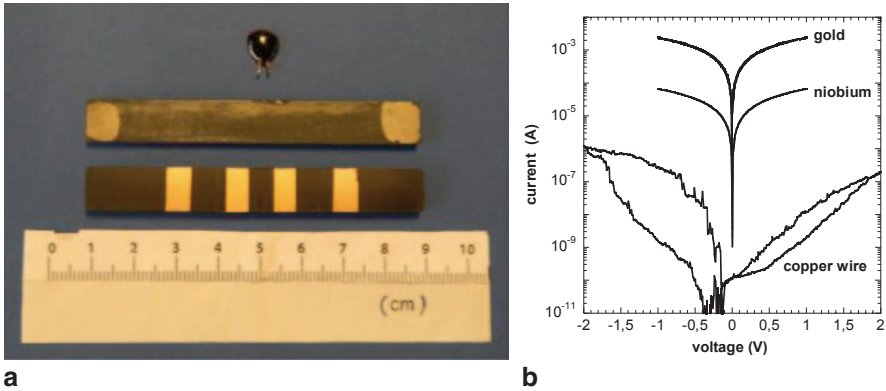
Fig. 58.1 a Image of three Epoxy/MWCNT samples, contacted with gold pads (4-point geometry), niobium pads (*middle* sample) and immersed copper wire contacts (*upper* sample) and **b** I-V characteristics of the three samples before temperature cycling

about 0.5 S/m [4, 6] and the underlying current transport process has been investigated using temperature dependent conductivity measurements and low-frequency noise spectroscopy [7, 8]. In the present study we investigate the possibility to use other materials than gold for the realization of the electrical contacts to the active composite temperature sensor material and to use simpler metallization methods than evaporation.

58.2 Experimental

58.2.1 Sample Preparation

Epoxy diglycidyl-ether bisphenol-A (DGEBA) with DDS, both from Sigma-Aldrich, and commercial non-functionalized MWCNTs from Nanocyl have been used as base components. The curing process and material properties are reported in detail elsewhere [4]. The two types of devices, used in the present study, have been prepared with different metallizations, either by the evaporation of niobium contact pads or by the immersion of copper wires into a small drop of epoxy/CNT liquid before curing. The sample geometries and respective electrical characteristics are shown in Fig. 58.1 together with the ones of a reference sample with gold pads. We found perfect linear electrical behavior for the evaporated gold and niobium contact devices and an asymmetric I-V characteristic with large hysteresis in the case of the copper wire based device.
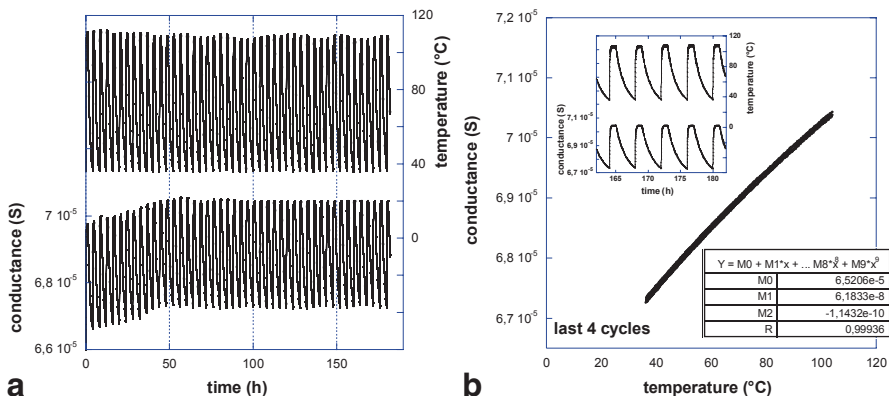
Fig. 58.2 **a** Monitoring of the oven temperature and niobium metallized sample conductance during multiple temperature cycles with an applied voltage of 1 V and **b** temperature-conductance plot for the last 4 temperature cycles with polynomial fit parameters and zoom into the last cycles (inset)

58.2.2 Measurement Setup

The electrical measurements of Epoxy/MWCNT composites, reported in this contribution, have been performed in a two-contact geometry using a Keithley model "2400" Source-Measurement-Unit (SMU) and temperature dependent measurements from room temperature up to 110 °C have been done using a HERAEUS type "T5042EK" oven. The oven temperature has been monitored with a small size thermocouple and a FLUKE model "45" Voltmeter.

58.3 Results and Discussion

The results of the conductance monitoring during the multiple thermal cycling at 1 V are shown in Fig. 58.2a. One observes a very regular variation of the conductance with temperature during all cycles, but the minima and maxima are linearly increasing with increasing cycle number up to about 50 h and remain further on stable. This can be explained by an initial decrease of the sample humidity, that results for this material in a linear increase of conductivity [5]. This can be seen in the inset of Fig. 58.2b, where we zoom into the last 5 cycles.

The ratio between the 100 and 40 °C conductance has a constant value of about 1.04. In Fig. 58.2b we show the complete temperature dependence of the conductance for the last 4 complete cooling periods. It can be expressed by a 2nd order polynomial function.

In an attempt to lower the production costs of these kind of sensors and to decrease the response time, we fabricated a series of composite drop on copper wire
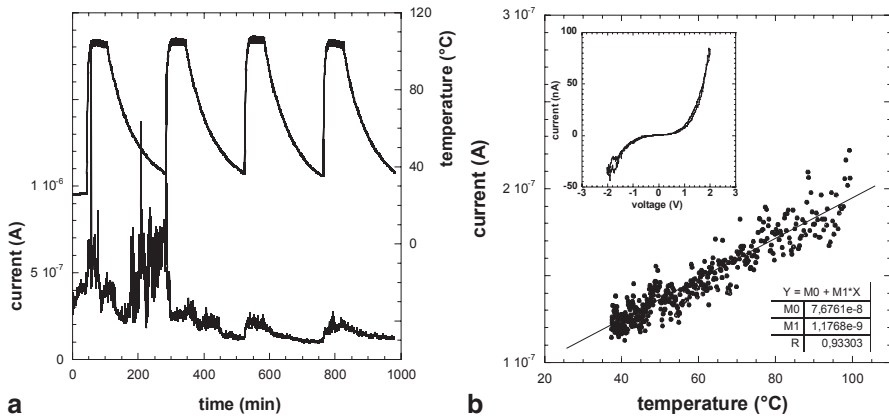
Fig. 58.3 **a** Monitoring of the oven temperature and copper wire metallized sample current during 4 temperature cycles with an applied voltage of +2 V and **b** temperature dependence of the sample current during the last cooling period

samples. First I-V characteristics were unstable, non-monotonic and noisy. In some cases even, there was no conduction before the application of elevated voltages for a short time. The current-voltage characteristics of such a device after voltage pulse "animation" is shown in Fig. 58.1b. We observe an asymmetrical behavior with hysteresis and for negative voltages even sharp switching. However, the temperature sensor performance of this sample has been monitored with an applied voltage of +2 V (Fig. 58.3a). A rather noisy and non-monotonic behavior with current spikes during the first 2 cycles, was followed by an almost regular behavior during the last 2 cycles with a monotonic increase of the conductance with increasing temperature. The resulting temperature-current plot during the last cooling with a linear fit is shown in Fig. 58.3b. Surprisingly the sensitivity of the however less stable, sensor is strongly increased as compared to the niobium and gold contacted sensors. Most probably the overall resistance is not any more dominated by the nanotube network interconnection [7, 8], but by the very weak and fragile nanotube—copper wire contact points. Copper, however, has been shown in another configuration with large areas to give good electrical contacts to the composite material [6].

58.4 Conclusions

The substitution of the usual gold contact pads with niobium pads as electrical contacts for epoxy/CNT based temperatures is possible and excellent long-term stability has been observed for temperatures up to 100 °C. On the other hand did we get no satisfactory results with copper wire contacts, simply immersed into the composite material, even if the sensor sensitivity was strongly increased.

References

1. K.M.F. Carmen, T.S.W. Victor, H.M.C. Rosa and J.L. Wen. Dielectrophoretic batch fabrication of bundled carbon nanotube thermal sensors. IEEE Trans. on Nanotechnology **3**, 395–403 (2004)
2. X. L. He, J. H. Du, Z. Ying, H. M. Cheng and X. J. He, Positive temperature coefficient effect in multiwalled carbon nanotube/high-density polyethylene composites. Appl. Phys. Lett. **86**, 062112 (2005)
3. R. DiGiacomo, B. Maresca, M. Angelillo, G. Landi, A. Leone, M.C. Vaccaro, C. Boit, A. Porta and H.C. Neitzert. Bio-Nano-Composite Materials Constructed With Single Cells and Carbon Nanotubes: Mechanical, Electrical, and Optical Properties. IEEE Trans. on Nanotechnology **12**, 1026–1030 (2013)
4. H.C. Neitzert, L. Vertuccio and A. Sorrentino. Epoxy/MWCNT composite as temperature sensor and electrical heating elements. IEEE Trans. on Nanotechnology **9**, 688–693 (2010)
5. H.C. Neitzert, A. Sorrentino and L. Vertuccio. Humidity sensing of an epoxy/MWCNT composite by electrical conductivity measurements. SPIE Proceedings **8766**, 87660D (2013)
6. H.C. Neitzert, A. Sorrentino L. Vertuccio and V. Vittoria Curing monitoring of an epoxy/carbon nanotube composite using DC conductivity measurements, Proceedings of the 26th Polymer Processing Society (PPS) meeting, July 4–8, (2010), Banff, Canada, p. R02–108.
7. C. Barone, S. Pagano and H.C. Neitzert. Transport and noise spectroscopy of MWCNT/HDPE composites with different nanotube concentrations. J. Appl. Phys. **110**, 113716 (2011)
8. C. Barone, D. Imparato, S. Pagano, L. Vertuccio, A. Sorrentino and H.C. Neitzert, Electrical Noise Characterization of Epoxy/MWCNT Composites. Proc. of the AISEM 2010, Sensors and Microsystems: Lecture Notes in Electrical Engineering, **9**, Springer, Berlin, 49–53 (2011)

Chapter 59
An Integrated Thermal Flow Sensor for Liquids Based on a Novel Technique for Electrical Insulation

Massimo Piotto, Alessia Di Pancrazio, Luca Intaschi and Paolo Bruschi

A novel method to electrically insulate integrated thermal flow sensors from liquids is proposed. The sensor is fabricated with a post-processing technique applied to chips designed with a commercial CMOS process. A low cost packaging technique is used to convey the liquid to the sensing structures. After packaging, a simple technique is used to coat the flow channel and the chip area exposed to the fluid with silicone. Preliminary tests in water confirm the effectiveness of the proposed method.

59.1 Introduction

Accurate measurements of small liquid flow rates are required in many application fields including semiconductor industry, microanalysis systems (μTAS), microchemical reaction systems and biomedical instrumentation. Different solutions based on MEMS devices have been proposed in the literature [1–4] and a few commercial products are now available [5].

The direct interaction between liquids and micromechanical structures poses diverse problems in terms of mechanical and electrical reliability. For this reason, the flow microsensor is usually separated from the liquid by an intermediate material. In the case of flow sensors based on a thermal principle, a thin thermally conductive membrane, in some cases the pipe wall itself, is usually used to separate the temperature microprobes from the liquid. This simple solution comes at the price of reducing the device sensitivity.

In this work we propose a thermal flow sensor for liquids based on a novel method for separating the fragile microstructures from the fluid. The separation

M. Piotto (✉)
IEIIT—Pisa, CNR, via G. Caruso 16, Pisa, Italy
e-mail: massimo.piotto@ieiit.cnr.it

A. D. Pancrazio · L. Intaschi · P. Bruschi
Dipartimento di Ingegneria dell'Informazione, University of Pisa, via G. Caruso 16, Pisa, Italy

Fig. 59.1 Photo of the sensing structure after the post-processing
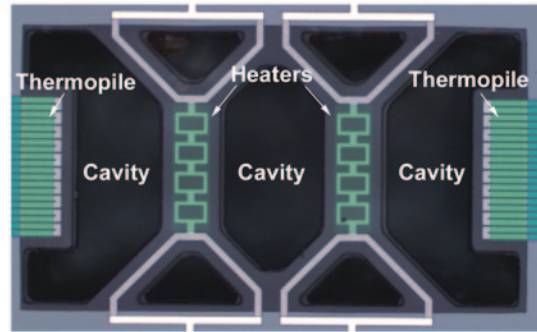
consists in a silicone layer that covers the integrated sensing structure fabricated by means of a post-processing technique applied to chips designed with a commercial CMOS process of STMicroelectronics. The silicone layer guarantees the electrical insulation between the chip and the liquid and it improves the mechanical robustness of the structures. The silicone film is applied after the packaging phase so the proposed method is independent from the technology used to fabricate the device.

59.2 Device Description and Fabrication

The sensing structure is a microcalorimeter made up of two polysilicon heaters symmetrically placed between two p^+ polysilicon/n^+ polysilicon thermopiles, used as temperature probes. The heaters are placed on suspended silicon dioxide membranes; the hot contacts of the thermopiles are at the tip of cantilever beams while the cold contacts are placed onto the silicon substrate. The sensors have been designed with the BCD6s process of STMicroelectronics while the membranes and the cantilever beams were fabricated in the post-processing phase by means of silicon anisotropic etching. Details about the design and fabrication of the device are reported in [6]. Figure 59.1 shows the sensing structure after the post-processing.

The connection of the chip to the liquid feed line was performed by means of a simple and cheap packaging technique based on a poly-methyl-methacrylate (PMMA) conveyor [7]. Details about the conveyor fabrication and the procedure used to align and fix it to the chip are reported in [8]. Figure 59.2 shows the device with the PMMA package connected to the feed line.

After packaging, a low-viscosity silicone, the Dow Corning® 3-1965, was directly inserted with a syringe into the feed line and the channel including the sensing structures was completely filled. Then, a nitrogen flow (100 sccm for 5 min) was used to remove the silicone in excess obtaining a good conformal coating. In order to avoid the channel clogging during silicone drying, a lower flow (10 sccm) was maintained for 30 min.
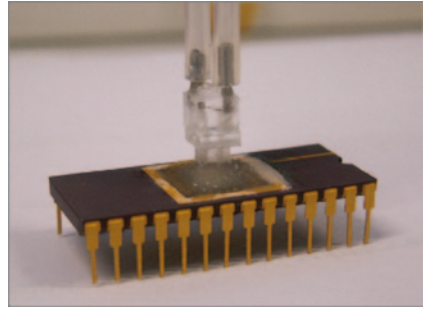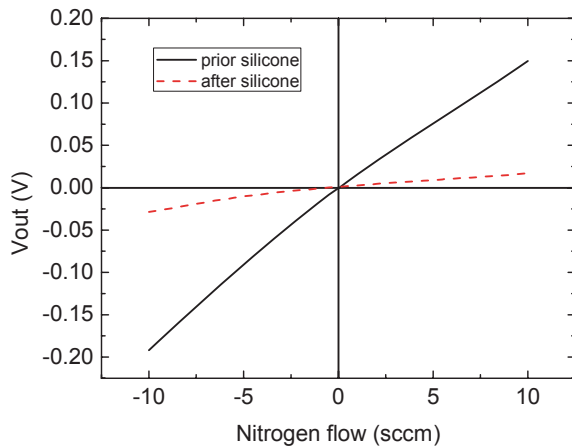
Fig. 59.2 Photo of the finished device

Fig. 59.3 Response to a nitrogen flow prior and after the silicone coating

59.3   Device Characterization

The device has been tested delivering a constant power of about 1 mW to each heater. A preliminary test in nitrogen prior and after the silicone coating has been performed and the result is shown in Fig. 59.3.

Negative flows meant swap of the inlet and outlet sensor fittings. It can be noted that the silicone coating causes a significant reduction of the sensitivity and the output voltage. This result is consistent with a reduction of the thermal insulation of the heaters and thermopiles caused by silicone.

The electrical insulation has been tested filling the channel with a highly conductive fluid (NaCl water solution) and measuring the resistance between the silicon substrate and the fluid. An increase of about four orders of magnitude in the resistance value has been observed after the silicone coating.

The sensor response to a deionized water flow is shown in Fig. 59.4. A clear reduction of the output range occurs in this case, while not significant changes in the sensitivity have been observed. A resolution of 30 µg/s has been estimated. Note that a non monotonic response has been observed for high flow rates when
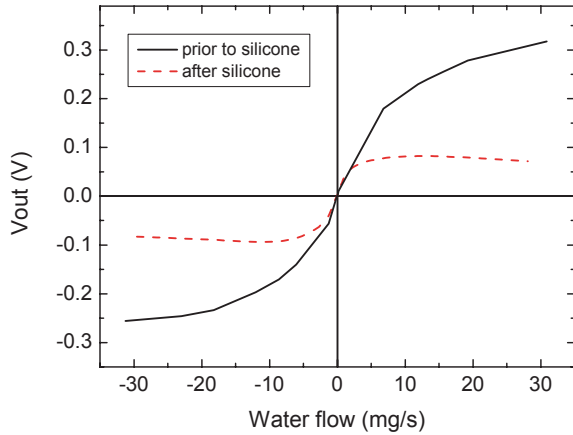
the sensing structure is coated with silicone. This behavior is usually ascribed to the decrease of the heater temperature.

59.4 Conclusions

An integrated thermal flow sensor for liquids has been fabricated and characterized. A silicone coating is used to increase both the electrical insulation and the mechanical robustness of the sensing structures. A sensitivity decrease caused by the coating has been observed with nitrogen flow. Differently, preliminary tests performed with deionized water show a decrease in the output range with not significant changes in the sensitivity. Further investigations will be devoted to characterize the device behavior with different liquids.

References

1. J. T. W. Kuo, L. Yu, E. Meng. Micromachined Thermal Flow Sensors—A Review. Micromachines **3**, 550–573 (2012)
2. T.S.J. Lammerink, N.R. Tas, M. Elwenspoek, J.H.J. Fluitman. Micro-liquid flow sensor. Sensors and Actuators A **37–38**, 45–50 (1993)
3. M. Ashauer, H. Glosch, F. Hedrich, N. Hey, H. Sandmaier, W. Lang. Thermal flow sensor for liquids and gases based on combinations of two principles. Sensors and Actuators A **73**, 7–13 (1999).
4. M. Piotto, M. Dei, P. Bruschi. Low pressure drop, CMOS compatible liquid flow sensor with sub ml/h resolution. Procedia Chemistry **1**, 96–99 (2009)

5. Sensirion Online Product Catalog. (2013) [Online]. Available: http://www.sensirion.com.
6. M. Piotto, M. Dei, F. Butti, G. Pennelli, P. Bruschi. Smart flow sensor with on-chip CMOS interface performing offset and pressure effect compensation. IEEE Sensors Journal **12** (12), 3309–3317, (2012)
7. P. Bruschi, M. Dei, M. Piotto. A single chip, double channel thermal flow meter. Microsystem Technologies 15 (8), 1179–1186 (2009)
8. M. Piotto, F. Butti, G. Pennelli, P. Bruschi. Smart flow sensors based on advanced packaging techniques applied to single chip sensing devices. Lecture Notes in Electrical Engineering **162**, 57–62 (2014)

Chapter 60
3D Ultra High Sensitive Superconductive Magnetic Nanosensor

C. Granata, A. Vettoliere, M. Fretto, N. De Leo and V. Lacquaniti

60.1 Introduction

It is well established that the magnetic nanoparticle studies play a fundamental role for the modern material science.

In the recent years, several efforts were devoted to the development magnetic nanosensor having an ultra high sensitivity approaching to the single spin level. In this framework, nano Superconducting Quantum Interference Devices (nano-SQUIDs) [1] seem to be the most promising sensors for the nanoscale applications because they exhibit an ultra high magnetic moment sensitivity (few spin or Bohr magnetons per unit of bandwidth) and allow direct magnetization changes in small spin systems [2–6]. NanoSQUIDs are typically based on nano-constrictions in a superconducting film, (Dayem nano-bridges), easily fabricated by a single nanopatterning step [1, 2]. However, they exhibits a quite different behavior compared to a standard one based on Josephson tunnel junctions. In particular, the critical current modulation depths are small leading to an increase of magnetic flux noise. Moreover, the nanobridge-based SQUIDs do not show a good critical current reproducibility and a robustness against the thermal cycles. In this paper, a very low noise three-dimensional (3D) nanoSQUID based on deep submicrometer Josepshon tunnel junctions fabricated by a Focused Ion Beam (FIB) sculpting technique is presented.

Compared to typical nanoSQUIDs, the main advantages of the proposed nanosensor, are a better control of the critical current, the high modulation depth of the critical current and the ultra low noise. Furthermore, being based on a fully reliable niobium technology, this 3D nanoSQUID is more reliable and robust with respect to the thermal cycles.

C. Granata (✉) · A. Vettoliere
Istituto di Cibernetica "E. Caianiello" del Coniglio Nazionale delle Ricerche, 80078 Pozzuoli, Napoli, Italy
e-mail: c.granata@cib.na.cnr.it

M. Fretto · N. De Leo · V. Lacquaniti
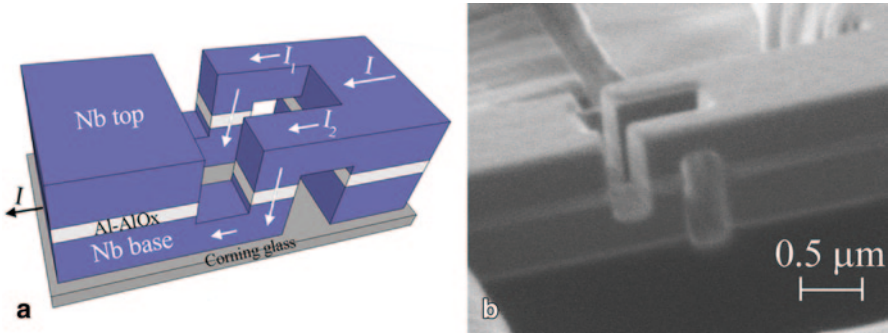Istituto Nazionale di Ricerca Metrologica, Torino, Italy

Fig. 60.1 **a** Sketch of the device, showing the current paths through the device. **b** Scanning electron micrograph of a 3D nanoSQUID fabricated using Focused Ion Beam (FIB) sculpting tecnique

60.2 Sensor Design and Fabrication

The device consists of a loop area down to 0.2 μm^2, and two square sub-micron Josephson junctions having a side length of 0.3 μm. The nanoSQUIDs are based on Nb/Al-AlOx/Nb S/N-I/S (Superconductor-Normal metal-Insulator-Superconductor) junctions and are fabricated by using an innovative 3D FIB based nanomachining [6]. The first step consists in the deposition of Nb/Al-AlO$_x$/Nb multilayer structure by a RF magnetron sputtering in a high vacuum ambient. The thickness of the two niobium electrodes is 350 nm, while the aluminium layer is 80 nm thick. The tunnel barrier is obtained by oxidizing Al in pure oxygen, without breaking the vacuum. The following step was the definition of the SNIS junctions and consequently the loop by the 3D FIB sculpting method. In detail, positioning the sample perpendicular to the ion beam trajectory, a multilayered microstrip was roughly narrowed by a multi-step etching down to 1.5 μm. Afterwards, a rectangular hole was realized in the centre of the strip, resulting in two parallel lamellae and defining both the Josephson junction's width and the loop of the nanoSQUID device. At the end, the sample was tilted parallel to the beam and two side cuts through the two lamellae were performed (Fig. 60.1).

60.3 Sensor Performance

The nanoSQUIDs have been characterized in liquid helium (T=4.2 K) shielded by a coaxial lead/cryoperm double cylinders and a low noise electronics [6].

Figure 60.2a reports the voltage vs external magnetic flux (V−Φ) characteristic for a bias current of 160 μA. Note that the V−Φ curve are resonance-free allowing the device to work in a wide region of bias points. This circumstance guarantees a good stability of device operation in both small signal mode and in flux locked loop configurations. The maximum voltage swing is ΔV=60 μV. In Fig. 60.2b, the
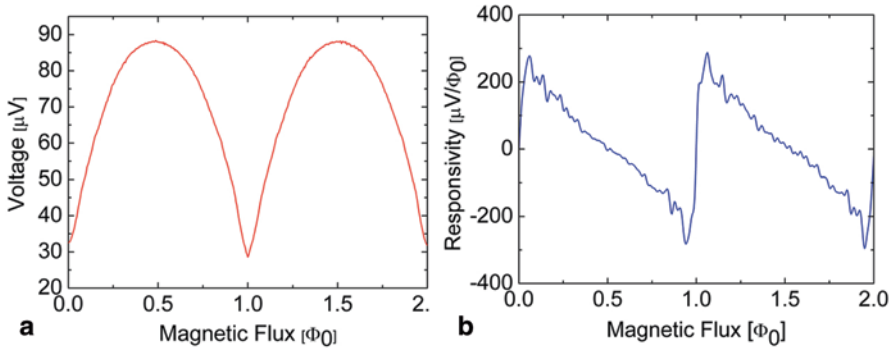
Fig. 60.2 a Voltage vs external magnetic flux (V-Φ) characteristics for a bias currents of 160 μA measured at T=4.2 K. **b** Voltage responsivity as a function of the external magnetic flux
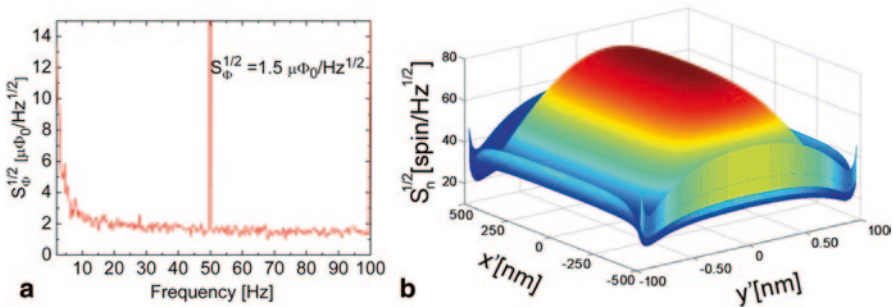
Fig. 60.3 a Spectral density of the magnetic flux noise measured at T=4.2 K in small signal mode using a low noise readout electronics. **b** Distribution of magnetic moment or spin noise spectral density $S_n^{1/2}$ of a rectangular nano-SQUID as a function of the position within its loop

magnetic flux-to-voltage transfer factor as a function (responsivity, $V_\Phi = \partial V/\partial \Phi$) of the external magnetic flux is reported. It is obtained by taking the maximum derivative of the V−Φ characteristic. We found a responsivity value as high as 300 μV/Φ_0 for an external magnetic flux of about 0.1 Φ_0. In the Fig. 60.3a, the spectral density of magnetic flux of the nanoSQUID under investigation is reported. It is measured in small signal mode by employing a low noise read–out electronics with a direct coupling scheme. In the white region, the nanoSQUID exhibited an intrinsic magnetic flux noise level as low as 1.5 μΦ_0/Hz$^{1/2}$, while the peak at the frequency value of 50 Hz and its multiple, are due to the electric power distribution disturbances.

An important factor of merit of a nanoSQUID is the magnetic moment or spin sensitivity. As reported in reference [7], an estimation of the spin sensitivity can be obtained by computing the magnetic flux $\Phi(x', y', z')$ produced by a single elementary magnetic moment oriented along the axis normal to the plane of the SQUID loop and positioned in a generic point (x', y', z') within the loop, where z' is the distance from the coil's plane and x', y' are the position in the loop plane. The z'

value is much smaller than the loop side length, thus the particle can be reasonably considered in the plane of the loop and no field divergence arises in correspondence of the loop edges. In order to have an estimation of the spin noise as a function of its position within the nanoSQUID sensitive area, the distribution of the spin noise over the capture area of the device (Fig. 60.3b) has been computed. It is evident from the Fig. 60.3b the presence of a frame within the loop where the sensor is more sensitive. The spin noise in the central region is about 80 $\mu_B/Hz^{1/2}$ while close to the edges and corners it is less than 20 $\mu_B/Hz^{1/2}$.

60.4   Conclusions

In conclusion, an ultra high sensitive 3D nanoSQUID based on a reliable niobium submicron Josephson tunnel Junctions and fabricated by 3D FIB sculpting technique, has been presented.

Due to its reliability, robustness and high performances in terms of magnetic flux noise and spin sensitivity, the presented magnetic sensor represent a powerful tool for nanoscience applications.

References

1. C. P. Foley and H. Hilgenkamp, Why NanoSQUIDs are important: an introduction to the focus issue. Supercond. Sci. Technol. **22**, 064001 1–5 (2009)
2. R. Russo, C. Granata, E. Esposito, D. Peddis, C. Cannas, A. Vettoliere, Nanoparticle magnetization measurements by a high sensitive nano-superconducting quantum interference device. Appl. Phys. Lett. **101**, 122601 1–4 (2012)
3. C. Granata, A. Vettoliere, M. Russo, and B. Ruggiero, Noise theory of dc nano-SQUIDs based on Dayem nanobridges. Phys. Rev. **B 84**, 224516 1–7 (2011).
4. D. Vasyukov, Y. Anahory, L. Embon, D. Halbertal, J. Cuppens, et al., A scanning superconducting quantum interference device with single electron spin sensitivity. Nature Nanotech. **8**, 639–644 (2013)
5. R. Wölbing, J. Nagel, T. Schwarz, O. Kieler, T. Weimann et al., Nb nano superconducting quantum interference devices with high spin sensitivity for operation in magnetic fields up to 0.5 T. Appl. Phys. Lett. **102**, 192601 1–4 (2013)
6. C. Granata, A. Vettoliere, R. Russo, M. Fretto, N. De Leo and V. Lacquaniti, Three-dimensional spin nanosensor based on reliable tunnel Josephson nano-junctions for nanomagnetism investigations. Appl. Phys. Lett. **103**, 102602 1–4 (2013)
7. C. Granata, A. Vettoliere, P. Walke, C. Nappi, and M. Russo, Performance of nano superconducting quantum interference devices for small spin cluster detection. J. Appl. Phys. **106**, 023925 (2009)

Chapter 61
High Resolution Ultrasonic Images by Miniaturized Fiber-Optic Probe

**Enrico Vannacci, Simona Granchi, Elena Biagi,
Luca Belsito and Alberto Roncaglia**

A new Micro-Opto-Mechanical System (MOMS) probe on optical fiber is presented. High miniaturization levels are reached in the MOMS devices (fiber-optic emitters and detectors with minimum diameter around 350 and 250 μm respectively). The transmitting element consists of an optical fiber with a graphite-compound absorbent layer on the tip. The receiving element is an extrinsic fiber hydrophone based on a Fabry-Perot interferometer, the thickness of which is modulated by ultrasonic signals. The possibility to use optoacoustic sources in conjunction with the fiber-optic acousto-optical detectors within a minimally invasive probe is demonstrated by successfully measuring the ultrasonic echo reflected from a fingerprint made of cornstarch flour and from a silicon substrate with micrometric machining. The ultra-wide bandwidth and the high frequencies allowed by photoacoustic generation, in conjunction with the extreme miniaturization derived from the MOMS technology, can generate images at very high resolution and permits to obtain different "ultrasonic views" of the investigated object.

61.1 Introduction

In recent years, optoacoustic emission of ultrasounds has been intensively studied as a possible solution for high-resolution biomedical imaging and tissue analysis [1–3]. The challenge of developing complete transmitting receiving ultrasonic transducers, based exclusively on fiber optic technology, is extremely important to define a new generation of ultrasonic probes. A high-frequency, wide-band ultrasonic

E. Vannacci (✉) · S. Granchi · E. Biagi
Dipartimento di Ingegneria dell'Informazione(DINFO), Università degli Studi di Firenze,
Via Santa Marta 3, 50139 Firenze, Italy
e-mail: enrico.vannacci@gmail.com

L. Belsito · A. Roncaglia
Istituto per la Microelettronica e i Microsistemi(IMM), CNR, Via Piero Gobetti 101, 40129
Bologna, Italy
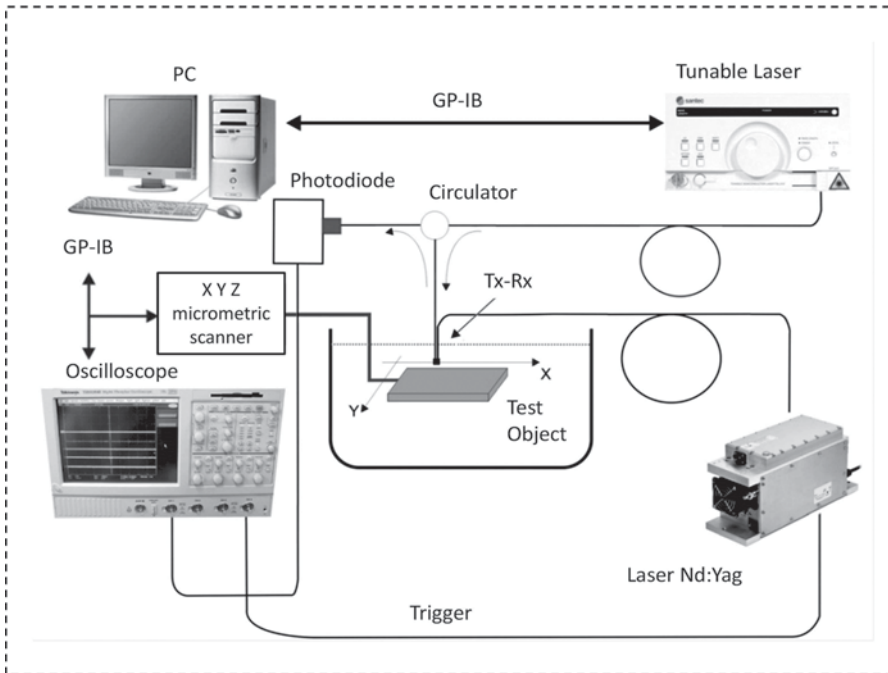
Fig. 61.1 Experimental set-up

probe based on opto-acoustic and acousto-optic devices, has been developed by our group [1–4] by the use of a Micro-Opto-Mechanical-System (MOMS) technology on micro-machined silicon frames.

61.2 Experimental Setup

The setup used for characterize the fiber optic probes is presented in Fig. 61.1. The transmitter present a cylindrical shape with a diameter respectively of roughly 350 μm and was mounted on a 200 μm multi-mode optical fiber. A Nd:YAG laser (PowerChip NanoLaser) with a wavelength of 1064 nm, a pulse energy of 50 μJ and a pulse Full Width Half Maximum (FWHM) of 500 ps was employed to irradiate the emitters.

The detector present a diameter of 250 μm and was mounted on a 125 μm single-mode optical fiber. The optical signal was generated by interrogating the Fabry-Perot cavity of the acousto-optical detector with a laser power of 8 mW using a San-tec TSL-210H tunable laser. The optical signal reflected by the cavity was splitted by an optical circulator (model 6015-3-FC, Oyokoden Lab Co.) in order to assure that the light generated by the laser source was only transmitted to the fiber-optic

Fig. 61.2a–c Three different "Ultrasonic Views" of the Fingerprint test object obtained by filtering the echo signals respectively at 10 MHz, 35 MHz and 70 MHz
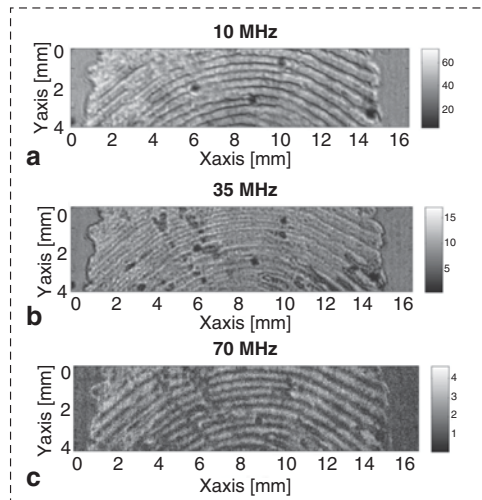
detector and did not interfere with the reflected light measured by a InGaAs photodiode (PDA10CF, Thorlabs Inc). A TDS Tektronix oscilloscope was used to acquire the signal from the detector.

All the measurements were carried out in a pulse-echo technique keeping the ultrasound source and the detector immersed in deionized water and positioned confocally at a 10° angle. The distance from the transducer faces and the acoustic beam intersection is 1 mm.

A bidimensional automatic XYZ scanner was used to reconstruct C-Scan images of the objects under investigation.

61.3   Results

In Fig. 61.2 and in Fig. 61.3 two results, obtained by a bi-dimensional automatic echo scan performed with a 50-μm step, are presented.

For each position of the scans, the acquired RF signals, gated at a depth corresponding to the echo position, have been filtered at different frequencies in order to highlight different details of the acoustic images; indeed by increasing the frequency of the filter it is possible to detect smaller details and different "ultrasonic views" of the object under investigation can be generated. The presented images were normalized with respect to their maximum value.

The first test object consists in a fingerprint covered with cornstarch flour pressed on a steel plate and sealed with waterproof transparent tape. In Fig. 61.2a four air bubbles positioned on the tape surface are visible. The micro cutting on the left of the fingerprint appears in Fig. 61.2b and it is evident in Fig. 61.2c.
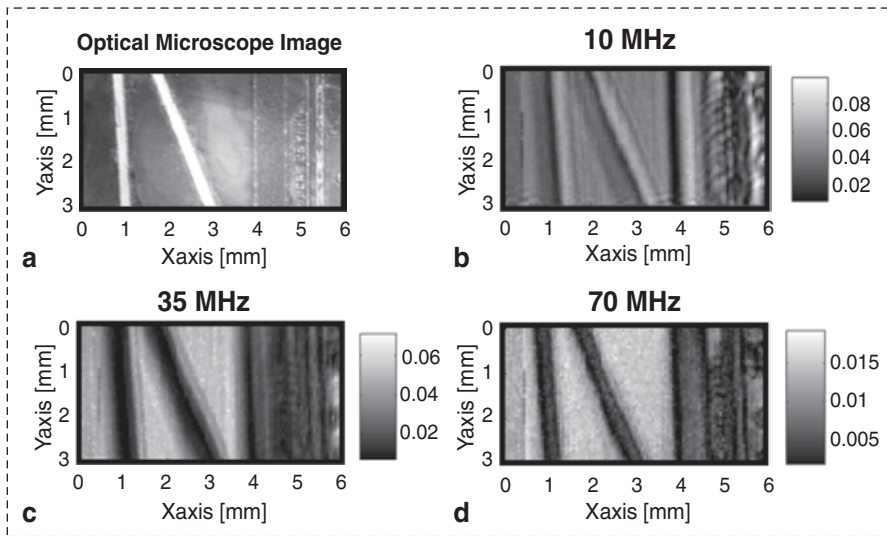
Fig. 61.3 In **a**: Optical image of the silicon substrate test object. In **b**, **c** and **d**: three different "Ultrasonic Views"

The second test object is constituted by a silicon substrate with some micrometric machining operations.

In Fig. 61.3 it is worth to note that in the 10 MHz filtered image of Fig. 61.3b it is impossible to distinguish between the different component of the test object. As the frequency increases more details of the micrometric machining operations are present in the ultrasonic image and in Fig. 61.3d it is possible to recognize almost all the details present in the optical image of Fig. 61.3a.

In particular it is worth noting that the resolution increases as the frequency increases. In fact, as and it can be observed in the images of Fig. 61.2 and Fig. 61.3, the high frequencies remain collimated for longer distances with respect to the low frequencies, because the near field zone directly depends on the frequency [5].

61.4 Conclusion

This work shows how the combination of the high frequencies allowed by photoacoustic generation, in conjunction with the extreme miniaturization derived from the MOMS technology, can generate images at very high resolution and permits to obtain different "ultrasonic views" of the investigated object. Furthermore it could open a way towards "virtual biopsy",intended as the possibility for studying and characterizing the nature and health conditions of living tissues "in situ".

References

1. E. Biagi, S. Cerbai, P. Gambacciani, and L. Masotti "Fiber Optic Broadband Ultrasonic Probe," *IEEE Sensors Journal*, n.10, pp.363–366, 2008.
2. E. Biagi, F. Margheri, and D. Menichelli, "Efficient Laser Ultrasound Generation by using Heavily Absorbing Films as Targets," *IEEE Trans. Ultrason., Ferroelectr., Freq. Contr.*, vol. 48, no. 6, pp. 1669–1680, Nov. 2001.
3. A. Acquafresca, E. Biagi, L. Masotti, and D. Menichelli, "Toward Virtual Biopsy Through an All Fiber Optic Ultrasonic Miniaturized Transducer: A Proposal", *IEEE Trans. Ultrason. Ferroelectr. Freq. Control.*, vol. 50, no. 10, pp. 1325–1335, Oct. 2003.
4. E. Biagi, S. Cerbai, L. Masotti, L. Belsito, A. Roncaglia, G. Masetti and N. Speciale, "MOMS Technology for Fully Fiber Optic Ultrasonic Probes: a Proposal for Virtual Biopsy," in IEEE Sensors, Hilton Waikoloa Village, Waikoloa, HI, USA, Nov. 1–4, 2010, pp. 1156–1160
5. G. S. Kyno, Acoustic Waves: Devices, Imaging, and Analog Signal Processing, Prentice-Hall, 1987, pp. 164–171.

Chapter 62
An Experimental Platform for the Analysis of Polydisperse Systems Based on Light Scattering and Image Processing

E. Viviani, F. Armani, A. Boscolo, B. Piuzzi and D. Salvalaggio

In this work an experimental platform for light scattering analysis has been developed using image sensors, as CCD or CMOS. The main aim of this activity is the investigation of the feasibility of using these types of sensors for polydisperse systems analysis. The second purpose is the implementation of an experimental platform which is enough versatile to permit the observation of different phenomena in order to develop novel sensors/approach using data fusion.

62.1 Introduction

A polydisperse system is a mixture composed by a continue phase and two or more dispersed phases which have different characteristics like state of matter, shape, dimension and mass. Typical examples of this kind of systems are colloids and suspensions. Polydisperse systems can be found in different fields and their analysis is essential in a wide range of scientific and technological applications. For example in microbiology this type of analysis is used for the observation of microorganism behaviour and in biochemistry for the study of macromolecules. This method is widely used in the industry, both in synthesis and production processes, as pharmaceutical, cosmetic and detergent production processes.

One of the physical phenomena that can be used to investigate these systems is the light scattering. This has been modelled for the first time by Rayleigh and Mie, from the end of '800 and beginning of '900 [1–3]. Other models and different methods of analysis were developed for particles dispersed, like SLS (Static Light Scattering), DLS (Dynamic Light Scattering) and turbidimetry/nephelometry [4, 5]. Various evolutions of these techniques have been developed recently allowing their use in new applications. The last years have been interested by a rapid development

E. Viviani (✉) · F. Armani · A. Boscolo · B. Piuzzi · D. Salvalaggio
Department of Engineering and Architecture, University of Trieste, via Valerio 10, 34127, Trieste, Italy
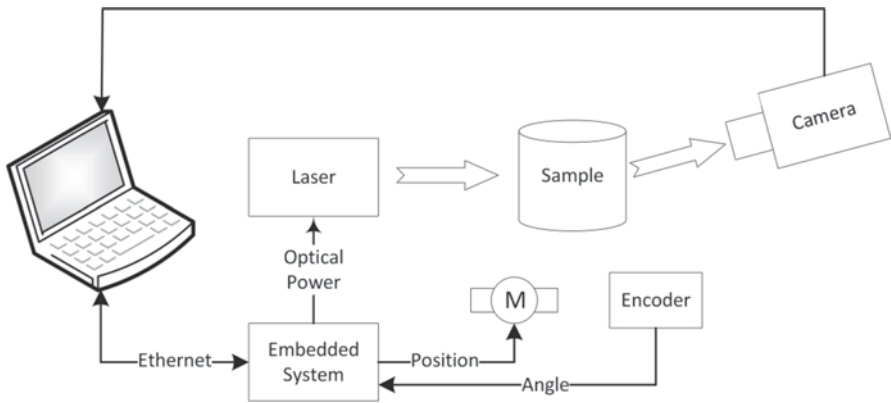e-mail: emanuele.viviani@studenti.units.it

355

Fig. 62.1 Block diagram of platform architecture

of new techniques like SALS (Small Angle Light Scattering), NFS (Near Field Scattering) and different type of cross-correlation methods [6, 7].

Current solutions that can be found on the market are often expensive and are designed for laboratory or in-line application. These solutions aren't cost effective, thus they can't be applied in consumer products. However, there is the necessity of having low cost sensors that could provide some information about the characteristics of the dispersed particles. Moreover a first estimation of the properties of the polydisperse system could be sufficient in many applications, in which the accuracy requirements are weak. However often is not possible to discriminate between two system states when observing a single phenomenon.

The idea behind this work is to observe multiple phenomena involving light scattering and to apply data fusion to infer information about the system.

62.2 Platform Architecture

The composition of polydisperse systems influences several properties of scattered light: its intensity depends on wavelength and angle of observation; the dispersed particles could produce a polarization variation of scattered light or even a depolarization; movements of particles produce time variation behaviour of light intensity. Another effect that can be observed is the spatial distribution of scattered light when observing the phenomena with a camera.

In this work a video camera was chosen as the main sensor. This can be used in any of the aforementioned case. Some solutions are the use of external tools as polarization filters or multiple light sources of different wavelength.

In order to develop a versatile architecture, a classical goniometer-based setup was chosen for the platform [3, 4] (Fig. 62.1).

The particular solution that was implemented consists of two concentric plates, one of which can rotate with an angular position actuator. Light sources and sensors can be mounted on both planes depending on which components need to be moved.
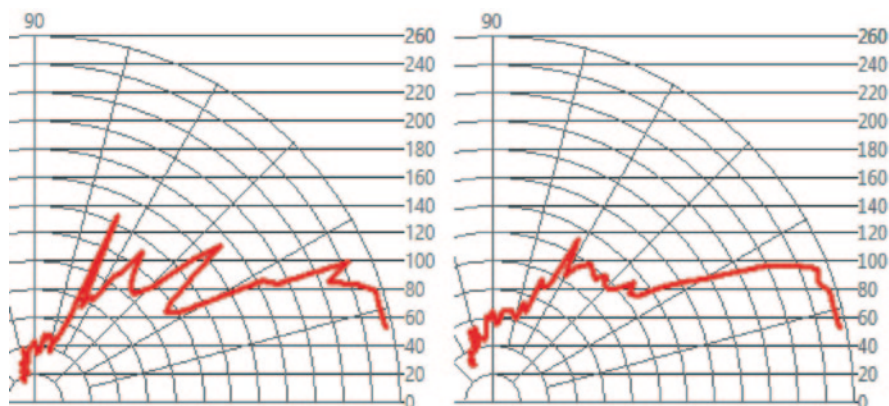
Fig. 62.2 Examples of light scattering polar diagram

A custom embedded electronic system control the platform. It was designed to have both digital and analog input-output capabilities. These allow managing more than one light source, like LEDs or laser diodes, and other optional light or temperature sensors.

A computer manages the whole system, acquiring signals from camera and communicating over Ethernet with the embedded system.

The platform is entirely modular so that it can be customized depending on the test type for which it will be used. A dedicated software can record both photo and video taken at fixed angle of view or in a continuous range. Moreover, it is capable of processing acquired images in real time or in a post processing step, even with the use of commercial image processing software.

The system has been calibrated using toluene as a reference. The detected scattered light has been used to normalize the response of the sensor. By this mean it was possible to compensate the intrinsic angular dependence of the goniometer-based setup [4].

62.3   Preliminary Tests

Some tests were done in order to verify the observability of various phenomena with the developed platform.

Figure 62.2 shows two polar diagrams of different colloids which were obtained by averaging the light intensity signal of acquired images.

In a second test, the use of a polarized filter was evaluated. This filter was placed in front of the camera, oriented orthogonal compared to the polarization of incident light. The test showed a good capability of the system to highlight the particles that induce light depolarization.

Fig. 62.3 a Original acquired
image. **b** High-pass filtered
image. **c** Low-pass filtered
image

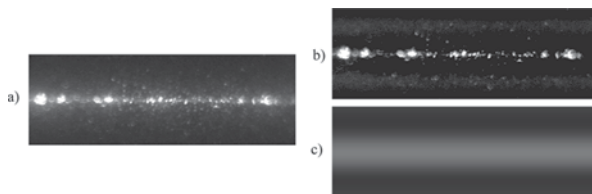Figure 62.3 shows results of applying high-pass and low-pass spatial filters. With this processing example it is possible highlight either the particles or the background luminance. The latter component of the image is due to particles smaller than camera resolution. For example this techniques can be applied to improve signal to noise ratio when one of the two components represent a noise for the measurement.

Additional tests were done in order to consider image processing that use time variations of the signal, like time averaging and time correlation.

62.4   Conclusions

The presented work represent a first step in the development of novel sensors for polydisperse systems analysis. On one hand the developed platform allows observing various phenomena; on the other it is a useful tool to test new techniques that merge different observed properties of scattered light. The use of a camera as a sensor allows the use of image processing tools. This will also enable the development of new analysis methods.

Future works will concern the metrological characterization of the system and the implementation of other type of processing. In a later stage a method to measure concentrations of components of a polydisperse system will be developed, in order to compare its performance to commercial solutions.

References

1. H. C. Van de Hulst, Light Scattering by Small Particles, Courier Dover Publications, 1957.
2. D. R. H. Craig F. Bohren, Absorption and Scattering of Light by Small Particles, Wiley, 1983.
3. R. Xu, Particle characterization: light scattering methods, Professor Brian Scarlett, 2002.
4. W. Schärtl, Light Scattering from Polymer Solutions and Nanoparticle Dispersions, Springer, 2006.
5. M. Sadar, Turbidity Standards; Technical Information Series, Booklet 12; Hach Company: Loveland, CO, USA.
6. F. Scheffold, R. Cerbino, New trends in light scattering, Current Opinion in Colloid & Interface Science 12, 2007, 50–57.
7. N. C. Alvarez, M. T. Garea, F. P. Quintian, Implementation and comparison of dynamic and static light scattering techniques for polydisperse particle sizing using a CCD camera, Journal of Physics: Conference Series 274, 2011.

Chapter 63
Structural Health Monitoring in the Railway Field by Fiber-Optic Sensors

Aldo Minardo, Agnese Coscetta, Giuseppe Porcaro, Daniele Giannetta, Romeo Bernini and Luigi Zeni

63.1 Introduction

In railway infrastructure monitoring, structural health monitoring (SHM) is a key element of industrial businesses. Standard inspection techniques may fail in revealing defects or unusual features, and some components may not receive close up examination if, for example, access is difficult or operating conditions do not permit it. Distributed optical fiber sensing techniques allow distributed temperature and strain measurements to be captured in real time over lengths of a few meters to tens of kilometers [1]. A permanently installed optical fiber cable provides continuous information about the status of the structure during its whole life cycle, thereby offering a unique opportunity in long-term SHM [2, 3].

Also, distributed sensors are able to acquire in real time the deformation of the rail track induced by train passage [4].

In this work, we report dynamic strain measurements performed by using the Brillouin Optical Time-Domain Analysis (BOTDA) in the Slope-Assisted configuration [5]. The tests were performed on the Peschici–San Severo regional railway line, connecting the northern coast of Gargano to the Adriatic railway, and operated

A. Minardo (✉) · A. Coscetta
Dept of Industrial and Information Engineering, Seconda Università di Napoli, Via Roma 29, 81031 Aversa, Italy
e-mail: aldo.minardo@unina2.it

G. Porcaro
Tecnomatica SaS, Corso del Mezzogiorno III trav., 71122 Foggia, Italy

D. Giannetta
Direzione di Esercizio, Ferrovie del Gargano, San Severo, 71016 Foggia, Italy

R. Bernini
Istituto per il Rilevamento Elettromagnetico dell'Ambiente, Consiglio Nazionale delle Ricerche, Via Diocleziano, 328, 80124 Napoli, Italy

L. Zeni
Dept of Industrial and Information Engineering, Seconda Università di Napoli, Via Roma 29, 81031 Aversa, Italy
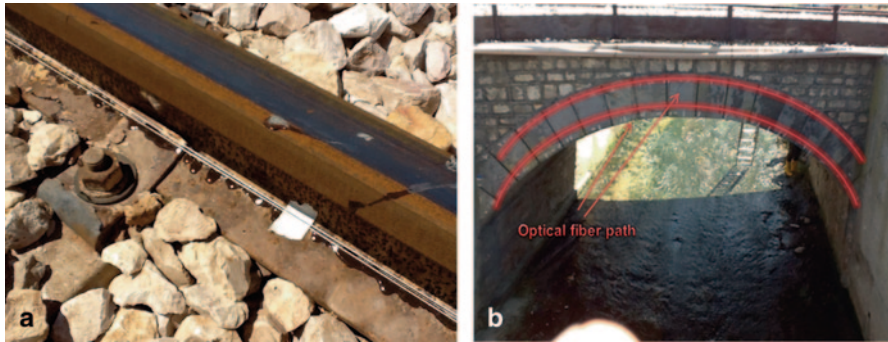
Fig. 63.1 **a** Instrumented rail sector and **b** instrumented rail bridge (picture of "sea side"). *The red curves* indicate the path of the glued optical fiber

by Ferrovie del Gargano. In particular, dynamic tests were performed along a 60 m length of rail sector (see Fig. 63.1a) and a stone bridge, (see Fig. 63.1b) located in proximity of the San Menaio Station.

63.2 Results of Dynamic Strain Measurements Along the Rail Track

The acquisition of dynamic strain along the rail track during train passage offers a mechanism to derive a number of useful parameters in the context of railway traffic monitoring, such as axle counting and spacing, speed detection, and dynamic load estimation [4].

Dynamic strain was acquired along a standard telecommunications single-mode optical fiber, glued along the rail foot for a length of 60 m by use of epoxy adhesive. Details on the installation procedure can be found in Ref. [4]. When the train passes over the instrumented rail, the weight of each axle induces a deformation on the rail itself, which is transferred to the optical fiber. If the latter is disposed below the neutral axis of the rail, a localized, tensile strain peak is recorded by the sensor at each axle passage. Therefore, axle counting can be easily achieved by counting the number of strain peaks associated to the passing train, provided that the acquisition rate is sufficiently high [4, 6]. Furthermore, a dynamic strain temporal waveform is retrieved for each sensed position, thereby offering the opportunity to retrieve other pieces of information such as axle spacing and train speed [4]. We show in Fig. 63.2a the map of dynamic strain captured by the Slope-Assisted BOTDA sensor at a spatial resolution of 1 m and an acquisition rate of 31 profiles/s, when the instrumented rail sector is crossed by a diagnostic car. The latter was composed of a two-bogies (four axles) motor car, followed by two trailer cars, each one composed of two bogies. The measurement was performed in a special condition, in which the train, bound for Rodi, was accelerating when passing over the monitored sector.
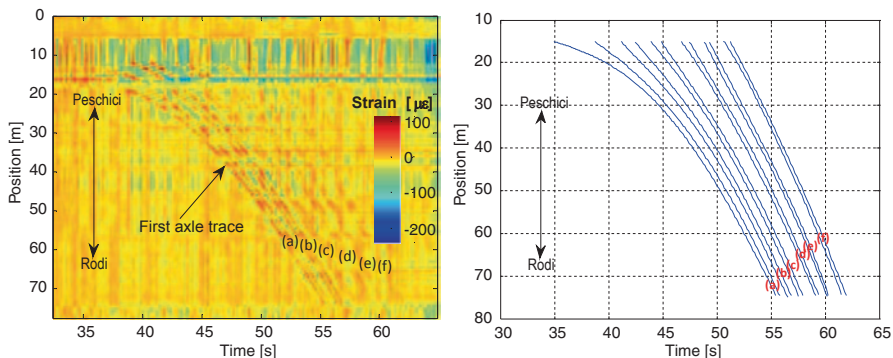
Fig. 63.2 Strain induced on the rail track by diagnostic car passage as a function of time and position. The letters from (*a*) to (*f*) indicate the six bogies of the train

Note that the positions corresponding to the fiber portion attached to the rail, range from z ~ 12 m to z ~ 72 m. Carefully examining the strain map, up to six bogies (12 axles) are recognized: two of them belong to the motor car (e–f), the other four belong to the trailer cars (a–d). We observe that the axle traces are not straight lines, rather they show some curvature. A curvature in the space-time representation is a clear indication of acceleration. In particular, the measurements indicate a positive acceleration of the train during its passage over the monitored sector. Note that, along the very first meters of the instrumented rail (from z ~ 12 m to z ~ 20 m), the slopes of the various axle traces are not uniform, instead they increases when moving from bogie (f) to bogie (a). This is due to the fact that, while the motor car is accelerating, the two trailer cars move at lower speed due to inertia, as it is also confirmed by the fact that the axle traces get increasingly closer during the measurement interval. It is also interesting to observe that the last trailer car (boogies (a) and (b)) induces a larger deformation than the other two cars, although all the cars have the same nominal load. This is an obvious consequence of the fact that the train is accelerating, resulting in a load transfer from front to rear axles.

63.3   Results of Dynamic Strain Measurements Along the Rail Bridge

The second test was performed on a railway bridge located close to the instrumented rail sector. The bridge is a 3 m-long, single span, stone arch bridge, showing evident signs of ageing. A piece of single-mode standard fiber, identical to the one employed in the previous test, was glued directly over the bridge following four paths, two of them are highlighted in Fig. 63.1b, while the other two lied on the opposite side. The measurements, carried out at 1 m spatial resolution and 43 profiles/s acquisition rate, were performed during the passage of a two-bogies (four axles) train over the bridge. The results, summarized in Fig. 63.3a, reveal two definite, compressive
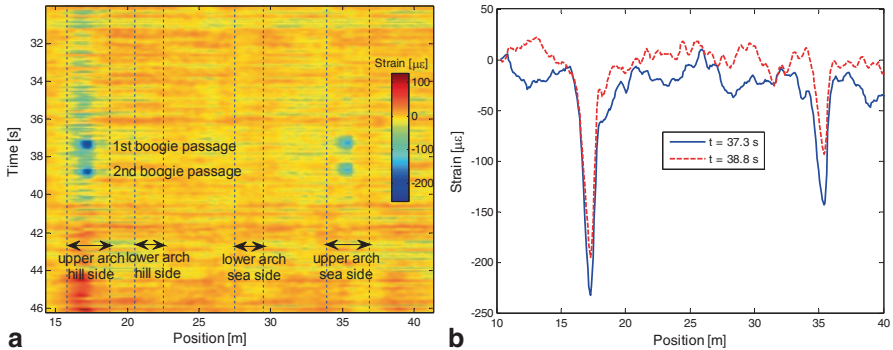
Fig. 63.3 **a** Strain induced on the arch bridge by train passage, as a function of time and position. **b** Strain induced on the arch bridge by train passage as a function of position, at $t=37.3$ s (*blue solid line*) and $t=38.8$ s (*red dashed line*)

strain peaks acquired at the passage of each bogie. Mapping these two fiber positions on the monitored structure, these two sections correspond to the upper part of the arch keystone. Figure 63.3b reports the strain acquired at the instants in which the two train bogies pass over the bridge.

63.4 Conclusions

A fiber-optic distributed sensor has been employed for integrated monitoring of railway infrastructures. The sensor is based on stimulated Brillouin scattering in an optical fiber. The results indicate that, gluing an optical fiber along the rail track, running conditions of passing trains can be determined. Furthermore, dynamic strain measurements on a rail bridge have been reported, aimed to detect potential structural defects. It is believed that health monitoring systems based on distributed optical fiber sensors may offer valuable information in evaluating structural integrity, durability and reliability, and in ensuring optimal maintenance planning and safe operation.

References

1. X. Bao, L. Chen, Recent Progress in Brillouin Scattering Based Fiber Sensors. Sensors **11**, 4152–4187 (2011)
2. A. Minardo, R. Bernini, L. Amato, L. Zeni. Bridge Monitoring Using Brillouin Fiber-Optic Sensors. IEEE Sensors J. **12**, 145–150 (2012)
3. M. Ko, Y. Q. Ni. Technology developments in structural health monitoring of large-scale bridges. Eng. Struct. **27**, 1715–1725 (2005)

4. A. Minardo, G. Porcaro, D. Giannetta, R. Bernini, L. Zeni. Real-time monitoring of railway traffic using slope-assisted Brillouin distributed sensors. Appl. Opt. **52**, 3770–3776 (2013)
5. R. Bernini, A. Minardo, L. Zeni. Dynamic strain measurement in optical fibers by stimulated Brillouin scattering. Opt. Lett. **34**, 2613–2615 (2009)
6. M. L. Filograno, P. Corredera Guillen, A. Rodriguez-Barrios, S. Martin-Lopez, M. Rodriguez-Plaza, A. Andres-Alguacil, M. Gonzalez-Herraez. Real-Time Monitoring of Railway Traffic Using Fiber Bragg Grating Sensors. IEEE Sensors J. **12**, 85–92 (2012)

Chapter 64
Wireless Telemetric Technique for Resistive Sensors in Biomedical Applications

Emilio Sardini and Mauro Serpelloni

The measurement of different quantities inside the human body has considerable difficulties due to various factors, including the characteristics of the environment itself, which may not allow the proper use of electronics or cabled connections between the inside and outside of the human body. The proposed solution is given by a passive telemetric system consisting of a passive sensor positioned within the human body and an external readout unit. In this paper, the passive sensor is a resistive sensor connected to an inductor, while the readout unit is connected to a second inductor positioned externally the measurement environment. No batteries are requested inside the human body, avoiding maintenance and risks for the subject. The proposed telemetric technique is based on a measurement of the impedance at the readout inductor's terminals and on a mathematical processing that extracts the sensor resistance value. Further experimental results are in progress.

64.1 Introduction

In the literature, telemetry systems providing a measurement of a wireless passive capacitive sensor positioned in a protected environment are reported, for example within the human body [1, 2] or in environments in which the proper functioning of electronics is not possible [3, 4]. The research group has been working for several years on these techniques and different solutions are proposed in the literature concerning telemetric techniques for capacitive sensors and proposing both measurement techniques [5, 6] and innovative circuit solutions [7]. However, the study of solutions that make it possible to apply such techniques, or new techniques, even at resistive sensors can allow to extend the measurement capabilities to resistive sensors and therefore in quantities that cannot be measured with capacitive sensors.

M. Serpelloni (✉) · E. Sardini
Dip. di Ingegneria dell'Informazione, Università di Brescia, via Branze 38, 25123 Brescia, Italy
e-mail: mauro.serpelloni@ing.unibs.it

In a previous work, a technique for low-value resistive sensors is proposed [8]. In this paper, a measuring method for telemetric sensors based on resistive transduction for biomedical application is presented. The proposed solution is presented for resistive sensors of worth tens of kilo ohms.

64.2   Telemetric Technique

The proposed circuit that models the designed telemetric system for resistive sensors is reported in Fig. 64.1. The symbols are defined as follows: Rp and Rs are the inductor parasitic resistances; Cs and Cp are the inductor parasitic capacitances; Lp and Ls are the leakage inductances; Lm is referred to coupled flux; $N1$ and $N2$ are the equivalent number of the inductor windings; Rx is the sensor resistance and Cx is a fixed capacitor, which is used as a parameter for tuning the resonant frequencies. Since the working frequency is high, Rp and Rs are neglected, and Cps can be neglected since its value can be greatly reduced by a proper design. Consequently a simplified model is reported in the low part of Fig. 64.1; Ct is the parallel between Cs and Cx, whereas Ca and L are the capacitance and inductance seen by the readout as shown in Fig. 64.1. The configuration has an impedance diagram Z of the modulus and phase of as reported in Fig. 64.2; four frequencies were analyzed (f_a, f_b, f_c and f_{min}). f_{min} represents the frequency at which the impedance phase is minimum in a short interval.

The impedance Z was calculated and reported in the following.

$$Z(s) = \frac{(L_m + L_p)Rs + (L_m L_p + L(L_m + L_p))s^2 + C_a(L_m L_p + L(L_m + L_p))Rs^3}{R + (L + L_m)s + (C_a(L + L_m) + C_p(L_m + L_p))Rs^2 + C_p(L_m L_p + L(L_m + L_p))s^3 + C_a C_p(L_m L_p + L(L_m + L_p))Rs^4}$$

In Table 64.1, the values used in the model are those of a real experimental system (Fig. 64.3) and in Table 64.2 the commercial resistors. Cx was chosen through a sensitivity analysis done by Wolfram Mathematica. The analysis showed that increasing Cx is possible to neglect the effect of Cp allowing a simpler model formulation. Thus,

$$\bar{Z}(s) = \frac{(L_m + L_p)Rs + (L_m L_p + L(L_m + L_p))s^2 + C_a(L_m L_p + L(L_m + L_p))Rs^3}{R + (L + L_m)s + C_a(L + L_m)Rs^2}$$

The analysis showed that the sensitivity of the phase value φ measured at f_{mim} with respect to Rx decreases with increasing of Cx. Therefore, it was necessary to choose a value of Cx (549.87 pF) allowing one side to neglect the effect of Cp and the other to have a good sensitivity.
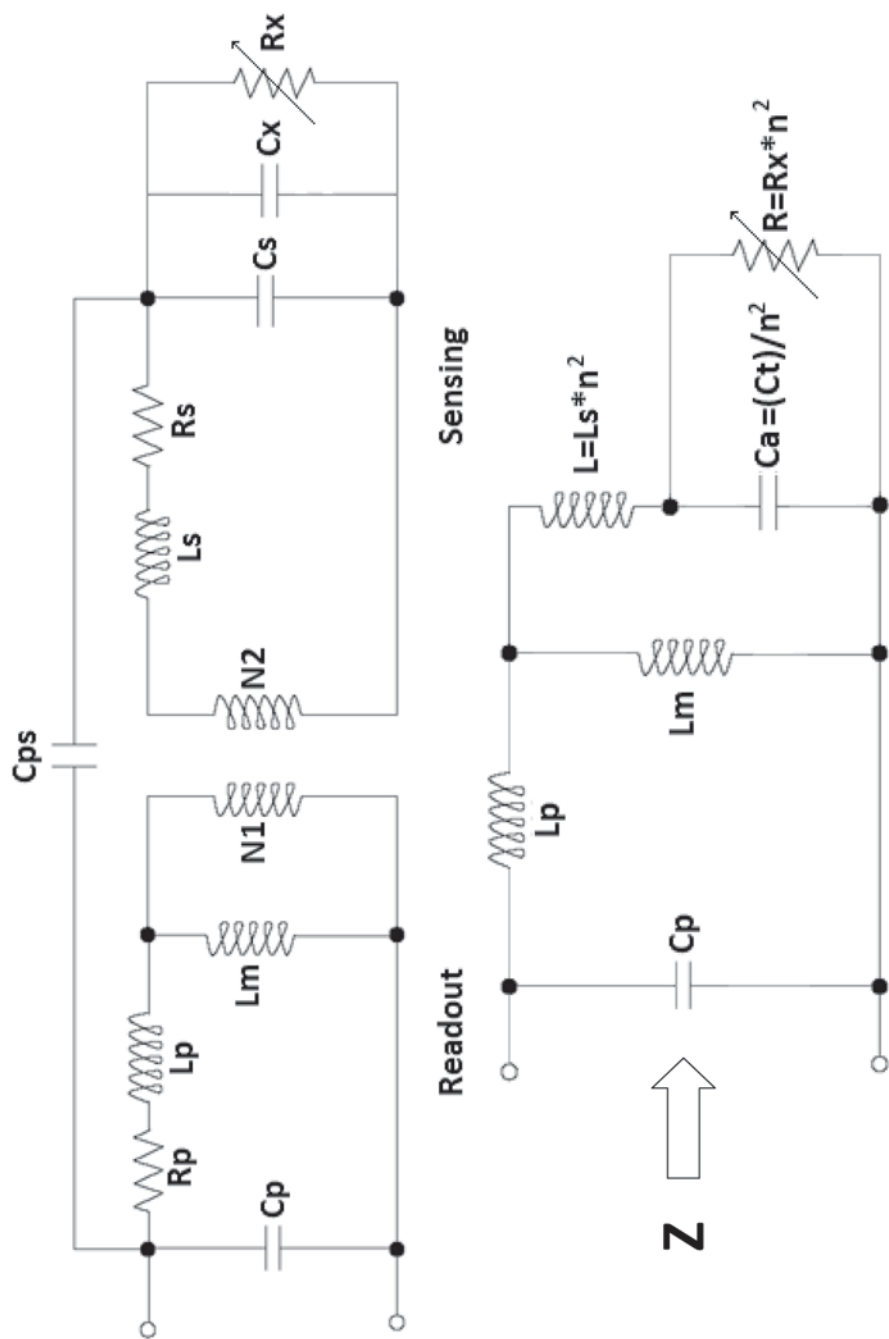
Fig. 64.1 Circuit model of a telemetric system suitable for resistive sensors

Fig. 64.2 Modulus and phase diagrams of the impedance at the readout inductor's terminals
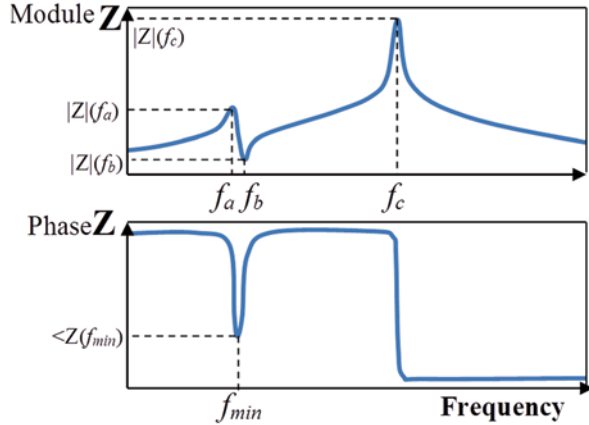
Table 64.1 Values of the model components used for mathematical analysis

Components	Values
Lp	31.94 μH
Lm	16 μH
Ls	12.58 μH
Cp	3.58 pF
Cs	1.73 pF
Cx	549.87 pF
n	1

Solving the simplified model it was possible to calculate the expression of R, which allows calculating the sensor resistance Rx by a measure of the phase φ at f_{min}. Thus,

$$R = \frac{1}{2bd}(-tan\varphi(ab - cd)) - \sqrt{(tan\varphi)^2 b^2 c^2 - 2(tan\varphi)^2 abcd + (tan\varphi)^2 a^2 d^2 - 4abcd}$$

Where,

$$a = (L_m L_p + L(L_m + L_p))\omega; \quad b = (L_m + L_p) - C_a a\omega; \quad c = (L + L_m)\omega; \quad d = 1 - C_a c\omega$$

64.3 Preliminary Experimental Results

An experimental system was developed to analyze the proposed solution; two planar inductors, one for the sensing circuit and one for the readout circuit (Fig. 64.3) was fabricated in PCB technology. The experimental system is composed by a

Fig. 64.3 Photos of the fabricated inductors and block diagram of the realized experimental setup
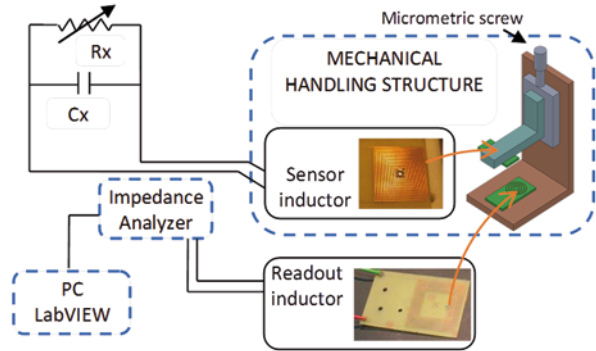
Table 64.2 The adopted Rx values

Rx values (Ω)
8170
9970
12020
14900
17940
21800
26700

wood structure with a micrometric screw for the correct positioning of the readout inductor respect the sensing inductor, at which *Rx* and *Cx* are connected.

The impedance at the readout inductor's terminals was measured using an impedance analyzer (HP4194A) and a PC (Personal Computer) with a LabVIEW program for the measurement process control. The mathematical and experimental results are briefly reported in Fig. 64.4. The calculated sensitivity is about 2°/kΩ. The experimental results obtained for the proposed configuration are reported; the data shows a good linearity and sensitivity, comparable with the data obtained with the mathematical analysis. Further experimental results concerning commercial sensors are in progress.

64.4   Conclusions

The preliminary experimental results demonstrate that the technology under study can be a viable solution for applications in hermetic and/or harsh environments that require the use of resistive sensors. Nevertheless, some considerations should be done to define its applicability; tuning capacitance *Cx* should be chosen properly to guarantee sensitivity and model applicability. Furthermore, during the measurement phase, the relative distance between the two inductors must be kept fixed. Further studies to investigate these aspects are in progress.
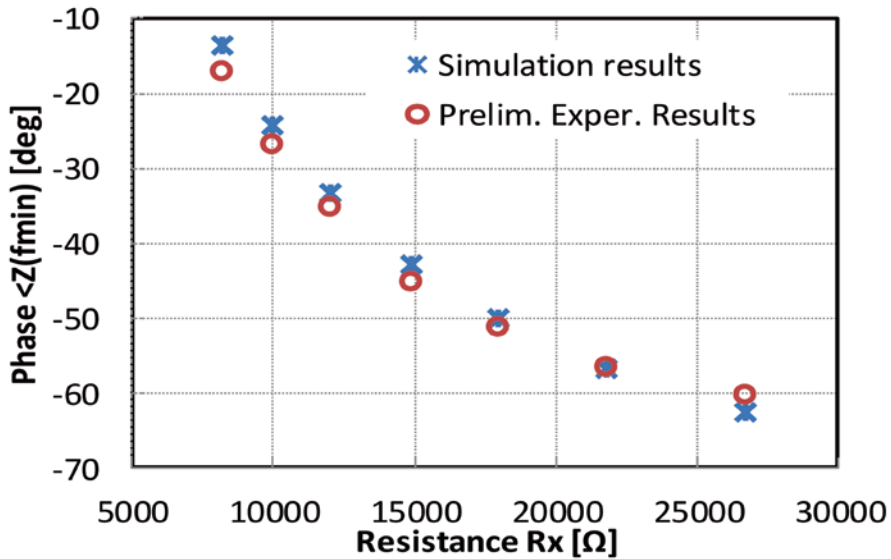
Fig. 64.4 The min-phase values vs. the sensor resistance values *Rx*

References

1. P.J. Chen, S. Saati, R. Varma, M.S. Humayun, Y.C. Tai. Wireless intraocular pressure sensing using microfabricated minimally invasive flexible-coiled LC sensor implant. Journal of Microelectromech. Systems **19**(4), 721–734 (2010).
2. N. Xue, J. B. Lee, S. Foland, S.P. Chang. Biocompatible polymeric wireless pressure sensor for intraocular pressure sensing application. Sensors, 2011 IEEE conference, 28–31 Oct. 2011, 1748–1751, (2011).
3. T. Salpavaara, J. Verho, P. Kumpulainen, J. Lekkala. Wireless interrogation techniques for sensors utilizing inductively coupled resonance circuits. Procedia Engineering **5** 216–219 (2010).
4. G. Jacquemod, M. Nowak, E. Colinet, N. Delorme, F. Conseil. Novel architecture and algorithm for remote interrogation of battery-free sensors. Sensors and Actuators A **160** 125–131 (2010).
5. D. Marioli, E. Sardini, M. Serpelloni, A. Taroni. A new measurement method for capacitance transducers in a distance compensated telemetric sensor system. Measurement Science and Technology, **16** (8), 1593–1599 (2005).
6. D. Marioli, E. Sardini, M. Serpelloni. An inductive telemetric measurement system for humidity sensing. Measurement Science and Technology, **19** (11), art. no. 115204 (2008).
7. E. Sardini, M. Serpelloni. Wireless measurement electronics for passive temperature sensor. IEEE Transactions on Instrumentation and Measurement, **61** (9), art. no. 6209429. 2354–2361 (2012).
8. E. Sardini, M. Serpelloni. Wireless measurement technique for telemetry low-value resistive sensors, Procedia Engineering, **25**, 1261–1264 (2011).

Chapter 65
Non-contact Measurement of the Heart Rate by a Image Sensor

Natascia Bernacchia, Paolo Marchionni, Ilaria Ercoli and Lorenzo Scalise

Nowadays there is a great attention in the biomedical field on the possibility to measure physiological parameters on a subject using a minimal invasive approach. In this paper, the authors propose an innovative, non-contact measurement method for the assessment of the heart rate (HR). The novel approach is based on the use of a digital camera to assess the color variation measureable on a subject face and caused by the periodic pumping action operated by the heart which allows the blood circulation. The paper report the methodological approach followed and the results obtained on ten voluntary subjects. Measured data are compared with HR values simultaneously measured by reference instruments. Cameras are available in many devices and this permits a large diffusion of this new method for the measurement of the heart rate that is the most important parameters to determinate a subject status of health.

65.1 Introduction

In the world, every year, 17 million of people die of cardiovascular diseases particularly heart attacks and strokes. The heart is one of the most important organ of the body and therefore the monitoring of its activity, in some cases, could be of primary interest for diagnosis purposes. The heart is a muscle which function is to periodically pump blood throughout the blood vessels allowing blood to reach the various parts of body. The energy that stimulates the heart occurs in the sinoatrial node, where an action potential is produced, which is sent across the atria and later to the ventricles. This periodic electric pattern, which invest the whole cardiac muscle, generates its contraction and consequently its pumping action. The frequency of the periodic contractions per minutes (bpm) is named Heart Rate (HR) and, in an adult, its normal rage can vary between 50 and 200 beats-per-minutes [1].

L. Scalise (✉) · N. Bernacchia · P. Marchionni · I. Ercoli
Dipartimento di Ingegneria e Scienze Matematiche, Università Politecnica delle Marche, via Brecce Bianche Monte Dago, 60131 Ancona, Italy
e-mail: l.scalise@univpm.it
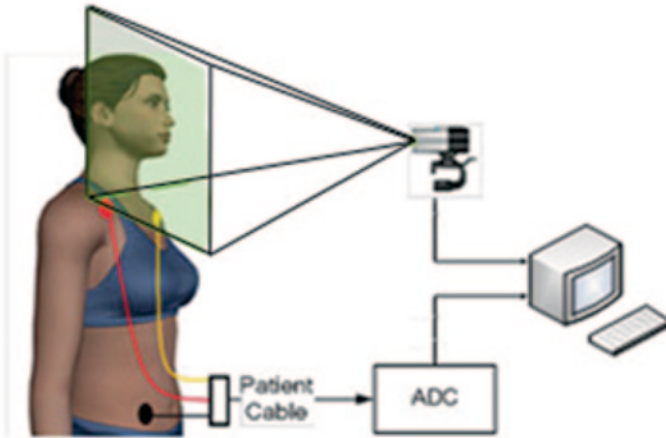
Fig. 65.1 The experimental setup used is composed by: CMOS Camera, ECG and an *ADC* board, a PC is used to record video and ECG signals and to operate the data computation

Routinely, the electric heart activity is monitored using an electrocardiogram (ECG) [2] which provides a time signal related to the different phases of the electrical activity of the heart. The sensing action is operated through the use of many skin-electrodes (up to ten electrodes) which are attached to the skin surface. HR is universally considered one of the most important physiological parameter and it is related to the health status of a subject [3]. Its values are related to his/her health status and also to his/her metabolic rate [4].

In this paper, the authors propose a novel measurements method for the measurement of the heart rate on a subject, based on the use of a digital imaging sensor (in our case a CMOS camera) which is characterized by complete absence of direct contact with the subject.

65.2 Materials and Methods

The measurement method proposed is based on the test set-up schematically reported in fig. 65.1. It is composed by a CMOS Camera (Microsoft LifeCam Studio, CMOS Technology) connected to a personal computer via USB and a reference ECG (ADInstruments) used to simultaneously measure the subject HR values. ECG is also connected to the PC via an analog-to-digital board and an USB. The camera video frames are acquired at 30 fps and are composed of single frame with a resolution of 320×240 pixels. The ECG measures the II lead and the sampling frequency set is of 1 kHz; an antialiasing filter is used on the ECG signal.

The passage of the blood pressure pulse along the vessels tree causes a local vasodilatation during the systolic pressure peak. This phenomenon is in particular
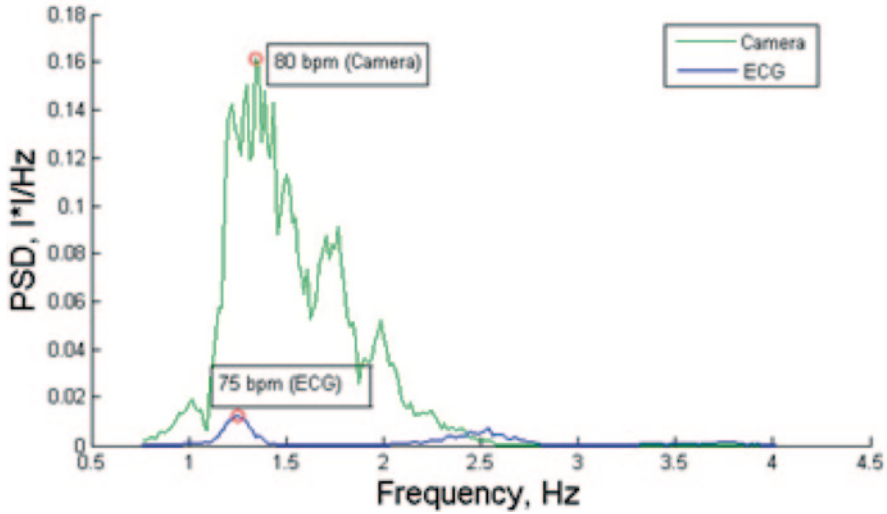
Fig. 65.2 Power spectrum densities of the measured (Camera) and reference (ECG)signals

visible in correspondence to the face surface vases. In fact, it causes an variation of the skin color intensity in correspondence to the vases. Typically the variation of color change is little and could not be perceived by eye. In this work a dedicated algorithm has been realized in order to emphasize the color variations due to passage of the blood pulse. In our experiments, 10 (5 male, 5 female) subjects have been used. The procedure consists of recording a video frame (duration 30 s) of the subject's face and simultaneously to acquire the ECG signal. A region of interest (ROI) is automatically select as rectangular box of the subject face.

The RGB channels from the digital camera are separated and from a specific study it resulted that the most sensitive channel for HR extraction is the green. Following the approach presented in [5], an Independent Component Analysis (ICA) [6] algorithm is applied and a wavelet decomposition is operated in order to obtain a signal with the same periodicity of the heart. A Power Spectrum Density (PSD) is applied on the signal in order to extract the HR values from its maximum peak (multiplying by 60) as reported in Fig. 65.2.

65.3   Results

The scatter plot obtained from the tests operated on the ten subjects (Fig. 65.3) shows a good correlation between the data measured with the proposed method and the data measured with the reference method (ECG): Pearson coefficient of 0.91. From our analysis, the HR values are affected by an uncertainty of ± 4 bpm (k = 1).
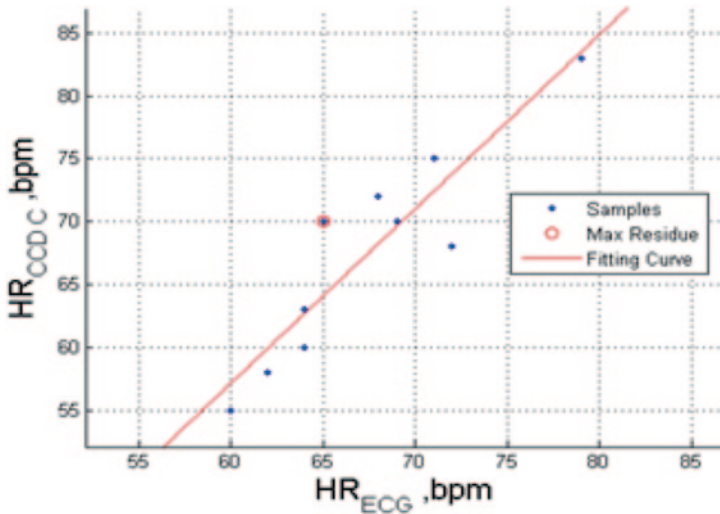
Fig. 65.3 Scatter plot of HR data measured with the proposed method (HR_CCD C) vs reference method (HR_ECG)

Identified possible sources of uncertainty are: the relative position of the digital camera respect to the subject face and his eventual movements artifacts during the test, the illumination pattern and also the color characteristics of the skin.

65.4 Conclusions

In this paper, the use of a standard digital camera for PC has been demonstrated to be feasible for non-contact remote heart rate monitoring. Result have been compared with a reference method/ECG) and a uncertainty of ± 4 bpm ($k = 1$) is reported from our tests.

The proposed method is characterized by the important advantage to operate without contact with the subject and its contactless nature is very important in particular operative conditions where the traditional ECG cannot be used (i.e. contaminated or dangerous area, such as the MRI machines) or where its use can be limited due to the skin conditions (i.e. burned or infectious patient).

From our tests, it results that the illumination conditions of the subject, rapid movements and camera to subject directions are the main limiting factors. To address such limits, redundancy of the imaging systems and optimization of the processing algorithm are under study.

Possible future use of the proposed method could also see non clinical scenarios such as the domestic environment where digital camera are already largely present (TV, smart phones, tablets, notebooks, home games, etc.).

References

1. Kumar; Abbas; Fausto (2005). *Robbins and Cotran Pathologic Basis of Disease* (7th ed.). Philadelphia: Elsevier Saunders. p. 556. ISBN 0-7216-01871-1.
2. J. Bronzino, The Biomedical Engineering Handbook (Vol 1), New York: Springer, 2000.
3. Jean Hopkins, Human Biology and Health., New Jersey: Englewood Cliffs, 1993.
4. Marie Dunford, Nutrition for Sport and Exercise, Cengage Learning, 2007.
5. Scalise, L.; Bernacchia, N.; Ercoli, I.; Marchionni, P., Heart rate measurement in neonatal patients using a webcamera. 2012 IEEE International Symposium on Medical Measurements and Applications Proceedings (MeMeA), pp. 1–4, 18–19 May 2012.
6. J. V. Stone, Independent component analysis: a tutorial introduction, MIT Press, n. ISBN 0-262-69315-1. Cambridge, Mass, 2004.

Chapter 66
Portable Low-power System for One-Lead ECG Monitoring and Datalogging

M. Baù, M. Ferrari and V. Ferrari

This work proposes a portable system for the measurement of ECG with a one-lead configuration for long term recording. The collected data are stored on high-density SD card for off-line examination. The present implementation focuses on low-power electronics to increase the battery lifetime, achieving about 16-h duration with two 158 mAh-capacity batteries. The system has proved to be able to detect heart rate anomalies on test subjects.

66.1 Introduction

ElectroCardioGram (ECG) and derived parameters like Heart Rate Variability (HRV) are of main concern in widely pervasive home care systems aimed to monitor patients for prevention or investigation of heart-related diseases or for after-incident follow-up [1]. Heart monitoring during daily or sleepy activity can be of particular interest for neurological disorders or sleep apnea detection. Nonclinical uses for home monitoring are also increasing. This scenario demands for portable, minimally-invasive, long-lasting battery-powered ECG monitors. With respect to clinical instruments, portable ECG monitors typically adopt a one-lead measurement configuration [2], which does not allow the measurement of the complete set of ECG derivations, but can provide relevant information in monitoring contexts. In portable systems, collected data can be transmitted on a wireless link to a dedicated subsystem for elaboration [3]. This solution possibly offers the advantage of real-time monitoring and readiness of intervention when anomalies are detected, but it is critical for battery duration of the portable device. Alternatively, in a more power saving approach, data can be permanently saved on on-board high-density mass storage devices for subsequent off-line examination. This work proposes a portable system for one-lead ECG measurement with on-board storage capability

M. Baù (✉) · M. Ferrari · V. Ferrari
Dept. Information Engineering, University of Brescia, Via Branze 38, 25123 Brescia, Italy
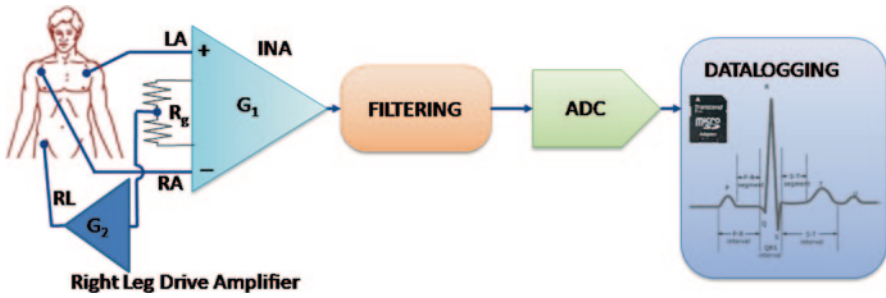e-mail: marco.bau@unibs.it

Fig. 66.1 Schematic block diagram of the proposed system

for long term recording and focuses on low-power electronics to increase the battery life-time. A first prototype has been fabricated and tested on human subjects to investigate both the capability of detecting different ECG derivation signals and evaluating the power consumption and related time duration.

66.2 System Description

The schematic diagram of the proposed system is shown in Fig. 66.1. The differential signal from the Left Arm (LA) and Right Arm (RA) electrodes is conditioned by a low-noise and low-power instrumentation amplifier (INA) with gain G_1. The common-mode signal is amplified with gain G_2 to drive the Right Leg (RL) electrode, used as the active reference, according to the one-lead measurement configuration [4]. The signal from the front-end is filtered for noise and 50-Hz interference suppression and digitized with a 10-bit ADC with a sampling frequency of 100 Hz. With the present configuration, the minimum detectable differential voltage from the electrodes is 5 μV and the overall bandwidth of the system, primarily set by the analog filter, is about 25 Hz. Digitized data are saved on a micro SD card from which they can be subsequently retrieved and analyzed. Figure 66.2a and Figure 66.2b show a picture of the realized prototype and a screenshot of the software interface for off-line retrieval, elaboration and visualization of collected data, respectively. Commercial general purpose ECG electrodes have been used during the experimental activity. By a proper collocation of the electrodes on the torso and depending on the differential voltage measured, different ECG signals can be obtained. In particular LEAD I, LEAD II, LEAD III, MCL1 signals have been considered [5].

66.3 Experimental Results

The capability of the circuit to measure the ECG signal has been tested on different volunteer subjects. Figure 66.3a shows a typical LEAD II signal measured with the proposed system, where the electrodes have been collocated on the torso according
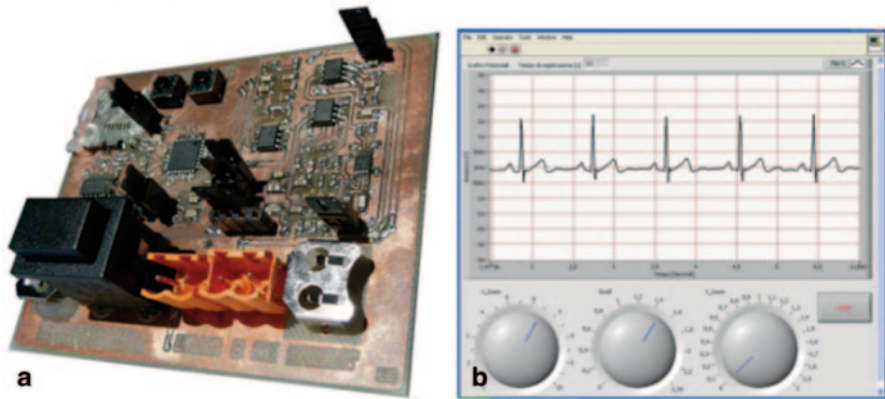
Fig. 66.2 a Picture of the realized prototype. **b** Screenshot of the software interface for off-line retrieval, elaboration and visualization of collected data
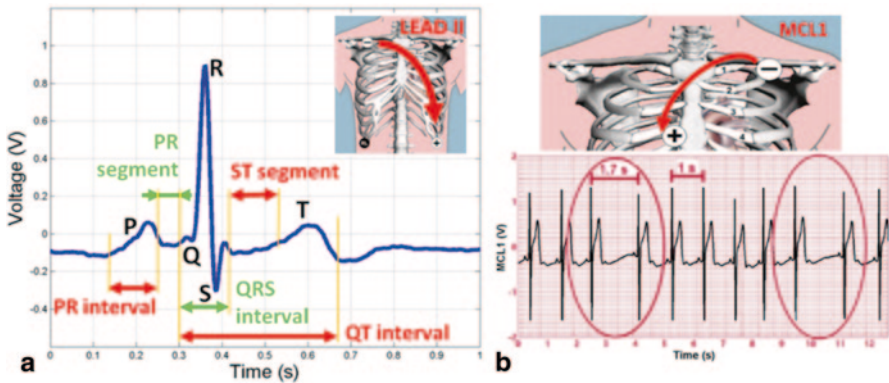
Fig. 66.3 a Waveform corresponding to a peak of LEAD II signal. The main characteristics of the ECG signal can be identified, namely the P wave, the T wave and the QRS complex. **b** ECG measured with the developed system corresponding to LEAD MCL1 on a subject affected by arrhythmia, later confirmed by clinical tests

to the diagram shown in the inset. In the 1-s recorded waveform, the P wave, the QRS complex and the T wave can be clearly identified as well as the PR and QT intervals, and the PR and ST segments, demonstrating that the proposed system is able to detect the distinctive characteristics of an ECG signal. To further investigate the proposed system, a different configuration of the electrodes according to the diagram of Fig. 66.3b, namely a LEAD MCL1 signal, has been tested on a different subject. Interestingly enough, the measured data reported in Fig. 66.3b show the detection of anomalous random heart-rate periods of about 1.7 s between normal heart-rate periods of about 1 s. Over a time record of about 12 s this anomaly, namely an arrhythmia, has been detected twice. The arrhythmia has been subsequently confirmed by rigorous clinical tests.

Fig. 66.4 Measured current
consumption of the system.
The peaks correspond to writ-
ing operation in the SD card.
In the inset a detail of the
writing cycle
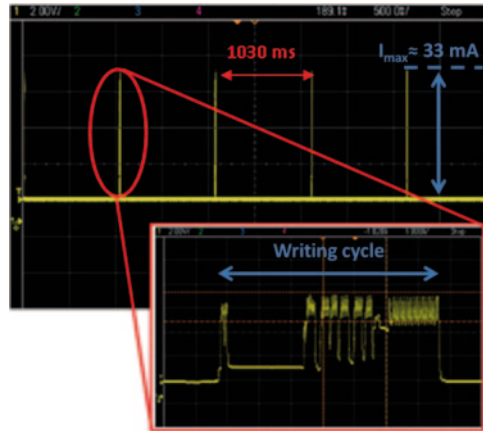
The energy consumption of the circuit has been also evaluated. The circuit has
been supplied by two 1.5-V LR44 alkaline batteries with nominal charge capacity
of 158 mAh. Figure 66.4 shows the typical working cycle of the system which con-
tinuously samples the conditioned signal from the electrodes and writes data on the
SD card every 1030 ms. In the inset the current during a write operation to the SD
card is shown. The writing operation is the most power-demanding task requiring
about 33 mA, while the analog and digital parts require 0.78 and 3.1 mA, respec-
tively. An average current consumption of about 4 mA has been estimated which
sets the duration of the current implementation at about 16 h.

66.4 Conclusions

In the present paper a prototype of a portable battery-powered system for measur-
ing the ECG by means of a one-lead configuration has been realized and tested on
different human subjects. The system is intended for continuous monitoring during
daily activity and logging the ECG on an on-board SD card for subsequent off-line
examination of data. With 158-mAh capacity batteries a duration of 16 h can be at-
tained that can be readily extended in the ongoing work.

References

1. S. Kumar, K. Kambhatla, F. Hu, M. Lifson, Y. Xiao, Ubiquitous Computing for Remote Cardiac Patient Monitoring: A Survey. International Journal of Telemedicine and Applications, 1–19 (2008).
2. P. Augustyniak, Wearable wireless heart rate monitor for continuous long-term variability studies. Journal of Electrocardiology **44**, 195–200 (2011).
3. M. Marzencki, K. Tavakolian, Y. Chuo, B. Hung, P. Lin, B. Kaminska, Miniature Wearable Wireless Real-time Health and Activity Monitoring System with Optimized Power Consumption. Journal of Medical and Biological Engineering **30** (4), 227–235 (2010).
4. B. B. Winter, J. B. Webster, Reduction of Interference Due to Common Mode Voltage in Biopotential Amplifiers. IEEE Transactions on Biomedical Engineering **30** (1), 62–66 (1983).
5. D. B. Geselowitz, On the Theory of the Electrocardiogram. Proceedings of the IEEE **77** (6), 857–896 (1989).

Chapter 67
Determination of the Minimum Resistor Area for Quasi-Simultaneous Heating and Temperature Sensing with Constant Thermal Resistance

Ivan Pini and Christian Falconi

67.1 Introduction

The specifications of our interest are: duty cycle d (*i.e.* the ratio between the time duration of the heating sub-cycle and the total "control period"); reference temperature T_0, minimum operating temperature, T_{MIN}, and maximum operating temperature, T_{MAX}, of the resistor; electrical resistivity ρ_0 and temperature coefficient α at the reference temperature T_0; minimum and maximum values for the thickness (t_m and t_M, respectively) and the width (W_m and W_M, respectively) of the resistor; input equivalent voltage error of the electronic interface, ΔV_{ERR}; heating power above a minimum required value $P_{HEAT, m}$; temperature measurement error ΔT_{ERR} below the maximum acceptable temperature measurement error $\Delta T_{ERR,M}$; maximum possible self-heating during temperature measurement $\Delta T_{MEAS,\max}$ below a maximum acceptable value $\Delta T_{MEAS,\max,M}$ for heaters whose minimum operating temperature is environment temperature; maximum current density (*i.e.* current density during heating) below a certain value $J_{MAX.}$

67.2 Mathematical Relations

The resistance can be expressed as

$$R = R_0\left[1 + \alpha(T - T_0)\right] = R_0 a = \left(\rho_0 \frac{L}{S}\right)a = \left(\rho_0 \frac{L}{tW}\right)a = \left(\rho_0 \frac{L^2}{tA}\right)a \quad (67.1)$$

I. Pini (✉) · C. Falconi
Dept. of Electronic Engineering, University of Rome Tor Vergata, Via del Politecnico 1, 00133 Rome, Italy
e-mail: ivan.pini@uniroma2.it

where a is a positive real coefficient. The maximum self-heating, if we neglect the temperature dependence of the thermal resistance between the microheater and the environment, is

$$\Delta T_{MEAS,\max} = P_{MEAS,\max} R_{TH} \tag{67.2}$$

ΔT_{ERR} is related to the error in the resistance measurement, ΔR_{ERR}, by the relation $\Delta T_{ERR} = \dfrac{\Delta R_{ERR}}{dR/dT} = \dfrac{\Delta R_{ERR}}{R_0 \alpha} = \dfrac{\Delta V_{ERR}}{R_0 \alpha I_{MEAS}} \leq \Delta T_{ERR,M}$, therefore ($I_{MEAS}$ is the measurement current that, ideally, does not depend on temperature):

$$k_0 \equiv \frac{\Delta T_{ERR,M}}{\Delta V_{ERR}} \geq \frac{tA}{\rho_0 L^2 \alpha I_{MEAS}} \tag{67.3}$$

From this relation, by using analytical expressions found in [3], we find the following limits for the area A

$$A \geq \frac{W}{\rho_0 \alpha k_0 J_{MAX}} \sqrt{\frac{a_{\max}}{a_{\min}} \frac{1-d}{d} \frac{R_{TH} P_{HEAT,m}}{\Delta T_{MEAS,\max,M}}} \equiv F_W(W) \geq F_W(W_m) \tag{67.4}$$

$$A \geq \frac{P_{HEAT,m}}{d \rho_0 a_{\min} J_{MAX}^2 t} \geq \frac{P_{HEAT,m}}{d \rho_0 a_{\min} J_{MAX}^2 t_M} \tag{67.5}$$

$$A \leq \frac{V_{DD}^2 d a_{\min}}{P_{HEAT,m} \rho_0 a_{\max}^2} W^2 t \tag{67.6}$$

67.3 Design Example

As an example, we assume that in the MEMS process of interest, due to technological limits, the width W and the thickness t of the integrated resistors must satisfy $10nm \leq t \leq 1\mu m$ and $1\mu m \leq W$ [2], [3]. Moreover, we consider the set of temperature-control specifications given in the following Table 67.1.

With these specifications, by using the analytical relations found in the previous paragraph, we obtain $A_{\min} = 0.025$ mm² which is the ultimate limit for the minimization of the area; however, in practice, similar to [1], it may be necessary to use slightly larger areas so that the specifications can be satisfied with some margin (e.g. even in presence of spread and drift). After determining the minimum possible area ($A_{\min}$) as the maximum of the last two members of (67.4) and (67.5), as schematically illustrated in Fig. 67.1, we can find the portion of the (W, t) plane which allows to design a minimum area heater; in practice, the coordinates W and t must both satisfy their respective technological limits as well as (by combining (67.4) with (67.6) and (67.5) with (67.6)) the inequality

Table 67.1 Temperature-control specifications

Parameter	Value
d, duty cycle	0.9
T_0, reference temperature	20°C = 293.15 K
T_{MIN}, reference temperature	300°C = 573.15 K
T_{MAX}, maximum temperature	500°C = 773.15 K
α, temperature coefficient of R at the reference temperature T_0	3920 ppm K^{-1}
ρ_0, electrical resistivity (platinum)	$1.06 \times 10^{-7} \Omega \cdot m$
J_{MAX}, maximum current density	$10^{10}\ \text{A}/\text{m}^2 = 10^6\ \text{A}/\text{cm}^2$
ΔV_{ERR}, input equivalent voltage error of the electronic interface	50 μV
$\Delta T_{ERR,M}$, maximum acceptable temperature measurement error	0.25 K
$\Delta T_{MEAS,max,M}$, maximum acceptable self-heating during temperature measurement	0.25 K
$P_{HEAT,m}$, minimum acceptable value for the heating power	0.5 W
R_{TH}, typical for membrane type resistors	2000 K$/$W
V_{DD}, supply voltage	5 V
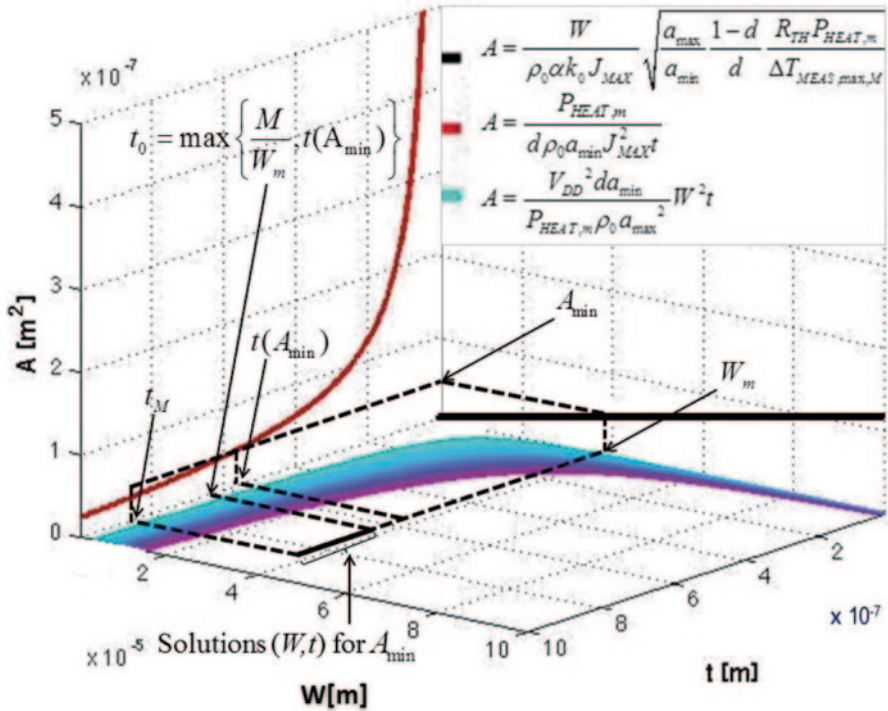
Fig. 67.1 Schematic representation of the solutions (W, t) for our design example

$$Wt \geq \max \left\{ \frac{P_{HEAT,m}\rho_0 a_{\max}^2 F_W(W_m)}{V_{DD}^2 da_{\min}W_m}, \frac{P_{HEAT,m}a_{\max}}{da_{\min}J_{MAX}V_{DD}} \right\} \equiv M \qquad (67.7)$$

References

1. C. Falconi, Systematic Design of Micro-Resistors for Temperature Control by Quasi-Simultaneous Heating and Temperature Sensing, Sensors and Actuators B: Chemical, 179, pp 336–346 (2013).
2. C. Falconi, E. Zampetti, S. Pantalei, E. Martinelli, C. Di Natale, A. D'Amico, V. Stornelli, G. Ferri, Temperature and flow velocity control for quartz crystal microbalances, Circuits and Systems, 2006. ISCAS 2006. Proceedings. 2006 IEEE International Symposium on, 4 pp.—4402 (2006) .
3. M. Lenz, G. Striedl, U. Fröhler, Thermal Resistance, Theory and Practice, Infineon Technologies AG, Munich, Ger. Special Su, 6-19 (2000).

Chapter 68
Gas Turbine Thermoelements Availability Analysis

T. Addabbo, O. Cordovani, A. Fort, M. Mugnaini, V. Vignoli and S. Rocchi

68.1 Introduction

The proposed configurations are usually used both in aero derivative and heavy duty gas turbine design in order to maximize the sensor information. Of course, in the selection of one of the alternatives, availability plays a crucial role. Some previously developed approaches as reported in [1–4] have been exploited to carry on the investigation on the most suitable solution for gas turbine systems. The Markov modeling approach [5–7] based on state flow analysis is the one applied to compare results of different configurations. Constant failure and repair rates are supposed and performance evaluation is summarized in terms of steady state availability. The availability performance at steady state shows that the $2006 + 3$ consecutive failures presents the highest value and therefore is to be selected in such applications. This is due also in consideration that the 3 consecutive failures configuration allows for gas turbine section monitoring improving the analysis without any loss related to safety constraints. The possibility to be able to grant a general mapping of the temperature in the exhaust section is crucial to extend the system operability and part life. Simulation results show that the following steady state values for the three configurations are: 0.999424 (4006), 0.999788 ($3006 + 2c$), 0.999803 ($2006 + 3c$) respectively.

M. Mugnaini (✉) · T. Addabbo · O. Cordovani · A. Fort · V. Vignoli · S. Rocchi
Department of Information Engineering and Mathematics (Unita' GMEE Siena),
University of Siena, Siena, Italy
e-mail: mugnaini@dii.unisi.it
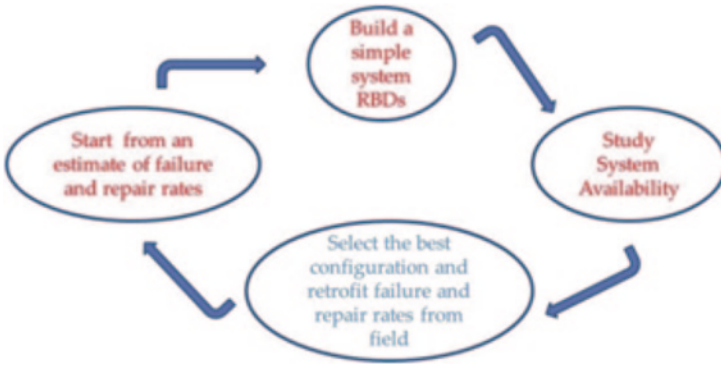
Fig. 68. 1 Process flow diagram to implement the system configuration evaluation and retrofit

$$\frac{dP(t)}{dt} = \begin{pmatrix} -6\lambda & 0 & 0 & \dfrac{\mu}{3} \\ 6\lambda & -5\lambda & 0 & 0 \\ 0 & 5\lambda & -4\lambda & 0 \\ 0 & 0 & 4\lambda & -\dfrac{\mu}{3} \end{pmatrix} P(t)$$
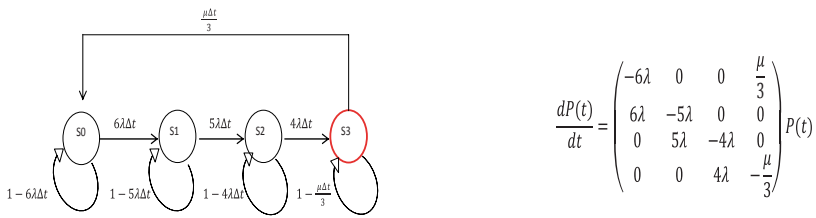
Fig. 68. 2 Markov State flow diagram of 4006 configuration
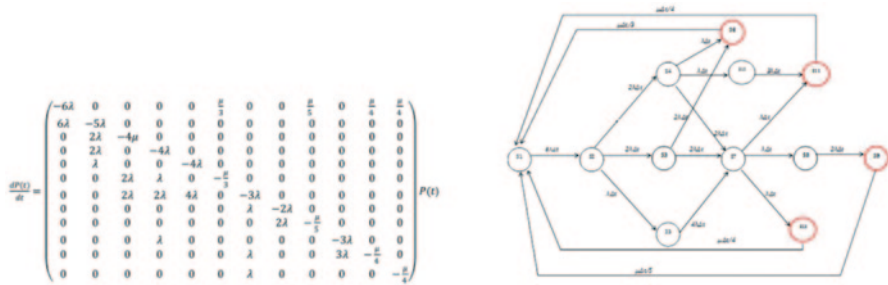
Fig. 68. 3 Markov diagram of the 2006 + 3 consecutive failures

68.2   Method and Modeling

In fig. 68.1 the flow diagram describing the general approach is reported. Starting from the estimation of both the failure and repair rates for each sensor, a reliability block diagram (RBD) is designed and consequently simulated to assess the steady state availability. Eventually the system parameters can be retrofitted if needed in order to improve the previsions adherence to actual behavior.

Three possible configurations were taken into account: a classical k/n configuration where at least k elements over n should work in order to consider the system working and two other hybrid configurations where an additional constraint of a minimum number of consecutive working sensors is mandatory in order to consider the system acceptable. In fig. 68.2 the representation of the Markov system for a 4006 configuration is reported and the corresponding probability transition matrix is reported while in fig. 68.3 the same diagram is represented for the 2006+3 consecutive failures together with the transition matrix (analogously the 3006+2 consecutive diagram can be easily derived).

Of course the dimension of the transition matrix is linked to the complexity of the problem and to its representation. It can be seen in fig. 68.4 that the availability of the three configurations are very different both in terms of dynamics and in terms of steady state values. It can be noted that the 2006+3 consecutive failures configuration should be preferred with respect to the others even if the final results depend on the possibility to act on the repair rates. Actually improving the repair rates for example of the alternative configuration 3006+2 consecutive it is possible to get acceptable results as well.
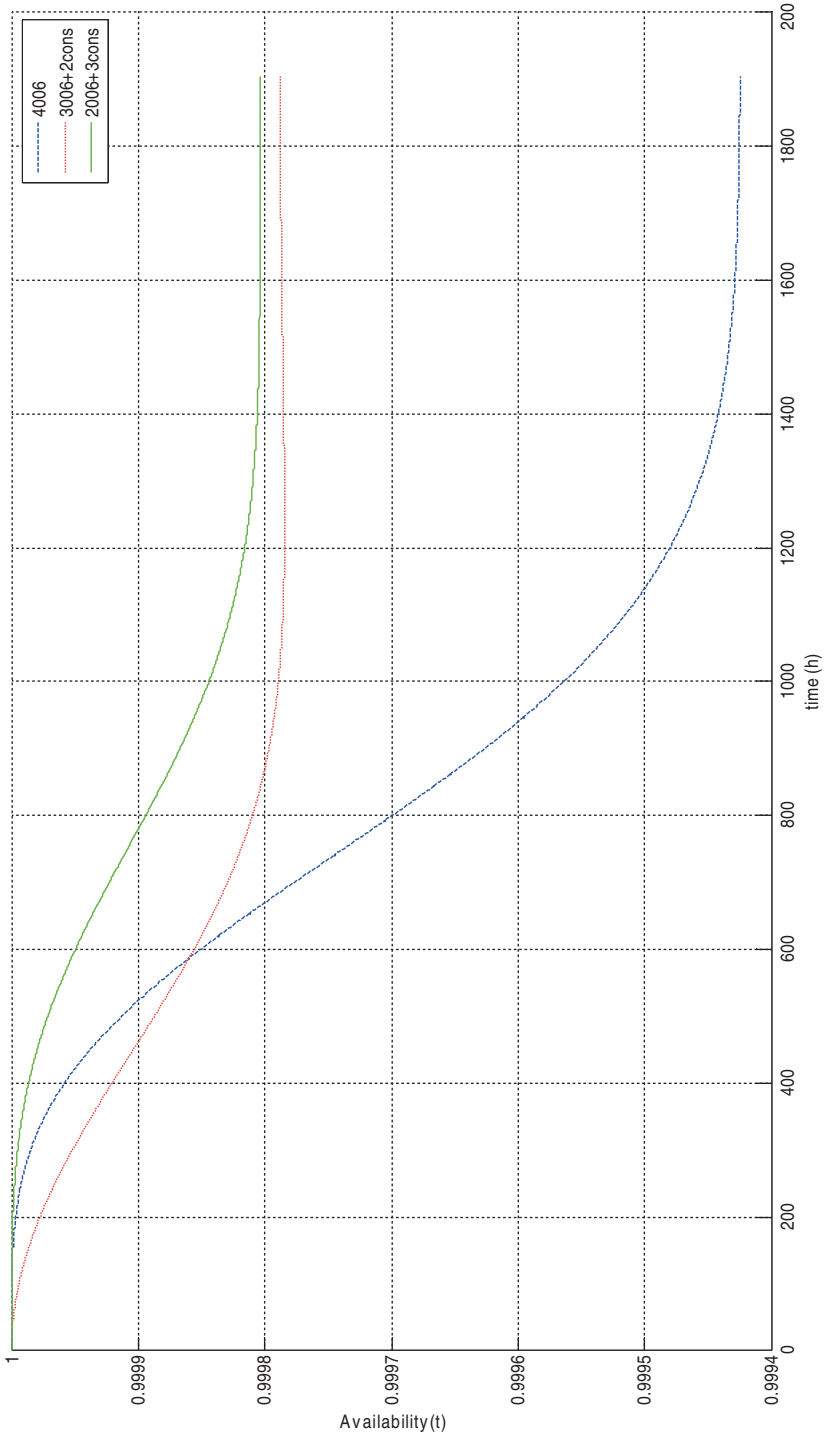
Fig. 68. 4 Availability comparison of the three proposed configurations

References

1. Hua-dong, Yang Xu Hong "Reliability Analysis of Gas Turbine Based on the Failure Mode and Effect Analysis Power and Energy Engineering Conference (APPEEC), 2011 Asia-Pacific
2. M. Mugnaini, M. Catelani, G. Ceschini, A. Masi, F. Nocentini "Pseudo Time-Variant parameters in centrifugal compressor availability studies by means of Markov models" in Microelectronics Reliability, vol. 42, 2002, p. 1373–1376, ISSN: 0026-2714
3. Chowdhury, A.A., Koval, D.O. "Reliability Assessment of a Backup Gas Turbine Generation System for a Critical Industry Load Using a Monte Carlo Simulation Model" Industry Applications, IEEE Transactions on Volume:45, Issue:1 10.1109/TIA.2008.2009495 Publication Year: 2009, Page(s): 310–316
4. G. Ceschini, M. Mugnaini, A. Masi "A reliability study for a submarine compression application" Microelectronics Reliability, vol. 42, 2002, p. 1377–1380, issn: 0026-2714
5. S.S. Rao "Reliability engineering Design" McGraw Hill
6. A. Birolini "Reliability Engineering: Theory and Practice" Springer 6th Edition 2010
7. M. Catelani, M. Mugnaini, R. Singuaroli. "Effects of test sequences on the degradation analysis in high speed connectors" Microelectronics Reliability, vol. 40, p. 1461–1465, ISSN:0026-2714.

Chapter 69
IR Sensor for Gas Turbine Inlet Temperature (TIT) Measurement: Experimental Results of a Laboratory Test

E. Golinelli, S. Musazzi, U. Perini and F. Barberis

69.1   Introduction

Although the Turbine Inlet Temperature (TIT) is a critical parameter for the optimization of Gas Turbine (GT) working conditions, no reliable method capable of providing this measurement has so far been implemented because of the very severe environment the sensor has to deal with. For this reason, we are studying an innovative temperature sensor that, in principle, could fill this gap. This sensor is based on spectroscopic photometric measurements of the infrared radiation emitted in a selected wavelength band by the CO_2 molecules present in the combustion gases.

69.2   Principle of Operation

The measured quantity is the grey body spectral irradiance H (λ,T) defined by the product of the blackbody spectral irradiance W_B (λ,T) and the grey body absorption Abs (λ,T), the blackbody spectral irradiance being defined by the well known Planck's law [1]. For a carbon dioxide gas mixture to achieve a black body condition, irradiance measurements have to be carried out in a very narrow spectral range (about 15 nm wide, around 4 microns) where the carbon dioxide molecules strongly absorb the IR radiation. In this way the detected signal can be related to the gas temperature so to allow real time monitoring of its temporal behavior. Unfortunately, since the measured signal depends also on geometrical and optical parameters of the detection chain that can hardly be theoretically evaluated, it turns out that it is very difficult to get the absolute gas temperature in the absence of an external independent reference measurement. In addition, since the measured quantity is an integral

E. Golinelli (✉) · S. Musazzi · U. Perini · F. Barberis
T&D Technologies Department, RSE—Ricerca sul Sistema Energetico, Milano, Italy
e-mail: elena.golinelli@rse-web.it

value resulting from the sum of many irradiance contributions coming from different regions of the investigated gas volume; it cannot be related to a given position of the test region. Therefore, it would be desirable to get the real temperature spatial distribution responsible of the measured signal. To cope with these problems we have implemented an innovative method based on a preliminary calibration of the measuring system and a proper modeling of the irradiance absorption/emission processes in the test volume. It consists of the following steps:

1. Perform a calibration of the measuring system by means of a thermally controlled source (like e.g. a hot metallic surface that closely mimics the behavior of a black body). In this way it is possible to get the calibration coefficients that allow to connect the measured signal to the true blackbody spectral irradiance as a function of the temperature.
2. Carry out a computation of the resulting spectral irradiance as a function of the gas temperature spatial distribution in the test region. This task is performed by assuming a discrete temperature profile (i.e. by dividing the test region in N adjacent layers of known constant temperature) and by calculating via the Hitran code [2] the absorption/emission contribution of each layer. The resulting irradiance can be derived according to the procedure described in the literature [3]. In this way it becomes possible to correlate the measured signal to the actual temperature profile in the test region.

69.3   Experimental Apparatus

The measuring system (schematically shown in Fig. 69.1) is made by three units:

- An optical probe that collects the radiation emitted by the hot gas. It has been properly designed to bear typical experimental conditions (high temperature, high pressure) existing in a real GT plant.
- A detection unit (connected via an optical fiber to the optical probe) where different narrowband interference filters can be positioned on the optical path to select the spectral region of interest.
- A data acquisition and analysis unit (based on a LabView program).

To check the validity of the proposed method, several laboratory tests have been carried out utilizing as a test object a properly prepared gas mixture whose temperature and pressure can be modified in a controlled way. The desired operating conditions have been achieved by using a thermally controlled cylindrical metallic cell filled with the desired gas mixture. Temperature variations (up to about 1000 °C) can be obtained by positioning the cell in a programmable cylindrical vertical axis furnace. To let the inner generated optical radiation escape from the hot gas region and be revealed, the cell is provided with a properly cooled optical access. The

a: Test cell
b: IR source
c: Mobile mirror
c': Mirror
d: Optical probe
e: Optical fiber
f: Filter holder
g: IR detector
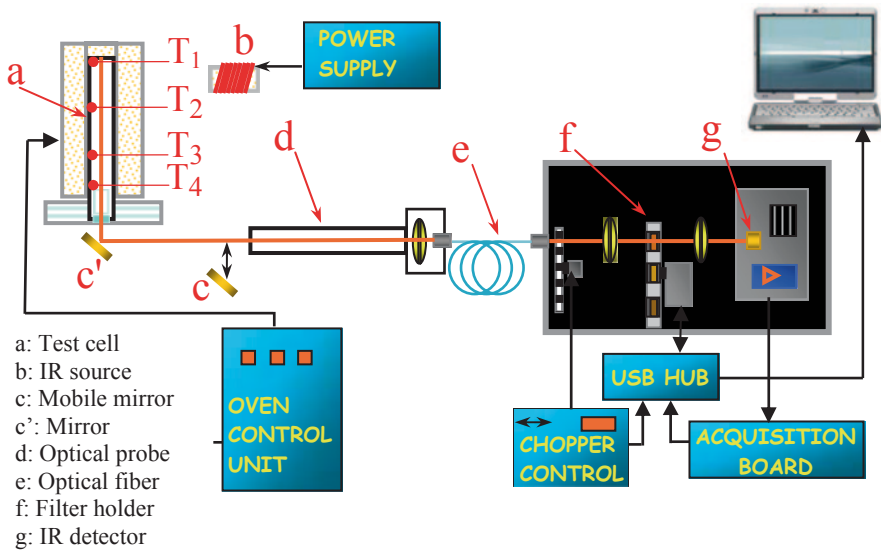
Fig. 69.1 Schematic of the measuring system

vertical temperature profile inside the cell can be monitored by means of four thermocouples (T_1, T_2, T_3 and T_4 in Fig. 69.1) placed at different heights in contact with the gas (see Fig. 69.1).

69.4   Experimental Results

Tests have been carried out with the experimental cell filled with a mixture of 4% CO_2 in N_2 atmosphere, at a pressure of about 15 bars (to reproduce a typical GT environment) during a thermally controlled temperature ramp (up to about 1000 °C). Measurements have been performed by gradually increasing the furnace temperature (by incremental steps of about 100 °C) and by recording the IR output signal after each temperature step. To get stable measurements, the IR signal was recorded only after reaching a stationary thermal condition in the gas (i.e. when a stable temperature profile was established inside the cell).

As an example of the experimental results obtained during this test campaign we show in Fig. 69.2 the comparison between the calculated and the measured signals as a function of the increasing gas temperature in the test cell (measured by one of the four thermocouples).

As it can be noticed, the measured IR signal (properly multiplied by the calibration factor) exhibits a good correlation with the theoretical one (calculated by assuming a discrete temperature profile in the cell).
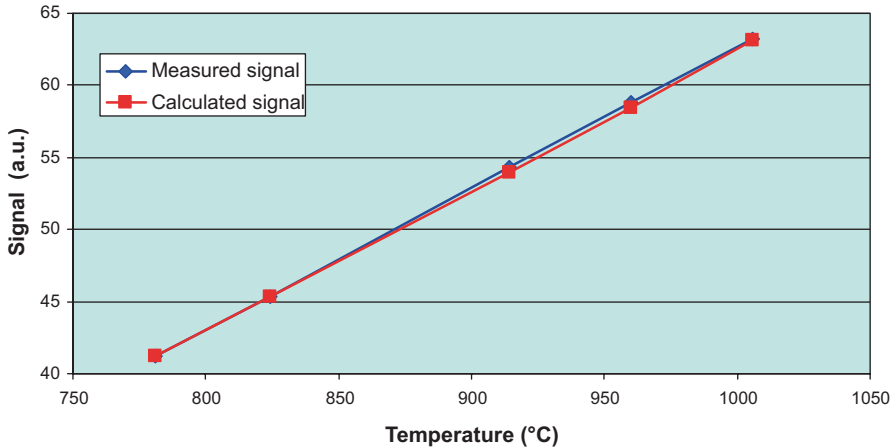
Fig. 69.2 Comparison between the calculated and the measured signals as a function of the increasing gas temperature

69.5 Conclusions

We presented preliminary experimental results of laboratory tests carried out on an innovative optical probe properly designed for measuring the temperature of the gases downstream the burner of a gas turbine machine. As described, we observed a good agreement between the measured signal and the theoretically calculated one, thus providing evidence that it is possible to construct the signal vs temperature calibration curves for any real case where the spatial temperature profile in the test region can be reasonably hypothesized.

References

1. J. Caniou, Passive Infrared Detection (Kluwer Academic Publisher, Boston, 1999)
2. University of South Florida, HITRAN Database. Copyright 1997.
3. R.H. Tourin, B. Krakow. Applicability of Infrared Emission and Absorption Spectra to Determination of Hot Gas Temperature Profiles. Appl. Opt. 4, 237–242 (1965)

Chapter 70
Simulation of an Ultrasonic Flow Meter for Liquids

Fabio Lo Castro, Massimiliano De Luca and Sergio Iarossi

Today's a most popular technology of flow measurement is based on ultrasound. An ultrasonic flow meter is a complex devices that, for its development, involves different disciplinary fields such as the electronics, the mechanics, the acoustics and the material science. For this purpose, it has been developed both a simulator of an ultrasonic flow meter and an ultrasonic flow meter in order to validate the simulator. The simulation take into account of the transducer property, of the fluid dynamics and of the acoustic propagation inside the measurement conduct of flow meter. In this work, the results of the simulations used to describe the performance of an ultrasonic flow meter for liquid is presented. Furthermore the validation of the adopted models has been performed comparing the simulation results with the collected data.

70.1 Introduction

The flow measurement in the fluid using ultrasonic probes offers the advantage of having no moving parts, which are prone to wear and unreliability, and it is able to detect very low flow rate less than 1 ml/min [1]. Furthermore it is potentiality insensible to change in temperature, installation condition, fluid viscosity, density and pressure.

Limitations are due especially to air spaces, bubbles and changing in the flow velocity field in the measuring duct, that can span from laminar to turbulent. Without bubble and air spaces turbulences are the mayor source of fluctuations in the measurement [2]. Accuracy, repeatability and measurement range of any measurement device are important parameters to determine if the meter is appropriate for a given application.

F. Lo Castro (✉) · M. De Luca · S. Iarossi
IDASC-CNR, Area della Ricerca di Roma Tor Vergata, Via Fosso del Cavaliere 100, 00133 Roma, Italy
e-mail: fabio.locastro@idasc.cnr.it
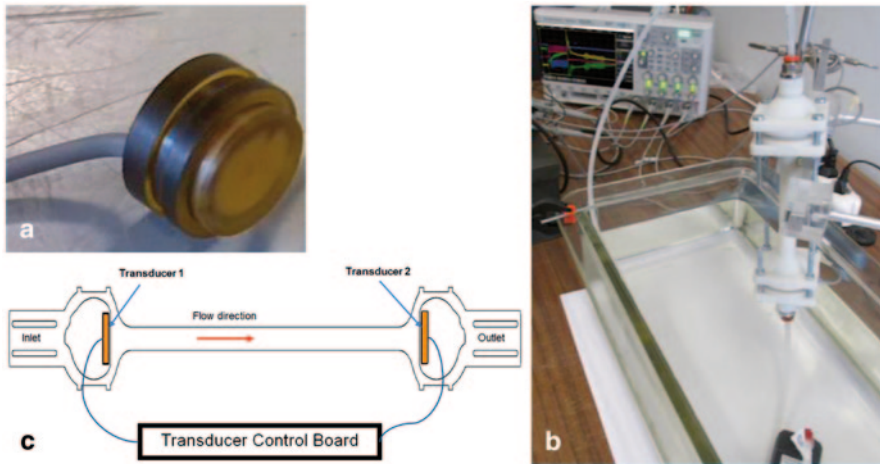
Fig. 70.1 **a** Piezoelectric transducer. **b** Experimental setup. **c** Flow meter working diagram

In order to comply with these three requirements different solutions are available on flow meter devices both in methods of measurement such as direct time of flight [3], phase shift [4], cross correlation [5] and in the position of the transducers with respect to the flow direction that can be axial [6], perpendicular [1] and oblique [3].

70.2 Experimental Setup and Simulation

The ultrasonic flow meter taken under consideration was an axial flow meter for liquid that has been developed able to measure flows in the range of 0–20 L/h with a resolution less of 0.1 L/h. It has been made using a 3D printer based on photopolymer VeroWhite [7]. The piezoelectric transducers have a central frequency of 1 MHz. The measurement technique of the flow is based on the phase shift [4]. The drafting has been aided by a proper 2D-Axial simulator (Fig. 70.1).

The simulator has been developed under the Matlab [8] environment. It is divided in four main stages (Fig. 70.2a). The first stage implements the KLM model [9–10] for the electro-acoustic simulation of transducer used both in transmission and reception. Both the measured impedance curve and the knowledge of the transducer materials have been used to find values of the equivalent circuit model parts. The KLM model has allowed to find the transfer function between the electrical driver signal of the piezoelectric transducer and the radiated pressure output. Figure 70.2b shows the normalized pressure output used in the simulation. The second stage of the simulator deals with the sound propagation in a moving media. It is based on a proper developed ray-tracer algorithm [11–12], in Matlab, that considers: the far
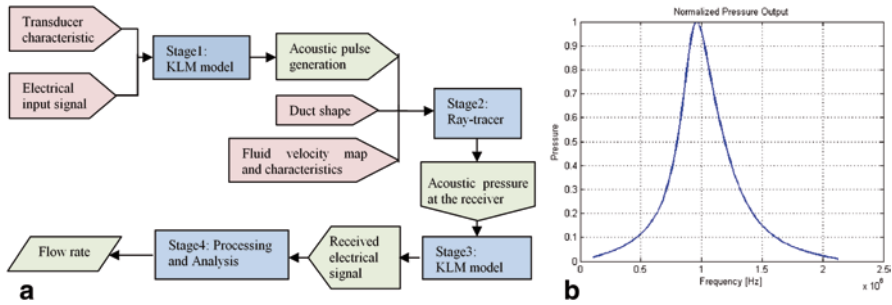
Fig. 70.2 a Block diagram of the flow meter simulator. **b** Normalized pressure output of the piezo-electric transducer, function of frequency

field propagation, the multiple reflections on the wall of the duct of the flow meter, the refraction due to velocity gradient of the medium. The velocity map in input at the simulator has been performed using COMSOL [13], a computational fluid dynamics (CFD) simulator. Figure 70.3a shows an example of velocity input map. SolidWorks [14], another CFD simulator, has been allowed to better show and to reduce the vorticosity in front of the inlet transducer, changing the shape of the duct, in presence of an high flow rate (Fig. 70.3b).

The third stage implements again the KLM model in order to convert the pressure acoustic wave in an electrical signal.

The last stage performs the phase shift measurement between the clock signal, also used to drive the ultrasonic transmitter, and the received electrical signal at the lead of the receiver.

70.3 Results

Flow meter simulator performance has been validated comparing numerical results with the corresponding theoretical values. Table 70.1 shows the flow rate evaluated changing the inlet fluid velocity and the values given by the simulator.

Figure 70.4 shows an example of the attenuation distribution inside the whole flow meter.

70.4 Conclusions

The objective of this research has been the development of a simulator for a fast and accurate reconstruction of the received electrical signal at the leads of the piezoelectric transducer inside an ultrasonic flow meter. This allows to compute the measurement of the flow rate using the phase shift technique.
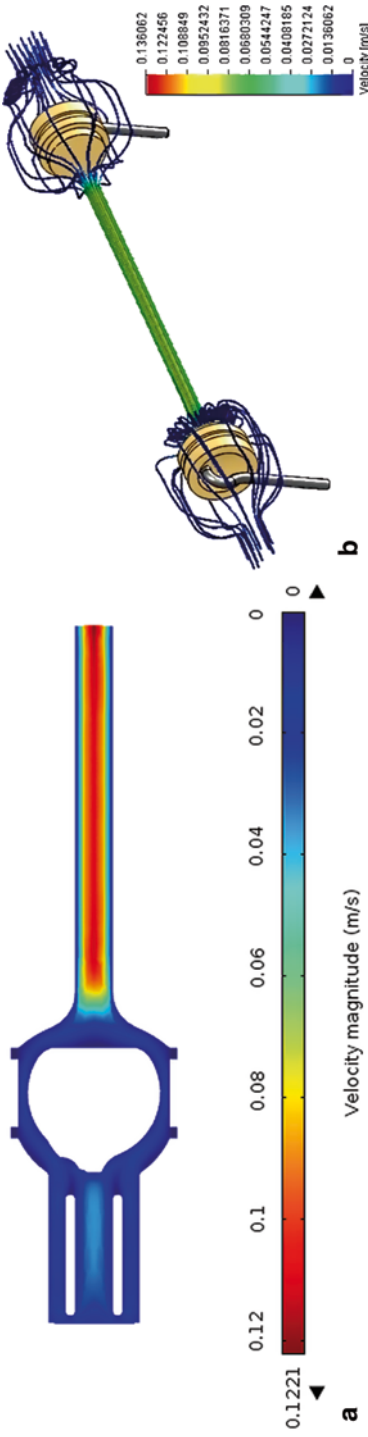
Fig. 70.3 **a** COMSOL fluid dynamic simulation of the inlet duct at the inlet. **b** SolidWorks fluid dynamic simulation shows vortexes in front of the transducer

Table 70.1 Comparison between theoretical values and simulated

	Flow rate					Unit
Theoretical	0.1	1	2	5	10	L/h
Simulated	0.08	0.97	1.97	4.96	9.93	L/h
|Error|	20	3	1.5	0.8	0.7	%
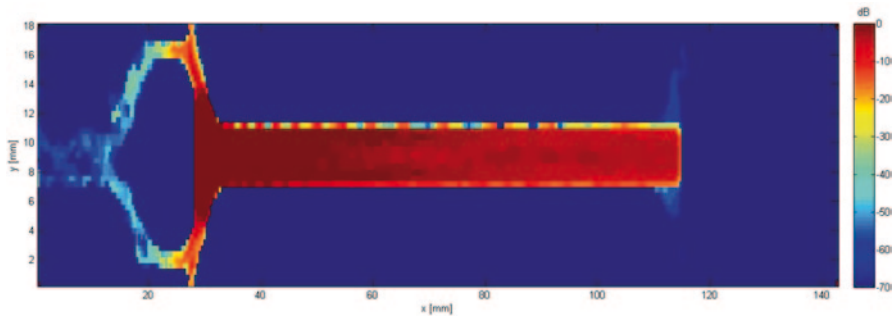
Fig. 70.4 MatLab simulation of the acoustic attenuation during sound propagation inside the flow meter

In order to validate the simulation it has also been developed a flow meter where has been performed the test.

Future development will be focused on the development of a 3D simulator in Matlab for a better and more accurate simulation.

References

1. H. Ishikawa, M. Takamoto, K. Shimizu, H. Monji, G. Matsuj. Development of a new ultrasonic liquid flowmeter for very low flow rate applicable to a thin pipe. IEEE Proc. of The Ninth International Symposium on Semiconductor Manufacturing, 383–386 (2000)
2. T. Strunz, A. Wiest, A. Fleury, A and T. Fröhlich. Influence of turbulence on ultrasonic flow measurements. Proc. of the 5th International Conference on Hydraulic Efficiency Measurements, IGHEM'2004. 1–6. (2004)
3. C. Buess, P. Pietsch, W. Guggenbuhl and E.A. Koller. Design and construction of a pulsed Ultrasonic air flowmeter, IEEE Transaction on Biomedical Engineering, BME-33 (8) 768–773 (1986)
4. Keefer S. Stull. Ultrasonic phase meter measures water velocity. Electronics 28 (9) 128–131 (1955)
5. Coulthard J. Ultrasonic cross-correlation flowmeters. Ultrasonics, 11 83–88 (1973)
6. Neil C. Temperley, Masud Behnia, Anthony F. Collings, Application of computational fluid dynamics and laser Doppler velocimetry to liquid ultrasonic flow meter design, Flow Measurement and Instrumentation, 15155–165 (2004)
7. VeroWhite http://www.stratasys.com. Accessed 20 May 2014
8. Matlab. http://www.mathworks.com. Accessed 20 May 2014
9. R. Krimholtz, D.A. Leedom, G.L. Mattaei, New equivalent circuits for elementary piezoelectric transducer, Electron. Lett. 6 398–399 (1970)

10. G. S. Kino. Acoustic waves: devices, imaging, and analog signal processing. Englewood Cliffs, NJ:Prentice-Hall (1987)
11. Don Cross, Fundamentals of Ray Tracing, (2013)
12. U. R. Krockstadt, "Calculating the acoustical room response by the use of a ray tracing technique," J. Sound Vib. 8 (18) 118–125 (1968)
13. COMSOL. http://www.comsol.com. Accessed 20 May 2014
14. Solidworks. http://www.solidworks.com. Accessed 20 May 2014

Chapter 71
Portable Wireless Distance Measurement System Powered By Intentional Human Action

D. Alghisi, M. Ferrari and V. Ferrari

This work proposes and experimentally validates an handheld distance measurement system powered by energy harvesting through the ElectroMagnetic (EM) effect. The system is entirely battery-less and powered on-demand by the user force exerted on the lever of an hand-crank EM converter. With a single excitation force of about 19.6 N over a lever travel of 2 cm, the proposed system is able to perform a distance measurement between a target object and the embedded ultrasonic sensor, show the reading on a LCD display, and transmit the data through a 433-MHz wireless-UART link to an host PC.

71.1 Introduction

A trend in the field of portable measurement instrumentation is to implement more functionality in the device, in particular the sharing of the measures through wired or wireless connectivity to a host, which can be a smartphone, a tablet or a PC. Battery life has to be increasingly extended to ensure operation over an extended time. With portable instruments that are operative only when they are handheld by the user who intentionally requests their operation, for example by pressing buttons, then batteries can be replaced by appropriate energy harvesting systems operated by human action [1, 2]. In this way the user himself provides the power to the device, making its operation battery-free.

In this context, this work presents a portable wireless distance measurement system powered on-demand by the user force applied to an ElectroMagnetic (EM) energy converter [3].

D. Alghisi (✉) · M. Ferrari · V. Ferrari

Department of Information Engineering, University of Brescia, Via Branze 38,

25123 Brescia, Italy

e-mail: davide.alghisi@ing.unibs.it
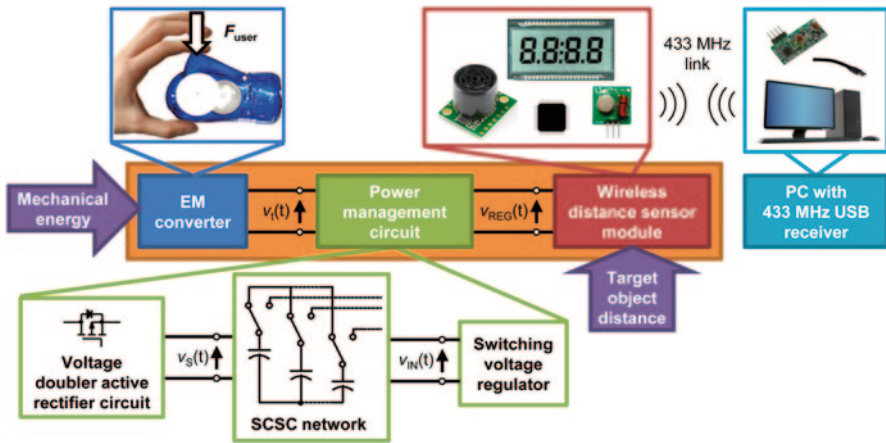
Fig. 71.1 Block diagram of the proposed portable wireless distance measurement system

71.2 Proposed Measurement System

The block diagram of the proposed measurement system is shown in Fig. 71.1. It is composed of the commercial hand-crank EM converter, the active power management circuit, and the custom wireless distance sensor module.

The user compressive force F_{user} exerted on the lever of the EM converter puts in rotation a group of permanent magnets coupled with a coil. The induced AC voltage $v_t(t)$ has typical open circuit peak values between 3.5 and 7 V, and its duration is in the order of few seconds, depending on the applied force. To perform AC–DC conversion, an enhanced version of the voltage doubler is adopted, in which MOS transistors are used as analog switches instead of diodes with lower power dissipation [4–6].

To extract more energy from the converter than with traditional rectifier circuits, the SCSC network is herein implemented [7].

The wireless distance sensor module is composed of a Maxbotix LV-EZ0 sonar range finder, a Varitronix VI-402-DP 4-digit 7-segment LCD display, a FS1000A 433-MHz transmitter and a Microchip PIC18F45K20 microcontroller. The ultrasonic distance sensor works at 42 kHz and is able to detect a 2.54-cm diameter dowel with a resolution of 2.54 cm over a range from 20 to 250 cm. The microcontroller manages the sensor operations, receiving the distance data through the UART input. The data are sent through the UART output of the microcontroller at 9600 bps, 8 data bits, no parity bit, and one stop bit, modulating the carrier wave of the transmitter by On-Off Keying (OOK) modulation.

The data packet is composed of 7 bytes: a header (1 byte), the device identification (1 byte), the distance data (4 byte), and the checksum (1 byte). The distance measurement is cyclically performed about every 1.5 s and the readings are shown on the LCD display directly driven by the microcontroller pins. The flow chart of the firmware executed by the microcontroller is shown in Fig. 71.2. The distance
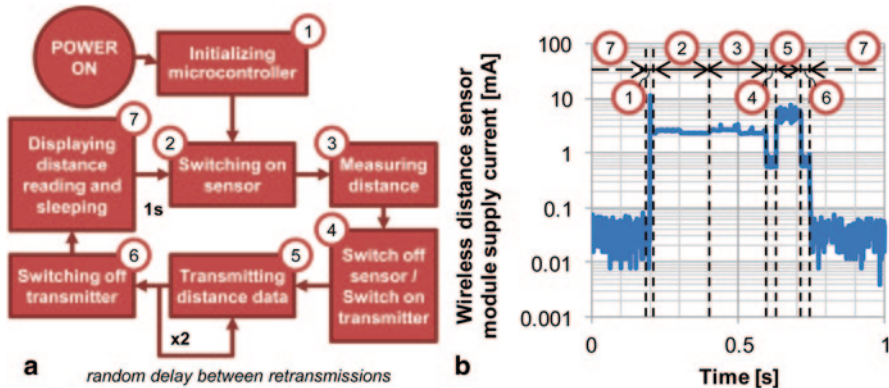
Fig. 71.2 Flow chart of the firmware executed by the microcontroller (**a**) and corresponding timing and current consumption measured at 3.3-V supply (**b**)

data are received by an host PC running National Instruments LabVIEW through a custom wireless-UART USB adapter, and shown on the VI front panel.

71.3 Experimental Results

The typical supply current of the power management circuit is between 7 and 12 µA, measured for the minimum allowed supply voltage of about 2.5 V. The wireless distance sensor module powered at 3.3 V draws about 2.5 mA for 0.4 s to perform a measurement, about 6 mA for 87 ms to transmit three times the data packet, and less than 0.1 mA to display the readings, as shown in Fig. 71.2b.

Figure 71.3a shows the charging process of six 1-mF capacitors performed by the active rectifier circuit with the SCSC network with an applied force to the EM converter of about 19.6 N over a lever travel of 2 cm. The 16.5 mJ of stored energy are used by the portable wireless distance measurement system shown in Fig. 71.3b to perform a measurement, to transmit the measure, and to display the reading for about 1 s.

The system has been tested by performing a series of measurements at different reference distances from a target into the measuring range 20–250 cm. The results after offset correction are shown in Fig. 71.4. It can be observed that a linearity error of about 2 % of the Span is present. As can be seen by the linear trend the error is dominated by a residual inaccuracy in the system sensitivity which can be reduced by calibration if required by the application.

71.4 Conclusions

A wireless distance measurement system powered by energy harvesting from intentional human action was presented. The system consists of an EM hand-crank energy converter, a power management circuit which implements active rectification
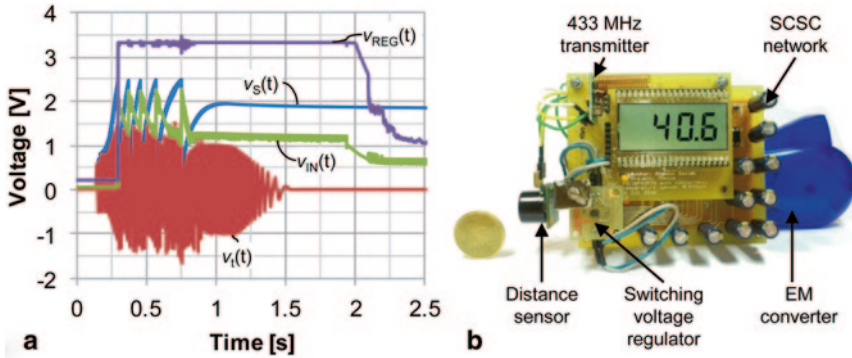
Fig. 71.3 Measured output voltage $v_t(t)$ of the EM converter, voltages $v_S(t)$ on 1-mF storage capacitors for the voltage doubler active rectifier circuit with the SCSC network, input voltage $v_{IN}(t)$ and output 3.3-V regulated voltage $v_{REG}(t)$ for the switching voltage regulator (applied force $F_{user} = 19.6$ N) (**a**). Prototype of the portable wireless distance measurement system (**b**)
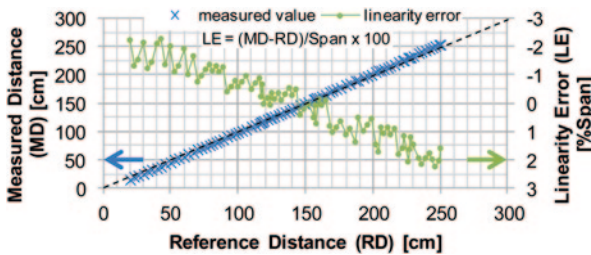
Fig. 71.4 Measured values versus reference values of the distance from the target and corresponding linearity error referred to the span

and the SCSC technique, and a wireless distance sensor module. With a single excitation force of about 19.6 N exerted on the lever of the converter by the user hand, the proposed system is able to perform a distance measurement between a target object and the ultrasonic sensor within the module, show the reading on a LCD display, and transmit the data through a 433-MHz wireless-UART link to an host PC.

References

1. R. Riemer, A. Shapiro. Biomechanical energy harvesting from human motion: theory, state of the art, design guidelines, and future directions. Journal of NeuroEngineering and Rehabilitation **8** (22), 1–13 (2011)
2. D. Alghisi, M. Ferrari, V. Ferrari. Portable Battery-Less Noncontact Temperature Measurement System Powered on Demand by Human Action. Proc. of the 18th IEEE Conference on Emerging Technologies & Factory Automation, Sept 10–13, 2013, Cagliari (Italy), 1–4 (2013)

3. D. Dai, J. Liu. Human powered wireless charger for low-power mobile electronic devices. IEEE Transactions on Consumer Electronics **58** (3), 767–774 (2012)
4. D. Marinkovic, A. Frey, I. Kuehne, G. Scholl. A New Rectifier and Trigger Circuit for a Piezo-electric Microgenerator. Procedia Chemistry **1** (1), 1447–1450 (2009)
5. C. Peters, J. Handwerker, D. Maurath, Y. Manoli. A Sub -500 mV Highly Efficient Active Rectifier for Energy Harvesting Applications. IEEE Transactions on Circuits and Systems I: Regular Papers **58** (7), 1542–1550 (2011)
6. S. Cheng, Y. Jin, Y. Rao; D.P. Arnold. An Active Voltage Doubling AC/DC Converter for Low-Voltage Energy Harvesting Applications. IEEE Transactions on Power Electronics **26** (8), 2258–2265 (2011)
7. D. Alghisi, M. Ferrari, V. Ferrari. Active rectifier circuits with sequential charging of storage capacitors (SCSC) for energy harvesting in autonomous sensors. Procedia Engineering **25**, 211–214 (2011)

Chapter 72
Nonlinear Snap-Through-Buckling Devices for Energy Harvesting from Vibrations

Bruno Ando', Salvatore Baglio, Vincenzo Marletta, Elisa Pergolizzi, Vittorio Ferrari, Marco Ferrari and Adi R. Bulsara

In this work authors present two low-cost nonlinear devices for vibrational energy harvesting which are able to convert low frequency mechanical vibrations into electrical energy. The two developed solutions exploit the advantages of a bistable device in a Snap-Through-Buckling (STB) configuration and a piezoelectric mechanical to electrical conversion mechanism. In fact it has been demonstrated that bistable systems, under the proper conditions, can provide better performances, compared to linear resonant oscillators, in terms of the amount of energy extracted from wide spectrum vibrations.

72.1 Introduction

In last years, researchers have focused on power harvesting solutions to make low-power electronic devices autonomous, or at least to extend the life of electrochemical batteries by exploiting the energy that can be harvested from their surroundings. Among different energy sources, environmental mechanical vibrations represent one of the most ubiquitously available sources that can, potentially, deliver a useful amount of energy [1]. Ambient mechanical vibrations come in a large variety of forms whose energy may be, sometimes, confined to a very specific region of the frequency spectrum, however, quite often, the available energy is distributed over a wide range of frequencies. Typically, vibrational energy harvesters are based

B. Ando' (✉) · S. Baglio · V. Marletta · E. Pergolizzi
Dipartimento di Ingegneria Elettrica Elettronica e Informatica (DIEEI), University of Catania, Catania, Italy
e-mail: bruno.ando@diees.unict.it

V. Ferrari · M. Ferrari
Dipartimento di Ingegneria dell'Informazione (DII), University of Brescia, Brescia, Italy

A. R. Bulsara
Space and Naval Warfare Systems Center Pacific, Code 71000, San Diego, CA, USA
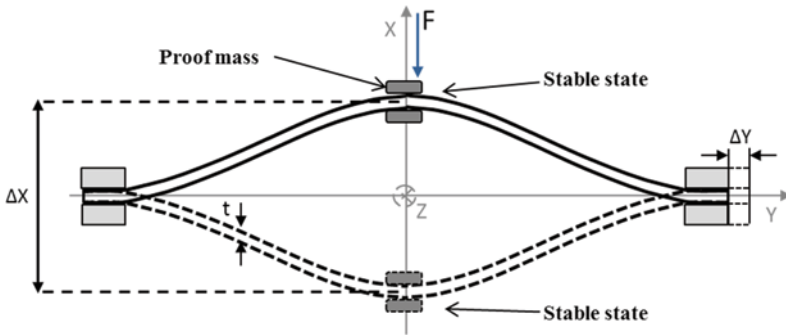
Fig. 72.1 Working principle of a bistable Snap-Through Buckling (*STB*) membrane (*top view*) and representation of the two stable equilibrium states. *F* is the force to allow transitions

on linear resonant mechanical structures like cantilever beams, which are very efficient when stimulated close to their resonance frequency. However, it has been demonstrated that bistable systems, under the proper conditions, can provide better performances, compared to linear resonant oscillators, in terms of the amount of energy extracted from wide spectrum vibrations [2]. In this framework, researchers at DIEEI of the University of Catania, are investigating novel low-cost devices for energy harvesting which are able to convert low frequency mechanical vibrations into electrical energy [3–5].

72.2 The Developed Devices

In the following two different solutions exploiting the advantages of a bistable device in a Snap-Through-Buckling (STB) configuration are addressed.

A schematization of a bistable Snap-Through-Buckling (STB) configuration is shown in Fig. 72.1.

If a fixed-fixed beam is subjected to an axial compression *ΔY*, it exhibits a bistable behavior due to the buckling [6]. The two stable equilibrium positions are separated by a distance *ΔX*. In order to achieve switching events between these stable states, a force *F* having amplitude larger than a certain threshold (imposed by the energy barrier inherent in the bistability) must be applied in the out-of-plane direction of the beam. The force *F* is generated by external vibrations and it increases as the beam mass increases. The total mass of the harvester can be increased by additive proof masses.

The bistable harvesting device exhibits rapid switching between the two states and large displacements, both of which are crucial in power conversion [3, 4].
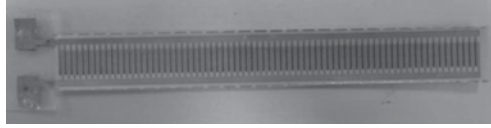
Fig. 72.2 A real view of the inkjet printed STB harvester
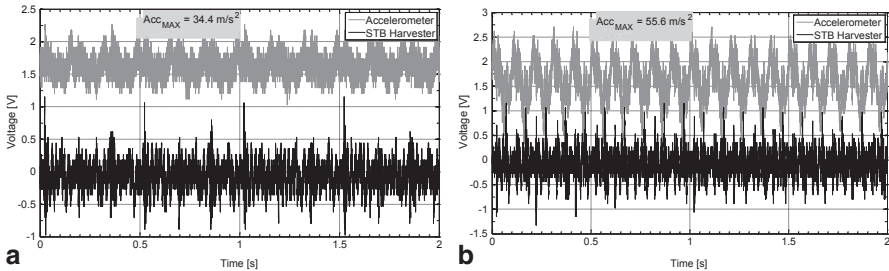
Fig. 72.3 Experimental results for two frequencies of the acceleration applied to the beam. Voltage signals from the harvester and the accelerometer at **a** 6 Hz and **b** 10 Hz, are shown in case of a pre-compression $\Delta Y = 3$ mm

72.2.1   A Inkjet Printed STB Vibrational Energy Harvester

The STB harvester here addressed consists of a cantilever beam with InterDigiTed (IDT) electrodes and one active layer deposited on top; the device is shown in Fig. 72.2. The STB beam is implemented via a PET (PolyEthylene Terephthalate) substrate 9 cm by 1 cm with a thickness of about 100 µm.

IDT electrodes have been realized by inkjet printing a conductive pattern of a silver nano-particle solution (Metalon® JS-B15P by Novacentrix), through a cheap commercial deskjet printer [7]. Strains stemming from the beam switching (between the two stable states) are converted into an output voltage by the screen printed Lead Zirconate Titanate (PZT) layer [5]. An example of observed signals in case of $\Delta Y = 3$ mm and for two frequencies (6 Hz and 10 Hz) of the input solicitation is shown in Fig. 72.3a and 72.3b, respectively.

Powers in the order of 10^2 nW have been experimentally estimated by a lab-scale prototype which merely aims at the proof-of-concept of the Snap-Through Buckling mechanism for energy harvesting.

72.2.2   A Double-Piezo STB Vibrational Energy Harvester

In the DP-NLH (Double Piezo-NonLinear Harvester) the beam switching is activated by environmental vibrations while the mechanical-to-electrical energy conversion is performed by two piezoelectric transducers [3, 4].
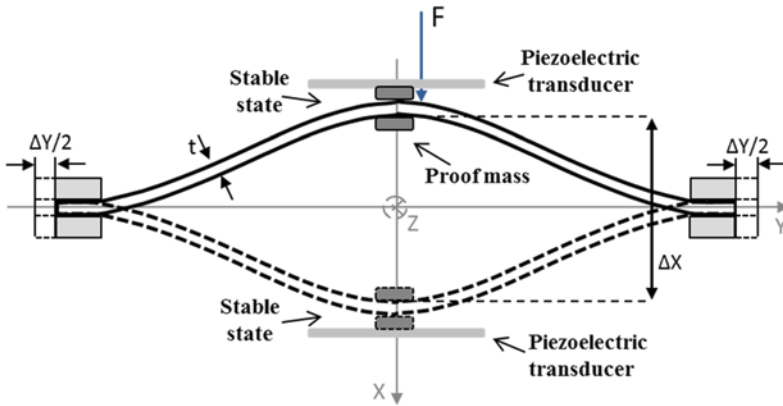
Fig. 72.4 Schematization of the DP-NLH vibrational energy harvester (*top view*)

Table 72.1 Observed electrical power produced by the DP-NLH device on a load $R=5$ kΩ, in case of forcing stimuli with the same amplitude producing an acceleration of 16.81 m/s^2 and increasing frequency

Frequency (Hz)	Power (μW)
4	284.8
5	296.3
8	309.4
10	313

A schematization of the DP-NLH harvester is shown in Fig. 72.4. It consists of a pre-compressed flexible PET beam in a clamped-clamped configuration, with only two allowed (i.e. stable) steady states. The PET beam dimensions are 10 cm by 1 cm while its thickness is 100 μm. Two low cost piezoelectric diaphragms 7BB-35-3L0 (Murata) are used to convert the beam impacts (in each steady state) into electric charges. The piezoelectric devices are electrically connected in a parallel configuration to supply the down-line electronics with charges produced during the impacts. An inertial mass of 10 g, placed in the middle of the beam, is used to optimize the trade-off between the operative frequency band and the minimum force that allows the switching.

Table 72.1 summarizes the powers experimentally computed on a resistive load of 5 kΩ by taking into account the non-normalized V_{RMS} voltages in case of forcing stimuli with the same amplitude producing an acceleration of 16.81 m/s^2 and increasing frequency. Although the generated powers weakly depend on the forcing frequency, their values are comparable thus confirming the frequency broad band operation of the device.

72.3 Conclusions

In this paper, the authors present two low cost solutions for energy harvesting from vibrations based on a bistable clamped-clamped PET beam. The beam switching is supposed to be activated by environmental vibrations. The mechanical-to-electrical energy conversion is performed by piezoelectric transducers. In the case of the ink-jet printed STB vibrational energy harvester, a layer is deposited on top the beam, while two piezoelectric transducers experiencing the beam impacts are used in the "Double Piezo-NonLinear Harvester". It has been demonstrated that the latter proposed solution is able to supply enough energy to power a wireless node.

References

1. S. Roundy, P. Wright, and J. Rabaey, A study of low level vibrations as a power source for wireless sensor nodes, Computer Communications, vol. 26, no. 11, pp. 1131–1144, 2003.
2. M. Ferrari, V. Ferrari, M. Guizzetti, B. Andò, S. Baglio, and C. Trigona, Improved Energy Harvesting from Wideband Vibrations by Nonlinear Piezoelectric Converters, Sensors & Actuators: A. Physical, vol.162, no. 2, pp.425–431, 2010.
3. B. Andò, S. Baglio, A. R. Bulsara, V. Marletta, I. Medico, S. Medico, A Double Piezo—Snap Through Buckling Device For Energy Harvesting, Proc. of the 17th International Conference on Solid-State Sensors, Actuators and Microsystems, Transducers '2013 & Eurosensors XXVII, June 16–20, 2013, Barcelona, Spain.
4. B. Andò, S. Baglio, A. R. Bulsara, V. Marletta, A bistable buckled beam based approach for vibrational energy harvesting, Sensors and Actuators A: Physical, n. 211, pp. 153–161, 2014.
5. B. Andò, S. Baglio, M. Baù, A.R. Bulsara, V. Ferrari, M. Ferrari, G. L'Episcopo, A Nonlinear Energy Harvester by Direct Printing Technology, Proc. Eurosensors XXVI, Procedia Engineering vol. 47, pp. 933–936, September 9–12, 2012, Kraków, Poland.
6. F. A. Leckie and D. J. Dal Bello, Strength and Stiffness of Engineering Systems, Mechanical Engineering Series, (Springer Science + Business Media, LLC 2009), 293
7. B. Andò, S. Baglio, Inkjet-Printed Sensors: A Useful Approach for low cost, rapid prototyping, IEEE Instr. Meas. Magazine, Vol.14–5, 2011.

Chapter 73
Modular Acquiring System for Lower Limb Rehabilitation Machines

M. Bona, E. Sardini and M. Serpelloni

The present paper refers to a research work aiming at implementing a modular acquiring system to be exploited in machines designed for lower limb muscles active rehabilitation. Mechatronic devices, as explained in [1] and [2], have given a relevant contribution to this field during last years, offering intensive treatments allowing individuals to restore as much as possible their motion capabilities, damaged by an injury, a disease or a lesion. But many machines do not have the possibility to obtain information about patient's biomechanical parameters during an active rehabilitation exercise. Starting from this concept, sensors, whether introduced into such devices, make accurate measurements and provide real-time data, which could be useful performance indicators, helping the physician to evaluate subject's condition and therapy efficiency, [1]. This work is articulated as follows: after having described the system, performed experimental analysis will be illustrated, and obtained results will be provided.

73.1 System Description

The acquiring system allows to get data about different parameters related to several magnitudes: (I) displacement carried out by moving mechanical structures, a sliding cart for instance, through a linear position transducer; (II) patient's Biceps femoris activity, thanks to an electromyographic analysis (EMG), by using three superficial electrodes attached to the thigh; (III) hip and knee flexion angles, with two accelerometers applied to leg and thigh, and (IV) machine resistant force, through a load cell. Sensors make the necessary measurements, while their analog outputs are received and converted by an acquiring board connected, through a USB port, to a PC, which executes an interface program, realized using LabVIEW software;

M. Serpelloni (✉) · M. Bona · E. Sardini
Dipartimento di Ingegneria dell'Informazione, Università degli Studi di Brescia, via Branze 38, 25123 Brescia, Italy
e-mail: mauro.serpelloni@unibs.it

such program elaborates the values coming from the board, to obtain the above mentioned information. When acquisition stops, all data are saved, in such a way they can be utilized whenever physician needs, for example to compare them with the ones resulting from previous therapy sessions. Sensors can be connected to the acquiring board in different ways, according to the desired analysis; this gives a great degree of flexibility and modularity to the system, allowing it to be utilized for a wide variety of applications. Its block scheme is represented in Fig. 73.1.

73.2   Experimental Analysis

Different analyses were performed, exploiting the acquiring system capability of collecting several types of data, according to rehabilitation purposes. Through the first one biomechanical parameters (i.e. angles and EMG signal) corresponding to the exercises proposed by two machines, called "a" and "b" for simplicity, involving the same muscular group, were compared. For both cases, electrodes were placed in the middle of subject's thigh (to study Biceps femoris contraction), in correspondence of Pes anserinus and on tibial condyle, while accelerometers were attached to thigh and leg through two elastic bandages. Then, subject performed both exercises (firstly on a machine, then on the other one) flexing and extending his knees many times, while LabVIEW program was registering all the useful values.

Second analysis aimed at getting objective data about resistant force provided by device "a", under different conditions (set by fixing a determined number of rubber bands), to obtain the one required to make properly the therapy exercise. One of load cell extremities was fixed, through a rope, to machine handle. Subject was standing and holding the other extremity with his hand. While LabVIEW program was running on the PC, he exerted a pulling action on that sensor to move the cart towards himself, until its limit, keeping the rod horizontal, as much as possible, with a velocity similar to the one employed during an ordinary exercise. He has maintained such position for a few seconds (typically between 15 and 25 s). Then, acquisition was stopped and subject released the cart. Many trials were performed, on different days and by more people, with increasing loads. In both cases, data were saved at the end of the acquisition and were elaborated using Microsoft Excel and MATLAB software.

73.3   Experimental Results

Figure. 73.2 shows the results obtained from the first analysis, i.e. flexion angles and EMG signal graphs related to the movements corresponding to the exercises performed with both rehabilitation devices.

It is evident that the one with machine "b" implies only knee flexion (while hip movement is negligible), whereas the one with device "a" assures hip and knee
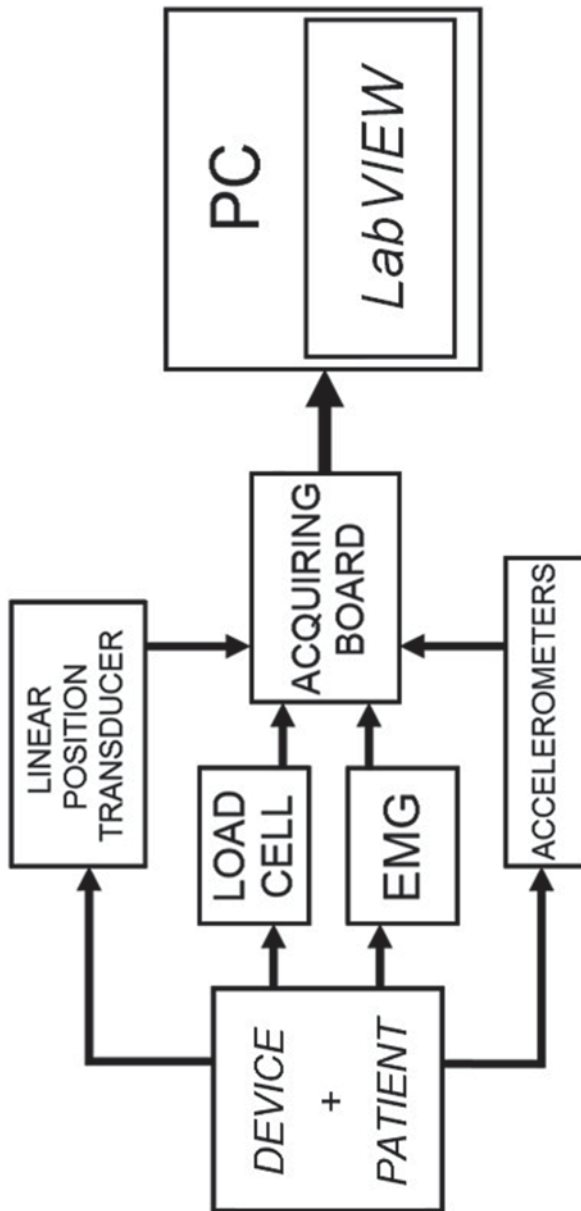
Fig. 73.1 Acquiring system block scheme
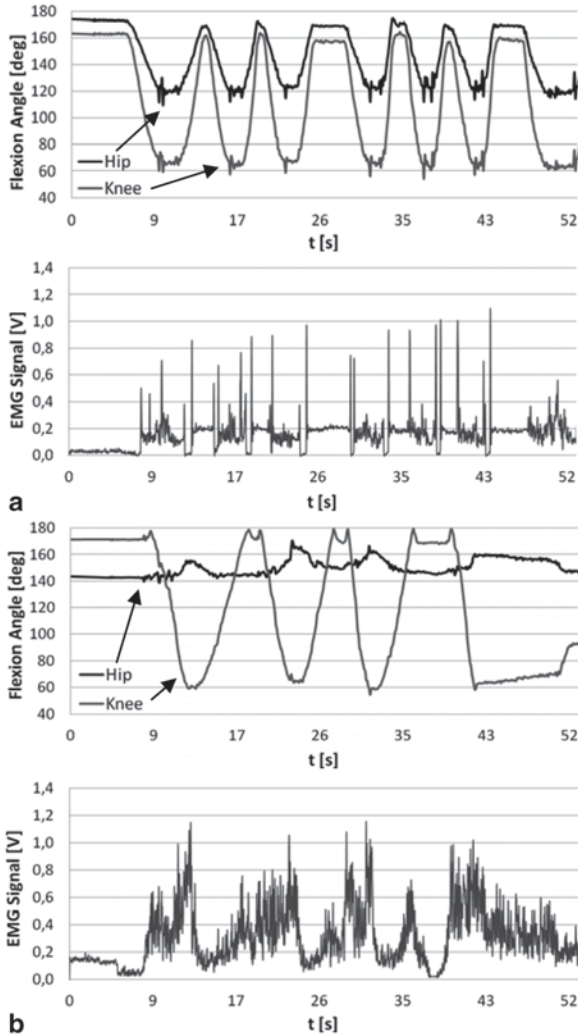
Fig. 73.2 Graphs of biomechanical parameters (hip and knee flexion angles and EMG signal) referring to the exercises performed with: **a** machine "a", **b** machine "b"

synchronous flexion, according to patient's natural kinetic chain; furthermore, EMG exam on Biceps femoris helps to understand that movement with machine "b" starts to activate this muscle at the beginning of knee flexion (concentric phase), with a peak when knee angle reaches its minimum value, whereas device "a" implies a more controlled and gradual muscle activation, mostly during extension (eccentric phase, as happens in running); in fact related signal is less noisy and the greatest part of its peaks is in correspondence of the beginning of such phase, or when

Table 73.1 Force intervals corresponding to different conditions

Rubber bands	Maximum force (kg)	Position maintaining force (kg)
1	12.0±0.9	6.0±0.7
2	16.5±1.4	12.4±1.0
3	23.8±2.0	17.3±0.6
4	28.2±1.5	22.8±0.5
5	34.5±2.2	28.1±1.1
6	41.4±1.1	33.6±1.0

knee angle reaches its maximum. A few peaks, less intense, are present also at the beginning of concentric phases; this can be due to the use of superficial electrodes, which could have involved fibers from other muscles.

Second analysis allowed obtaining proper force intervals for different numbers of rubber bands. They are listed in Table 73.1. Thus an indication about the force to provide in order to perform a suitable exercise is achieved. Maximum force refers to total effort for cart moving until its limit, whereas Position maintaining force is related to the one for keeping such position.

73.4   Conclusions

This article describes an acquiring system which has been implemented in two lower limb active rehabilitation devices (its modularity and most of all its capability of gathering different data for specific aims has allowed its efficient adaptation to these machines), to monitor biomechanical parameters during treatment, helping the physician to evaluate patient's condition and therapy effects. Furthermore, it has proved to be very useful to show the differences between the exercises proposed by such instruments and to obtain reasonable force intervals related to a proper execution of the exercise with machine "a".

References

1. H.S. Lo, S.Q. Xie. Exoskeleton robots for upper-limb rehabilitation: state of the art and future prospects. Med. Eng. & Phys. **34**, 261–268 (2012)
2. X. Cheng, Y. Zhou, C. Zuo, X. Fan. Design of an upper limb rehabilitation robot based on medical theory. Proc. Eng. **15**, 688–692 (2011)

Chapter 74
RGB-D Sensor-based Platform for Cognitive Rehabilitation in Alzheimer Disease

Alessandro Leone, Andrea Caroppo and Pietro Siciliano

The paper presents an digital platform integrating advanced Natural User Interface technologies for multi-domain Cognitive Rehabilitation. The platform is made up of a set-top-box connected to a TV monitor with Internet connection, a commercial RGB-D sensor as interactive device and an optional e-shirt with textile electrodes for clinical signs detection. A novel hand tracking procedure has been implemented improving the interaction between the end-user and the Graphical User Interface designed for specific cognitive domains. For proper interaction, gestures of Alzheimer Disease's patients with mild form are acquired by the active vision sensor in the nominal functioning range, allowing 100 % hands detection rate, useful for an error free human-machine interaction.

74.1   Introduction

Although no cure is available, Cognitive Rehabilitation (CR) for mild form [1, 2] of Alzheimer's Disease (AD) patients appears as an attractive treatment. In order to increase the chances of an appropriate care, the development of a cost-effective home-care service with CR functionalities appears as very attractive. In the field of healthcare, enabling technologies such as virtual reality, augmented reality and more in general digital tools (including serious games) have being applied for long time, including cognitive training and rehabilitation [3–6]. In the last years, the large diffusion of interaction devices enabling body movements for systems control have been investigated, with specific focus on ICT technologies for natural interaction. Microsoft Kinect [7] is the widely used RGB-D sensor allowing motion capture and gesture recognition [8].

A. Leone (✉) · A. Caroppo · P. Siciliano
CNR-IMM, Via Monteroni presso Campus Universitario, Lecce, Italy
e-mail: alessandro.leone@le.imm.cnr.it
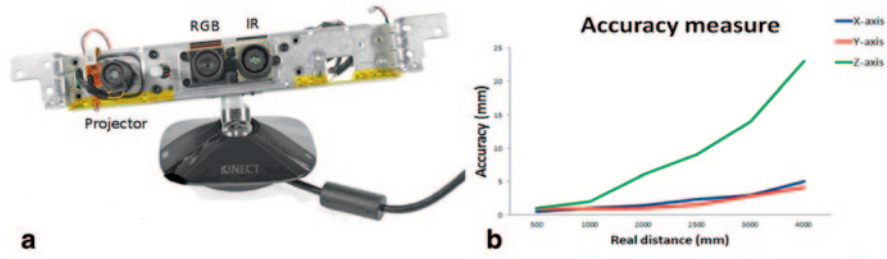
Fig. 74.1 **a** Details of Microsoft Kinect **b** Measurement accuracy along X, Y, Z-axis

A Natural User Interace (NUI) platform for remote CR has been designed with the aim to support AD patients during the multi-domain rehabilitation practice (temporal-spatial orientation, visual-topographical-verbal memory and fluency, visual-hearing attention, etc.) without the presence of any caregiver. A new hands tracking filter has been implemented in order to overcome the well-known limitations of the royalties-free NUI middleware architecture used in the platform. The paper is organized as follows: Sect. II describes the overall ICT platform with specific focus on the used sensor. In Sect III the hand tracking module is described whereas Sect IV presents perspective of the proposed technology and an overview of open research issues.

74.2 AL.TR.U.I.S.M. Platform

The developed ICT platform (called AL.TR.U.I.S.M.—Alzheimer patient's home rehabilitation by a Virtual Personal Trainer-based Unique Information System Monitoring) provides a digital tool for CR through a customized Virtual Personal Trainer (VPT) allowing the patients to perform the rehabilitation practice at home. The system provides a web-based platform allowing the physician to customize directly the therapy. The process is a highly innovative compared to existing systems [9] as the caregiver/physician defines a specific sequence of exercises (the therapeutic session) according to the residual abilities of the patient. The core of the platform is represented by the sensor-based architecture that permits the natural interaction of the end-user with the system. Technical details about the key modules of the platform are reported in the following.

74.2.1 Microsoft Kinect RGB-D Sensor

Microsoft Kinect (Fig. 74.1a) is a motion sensor that allows users to interact intuitively and without any intermediary device with a GUI. According to the structured-light functioning paradigm, the device acquires RGB frames at 640×480

Table 74.1 RMSD values at different distances for HDESF and EWMAF

Distance from Kinect (m)	RMSD (HDESF, in pixel)	RMSD (EWMAF, in pixel)
1.5	60.30	22.87
2.5	61.06	23.36
3	68.12	25.67
4	87.98	28.32

spatial resolution (30 fps), revealing nominal depth measurements in the 0.5–4 m range. While increasing distance from the sensor, the accuracy of the measurements decreases remaining within a functional range (Fig. 74.1b) compatible with the considered application scenario (however lower than 25 mm at the maximum distance range). Through the skeleton procedure provided by Microsoft Kinect SDK (or other free middleware platform as OpenNI), the spatial position of each joints of the body is recovered (or estimated) in a real-time way.

74.3   Hand Tracking Procedure for Contact-less NUI

The interaction with the platform is achieved by hand gestures performed by the patient according to the ad-hoc designed GUI, compliant the specific CR exercise. As AD patient may have troubles moving the hands, the procedure for hand tracking and gesture recognition provided by the Microsoft Kinect SDK may be affected by critical issues. In order to compensate jitter effects, a noise reduction filter has been designed. The suggested filter operates as a smoothing filter overcoming the performances of the Holt Double Exponential Smoothing Filter (HDESF) [10] built-in the SDK. From the analysis of the state of the art, the Exponential Weighted Moving Average Filter (EWMAF) [11] appears as the best trade-off between smoothing effect, jitter control and latency. The EWMAF is given by the following formula:

$$S_t = \alpha X_{t-1} + (1 - \alpha) \, S_{t-1} \quad t > 1 \tag{74.1}$$

where X_t is the 2D coordinate sample (in the image plane) at a time period t, S_t is the smoothed statistic as simple weighted average of the previous observation X_{t-1} and the previous smoothed statistic S_{t-1}. The coefficient α is constant smoothing factor between 0 and 1 and it represents the decreasing weighting degree. The evaluation of hand tracking procedure was made analyzing the difference between ground-truth values of the hand positions and the tracked values recorded using both HDESF and EWMAF. For this purpose, a frequently used measure is the Root-Mean-Square Deviation (RMSD), that represents the sample standard deviation of the difference between predicted and observed values.

Table 74.1 shows the results obtained at four different distances. The average RMSD values for EWMAF never exceeds the value of 30 pixel, allowing greater precision in the selection of a graphic item on the GUI. Instead, HDESF performs

Table 74.2 Performance of EWMAF for different α smoothing factor and number of observations

# of observations	α=0.1	α=0.3	α=0.7	α=0.9
5	34.3212	29.1258	25.3427	23.0045
10	33.5662	28.9083	24.9980	22.6754
15	32.0113	28.3397	24.6548	22.3359
20	32.9675	28.0989	24.1765	21.8675
30	31.3444	27.5674	23.8413	21.6754

an average error always greater than 60 pixels, so that the gap in some cases affects the correct selection of a graphic element. On the other hand, EWMAF introduces a quite limited lag relative to the input data. In real-time application, latency is a critical factor so it is essential to tune up in the right way the parameters of the filter, with the aim of obtaining the best performance with the lowest latency.

The choice of α=0.9 allows EWMAF to reduce significantly the RMSD compared to the result obtained with α=0.1 and α=0.3 (see Table 74.2); when the amount of past observations grows in size, results are better although a latency effect is introduced in the hand tracking procedure. For all considered CR scenarios, the best tradeoff is achieved for α=0.9 and the amount of past observations equal to 10 (as 300 ms).

74.4   Conclusions

The proposed system promotes multi-domain Cognitive Rehabilitation of Alzheimer's Disease patient at home through an ICT platform integrating low-cost contact-less Natural User Interface devices. The proposed platform allows both the evaluation of the progress of the dementia and the cognitive stimulation of the end-user in several domains. In this work an accurate interaction of the end-user, even in the presence of complex GUI, has been obtained through to a low-latency hand tracking procedure. Future works are addressed to deploy the platform to a wide class of patients with dementia or other kind of impairments related to ageing (including motor impairment) in order to have the measurable outcome of the technological tool usage. This will allow to tune up each component of the platform in order to make it highly compliant with the needs and the requirements of the patients, according to the recent User Centered Design paradigm.

References

1. Clare, L., et Al.: Cognitive Rehabilitation in Dementia, in Neuropsychologistical Rehabilitation, Psychology Press Ltd, 193–196 (2001)
2. Neal, M., Briggs, M.: Validation therapy for dementia (Cochrane Review). The Cochrane Library, Issue 2. Chichester, UK (2004)

3. Richard, E., et Al.: Augmented Reality for Rehabilitation of Cognitive Disable Children: A preliminary Study, Virtual Rehabilitation, 102–08, (2007)
4. Taylor, M.J.D., et Al.: Activity-promoting gaming systems in exercise and rehabilitation, Journal of Rehabilitation Research 48 (10), 1171–86. (2011)
5. Nacke, L.E., et Al.: Brain training for silver aged gamers: effects of age and game form on effectiveness, self-assessment, and gameplay", in Cyberpsychology & Behavior, 12(5), 493–499 (2009)
6. Imbeault, F., et Al.: Serious Games in Cognitive Training for Alzheimer's Patients, in IEEE Int. Conference on Serious Games and Applications for Health, 122–129 (2011)
7. http://www.microsoft.com/en-us/kinectforwindows
8. Da Gama, A., et Al.: Improving Motor Rehabilitation Process through a Natural Interaction Based System Using Kinect Sensor, Proceedings of IEEE Symposium on 3D User Interfaces, 145-46 (2012)
9. Solana, J. et Al.: PREVIRNEC, A new platform for cognitive tele-rehabilitation, in the Third Int. Conference on Advanced Cognitive Technologies and Applications (2011)
10. Holt, C.C.: Forecasting seasonals and trends by exponentially weighted moving averages, ONR Memorandum, vol. 52Carnegie Institute of Technology, Pittsburgh, PA, available from the Engineering Library, University of Texas at Austin (1957)
11. Roberts, S.W.: Control Chart Tests Based on Geometric Moving Averages, Technometrics (1959)

Chapter 75
Fall & ADL Detection Methodologies for AAL

Bruno Andò, Salvatore Baglio, Cristian O. Lombardo, Vincenzo Marletta and Elisa A. Pergolizzi

The monitoring of falls and Activities of Daily Living (ADL) is a fundamental task to implement a rigorous remote monitoring of weak users with particular regards to elderlies. Actually, unintentional falls cause a lot of hospitalizations and could produce serious consequences due to long-lie happenings. ADL monitoring by using poor invasive and easy to use devices would really change the way of achieving awareness on the user status thus reducing times for the implementation of emergency actions. In this paper authors present two different methodologies for falls and ADLs detection. The proposed methodologies allows for ADL classification with sensibility and specificity features in line with real applications in AAL context.

75.1 Introduction

Detection of ADLs is a mandatory and challenging task to implement a rigorous remote monitoring of weak users. Falling, stair negotiation, user posture are just few examples of events and daily activities to be monitored. A reliable monitoring of ADL by using poor invasive and easy to use devices would really change the way of achieving awareness on the user status thus reducing times for the implementation of emergency activities. Different approaches have been proposed to develop systems for ADL detection in the Ambient Assisted Living contexts, such as customized devices [1] and smartphone based platforms [2–3]. Researchers at DIEEI of the University of Catania are investigating novel methodologies and solutions providing useful and reliable information for the efficient implementation of remote

B. Andò (✉) · S. Baglio · C. O. Lombardo · V. Marletta · E. A. Pergolizzi
Dipartimento di Ingegneria Elettrica Elettronica e Informatica (DIEEI), University of Catania, Catania, Italy
e-mail: bruno.ando@diees.unict.it
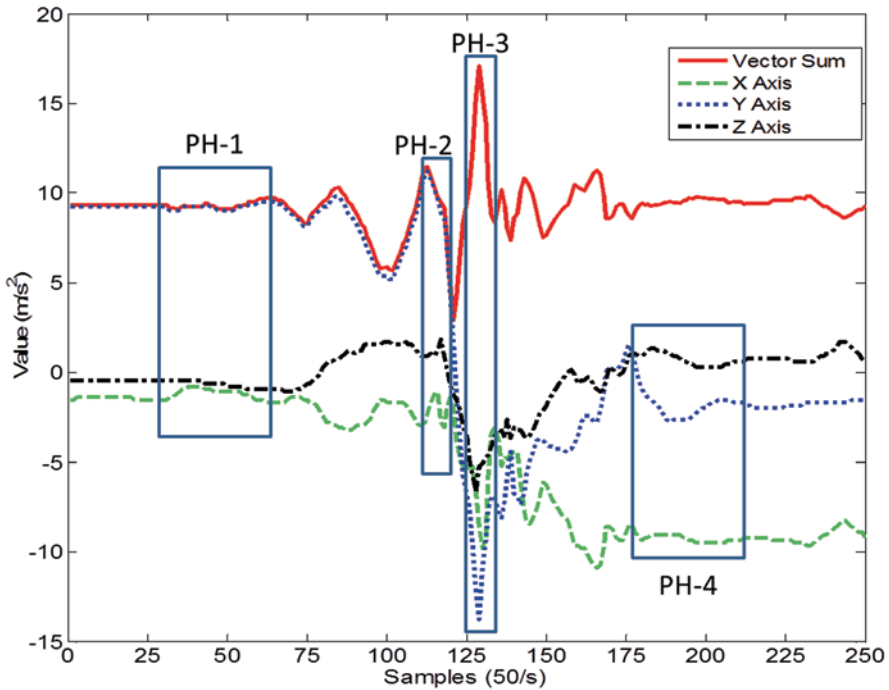
Fig. 75.1 Acceleration signals observed during a typical fall event

elderly monitoring with particular attention to falls and ADL detection [4–6]. In this paper two different methodologies for fall events detection and ADL classification are addressed.

75.2 Fall Detection Algorithm Based on Fall Dynamics

This section deals with a methodology for falls' identification exploiting the analysis of acceleration curves during fall events [7]. In particular, the fall event present four critical peculiar phases characterized by typical accelerations observed on the three axes and time span. The recognition of these characteristics in the dynamics of the monitored movements allows detecting of the fall events. Figure 75.1, schematically shows the time trend of the acceleration signal observed on the three axes during the fall event and the four phases. The vector sum of accelerations is also represented.

An initial phase (PH-1) in which the acceleration signals assume values which depend on the human body posture, can be identified. Subsequently, at the start of the fall a "free fall" condition is experienced by the accelerometer and acceleration signals tend towards zero (PH-2). Obviously, except for falls from great heights,

Table 75.1 Typical Parameters of the four phases representing fall event dynamic evolution

	PH-1	PH-2	PH-3	PH-4
	Initial posture	Free fall	High activity	Final posture/inactivity
Accel. Typol.	Static	Dynamic	Dynamic	Static/Dynamic
Amplitude (m/s^2)	0–11.8	<5.5	>17.2	<1.8 (Dynamic) 0–11.8 (Static)
Period (ms)	–	>30	<200	<200

the acceleration signals will never reach zero. In the third phase (PH-3), the human body impacts the ground and a peak on the amplitudes of the acceleration on all axes is observed. Finally, the last phase (PH-4) is essentially characterized by a condition of inactivity. Typically a different final static configuration as respect to the initial one is observed due to the different postural configuration. Detection of a fall event takes place after identification of phases 2, 3 and 4. A change in the static position on at least two axes between PH-1 and PH-4 should be observed. The detection algorithm was implemented by a microcontroller board employing a low power 8-bit ATmega168. The accelerometer ADXL345 (Analog Devices) was used to sense accelerations onto the three axis. The typical accelerations and time span of the four phases observed experimentally in case the device was mounted in the pelvis of the user are shown in Table 75.1.

75.3 A Smartphone Based Methodology for ADL Classification

Smartphone based solutions could represent a promising way to monitor weak users involved in common daily activities, especially when they do not require user interaction. In this section a smartphone based platform aimed to provide effective solutions for ADL detection in Ambient Assisted Living (AAL) contexts is addressed [4–6]. The main task of the assistive system is to acquire awareness of fall events and common ADLs such as stair negotiation and sitting, in order to provide weak users with a suitable degree of assistance. The system is based on a smartphone positioned on the hip and exploits embedded sensors and advanced signal processing paradigms to detect and classify ADLs. In particular, two different classification algorithms have been developed. The first one exploits a threshold mechanism while the other one is based on Principal Component Analysis (PCA). The threshold definition mechanism implemented use ROC theory which allows to properly define thresholds values on the basis of constraints on the system sensibility and specificity. Advantage of the PCA approach resides in the possibility to improve the system specificity in classifying different kind of falls and a reduction of the classification problem complexity. Each event is characterized by a typical signature of the acceleration magnitude signal. A suitable dedicated algorithm for the normalized signature extraction has been developed. Normalization in the

Fig. 75.2 Flow diagram
of the threshold algorithm
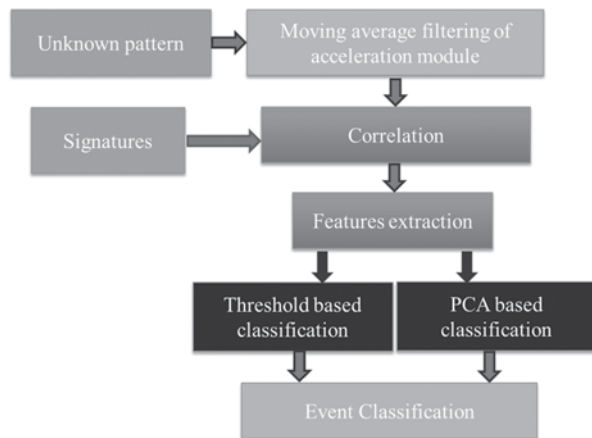adopted for the sake of events
classification

Table 75.2 Performances of classification paradigms in terms of sensitivity and specificity

	Sensibility of threshold algorithm	Sensibility of PCA algorithm	Specificity of threshold algorithm	Specificity of PCA algorithm
FF1	1	1	0.94	1
FF2	1	1	0.79	1
FF3	1	1	0.92	0.96
FBW	0.78	1	0.92	1
BF	0.78	1	0.86	1
LF	0.89	1	0.87	0.96
SU	1	1	1	1
SD	1	1	1	1
SI	0.89	1	0.68	1

range $[-1,1]$ has been employed thus preserving signals dynamics while leading
to a signature generalization. Class of performed actions are: forward fall starting
from standing (FF1), forward fall from walking (FF2), fainting fall (FF3), backward
fall (BF), lateral fall (LF), forward fall starting from bending (FFB), stair negotia-
tion (step up 'SU', step down 'SD') and sitting down (SI). The flow diagram of
the threshold classification approach is sketched in Fig. 75.2. The maximum val-
ues of the cross-correlation between the obtained signal and the set of signatures
of candidate class of events are used as features for the classification procedure.
The last step of the algorithm consists in comparing extracted features to threshold
values in order to define the potential class or classes to which the unknown target
belongs. A second classification solution based on PCA has been used for the sake
of comparison. In order to test the system, simulated intentional actions were per-
formed by healthy subjects exploiting if necessary a mattress. Each action has been
repeated nine times. A comparison of results in terms of sensitivity and responsivity
for the two classification algorithms is given in Table 75.2. As it can be observed
performances of such approach are definitively better than the threshold based clas-
sification solution and as respect to the State Of The Art.

75.4   Conclusions

In this paper authors present two different methodologies for fall and ADLs detection. In particular a methodology of identification of the falls based on the exploitation of a customized solution and some considerations on the acceleration change curves during the fall event and a smartphone based platform aimed to provide effective solutions for ADL detection in AAL contexts exploiting embedded sensors and advanced signal processing paradigms have been presented. The proposed methodologies allows for ADLs classification with sensibility and specificity features in line with real applications in AAL context. Results obtained encourage the development of this kind of assistive systems.

References

1. G. Rescio, A. Leone, P. Siciliano, Supervised Expert System for Wearable MEMS Accelerometer-Based Fall Detector, Journal of Sensors, vol. 2013, Article ID 254629, 11 pages, 2013. doi:10.1155/2013/254629
2. J. Dunkel, R. Bruns, S. Stipkovic, Event-based smartphone sensor processing for ambient assisted living, Autonomous Decentralized Systems (ISADS), 2013 IEEE Eleventh International Symposium on, pp. 1–6, Mexico City, March 6–8 2013
3. C. Tacconi, S. Mellone, L. Chiari, Smartphone-Based Applications for Investigating Falls and Mobility, 5th International Conference on Pervasive Computing Technologies for Healthcare (PervasiveHealth) and Workshops, pp. 258–261, Dublin, May 23–26, 2011.
4. B. Andò, S. Baglio, C. O. Lombardo, V. Marletta, E. A. Pergolizzi and A. Pistorio, RESIMA: a new WSN based paradigm to assist weak people in indoor environment, 2013 IEEE International Workshop on Measurement and Networking (M & N), Naples, October 7–8, 2013.
5. B. Andò, S. Baglio, C. O. Lombardo, V. Marletta, An advanced tracking solution fully based on native sensing features of smartphone, IEEE Sensors Applications Symposium (SAS), pp. 141–144, Queenstown, New Zealand, February 18–20, 2014.
6. B. Andò, S. Baglio, C. O. Lombardo, V. Marletta, E. A. Pergolizzi, A. Pistorio, An event polarized paradigm for ADL detection in AAL context, 2014 IEEE International Instrumentation and Measurement Technology Conference (I2MTC), Montevideo, Uruguay, May 12–15, 2014.
7. N. Jia, Fall Detection Application by Using 3-Axis Accelerometer ADXL345, Analog Devices, Application Note 1023.

Chapter 76
Semi-active RFID Devices for Traceability

Francesco Abate, Consolatina Liguori, Vincenzo Paciello, Antonio Pietrosanto, Ciro D'Apice and Rosanna Manzo

In this paper a semi-active RFID module for remote monitoring of storage conditions during the transportation is proposed. It integrates one SmartTag and some sensors, and allows also to locate the object to the one which is related. In order to obtain the real time observing on the transportation vehicle an On Board Unit (OBU) is installed that works as a concentrator and communicates with a central control room.

76.1   Introduction

Traceability is defined as the ability to trace the history, use or location of which is being considered [1]. The internal traceability is limited to the design cycle of a given product and is easily confined to a single place of work, or even to a single company; whilst the supply chain traceability is therefore the ability to reconstruct the history and to follow the use of a product. A delicate aspect is the monitoring of goods in transit, especially for perishable goods [1], which the constant monitoring of the quality of the environment in which they are placed during transport, it is a very important issue for [3, 4].

The purpose of an advanced tracking system is to monitor the product not only in production but also in all the different stages of the supply chain, including the inter-factory transportation. The encoding of the information to be transported is very important for the traceability system. Among the most used techniques the

---

A. Pietrosanto (✉) · F. Abate · C. Liguori · V. Paciello
Department of Industrial Engineering, University of Salerno, via Giovanni Paolo II,132, Salerno, Italy
e-mail: apietrosanto@unisa.it

C. D'Apice · R. Manzo
Department of Electronic and Computer Engineering, University of Salerno, via Giovanni Paolo II,132, Salerno, Italy
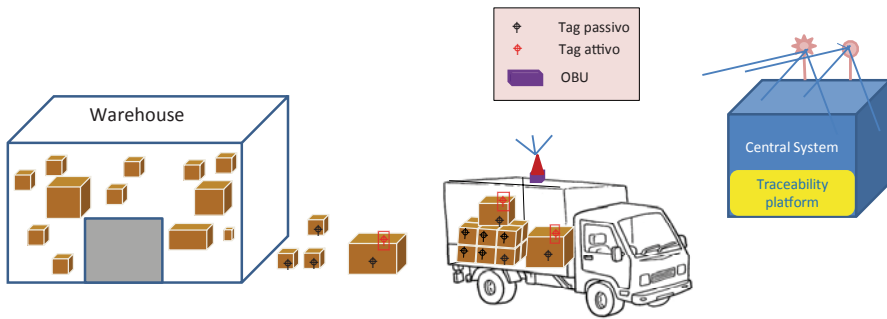
Fig. 76.1 Traceability system

radio-frequency identification (RFID) tags are becoming more and more widespread. The reader is used to remotely read and write data on the smart tag in real time, it sends an activation signal to the tag, which responds with the transmission of information loaded into memory.

In this paper, we propose a semi-active RFID [5] module where one SmartTag and some sensors for remote monitoring of storage conditions of the products during handling are integrated. It also allows you to track the location of each object thanks to an On Board Unit (OBU) installed on the transportation vehicle [6].

76.2 The Proposed Traceability System

In Fig. 76.1, the proposed traceability system is schematically shown.

The main components of the system are five: (i) reader RFID, (ii) passive TAGs, (iii) semi-active TAGs, (iv) the On Board Unit (OBU), and (v) the central system.

All the packages to be tracked are labeled with a passive TAG [5] that uniquely identifies them, it stores the unique code of the product. The reader transmits interrogator signals and all the TAGs, which are in the antenna field, respond with the unique identifier (utilizing an anti-collision protocol), and some other data stored in the memory of TAGs.

Several special packages are featured also with an semi-active TAG that integrates sensors, in order to monitor the preservation of environmental conditions; data coming from sensors are sent to the OBU.

The OBU works as a concentrator and communicates with a central control room; OBU and active TAGs are then nodes of a wireless sensor network [7–11].

76.2.1 The RFID Reader

The RFID reader is based on the OEM RFID UHF ISC.MU02.02 module by Feig Electronic®, it works in the 860÷960 MHz (UHF) frequency range, ad is suitable

Fig. 76.2 The passive TAG

for short and medium distance range and is characterized by low power consumption. The read TAG codes are periodically sent to the OBU. (Fig 76.2)

76.2.2   The Passive TAG

The used TAG are the ALN-9662, by Alien®; it uses EPC Gen 2 coding, RFID UHF operation (840–960 MHz); it is pre-programmed with a 64-bit serial number. The User Memory can be write, and it is possible to protect the data with password in 64-bit blocks.

76.2.3   The Semi-Active TAG

The semi-active TAG is based on the CC1111Fx by Texas Instruments®, includes temperature, humidity and light sensors. Each semi-active TAG is related to a passive TAG storing the ID of the microcontroller in the passive TAG user memory. The sensor data are acquired with a period of five seconds, and the measured values are pre-processed on board, finally the outputs are sent to the OBU.

76.2.4   The OBU

The OBU acts as linker between the vehicle and the traceability framework; consequently, its tasks are numerous, it has to collect all the information on the vehicle status and operates as a wireless network concentrator [7], it always has to be geographically localized and continuously sends data to the central system.

The OBU prototype is schematically shown in Fig. 76.3: it is based on STM-32F103RE microcontroller, manufactured by STMicroelectronics, in ARM Cortex M3 technology. The OBU is featured with several modules: the RFID reader, a GM862-GPS module by Telit that integrates GPS/GPRS functionality module, SD memory. All these devices are interfaced via RS232 to the OBU microcontroller [8, 9]. The GPS module gives the geographic location and time. The OBU is also equipped with an SD memory since the system requires a memory buffer, to save the information when the system cannot send data to the server.

The OBU periodically read data by the semi-active TAGs, the communication is made by a star topology with a carrier to about 868 MHz. The used protocol is
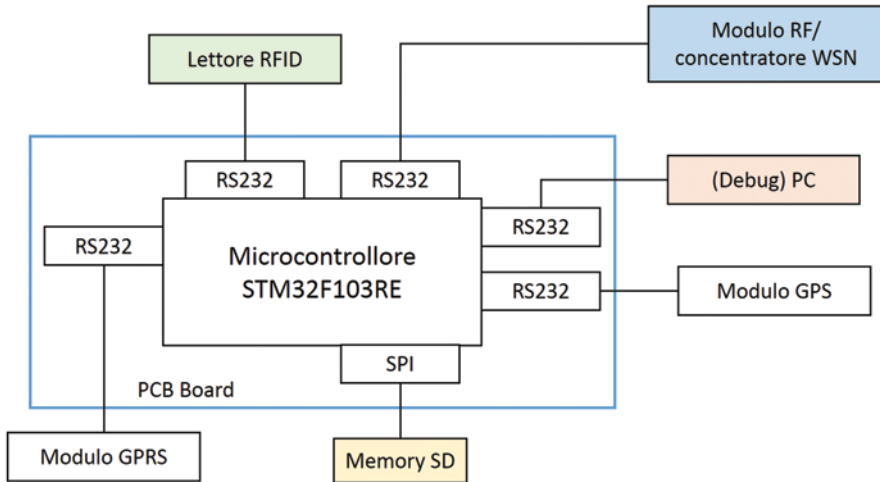
Fig. 76.3 Block diagram of the OBU

SimpliciTI by Texas Instruments. After the acquisition and processing phases the microcontroller creates a data packet for each minimum traceable unit and sends data to a server through the GPRS module.

76.2.5 The Central System

The server processes the received packets, visualizes on a map the package localization and shown all the collected data concerning the condition of each special package, moreover some alarm indications are provided in case of the specifications on the storage condition are not satisfied or the package route is not followed.

76.3 Conclusions

In the paper the design and the use of semi-active RFID devices featured by environmental sensors for innovative traceability application is presented. Thanks to the adopted solutions both in the semi-active devices realization and on the wireless sensor network [10, 11] implementation allow the continuous tracking of packaging also in the transportation phase.

References

1. Regulation (EC) No 178/2002 of the European Parliament and of the Council, (2002).
2. Che-Fu Hsueh and Mei-Shiang Chang, "A Model for Intelligent Transportation of Perishable Products", International Journal of Intelligent Transportation Systems Research (2010), Vol. 8, no 1, pp. 36–41.
3. Yu-Chih Huang Wen-Chung Kuo Min-Chih Kao, "A RFID Field Operation System Design for Agricultural Traceability", Pervasive Computing Signal Processing and Applications (PCSPA), 17–19 September 2010 First International Conference on, pp. 423–426 (2010).
4. DIRECTIVE 2001/95/EC OF THE EUROPEAN PARLIAMENT AND OF THE COUNCIL, 3 December 2001 (2001).
5. Thakur, M., et al. Managing food traceability information using EPCIS framework. Journal of Food Engineering, (2011) Vol. 103, no 4, pp. 417–433.
6. Moe, T., Perspectives on traceability in food manufacture. Trends in Food Science & Technology, (1998) no. 5, pp. 211–214.
7. D. Capriglione, L. Ferrigno, A. Attianese, A. Pietrosanto, V. Paciello (2013) "Experimental Analysis of Wireless Sensor Network Synchronization Protocols Under Real Operating Conditions" Springer, pp. 529–533, Vol. 162, Sensors, 15–17 February, 2012, Roma.
8. L. Ferrigno, D. Capriglione, V. Paciello, A. Pietrosanto (2012) "A step forward the on-line minimization of the synchronization events in TPSN", Proceeding of International Instrumentation and Measurement Technology Conference I2MTC 2012. pp. 2780–2784, IEEE, ISBN: 9781457717710.
9. L. Ferrigno, V. Paciello, A. Pietrosanto, "Visual sensors for remote metering in public networks" IEEE International Instrumentation and Measurement Technology Conference (I^{2}MTC), Hangzhou, Cina, 9-12 May 2011, pp. 1–6, DOI 10.1109/IMTC.2011.5944237.
10. L. Ferrigno, V. Paciello, A. Pietrosanto, "Performance Characterization of a Wireless Instrumentation Bus", IEEE Transactions on Instrumentation and Measurement, Vol. 59, no. 12, DOI: 10.1109/TIM.2010.2047307, pp. 3253–3261, 2010.
11. L. Ferrigno, V. Paciello, A. Pietrosanto, "Experimental Characterization of Synchronization Protocols for Instrument Wireless Interface", IEEE Transactions on Instrumentation and Measurement, Vol. 60, no. 3, DOI: 10.1109/TIM.2010.2060224, pp. 1037–1046, 2011.

Chapter 77
Some Notes on the Performance of Regression-based Time Synchronization Algorithms in Low Cost WSNs

Giovanni Betta, Deborah Casinelli and Luigi Ferrigno

Time synchronization in low-cost wireless sensor networks based on synchronization algorithm is a today relevant issue as for the networks costs, energy consumption and indoor uses aspects. Among the other those based on the one way messaging and, in particular, on the adoption of regressive algorithms are widely used in many application contexts. This paper proposes a preliminary performance analysis aimed at highlighting the sensitivity of the regression-based algorithms versus some influence factor typical of the low cost applications, such as the finite resolution of the timing clock, the presence of clock drift, clock jitter and wander, the presence of real latencies of the radio devices, the presence of real latencies of the microcontroller device. The aim is to weight the influence of each one of these influence factors on the overall synchronization performance. The analysis is carried out a suitable and controlled experimental environment.

77.1 Introduction

In the most of short range and low cost Wireless Sensor Networks (WSNs) applications, sensor nodes have to "share" the same sense of time to obtain cooperation, synchronized measures, reliable data fusion, and localization to cite a few. Recent literature is proposing many efficient algorithms for WSNs synchronization. Among the others, those based on time regression are widely used and try to establish a linear relationship between clocks at different sensor nodes with the aim of predicting a reference clock based on collected timestamps [1]. In this context the authors have paid their attention to the performance characterization of these synchronization protocols when low cost wireless sensor nodes are used [2, 3]. In particular, their studies evidenced that even though such algorithms had been thought for small

G. Betta (✉) · D. Casinelli · L. Ferrigno
DIEI, Università di Cassino e del Lazio Meridionale, Via G. Di Biasio, 43, Cassino, Italy
e-mail: betta@unicas.it

scale and low cost WSNs, their performance had been either predicted in simulation environment, or achieved with nodes equipped with the capability of read and write timestamps at medium access channel (MAC) level. On the contrary, in typical industrial and user applications these synchronization protocols are performed by devices that do not have such a feature. In addition, further non-idealities are generally present as reference clocks that might change versus some influence factors as the temperature, the aging, the battery voltage, the employment of commercial radio device as the WiFi, the BlueTooth (BT) and so on. Starting from these results, from the experiences in the field of communication systems testing and algorithm characterization [4–6], this paper extends the above-mentioned studies and carries out a systematic characterization of the regression based algorithms. In particular, the influence of some factors as (i) the implementation on real low cost wireless sensor nodes, (ii) the adoption of commercial radio systems, (iii) the use of real clock that exhibit drifts and variation over time, have been considered.

77.2   Test Setup and Results

To perform the above-mentioned tasks the authors propose a suitable set-up able to generate precise clock frequencies, to impose desired clock behaviors (i.e. variation of clock over time according the desired waveforms), to emulate fixed and variable latencies due to the communication channels, the serial tunneling and the application software has been adopted. It is made up of the PC controller, the Tektronix TLA5202 Logic Analyzer, the Tektronix AFG3022B dual channel waveform generator, and two sensor nodes connected through a wired link. The PC controller is embedded in the logic analyzer but it is represented as an external unit for the sake of clarity. It supervises all the instruments in the measurement setup. The logic analyzer captures the time related to each happened event during the execution of experimental tests as better described below. The dual channel waveform generator provides clocks to the two sensors involved in the measurement setup. The two sensor nodes perform the synchronization procedure and run the software routines conceived to be able to emulate the behavior of different radio devices.

In the following some of the obtained results are reported. In particular, Fig. 77.1 shows the residual clock delay, evaluated after the synchronization procedure, between the clock sender and the clock receiver versus the variable latency of the radio channel modeled as an uniform distributed time delay. Two clock drifts equal to $\pm 0.025\%$ between sender and receiver clocks have been considered. It is possible to highlight that there is a dependency between the performance of the radio channel (i.e. the radio standard adopted) and the synchronization results.

Figure 77.2 sums also the presence of a latency due to the communication channel between the microcontroller and the radio device. It is possible to highlight the combined effect in the worsening of the CPD. Scarce influence of the total synchronization time, defined as the time interval between consecutive synchronization
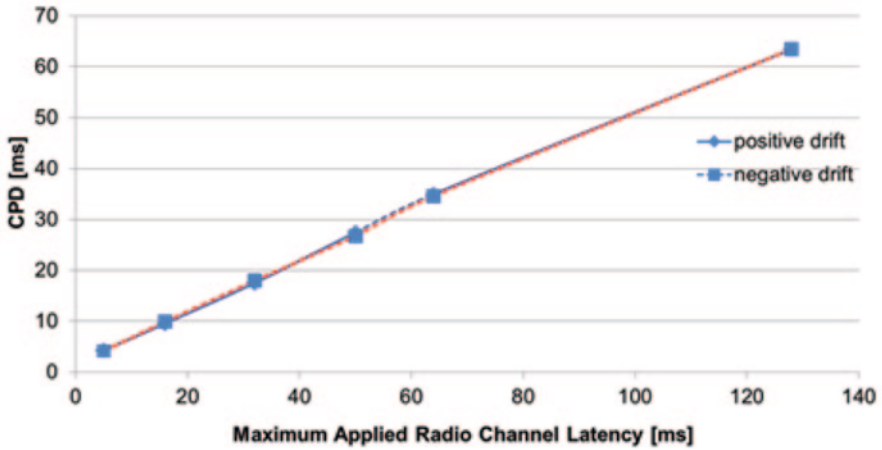
Fig. 77.1 Residual clock delay between the clock sender and the clock receiver versus the variable latency of the radio channel (*red dotted line* is for positive drift and *blue solid line* is for negative drift)

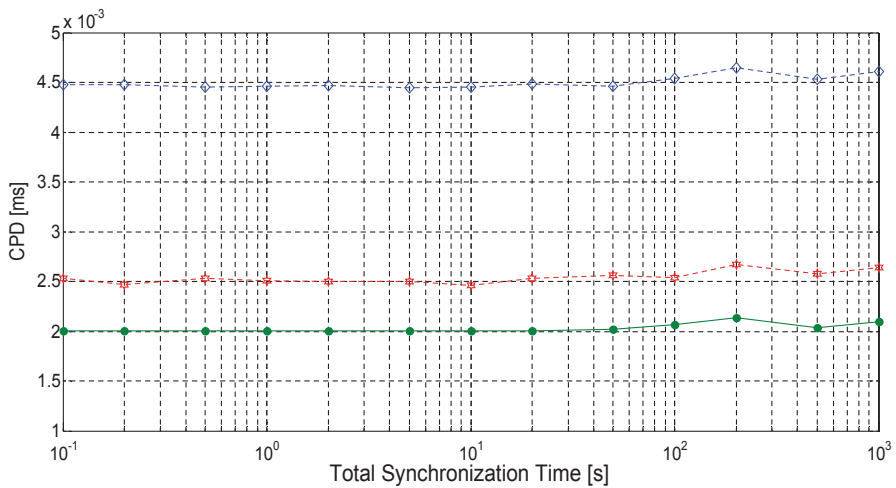**Fig. 77.2** Residual clock delay between the clock sender and the clock receiver versus the total synchronization time in presence of microcontroller latency *(green solid line with circle marker)*, variable latency of the radio channel *(red dashed line with asterisk marker)* and both of them *(blue dotted line with diamond marker)*
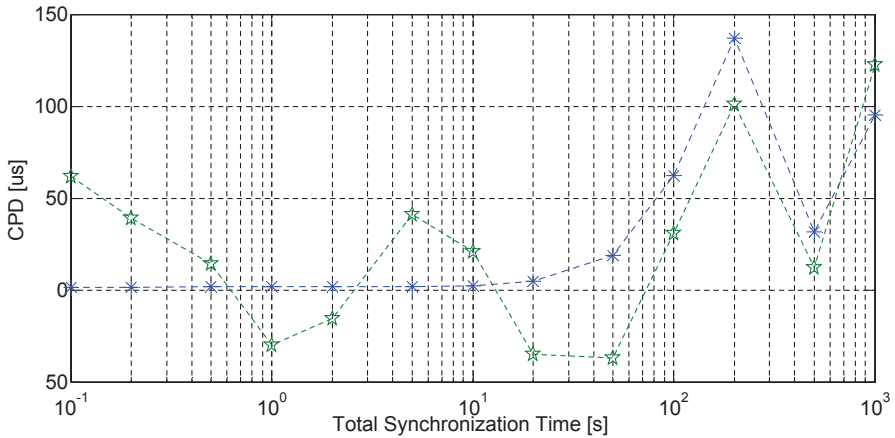
Fig. 77.3 Effect of the correction of the mean latencies of the microcontroller and radio channel latencies (*green dotted line* with *star markers*) versus the total synchronization. The *blue dashed line* with *asterisk markers*, shows the case of ideal radio channel and absence of microcontroller latencies

time-stamps, is observed. Finally, Fig. 77.3 shows the effect of the correction of the mean values of these latencies respect to the ideal case. Deep improvements in the synchronization performance are observed.

77.3 Conclusions

A preliminary characterization of synchronization algorithms based on linear regression and operating on low costs wireless sensor nodes has been carried out. Typical latencies and synchronization worsening factors that commonly occur in these types of sensors have been identified and suitably analyzed by the way of a reliable measurement set-up. In particular, the effects of more persuading factors such as the clock drift, the latency of radio channels, and the limited bandwidth of the transmission channel have been accounted for. The achieved results have highlighted the effect of each of the above mentioned influence factor and the benefit obtaining by the application of some simple correction factors which could be estimated by means either of datasheet or preliminary experimental campaign.

References

1. M. Maroti, B. Kusy, G. Simon, and A. Ledeczi, "The flooding time synchronization protocol," in Proceedings of the 2nd International Conference on Embedded Networked Sensor Systems. New York: ACM Press, 2004, pp. 39–49.

2. L. Ferrigno, V. Paciello, A. Pietrosanto, "Experimental Characterization of Synchronization Protocols for Instrument Wireless Interface," IEEE Transactions on Instrumentation and Measurement, Vol. 60, Issue: 3, 2011.
3. D. Capriglione, D. Casinelli, E. D'Orazio, L. Ferrigno, "Time synchronization based on linear regression in low cost WSNs: A performance analysis", proceedings of the IEEE International Workshop on Measurements and Networking (M & N), 2013, Napoli, 7–8 Oct. 2013, pp. 25–30.
4. L. Ferrigno, V. Paciello, A. Pietrosanto, "Low-cost visual sensor node for BlueTooth-based measurement networks,"; IEEE Transactions on Instrumentation and Measurement, vol. 55, no. 2. pp. 521–527, April 2006.
5. L. Ferrigno, M. Laracca, C. Liguori, A. Pietrosanto, "An FPGA-Based Instrument for the Estimation of R, L, and C Parameters Under Nonsinusoidal Conditions", IEEE Transactions on Instrumentation and Measurement, Vol. 61, Issue 5, pp. 1503–1511, 2012,
6. Angrisani L., Capriglione D., Ferrigno L., Miele G., "A methodological approach for estimating protocol analyzer instrumental measurement uncertainty in packet jitter evaluation", IEEE Transactions on Instrumentation and Measurement, Vol. 61 issue 5 pp. 1405–1416, 2012.

Chapter 78
A Software Sensor for Motorcycle Suspension Stroke

Domenico Capriglione, Consolatina Liguori, Vincenzo Paciello, Antonio Pietrosanto and Paolo Sommella

78.1   Introduction

Soft Sensors are generally meant the process of estimation of any system or process variable by using mathematical models, substituting some physical sensors and using data acquired from some other available ones [1]. Since the direct implications on cost-saving and safety, the smart sensing has become an interesting topic also for the field of two-wheeled vehicles, where the spread of electronic control systems is still in its infancy (for example, today, only a few commercial motorbikes are equipped with ABS control systems). A typical approach is the adoption of Kalman filters: in [2] they were proposed as real-time acceleration-based estimators of the elongation velocity and damping force for single semi-active shock-absorber in order to improve noise filtering and/or implement virtual sensor. Since measurement information about suspension dynamics (in terms of elongation and/or velocity) is necessary to implement whichever strategies for controlling the damper characteristics of semi-active and active shock absorbers [3,4], a straightforward extension of the previous approaches is the soft sensing of the rear suspension behavior (stroke), which the authors aim to, by exploiting the analytical redundancy between vertical dynamics of the motorcycle suspension system as whole. Indeed, according to the half-car model (which linearly approximates the in-plane dynamics) the rear suspension response to the road disturbances is strongly influenced by the heavy and pitch movements of the front suspension and the motorcycle body respectively as well as by the road profile actually experienced by the front wheel. In the present

---

D. Capriglione (✉)
DIEI, University of Cassino, via G. Biasio, 43 Cassino, Frosinone, Italy
e-mail: capriglione@unicas.it

C. Liguori · V. Paciello · A. Pietrosanto · P. Sommella
DIIn, University of Salerno, via Giovanni Paolo II,132 Fisciano, Salerno, Italy
e-mail: apietrosanto@unisa.it

work, the mathematical model allowing to infer the rear suspension stroke on the basis of its dependence on a set of influential variables is developed according to the data-driven approach.

78.2   Methods and Material

The typical steps that a softer designer is faced with are reported in the following as well as the correspondingly adopted techniques.

a. *Data Collection.* The model designer might select data that represent the whole system dynamics by running measurement campaign on the process, which give insight into relevant variables, system order, delays, sampling time, operating range, nonlinearity. This identification step was performed by taking into account the following riding conditions: a stretch of cobblestone (which excite the suspension response to the pitch); a rough urban road negotiated at low-medium speed (accordingly the motorcycle receives a mixed pitch-have excitation simultaneously, on a broad spectrum), an extra-urban road negotiated at high-medium speed (which mainly introduces pure heavy excitation), a region with multiple speed bumps (in order to highlight the suspension behavior against concentrated obstacles and significant load transfer). About 1 hour of data acquisition (12 records of the test lap) has been collected for the following signals: fork stroke, pitch rate, roll rate, longitudinal speed, breaking activation (as independent variables) and rear shock stroke (as dependent variable).

b. *Data Filtering.* The recorded data came from the sampling process of the analog signals at 1 kHz. Digital data filtering has been introduced to remove high frequency noise and offsets. To prevent larger magnitude variables to be dominant over smaller ones during the identification process, data scaling has been also performed according to the min-max normalization method. Finally, since the presence of outliers can affect the performance of data-driven soft sensor design, the Hampel identifier has been adopted as detection strategy [5].

c. *Model Structure & Regression Selection.* Model structure is a set of candidate oriented representations, where a set of dependent variables (i.e. the system outputs) are the consequence of a set of independent variables (i.e. the system inputs). When the variable inferred by the soft sensor is the output of a dynamic system, two possible choices are common: Nonlinear Moving Average (NMA) models and Nonlinear Auto-Regressive with exogenous inputs ARX (NARX) models. Since the half-car model hypotheses that the suspension system works close to a steady state condition and does not account for the steering and linkage nonlinear effects which mainly results in a varying wheel base and transfer load, the NARX model has been appeared as the most straightforward choice. About the Regression selection, the estimated normalized cross-correlation function between each candidate independent variable and the system output has been investigated in terms of the peak magnitude. As result, fork stroke, pitch rate and
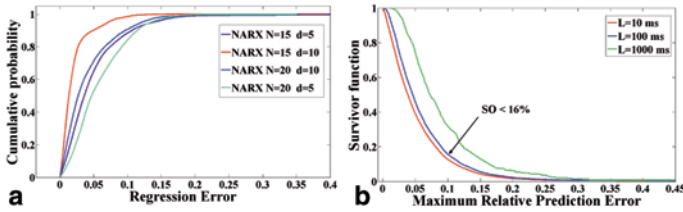
Fig. 78.1 Graphical tools for model validation applied to the rear stroke sensor: **a** *REC curves* for comparing NARX Neural Network (*N*, number of hidden nodes; *d*, time delay). **b** *SOE curves* for NARX Neural Network (*N*=15, d=10) as the window length is varying

longitudinal speed emerged as the most relevant inputs and further considered in the next design steps.

d. *Model Estimation.* The NARX Network is a recurrent dynamic network, with feedback connections enclosing several layers. The model identification has been carried out with reference to the number N of neurons in the hidden layer (ranging from 5 to 25), the tapped delay line d (range from 10 to 100 ms) resulting in a total of 25 combinations. Moreover, a Training Set including more than 30.000 successive samples (randomly selected from the re-sampled and filtered data) and 100 epochs have been considered.

e. *Model Validation.* The Regression Error Characteristics (REC) and Sliding Occurrence Error (SOE) curves introduced in [6] to provide both synthetic and detailed indication about the ANNs performance have been considered to compare the proposed architectures. REC curves plot, for each point (x, y), the relative occurrences of regression function outputs (on the y-axis) that are within a given error range (tolerance) (on the x-axis). The resulting curve estimates the cumulative distribution function (CDF) of the error that may be defined as the relative difference between the ANN prediction and the actual system output. The area over the curve (AOC) is a biased estimate of the expected mean error and provides a measure of the mean accuracy; the closer the curve to the y-axis the better the performance expected for the regression function. Thus, the REC curve has been adopted to select the NARX Network (in terms of neurons and delay) which guarantee the best accuracy over the Test Set (about 330.000 samples from the recorded data). As an example, Fig. 78.1a reports the REC curves corresponding to the proposed architectures: the model with N=15 and d=10 is able to keep the regression error lower than 10% for over the 95% of the Test Set. The REC curve gives only integral information disregarding the time distance between regression errors ("local accuracy"). On the other hand, within the sensor validation (where focus is on the fault detection performance), once a suitable threshold is fixed as the maximum tolerable error, it is preferable to use the ANN able to warrant a small percentage of errors exceeding the threshold in a time interval rather than a ANN that assures the lowest mean error even if characterized by some time windows in which a higher percentage of threshold overcoming occurs.

This feature may be highlighted by the SOE curve: with reference to a moving window constituted by L successive samples, it plots the error tolerance (defined as the maximum relative deviation) on the x-axis and the corresponding relative occurrences in L of the regression function on the y-axis (in other words, the SOE curve represents the survivor function of the error tolerance). As an example, Fig. 78.1b show the SOE curves for different window length L over the Test Set corresponding to the most accurate NARX model. You may easy note that the maximum (relative) prediction error exceed 10 % only for a small quote (16 %) of the Test Set when a 100 ms windows is considered.

78.3   Conclusions

The NARX models have been investigated for the development of suitable schemes about the sensor validation within the motorcycle field. As result, the NARX model can be effectively adopted as benchmark (in terms of false alarms and correct faults) in the improvement of off-line fault detection strategies (i.e. threshold identification) aiming to the sensor validation of the rear suspension stroke. Further research will be addressed to the effective implementation and metrological characterization of the suggested models for on-line IFDI (Instrument Fault Detection and Isolation) schemes.

References

1. L. Fortuna, S. Graziani, A. Rizzo, M. G. Xibilia, "Soft Sensors for Monitoring and Control of Industrial Processes", Springer Book, 2007, ISBN 978-1-84628-480-9.
2. D. Delvecchio, C. Spelta, G. Perico, S. M. Savaresi, "Accelerometer-based estimation of the elongation speed in a motorcycle suspension via Kalman-filter techniques", Proceedings of 49th IEEE Conference on Decision and Control, pp. 5566–71, 2010.
3. C. Liguori, V. Paciello, A. Paolillo, A. Pietrosanto, "Real-Time Detection of Low Frequency Components", IEEE Transactions on Instrumentation and Measurement, Vol. 62, no. 5, pp. 1118–1129, May 2013.
4. V. Paciello, P. Sommella, "Smart sensing and smart material for smart automotive damping "Instrumentation and Measurement Magazine, IEEE Vol. 16, no. 5, pp 24–30, October 2013.
5. F. R. Hampel, "The influence curve and its role in robust estimation", Journal of the American Statistical Association, 69, pp. 382–393, 1974.
6. G. Betta, D. Capriglione, A. Pietrosanto, P. Sommella, "ANN-based sensor fault accommodation techniques", 2011 IEEE International Symposium on Diagnostics for Electric Machines, Power Electronics and Drives (SDEMPED), 5–8 September 2011, Bologna, pp. 517–524.

Chapter 79
The Use of Uncertainty for Improving the Reliability of Classification in Face Based Recognition Algorithms

G. Betta, D. Capriglione, M. Corvino, C. Liguori, A. Paolillo and P. Sommella

The paper proposes a new approach to classification and recognition problems which takes into account the measurement uncertainty affecting input data for improving the overall reliability of such kind of processes. The proposed method is based on an effective probabilistic approach for the evaluation of the confidence level of system outputs and the suitable use of such information for improving the performance in terms of correct decision.

79.1 Introduction

In a face recognition system the identification is made by comparing some quantities, extracted from an image of the unknown subject to be classified, with the corresponding ones extracted from a preexisting database [1]. Afterwards, a maximum likelihood approach is generally adopted to classify and recognize the input subject. The quantities measured for the classification are generally affected by uncertainty, thus generating a clear risk in accepting the decision. This risk could be quantified and reduced by suitably taking into account the measurement uncertainty in the comparison stage.

In this field, the authors tackled the problem of the metrological characterization of a face recognition classification system [2, 3]. They proposed an original method which, starting from the analysis of the acquired image, estimates the uncertainty of the quantities employed in the classification stage. Starting from these results, target of this paper is the design of a new classification scheme, able to effectively manage

G. Betta (✉) · D. Capriglione · M. Corvino
Dipartimento di Ingegneria Elettrica e dell'Informazione, Università di Cassino e del Lazio
MeridionaleVia G, Di Biasio 43, 03043 Cassino, FR, Italy
e-mail: betta@unicas.it

C. Liguori · A. Paolillo · P. Sommella
Dipartimento di Ingegneria Industriale, Università degli studi di Salerno, Via Giovanni Paolo II,
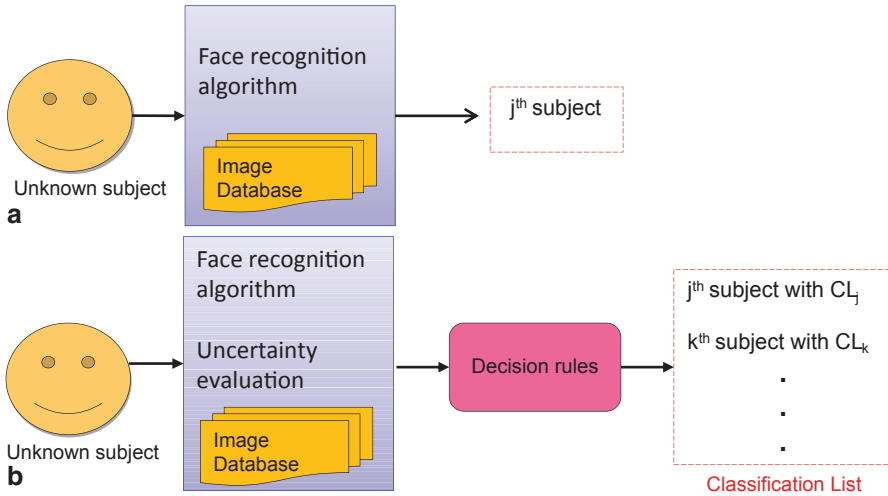132, 84084 Fisciano, SA, Italy

Fig. 79.1 Simplified block diagram of: **a** traditional classification system, **b** the proposed classification system

the overall uncertainty of the recognition system. In particular, Fig. 79.1 compares the proposed face recognition scheme with a traditional one. The main novelty is in the output results that do not consist only in the class which the subject belongs to, but in a list of possible classes each one characterized by a certainty level. Consequently the decision will be provided with a better knowledge with respect to a traditional classification scheme.

79.2 The Uncertainty Model

The model of the uncertainty of the evaluated scores is obtained using a "black box" approach [4]. It is based on a large experimental analysis for the identification of the main quantities of influence and the related uncertainty model [5] is achieved through the fitting of simple models onto experimental data. The free access database Pointing'04 [6] developed at Cambridge University was used in the test for determining the uncertainty using a black box approach.

In particular, for each influence quantity [7], q_i (i=1,..,N where N is the number of quantities of influence), the relationship with the uncertainty on the score, u_i is evaluated as:

$$u_i = f_i(\Delta_i) \tag{79.1}$$

where Δ_i is the difference between the actual measured value, q_i, and its correspond-ing reference value. All the influence quantities are considered uncorrelated with the other ones, then the combined uncertainty on the score is evaluated as [8]:

$$u_s = \sqrt{\sum_{i=1}^{N} u_i^2} \tag{79.2}$$

79.3   Proposal for Classification Phase

The system output is constituted by a classification list reporting all the classes in which the subject could be recognized. The decision phase is aimed at creating this list. The probability that the new subject belongs to each j-th class, P_j, is evaluated, then a classification list is created with a selection of the probable classes; finally, the confidence level of each class in the list is evaluated. The probability of each class represents the probability that the corresponding score was equal to zero, P_j; and it is evaluated considering the score as a random variable [9–11]. P_j represents the probability that the Score of the jth class is equal to zero given a measured value $\overline{S}_j$; we propose to estimate it starting by the score probability density function, $p(s)$ as follows:

$$P_j = P\left(S_j = 0 | \overline{S_j}\right) = \begin{cases} 1 & \text{if } \overline{S}_j \leq th \\ \int_{\overline{S}_j}^{\infty} p(s - th) ds & \text{if } \overline{S}_j > th \end{cases} \tag{79.3}$$

Once the scores have been evaluated, the classification list is composed by all the classes with a probability greater than a further threshold, namely **TH**. The selection of the optimum value of **TH** is achieved by identifying the best tradeoff between the system performance in terms of True Acceptance Rate (TAR) and False Accep-tance Rate (FAR). Since the proposed statistical post processing reduces the false positive, the selection of **TH** can be made to preserve the system sensitivity (i.e. the TAR parameter).To this aim the analyses of TAR and FAR versus **TH**, together with the Receiver Operating Characteristic (ROC) curve have been performed. As result, a **TH** equal to 0.40 has been chosen which provides a TAR greater than 0.99 and a FAR lower than 0.15.

The probabilities of all the classes included in the classification list are used for evaluating a normalization factor, K, defined as follows:

$$K = \sum_{j} P_j \text{ all j whose } P_j > TH \tag{79.4}$$

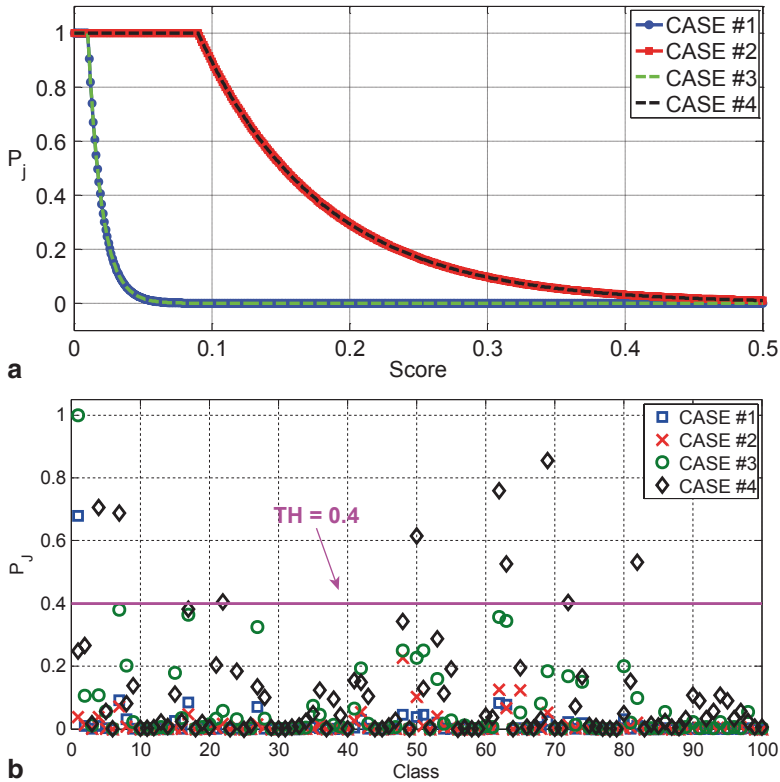Then the level of confidence of each class belonging to the list is evaluated as the probability P_j divided by K:

Fig. 79.2 Pj versus **a** score, **b** class

$$LC_j = \frac{P_j}{K} \tag{79.5}$$

In Figs. 79.2 the application of the proposed function is reported as example of application to a scenario involving four cases: Case #1 and Case #3 deal with a subject included in the database, but the acquisition conditions are different from those related to the training phase, whereas, Case #2 and Case #4 refer to a subject not included in the training database but related to images characterized by high uncertainties. Table 79.1 reports the corresponding output of the system.

79.4 Conclusions

The paper has introduced and discussed a novel approach to the decision task in face recognition algorithms. The proposed approach exploits the knowledge of the uncertainties of relevant quantities involved in the classification process, in order to

Table 79.1 Classification list based on the Level of confidence (*LC*)

Case #1	Case #2	Case #3	Case #4
Subject 1	Subject *j* (*j*=1,..N)	Subject 1	Subject 4 LC=0.19
LC=1	LC=0	LC=1	Subject 5 LC=0.19
			Subject 6 LC=0.21
Subject *j* (*j*≠1)		Subject *j* (*j*≠1)	Subject 12 LC=0.19
LC=0		LC=0	Subject 15 LC=0.22

provide recognition outcomes with their own level of confidence. As an example, in order to better highlight the procedure of behavior and performance this approach was applied to a case study, namely to a biometry face recognition task based on a LDA algorithm. The experimental results have shown the goodness of the proposal.

References

1. "Handbook of face recognition", Stan Z. Li, Anil K. Jain Editors, Second Edition, Springer.
2. G. Betta, D. Capriglione, F. Crenna, G.B. Rossi, M. Gasparetto, E. Zappa, C. Liguori, A. Paolillo, "Face-based recognition techniques: Proposals for the metrological characterization of global and feature-based approaches", (2011), Measurement Science and Technology, 22 (12).
3. G. Betta, D. Capriglione, M. Corvino, C. Liguori, A. Paolillo, "Face Based Recognition Algorithms: A First Step Toward a Metrological Characterization", IEEE Transactions on Instrumentation and Measurement, 62 (5), 1008–1016, (2013).
4. G. Betta, D. Capriglione, A. Pietrosanto, P. Sommella, "A methodology to test instrument software: an automotive diagnostic system application", IEEE Transactions on Instrumentation and Measurement, 57 (12), 2733–2741, (2008).
5. G. Betta, D. Capriglione, C. Liguori, A. Paolillo, "Uncertainty evaluation in face recognition algorithms", IEEE Proceedings of Instrumentation and Measurement Technology Conference I²MTC11, Binjiang, China, May 2011.
6. Face database Pointing'04. Avalilabe on line: http://www-prima.inrialpes.fr/Pointing04/data-face.html.
7. G. Betta, D. Capriglione, M. Corvino, C. Liguori, A. Paolillo, "Estimation of Influence Quantities in Face Recognition", IEEE Proceedings of Instrumentation and Measurement Technology Conference I²MTC12, Graz, Austria, May 2012.
8. JCGM 100, "Evaluation of measurement data—Guide to the expression of uncertainty in measurement", 2008.
9. G. Betta, D. Capriglione, M. Corvino, C. Liguori, A. Paolillo, "Face based recognition algorithms: The use of uncertainty in the classification", IEEE Proceedings of Instrumentation and Measurement Technology Conference (I²MTC), pp. 1098–1103, Minneapolis 2013.
10. L. Angrisani, D. Capriglione, L. Ferrigno, G. Miele, "A methodological approach for estimating protocol analyzer instrumental measurement uncertainty in packet jitter evaluation", IEEE Transactions on Instrumentation and Measurement, 61 (5), pp. 1405–1416.
11. L. Angrisani, E. Atteo, D. Capriglione, L. Ferrigno, G. Miele, "An efficient experimental approach for the uncertainty estimation of QoS parameters in communication networks",, IEEE Proceedings of Instrumentation and Measurement Technology Conference (I²MTC), pp. 1186–1191, Minneapolis 2010.